Proceedings of the International Conference on Innovations in Energy Engineering & Cleaner Production

29–30 July 2021

Silicon Valley, San Francisco, CA – USA.

Preface

Renewable energy is the fastest-growing energy source since the beginning of the century and the demand growth with the fast development in industrial and transportation sectors. According to the C2ES, renewables made up more than 20 percent of net U.S. energy consumed globally for heating, power, and transportation. Nearly 60 percent came from modern renewables (i.e., biomass, geothermal, solar, hydro, wind, and biofuels). In the industrial sector, biomass makes up 98 percent of the renewable energy use with nearly 60 percent derived from biomass wood, 32 percent from biofuels, and nearly 7 percent from biomass waste. In the transportation sector, renewable fuels, such as ethanol and biodiesel, have increased significantly during the past decade. E85 (ethanol transportation fuel) is expected to be the fastest growing renewable energy type, growing at an average annual rate of 9.7 percent over the next 30 years.

The International Conference on Innovations in Energy Engineering & Cleaner Production (IEE^{CP}'21) aims to investigate innovation applications and last researches in the areas of energy production, alternative and renewable energy supply, energy savings analysis, cleaner production, optimization of energy processes and the environmental impacts. The volume contains the proceedings of the international conference on Innovations in Energy Engineering & Cleaner Production (IEE^{CP}'21). The IEE^{CP}'21 conference is a scientific event which gathered leading researchers and practitioners who will present ideas to more than 100 attendees. Authors have provided high quality contributions reviewed by a program committee featuring renowned international experts on a broad range of knowledge management topics. More than 200 papers were submitted to the IEE^{CP}'21 conference from authors of many countries and continents. Two or three reviewers were assigned to each paper and according to these reviews, 73 papers were accepted which makes acceptance rate of 36.5%.

We are grateful to the Chairs, Program Committee, External Reviewers, Organizing Committee and the keynote speakers for their wonderful work and efforts. Finally, we would like to thank all the participants and sponsors hoping to meet them soon for other collaboration in scientific events.

Sincerely yours,

IEE^{CP}'21 Chair

Program Committee IEE^{CP}'21

International Advisory Board

- Dr. Hwai Chyuan Ong, University of Technology Sydney, UTS, Australia
- Prof. Werner J.F., Christian-Albrechts-University, Germany
- Dr. Jae-Jin Shim, School of Chemical Engineering, Gyeongsan-si, South Korea
- Dr. Jei-Pil Wang, Pukyong National University, South Korea
- Pr. Vaidotas Kažukauskas, Institute of Photonics and Nanotechnology, Vilnius University, Lithuania
- Dr. Ishwar Chandra Yadav, Tokyo University of Agriculture and Technology (TUAT), Japan
- Dr. Shtangeeva Irina, Department of Soil Science & Soil Ecology, St.Petersburg State University, Russia
- Dr. Farhad Shahnia, Murdoch University, Australia
- Dr. Bimal Kumar Ghimire, College of Sanghuh Life Science, Konkuk University, Seoul, Korea
- Prof. Hui Li, College of Transportation at Tongji University, Shanghai, China
- Dr. Javier Velázquez Saornil, Universidad Católica de Ávila, Spain
- Dr. Hugo Morais, GECAD, Polytechnic Institute of Porto (IPP) Porto, Portugal
- Dr. Jan Bocianowski, Dept. of Mathematical and Statistical Methods, Poznan University, Poland
- Dr. Jania Betania Silva, Universidade Federal da Bahia, Brazil
- Dr. Jesus David Coral Medina, Mariana University, Federal of Paraná University, Colombia
- Dr. Jaime Andrés Pérez Taborda, Universidad de los Andes, Colombia
- Dr. Isam H. Aljundi, King Fahd University of Petroleum and Minerals, Dhahran, Saudi Arabia

International Chairman Board

- Dr. Roselita Fragoudakis, Merrimack College, North Andover, MA, USA
- Dr. Maria Laura Tummino, Italian National Research Council (CNR), Biella, Italy
- Dr. Man Pun Wan, Nanyang Technological University, Singapore
- Dr. Talieh Rajabloo, IMO-IMOMEC, Energyville II, University of Hasselt, Genk, Belgium
- Dr. Chaiwat Prapainainar, King Mongkut's University of Technology, Bangkok, Thailand
- Prof. Majid Ali, Capital University of Science and Technology, Islamabad, Pakistan
- Dr. Chibuisi C. Okorieimoh, Technological University Dublin Dublin, Ireland
- Dr. Mohd Hasmizam Razali, Universiti Malaysia Terengganu, Malaysia
- Dr. Francesca Deganello, Istituto per lo Studio dei Materiali Nanostrutturati, Palermo, Italy
- Dr. Guohai Chen, National Institute of Advanced Industrial Science and Technology (AIST), Japan

- Prof. Fei Wang, Qingdao University of Science & Technology, China
- Dr. Kumaran Vediappan, SRM Institute of Science and Technology (SRMIST), India
- Dr Hongwei WU, School of Physics, University of Hertfordshire, UK
- Dr. Eman Ragab Mohamed Nofal, National Water Research Center (NWRC), Egypt
- Dr. Ajay Kumar Kaviti, VNR Vignana Jyothi Institute of Engineering & Technology, India
- Dr. Christopher Jeyakumar T, American College, Madurai India
- Prof. Alina Adriana Minea, Technical University Gheorghe Asachi from Iasi, Romania
- Dr. Alban Kuriqi, Instituto Superior Técnico, University of Lisbon.
- Dr. Jesús David Coral M, Federal of Paraná University, Brazil

Technical Program Committee

- Prof. Bo Jin, College of Materials Science and Engineering, Jilin University, China
- Prof. Jun Li, Kansas State University, Department of Chemistry, Manhattan, USA
- Dr. Junbo Zhao, Mississippi State University, USA
- Prof. Eddie YK NG, College of Engineering, Nanyang, Technological University, Singapore
- Dr. Guohai Chen, CNT-Application Research Center, AIST, Japan
- Prof. Fei Wang, Qingdao University of Science & Technology, China
- Dr. Hongwei WU, School of Physics, University of Hertfordshire, UK
- Dr. Eike Marie Thaysen, School of Geosciences, University of Edinburgh, UK
- Prof. Guimin Chen, School of Mechanical Engineering, Xi'an Jiaotong University, China
- Dr. Feng Lin, Natural Resources Canada
- Dr. Eliseu Leandro de Magalhães Monteiro, University of Coimbra, Portugal
- Dr. Esmaeil Zarei, Memorial University, St. John's, NL, Canada
- Dr. Francesca Deganello, CNR-ISMN Palermo, Via Ugo La Malfa, Italy
- Dr. Géremi Gilson Dranka, Department of Production and Systems Campus Azurem, Portugal
- Dr. Hock Jin QUAH, INOR, Universiti Sains Malaysia
- Dr. Hao Yi, College of Mechanical Engineering, Chongqing University, China
- Dr. Mesfin Kebede, Energy centre, CSIR – South Africa
- Dr. Gaetano LISI, e-Campus University, Department of Economics, Novedrate (CO), Italy
- Dr. Grzegorz Woroniak, Bialystok University of Technology, Poland
- Dr. Fiseha TESFAYE, Faculty of Science and Engineering, Åbo Akademi University, Finland
- Prof. Haitham M. S. Lababidi, College of Engineering, Petroleum, Kuwait University, Kuwait
- Dr. Guohua Xie, Department of Chemistry, Wuhan University, China
- Dr. Ellen Cristine Giese, Centro de Tecnologia Mineral (CETEM), Brazil
- Dr. Hassan Abdulmouti, Sharjah Men's College, Sharjah, UAE
- Prof. Edimilson Costa Lucas, Federal Univesity of Sao Paulo (EPPEN-UNIFESP), Brazil
- Dr. Liu Hongfei, Institute of Materials Research and Engineering (IMRE), Singapore

Table of Contents

Articles (Abstracts, Short and Full Papers)

Article 015 (ID: 57) Interplay Bewteen Diradical Character and Stability in Singlet Fission Chromophores.
Vaska Petakova, Joanna Stoycheva, Alia Tadjer and Julia Romanova.

Article 016 (ID: 58) Unlocking New Opportunities for the Photovoltaic Materials Market.
Joanna Stoycheva, Alia Tadjer, Julia Romanova.

Article 017 (ID: 59) A comparative study of the thermal behavior of Li-ion batteries with different geometries,capacities,cathode materials.
Khalid ZIAT, Hasna LOUAHLIA, Hamid GUALOUS.

Article 018 (ID: 61) Study of CZTSSe based solar cells with different ETMs by SCAPS.
Lhoussayne Et-taya ,Touria Ouslimane,Abdellah Benami.

Article 019 (ID: 62) Thermodynamic study of a membraneless electrochemical process for the hydrogen and oxygen high-pressure generation.
Andrii Shevchenko, Nguyen Tien Khiem, Bui Dinh Tri, Anatolii Kotenko.

Article 020 (ID: 63) Description of Colombian Electricity Pricing Derivatives.
Sellamuthu Prabakaran.

Article 021 (ID: 70) Ethanol Demand in Brazil: a contribution to a better estimate.
Anderson Luís da Silva, Juan Castañeda-Ayarza.

Article 022 (ID: 72) Identification of wind energy deployment determinants: Fuzzy cognitive map-based method.
Sara Ghaboulian Zare, M. Alipour, R. Parsaei Tabar, Mehdi Hafezi.

Article 023 (ID: 73) Research on Mud Loss Prevention and Control for Deep Wells with Complex Pressure System in Mingebrak Oilfield, Uzbekistan.
Wanjun Li, Qi Liu, Huifeng Liu, Jun Yan, Yong Wang, Shujiu Feng, He Ba and Yue Xiao.

Article 024 (ID: 76) Optical-Electronic Matrix System for the monitoring of nocturnal migration of birds.
Alexandra Sinelschikova, Mikhael Vorotkov, ,Victor Bulyuk.

Article 025 (ID: 78) In situ FTIR studies for photocatalytic reduction of CO2 by TiO2 nanotubes.
H.-H. Chang, H.-Y. Chang, H.P. Wang.

Article 026 (ID: 79) Photocatalytic Reduction of CO2-to-C1 by Dual Photoelectrode Reactor.
H.-Y. Chang, L.-W. Wei, H.P. Wang.

Article 027 (ID: 80) Electrokinetic Remediation of Arsenic in a Gold Tailing Studied by in situ EXAFS.
C.Y. Peng, P.-A. Chen, P.-C. Chang, H. Paul Wang

Article 028 (ID: 81) Capacitive deionization of salt water using thin stainless steel and graphite collectors in the FdCDI process.
C.-H. Wu, P.-A. Chen, P.-C. Chang, H. Paul Wang.

Article 029 (ID: 82) Enhanced extraction of PAHs from fly ashes with variable dielectric-constant supercritical fluids.
K.-A. Hsueh, Y.-C. Tsai , T.-E. Wu, I-H. Chen, Y.-J. Tuan, H.-P. Wang.

Article 030 (ID: 83) High-temperature desulfurization by ZnO/Raney CuO absorbents.
T.-C. Wang, T.-E. Wu, Y.-C. Tsai, Y.-J. Tuan, and H. Paul Wang.

Article 031 (ID: 84) Photocatalytic reduction of CO2 to C1 fuels by (Ni/ZnO)@C nanoreactors.
M.-L. Liu, L.-W. Wei, H.-P. Wang.

Article 032 (ID: 85) In situ EXAFS studies of photoelectrocatalytic reduction of gold and lanthanum ions recycled from E-wastes.
T.-E. Wu, Y.-C. Tsai, Y.-J. Tuan, and H. Paul Wang.

Article 033 (ID: 86) Photocatalytic reduction of CO2 to methanol by Cu2O/TiO2 heterojunctions.
S.-P. Cheng, L.-W. Wei, H.-P. Wang.

Article 034 (ID: 87) Low-Cost DSSCs using FeNi3@C counter electrodes.
C.-C. Chen, Y.-F. Liou, L.-W. Wei, H. Paul Wang.

Article 035 (ID: 88) Solar-driven H2O-to-H2O2 effected by promoters NiP and CoP on g-C3N4/BiOI composites.
Y.-F. Liou, L.-W. Wei, H. Paul Wang.

Article 036 (ID: 89) Selective extraction of cobalt from spent lithium-ion batteries.
Y.-C. Tsai, T.-E. Wu, I-H. Chen, Y.-J. Tuan, H.-P. Wang.

Article 037 (ID: 91) Examination of Nuclear and Renewables Potential in Malaysia.
Pei Jia Pok, Man-Sung Yim.

Article 038 (ID: 92) Dechloriation of incineration fly ash by fluidized capacitive deionization for utilization.
P.-C. Chang, P.-A. Chen, H. Paul Wang.

Article 039 (ID: 93) Liquefaction of scrap tires for recycling of fuel oils.
H.-A. Lee, P.-C. Chang, P.-A. Chen, H. Paul Wang.

Article 040 (ID: 95) Numerical simulation of highly-efficient lead free tin-based perovskite solar cell with Sb2S3 as novel hole transport layer.
Most. Marzia Khatun, Sabrina Rahman, Adnan Hosen, Md. Nur Hossain Riyad, Adil Sunny, Sheikh Rashel Al Ahmed.

Article 041 (ID: 96) Improving Energy Performance and Thermal Comfort for Heritage Buildings: A Case Study Murabaa Palace.
Abobakr Al-Sakkaf, Sherif Mahmoud and Eslam Mohammed Abdelkader.

Article 042 (ID: 99) Integration of vanadium redox battery with PV systems : Modeling and simulation of Vanadium Redox flow batteries based on MATLAB/Simulink.
BABAY Mohamed-Amine, Mustapha ADAR and Mustapha Mabrouki.

Article 043 (ID: 104) Vibration Characterizations of motor-gear-rotor system with considering the lateral-torsional-axial coupling effect.
Wenyu Bai,Hongyu Xi, Xiaohang Zhang, Zhouxin Wu,Libin Zhang.

Article 058 (ID: 145) Energy and Typological Building Characterization of the Social Housing Stock in Southern Spain.
Carmen María Calama-González, Á.L. León-Rodríguez and R. Suárez.

Article 059 (ID: 146) Development of Underground transportation Hazard management System (UTHMS) for Indian underground hard rock mines.
Falguni Sarkar , Sabyasachi Nayak.

Article 060 (ID: 147) Effectiveness of Hybrid Fibers in Cementitious Composites Towards Sustainability: A Review.
Ali Rehman, Majid Ali.

Article 061 (ID: 149) Treatment of Natural Fibers for Improving Cement Composites Behavior-An Overview.
Sami Ullah, Majid Ali.

Article 062 (ID: 150) Numerical Modeling of Heat Flow of Kangding Area with New Borehole Data for Purpose of Geothermal Resources Development Evaluation.
Chao Zhang, Ming Wu, ZaoBao Liu.

Article 063 (ID: 151) Intensified extractive distillation process for the separation of n-heptane-toluene mixture using the ionic liquid 1-Ethyl-4-methylpyridinium Bis(trifluoromethanesulfonyl)imide.
Fadia Guella, Hassiba Benyounes.

Article 064 (ID: 153) Recycling of waste plastic with least effect to environment: A review.
Aaroon Joshua Das and Majid Ali.

Article 065 (ID: 155) A Review on Durability Methods for Natural Fibers in Polymer Matrices from Sustainability Aspects.
Blawal Hasan, Majid Ali.

Article 066 (ID: 156) Aspergillus niger a local isolate from rice husk as potential source of single cell protein production.
R.Monisha and R. Jaya Madhuri.

Article 067 (ID: 157) Submerged fermentative production of L-Asparaginase Enzyme by Aspergillus niger.
K.Sowbhagya Lakshmi, M.Bhargavi and R.Jaya Madhuri.

Article 068 (ID: 158) Gradient algorithms for artificial neuron network teaching.
Erkin Uljaev, Shohrukh Narzullayev, Utkirjon Ubaydullaev, Elyor Khudaoyberdiyev.

Article 069 (ID: 164) Impact of window wall ratio in office building envelopes on operational energy consumption in the temperate climatic zone of India.
Deepali Sahu, Pradeep Kini, Pranav Kishore, Anir Upadhyay, Kiran Kamath.

Article 070 (ID: 165) Energy Conservation Building Code compliant material optimization of lightweight building envelope wall construction for different climate zones of India.
Pranav Kishore, Vanshika Chanani, Stuthi Shetty, Srijan Didwania, Vatsala Bajpai, Pradeep Kini.

Exergy Methods for Addressing Climate Change and Other Environmental Impacts

Marc A. Rosen
Faculty of Engineering and Applied Science
University of Ontario Institute of Technology
Oshawa, Ontario, Canada
marc.rosen@ontariotechu.ca

Abstract

The use of exergy methods is described as tools for addressing climate change so the benefits can be appreciated and attained. Exergy can be used to understand climate change measures and to assess and improve energy systems, and can help better understand the benefits of utilizing sustainable energy by providing more useful and meaningful information than energy provides. Exergy clearly identifies efficiency improvements and reductions in wastes and environmental impacts attributable to sustainable energy. Exergy can also identify better than energy the environmental benefits and economics of energy technologies. Exergy should be applied in addressing climate change.

Keywords: *Exergy; climate change; environment; ecology; energy*

Biography

Marc A. Rosen, Ph.D., is a Professor at University of Ontario Institute of Technology in Oshawa, Canada, where he served as founding Dean of the Faculty of Engineering and Applied Science. Dr. Rosen has served as President of the Engineering Institute of Canada and of the Canadian Society for Mechanical Engineering. He has acted in many professional capacities, including Editor-in-Chief of various journals and a Director of Oshawa Power and Utilities Corporation. With over 70 research grants and contracts and 900 technical publications, Dr. Rosen is an active teacher and researcher in sustainable energy, sustainability, and environmental impact. Much of his research has been carried out for industry. Dr. Rosen has worked for such organizations as Imatra Power Company in Finland, Argonne National Laboratory near Chicago, the Institute for Hydrogen Systems near Toronto, and Ryerson University in Toronto, where he served as Chair the Department of Mechanical, Aerospace and Industrial Engineering. Dr. Rosen has received numerous awards and honours, and is a Fellow of numerous societies.

IEECP'21, July 29-30, 2021, Silicon Valley, San Francisco, CA – USA

DAI : *https://sci-index.com/DAI/2021.99101/IEECP/14991615*

Modelling of wake velocity and turbulence intensity of a wind turbine using machine learning algorithms

E. Y. K. Ng*, Shantanu Purohit, Ijaz Fazil Syed Ahmed Kabir
School of Mechanical and Aerospace Engineering
College of Engineering, Nanyang Technological University
(of Affiliation)
50 Nanyang Avenue 639798, Singapore
MYKNG@ntu.edu.sg

Abstract

In this talk, three machine learning (ML) algorithms viz. Support Vector Regression (SVR), Artificial Neural Networks (ANN), and Extreme Gradient Boosting (XGBoost) are implemented to predict wake velocity and turbulence intensity from a wind turbine at different downstream distances. To this end, a set of high-fidelity numerical simulations are performed for the NREL Phase VI wind turbine to produce training and test datasets for the three machine learning algorithms. Using the trained model, the wake flow field downstream of the blade and turbulence intensity are predicted on the test datasets which are hidden from the trained model. The prediction of wake velocity deficit and turbulence level in the wake from the machine learning algorithms are commensurate to the Computational Fluid Dynamics (CFD) simulations while running as fast as low-fidelity wake models. The wake velocity and turbulence intensity obtained from the ML models are also compared with some of the analytical wake models. The results reveal that machine learning-based algorithms can approximate wake and turbulence intensity characteristics better than the traditional analytical wake models**.**

Keywords: *Wake velocity, turbulence intensity, Support Vector Regression (SVR), Artificial Neural Networks (ANN), eXtreme Gradient Boosting (XGBoost)*

* *Conf. presenter and Corresponding author. School of Mechanical and Aerospace Engineering, Nanyang Technological University, Singapore*

Short biography

Eddie is elected as:
Academician for European Academy of Sciences and Arts (EASA, EU);
Fellow of the American Society of Mechanical Engineers (FASME, USA);
Fellow of Institute of Engineering and Technology (FIET, United Kingdom);
Fellow of International Engineering and Technology Institute (FIETI, Hong Kong),
Distinguished Fellow for Institute of Data Science and Artificial Intelligence, (DFIDSAI, China), and, Academician for Academy of Pedagogy and Learning, (USA).
He has published numerous papers in SCI-IF int. journal (430); int. conf. proceedings (130), textbook chapters (>105) and others (32) over the 29 years. Co-edited 14 books in STEM areas.
He is the:
Lead Editor-in-Chief for the ISI Journal of Mechanics in Medicine and Biology for dissemination of original research in all fields of mechanics in medicine and biology since 2000;
Founding Editor-in-Chief for the ISI indexed Journal of Medical Imaging and Health Informatics;
Associate editor or EAB of various referred international journals such as Applied Intelligence, BioMedical Engineering OnLine, Computers in Biology & Medicine, and, Journal of Advanced Thermal Science Research.
More details can be found in: Cv: https://dr.ntu.edu.sg/cris/rp/rp00847

IEECP'21, July 29-30, 2021, Silicon Valley, San Francisco, CA – USA

DAI : https://sci-index.com/DAI/2021.99101/IEECP/14991633

Recent and Future Research on Microgrid Clusters

Farhad Shahnia
Murdoch University, Australia
F.Shahnia@Murdoch.edu.au

Abstract

Electricity systems around the world are experiencing a radical transition as the consequence of replacing fossil fuels, used for electricity production, by sustainable and cleaner energies. The growing penetration of renewable energies requires smarter techniques capable of handling the uncertainties of these intermittent sources. Along with this change, traditionally centralized power systems are also converting into distributed self-sufficient systems, often referred to as microgrids, that can operate independently. This talk will focus on remote area microgrids as a hot research topic in Australia and Southeast Asia that have hundreds of remote and off-grid towns and communities, and islands. It is expected that remote area microgrids will strongly benefit these remote locations in the forthcoming years. This talk will briefly introduce the progress of research in this field around the world and Australia, and will also discuss some of the technical challenges associated with interconnection of neighbouring microgrids as a key step to improve their survivability in the course of unexpected imbalances between the demand and the available generation from intermittent renewable resources**.**

Keywords: *Microgrid Clusters, cleaner energies, renewable energy.*

Short biography

A/Professor Farhad Shahnia received his PhD in Electrical Engineering from Queensland University of Technology (QUT), Brisbane, in 2012. He is currently an A/Professor at Murdoch University. Before that, he was a Lecturer at Curtin University (2012-15), a research scholar at QUT (2008-11), and an R&D engineer at the Eastern Azarbayjan Electric Power Distribution Company, Iran (2005-08). He is currently a Fellow member of Engineers Australia, Senior Member of IEEE, and member of the Australasian Association for Engineering Education.

Farhad's research falls under Distribution networks, Microgrid and Smart grid concepts. He has authored one book and 11 book chapters and 100+ peer-reviewed scholarly articles in international conferences and journals, as well as being an editor of 6 books.

Farhad has won 5 Best Paper Awards in various conferences and has also received the IET Premium Award for the Best Paper published in the IET Generation, Transmission & Distribution journal in 2015. One of his articles was listed under the top-25 most cited articles in the Electric Power System Research Journal in 2015 while one of his 2015 journal articles has been listed under the top-5 most read articles of the Australian Journal of Electrical and Electronics Engineering. He was the recipient of the Postgraduate Research Supervisor Award from Curtin University in 2015 and the Australia-China Young Scientist Exchange Award from the Australian Academy of Technology and Engineering in 2016.

Farhad is currently a Subject Editor, Deputy Subject Editor, and Associate Editor of several journals including IEEE Access, IET Generation, Transmission & Distribution, IET Renewable Power Generation, IET Smart Grid, IET Energy Conversion and Economics, and International Transaction on Electrical Energy Systems and has served 35+ conferences in various roles such as General, Technical, Publication, Publicity, Award, Sponsorship, and Special Session Chairs.

Farhad is currently the Chair of the IEEE Western Australia Section and a member of IEEE's Industrial Electronics Society (IES)'s Technical Committees of Smart Grid and Energy Storage

IEECP'21, July 29-30, 2021, Silicon Valley, San Francisco, CA – USA

D!f: *https://sci-index.com/DAI/2021.99101/IEECP/14991684*

Ceramic Electrolytes and Electrodes for All-Solid-State Batteries with High Energy and Power Density – Environmentally Benign, Inexpensive, Safe and Long Lasting

Werner J.F. Weppner
Institute of Materials Science, Faculty of Engineering
Christian-Albrechts University, Kiel, Germany
ww@tf.uni-kiel.de

Abstract

Solids can have a wide variety of structural and functional properties. In terms of electrical conductivity, they are used as metallic conductors, semiconductors or insulators. Ceramic materials can even show superconductivity at practically usable temperatures. In addition, ceramics are also able to transport ions. In many cases this conductivity is low, but in some cases it is very high and of practical importance due to structural disorder in the crystal lattice. As a result, solids can take on tasks that electrons are unable to perform. These are particularly important in the area of energy conversion and storage as well as environmental protection. In times of climate change and resource conservation, they are of outstanding practical importance. Applications include new generations of solid state batteries, fuel cells, electrochromic windows, and chemical sensors. In addition to ceramics with predominantly ionic conduction, such solids with mixed electronic-ionic conduction play an important role that has so far been neglected, e.g. for electrodes for rapid charging and discharging.

The possibilities of developing and using such ceramics with predominantly ionic conduction as well as mixed electronic-ionic conduction are shown in particular using the example of all-solid-state high-performance batteries. Applications in fuel cells and electrochromic systems are also briefly touched upon**.**

Keywords: *Ceramic Electrolytes and Electrodes, Batteries, Energy*

Short biography

Prof. Werner Weppner holds since 1993 the Chair for Sensors and Solid State Ionics at the Faculty of Engineering of Christian Albrechts University, Kiel, Germany. He has been earlier at the Max-Planck-Institute for Solid State Research, Stuttgart and a Research Professor at Stanford University, CA, USA, in the Department of Materials Science and Engineering. Prof. Weppner holds a diploma in physics from Mainz University and a Ph.D. in chemistry from Dortmund University, both Germany. His research interests are based on fast ionic transport in solids and include both fundamental understanding and practical application aspects

IEECP'21, July 29-30, 2021, Silicon Valley, San Francisco, CA – USA

D!f: *https://sci-index.com/DAI/2021.99101/IEECP/15048621*

CO_2 photoreduction into fuels using TiO_2 based photocatalyst

Mohd Hasmizam Razali
Faculty of Science and Marine Environment,
Universiti Malaysia Terengganu
Kuala Nerus, Terengganu, Malaysia
mdhasmizam@umt.edu.my

Abstract

Carbon dioxide (CO_2) emission from fossil fuel utilization poses a potential thread to global climate. Recent development in CO_2 reduction opens up new possibilities of utilization of CO_2 as a carbon feedstock for fuel generation and commodity chemicals. In this research, TiO_2-based photocatalysts have been extensively investigated for the CO_2 photoreduction into hydrocarbons in aqueous solutions under environmental conditions to understand their reduction activity and selectivity. The physiochemical properties of the photocatalysts were characterised by X-ray diffraction (XRD), field emission scanning microscopy (FESEM), transmission electron microscopy (TEM), high resolution transmission electron microscopy (HRTEM) and X-ray photoelectron spectroscopy (XPS). The adsorption, surface area, and porosity were studied using nitrogen gas adsorption and UV-Vis DRS was used for band gap measurement. The photocatalytic activity of the synthesised photocatalysts was tested for carbon dioxide (CO_2) photoconversion into fuels using home-buil micro reactor system. The results obtained show that, CuO loaded TiO_2 nanotubes demonstrated the highest CO_2 conversion (100%) because of their effective separation of photogenerated electron-hole pairs with the presence of CuO particles.

Keywords: *CO_2; reduction; TiO_2; fuels; photocatalyst.*

Short biography

Mohd Hasmizam Razali has a PhD degree in Materials Engineering (Nanomaterials) from Universiti Sains Malaysia (USM), MSc. in Chemistry (Catalyst) and B.Sc (Hons) in Chemical Industry from Universiti Teknologi Malaysia (UTM). Currently he is an Associate Professor at Faculty of Sciences and Marine Environment, Universiti Malaysia Terengganu (UMT), Malaysia. He has published more than 60 technical papers in journals and conference proceedings locally and internationally related to the functional nanomaterials research. Owing to their significant impacts to the science, economy and society, his innovative research and inventions have attracted global and national interests, enabling him to secure financial support from both private and government agencies. He has been awarded Who's Who in the World for 3 years in a row 2013, 2014 and 2015 by The Marquis Who's Who Publications Board. In 2014, the Cambridge Biographical Centre listed him as one of 2000 Outstanding Intellectuals of the 21st Century. On top of that, he is also the recipient of the MAWHIBA Award and GENEVA Gold Medal Award in 1999.

DAI : *https://sci-index.com/DAI/2021.99101/IEECP/14525649*

A Review of Fiber Reinforced Plastic Laminated Structures for more Efficient and Clean Transportation

Roselita Fragoudakis Department of Mechanical Engineering Merrimack College
North Andover, MA, USA
fragoudakisr@merrimack.edu

Abstract

Laminated composite materials are a lighter and of customizable flexibility material alternative for road vehicles. FRP laminated structures in the automotive industry may be an ideal solution for lighter and safer vehicles, while the weight reduction is also associated with lower fuel emissions. In this paper, we investigate the behavior of laminated FRP structures under bending and more specifically how the number of layers and stacking sequence of the structures affect their performance. A theoretical approach to the design of such structures, more specifically laminated FRP beams under cyclic bending, is presented in the first part of the review. The design of FRP laminates is based on Classical Lamination Theory (CLT) and interactive failure theories. The second part of the review examines the potential of FRP laminated structures to become the host of piezoelectric fibers and be used as energy scavenging devices, while maintaining their desirable and tailored stiffness and high performance, at a low weight. Two examples where laminated FRP beams are used as the host of piezoelectric layers to produce energy scavenging structures are presented. These examples examine beam structures under cyclic loading where the fiber stacking sequence allows for tailoring of the degree of deformation under bending. The deformation affects the amount of energy produced as the electromechanical behavior of the piezoelectric layer is guided by the mechanical behavior, more specifically deflection under a bending moment, of the FRP structure. The fiber material in each example addresses a different possible application area: E-glass fibers for applications where moisture effects may be a concern, and natural fibers in those where moisture effects are negligible.

Keywords: *Fiber Reinforced Plastics (FRP), Classical Lamination Theory (CLT), Interactive Failure Theories, Piezoelectric Fibers, Energy Scavenging.*

Short biography

Roselita Fragoudakis is an Assistant Professor in Mechanical Engineering at Merrimack College in North Andover, Massachusetts, USA. Her research is on materials. Dr. Fragoudakis has worked on a comparison of steel and Fiber Reinforced Plastic (FRP) applicable in heavy duty vehicle suspension systems. She has conducted experimental and computational analysis on Lateral Diffused Metal Oxide Semiconductor (LDMOS) packages and the dielectric properties of polymers. Currently she directs computational analysis of fiber orientations around geometric discontinuities. Additionally, she investigates ethical dilemmas in the innovative technological advances in her field and has created a course exploring the ethics of innovation and matters of intellectual property. Dr. Fragoudakis has served as a reviewer on multiple journals and periodicals, including the International Journal of Fatigue and Mechanics of Advanced Materials and Structures.

DAI : *https://sci-index.com/DAI/2021.99101/IEECP/14525259*

A cleaner process for heavy oil extraction from oil sand using a bio-based solvent

Feng Lin
Natural Resources Canada, CanmetENERGY Research Centre
One Oil Patch Drive, Devon, Alberta, Canada
feng.lin@canada.ca

Abstract

Non-aqueous extraction (NAE) at ambient conditions provides many advantages over the current commercial hot water method for processing mined oil sand, but several challenges remain largely due to the use of a hazardous conventional organic solvent (COS) such as toluene or heptane. In this work, a cleaner, more sustainable NAE process using a low-cost, eco-friendly, bio-based solvent, was developed. Results indicate that the bio-solvent extraction could achieve oil recoveries of close to 100% for different grades of ores, the highest yield compared to those often obtained using a COS (toluene or heptane). The total water and solids contents in the supernatant of the extract were very low and as comparable to those extracted using toluene. Importantly, the quantity of residual bio-solvent in the sand after simple evaporation was limited to a level significantly below the regulation target for a COS. The application of bio-based solvent in NAE could dramatically reduce the safety, environmental, and health concerns associated with the use of a COS. Equally important, this bio-solvent extraction inherits all the advantages of NAE, e.g., dry tailings, ready for land reclamation, lower carbon footprint, and ability to efficiently recover low-grade and oil-wetted ores.

Keywords: *Bio-based solvent, Solubility, Oil recovery, Advanced separation, Sustainability*

Short biography

Dr. Feng Lin obtained Ph.D. and M.Sc. degrees, both in Chemical Engineering, from the University of Alberta and the University of Waterloo, Canada, respectively. He is currently a Research Scientist at CanmetENERGY research centre in Devon within the department of Natural Resources Canada. His research expertise covers interfacial transport phenomena, colloids, wetting and adhesion, heavy petroleum production, minerals processing, polymers and nanomaterials synthesis, and renewable energy engineering. To date, Dr. Lin has managed 10 projects with more than 2 million dollars funding, supervised 8 technologists and postgraduate students, and authored about 40 referred journal publications and government-wide scientific reports, in relation to the fundamental research and scale up of cleaner oil recovery and minerals processing technologies. His passion to research and technology development is to be one of many contributors for searching cleaner solutions and materials to fuel our homes, societies, and economies.

IEECP'21, July 29-30, 2021, Silicon Valley, San Francisco, CA – USA

DAI : *https://sci-index.com/DAI/2021.99101/IEECP/14575251*

Lignocellulose as a fundamental resource for a sustainable development

Maria Laura Tummino
Intelligent Industrial Technologies and Systems for Advanced Manufacturing (STIIMA)
Italian National Research Council (CNR)
Biella, Italy
marialaura.tummino@stiima.cnr.it

Abstract

Nowadays, the topic of environmental preservation and remediation plays an important role within the activities of the scientific community. Indeed, the procrastination of effective measures to mitigate the environmental damages caused by human activities is no longer possible. In particular, the use of non-fossil substances should be promoted for different reasons: to reduce the environmental disequilibria of the areas involved in the fossil fuel extraction; to decrease the impact of emissions and by-products related to the industrial transformation of fossil-based products; possibly, to exploit biomasses as sources of organic carbon with net zero carbon emission. As regards the type of biomass, herein, a focus on the use of lignocellulose biomass (LCB) will be presented, in particular when it is in the form of waste, often non-correctly disposed or incinerated, representing a biohazard. Waste-LCB are low-cost, easy-available and green raw material. Despite of the variability among different lignocellulose biomasses, in general, they present convenient chemical-physical features that make them suitable compounds for several purposes. An overview of the multiple functions of lignocellulose biomass in the broad field of green chemistry and green catalysis will be explored. Thanks to the versatility of LCB, it has found application as an adsorbent for aqueous pollutant removal, as a precursor of bio-carbons with multi-purpose applications and reinforcing agent for plastics and construction materials. Within the catalysis field, LCB can be the substrate of catalytic transformation, when their constituting biopolymers (cellulose, hemicellulose, lignin) are converted to platform molecules and strategic building blocks, which can substitute some petroleum derivatives for the production of biochemicals and biofuels, in a perspective of lessening the petroleum dependence. Strong efforts have to made to make this kind of processes sustainable, i.e. the employment of heterogeneous catalysts able to catalyze one or multi-step sequences, as well as the choice of solvent that, in most of the cases, plays a significant role for the reaction evolution. LCB can be considered also as a precursor for humic-like substances, isolated from waste-LCB, which are photocatalytically active compounds, able to degrade water contaminants under light irradiation, through the production of excited species and whose activity is strictly related by their origin and chemical structure. Lastly, LCB has been recently considered also as a support for metal/metal oxide catalysts and in other high-technological applications. Given the wide scenario involving lignocellulose-based compounds, this presentation is aimed to propose food for thought about a multifunctional approach on the valorization of waste-LCB for an eco-sustainable development.

Keywords: *Lignocellulosic biomass, waste valorization, environmental remediation, biorefinery*

Short biography

Maria Laura Tummino is a Permanent Researcher at STIIMA Biella of the Italian National Research Council. She received her Master's Degree in Industrial Chemistry in 2013 and the PhD in Chemical and Material Sciences in 2017 at Università di Torino (North-West of Italy). Maria Laura has devoted her career to green chemistry research, developing different materials for energy and environmental remediation. Her research was focused on photocatalysts for water depuration, biomass-based adsorbents for organic and inorganic aqueous pollutant removal and cathodes for electrochemical devices. She has combined the basic research on national and international levels with job experiences in different companies. She is (co-)author of more than 30 works (papers, congress presentations and publications in a database) and she is involved in scientific dissemination projects and outreach events.

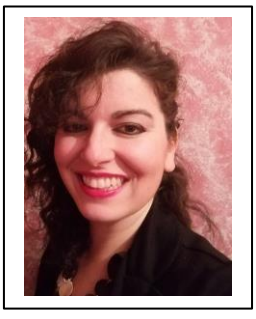

IEECP 21, July 29-30, 2021, Silicon Valley, San Francisco, CA – USA

D!f: *https://sci-index.com/DAI/2021.99101/IEECP/14525574*

Model Predictive Control for Intelligent Building Energy Management

Man Pun Wan[1], Shiyu Yang[2]
School of Mechanical and Aerospace Engineering
Nanyang Technological University
Singapore
mpwan@ntu.edu.sg[1], yangshiyu@ntu.edu.sg[2]

Abstract

The building sector consumes over 30%, with an annual growth rate of 1.3%, of global final energy and is responsible for nearly 40% of global carbon emissions. Building energy efficiency harbours enormous potential as a major contributor to global carbon footprint reduction and urban sustainability. In this context, World Green Building Council announced the Net Zero Carbon Buildings Commitment of achieving net zero carbon operation for buildings under their control by 2030 and all buildings by 2050. Advances in building energy management systems (BEMS) offer significant potential to improve building energy efficiency and occupant well-being. Current BEMS are mostly based on reactive control (e.g., proportional–integral–derivative control), which lacks the level of intelligence needed to handle challenges such as increasing demand for occupant's well-being and the proliferous adoption of multiple energy systems (e.g., renewable energy and energy storage) in buildings. Empowered by the increased connectivity and access to diverse data in buildings brought by emerging digital technologies (e.g., internet of things (IoT), wireless communication network and cloud/edge computing), adopting more sophisticated building energy management solutions is expected to be a major path to achieve building energy efficiency and carbon footprint reduction goals. Model predictive control (MPC) and data-driven approaches (e.g., machine learning (ML)) are widely identified as key technology enablers e.g., International Energy Agency (IEA) through its global initiatives of IEA-EBC Annex 67 Energy Flexible Buildings and Annex 81 Data-Driven Smart Buildings. This talk presents our research work on the development and application of MPC as well as ML-based MPC for building energy management. The key feature of MPC is that it exploits a predictive building model for predicting future building states and, subsequently, performing optimal controls based on the predictions. We proposed a multi-objective MPC scheme for coordinated control of multiple building services (air-conditioning, dimmable lighting and automated shading). The multi-objective MPC can optimize these multiple building services simultaneously and achieve the overall optimum of energy efficiency and human comfort in buildings. To further enhance the adaptability of MPC for building energy management applications, we proposed two novel MPC schemes incorporating ML, i.e., adaptive ML-based MPC and ML-based approximate MPC. The key feature of adaptive ML-based MPC is that it employs an adaptive ML-based model as the predictive building model. The ML-based approximate MPC employs a ML model to approximate the control laws of MPC, then, uses the ML model to replace MPC for building control. The control-oriented building modelling, optimization formulation, control implementation in real buildings (a lecture theatre, an office and laboratory test facility) as well as experimental results of the three proposed MPC schemes will be presented and discussed. Finally, open problems and our ongoing/future research efforts are discussed.

Keywords: *Model Predictive Control, Building Energy Management, Machine Learning, Energy Efficiency*

Short biography

Dr. Wan is currently an Associate Professor in the School of Mechanical & Aerospace Engineering at Nanyang Technological University. Prior to joining NTU, he was an Assistant Professor of Mechanical Engineering at Kyungpook National University, Korea. His research interests cover aerosol sciences, building energy, smart buildings, indoor environmental quality, catalytic oxidation systems and numerical simulations. Dr. Wan led numerous government- and industry-funded research projects ranging from fundamental studies of fundamental thermos-fluids sciences, aerosol sciences and impacts of indoor environmental quality on occupant cognitive function. He has also been working on development of novel green building technologies such as high-performance Cool materials for buildings and pavements, advanced building control and automation systems, integrated dimmable lighting and dynamic shading system, chilled ceiling system and other technologies for energy efficiency and occupant well-being. Dr. Wan has published over 100 international refereed journal and conference articles and is inventor of 3 patents. He is a member of American Society of Mechanical Engineers (ASME), American Chemical Society (ACS) and American Society of Heating, Refrigerating and Air-Conditioning Engineers (ASHRAE).

D!f: *https://sci-index.com/DAI/2021.99101/IEECP/14525589*

Energy and environment: important role of chemistry in meeting the new demand for sustainable solutions

Francesca Deganello
Istituto per lo Studio dei Materiali Nanostrutturati
Consiglio Nazionale delle Ricerche
Palermo, Italy
francesca.deganello@cnr.it

Abstract

Sustainability has been worldwide recognized as the only possible bridge to the future, and chemistry has to be rethought in this new perspective. Materials production through chemical methods needs to be designed through sustainable actions, from the choice of primary resources to the efficiency of the synthesis process, from the functional performance of the materials to their present and future impact in society, environment, and economy. Apparently, this is an unaffordable goal. This presentation will give a chemistry perspective on sustainable materials for energy and environment, highlighting some little steps to take in the way toward sustainable development and discussing how chemistry can help to reach sustainable development goals, such as responsible consumption and production (n°12), affordable and clean energy (n°7), clean water and sanitation (n°6), sustainable cities and communities (n°11) and quality education (n°4).

Keywords: *sustainability, sustainable development goals, materials synthesis, energy and environment, waste precursors, chemistry, mixed oxides, solution combustion synthesis.*

Short biography

Dr. Francesca Deganello is researcher at CNR-ISMN Palermo (Italy) since 2001. In March 1996 she got the Chemistry degree at the Università degli Studi di Palermo (110/110 cum laude). In February 2002 she obtained her Ph.D certificate in Chemical Sciences at Università degli Studi di Palermo, Italy. She is involved in several national and international projects on the preparation and characterization of sustainable nanomaterials, especially mixed oxides with perovskite-type structure for solid oxide fuel cells operating at intermediate temperatures, for metal-air batteries, and for the degradation of pollutants in the air and in industrial wastewater. Dr. Deganello is the author of 37 peer reviewed scientific publications, 10 structures in the ICDD database, and about 60 oral, poster communications and invited presentations. She is also involved in outreach activities for schools and public.

DAI : ***https://sci-index.com/DAI/2021.99101/IEECP/14525670***

Decarbonization for the energy transition and green production

Talieh Rajabloo
IMO-IMOMEC, Energyville II
University of Hasselt
Genk, Belgium
talieh.rajabloo@uhasselt.be, rajabl67@imec.be, talieh_rajabloo@yahoo.com

Abstract

A considerable part of the fossil CO_2 emissions comes from the energy sector, in which the main parts are released through energy-intensive industries, namely metal production, chemicals, and manufacturing. Hence, decarbonization of industries is considerably important beside the other sectors such as net zero buildings and transformation. The main concept of this speech will cover renewable energy/resources solutions after looking into potential classic decarbonization. First objective is about the upgrading of the existing processes, equipment, and plants besides implementing the heat recovery/integration based on the innovations toward reducing the energy requirements and efficiency increments. Then, the renewable resources are going to be introduced. Moreover, energy production and conversion methods, feedstocks, carbon capture and storage, and electrification will be discussed.

Overall, both classic and innovative renewable attempts are required to reach the deep decarbonization targets. At the end, the objectives are going to be expanded toward chemical industries by introducing the potential technology implementation at different subsectors. For this purpose, the assessed roadmaps and pathways will be discussed further. The primary research results of my current study reveal that although all of the inventive suggestions are not available at an industrial scale or are not economically viable yet, they will play a crucial role in the energy transition at upcoming decades.

Keywords: *Industrial decarbonization, energy intensive sector, Renewable energy and resources, CO_2 mitigation*

Short biography

Experienced senior researcher in the field of industrial decarbonization with broad experience in fulfilling and managing research and development projects. Specialist in the field of renewable energies with a demonstrated history of working more than 10 years, on process design, decarbonization research and energy conversion. Skilled in Aspen Plus, Power Plants, Process simulation and design, Heat Exchangers, petrochemicals processes, Python, and scientific publications. Ambitious research professional with a Doctor of Philosophy (PhD) focused in Mechanical Engineering for systems of energy from University of Brescia. Background in Chemical engineering and process design. Able to work effectively with scientists and engineers of multiple disciplines.

Dr. Talieh Rajabloo

DAI : ***https://sci-index.com/DAI/2021.99101/IEECP/14525661***

Computational Screening for New Generation Photovoltaic Materials

Julia Romanova
Sofia University, Faculty of Chemistry and Pharmacy
Sofia 1164, Bulgaria
jromanova@chem.uni-sofia.bg

Abstract

The present study is devoted to singlet fission chromophores – a rare kind of molecules, which, upon excitation, may double the charge carriers in a solar cell, overcome the Shockley–Queisser limit and boost the development of new generation organic based solar cells. In order to find new potential singlet fission chromophores, we have developed computational screening procedure implementing quantum-chemical approaches, machine learning algorithms and chemometrics methods. The singlet fission propensity of the molecules is rated based on their diradical character. In order to prove our concept for finding new photovoltaics chromophores, we have created an open-access database. The computational screening procedure allows us fast preselection of potential singlet fission candidates, as well as to explore in detail the structure-properties relationships and to define new strategies for the design of such materials.

Keywords: *singlet fission, excited states, semi-empirical, diradical character*

Short biography

Dr. Julia Romanova is an assistant professor at the Department of Inorganic Chemistry of the Faculty of Chemistry and Pharmacy, University of Sofia. Her research interests are in the field of applied computational chemistry with special focus on organic and organometallic compounds with attractive optical, magnetic and conducting properties. Assist. Prof. Julia Romanova has co-authored 1 patent, 23 research papers and 3 book chapters. In 2011, she was received the national 'Eurika' Foundation Award for exceptional achievements in science for her work as an early-stage researcher. In the period 2012-2017 she gained international research experience working as a postdoctoral and research fellow at the University of Surrey (UK) and the University of Namur (Belgium). Assist. Prof. Julia Romanova was a fellow of the German Academic Exchange Service at the Max Plank Institute for Polymer research (Germany, 2006) and a fellow of the French Government at the University of Upper Alsace (France, 2007-2010). In 2019, she won a L'Oréal-UNESCO fellowship for Women in Science, Bulgaria.

DAI : *https://sci-index.com/DAI/2021.99101/IEECP/14525664*

Utilizing Metal Chelating Flavonols as Metal Ion Filter and Hydroxyl Detector in Aqueous System

Erum Jabeen
Department of Chemistry
Allama Iqbal Open University
Islamabad, Pakistan
erum.jabeen@aiou.edu.pk

Abstract

Flavonols are the group of compounds with conjugated structure having at least one hydroxyl and one keto group on adjacent C on ring C of flavone within planner structure. This particular arrangement provides flavonols with excellent radical scavenging potencies metal chelating properties and DNA intercalating ability at the same time. Apart from determining the pharmaceutical benefits of flavonols, they can be explored for brilliant environmental applications such as ROS detectors and water purifiers. In the current study, we are exploring the typical pharmaceutical benefits for engineering selective electrochemical ROS detector and metal trapping filters for water purification. Three Hydroxy flavones (HF); 2'PHF, 3'PHF and 5HF were subjected to metal complexation M-HF) with Mn and Ni followed by RSA and DNA binding analysis of bare flavonol (HFs) and their metal complexes (M-HFs). The antioxidant potencies of M-HF, Ni-HF and Mn-HF were described in terms of RSA (radical scavenging activity) against 1,1-diphenyl-2-picryhydrazyl radicals (DPPH$^{\bullet}$), hydroxyl radicals (OH$^{\bullet}$), tetramethyl-pipyridinyl radicals (TEMPO$^{\bullet}$) and superoxide radicals ($O_2^{\bullet-}$). The quantity required to scavenge the 50% of radicals IC_{50} were estimated form RSa vs concentration plots in physiological conditions. The computed ionization potential (IP) and ΔE_{HOMO} were complementary with IC_{50} trend. The comparative investigations indicated M-HF to be stronger scavenger then corresponding HF. So, metal complex were also used for OH$^{\bullet}$ sensor fabrication. The flavonols (HF) and their metal complexes (M-HF) were deposited over APTES-FTO (3-aminopropyl triethoxy saline−fluorine doped TiO_2) to fabricate (M-)HF-APTES-FTO electrode leading to stable sensor formation. This sensor responded to nano-molar concentrations of ROS through decrease in peak current. The anodic wave signal decayed upon incremental addition of OH$^{\bullet}$ at a concentration as low as 5nM leading to good sensitivity towards OH$^{\bullet}$ detection. The OH$^{\bullet}$ brought significant curret decay when compared with higher concentrations of other ROS suggesting reasonable sensitivity and selectivity of HF/M-HF-APTES-FTO for OH$^{\bullet}$

The DNA binding constant for HF, Mn-HF and Ni-HF were in the range of 10^2-10^4 (M^{-1}) with negative ΔG depicting stable and spontaneous DNA binding. The variation patterns of absorption spectra and voltammograms were explored to assign modes of binding such as intercalation, groove binding, electrostatic binding or mixed ones. The M-HF were found to be stronger DNA binders than respective HF which reveals that after metal chelation the DNA bound molecule will remain bound with it which can be utilized for engineering a DNA binding based filter for chelation of heavy metal ions from aqueous solutions. Three different assemblies were comparatively studied for their efficiency towards metal ion capture. There patterns of chelation and immobilization were tested for relative success towards ion capture which included (i) immobilization of DNA intercalated metal-flavonol, (ii) intercalation of M-HF on APTES pre-immobilized DNA (iii) chelating metal ion over pre-intercalated Flavonol over DNA-APTES matrix. The M-HF-DNA immobilization over APTES captured around 65% ions from solution. The M-HF have intercalated into DNA-APTES films up to 82%. However, M chelation over HF-DNA-APTES matrix was effective in ion capture from the solution phase up to 99%. Our results depicted that the DNA intercalation/interaction can be utilized to successfully remove hazardous ions from the solution up to safer limits.

Keywords: *Radical Scavenger, Hydroxyl Radical Detection, Metal ion removal, DNA intercalator*

Short biography

Dr. Erum Jabeen is currently working as a Lecturer at Department of Chemistry, Allama Iqbal Open University, Islamabad Pakistan. She got her PhD with specialization in Physical Chemistry from Quaid-i-Azam University Islamabad Pakistan in 2017. She got her MPhil in physical chemistry (2012) and MSc in physical chemistry (2010) from Quaid-i-Azam University Pakistan. During her stay at Quaid-i-Azam University Islamabad, she won QAU merit scholarship 2008-2010, 1st position award 2010 and HEC indigenous scholarship 2012-2017. Currently her research focuses on biosensor fabrication for hydroxyl radical sensing, electrode modifications for electrochemical enzyme kinetic assays, electrochemical enantioseparation techniques, biomedical DNA biomarkers, adsorption of inorganic pollutants such as CO_2 and toxic metals such as As, Pb, organic pollutants such as phenols. She is also focusing on DNA binding and antioxidant investigations for versatile applications, electrochemical water treatment, photo-electrochemical oxidation and reactor/systems for waste water treatment. She has won "AIOU research publication grant 2020-2021" at Allama Iqbal Open University Islamabad Pakistan.

DAI : https://sci-index.com/DAI/2021.99101/IEECP/14551191

Study of Liquid Desiccant Air Conditioning Using Flat Plate Solar Collector

Geleta Fekadu Daba (PhD)
Department of Mechanical Engineering
Wollega University, College Of Engineering And Technology
Ethiopia, Oromia. Nekemte
gelefeke@gmail.com /gelefiker@yahoo.com

Abstract

The present study deals with a liquid desiccant air conditioning system using a flat-plate solar collector. Initially, there is an investigation for the performance of a flat-plate solar collector using Al_2O_3–water nanofluid and pure water. Using nano fluids as heat transfer fluid instead of conventional fluid (water) improves heat transfer and thermal properties and also there is a remarkable effect on the collector efficiency. The experimental setup comprises of a flat plate collector of the aluminium absorber plate, a closed-loop working fluid system and measurement devices. The effect of various parameters like mass flow rate of fluid, collector inlet and outlet fluid temperature, solar radiation, and ambient temperature on the collector efficiency is investigated. The experimental results show that, each of these parameters can affect the collector efficiency differently by changing the value of the other parameters. The mass flow rate was varied from 1 to 5 L/min and the volume fraction is 0.1 vol. % of nano fluid. By suspending Al_2O_3 nanoparticles (particle size 20 nm) in the base fluid (water) the maximum collector efficiency attained is 83.2% and to the pure water is 59.7%, whereas exergy efficiency maximum is achieved 18.7% and 12.3% for the 20nm Al_2O_3 nanofluid and base water at the mass flow rate of 3 L/min. Hence, efficient solar flat plate collector is achieved.

Finally, liquid desiccant as air conditioning using solar flat plate collector. The main problem of liquid desiccant as air conditioning is the utilization energy for regeneration, corrosiveness and carryover. The dehumidifier is made of stainless steel tubes of 316L and these tubes are stacked in aluminium fins to maintain the desiccant solution temperature using the evaporative cooler. In this experiment, calcium chloride solution is used. The flat plate collector is used for heating water using closed-loop of thermosiphon as regeneration.

The flow rate for air is fixed at 10CFM and the concentration of calcium chloride is 33% by mass. The inlet air is humidified and controlled by a constant temperature bath. The inlet parameters are solution volume flow rate, inlet temperature, inlet relative humidity, regeneration, and solution temperature. The performance parameters are the absolute humidity reduction, outlet temperature and dehumidifier and enthalpy effectiveness of the dehumidifier. The solution volume flow rates of 14 L/min, 16 L/min, 18 L/min and 20 L/min are used for the experiments. The experiments show that for a fixed $T_{a,}$ inlet and RH% as solution volume flow rate increases, there is increase in absolute humidity reduction. The temperature of the dehumidified air is reduced compared to that of inlet air if this air is passed over the pad used for the evaporating cooler. It is seen that the increase in relative humidity from 68.88% to 92.8% for the flow rate of 20 L/min and fixed inlet air temperature, increases absolute humidity reduction from 5.56 to 13.3 g/kg. When the solution temperature changes from 31.5 to 34 ^{0}C, there are reductions in the absolute humidity reduction and dehumidifier effectiveness by 34.4% and 13.04% respectively.

Keywords: *Solar flat plate collector, Al_2O_3-water nanofluid, Efficiency, Heat transfer enhancement, Liquid desiccant, Dehumidifier, Evaporative cooler, Absolute humidity, Effectiveness.*

Short biography

Dr. Geleta Fekadu Daba Ph.D Degree obtained Thermal Engineering, in the Department of Mechanical and Industrial Engineering from Indian Institute of Technology Roorkee (IITR), India. Dr. Geleta obtained his Bsc and M. Sc degrees in Automotive Technology and Automotive Engineering respectively from Adama Science and Technology, Ethiopia, Oromia. After my first degree I hired one of Ethiopian government University Wollega University, College of Engineering and Technology, Department of Mechanical Engineering. After he served wollega University for one year,got scholarship to study Msc. and completed in Automotive Engineering, then he restated to give service for his University. After three years of his service and head of the department he got sponsorship to attend PhD; he wrote one project on solar assisted liquid desiccant air conditioning to department of science and Technology, India and won about 33lac.through his guide and completed his study from in Indian Institute of Technology Roorkee (IITR), Department of Mechanical and Industrial Engineering (Thermal Engineering) since 2020 and he returned back to his home country Ethiopia Wollega University as position of Assistant Professor, College of Engineering and Technology, Department of Mechanical Engineering. He published 4 international reputable journals, 2 book chapters, and 5 international conferences. So, he has keen interest to share his experience on renewable energy resources of solar assisted liquid desiccant air conditioning.

DAI : *https://sci-index.com/DAI/2021.99101/IEECP/14991585*

Analyzing the Effect of Cleaning on Anti Reflecting Coating of PV Module

Rohit Bhardwaj
Centre of Excellence for Energy &
Environmental Studies
Deenbandhu Chhotu Ram University of
Science & Technology
Murtha, Sonipat (India)
rohitbhardwaj6848@gmail.com

Abstract

Solar energy which is cheap and present in abundance in tropical and subtropical regions has been universally accepted as future source of energy and photovoltaic cells are considered as potential candidates to harness this energy. In the recent years, India being its proximity to equator has increased the installation of PV systems in a huge way because of the higher irradiation available in large part of the country. India has seasonal variations from extreme cold to scorching heat, sand & dust storms, fog and heavy rain fall during monsoon. All these extreme metrological conditions causes accumulation of soil on PV modules which adversely affect the optimized output of modules. Removing of dust & dirt from the surface of module require cleaning of the module surfaces at regular interval. For this study 12 PV module were selected out of which six were based on mono-crystalline silicon and another six were of poly-crystalline silicon technology of 6 samples each. All the PV modules were made up of 72 cells configuration with 6 rows x 12 columns. Initially, after recording the important parameters such as Voc, Isc, Vmp, Imp, and cell efficiency etc as per manufacturers information the Visual Inspection Test was conducted of all the 12 PV modules as IEC and internal standard protocol. Electroluminescence Test, STC Performance Test, ultrasonic thickness test, reflectance and soiling test were conducted and the data recorded as base data.
To simulate the extreme soiling conditions on the solar PV modules the desert soil which is mostly sandy soil (90-95%) was used. To study the soiling effect the scale of 100 cycles was taken which was further divided into 3 stages, first stage was from 0 to 30 cycle, second stage from 31 to 60 cyles and third stage from 61 to 100 cycles.

The desert soil was collected in a cloth bag of fabric with small pores through which fine sand particles were sprinkled manually on the solar PV modules. Initially, for first and second stage the 26 grams of fine desert soil taken in a cloth bag and out of which only 35 to 40% (approx 10gm) soil passes through the pores and accumulated on PV modules. For third stage a bag of 180 gm desert soil was used to sprinkle 50 gm of soil on the surface of test modules. Dry Robotic Cleaning Technology is used for cleaning of the panels. Impact of regular cleaning on panel performance was evaluated by analyzing the effect of cleaning on the glass surface and Anti-reflection coating present on the PV modules.

The parameters like; total reflectance, diffuse reflectance and spectral reflectance of light from the module surface were calculated and removal of ARC coating was assessed by performing Ultrasonic Thickness Measurement Test at eight different location of the PV modules.

Keywords: *soiling, anti reflection coating, PV modules*

IEECP'21, July 29-30, 2021, Silicon Valley, San Francisco, CA – USA

D!!: *https://sci-index.com/DAI/2021.99101/IEECP/14526999*

Zero-carbon footprint, mechanical intervention for potentially reducing forest fires and generating livelihood options in Western Himalaya

Kapil Kumar Joshi
Indian Forest Service Officer, Post-Doctoral Fellow, Department of Management Studies,
IIT Roorkee, Uttarakhand, 247667, India.
kapilkjoshi@rediffmail.com

Vinay Sharma
Professor, Department of Management Studies,
IIT Roorkee, 247667,Uttarakhand, India.
vinay.sharma@ms.iitr.ac.in

Abstract

This paper provides an appropriate technological intervention with a zero-carbon footprint operating model while converting a dangerous forest bio-residue into a usable commodity. In our study, the dangerous forest bio-residue consists of the dry and fallen pine needles of the trees that grow in the Western Himalayan region. The appropriate technological intervention is the evolution of a manually operated biomass briquetting machine, and the usable commodity is the bio-briquettes, which could be used as an alternative to fossil fuels. Dry and fallen pine needles induce devastating forest fires in the Himalayan region, which facilitates the release of huge amounts of carbon into the atmosphere without obtaining any productive use from it. The purpose of this research is to present an easy-to-operate manual intervention to densify the loose and dry bio-residue into a useful and salable fuel option while promoting community involvement. The studies propelling the evolution of the briquetting machine are based on reflexivity, where communities themselves have been demanding such types of basic and indigenous interventions to create reasonable livelihood options for themselves and to address the socio-climatic issues caused by forest fires in the Himalayan region.

Keywords: Forest bio-residue, Briquetting, Climate Change, Himalayas, Livelihood, Zero-carbon footprint

I. INTRODUCTION

The Indian Himalayan region comprises of about 12% of India's total landmass and approximately 30 % of India's total faunal diversity [30]. This area has a great influence on the ecology of the entire northIndian region as it hosts around 280 species of mammals, 940 bird species, 316 fish species, 200 species of reptiles, and around 80 amphibian species [12].The region has numerous lakes, ponds, rivers, glaciers, forests, and high-altitude grasslands that support different ecologies and additional flora-fauna species.

Unfortunately, climate change models implemented to estimate the climate of the Himalayan region predict ever-increasing temperatures and erratic precipitation [22], where in the tree and shrub lines moving up the mountains, glaciers will be melting at a faster rate, alpine meadows will decrease, quality forests will shrink, and flowering pattern of wild species will also change [12,26,21].

Although indigenous people in the Himalayan region clearly understand climate change and are well aware of global warming, melting glaciers, unpredictable rain patterns [4], loss of habitat, degradation, and deforestation, many of them strongly attribute these changes to spiritual causes and suggest prayers and ceremonial practices as solutions [27]. Since time immemorial, the traditional Himalayan livelihood had been carbon negative as communities used their natural resources, such as timber, grasses, medicinal plants, fire wood, flowers, fruits, tubers, and water, for sustained living. They never overexploited, destroyed, or polluted their natural resources and believed in sustainable consumerism. However, they knew well to arrest or mitigate climate change by implementing strong traditional ecological knowledge (TEK) in their day-to-day affairs. This knowledge would be shared from one generation to the other thereby creating a sustainable community-environment cycle.

Climate change has been strongly attributed to deforestation. Ironically, during the past decades, climate change in the Himalayas has not accelerated because of deforestation. This is evident from the aerial satellite data of the region pertaining to forest biomass; the data show that the opposite phenomenon of reforestation is being actively carried out in the region [5]. States of Himachal Pradesh and Uttarakhand (Himalayan states of North India) indicate degradation (rather than deforestation) to be the key problem. A majority of the forest area exhibits crown cover below the ecologically sustainable threshold of 40%; heavily lopped trees and stunted tree-growth with limited foliage is a common scenario in this region. Additionally, repeated forest fires in the Himalayan region are gradually becoming a major cause of degradation of forest areas.

IEECP'21, July 29-30, 2021, Silicon Valley, San Francisco, CA – USA

DAI : *https://sci-index.com/DAI/2021.99101/IEECP/14580096*

Among many other reasons, the chir pine(Pinus Roxburghii) forests in the region contribute substantially to the forest fires. Forest fires in Indian Himalayan states, such as Uttarakhand, have emerged as the biggest enemy of the unique megabio-diversity of this region. Over half a million hectares of forest land is covered with chir pine trees (Pinus Roxburghii), and they shed millions of tons of leaves annually during the summer season (March to June). Either intentionally or accidently , thedry and fallen pine needles catch fire, causing colossal damage to not just the unique biodiversity of the region but also the whole environment [28]. It is estimated that 4–5 million tons of dry and highly- inflammable chir pine leaves fall over the forest floor in the Indian Himalayan state of Uttarakhand alone [24, 29].

As pine needles are highly combustible because of their turpentine content, they spread fires with lightning speed. Although the incendiary nature of these pine needles is a major cause of forest fires in hot summers that can lead to destruction of life and ecosystems, they can still have precious use as an alternative fossil fuel; the fallen dry pine-needles could be conveniently converted into bio-briquettes. It is also worth mentioning that transporting these pine needles in loose form, from point of origin to the factory site, is highly cost-intensive because of its very high volume, which largely restricts the load capacity of the vehicle. As an example, a carrier vehicle designed to transport a load of nine tons can hardly transport two to three tons of loose pine needles, which drastically increases the transportation cost. Simultaneously, because of the absence of an appropriate briquetting technology, local communities find it impossible to create a value-added product from the fallen pine needles. As a result, this important resource is not only causing devastating forest fires and irreversible loss to the environment but is also getting wasted (owing to the fact that it can be a reliable fuel source if treated properly). Thus, producing briquettes from the needles will not only minimize the forest fires but also provide an alternative source of fuel. Additionally, this can be a great way to offer employment and reliable livelihoods to the local communities.

II. OBJECTIVES OF THE STUDY

In this study, we visualize the strengthening of the capacity and development of human capital in the Himalayan region by addressing the socio-economic scenario of the region with the support of technological interventions; using forest bio-residue as a source of renewable energy through bio-briquetting of dry and fallen pine needles, is a promising way to achieve this. This study aims to innovate and provide related knowledge interventions using indigenous green technologies to subsequently, curb migration, mitigate climate change, and capacity building which in turn will create good livelihood opportunities for the local communities residing in the nearby pine forests.

We aim to develop a manually operated briquetting machine for areas that are historically known for rich traditional knowledge practices to serve the larger goal of natural resource conservation. The objectives of the study are to address climate change issues along with providing sustainable livelihood options to the local communities.

III. LITERATURE REVIEW

The world is diligently searching for an alternative source of energy for domestic and industrial usage to ensure sustainable development [13]; corresponding to this need, researchers are working on unlocking renewable energy sources [14]. In the recent years, bio fuel has become a globally accepted form of energy owing to its easy availability [15]. Bio-briquetting, which is reported to be more effective than the other forms of renewable energy such as bio-diesel and bio fuel, requires more research and appropriate technology to use it efficiently and effectively [20].

Solid fuel can be produced through a briquetting technique involving the binding of pulverized carbonaceous matter with or without a binder [16]. This may be a manual or mechanical process involving screw, piston, or hydraulic presses [10]. To produce a bio-briquette, solid waste such as agro-residue, dry organic material, or forest bio-residue can be used [9]. The organic waste is compressed with or without a binder (a specific ratio is adhered to if a binder is used). The proper briquetting technique provides a good quality solid fuel with a low ash content, lower burning rate, better ignition time, and low moisture content [6]. Saw dust [1], groundnut shell [2], grass [11], rice husk, jute dust, de-oiled bran, and corncob are widely used as bio-briquetting materials. The use of forest bio-residue as a briquetting material has not gained much popularity because of factors such as high transportation cost of raw material, non-accessible areas, tough and remote forest terrain, lack of appropriate technology, and various non-cohesive government regulations that supervise forest production. Forests globally have the potential to produce considerable amounts of biomass in the form of forest residue, such as branches, tops, bark, litter, and stumps. Forest residues have the potential to produce 30–150 exa-joules of energy per year [3, 23, 8].

It is further noticed that during a periodic cycle of approximately 240 years, cumulative radioactive forcing is significantly reduced when forest residues are used for energy instead of fossil fuels, although it takes 10 to 25 years to obtain positive results after the fuels are replaced with the forest residue [25,19]. The forestry sector in India has a bio-residue generation capacity of 27.1 metric tons per annum [7]. With such a vast forest bio-residue resource, India can easily address the issue of renewable energy using a low-cost energy generation solution.

Because of the large quantity of inflammable material lying on the forest floor, pine forests of the Himalayas are highly prone to forest fires [17]. Only a small fraction of dry and fallen pine needles is used by the local communities for manure, packaging, mulching, and roof shedding, while the rest is burnt accidently or otherwise. There has been hardly any known and implementable commercial activity related to such vast forest residues that are easily available to local communities. In the past, some initiatives were taken by the Uttarakhand state government to convert pine needles into briquettes under macro-level entrepreneurship programs [18]. However, the efforts did not yield because of executive, economic, operational, or policy issues. The transportation of dry and fallen pine needles from the hillside to the factory site is a great concern for entrepreneurs because the collection of pine needles from the forest floor and its transportation to the factory is highly uneconomical.

Though the communities were involved in this but being a contractual or hired laborer, no entrepreneurship skills could be developed among the locals. When the bio-briquetting industries faced forced closures because of the unacceptable cost-benefit ratio, these communities lost their livelihoods and the forest fires continued to destroy the ecology of the region.

Corresponding to this, in another attempt at micro-level entrepreneurship, electrically-operated machines were introduced for coal-making in the year 2010 by the Forest Department in some of the hilly areas of Uttarakhand. This method of coal-making involved carbonization of the pine needles to later mix it with additives, such as molasses or cow dung, before feeding the mixture into the machine for making coal pallets of different sizes. This attempt also turned out to be unsuccessful because the villagers faced serious problems in the maintenance of the electrically-operated machine, they could not achieve perfection in the carbonization process, and it was very difficult for them to arrange cow dung or molasses for mixing as a binder.

This journey began when all the deterrents in the macro scale entrepreneurship as well as in the micro scale entrepreneurship were deeply analyzed, and a manually operated bio-briquetting machine was designed and developed. This machine was conceived and later manufactured, keeping in mind the basics of social entrepreneurship.

IV. METHODOLOGY

The perspective that emerged in this study is that thinkers, authors, researchers, academicians, and policy makers never viewed the subject of forest bio-residue management to create livelihoods for forest inhabitants and to mitigate climate change along with augmenting the associated policies.

Two different options were considered in order to design a manually operated bio-briquetting machine:

Option 1: Application of heat to soften the surface lignin of pine needles and simultaneously compacting it to make briquettes

Option 2: Application of pure hydraulic pressure of about 1500 to 2000 psi to compact the pine needles without the use of any additives.

Option 1 had many operational problems, as it was not easy to handle a heated machine. More than that using fire near a highly inflammable material, such as dry pine needles, was not really safe to operate.

Detailed experiments were conducted to validate option 2. Pascal's principle was applied for this purpose. Corresponding to this principle, the force delivered by the fluid at the delivery end is determined by multiplying the pressure and cross-sectional area. The pressure being the same in all directions, the smaller piston feels a small force whereas the larger piston feels a larger force. Therefore, a smaller force input can generate a large force output at the delivery end of a hydraulic system.

A line diagram is shown in figure 1 to illustrate the principle of hydraulics.

Figure 1 Diagram depicting principle of hydraulics

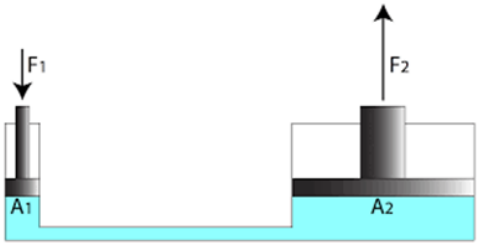

This hydraulic system mainly consists of:

- Moving piston connected to the output shaft in an enclosed cylinder
- Storage tank
- Filter
- Pressure regulator, control valves, and leak-proof closed-loop piping
- High density incompressible oil.

Force calculations for a hydraulic system

A hypothetical calculation is shown below in order to calculate the scope of force multiplication through a hydraulic unit.

- Force applied by a human hand:
  $(F_1) = 60$ N
- Area of the input side cylinder (0.25 m diameter):
  $A_1 = \pi r^2 = \pi(.25/2)^2$
  $= .05$ sq m
- Area of the output side cylinder (0.5 m diameter):
  $A_2 = \pi r^2 = \pi(.5/2)^2$
  $= .196$ sq m
- Force transmitted to the output cylinder:
  $F_2 = F_1 \frac{A2}{A1} = 240$ N

The above calculation shows that through a simple hydraulic piston cylinder design, the force on the delivery end is four times the input force. Similarly, if the force is applied by hand and foot simultaneously on the input side, a force almost equal to 500 to 1000 N could be easily developed on the output side for the same piston–cylinder dimensions.

- Force applied by a human hand and leg simultaneously:
  $F_1 = 160$ N
- Area of the input side cylinder (0.25 m diameter):
  $A_1 = \pi r^2 = \pi(.25/2)^2$
  $= .05$ sq m
- Area of the output side cylinder (0.5 m diameter):
  $A_2 = \pi r^2 = \pi(.5/2)^2$
  $= .196$ sq m
- Force transmitted to the output cylinder:
  $F_2 = F_1 \frac{A2}{A1} = 627$ N

The force on the delivery side will further multiply if the input side cylinder diameter is reduced. Variation in the input force and cylinder diameter will give a number of permutations and combinations to manufacture the perfect briquette.

The above principle of hydraulics was applied to the development of a manually operated bio-briquetting machine for compacting dry chir pine needles into bio-briquettes.

V. EXPERIMENT AND RESULTS

Attempts were made to design and fabricate a machine for making bio-briquettes from dry chir pine needles of the Himalayan region. This work was carried out at one of the pioneer institutes of India named the Indian Institute of Technology, Roorkee, Uttarakhand. Although it was quite a tough composition to densify loose and dry pine needles through a manually operated hydraulic machine, under the concept of grass root -level execution strategy and social entrepreneurship, it was mandatory to develop a machine keeping in mind the following points:

- The whole concept of chir pine bio-briquetting is strictly based on grass root-level implication strategy where villagers will work as entrepreneurs and not as collectors of dry and fallen pine needles.
- The machine must have low cost, low maintenance and easy operation so that villagers could not only afford it but also operate it sustainably.
- It should be manually driven as the Himalayan rural areas face heavy electricity cuts and lack consistent electric supply; an electrical machine would be of very little use to the villagers.
- It should be easily transported to the remote hilly terrain.
- Carbonization of pine needles should not be needed in making the briquettes as villages may not attain expertise in this.
- There should be no need of additives like cow dung and molasses.

- Transportation of pine needles in loose form should be ruled out.
- Multiple types of raw material may be used in this machine.

After a series of trials based on various piston–cylinder assemblies and hydraulic unit combinations, a pressure of 2000–2500 psi could be successfully generated at the delivery side of the machine through pure manual means. A series of initial problems like hose pipe burst, bench bend, die dislocation, piston misalignment, oil leakage, and nut and bolt fractures cropped up and were rectified. This finally resulted in the development of a manually-operated bio-briquetting machine, which could successfully convert dry and crushed pine needles into small briquettes of 30 to 40 g (weight) individually.

5.1 Flow Chart: briquetting process

The evolved briquetting machine had the basis of a simple but an appropriate technology in which the process flow chart consists of the following main steps:

- Crush the dry pine needles into small sizes of 1–2 centimeters
- Allow open air drying for a day or two
- Place the shredded needles in the die (cavity for imparting a desired shape)
- Manual application of pressure and compacting the loose mass in the die
- Ejecting the briquette from the die
- Packaging.

Figure 2 Flow chart of briquetting process

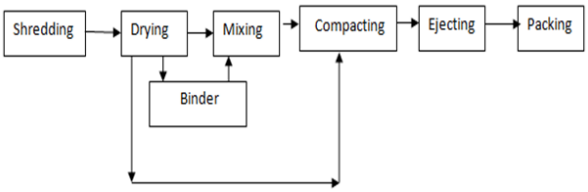

5.2 Manually operated briquetting machine

Figure 3 shows an actual photograph of the briquetting machine, and figure 4 shows the design of the briquetting machine with its various components.

Figure 3 Actual photograph of briquetting machine

Figure 4 Design of briquetting machine

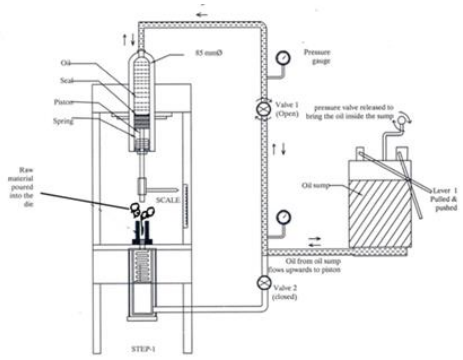

This briquetting machine has the following main components:

- Oil pump and hydraulic unit with lever 1 and lever 2
- 85 mm diameter output cylinder–piston assembly
- Mild steel die for making briquettes
- Valves, pressure gauges
- Ejection mechanism
- Compression scale.

5.3 Machine operations

Briquetting machine follows the following procedure to make a bio-briquette from chir pine needles:

a. Step 1:
- Crush the dry raw material
- Pour the raw material into the die
- Close valve no 2 (lower side valve)

b. Step 2:
- Close pressure valve to bring the oil inside the cylinder from oil pump
- Manually pump a desired pressure
- Observe desired compression level on the scale
- Open valve no 1 (upside valve)
- Open pressure-release valve and close valve no 1

c. Step 3:
- Close pressure-release valve
- Open value no 2

d. Step 4:
- Use lever no 2, operate the hydraulic pump until the briquette is ejected from the die

Figure 6 Briquetting on manually operated machine

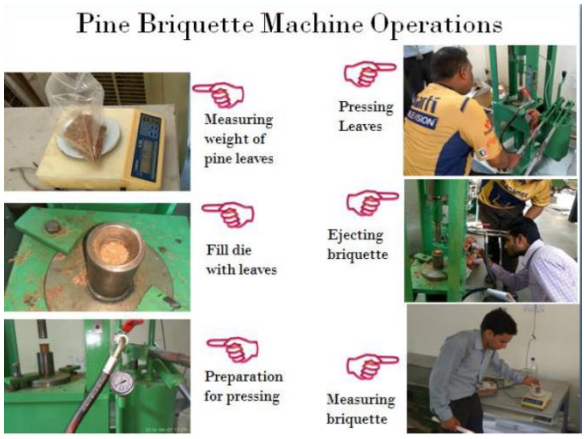

5.4 Briquette density calculation

A laboratory test was conducted for a variety of raw material mixtures and different input pressure applications. The findings of the test are given in Table 1.

Table 1 Pine briquette density analysis

Sr.No	Weight Before pressing (gm)	Weight after pressing (gm)	Compression pressure (PSI)	Ejection pressure (PSI)	Height of the brick (mm)	Time to make one briquette (min)	Compression ratio	Material type
1	14.73	14.41	500	300	31	2	2.1	
2	15.04	14.79	1000	400	23	2	2.9	Powder
3	15.01	14.37	1500	500	20	2	3.3	
1	7.38	7.25	500	300	18	2	3.7	
2	7.02	6.37	1000	400	11	2	6.0	Leaf
3	7.01	6.78	1500	500	10	2	6.7	
1	6.12	5.93	500	300	15	2	4.4	
2	6.07	5.98	1000	300	11	2	6.0	Mixed
3	6.18	5.97	1500	400	9	2	7.4	

Laboratory tests of various briquettes manufactured by this machine show the following results:

- Briquetting is possible with a pressure as low as 500 psi if the raw material is in almost powdered form (leaf size is 1–3 mm)
- As the size of the raw material increases, more pressure is needed to form a briquette
- For the same amount (weight) of raw material the height of the briquette varies from 31 mm to 9 mm i.e. varied density bricks may be manufactured from the same machine
- Average time taken to complete one cycle of briquetting is about 2 minutes
- There is no appreciable loss of weight while compacting the raw material and making a briquette
- Briquetting machine may satisfactorily work for a compression range between 2.1 to 7.4
- For ejecting a briquette, a pressure of 300–400 psi is sufficient.

5.5 Briquette

An actual photograph of pine needle briquettes made by this machine is shown in figure 5.

Figure 5 Pine needle briquettes

As mentioned in Section 5.4, the size of the briquette depends largely on the pressure and compression ratio as exerted by the machine. It is further observed that a 15–20 mm diameter briquette is conveniently made from this design; however, if a larger diameter die is attached to the machine, a much bigger briquette could be easily manufactured. On an average, a briquette of 20 g to 40 g weightis most convenient to manufacture with the least wear and tear of the machine. It was further observed that if the die diameter is larger in size, with the same effort, a bigger bio-briquette could be manufactured easily.

5.6 Barriers

As the machine is manually operated and supposed to work on rough and remote hilly terrain, it is associated with various technological limitations:

- There is a chance of corrosion of the storage tank, piping, cylinder, and piston; hence, the material must be selected carefully.
- Impurities of hydraulic fluid may have a damaging effect on the system.
- Proper sealing should be adopted to avoid the leakage of hydraulic fluid because this is a critical issue.
- The hydraulic fluid must be disposed of properly.
- The structural weight and size of the system is less and therefore, daily working hours on the machine have to be optimized in order to avoid unnecessary maintenance work.
- Some bottlenecks such as piston jam, fluid spray, nut and bolt loosening, briquette sticking to the die, cutter blade misalignment, and tilting of the machine frame may occur during operations. All these problems can be easily handled through minor mechanical interventions.
- Government regulations and policies will always have an impact on the process of bio-briquetting as the raw material used in this machine is treated as a forest produce.

5.7 Enablers

The briquetting machine is designed on a very simple fundamental of hydraulics. The cost of manufacturing a single machine is below USD 1000. This machine could easily be adopted under a social entrepreneurship strategy as the communities and the nearby villagers will obtain good livelihood opportunities from this venture. This machine is completely eco-friendly, and the carbon footprint while operating it is almost zero. In totality, if a complete analysis of this manufacturing process is made, it will certainly lead to a

negative carbon footprint. Moreover, the biggest enabler in this process is the willingness of the local communities. These communities want to reduce the repeated occurrence of forest fires and also wish to have sustainable livelihood options from nearby forest resources.

VI. ACKNOWLEDGMENTS

Attempt to collect dry and fallen pine needles from the hilly terrain and transporting it to the factory site before making the briquettes under a macro-level entrepreneurship program failed. Similarly, a micro-level entrepreneurship approach of pine needle coal-making by carbonizing the dry organic material and mixing it with additives, such as cow dung or molasses, before shaping it into a coal briquette through a motorized machine, could also not achieve success. With these two failed experiments, the problem of forest fires and the disposal of chir pine needles remained unsolved. The third intervention in the form of a manually operated, easily transportable briquetting machine was designed and fabricated, as mentioned in this paper. With this machine, dry biomass is directly compressed to give it a small brick shape. Upgrading raw biomass waste and providing it as a substitute for wood or coal may be useful cooking, industrial furnaces, domestic heating, and other applications.

It is worth mentioning that in a Himalayan state like Uttarakhand, every year, approximately 500,000 tons of dry pine needles fall on the forest floor, and this large mass is unproductively burnt because of the induced forest fires, releasing over a million tons of carbon into the atmosphere. This is clear waste of a useful resource of energy. The process of converting harmful forest bio-residue into a useful resource for energy under grass root-level execution strategy and social entrepreneurship, has great potential to not only provide sustainable livelihood opportunities to the communities, but also to get qualified under the Reduced Emission through Deforestation and Degradation (REDD +) scheme of the UNFCCC (United Nations Framework Convention on Climate Change) by facilitating carbon credits to the state.

This experiment of bio briquetting through a manually driven machine has immense potential to address issues such as climate change, economic gain to villagers, forest improvement, forest fire control, and many other tangible and intangible benefits. National missions on climate change, such as the Green India Mission, and the mission for sustaining the Himalayan region, strongly support such types of activities that address development with sustainability, promote community-based management of ecosystems, provide incentives to communities for protecting and enhancing forest areas, and enhance carbon sinks and ecosystem services; this helps us to view forests as carbon sinks and formulate socially accepted and scientific fire-management strategies for protecting the Himalayas. The evolution of a manually operated bio-briquetting machine, especially for the Himalayan region, is an extremely useful preposition to fulfill any international or national level commitment towards climate change issues

VII. ACKNOWLEDGMENTS

We are highly grateful to Professor Dr. R.P. Saini, Professor AHEC, IIT Roorkee for giving his valuable support in designing and manufacturing of the machine in his departmental laboratory. We are also thankful to the Forest Department and Forest Corporation Uttarakhand state for proving valuable financial help in physically conceptualizing the manually operated bio briquetting machine

VIII. REFERENCES

1. L. O. Adekoya, Investigation into briquetting of sawdust. The Nigerian Engineers. 1989, 24 (3):17-38.

2. J. A.Ajobo, Densification Characteristics of Groundnut Shell. 2014, 2(1):150–54.

3. G. Berndes, M. Hoogwijk, V. D.Broek, The contribution of biomass in the future global energy supply: a review of 17 studies. Biomass and Bio-energy. 2003, 25(1):1–28.

4. A. Bygand, A.Salick, Local Perspectives on a Global Phenomenon—Climate Change in Eastern Tibetan Villages. Global Environmental Change. 2009, 19:156–166.

5. A. Foster, M. Rosenzweig, "Economic Growth and the Rise of Forests", Quarterly Journal of Economics. 2003, 118:601–637.

6. P. D. Grover,S.K.Mishra, Biomass briquetting: Technology and practices. Regional Wood Energy Development Program in Asia. 2011, 46:1–48.

7. J.A.Hughes, The Philosophy of Social Research. Longman Social Research Series 3, 1990.

8. M. Hoogwijk, A.Faaij, B. De Vries, W.Turkenburg, Global potential of biomass for energy from energy crops under four GHG emission scenarios Part B: the economic potential. Biomass & Bio energy.2005b, 29:225-257.

9. S. O. Jekayinfa , V. Scholz, Potential availability of energetically usable crop residues in Nigeria. Energy Sources, 2009, 31(8):687–697.

10. S. O. Jekayinfa, V. Scholz, Laboratory scale preparation of biogas from cassava tubers, cassava peels, and palm kernel oil residues. Energy Sources,2013, 35(21):2022–2032.

11. S. Mani, L.G. Tabil, S.Sokhansanj, Effects of compressive force, particle size and moisture content on mechanical properties of biomass pellets from grasses no title, in biomass and bio-energy heat energy from value-added sawdust briquettes of AlbiziaZygia. Ethiopian Journal of Environmental Studies and Management. 2009, 2(1): 42–49.

12.R.K. Revisiting Shangri-La: Photographing a Century of Environmental and Cultural Change in the Mountains of Southwest China. China Intercontinental Press, Beijing, CN; 2011.

13. M.Nnabuchi, P.Ukpai, Comparative study of biogas production from cow dung, cow pea and cassava peeling using 45 litres biogas digester. PRIME Journal. 2012, 2(3):89–93.

14. J. T.Oladeji, Agricultural and forestry wastes and opportunities for their use as an energy source in Nigeria- an overview. Journal of Chemical Information and Modeling. 2013, 53(4);1689–1699.

15. K.Joshi, V. Sharma, Challenges in Community Based Forest Bio ResidueResource Utilization for Bio

Briquetting in the Western Himalayan Region ofUttarakhand:ARealCaseStudy.Community-basedForestManagementintheSAARC region, 2014, pp 61-68.

16 J.Oladeji, Theoretical aspects of biomass briquetting: A review study. Journal of Energy Technologies and Policy. 2015, 5(3):72–82.

17. S. Pandey, R. P.Dhakal, Pine needles briquettes: A renewable source of energy. IJES. 2013, 3(3):254–258.

18. Personal communications,Kumar Kabra: Owner, Suyasudyog private limited, Kiccha, Uttarakhand. 2014.

19. I. Savolainen, K.Hillebrand, Green house impacts of the use of peat and wood for energy. VTT research notes 1559, Espoo, Finland; 1994.

20. E.Saeidy, Technological fundamentals of briquetting cotton stalks as a bio-fuel. Berlin, Germany: Agricultural Engineering, Faculty of Agriculture and Horticulture, Humboldt University. Ph.D thesis, 2004.

21. J. Salick, Y.P.Yangand, AmendA. Tibetan Land Use and Change in NW Yunnan. Economic Botany. 2005, 59:312–325.

22. S.Solomon, D. Qin, Manning M, Chen Z, et al. Climate Change 2007: The Physical Science Basis: Working Group I Contribution to the Fourth Assessment Report of the Intergovernmental Panel on Climate Change. Cambridge University Press. Cambridge, UK; 2007.

23. E.Smeets, A. Faaij, Lewandowski I, Turkenburg W. A quick scan of global bio-energy potentials to 2050. Progress in Energy and Combustion Science. 2007. 33(1):56–106.

24. S. K.Singh, Annual report 2009-10. Uttarakhand Forestry Research Institute. Haldwani,Nainital; 2010.

25. R. Sathre, L.Gustavsson, Time–dependent climate benefits of using forest residues to substitute fossil fuels. Biomass and Bio energy.2011, 35:2506-2516.

26. J. Salick, R. Moseley, KhawaKarpo, Tradition Tibetanknowledge and conservation. Monographs in systematic botany from the Missouri botanical garden. Missouri Botanical Garden Press. St. Louis, MO;2012.

27. J. Salick , A. Bygand, K. .Bauer, Contemporary Tibetan Cosmology of Climate Change. Nature and Culture.2012, 6:447–476.

28. Uttarakhand Forest Department Order, Pine needles for bio briquetting. PCCF Letter no 1323/24-1(8) dated 18-02-2010.

29.Uttarakhand Renewable Energy Development Agency, Pine needle based biomass gasifier: A pilot project, 2010

30. Zoological Survey of India, ZSI Unravels 778 new faunal species: K Venkataraman. The Economic Times; Nov 15, 2015.

Can there be a universal phase locked loop?

Reyes Sánchez-Herrera
Dpto. Electric Engineering
University of Huelva
Huelva, Spain
reyes.sanchez@die.uhu.es

Gabriel Gómez
Dpto. Electronic Engineering
University of Huelva Huelva,
Spain
gabriel.gomez936@alu.uhu.es

Jose M Andújar
Dpto. Electronic Engineering
University of Huelva Huelva,
Spain
andujar@uhu.es

Marco Márquez
Dpto. Electronic Engineering
University of Huelva
Huelva, Spain
marcoa@pi.uhu.es

Andrés Mejías
Dpto. Electronic Engineering
University of Huelva
Huelva, Spain
mjias@uhu.es

Abstract

This paper aims to highlight the drawbacks of the most common phase locked loop (PLL) circuits to operate as universal PLLs. The phase locked loop tracks the phase of an input signal. These devices are necessary in different disciplines for which the input signal conditions are very different. In fact, they are used in synchronization to the grid waveforms, in the communications applications as frequency modulation or amplitude modulation, and in the measurement of the motors speed, among others. For each discipline, a different group of PLLs is used. Among all of them, the most appropriate to be used in several disciplines seems to be the designed to synchronize the grid. So, they are the chosen to be studied and test their behavior in different applications to find out the PLL which is useful in any application and which achieves to track the phase/frequency signal whose value is initially unknown. I. e. the universal PLL, useful in all the considered applications.

Thus, the most used PLL circuits to synchronize to the grid waveforms, able to work with an unknown initial value of the frequency, have been chosen from the technical literature. I.e. the Synchronous Reference Frame (SRF-PLL), the Second-Order Generalized Integrator (SOGI-PLL), and the Enhanced PLL (EPLL). Their performance has been studied in the monitoring of input signals with conditions different from those presented by the grid voltage, in synchronization. These different conditions are those that occur, for example, in communications applications. The results obtained, prove that the assessed PLLs present a good behavior if the filters and controlled involved in them are tunned to the input signal frequency. In this case, the PLLs provide a signal which tracks the input signal frequency. It could be thought they are universal PLL. However, if the value of the frequency is unknown, the tunning has to be carried out to an estimated frequency, different from the actual one. The results obtained in this paper prove that, in these new conditions, the assessed PLLs do not achieve to track the input signal frequency. Thus, the PLLs analyzed in this paper and carefully chosen are not able to carry out frequency sweeps. Therefore, any of them can be considered as the universal PLL.

Keywords: *phase locked loop, frequency locked loop, modulated frequency, distortion*

DAI : ***https://sci-index.com/DAI/2021.99101/IEECP/14526837***

A low-budget mathematically scalable sensor solution to reduce energy consumption in buildings.

Robinson Adrián Barrazueta Paccha
Department of Computer Science and Electronics
Universidad Técnica Particular de Loja
Loja, Ecuador
rabarrazueta@utpl.edu.ec

José Raúl Castro Mendieta
Department of Computer Science and Electronics
Universidad Técnica Particular de Loja
Loja, Ecuador
jrcastro@utpl.edu.ec

Abstract

Reducing the consumption of electrical equipment such as air conditioning and lighting in buildings is a challenge around the world. Sensor-based control systems supported by intelligent, adaptive mathematical algorithms can control electrical equipment optimally to save energy and maintain user satisfaction. The system combines PIR sensors, low-consumption temperature and lighting sensors that analyze the characteristics of the environment and allow efficient control decisions to be made in electrical equipment such as air conditioning and lighting system present in the building. This paper presents the design and implementation of the proposed system in a real room and the analysis of the system implementation in a simulation for a building. The simulations of total energy consumption during a period of one year of an occupied building were carried out to verify the performance and energy saving in some scenarios of climatic conditions. The proposed system reduces total energy consumption by 10%.

Keywords: wireless sensor networks, power management, energy efficiency.

I. INTRODUCTION

Energy efficiency in Latin American countries is a challenge and a long-term goal to achieve according to CEPAL, as detailed in [1]. Although there are sectors (such as industry) where energy savings are more noticeable, it is possible to implement these strategies in a house, a building, an office, among many other scenarios; the more environments that can be included, the energy consumption will be much lower. According to ECLAC reports, certain programs and policies are carried out in Ecuador to improve energy efficiency, such as: Renova Refrigeradores Program and the Energy Efficiency Plan for cooking and water heating. However, there is no policy to improve energy efficiency in lighting or air conditioning systems, since it is not considered a high consumption sector, such as transportation systems and industry, as explained in [2].

Under this premise, this paper presents the design of a space occupancy measurement system for control of energy consumption in a workspace. The system is based on the use of occupancy and vacancy sensors and environmental variables meters. In this way, it seeks to monitor the use of devices connected to the system.

The objectives to be achieved in this project respond to the proposal of a solution for the reduction of energy consumption of electrical equipment in buildings, through the study of people counting technologies and the design of a system for this purpose. From this information, it is possible to define the behavior of electrical equipment in this space, and provide a solution to optimize the use of electricity.

Based on the information collected by low-cost sensors that analyze the temperature and illumination of a room, which are environmental variables of the area, and the occupancy of the place, it is possible to obtain certain data that, after going through various mathematical methods that allow converting these values into useful information, will be useful for the automatic control of the devices that make up the air conditioning and lighting systems.

This document is structured as described below: Section II presents the analysis of technologies for estimating the occupancy of a system, and shows which one is the optimal technology for the system to be developed. Section III develops the system (hardware and software) for people counting to implement and its application in energy monitoring. Section IV shows the establishment of operating and control thresholds of the devices that make up the air conditioning and lighting systems, finally, in section V, present the results of the system, together with the simulations performed.

II. LITERATURE ANALYSIS

This section shows the four main technologies analyzed for the development of the electronic people counting and control system for air conditioning and lighting devices.

A. Open Computer Vision (OpenCV)

OpenCV, as described in [3], is an open source computer vision library, which allows the counting and tracking of people through an algorithm based on centroids analysis. In [4] it is shown that, by delimiting a person, establishing his location on a plane and analyzing the Euclidean distance of the person when he is moving, it is possible to identify the direction of the person, and the number of people that are interacting in that moment in that defined space.

B. Passive Infrared Sensor (PIR)

The PIR sensor is a device that detects and measures infrared radiation to analyze whether there is movement in the area it is analyzing. This sensor does not emit any type of radiation (hence its name of passive), but rather analyzes the radiation already existing in the environment and detects disturbances, as explained in [5]. Although this technology can be used as a complement to more robust systems, such as video surveillance systems, as observed in

IEECP 21, July 29-30, 2021, Silicon Valley, San Francisco, CA – USA

DAI : *https://sci-index.com/DAI/2021.99101/IEECP/14526846*

[6], the idea of using it as the main detection system for people is not ruled out.

C. Analysis of WiFi signal disturbances

As discussed in [7], it is possible to develop a people counting system by using a receiver and a transmitter of Wi-Fi signals at two defined points, knowing that the passage of people between these devices generates disturbances between the signals received and transmitted. By means of the received signal intensity indicator and an algorithm based on the Kullback-Leibler divergence, it is possible to know the estimated number of people in the studied area.

D. Sensors of environmental variables

Certain characteristics of the studied area, such as temperature, lighting, CO2, among others, provide information not only on the occupation or vacancy of a room, but also on the environment within it, data that would allow the air conditioning systems to and lighting are in operation according to the needs of the room at a given time, as discussed in [8].

III. ELECTRONIC SYSTEM DESIGN

The system designed for this project can be divided into two main parts: mathematical design and hardware and programming design.

A. Mathematical design

The mathematical design of the system is based on the work of [9], which carried out the implementation of two PIR sensors in each door of each room on a floor of a building. The distribution of sensors is shown in figure 1, and equation (1) shows the analysis of the entrance and exit sensors (i and j respectively), where the action of entering or leaving a room must be carried out in an equal time or less than Δt which for this project was defined in 3s.

$$S_{i,j} = \{ x_i(t_c), x_j(|t - t_c| \leq \Delta t) \} \quad (1)$$

To know the number of people in the room at a given time, it is necessary to add the content of the matrix shown in equation (2), which stores the values of the interactions in equation (1), knowing that when a person enters to the room, a value of +1 is stored, and when a person leaves, a value of -1 is stored.

$$S = \{ x_i(t_i),\ x_{i+1}(t_{i+1}),\ x_{i+2}(t_{i+2}), \dots, x_n(t_n) \} \quad (2)$$

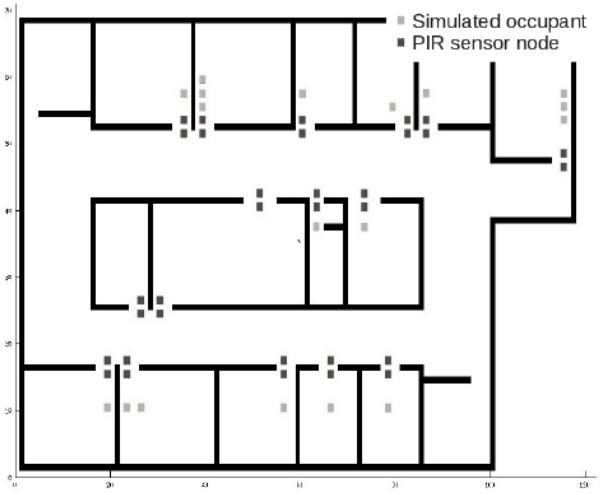

Figure 1. Initial state of the people counting experiment using PIR sensors. Adapted from Wahl et al., 2012.

B. Hardware and Programming design

The hardware used for the development of the system is composed of the HC-SR501 PIR sensor and a Raspberry Pi 4 Model B. Two sensors were used, one outside the room and the other inside, both connected to the Raspberry that analyzes the signals sent by them. It is possible to use the HC-SR501 sensor autonomously, that is, it does not need external hardware such as the Raspberry for its operation, but its use is recommended not only for powering the sensor, but also for storing the counting data of the room, for further analysis. Figure 2 shows the flowchart of the system's operation with the two sensors implemented, and figure 3 shows the connection of the sensors to the Raspberry.

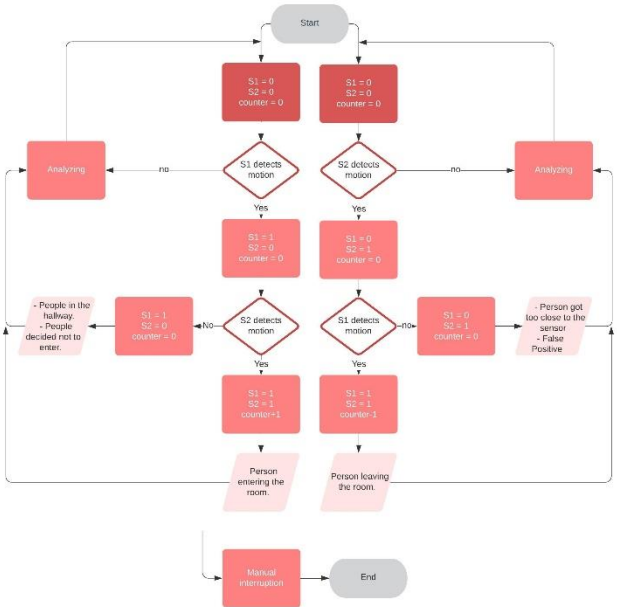

Figure 2. Flowchart of electronic people counting system using PIR sensors. Source: Author.

Figure 3. PIR sensors connected to Raspberry Pi 4. Source: Author.

IV. ANALYSIS OF ENVIROMENTAL VARIABLES

In order to analyze the environmental characteristics of the monitored room, sensors were used to analyze the temperature and lighting of the place. This, combined with the presence or vacancy status of people in the area, allow obtaining information that the air conditioning and lighting systems use to improve their energy consumption.

A. Performance standards

In order for the air conditioning and lighting systems to operate under the same parameters and to provide thermal and lighting comfort to people, several documents have been analyzed which describe the optimum temperature and lighting for office work, which are described in table 1 and 2.

Table 1. Recommended temperature levels in offices. Adapted from NTP 501, Calleja, 1998.

TYPE OF WORK	OPTIMAL TEMPERATURE (in °C)	HUMIDITY LEVEL	AIR SPEED (in m/s)
Intellectual work in seated position	18º to 24º	40% to 70%	0.1
Work in standing position	17º to 22º	40% to 70%	0.1 to 0.2
Hard work	15º a 21º	30% to 65%	0.4 to 0.5
Very hard work	12º to 18º	20% to 60%	1.0 to 1.5

Table 2. Recommended lighting levels in offices. Adapted from ISO 8995 - 2002 standard.

TYPE OF ACTIVITY PERFORMED	LIGHTING MAINTAINED (*E*m) in lx
Archiving, copying, circulation.	300
Writing, typing, reading, data processing.	500
Technical Drawing	750
CAD workstation	500
Conference and meeting room	500
Reception bureau	300
Archives	200

B. Temperature monitoring system

The room's thermal measurement system used a DS18B20 sensor and the Raspberry Pi 4 mentioned in the previous section. The program was designed in Python 3, using the w1thermsensor library, thanks to the 1-Wire protocol used by the sensor, which allows data to be sent to the Raspberry using a single physical communication pin. Figure 4 shows the flowchart of the data receiving and sending process.

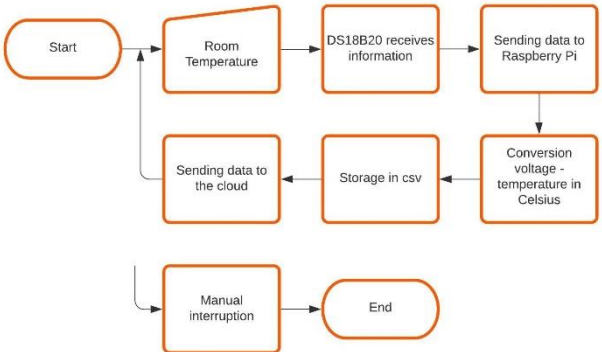

Figure 4. Flowchart of the electronic temperature monitoring system using the DS18B20 sensor. Source: Author.

The values obtained for temperature and lighting in the room were stored in a csv file for mathematical processing, which will be discussed later.

C. Lighting monitoring system

The system that monitored the lighting in the room is composed of a BH1750 sensor and the Raspberry Pi 4. The program was designed in Python 3 using the smbus library. The sensor operates using the I2C protocol, which requires two physical pins for communication. The temperature and lighting sensors receive a 3.3V power supply from the Raspberry and the analysis of the variables is carried out every 2 minutes continuously, thanks to the crontab tool. In this way, by not continuously analyzing the room, the sensors can be kept in a low power consumption state when the information is not required. Figure 5 shows the flowchart of the process for obtaining lighting information, and Figure 6, the physical connection of sensors to the Raspberry Pi 4.

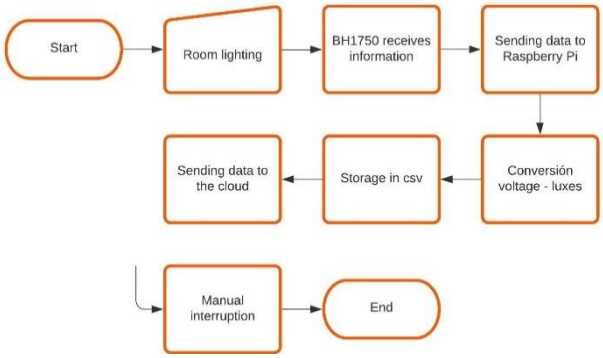

Figure 5. Flowchart of the electronic lighting monitoring system using the BH1750 sensor. Source: Author.

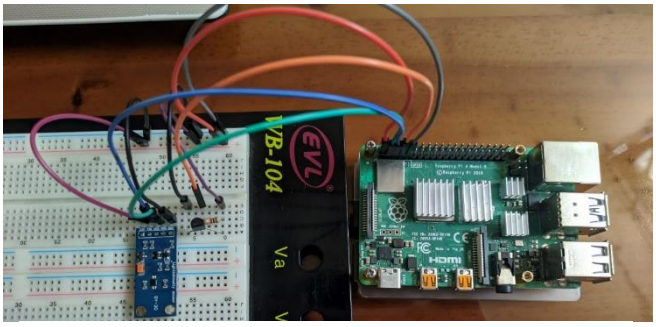

Figure 6. DB18B20 and BH1750 sensors connected to the Raspberry Pi 4. Source: Author.

D. Sensors of environmental variables

The experimental data obtained through the sensors were processed using mathematical modeling techniques (least squares) and grouping algorithms (K Means), in order to know the behavior of these variables and improve the accuracy of the data that will serve to control the air conditioning and lighting systems.

The least squares technique allows obtaining a polynomial equation based on experimental data, looking for the best possible fit (defined by the user) to the information to be modeled. In [10] the procedure to follow when using this method is detailed, whose main objective, after having defined the degree of the equation, is to find the coefficients corresponding to the independent variable. The equation obtained will have a level of error depending on the degree chosen; the lower the degree, the greater the error in the equation.

The K Means clustering algorithm differentiates elements of a group of data according to their characteristics, and define an average value to represent. This is done by measuring Euclidean distances and

defining a number of clusters, which will be the number of sets into which the data will be divided. The work of [11] shows that, in order to correctly define the number of clusters that the data require, techniques such as the "Jambú elbow" can be applied, in order to find the point where there are no noticeable changes between the sets already defined.

Thanks to the numpy and sklearn.cluster Python libraries, it is possible to process the sensor data stored in csv format directly from the Raspberry Pi. Through these techniques it will be possible to define the temperature and lighting level in the room with greater accuracy, in addition to contributing to the establishment of operating thresholds for air conditioning and lighting devices.

V. RESULTS OBTAINED

To corroborate the operation of the system, experimental tests and energy consumption simulations were carried out.

A. Results of the people counting system

The two PIR sensors were installed in a room in a residential building. Two hundred experiments were carried out, half oriented to the entrance to the room and the others, to the exit. Table 3 shows the results obtained, where the use of the HC-SR501 sensor obtains an average accuracy level of about 80%. Considering that the sensor used is one of the cheapest on the market and that high precision is not required to meet the objectives of this project, the use of this sensor is ideal.

Table 3. Results obtained from the people counting system using PIR sensors. Source: Author.

ACTION	PERCENTAGE
Entry to the room	84%
Exit from room	74%
False positives	10%
Average level of accuracy	79%

B. Results of the lighting monitoring system

The lighting values in the room were obtained experimentally in four days, placing the BH1750 sensor in different places each day; the same procedure was carried out for temperature measurement. The behavior of the lighting in the room is reflected in figure 7, in addition to the cubic equation generated by the least squares technique, which models the behavior of this variable to send more precise data to the lighting device control system.

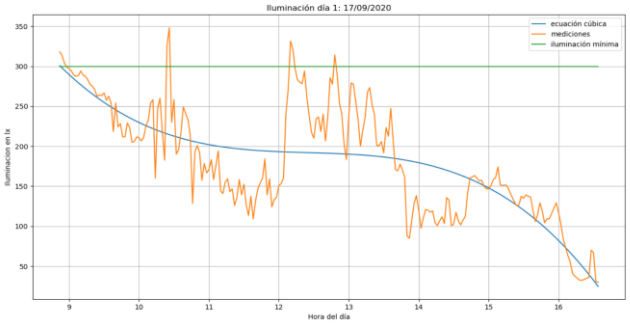

Figure 7. Graph of lighting behavior in the room with respect to the mathematically calculated values. Source: Author.

Equations (3), (4), (5) and (6) show the behavior of the room lighting in the working area, the most illuminated area, the least illuminated area and the center of the room, respectively. The graph shown in figure 7 corresponds to the values in the work zone. The units of the results are displayed in lux, a measure of lighting with respect to the area in m2 of the room.

$$-2.211x^3 + 82.43x^2 - 1027x + 4467 \quad (3)$$

$$0.6903x^3 - 31.12x^2 + 445.6x - 1962 \quad (4)$$

$$9.903x^3 - 471.8x^2 + 6926x - 28997.67 \quad (5)$$

$$-9.757x^3 - 366.9x^2 + 4552x - 19677.02 \quad (6)$$

For the analysis of the lighting data using the K Means clustering technique, it was expected to obtain a differentiation of lighting information with respect to the time of day, as will be observed later in the clustering of temperature data. However, since there is a great dispersion between the data obtained (because the information obtained was from natural light), the information of the clusters generated as seen in figure 8 is not useful for the purposes of this analysis.

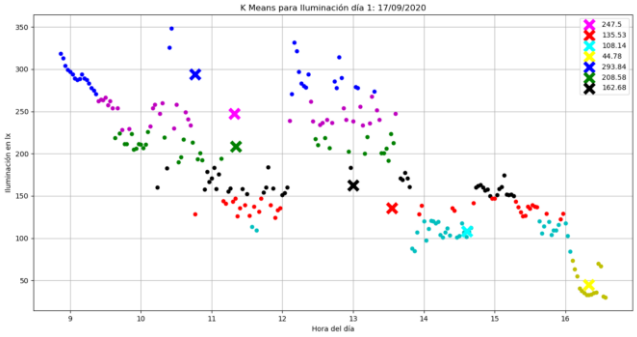

Figure 8. Clustering analysis of room lighting using K Means. Source: Author.

C. Results of the temperature monitoring system

The temperature values in the room were obtained experimentally in four days, following the same process explained for lighting monitoring, in this case using the DS18B20 sensor. Figure 9 shows the results obtained in the room, together with the graph of the cubic equation generated by least squares.

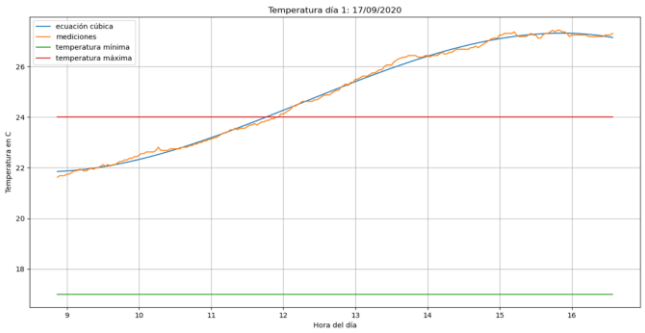

Figure 9. Graph of room temperature behavior with respect to mathematically calculated values. Source: Author.

Equations (7), (8), (9) and (10) show the behavior of the temperature in the room, in the same areas described for the previous lighting equations. Figure 9 shows the temperature values in the working area. Results units are displayed in Celsius.

$$-0.02967x^3 + 1.092x^2 - 12.25x + 65.31 \quad (7)$$

$$-0.01268x^3 + 0.4995x^2 - 6.018x + 44.13 \quad (8)$$

$$-0.004903x^3 + 0.1637x^2 - 1.3x + 23.5 \quad (9)$$

$$-0.008017x^3 + 0.285x^2 - 2.825x + 28.65 \quad (10)$$

In addition to the least squares analysis, the use of the K Means algorithm is proposed, in order to know the average temperature values that will be sent to the temperature device control system in a period of time. It is observed in figure 10 that the variation between experimental values and those calculated mathematically is reduced for this variable, contrary to what happens with the lighting data, for which the clustering analysis is effective only for the temperature values of the room.

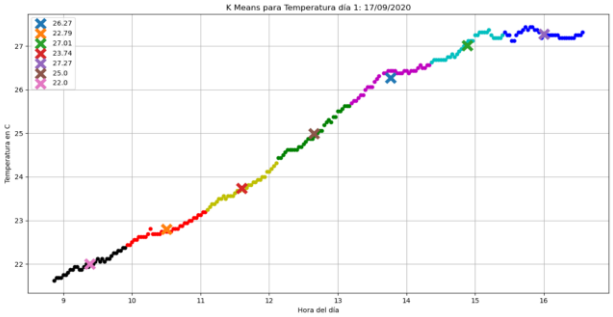

Figure 10. Clustering analysis of room temperature using K Means. Source: Author.

Once the clusters per working hour of the temperature data have been obtained, it is possible to perform the same procedure for the data mathematically calculated by means of least squares, as shown in table 4. Through this, an average value can be obtained between the two sources of information, which will be the data sent to the air conditioning control system to make decisions for its operation.

Table 4. Comparison between experimental and mathematically calculated clusters. Source: Author.

# Clúster (time of day)	Experimental Clusters	Clusters from equation	Average
1 (9–10 am)	22.00	22.05	22.03
2 (10–11 am)	22.79	22.81	22.80
3 (11 am–12 pm)	23.74	23.87	23.81
4 (12–13 pm)	25.02	25.01	25.02
5 (13–14 pm)	26.29	26.11	26.20
6 (14–15 pm)	27.02	26.97	27.00
7 (15–16 pm)	27.27	27.27	27.27

D. Sensors of environmental variables

In order to verify the effectiveness of energy saving through the implementation of this system, a simulation was developed using the OpenStudio program, software based on EnergyPlus, to analyze the consumption patterns of a building and observe the percentage of reduction in energy consumption implemented improvements in air conditioning and lighting systems.

Three simulations were carried out, the first with typical electrical energy consumption values, given by the ANSI/ASHRAE 189.1-2009 standard, as detailed in [12]. The second applies improvements to lighting systems, and the third applies improvements to air conditioning and lighting systems.

The improvements were applied in the "Hours" tab, where you can modify the times and operating values of lighting and air conditioning in the rooms of a building. Thanks to the information obtained by the environmental sensors, it is possible to know the state of the room in a period of time and define the moments in which these devices must operate. The operating levels are defined by the mathematical values discussed in the previous section, so that each device knows how to operate in response to the state of the current environment.

Table 5 shows the level of energy consumption of a building without the application of any improvement in energy consumption, and in contrast, the values of energy consumption with improvements implemented are shown in table 6. The level of savings is 9.95% compared to the building without improvements, which demonstrates the effectiveness of the designed system, even though OpenStudio cannot model the people counting system. If the occupancy level of the room was considered, the energy savings would be even greater.

Table 5. Results obtained from the simulation of energy consumption of a building without implementation of improvements. Source: Author.

Parameters	Value
Total net building area	132 m^2
Total annual energy consumption	5247 kWh
Energy consumption per m^2	39.66 kWh/m^2
Heating energy consumption	611 kWh
Cooling energy consumption	1783 kWh
Lightning energy consumption	1081 kWh
Energy consumption for electronic devices	1772 kWh

Table 6. Results obtained from the simulation of energy consumption of a building with implementation of improvements. Source: Author.

Parameters	Value
Total net building area	132 m^2
Total annual energy consumption	4725 kWh
Energy consumption per m^2	35.71 kWh/m^2
Heating energy consumption	742 kWh
Cooling energy consumption	1450 kWh
Lightning energy consumption	761 kWh
Energy consumption for electronic devices	1772 kWh

VI. CONCLUSIONS

Thanks to the results of the mathematical processing of the environmental variables data and the simulation performed in OpenStudio, it can be determined that the main objective of this work, defined as the reduction of energy consumption in an office, which was the case study used in the simulation, by 10%, was achieved. This model can be replicated in various scenarios, such as homes, hotels, restaurants, among others.

The development of the people counting system explained in this paper allows to know the occupation or vacancy of a room, in order to determine whether the air conditioning and lighting systems

should operate or not. If required, the devices will operate based on operating standards, to maintain thermal and lighting comfort, and based on information from the environment captured by environmental variables sensors, to reduce unnecessary energy consumption.

The mathematical processing used in the experimental data makes it possible to provide a certain degree of intelligence to the control system of air conditioning and lighting devices. Although the values provided by the sensors are already useful for decision-making, mathematical analysis allows studying the behavior of these variables in the room and defining the correct operating values and in the correct time periods. In addition, this information can be recorded for future review by users, as information about the state of the place in terms of temperature and lighting.

The use of mathematical methods of clustering and equation modeling are some of the many techniques that can be used to treat the data obtained from the sensors. Procedures such as data mining would allow an in-depth information analysis, which combined with more advanced hardware accuracy would make the percentage of savings and the operating thresholds of the devices more accurate and efficient.

VII. RECOMMENDATIONS

Based on the conclusions obtained from this work, several recommendations are made that, in the long term, could improve energy efficiency in a building. The proposed lighting improvements could be implemented when a room works with luminaires that operate independently of each other. Currently, these types of systems are not regularly found in buildings in Ecuador, so migration to autonomous lighting systems is recommended.

In this project we work with obtaining information about lighting and room temperature, for a subsequent mathematical analysis of the data. To improve the accuracy of the data obtained, it is recommended to carry out the mathematical processing at the same time as the data collection, a process that the Raspberry Pi used can carry out without any problem.

The data obtained by the sensors in this project does not reach 100% accuracy due to the hardware used, low cost devices and for experimental purposes. In order to achieve high performance in the system, it is recommended to use industrial-type devices, such as the Panasonic PIR sensor EKMB1101112, a sensor used in [9] that provides results with high accuracy.

VIII. REFERENCES

[1] B. Lapillonne, “Monitoreando la eficiencia energética en América Latina,” 2016.

[2] S. Espinoza, A. Orbe, F. Izurieta, and K. Arias, “Informe Nacional de Monitoreo de la Eficiencia Energética de la República del Ecuador, 2016,” 2016.

[3] “OpenCV.” [Online]. Available: https://opencv.org/. [Accessed: 18-Jun-2020].

[4] A. Rosebrock, “OpenCV People Counter,” *PyImageSearch*, 13-Aug-2018. [Online]. Available: https://www.pyimagesearch.com/2018/08/13/opencv-people-counter/. [Accessed: 18-Jun-2020].

[5] L. Llamas, “Detector de movimiento con Arduino y sensor PIR,” 24-Jul-2015. [Online]. Available: https://www.luisllamas.es/detector-de-movimiento-con-arduino-y-sensor-pir/. [Accessed: 19-Jun-2020].

[6] N. Surantha and W. R. Wicaksono, “Design of Smart Home Security System using Object Recognition and PIR Sensor,” in *Procedia Computer Science*, 2018, vol. 135, pp. 465–472.

[7] S. Depatla, A. Muralidharan, and Y. Mostofi, “Occupancy Estimation Using Only WiFi Power Measurements,” *IEEE J. Sel. Areas Commun.*, vol. 33, no. 7, pp. 1381–1393, Jul. 2015.

[8] C. Lino Ramirez, M. Zamudio Rodriguez V., V. del R. Ochoa López, and G. Muñoz López, “Wireless sensor networks applications for monitoring environmental variables using evolutionary algorithms,” in *Intelligent Data Sensing and Processing for Health and Well-being Applications*, Elsevier, 2018, pp. 257–281.

[9] F. Wahl, M. Milenkovic, and O. Amft, “A distributed PIR-based approach for estimating people count in office environments,” in *Proceedings - 15th IEEE International Conference on Computational Science and Engineering, CSE 2012 and 10th IEEE/IFIP International Conference on Embedded and Ubiquitous Computing, EUC 2012*, 2012, pp. 640–647.

[10] S. J. Miller, “The Method of Least Squares,” Williamstown, 2006.

[11] G. Medina Veloz, F. J. Luna Rosas, J. F. Tavarez Avendaño, and R. U. Narvaez Murillo, “Calibración y selección del modelo de aprendizaje no supervisado K-Medias, de una encuesta sobre factores de riesgo en el consumo de drogas entre estudiantes,” 2016.

[12] N. Long, E. Bonnema, K. Field, and P. Torcellini, “Evaluation of ANSI/ASHRAE/USGBC/IES Standard 189.1-2009,” Springfield, Jul. 2010.

Methane Reforming with Sulfur Dioxide on $Cr_2O_3/\gamma-Al_2O_3$

Sabrina Noemí Hernández Guiance
Universidad del Centro Educativo Latinoamericano.
Av. Pellegrini 1332 CP 2000 Rosario, Argentina.
rosse_1986@hotmail.com

Ignacio Daniel Coria
Universidad del Centro Educativo Latinoamericano.
Av. Pellegrini 1332 CP 2000 Rosario, Argentina.
dcoria@ucel.edu.ar

Isabel María Irurzun
CCT La Plata CONICET. Instituto de Investigaciones Fisicoquímicas Teóricas y Aplicadas (INIFTA), Facultad de Ciencias Exactas, Universidad Nacional de La Plata.
Diagonal 113 y 64, CP (1900), La Plata, Argentina.
i_irurzun@hotmail.com

Abstract

In this work we present a study on the methane oxidation reaction on Cr_2O_3 in the presence of sulfur dioxide using both infrared spectroscopy and simulations based on the density functional theory. The purpose of the work is to know the reasons why sulfur dioxide decreases the activation energy of the methane oxidation reaction. We found that sulfur dioxide promotes oxygen dissociation through the formation of sulfite species. Dissociated oxygen favors the dehydrogenation of methane, the formation of methoxy species, formaldehyde, dioxymethylene, and methanol.

Keywords: methane reforming, methanol, formaldehyde.

IEECP'21, July 29-30, 2021, Silicon Valley, San Francisco, CA – USA

DAI : https://sci-index.com/DAI/2021.99101/IEECP/14737989

I. INTRODUCTION

Methane reforming is a method for producing syngas (hydrogen and carbon monoxide) by the reaction of hydrocarbons with water. The main purpose of this technology is hydrogen production. The reaction is represented by

$$CH_4 + H_2O \rightleftharpoons CO + 3\ H_2 \qquad \text{(Eq. 1)}$$

Autothermal reforming (ATR) uses oxygen and carbon dioxide or steam in a reaction with methane to form syngas.
The reactions can be described by the following equations, using CO_2:

$$2\ CH_4 + O_2 + CO_2 \rightarrow 3\ H_2 + 3\ CO + H_2O \qquad \text{(Eq. 2)}$$

and using steam:

$$4\ CH_4 + O_2 + 2\ H_2O \rightarrow 10\ H_2 + 4\ CO \qquad \text{(Eq. 3)}$$

CH_4 is also one of the main greenhouse gases. To reduce its emission to the atmosphere, it can be retained by adsorption before it is released by industrial chimneys. O_2 is present in flue gases, but in the absence of a suitable catalyst, it does not react with CH_4.
CH_4 oxidation was previously studied on PdO(101), RuO_2(110) and IrO_2(110), Ni(111) and MgO(001) on Ni4 catalysts.
A major difficulty associated with the production of syngas is that the sulfur compounds in the fuel poison certain catalysts, making it difficult to operate this type of system with regular gasoline. We have carried out studies on various oxides, with emphasis on the oxidation of CH_4 and the reduction reactions of SO_2 [1, 6]. It has been concluded that the alumina-supported chromium oxide catalyst (Cr_2O_3 / Al_2O_3) is the most efficient for the adsorption of these greenhouse gases, because it is not deactivated by the presence of acid gases. In [4] we studied the oxidation of CH_4 on Cr_2O_3/γ-Al_2O_3 and experimentally determined an activation energy of the reaction (Ea = 0.57 eV). The SO_2 reduces the activation energy to Ea = 0.31 eV, the lowest value found so far to our knowledge. For example, the catalytic oxidation of methane in the presence and absence of SO_2 was investigated on palladium catalysts supported on Al_2O_3

and CeO_2/Al_2O_3 washcoats. The activation energies in the absence of SO_2 were 0.4 +/- 0.1 eV and 0:6+/- 0.15 eV for the 3 wt% Pd/Al2O3 and the 3 wt% Pd/12 wt% CeO_2/Al_2O_3 catalysts respectively.
In this work we carried out a combined FTIR + DFT study of the reaction

$$CH_4+SO_2+O_2 \rightarrow S^0+CO_2+2H_2O \text{ on } Cr_2O_3/\gamma\text{-}Al_2O_3 \qquad \text{(Eq. 4)}$$

in order to unveil its kinetic mechanism.
This work continues previous research on the oxidation of CH_4 with oxygen on Cr_2O_3/γ-Al_2O_3 [6]. The main purpose is to reveal the causes for the reduction of the activation energy mentioned above.
Additionally, we found the formation of intermediate species of industrial interest, such as methanol and formaldehyde.

II. EXPERIMENTAL WORK

A. Materials and Setup

Methane oxidation on Cr_2O_3/γ-Al_2O_3 and in the presence of SO_2 (Eq. 4) was studied on a fixed-bed reactor consisting of a quartz column of 0.6 cm diameter and 110 cm length placed in an adjustable temperature oven (Fig. 1). Reaction gases were provided by LINDE: SO_2 composition > 99:98%, CH_4 composition > 93%, O_2 composition > 99:5%. They were introduced in the reactor at a constant flow rate and a concentration of 10 ppm in N_2. In one experiment, a catalyst sample was exposed to the reaction gases at an initial temperature of 293 K, until the concentration of the produced CO_2 reached constant values. Then, the temperature was increased in steps until reaching 573 K. Each catalyst sample was subjected to three of these experiments. Finally, a Fourier transform infrared (FTIR) spectroscopic study was performed on each sample with Vertex 70 equipment from 2008.

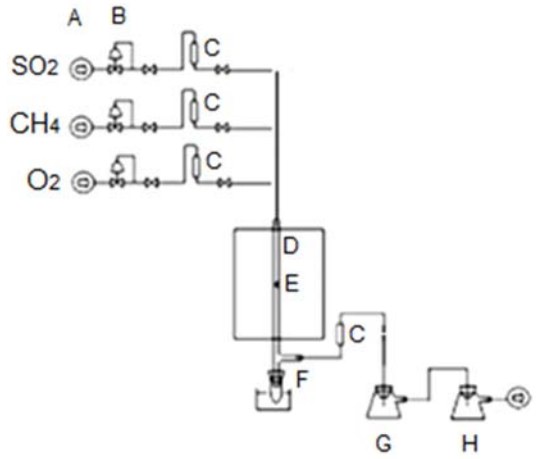

Figure 1. Experimental setup used in the present work. (A) Gas suppliers, (B) safety valves, (C) rotameters, (D) electrically heated oven, (E) reactor (quartz column), (F) sulfur trap, (G) bubbler with distilled water, (H) bubbler with a dilute sodium hydroxide solution.

Results

Figure 2 shows an FTIR spectrum obtained in this work. We identified bands at 2960 cm^{-1} and 2854 cm^{-1}, corresponding to the stretching modes of CH_3 and CH_2 groups respectively. There was also an O-H bond stretching band at 3446-3465 cm^{-1}. Stretching frequencies of adsorbed O-S-O bond were at 561-567 cm^{-1}.
Finally, we found bands at 1126 cm^{-1} and 1655 cm^{-1}. According to our DFT calculations we related them to formaldehyde adsorbed on the surface.

III. THEORETICAL WORK

A. Computational Calculations

First-principles calculations were performed using DFT+U as implemented in the Vienna Ab initio Simulation Package (VASP) code. The Kohn-Sham equations were solved using the projector augmented wave (PAW) method and a plane-wave base set that includes plane waves up to 400 eV. The DFT+ U method was used with values J = 1 and U = 5. The calculations were performed using pseudopotentials based on the generalized gradient approximation (GGA+U). The convergence of each calculation was achieved when the forces on the ions were less than 0.03 eV / Å. The periodic boundary conditions applied in all three perpendicular directions. The Hessian matrix of second derivatives was determined for basal structures within the harmonic approximation

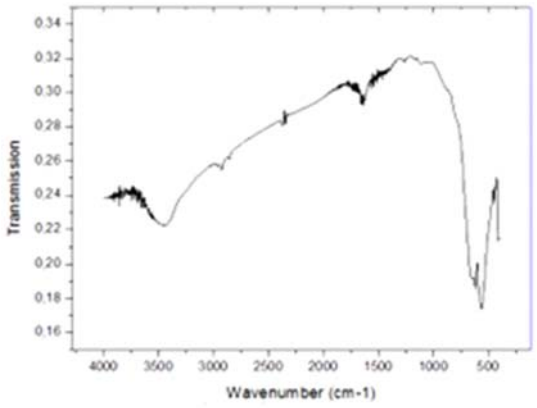

Figure 2. Infrared spectra of a sample used in this work.

by finite two-sided differences, using a displacement step of 0.01 Å. The adsorbed atoms were displaced in the calculations, and the diagonalization of the dynamic matrix produced the harmonic frequencies.
The Cr_2O_3(0001) surface was modeled as a rhomboid supercell with an edge size of 4.954 Å and 20 Å high. Each substrate layer was composed of one chromium atom, three oxygen atoms and one chromium atom, and was 2.263 Å thick (Fig. 3).
The face (0001) was selected because in its natural state, Cr_2O_3 has this type of structure in 97.20% of its volume, which is maintained up to temperatures of approximately 973 K (see Fig. 4).

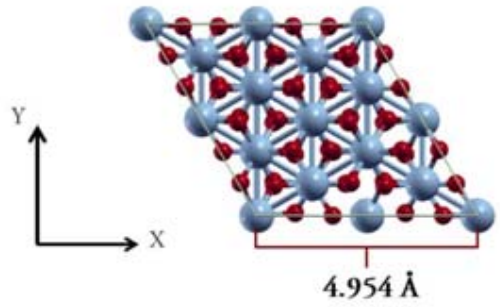

Figure 3. Cr_2O_3(0001) supercell [3]. Red: oxygen atoms, gray: chromium atoms.

The first Brillouin zone was sampled with a (331) gamma point centered mesh, and only the gamma point was used for the cubic supercell used for the optimization of isolated molecules.

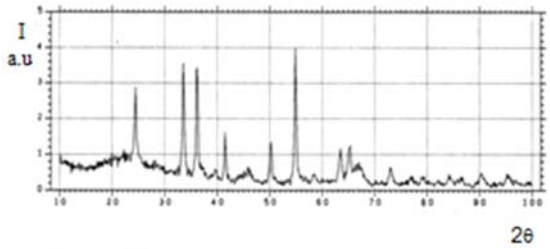

Figure 4. X-ray spectrum of a Cr_2O_3 sample calcined at 973 K.

The adsorption energy of each adsorbate molecule was calculated as

$Ea = E(Adsorbate/Cr_2O_3)-E(Adsorbate)-E(Cr_2O_3)$

The first term is the energy of the optimized configuration for the relaxed adsorbate molecule bonded to the clean surface. The second term is the energy of the optimized gas-phase adsorbate molecule (isolated), and the third term is the energy of the optimized surface. Based on this definition, negative values of Ea correspond to stable configurations.

B. Results

SO_2 is adsorbed onto Cr_2O_3 (0001) by bonding its two oxygen atoms to two different chromium atoms on the surface. The sulfur atom may or may not be attached to a surface oxygen atom. The first sulfite-like structure is the most stable and can be formed at various sites on the surface. The vibrational frequencies of the O-S-O bond are similar in all of these sites and for the asymmetric stretching they take values between 1000 and 940 cm^{-1}, for the symmetric stretching, about 600 cm^{-1}, and for the bending, around 490 cm^{-1}.

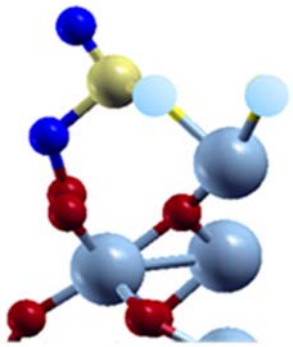

Figure 5. Sulfite-like species formed between SO_2 and oxygen previously adsorbed in molecular state. Gray: chromium atoms, red: surface oxygen atoms, yellow: sulfur atom, blue: oxygen atoms from SO_2, light blue: preadsorbed oxygen atoms.

The second structure, in which the sulfur atom is not bound to the surface, is an intermediate configuration, in a local minimum of energy, but it participates in the dissociation of adsorbed oxygen and in the dehydrogenation of methane, as explained below.

Oxygen is adsorbed on the clean surface of Cr_2O_3 (0001) both in molecular state and in dissociated form, the latter being the most stable. In the molecular state it has two stable configurations, with only one oxygen atom attached to a surface chromium atom, or with both oxygen atoms attached to a single chromium atom. In the dissociated state the two oxygen atoms are attached to the same chromium atom.

The presence of adsorbed SO_2 promotes the dissociation of oxygen and the formation of sulfite species (Fig. 5).

Methane does not adsorb on the clean Cr_2O_3(0001) surface or in the presence of molecular oxygen. However, it interacts with oxygen in a dissociated state, leading to the formation of both hydroxyl and methoxy species, the latter through the binding of the methyl group and a surface oxygen atom. The characteristic frequency of the CH_3 d-stretching mode is in the range 2960-3000 cm^{-1}.

The interaction between methane and adsorbed sulfur dioxide facilitates the dehydrogenation of methane. In this case, the methyl groups are attached to the sulfur atom not bound to the surface, but this configuration, although stable, is intermediate and should lead to the formation of methoxy and sulfite-type species.

Methoxy species can form at various sites on the surface, and their interaction with oxygen in the dissociated state promotes their dehydrogenation. The oxymethylene species then have a characteristic frequency of symmetric stretching around 2860 cm^{-1} (Fig.6).

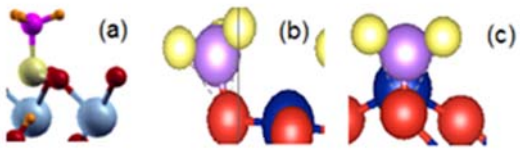

Figure 6. (a) Dehydrogenation of methane in the presence of sulfur dioxide, (b) methoxy species, (c) oxymethylene species

The subsequent oxidation of these species leads to the formation of dioxymethylene and formaldehyde.

According to [7,8] the adsorption of formaldehyde on Cr_2O_3(0001) would give rise to spectroscopic bands at 1650 cm^{-1} and 1126 cm^{-1}.
Interestingly, the methoxy species can interact with hydroxyl, leading to the formation of methanol, which in turn can react with the adsorbed species (Fig. 7).

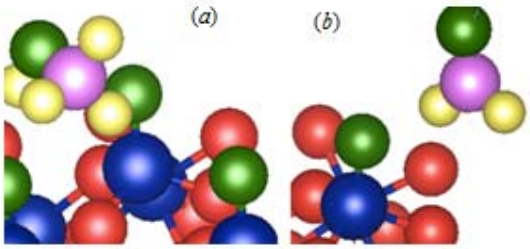

Figure 7. Formation of methanol (a) and formaldehyde (b) on Cr_2O_3 (0001) surface.

IV. CONCLUSIONS

In this work we presented a theoretical-experimental study of the methane oxidation reaction in the presence of sulfur dioxide on Cr_2O_3 / γ-Al_2O_3

$CH_4+SO_2+O_2 \rightarrow S^0+CO_2+2H_2O$ on Cr_2O_3 (Eq. 5)

The global activation energy of this reaction is lower than that of the oxidation reaction

$CH_4+2O_2 \rightarrow CO_2+2H_2O$ on Cr_2O_3 (Eq. 6)

and to our knowledge, it is the lowest found so far in different catalysts. Our objective was to try to unveil the role of sulfur dioxide as well as to detect intermediate species of possible industrial interest.
Sulfur dioxide is adsorbed on Cr_2O_3 (0001) in two different configurations, in both the oxygen atoms are attached to chromium atoms, but the sulfur atom may or may not attach to a surface oxygen atom. The sulfite configuration is the most stable, but it is the other one that acts as an intermediate to promote the dissociation of molecularly adsorbed oxygen or the dehydrogenation of methane. This effect facilitates the formation and subsequent oxidation of methoxy species up to the formation of dioxymethylene, formaldehyde, and methanol.
Our results suggest that the possibility of oxidizing methane on chromium oxide in the presence of sulfur dioxide deserves to be considered in the development of syngas production technologies.
Our research also points to an additional alternative to the green formation of methanol that deserves to be explored.

V. ACKNOWLEDGMENTS

This work was supported by the National Council of Science and Technology, the Faculty of Chemistry and Engineering Fray Roger Bacon, and the National University of La Plata, from Argentina.

VI. REFERENCES

[1] I. Coria, S. Medina, I.R. Ramos, A.G. Ruiz, "Estudio comparativo de la retencion del SO_2 en diferentes oxidos de metales de transicion soportados sobre alumina". Energeia 1, 49-65, 2003.

[2] I. D. Coria, O. Carattoli, S. Hernandez Guiance, Y. Malik, "Estudio de la reducción de SO_2 con CH_4 en presencia de O_2 a altas temperaturas, sobre catalizador de Cr_2O_3 soportado en alúmina." Energeia 5, 30-39, 2007.

[3] V.A. Ranea, S.N. Hernandez, S. Medina, I.M. Irurzun, I.D. Coria, E.E. Mola, "Formation of sulte-like species on Cr_2O_3 after SO_2 chemisorption." Surface Science 605 489493, 2011.

[4] S. N. Hernandez Guiance, I. D. Coria, I. M. Irurzun, E. E. Mola, "Experimental determination of the activation energies of CH_4, SO_2 and O_2 reactions on $Cr_2O_3/\gamma-Al_2O_3$.". Chemical Physics Letters 660123-126, 2016.

[5] S. N. Hernández Guiance. PhD Thesis. University of La Plata, Buenos Aires, Argentina, 2016.

[6] S. N. Hernandez Guiance, I. D. Coria, I. M. Irurzun, "A combined infrared spectroscopy (FT-IR) and density functional theory (DFT) study of the CH_4 and O_2 reaction on Cr_2O_3." unpublished.

[7] V. V. Kaichev, G. Ya. Popova, Yu. A. Chesalov, A. A. Saraev, D. Y. Zemlyanov, S. A. Beloshapkin, A.Knop-Gericke, R. Schlögl, T. V. Andrushkevich, V. I. Bukhtiyarov, "Selective oxidation of methanol to form dimethoxymethane and methyl formate over a monolayer V_2O_5/TiO_2 catalyst." Journal of Catalysis, 311, 59-70, 2014.

[8] G. Busca, A.S. Elmi, P. Forzatti, "Mechanisimof Selective Methanol Oxidation over Vanadium Oxide-Titanium Oxide Catalysts: A FT-IR and Flow Reactor Study", J. Phys. Chem. 91, 5263, 1987.

Optical Analysis for a Honeycomb Solar Receiver Using a Point-Focus Concentrator

N. Aracely Cisneros-Cárdenas Chemical Engineering Department at Universidad de Sonora Hermosillo, Mexico. ORCID 0000-0001-6176-3616

Rafael E. Cabanillas-López Chemical Engineering Department at Universidad de Sonora Hermosillo, México ORCID 0000-0003-0739-3348

Ricardo A. Pérez-Enciso Industrial Engineering Department at Universidad de Sonora Hermosillo, Mexico ORCID 0000-0001-5568-9624

Abstract

In this work we present an optical analysis for three different hydraulic diameter honeycomb receivers used to elevate working fluid temperature using concentrated solar radiation provided by a point-focus solar concentrating system. The analysis was carried out in order to determine the amount of concentrated solar radiation received in the volumetric receiver as well as the radiation distribution inside of it, also to determine the length of it. The study which determines the location of the receiver in the optical axis of the concentrating system is also presented, as well as the ray independence study to secure the reproducibility and repeatability of the results. The simulation was done in Tonatiuh software considering the physical characteristics of the point-focus concentrating system and the volumetric receivers. As results, it was revealed that around 96% of the concentrated solar radiation arrives to the receiver – inside and in the front side-, the rest of it is attributed to the losses due to different factors.

Keywords: Honeycomb solar receiver, Optical analysis, Point-Focus concentrator.

I. INTRODUCTION

Obtaining heat through the excessive use of fossil fuels to facilitate the production processes of fuels and materials is a serious problem today; however, a feasible alternative is the use of renewable resources and materials. Solar Thermal Energy is the most important in the type of solar energy and represents one of the most important sources of technology and electricity production used in various applications such as buildings, mobility and manufacturing [1]. The heat necessary for medium-high temperature processes can be obtained through the production of Concentrated Solar Radiation, this heat is obtained through systems with optical arrangements that involve the use of lenses and / or mirrors, which have the function of re-directing the sun's rays to an area smaller than the catchment area, thus increasing its energy density several times. There are different types of solar concentration technologies that achieve this process through different operating bases such as the parabolic disc, parabolic channel, linear fresnel reflector, central tower and solar oven[1]. Solar concentration technologies are still under development and are not accessible like conventional photovoltaic modules compared to the ease of operation of the latter[2]. However, its development provides significant advantages over conventional devices such as greater efficiency, high temperatures for energy production and to be used as process heat.

The transformation of RSC into thermal power is carried out using receivers, whose geometries and construction materials vary depending on their application. Volumetric receptors (Figure 1 (a)) are porous structures of different materials such as metal or ceramics. This type of receptor is very promising due to the volumetric effect; this effect causes the temperature of the irradiated part to be lower than the temperature in the final part of the receiver, causing less heat losses by radiation and making the process more thermodynamically efficient [3], it also reduces the local points high temperature that could damage the material and harm the process in general[4]. Despite this, there are significant difficulties in RV design due to the complexity of the volumetric effect. The heat transfer phenomena that occur within the structure - radiation, convection and conduction - are affected by each other, so the radiative and thermal study of RVs requires a large computational load[4].

The distribution of radiative flux has a significant impact on the temperature field of the receiver [5], that is why their study provides necessary information on its operating limits. Said study is carried out by applying the ray tracing method, which considers that light moves from a light source describing a path in the form of a line until it hits a surface that, depending on its assigned physical properties, can modify its direction by reflection or refraction. Ray tracing can be performed using three different techniques: Simple Ray Tracing Method, Convolution Ray Tracing Method and Monte-Carlo Method.

The simple ray tracing method refers to a systematic ray distribution of rays by mesh and ray projection of the solar cone individually; While convolution ray tracing is a mesh ray distribution and calculation of the degraded solar cone by the mathematical convolution technique, only the central ray is projected, and the cone is reconstructed in the receiver. On the other hand, the Monte Carlo Method, which is a numerical method that allows solving physical and mathematical problems by simulating random variables, is a

IEECP'21, July 29-30, 2021, Silicon Valley, San Francisco, CA – USA

DAI : ***https://sci-index.com/DAI/2021.99101/IEECP/14727252***

statistical simulation of the radiative transfer phenomenon based on the behavior of the emission, the reflection and the absorption of the surfaces of the optical system [6].

Studies have been reported in the literature that reveal the distribution of radiative flux in RV, through the application of the MCRT Method, where the source of CSR considered is a point focus concentrator [7–9], some reported works combine the X-ray computed tomography technique to reconstruct a realistic porous absorber with the MCRT to obtain the RSC distribution[10], while in other works theoretical assumptions are made to simulate the operating conditions of the receiver[11].

In this work, the methodology and results obtained by ray tracing simulation carried out in three volumetric receivers of different hydraulic diameters are presented to determine the amount of concentrated solar radiation received in it, as well as the way in which it is received. and it is distributed within the structure in addition to establishing the length of the same receiver; and which are the three diameters it presents favors the radiative phenomenon to a greater extent. The CSR source considered is a point focus concentrator (Figure 1 (b)), developed and built by researchers from the University of Arizona in collaboration with Rehnu[12], whose characteristics are described in Table 1.

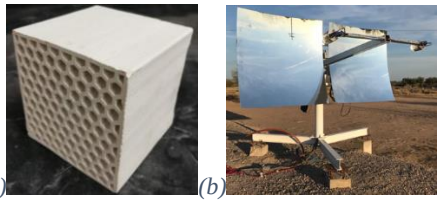

(a) (b)

Figure 1. (a) Ceramic volumetric receiver with dimensions of 10x10x10, dh = 0.0078 m. (b) Point focus concentrator system located in the Hermosillo Solar Platform.

II. METHODOLOGY

The simulations were carried out in the free license software Tonatiuh v.2.2.4 with three volumetric receivers of different porosities with hexagonal cylinders (Figure 2); For an orderly application of the methodology, the cases described in sections a), b) and c) were established, in addition the specifications described in Table 1 were considered and the receiver input was located 1.47 m from the vertex on the optical axis of the parable - as determined in the next section - considering it as a black body.

The simulation strategy used consisted of approximating the hexagonal cylinders to circular cylinders through the use of the hydraulic diameter, in addition to considering all the cylinders that are within a flat area of 0.05x0.05 m2 at the entrance of the receiver; This is because the system to be simulated must be as similar as possible to the physical system (Figure 3), which is why it is important to include in the simulation, the structure of the concentrator system to determine if it has an effect on the distribution of radiation in the receptor.

To consider the results obtained from the simulation acceptable, a radiative balance was carried out considering that the sum of the radiation received in the RV, as well as that which passes through it and which is overflowed, must be equal to what is received in a area of 0.01 m2 (which is the total receiving area 1.47 m from the vertex).

a) Case 1: DH = 0.004 m, L = 0.10 m, No. of cylinders = 99, fraction of holes = 0.498
b) Case 2: DH = 0.0057 m, L = 0.10 m, No. of cylinders = 42, fraction of holes = 0.428
c) Case 3: DH = 0.0078 m, L = 0.10 m, No. of cylinders = 25, fraction of holes = 0.802

A. Study of ray independence

The study of ray independence is mandatory in TR simulations to ensure the repeatability and reproducibility of the results obtained, which is why it must be carried out before the development of the aforementioned methodology. For this, the mesh size parameter was set at 25x25 while the number of rays was considered as the variable and an uncertainty was established as a function of this and in relation to the maximum value of flux less than 4% for the three cases a study. As results, we found that for case 1, 10 million rays were used and for cases 2 and 3 5 million were used.

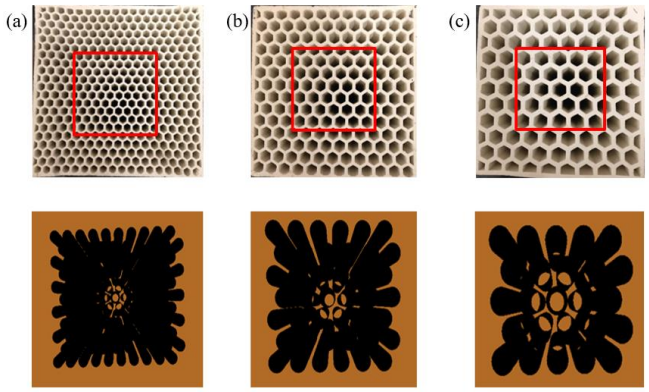

Figure 2. (a) case 1, (b) case 2, (c) case 3.

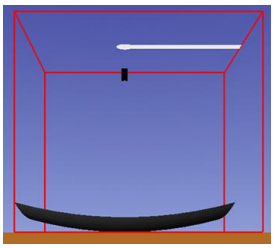

Figure 3. Physical system drawn in Tonatiuh software.

Table 1. Definition of parameters for TR simulation in Tonatiuh software

Definition of irradiance parameter	
Direct Normal Irradiance	1000 W/m^2
Sun Shape	Standard
CSR	0.02
Azimut	0°
Elevation	90°
Primary optical element	Parabolic mirror
Dimensions	1.65x1.65 m^2
Focal point	1.5 m
Reflectivity	0.9
Global optical error of the system	2.8 mrad

B. Determination of the location of the RV on the optic axis

It was established that the area of the receiver is 0.05 x 0.05 m^2, so through the simulations it was determined that at a distance of 1.47 m from the vertex and on the optical axis of the parabola, the RSC with the highest concentration illuminates an area of 0.0025 m^2 while the total reception area is 0.01 m^2. According to the results of the TR simulations, the support structure does not have a significant effect on the distribution of the RSC as shown in Figure 4; where it

is also established that the CSR presents a maximum peak of 2.5 MW/m^2 and an average of 236 kW/m^2.

Figure 5 shows the profiles of the distribution of concentrated solar radiation obtained from Figure 4, in the central part of the x and y axes, respectively. In the distribution profiles presented, it is observed that the shadowing effect of the structure on these is negligible, and that the flux value remains between 1.5-2.5 x10^6 W/m^2 in x, y = [- 2.5,2.5].

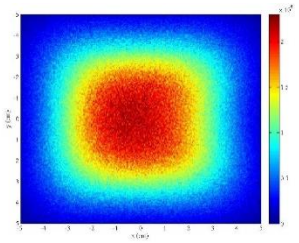

Figure 4. Spot of concentrated solar radiation obtained by simulation on the PPLR at 1.47 m from the vertex of the parabola. (The units of the color scale are W/m^2).

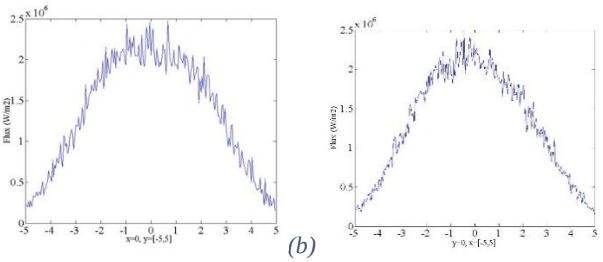

(a) *(b)*

Figure 5. Profiles in (a) x = 0; y = [- 5.5] y (b) y = 0, x = [- 5.5] of the distribution of concentrated solar radiation on the PPLR obtained by simulation.

III. RESULTS

A. Interpretation of results

For a proper interpretation of the energy balance, the following is established. "Received in the volumetric receiver" is understood as the radiation that is received in the frontal structure of the walls that are between the cylinders and that that is received in the interior walls. On the other hand, the radiation that overflows when reducing the area from 0.01 m2 to 0.0025 m^2 and that which leaves the receiver, whether a part of it has interacted with the interior walls, are considered as losses.

Before performing the energy balance within the volumetric receiver for the three cases, it is necessary to clarify what happens to the concentrated solar radiation when the receiver arrives. The solar rays can be intercepted by the frontal structure of the walls that is between the cylinders of the receiver as well as they can impact against the interior walls - reflect some percentage to hit another wall again depending on its direction - or pass through the cylinders without having directly interacted with the walls of the receiver; Another percentage of the rays may not even have reached the receiver and another percentage may overflow from the reception area. The radiation distribution that is observed in the following figures corresponding to this section are the result of the radiation phenomenon, because the physical properties of the receiver are considered, as well as the concentration system and the final scene of the phenomenon including optical system errors.

B. Results

Considering the total area of capture of solar radiation (2.7225 m2) and a normal direct irradiance of 1,000 W / m2, the radiation that would be received if a perfect concentrator were had would be 2,722.5 W; However, considering the global optical error of the system that has been determined previously, only 2.365 W are received, that is, 96% - in radiative terms - in a flat plate of 0.01 m^2 at 1.47 m and on the optical axis. From this, the balances presented above are determined.

The general and detailed energy balances presented in the previous tables are considered correct because, as expected, the sum of the energy received inside the cylinders is less than that received in a flat receiver. As can be seen in Tables 2, 3 and 4, there is no significant difference between one diameter size and another in terms of radiation received within the receiver or losses.

Regarding the distribution profiles of concentrated solar radiation formed on the interior walls of the volumetric receiver, only those corresponding to the central section are presented and analyzed in this section, while the rest of the graphs are found in the section of annexes. The foregoing is justified by corroborating that the radiation intensity was highest in the center of the receiver and decreases when moving away from the center, so reviewing the profiles at this location will provide sufficient information for the analysis.

To begin the analysis of the results of the ray tracing simulation, a general description of Figures 6, 7 and 8 is made. The x-axis corresponds to the hydraulic diameter of each case described above, while the y-axis describes the length of the cylinder. The input of the concentrated solar radiation to the cylinder is at y = 0 and the output at y = 0.10. The origin of the coordinates is on the lower left side.

In Figure 7, the results for case 1 are shown and in a general appreciation, it is observed that the radiation does not reach beyond y = 0.02, which means that the highest concentration is in the first fifth of the volumetric receptor. The maximum estimated flux value is 6 MW / m2. Figure 8 corresponds to the results of case 2 and the radiation slightly exceeds the length of y = 0.02 in the positions that correspond to items 1 to 4, which means that the radiation has a penetration greater than 1/5 of the length of the receiver; the maximum estimated flux value is 7 MW / m2. Regarding Figure 9, the distribution profiles of the concentrated solar radiation corresponding to case 3 are described. The radiation penetrates up to a maximum length of y = 0.04 m, that is, it reaches 2/5 of the total length of the receiver and the maximum estimated flux value is 7 MW / m2.

In all three cases it is possible to appreciate the volumetric effect from the perspective of the radiation distribution inside the walls. From this, it is established that a length of 0.10 m is not necessary for the receiver - in any of the cases-, but it is recommended that it have a maximum length of 0.05 m.

Table 2. Energy balance for case 1

		Balance in General Terms		
2365	W	Plane (0.01 m^2)	100.00	%
2273.7	W	Received in VR (0.0025 m^2)	96.14	%
91.3	W	Losses	3.86	%
		Detailed Balance	**Percentage**	
2365	W	Plane (0.01 m^2)	100.00	%
2279	W	Plane (0.0025 m^2)	96.36	%
86	W	Overflow	3.64	%
1299.8	W	Received within 99 cylinders	54.96	%
5.3	W	Come out of the receiver	0.22	%
973.9	W	Received in the structure	41.18	%

Table 3. Energy balance for case 2

		Balance in General Terms	Percentage	
2365	W	Plane (0.01 m^2)	100.00	%
2276.4	W	Received in VR (0.0025 m^2)	96.26	%
88.53	W	Losses	3.74	%
		Detailed Balance	**Percentage**	
2365	W	Plane (0.01 m^2)	100.00	%
2279	W	Plane (0.0025 m^2)	96.36	%
86	W	Overflow	3.64	%
1184	W	Received within 99 cylinders	50.07	%
2.53	W	Come out of the receiver	0.11	%
1092.3	W	Received in the structure	46.19	%

Table 4. Energy balance for case 3

		Balance in General Terms	Percentage	
2365	W	Plane (0.01 m^2)	100.00	%
2278.3	W	Received in VR (0.0025 m^2)	96.34	%
86.64	W	Losses	3.66	%
		Detailed Balance	**Percentage**	
2365	W	Plane (0.01 m^2)	100.00	%
2279	W	Plane (0.0025 m^2)	96.34	%
86	W	Overflow	3.64	%
1289.5	W	Received within 99 cylinders	54.53	%
0.64	W	Come out of the receiver	0.03	%
988.84	W	Received in the structure	41.81	%

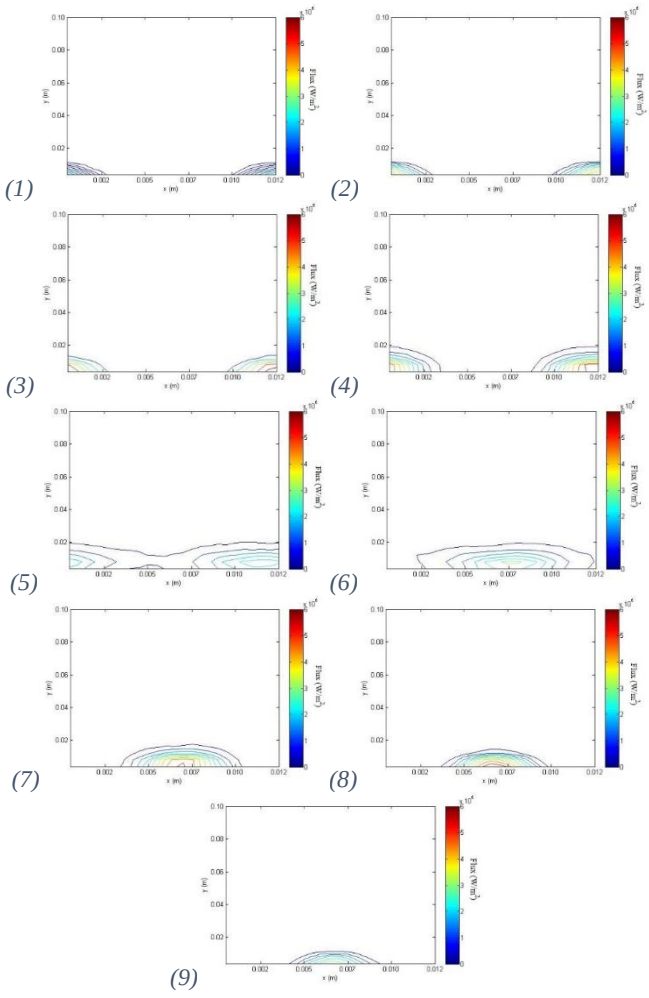

Figure 6. Distribution profiles of concentrated solar radiation on the interior walls of case 1.

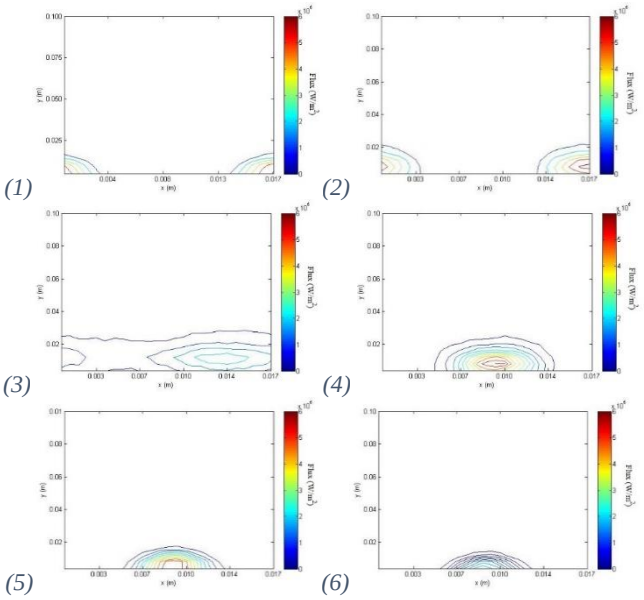

Figure 7. Distribution profiles of concentrated solar radiation on the interior walls of case 2.

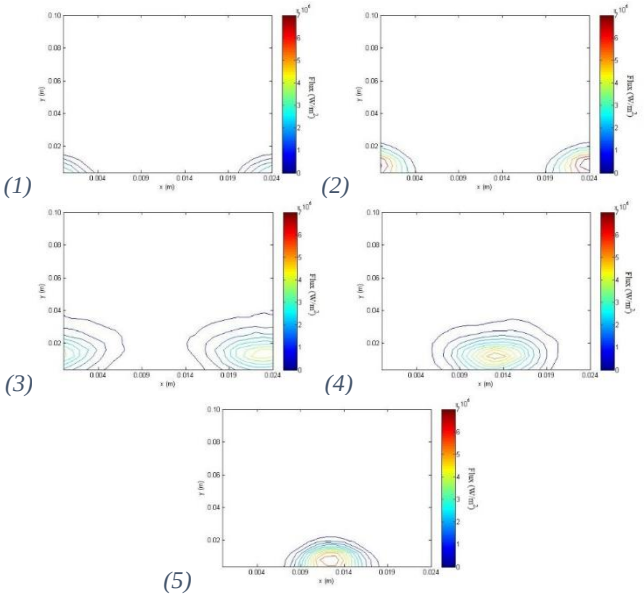

Figure 8. Distribution profiles of concentrated solar radiation on the interior walls of case 3.

IV. REFERENCES

[1] M.S. Raboaca, G. Badea, A. Enache, C. Filote, G. Rasoi, M. Rata, A. Lavric, R.A. Felseghi, Concentrating solar power technologies, Energies. 12 (2019) 1–17. https://doi.org/10.3390/en19061048.

[2] A. Guenounou, A. Malek, M. Aillerie, Comparative performance of PV panels of different technologies over one year of exposure: Application to a coastal Mediterranean region of Algeria, Energy Convers. Manag. 114 (2016) 356–363. https://doi.org/10.1016/j.enconman.2016.02.044.

[3] A.L. Ávila-Marín, Volumetric receivers in Solar Thermal Power Plants with Central Receiver System technology: A review,

Sol. Energy. 85 (2011) 891–910. https://doi.org/10.1016/j.solener.2011.02.002.
[4] M. Nakakura, K. Matsubara, S. Bellan, T. Kodama, Direct simulation of a volumetric solar receiver with different cell sizes at high outlet temperatures (1,000–1,500 °C), Renew. Energy. 146 (2020) 1143–1152. https://doi.org/10.1016/j.renene.2019.07.039.
[5] F. Wang, Y. Shuai, H. Tan, X. Zhang, Q. Mao, Heat transfer analyses of porous media receiver with multi-dish collector by coupling MCRT and FVM method, Sol. Energy. 93 (2013) 158–168. https://doi.org/10.1016/j.solener.2013.04.004.
[6] Y. Shuai, X. Xia, H. Tan, Numerical simulation and experiment research of radiation performance in a dish solar collector system, Front. Energy Power Eng. China. 4 (2010) 488–495. https://doi.org/10.1007/s11708-010-0007-z.
[7] F. Wang, Y. Shuai, H. Tan, C. Yu, Thermal performance analysis of porous media receiver with concentrated solar irradiation, Int. J. Heat Mass Transf. 62 (2013) 247–254. https://doi.org/10.1016/j.ijheatmasstransfer.2013.03.003.
[8] X. Chen, X.L. Xia, X.L. Meng, X.H. Dong, Thermal performance analysis on a volumetric solar receiver with double-layer ceramic foam, Energy Convers. Manag. 97 (2015) 282–289. https://doi.org/10.1016/j.enconman.2015.03.066.
[9] G. Barreto, P. Canhoto, M. Collares-Pereira, Three-dimensional modelling and analysis of solar radiation absorption in porous volumetric receivers, Appl. Energy. 215 (2018) 602–614. https://doi.org/10.1016/j.apenergy.2018.02.065.
[10] S. Du, M.J. Li, Q. Ren, Q. Liang, Y.L. He, Pore-scale numerical simulation of fully coupled heat transfer process in porous volumetric solar receiver, Energy. 140 (2017) 1267–1275. https://doi.org/10.1016/j.energy.2017.08.062.
[11] M. Ali, M. Rady, M.A.A. Attia, E.M.M. Ewais, Consistent coupled optical and thermal analysis of volumetric solar receivers with honeycomb absorbers, Renew. Energy. 145 (2020) 1849–1861. https://doi.org/10.1016/j.renene.2019.07.082.
[12] B.M. Coughenour, T. Stalcup, B. Wheelwright, A. Geary, K. Hammer, R. Angel, Dish-based high concentration PV system with Köhler optics, Opt. Express. 22 (2014) A211. https://doi.org/10.1364/oe.22.00a211.

A pilot study on implementation of sustainable design and construction activities in highway development

Raja Rafidah Raja Bt Muhammad Rooshdi
CENTER OF STUDIES FOR QUANTITY SURVEYING
UNIVERSITI TEKNOLOGI MARA SHAH ALAM
lSHAH ALAM, SELANGOR, MALAYSIA
raja_rafidah@uitm.edu.my

Noor Akmal Adillah Bt Ismail
CENTER OF STUDIES FOR QUANTITY SURVEYING
UNIVERSITI TEKNOLOGI MARA SHAH ALAM
SHAH ALAM, SELANGOR, MALAYSIA
noorakmal@uitm.edu.my

Shaza Rina Bt Sahamir
CENTER OF STUDIES FOR CONSTRUCTION MANAGEMENT
UNIVERSITI TEKNOLOGI MARA SHAH ALAM
SHAH ALAM, SELANGOR, MALAYSIA
shaza_rina@uitm.edu.my

Abstract

The construction industry is one of the major contributors to the CO2 emission which cause environmental impacts on the earth's climate. Malaysian government is committed in reducing the CO2 by 40% in 2020 and 45% by 2030 as compared to the levels in 2005. Hence, there is a need to reduce the impact on the environment. Currently, Malaysia had developed several assessment tools such MyGHI, pHJKR and Infrastar. However, the implementation was still in not too much. Therefore, the main objective of this paper is to identify the sustainable construction activities element that had been implement and to determine the most main criteria had been implemented in current highway construction project. The pilot study was based on sustainable design and construction activities scorecard in MyGHI. The case studies were chosen based on the stages of the project such as the designing and planning stage, constructing stage, and operating and maintaining stage. The results of the pilot test for case studies had been discussed in focus group discussion. The focus group had been chosen among the expertise in highway development. The experts agreed with all the results that had been gathered during the pilot test. The scorecard of sustainable design and construction activities would be used in the future assessment of highway. The experts had also agreed that highway development in Malaysia is ready for green highway development. All the case studies had gathered 47% until 80% of points. However, the total point scores obtained by different highway projects were considered comparatively and moderately and indicated that the current highway construction practices need to be improved with the sustainable element during highway development. Based on these results, it was clearly discovered that green practices in terms of design and construction were already applied by all three highway projects in Malaysia.

Keywords: *Sustainable development, green highway, assessment tools, pilot study*

IEECP 21, July 29-30, 2021, Silicon Valley, San Francisco, CA – USA

D!f: *https://sci-index.com/DAI/2021.99101/IEECP/14526909*

Modeling and simulation of a Web-of-Cells architecture using Matlab/Simulink

Mohamed Faradji
Systems and Telecommunications Engineering Laboratory. University of Boumerdes,Algeria
Email: m.faradji@univ-boumerdes.dz

Toufi Madani Layadi
Laboratory of Materials Physics,Radiation and Nanostructures, University of BBA, Algeria
Email: toufikmadani.layadi@univ-bba.dz

Colak Ilhami
Engineering and Architecture Faculty, Nisantasi University, Turkey
Email: *ilhcol@gmail.com*

Khaled Roubah
ETA Laboratory University of BBA, Algeria
Email: khaled.rouabah@univ-bba.dz

Abstract

Nowadays, the Web-Of-Cells (WOC) represents an alternative strategy for solving communication, generation and distribution problems in smart grids that integrate Hybrid Renewable Energy Sources (HRES). In this paper a simulation method of WOC architecture with a new voltage control model have been proposed.

The proposed method is summarized in three main points: First modeling of the WOC taking into account the voltage control model has been developed. Then, simulation of the WOC in Matlab/Simulink software is realized. During the simulation of the WOC architecture, profiles of data are considered. Finally, simulation results and explanations are discussed.

The study proved that the integration of voltage control technique in WOC architecture allows optimizing the reverse power flows, local congestions and voltage problems.

Keywords: *Web-Of-Cells Modeling, Smart grids, Hybrid Renewable Energy Sources, voltage control strategy,* Matlab/Simulink.

IEECP'21, July 29-30, 2021, Silicon Valley, San Francisco, CA – USA

DAI : *https://sci-index.com/DAI/2021.99101/IEECP/14526945*

Methodological basis for selecting experimental research for building materials

1st Tatiana Eremina
Institute of Integrated Safety in Construction
Moscow State University of Civil Engineering
Moscow, Russia
main@stopfire.ru

2nd Fedor Portnov
Institute of Integrated Safety in Construction
Moscow State University of Civil Engineering
Moscow, Russia
wastingtimefilmart@gmail.com

Abstract

This paper for the first time proposes methodological frameworks built by generalizing empirical data on the mechanochemical characteristics of materials using interdisciplinary methods. This methodology optimizes research for any composite materials while maintaining targeted research methods and eliminating impractical and related experimental studies with reduced work costs and as a result of environmental impact.

Keywords: Fire safety; the performance of the designs; The physical and chemical properties of the materials; fire retardant; planning of experiment; interdisciplinary research methods

I. INTRODUCTION

The problem of predicting the behavior of building materials in the conditions of their exploitation is one of the significant and promising issues in the development of the construction complex. The behavior of building materials and structures is described by a number of characteristics. Exploitation characteristics include mechanical characteristics - strength (depending on the type of design), shock resistance, wearability, etc., characteristics describing the features of the use of building materials and structures - adhesive ability, reflectivity, thermal insulation, characteristics describing the stability of water by external factors - laity, hydrophobic, etc. There is also a criterion such as durability, describing the minimum possible time of normal operation of materials and structures in certain climatic conditions. In addition, the operation of materials and structures can occur emergencies that create abnormal conditions, such as vibrational impact, elevated temperatures and fire, low temperatures, hurricane wind impact

The above features of building materials and structures suggest the existence of special regulatory methods of research. For example, in the Russian Federation there is a regulatory document GOST 30403-2012 "Building constructions. Fire hazard testing method." This method allows to assess the behavior of the construction structure in natural conditions - part of the sample is in the fire chamber, which simulates the fire, and part of the sample is separated by a partition with an ale, which allows to assess the behavior of unheated structures in the event of a fire. Based on the results of such tests, the structure is assigned a fire hazard class [1-3].

For most characteristics that describe the behavior of building materials and structures in emergency situations, there are a large number of appropriate assessment methods that create conditions for tests close to the real. However, a significant problem with such tests in research work aimed at the development of new building materials and structures is the high cost, labor costs, and negative impact on the environment (e.g., in fire tests of construction structures).

II. METHODOLOGICAL BASICS OF RESEARCH

As you know, in addition to operational and other characteristics described above, building materials also have all the known properties of physical and chemical systems. Accordingly, it is possible to conduct a comprehensive analysis of building materials and structures using physical and chemical research methods.

Physics and chemical analysis methods allow to study in detail the specifics of the behavior of building materials and structures in different conditions. Such methods include: methods of thermogravimetric analysis of the structure, X-ray spectroscopy, chromato-mass spectrograms, elemental analysis, IR spectroscopy, pH-metric [4-13].

Despite the significant results of the use of such methods in practice in the development of new building materials and structures, such methods are used as additional after-site tests.

In order to create a more efficient and optimal development environment for new building materials and structures, a methodological framework for the selection of experimental research needs to be developed.

Based on the large number of research carried out by the authors, the following approach is proposed, based on the separation of experimental methods on the application of them depending on the level (scale) of the objects under study (materials):

IEECP 21, July 29-30, 2021, Silicon Valley, San Francisco, CA – USA

DAI : https://sci-index.com/DAI/2021.99101/IEECP/14526858

- Micro level;

- supramolecular level;

- Research on the material;

- Design research.

The choice of this approach is related to the specifics of data processing, as well as the preparation of the samples under study. At the micro level, the results are based on the study and analysis of the quantitative patterns of intermolecular connections and their energy. A minimum sample canopy is used as samples for testing. The supramolecular level allows us to consider the structure of dispersal systems with the possibility of their detailed quantitative analysis. A fragment of the material is considered. In the study of the material, it is possible to prepare small reference samples reflecting the basic physical, chemical, mechanical and operational characteristics. In the study of structures, fragments of theoretical or actual functioning objects are selected as objects that allow to reproduce real conditions of operation, as well as emergencies.

Table 1. Interdisciplinary methods of microlevel research

Micro-level research methods
Physical and chemical characteristics:
Heat conductivity assessment
Temperature assessment
Heat-intensity assessment
Thermo-gravimetric analysis
Isothermic calorimetry
Determining Gibbs Energy
High-quality elemental analysis:
X-ray spectroscopy
Chromato-mass-spectrogram
Elemental analysis
IR-spectroscopy
pH-metro

Table 2. Interdisciplinary methods of supramolecular research

Methods of research at the supramolecular level
Assessment of the porous structure:
Specific surface
Porosity
Distribution of pores by size
Assessment of surface structure:
Electronic microscopy
The edge of wetting

Table 3. Interdisciplinary methods of research at the level of materials

Material-level research methods
Performance:
Assessment of water absorption
Assessment of water resistance
Assessment of hydrophobic
Assessment of permeability
Definition of adhesion
Assessment of heat resistance
Assessment of thermal aging
Fire retardant characteristics:
Assessment of fire hazards
Assessment of fire retardant efficiency
Mechanical characteristics:
Strength assessment
Stretching score
Evaluation of the shift
Bend assessment
Methods to control the quality of the material structure
Obtain data on the characteristics of the surface of compositions (electron microscopy)
Assess the edge angle of wetting
Ir-spectroscopy
Study of fire retardants by pH-marker (complex study of the chemical composition of water solutions (rigidity, anion chromatography, pH-metro))

Table 4. Interdisciplinary methods of research at the level of designs

Design-level research
Performance:
Assessment toorrosional durability
Evaluation erosie
Assessment of bio resilience
Assessment of UV sustainability
Assessment of heat resistance
Fire hazards:
Assessment of the fire resistance limit
Mechanical test:
Large-scale trials

The methods described above allow for a comprehensive assessment of building materials and structures of any type and are the methodological basis for a large-scale study.

III. STUDY COMPATIBILITY CHART

Despite the theoretical importance of the research methods described above, it is necessary to address the issue of optimization of research in order to predict the properties of construction structures and materials.

The authors' developments in the design of composite and fire retardant materials using interdisciplinary research methods suggest that the lowest-scale (micro and supramolecular level) studies are correlated with a larger level and can be extended to a number of assumptions that characterize the chosen scale. This is how an approach has been developed, which is described as a compatibility diagram

This diagram describes the relationship between interdisciplinary research methods at different levels and shows the possibility of using smaller test results to predict the behavior of the subject at a larger level.

The use of such a diagram is associated with extensive research on the results of interdisciplinary research methods on a limited number of sites. This selects a functional criterion, the indicators derived from studies that can allow the prediction of the properties of similar building materials and structures to obtain the necessary conclusions (see Figure 1).

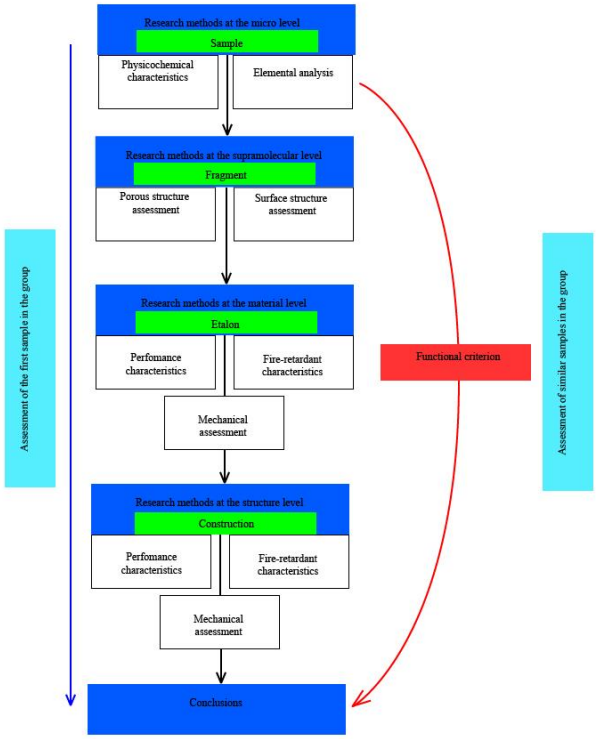

Figure 1. Study compatibility chart

An example is the study of wood fire danger. A number of papers provide examples of research into the various factors that influence these characteristics. In most cases, a wide range of methods are used, which fits into the proposed compatibility chart. At the same time, several types of elemental analysis, thermal research methods and methods for determining fire hazard characteristics can be used, as well as detailed structural analysis for a large list of similar properties of samples. It should be taken into account that such groups of samples may have a similar functional criterion (e.g., functional chemical link), the change of which in different samples can lead to a change in performance. Therefore, in such cases, one micro-level method of research, such as X-ray analysis, can be selected to predict performance characteristics that relate to the level of the structure.

IV. CONCLUSIONS

For the first time, an algorithm for generalizing empirical data on the mechanochemical characteristics of materials using interdisciplinary methods in the form of a compatibility diagram has been proposed;

A practical example of how to use a compatibility chart is shown.

This methodology optimizes research for any composite materials, preserving targeted research methods and eliminating impractical and related experimental studies with reduced labor costs and, as a result, environmental impact

V. ACKNOWLEDGMENTS

This work was financially supported by the Ministry of Science and Higher Education of the Russian Federation (Project: Theoretical and experimental design of new composite materials to ensure safety during the operation of buildings and structures under conditions of technogenic and biogenic threats #FSWG-2020-0007).

VI. REFERENCES

[1] Telichenko V.I., Roitman V.M. Ensuring the resilience of buildings and structures with combined special impacts involving fire is a basic element of the integrated safety system. 2010.

[2] Roitman V.M. Resilience of buildings and structures against progressive collapse with combined special impacts involving fire / Moscow State University Herald. 2009. Vol. No 2. pp. 37-59.

[3] Roitman V.M. Basics fire safety high-rise buildings. M. : MSSU, 2009. 107 p.

[4] Nalimov V.V. Application of mathematical statistics in substance analysis. Moscow: Fizmatgiz, 430 p., 1960

[5] A.M. Aisenstadt, Innovative materials and technologies for construction in extreme climatic conditions, 2014, 244 p.

[6] B.V. Deryagin, I.I. Abrikosova, E.M. Lifshits, Successes in physical sciences, **3**, 1958 pp.494-526,

[7] B.V. Deryagin, N.V. Curaev, *Wetting membranes*, 1984

[8] P. Dzh. Gudkh'yu, Practical Methods in Electron Microscopy,1980

[9] Dzh. Gouldsteyn Practical raster microscopy,1978

[10] B.A. Kalin, Raster electron microscopy. Laboratory work, 2008

[11] A.A. Abramzon, L.Ye. Bobrova, L.P. Zaychenko, Surface phenomena and surface-active substances: handbook, 1984

[12] A.S. Vyacheslavov, Ye.A. Pomerantseva, Measurement of surface area and porosity by the method of capillary nitrogen condensation (preparation of masters - operators of modern scientific equipment): Methodological development, 2006

[13] YU.A. Podkamennyy, A.A. Nosenko *Innovative method for determining the specific surface area of disperse systems and porous materials, 2013* Available at: http://conf.sfu-kras.ru/sites/mn2013/section060.html

Aggregation and Flexibility for Grids' Operation: the EU Path Toward the Opening of the Ancillary Services Market to Distributed Energy Resources

Davide Falabretti, Francesco Gulotta
Department of Energy
Politecnico di Milano
Milano, Italy
{davide.falabretti; francesco.gulotta}@polimi.it

Dario Siface
Institute of Integrated Safety in Construction
Ricerca sul Sistema
Energetico (RSE) Milano, Italy
wastingtimefilmart@gmail.com

Abstract

The present paper proposes an analysis of EU policies related to the enabling of the Distributed Energy Resources (DERs) participation into the Ancillary Service Market (ASM). Indeed, the rising of renewables and DERs penetration in the power system recently called for the enlargement of the pool of actors that can actively participate in the grid balancing. Therefore, Europe, through directives and guidelines, is gradually fostering the involvement of DERs into the ASM. This paper firstly provides an overview of the regulations actually in place in the EU Member States concerning the participation of DERs into the energy markets. Then, a detailed analysis of the Italian framework is proposed. In the last years, Italy has undertaken a process aimed to increase the observability of DERs, through the installation of suitable monitoring and communication devices, and to enable the provision of ancillary services by dispersed units. The main features and the preliminary results of this process are analyzed and commented, highlighting the benefits and opportunities related to it.

Keywords: electricity markets, aggregation, ancillary services, distributed resources, energy policies

I. INTRODUCTION

In the last years, the ambitious environmental policies defined by the Paris Agreement [1] and promulgated by the European Community through the "Climate and Energy Package" [2] and "2050 Long Term Strategy" [3] have imposed ambitious environmental targets in Europe, such as 32% share of gross final energy consumption from Renewable Energy Sources (RESs) by 2030 and the net-zero greenhouse gasses by 2050. These environmental targets are clearly modifying many sectors, among which the energy one. Indeed, the sustainability targets set by these agreements have promoted the increasing share of Distributed Energy Resources (DERs) connected to medium and low voltage distribution grids and the exploitation of Non- Programmable Renewable Energy Sources (NP-RESs), introducing higher requests of flexibility from the power system to manage the intermittent and scarcely predictable nature of these new energy sources. Additionally, conventional power plants, historically in charge to provide Ancillary Service (ASs) to the power system, are undergoing a gradual phase-out, due to the above-mentioned need for greater sustainability and a reduction in their competitiveness. This process has firstly caused a progressive decrease of the electric system inertia. As a consequence, in many countries worldwide, more challenging performance requirements have been introduced for the AS provision. Moreover, more recently, some national authorities have foreseen the opening of the relevant Ancillary Service Market (ASM) to new actors, as for example DER and NP-RES units, in order to enlarge the number of actors enabled to provide services to the grid [4][5].

Even if the involvement of DER and RESs in ASMs in perspective will have clear benefits for the grid's operation, the participation of these small units in the market as disaggregated entities is infeasible, both for technical (i.e. market resolution issues, low controllability, etc.) and practical reasons (in Italy, for example, there are almost 800,000 power plants connected to MV/LV grids) [6]. A promising way to address these issues, enabling the provision of ASs from DERs, is to aggregate and manage as a single entity several flexibility resources [7].

In the EU, this concept was first introduced by the European Parliament's directive 2012/27/UE [8], which defined the Aggregator as the subject that, controlling several energy resources, is enabled to offer the resulting flexibility in the electricity markets. Therefore, according to this definition, the Aggregator can be considered as an intermediary between the System Operator, which manages the electricity market as a central counterpart to collect ASs, and the owners of DERs units. To this purpose, the Aggregator should group, on a voluntary basis, the resources connected on the distribution network and, by implementing adequate controls tools, it has to manage the units in its portfolio making them act as a single

IEECP 21, July 29-30, 2021, Silicon Valley, San Francisco, CA – USA

DAI : *https://sci-index.com/DAI/2021.99101/IEECP/14526870*

controllable power plant (concept also known in the literature as Virtual Power Plant [9]). Usually, the Aggregator's portfolio (i.e. the resources through which it can offer flexibility to the system) can be extremely diversified, including: i) distributed production units, typically from RESs and characterized by a small power capacity; ii) energy storage systems, such as stationary Electrochemical Storage System (ESS) and Electric Vehicles (EVs); iii) flexible consumption units, capable to change their absorbed power.

In this framework, the European Community is promoting the opening of the electricity markets to aggregates of DERs, through directives envisaging the activation of demonstration projects and the setting up of a framework of rules enabling in the future new opportunities for network operators. In this process, Italy is playing a pivotal role, since the national Energy Authority (ARERA), together with Terna (the Italian Transmission System Operator), and other stakeholders of electricity sector, has recently started a procedure to reform the existing dispatching discipline. As a first result, a pilot project that unlocks, for the first time in Italy, the participation in the ASM of aggregated DERs managed by an Aggregator has recently started.

The remainder of the paper is structured as follows: in Section II it is proposed a detailed literature review of works proposing an optimized management of aggregates of DERs. Section III analyzes the regulations actually in place in some EU countries regarding the participation of DERs in the electricity markets. Section IV focuses on the path adopted in Italy for a better DER integration. Finally, some conclusions are drawn.

II. AGGREGATION METHODOLOGIES IN THE SCIENTIFIC LITERATURE

In the present energy scenario, characterized by high penetration of distributed and renewable generation and by increasing electrification of consumptions [10], it is universally recognized that the figure of the Aggregator could bring many advantages for the power system. In particular:

- the target fixed by the EU to achieve the climate neutrality by 2050, with an expected percentage of energy production from RES of 54%, requires the exploitation of all the flexibility resources, including DERs, to guarantee an efficient and reliable operation of the electric grid;
- a greater number of units enabled to participate in the ASM is expected to boost the competition on the market and, consequently, the economic efficiency of the latter is also supposed to enhance;
- thanks to the technological diversification and the redundancy of units in the Aggregator's portfolio, the ASs provided by a coordinated aggregate of DERs can be characterized by a degree of programmability and reliability higher than the same units operating with a disaggregated approach;
- the involvement of domestic and industrial users in the portfolio can promote the spreading of demand response techniques among passive users, which has been recognized as one of the fundamental steps to achieve the emission targets [8].

However, the management of a heterogeneous aggregate of units, highly dispersed on the network and characterized by hardly predictable power profiles, is particularly challenging for an Aggregator. Therefore, researchers have dedicated many works on the development of suitable tools aiming to allow the participation of DERs in the electricity market.

An example of these works can be found in [11], where an approach is described to optimize the participation into the Day Ahead Market (DAM) and in the ASM of an aggregate composed of wind turbines and a natural gas microturbine. Starting from the power forecasted for NP-RESs and the corresponding level of uncertainty, the quantity and price offered on the DAM by the Aggregator are first optimized. In order to properly take into account the uncertainty of the NP-RESs production and the DAM prices, the authors propose a multi-stage stochastic algorithm. Subsequently, the AS provision is analyzed. The Aggregator, taking advantage of the forecast update of the wind turbine power production and considering the gas turbine regulating margins and technical limits (i.e., ramp rates, maximum power, etc.), offers the remaining power capacity as flexibility on the market. More recently, the constant reduction in the prices of ESS and the significant growth in the electrification of final uses have fostered the exploitation of innovative flexibility resources, such as residential storage systems and domestic loads [12][13]. However, as analyzed in [14], the stringent privacy issues that emerge when residential loads are managed by an Aggregator and the need of avoiding detrimental impacts on the user caused by participation in the market, are slowing down the exploitation of these resources. To face these concerns, the scientific community has designed some decentralized approaches to coordinate and manage the residential loads and ESSs, limiting the amount of information needed to share [15]. In the decentralized approach, the Aggregator does not directly manage the resources in its portfolio, but it informs each user about the price at which it is willing to pay their flexibility. Then, each unit, considering the price signal and anticipating the user's needs, decides whether to perform or not the service requested. Adopting this approach, data exchanged between the Aggregator and the users only refer to price signals, with clear benefits on privacy issues; moreover, the user's freedom to use his own devices as/when he wants is also respected.

An example of decentralized approach can be found in [16], where an aggregate of NP-RESs, residential ESSs, and loads is considered. In particular, the Aggregator during the real-time directly manages the dispersed production and the ESSs, and exploits the loads' flexibility by sending adequate price signals in order to optimize the energy exchanges with the grid. To consider the uncertainties of power production and flexibility delivered by loads, a stochastic optimization algorithm is implemented. Finally, the results obtained by the optimization process are evaluated by means of Value-at-Risk (VaR) and Conditional Value-at-Risk (CVaR) methodologies.

As analyzed in the following, EU countries are increasingly opening their electricity markets to DERs managed by Aggregators. However, due to the intrinsic uncertainties of these markets (e.g. prices and quantity cleared), the development of bidding strategies is particularly complex. In this regard, in [17] a comprehensive methodology is proposed to optimize the markets participation of an aggregate of ESS and dispersed NP-RES. During the market sessions, the Aggregator is considered as a price-maker (i.e. its offers are assumed to modify the clearing process results), therefore the authors modeled the bidding strategy of all market actors. Moreover, to consider the errors committed in the forecasting of the power production by NP-RESs, the authors implemented a robust optimization algorithm aiming to define the quantities and prices offered by the Aggregator in both DAM and ASM. To simulate the ASM participation, the power grid structure is modeled to ensure acceptable levels of reserve capacity and the real-time balancing. Finally, the real-time energy exchanges between users in the aggregate and the power grid are managed by using two distinct approaches: ESSs are directly controlled by the Aggregator by a centralized approach, while the power absorbed by flexible loads is regulated indirectly through the price signals sent to users. This (decentralized) approach allows guaranteeing the respect of the privacy issues that could arise in some circumstances.

As emerged from the literature review, different approaches can be adopted to model the behavior of the Aggregator's portfolio.

However, despite the methods proposed can be different, it is usually possible to identify some common steps:

i. Forecasting phase, in which the Aggregator predicts the energy exchanges for the following days (up to 1-2 days ahead). Usually, the forecasted quantities are the power produced by NP-RES, the availability of storage systems (also including the presence of EVs under charge) and the power absorbed by consumption units. The forecasted profile, and the related uncertainty, will be used to optimize the bidding strategy on the market.

ii. Electricity market participation, during this phase, the Aggregator, according to the predicted power profiles and the availability of the units in its portfolio, optimizes the quantity and the price offered on the market. In most of the countries worldwide, each unit or aggregate of units must participate first in the DAM, in which each actor sells/buys the power produced/absorbed for the next day, and then in the ASM, where margins of flexibility with respect to the bidding schedules agreed on the DAM are offered. These margins are then exploited by the Transmission System Operator (TSO) to balance the grid during the real-time operation and to solve other operational issues (e.g. congestions).

iii. Real-time operation, in which the Aggregator adjusts the energy exchanges between the units in its portfolio, according to the results of the market and considering the actual energy production/consumption, the ESSs' state of charge and the units' availability. In this phase, the Aggregator is also requested to exchange data with the relevant plants, to monitor them, and to deliver control signals according to TSO's requests.

Starting from the encouraging results obtained by researchers, and considering the tecno-economic advantages that a better involvement of distributed resources would bring to the energy scenario, national regulating authorities are progressively enabling the participation of DERs into the electricity markets. To have a clearer picture of the situation in place in the EU, in the following Section an overview of the regulatory frameworks and initiatives devoted to achieving a more effective DERs integration is provided.

III. AGGREGATION IN EUROPE

To achieve the environmental targets described in Section I, the EU is seeking to reform the electricity market regulations of Member Countries. In particular, about 20 years ago, Europe started a gradual harmonization process of national electrical grid codes, with the purpose to evolve toward a unique and fully integrated European ASM [18]. Indeed, as stated by Regulation

2016/631 [19], the completion of a fully functioning and interconnected European energy market is crucial to ensure a suitable security of energy supply also in case of high RES integration. Moreover, the Regulation promotes a closer cooperation between national authorities to favor investments and to support the spreading in the energy sector of new actors (as the Aggregator) and technologies.

Although this harmonization process started several years ago, given the complexity of the matter and the need to align national regulatory and technical frameworks very far each other, it is still in an early stage, defining standardized flexibility products exchangeable in national and European ASMs.

Actually, the EU guideline on electricity transmission system operation 2017/1485 [20] identified a set of products to manage congestions in the transmission lines, to regulate system frequency and control voltage profiles. This work will focus on the products devoted to the frequency regulation and power balance, because they are strictly related to system operation security. Moreover, given that the provision of these "global" services is marginally influenced by the position of the resources within the network, they can be theoretically offered by a greater number of actors, including the distributed resources.

In particular, the EU's guidelines define the following services related to the provision of frequency regulation and balancing:

- Frequency Containment Reserve (FCR), aimed to contain the system frequency deviation after the occurrence of an imbalance. The FCR has an activation time up to 30 s and it is usually provided automatically by enabled units.
- Frequency Restoration Reserve (FRR), activated automatically (aFRR) or manually (mFRR), and which shall be supplied in a continuous manner. This product has an activation time typically between 30 s and 15 minutes and it is used to restore the system frequency.
- The Replacement Reserves (RR), an active power reserve that is used to restore the required level of FRR. The activation time for this product is usually 15 minutes.

In Figure 1 the standardized products for frequency and reserves restoration in place in EU are shown. More recently, a new ancillary service has been established: the Enhanced Frequency Control (EFC) [21]. This product has been introduced to cope with the progressive reduction of the power system inertia. Indeed, it is designed to rapidly limit the variation of the system frequency deviation and therefore it is characterized by a very small activation time, i.e. 1 s.

Despite the ongoing harmonization process, the regulations about the participation of aggregated DERs in the ASM are however still different in EU Member States, slowing down the spread of the Aggregator figure in the electricity sector. Therefore, in the following, a brief review of the regulatory frameworks in place in EU countries is provided, analyzing the abovementioned products negotiable by Aggregators in the national ASMs, the corresponding bid size and the possible regulatory barriers in place.

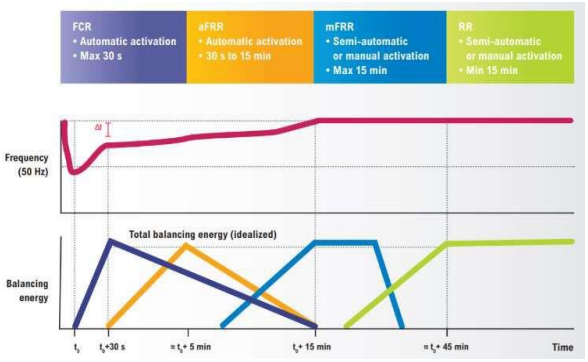

Figure 1. Products for frequency restoration in Europe [22].

A. Germany

Over the past years, the German electricity scenario has undergone a major change due to the large deployment of DERs, especially based on renewables [23]. The main driver for the spreading

exploitation of RESs in Germany is the Renewable Energy Act, first adopted in 2000 and subsequently revisited several times. This Act introduced different aspects promoting the use of RESs, such as the obligation for the DSOs to allow the connection of new RESs to the distribution grid and a remuneration scheme for these resources, with fixed price, usually guaranteed for 20 years [24]. In addition to that, the ongoing decline in prices for rooftop photovoltaic plants has increased the use of NP-RESs, reaching 90% of renewable capacity connected to the distribution grid [25].

This transformation has introduced a range of technical challenges, since in the past distribution grids were not designed to accommodate high penetration of DERs. To overcome these technical issues, German national authorities have introduced the possibility for the DSO to curtail NP-RES production in critical situations [26]. However, it is clear that this curtailment highlights inefficiencies in the system, causing, for example, a significant increase of relevant costs (it is estimated that during

2016 this procedure costed 375 M€) [27]. Therefore, to enhance the network's hosting capacity for DERs and to improve their coordination, the figure of the Aggregator has been introduced in

Germany, initially with the purpose of better coordinating the resources to limit congestions and so the NP-RSE curtailment. Subsequently, starting from 2018, the Aggregator has been enabled to provide ASs to the power system. To date, all the above-mentioned services (FCR, aFRR and mFRR) are open to DERs, as long as they fulfill the technical requirements prescribed by the national grid code. The minimum bid size to participate in the market is 1 MW for FCR and 5 MW for aFRR and mFRR.

B. France The French energy framework has been characterized, during the last years, by the creation of different Energy communities through the decrees "Self-consumption Ordinance" and the "Self-consumption Decree" [28][29]. Following the French regulation, an Energy community is an entity in which geographically close consumers and produces, connected to the low voltage distribution grid, are brought together to obtain a single self-consumption unit. Actually, the nominal capacity of each Energy community is fixed to 3 MW and the maximum geographical distance between community's members is limited to 20 km [30].

These decrees led to a great deployment of small-scale photovoltaic power plants, almost 500,000 at the end of 2019, some of which (15% of the total) devoted to the self-consumption communities. More recently, the high penetration of DERs has also pushed national agencies to enable the qualification to the ASM of DERs suitably aggregated. Therefore, today, aggregates of distributed resources are allowed to provide all the three services previously described. The minimum bid size is equal to 1 MW for the FCR and aFRR services, and equal to 10 MW for the mFRR one. The participation of DERs in the FCR balancing market is still limited, since 70 MW of DERs are enabled. Instead, for the mFRR product, a total capacity of 500 MW from distributed resources is enabled [24].

C. United Kingdom Even if, after Brexit, United Kingdom is no more an EU Member State, it has been included in this analysis because its current regulation has been also influenced by the abovementioned EU directives. UK was one of the first European countries that allowed the participation of DERs in electricity markets to support the stability of the grid [24].

Indeed, as result of the poor transmission capacity with Continental Europe, the electrical balancing of UK has always been characterized by severe criticalities. These issues required the introduction of balancing products on the ASM particularly diversified and technology specific. However, this complex technical framework represented a potential barrier to the integration of DERs in balancing markets.

Currently, only the primary control service (FCR) and the downward Replacement Reserve have a minimum bid size compatible with the typical aggregation size (i.e. 1 MW) [31]. Concerning the EFC and the mFRR, the former is characterized by a minimum bid size too elevate to allow the participation of DERs' aggregates (i.e. 25 MW). While, the latter is procured through a different mechanism, based on a pay-as-bid tender with a minimum bid size of 3 MW [24].

D. Finland

Finland is one of the most virtuous EU countries in terms of accessibility to electricity markets by DERs. These resources are enabled to procure all the three products defined by the European guidelines [20]. Moreover, thanks to the low minimum bidding size, equal to 0.1 MW for the FCR in normal condition and 5 MW for aFRR and mFRR services, the aggregated resources participate actively in the ASM. Indeed, during 2018, the DERs have provided approximately one third of the energy required in the mFRR market [24].

E. Italy

Currently, in Italy, only conventional power plants with a power capacity higher than 10 MVA can access to the ASM, providing ASs to the grid. However, during the last years, the Italian Regulatory Authority for Energy, Networks and Environment (ARERA) has moved to enable also the participation of DERs. In this regard, in 2017, Resolution 300/2017/R/eel [32] started a pilot project allowing the provision of RR service from dispersed generation, properly aggregated and coordinated [33]. A further extension to the aFRR service (secondary frequency reserve) is also foreseen [34]. Actually, the minimum bid size is set at 1 MW; however, a reduction of this threshold to 0.2 MW is under discussion [35].

Despite the harmonization process ongoing in Europe, there are still many differences in terms of participation of DERs into the ASM between the EU countries. However, in spite of national peculiarities, the survey underlined a common path of Member States toward the opening of their ASMs. In this framework, Italy is playing a pivotal role to progressively enable the participation of the distributed resources into the ASM. In the next section, the path undertaken in Italy in this regard and the preliminary results of the Italian pilot project are depicted.

Table 1. Minimum bidding size required to the participation of aggregate of units in ASM.

Country	Minimum bidding size [MW]		
	FCR	aFRR	mFRR or RR
Germany	1	5	5
France	1	1	10
United Kingdom	1	/	3
Finland	0.1	5	5
Italy	/	(Under discussion)	1

IV. THE ITALIAN PATH TOWARD THE OPENING OF THE ASM TO DERS

Similarly to the evolution of many EU countries, also Italy has been characterized by a large deployment of DERs driven by environmental targets and economic incentives. For example, during the decade 2008-2018, the yearly energy production from DERs increased by 3 times, reaching 20% of the national annual consumption. This rapid evolution has required a process of standardization of the technical requirements to enable the connection of power plants to the grid. This process started in 2008 with the introduction of the technical standard CEI 0-16 of the Italian Electrotechnical Committee, defining the technical prerequisites to apply for the connection of loads and generators to the medium voltage distribution grid [36]. With a similar approach, the standard CEI 0-21 defined the prescriptions to follow for the connection of power plants to the low voltage grid. These rules were updated in 2012 and 2014, introducing further requirements for DER power plants, such as the obligation to control the reactive power to adjust the voltage profile over the grid and to limit the active power injected in critical circumstances (e.g. overfrequency transients). However, the exploitation of distributed resources to provide grid services cannot be limited to critical conditions. Indeed, as expressed by the EU Regulation 2019/943 [37], there is the need to completely integrate all the resources, connected at any voltage level, to achieve a safe and reliable system operation. Therefore, to this purpose, ARERA has recently initiated two paths to improve this integration:

i) increasing the observability of DERs by the system operator through the installation of suitable monitoring and communication devices (also enabling the sending of control signals to dispersed units, when needed);

ii) opening the national ASM to aggregate of DERs.

i) Increase of DERs osservability

One of the main problems introduced by large penetration of DERs is related to the limited data available on their real-time production and predictability of their energy exchanges. To overcome these issues, ARERA, following the directions of EU guideline 2017/1485 [38], has opened to the possibility of collecting measurements on DER power plants to be delivered to the TSO. This process, started by the Resolution 628/2018/R/eel [39], provided the installation of an innovative device specified by the last release of technical standard CEI 0-16, which is aimed to monitor and, in perspective, to enable the remote control of dispersed units: the Centralized Plant Controller (following the Italian nomenclature “Controllore Centrale di Impianto”: CCI). The CCI is an integrated device capable to supervise the performances, in terms of active and reactive power exchanges, of a single power plant or aggregate of DERs. It is equipped with a modem capable to provide a bidirectional communication between the local generator, the system operators (i.e. TSO, DSO) and the Aggregator. Hence, the implementation of this device allows achieving not only a higher observability of DERs, but also promotes a greater spreading of the Aggregator concept, since it facilitates and standardizes the exchange of data and signals between the Aggregator and the units in its portfolio. According to the Italian regulation (still under definition), probably the CCI will be mandatorily installed on all the new generators or group of generators with a total power greater than 1 MW and aggregates of units that are enabled, through pilot projects, to provide ASs to the power grid. It is also foreseen a further extension to plants and ESSs already installed and clusters of units having a nominal power between 11.08 kW and 1 MW [39].

As already anticipated, Italy is also playing an important role in experimenting the supply of ASs from DERs. In this regard, in the next subsection, the preliminary results of the Italian pilot project enabling the provision of ASs from aggregates of dispersed resources are presented.

ii) Opening of the ASM to DERs

Recently, the Italian Regulatory Authority (ARERA) started a pilot project to test the provision of ASs from aggregates of distributed resources. This pilot project started in 2017 and defined, for the first time in Italy, the concept of Virtually Aggregated Unit (in Italian “Unità Virtuale Abilitata”: UVA) [32]. Based on the latest resolution, published in 2018, an UVA is defined as an aggregate of many small-scale generation plants, consumption units and energy storage systems (e.g. also including electric vehicles). These resources are grouped and coordinated by an Aggregator, which, by using suitable control tools, can participate to the ASM offering the units’ flexibility.

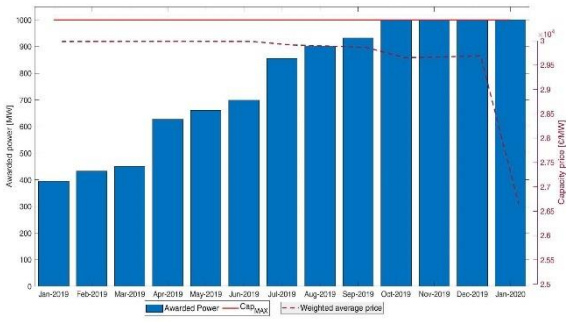

Figure 2. Capacity allocation and average price of the capacity auctions

To favor a larger involvement of stakeholders, ARERA has introduced a dual remuneration scheme for Aggregators. In particular, it was introduced a remuneration based on long term capacity contracts, in addition to the standard mechanism based on the energy supplied during the regulation. In these contracts, the TSO acquires a certain amount of capacity from the Aggregators (i.e. 1 GW in total for 2020) through annual and intra-annual auctions, with a strike price of 30,000 €/MWh. The Aggregators receive the capacity remuneration monthly upon the commitment to submit offers in the ASM during the peak hours (i.e. from 2 p.m. to 8 p.m. of the weekdays). The introduction of a capacity remuneration has produced two main advantages: i) it has favored the Aggregators’ involvement, covering part of the investment costs required to equip the coordinated DERs; ii) it has also facilitated the creation, during the peak hours, of the high margin of reserve required by the TSO [40].

Secondly, to further facilitate the aggregation of DERs, the aggregation perimeter, i.e., the geometrical area within which the Aggregator can group DERs, has been opportunely defined. Following the actual regulations, this perimeter can group a few provinces. However, it is expected that in the next future this aspect will be revised, because to avoid congestions in the transmission lines due to energy exchanges between the units in the aggregate, the aggregation perimeters should consider the transmission network topology and not the geographical area. The results of 2020 auctions for the capacity contracts showed a large involvement of the stakeholders in the pilot project. Indeed, all the capacity issued available by the Italian TSO (1 GW) has been assigned to the

Aggregators. Analyzing the auctions from an economic perspective, it is possible to highlight a constant decrease of the weighted average price paid by the TSO for the capacity remuneration. Indeed, the mean weighted price accepted in the annual auction decreased by 13% between 2019 and 2020 (i.e. from 29,980 €/MWh to 26,500 €/MWh). Therefore, as presented in Figure 2, the growing involvement of Aggregators in the project (the blue bars in the plot indicate the capacity awarded) led to a more competitive market, pushing for a reduction of the average capacity remuneration price (the magenta dotted lines).

During the project, 231 aggregates, with an overall capacity of 1,348.9 MW, have participated. Most of them, almost 75% of the total, are currently located in the North of Italy. Concerning the technical composition, a positive aspect that should be underlined is related to the large participation of consumption units: almost 80% of the Aggregators have at least one flexible load in their portfolio. However, the participation of aggregates of dispersed RES is still limited. This is caused by the fact that, on the one hand, many of these resources in Italy benefits of incentive schemes, which push users to maximize their energy production.

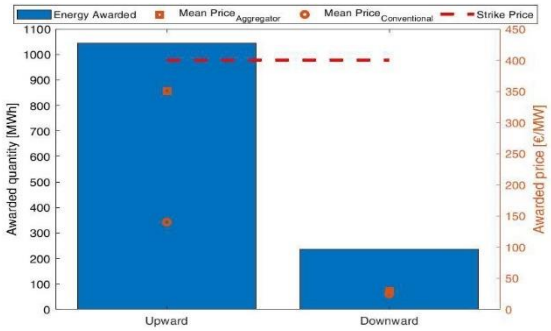

Figure 3. Quantity and mean price accepted from the Aggregators' bids

On the other hand, usually the regulation performed by RES is carried out by curtailing their power. Therefore, the participation to the ASM of these resources is not convenient without the adoption of proper expedients (e.g. ESS) able to avoid the loss of production.

Another critical aspect emerged in the Italian pilot project is related to the small number of units currently involved in the Aggregator's portfolio. Indeed only 8 aggregates operate with a portfolio with at least 10 units, and in 25% of the cases, the portfolio is composed by a single unit. This result can be justified considering the greater ease to control and manage, in this first phase, a small aggregate of plants. However, even though the management of a larger and diversified portfolio could be more complex, it is expected to bring in the future greater technical and economic advantages: a wide and heterogeneous portfolio, as described in Section II, implies a higher possibility to provide services to the market, but also allows to increase the reliability of the AS provision, reducing for example possible penalties for the non-fulfilment of the requested service.

Despite the advantages related to the procurement of capacity margins, so far, UVAs have been only partially exploited for the provision of ASs. In particular, during the period 2019-2020, only 1,045.23 MWh of upward regulation (i.e. request to increase the power produced) has been acquired from Aggregators. In relative terms, the awarded bids represent only 0.02% of the total quantity offered. This limited exploitation of the flexibility made available can be justified considering the prices at which the upward service has been offered: the average price of the Aggregators' bids was about 351 €/MWh, which is close to the strike price (i.e. 400 €/MWh), and it is 2.5 times the average price offered by conventional power units (see Figure 3). Clearly, since the offers selection process in the ASM aims at minimizing the overall system costs, the offers of the Aggregators have less probability of being selected. Considering the bids submitted for the RR downward service, only 234.83 MWh submitted by the Aggregators have been accepted (i.e. 0.5% of the total bids). However, in this case the average price submitted was 30 €/MWh, value in line with the average value offered by traditional power units, which is 25 €/MWh.

In spite of the fact the UVA pilot project is still at a preliminary stage, where the actors involved are still shaping their dynamics of participation into the market and there is a scarce competition among offers, the Italian TSO has frequently declared the importance of this project to prove the feasibility of the proposed approach and to support the creation of the reserve margins requested by the TSO.

V. CONCLUSIONS

In this paper, a comprehensive analysis of the EU path toward the opening of the ASM to DERs has been proposed. The survey has shown that, despite differences are still present, EU countries are moving toward a higher integration of DERs in their ASMs. In this rapidly changing scenario, Italy is playing a key role. To face the issues introduced by the massive penetration of RES, the Italian Regulatory Authority (ARERA) has moved to allow a better integration of DERs into the power system and electricity market. The preliminary results of the UVA pilot project, which opened the Italian ASM to aggregates of distributed resources, have shown the potential of DERs to contribute to the ASs provision. The opportunities related to the involvement of DERs in the market are expected to further increase in the next future, with the adoption of the communication and monitoring devices prescribed by Italian technical standard CEI 0-16, aimed to allow a better observability of dispersed resources and to enable their remote control and coordination by Aggregators

VI. ACKNOWLEDGMENTS

This work has been financed by the Research Fund for the Italian Electrical System in compliance with the Decree of Minister of Economic Development April 16, 2018.

VII. REFERENCES

[1] United Nations (UN), "Paris Agreement report of the Parties", 2015, available online: https://unfccc.int/process/conferences/pastconferences/paris-climate-change-conference-november-2015/paris-agreement.

[2] European Commission, "GREEN PAPER A 2030 framework for climate and energy policies", Brussels, 27.3.2013, COM(2013), 169.

[3] European Commission, "Regulation of the European parliament and council establishing the framework for achieving climate neutrality" Regulation (EU) 2018/199, 4.3.2020, COM(2020) 80

[4] USA FERC, Docket N. RM10-17-000; Order N. 745, "Demand Response Compensation in Organized Wholesale Energy Markets", Mar. 2011.

[5] AEMC 2016, "Demand Response Mechanism and Ancillary Services Unbundling", Final Rule Determination, Nov. 2016, Sydney

[6] Italian Energy Authority (ARERA), Consultation Document 207/2019/I/EEL, May 2019, available online: https://www.arera.it/allegati/docs/19/207-19.pdf

[7] H. Saboori, M. Mohammadi, R. Taghe, "Virtual Power Plant (VPP), Definition, Concept, Components and Types," 2011 Asia-Pacific Power and Energy Engineering Conference, Wuhan, China, 2011, pp. 1-4, doi: 10.1109/APPEEC.2011.5749026.

[8] Directive 2012/27/EU of the European Parliament and of the Council of 25 October 2012 on energy efficiency, available online: http://data.europa.eu/eli/dir/2012/27/2021-01-01.

[9] G. Plancke, K. De Vos, R. Belmans, A. Delnooz, "Virtual power plants: Definition, applications and barriers to the

implementation in the distribution system," 2015 12th International Conference on the European Energy Market (EEM), Lisbon, Portugal, 2015, pp. 1-5, doi: 10.1109/EEM.2015.7216693.

[10] M. Trieu, P. Jadun, J. Logan, C. McMillan, M. Muratori, D. Steinberg, L. Vimmerstedt, R. Jones, B. Haley, B. Nelson, "Electrification Futures Study: Scenarios of Electric Technology Adoption and Power Consumption for the United States" , National Renewable Energy Laboratory. NREL/TP-6A20-71500,available online: https://www.nrel.gov/docs/fy18osti/71500.pdf.

[11] C. Dong, X. Ai, S. Guo, K. Wang, Y. Liu, L. Li, "A study on short-term trading and optimal operation strategy for virtual power plant", 5th International Conference on Electric Utility Deregulation and Restructuring and Power Technologies (DRPT), Changsha, 2015.

[12] International Renewable Energt Agency (IRENA), "Electricity Storage and Renewables: Costs and Markets to 2030", Abu Dhabi, October 2017.

[13] EU-SysFlex, "Demonstrators for Flexibility Provision from Decentralized Resources, Common View, Document 6.6",2019.

[14] B. J. Claessens, S. Vandael, F. Ruelens, M. Hommelberg, «Self-learning demand side management for a heterogeneous cluster of devices with binary control actions», 2012 3rd IEEE PES Innovative Smart Grid Technologies Europe (ISGT Europe), Berlin, 2012.

[15] S. Cheng, Y. Feng, X. Wang, "Application of Lagrange Relaxation to Decentralized Optimization of Dispatching a Charging Station for Electric Vehicles," Electronics, vol. 8, no. 3, p. 288, Mar. 2019.

[16] C. Meng, P. Qin, Y. Wang, X. An, H. Jiang, Y. Liang, «A revenue-risk equilibrium model for distributed energy integrated virtual power plants considering uncertainties of wind and photovoltaic power,», 2020 5th Asia Conference on Power and Electrical Engineering (ACPEE), Chengdu, China, 2020.

[17] W. Tang, H. Yang, "Optimal Operation and Bidding Strategy of a Virtual Power Plant Integrated With Energy Storage Systems and Elasticity Demand Response", IEEE Access, vol. 7, pp. 79798-79809, 2019.

[18] 50hertz, Amprion Tennet, APF, Elia, Transnet BW," Consultation on the design of the platform for automatic Frequency Restoration Reserve (aFRR) of PICASSO region", November 2017.

[19] European Commission, "Establishing a network code on requirements for grid connection of generators", Commission Regulation 2016/631, 14 April 2016.

[20] European Commission, "Establishing a guideline on electricity transmission system operation", 2017/1485 of 2 August 2017, available online: http://data.europa.eu/eli/reg/2017/1485/oj.

[21] ENTSO-E, "Technical Requirements for Fast Frequency Reserve Provision in the Nordic Synchronous Area – External document", 24 February 2020.

[22] ENTSO-E "Electricity Balancing in Europe: An overview of the European balancing market and electricity balancing guideline", November 2018.

[23] 50hertz, Amprion Tennet, Transnet BW, "Prequalified performance in Germany for the reserve quantity", September 2020, original title: Präqualifizierte Leistung in Deutschland.

[24] Smart Energy Europe (SmartEn), "European Balancing Markets Edition", 2018.

[25] P. Matschoss, B. Bayer, H. Thomas, A. Marian, "The German incentive regulation and its practical impact on the grid integration of renewable energy systems", Renewable Energy, Volume 134, 2019, Pages 727-738.

[26] Interflex project, "Deliverable D5.6: Documentation of Use Case Algorithms", June 2018.

[27] M. Joos, I. Staffell, "Short-term integration costs of variable renewable energy: Wind curtailment and balancing in Britain and Germany", Renewable and Sustainable Energy Reviews, 2018, V. 86, p. 45 -65.

[28] Francaise National Assembly and Senate, Law 2015-992, "Energy transition for green growth", August 2015.

[29] Ordinance N°2016-2019 of the Francaise Republique , "Self-consumption of electricity", July 2017.

[30] Caramizaru, A. and Uihlein, A., "Energy communities: an overview of energy and social innovation", Publications Office of the European Union, Luxembourg, 2020, doi:10.2760/180576, JRC119433.

[31] National gridESO website, Replacement Reserve, 2020, available online: https://www.nationalgrideso.com/industryinformation/balancing-services/reserve-services/replacementreserverr

[32] Italian Energy Authority (ARERA), "Consultation Document 300/2017/R/eel", 2017, available online: https://www.arera.it/it/docs/17/300-17.htm

[33] D. Falabretti, F. Gulotta," An Algorithm for the Ancillary Services Provision by E-Mobility-based Virtually Aggregated Mixed Units", 2020 IEEE International Conference on Environment and Electrical Engineering, Madrid, Spain, 2020, doi: 10.1109/EEEIC/ICPSEurope49358.2020.9160737.

[34] Italian Energy Authority (ARERA), "Memorandum for the Industrial Commission, Commerce, Tourism Commission of the Senate of the Italian Republic", 6 Oct. 2020, available online: https://www.arera.it/it/docs/20/370-20.htm

[35] Italian Energy Authority (ARERA), "Consultation Document 3 June 2020 201/2020/R/eel", 2020, available online: www.arera.it/it/docs/20/20-20.htm

[36] Italian Electrotechnical Committee, "Reference technical rules for the connection of active and passive consumers to the HV and MV electrical networks of distribution Company", 2020.

[37] Regulation (EU) 2019/943 of the European Parliament and of the Council of 5 June 2019 on the internal market for electricity, OJ L 158, 14.6.2019, p. 54–124.

[38] European Commission, "Establishing a guideline on electricity transmission system operation", 2017/1485 of 2 August 2017.

[39] Italian Energy Authority (ARERA), "Resolution 628/2018/R/eel", December 2018.

[40] F. Gulotta, A. Rossi et al., "Opening of the Italian Ancillary Service Market to Distributed Energy Resources: Preliminary Results of UVAM project," 2020 IEEE 17th International Conference HONET, Charlotte, NC, USA, 2020, pp. 199-203, doi: 10.1109/HONET50430.2020.9322822

New urbanstyle technology – modular green roof and wall system

Natalia Shushunova
Department of Integrated Safety in Construction
National Research Moscow State University of Civil Engineering
Moscow, Russia
nshushun@gmail.com

Elena Korol
Department of Housing and Communal Services
National Research Moscow State University of Civil Engineering
Moscow, Russia
professorkorol@mail.ru

Piero Bevilacqua
Department of Mechanical, Energy and Management Engineering
University of Calabria
Rende, Italy
piero.bevilacqua@unical.it

Abstract

In this paper, we describe the most innovative environmental projects and modular green technology as a key element of our urban spaces and the lungs of the cities. The decision to completely eliminate carbon fuels and reduce environmental pollution, make urban style more sustainable and friendly to the environment is reflected in the use of modular design and technological solutions for the building facades and roofs. A comprehensive analysis of the presented green systems allows to identify their shortcomings and show the advantages of modern modular greening technology using devices that integrate and convert solar and wind energy such as solar panels, micro wind turbines and modern automatic irrigation system. Ergonomic design is provided with the installation in various roof configurations and types such as green and blue roofs and using the system as a vertical gardening by construction of multilevel modular pot system. Another motivating factor will be the deeper appreciation of Green Environmental Protection and the relentless efforts of many governments to this end.

Keywords: *Green building, green roof technology, manufacturability, sustainable development, urban health*

I. INTRODUCTION

The relevance in this work is determined by the fact that at present new construction technologies are being formed with integrated greening systems on the roofs and facades of buildings in order to create a comfortable and healthy urban environment for future generations. Nowadays in many countries, environmental policy is aimed at getting rid of excess carbon footprint and making the urban spaces environmentally friendly for a favorable living environment for its citizens. The greening of roofs and walls of buildings is a necessary element of sustainable ecological development of modern cities. «Clean air and a livable climate are inalienable human rights and solving this crisis is not a question of politics, it is a question of our own survival. This is the most urgent of times, and the most urgent of messages», Leonardo DiCaprio, United Nations Messenger of Peace for Climate, said it on the United Nations Climate Summit in 2014, and we have to influence it as soon as possible [1].

IEECP'21, July 29-30, 2021, Silicon Valley, San Francisco, CA – USA

DAI : *https://sci-index.com/DAI/2021.99101/IEECP/14526939*

II. GREEN ROOFS AND PV TECHNOLOGY

The combination of green roof and PV technology can be beneficial and provide several advantages. It is well known that an increase in PV cells' temperature adversely affects the conversion efficiency, limiting the ability of a PV module (figure 1) to produce energy in favorable conditions, such as with high level of solar irradiation [2], [3].

Figure 1. Integration of PV panels on the green roof.

Vegetation and substrate on a green roof are responsible for the evapotranspiration effect, that is believed to reduce the air and system temperature converting solar radiation into latent heat released in the atmosphere, producing consequently savings in terms of cooling energy need [4]. Furthermore, the green roof reduces the surface temperature, with consequent cooler near-surface air temperature, thus providing enhanced conditions for PV operation and production.

The recent research has analyzed the combination of these two technologies in order to assess the cost-effectiveness as well as the environmental benefits [5]. The experimental evaluation of Photovoltaic (PV) – green roofs under Mediterranean climate summer conditions was performed in [6] selecting two autochthonous plants, (Gazania rigens and Sedum clavatum) and a PV-gravel configuration as the reference roof. The results revealed that the green roof caused a positive effect leading to the

improvement of PV electrical performance, with maximum power output increase for PV-gazania and PV-sedum of 1.29% and 3.33%, respectively, when compared to a PV-gravel roof. A study [7] evaluated the overall profit considering the energy generated and saved thanks to the installation of PV and green roofs considering also climate uncertainties with a two-stage stochastic programming mode. With a 20-year time span, more consistent with PV and green roof lifespan, the results showed the importance of the integration of PV-GR for efficiency increase as it can significantly change the optimal solutions and that the model is highly sensitive to GR parameters that must be properly calibrated. The effect of different roofing technologies was explored in [8], where it was found that a white-PV roof can reduce the total flux by 55%, whereas a green-PV roof reach a total flux reduction of about 42%, both compared to a traditional black roof. The relationship between ambient temperature and PV output by comparing the performance of green roof–PV and black roof–PV systems considering a one-year field experiments was investigated in [9]. The results revealed that the green roof was expected to increase the PV power generation by 0.9% under high temperature scenario, for the climate conditions of Pittsburgh.

It is important evaluate the performance of the various plant layers which enhance the PV-green roof integration in order to maximize the power output [10] and therefore there is a need to select the best vegetation according to climate conditions of the specific locality. It was highlighted that the integration of a PV on a green roof can affect the plant development and community [11]. The main effect of the PV is the shade provided by the modules. Shade can be useful to developing plants in dry environments because of the increased moisture while it appears unnecessary in moist environments.

Since extensive green roofs in Mediterranean climates generally lose moisture quickly following the end of seasonal precipitation, PV would be expected to contribute to higher moisture levels on the green roof, and thus benefit plants. Several studies that have examined the effects of shade on multiple species found that only some of them responded positively [12], [13]. Shade heterogeneity can allow competing species to coexist [14]. Since shade and its effects benefit some species, but are detrimental to other species, a green roof with PV, where there is a heterogeneous environment with different levels of shade, would be expected to produce a diverse plant community [11].

A more interesting and appealing solution that allows to exploit even better the characteristic of the green roof is the use of Bi-facial PV modules. The use of conventional photovoltaic system often installed with low-tilt angles, prominently in South, South-East or South-west directions, and the close placements of modules to each other, in order to optimize the available space, can results in an almost coverage of the roof surface, completely shading the vegetation. Or, if PV panels are installed at a low height from the roof plane, the plants growing in between the modules can generate undesirable shading of the collector surface with the risk to reduce the annual energy yield. So, in such cases, it becomes important a frequent maintenance procedure, that can be however, complicated by dense PV system layouts.

In order to overcome these limitation vertically mounted bifacial modules were proposed [15]. They tested a standard green roof substrate with a standard mixture of green-leaved plants and a recycled green roof substrate with silver-leaved plants to achieve a higher albedo. Despite the East-West orientation, the bifacial modules were able to achieved a specific yield close to typical values of south-facing systems in the same region. It was also shown that plants with silvery leaves improve the system yield compared higher resilience of the plants that provides a more stable albedo.

The PV-green roof is believed to be a promising technology to enhance the PV output on a building scale. However, there are several challenges for combining the two technologies together which obstacle its application. Challenges relating to green roofs include high investment costs, a lack of sustainable materials, and the difficulty of real-life applications in larger projects [5]. Most importantly the biggest challenge for the PV-green roof application is the limited availability of case studies and experimental data making it difficult to draw robust conclusion on the feasibility of such integration.

III. GREEN ROOF INSTALLATION PROCESS

When installing green roofs, we took into account:

- the load that the structure of this roof can withstand; taking it into account, the type of green spaces is selected;

- the volume of the soil layer required to accommodate plant roots;

- the required amount of moisture to provide plants with water; the need for drainage to remove excess moisture, gets operational coverage during precipitation or watering plants;

- the need to protect structural elements from root penetration;

- the possibility of arranging energy converting systems such as PV modules, wind turbines and others.

At the same time, we were analyzed the continuous and modular device of greening systems:

- continuous green roof with devices for independent irrigation - variant 1(Figure 2);

- modular green roof system with the cells - variant 2 (Figure 3);

- modular green roof system, designed by authors - variant 3 (Figure 4).

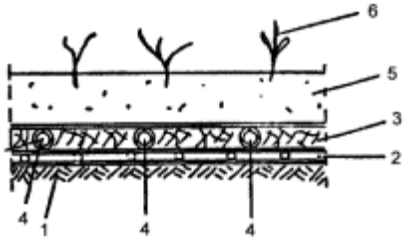

Figure 2. Continuous green roof with devices for independent irrigation: 1 - Concrete vault; 2 - Sealing (sealing) gasket; 3 - a layer of fiberglass; 4 - Flexible tube; 5 - Root checkmate; 6 - Vegetation layer.

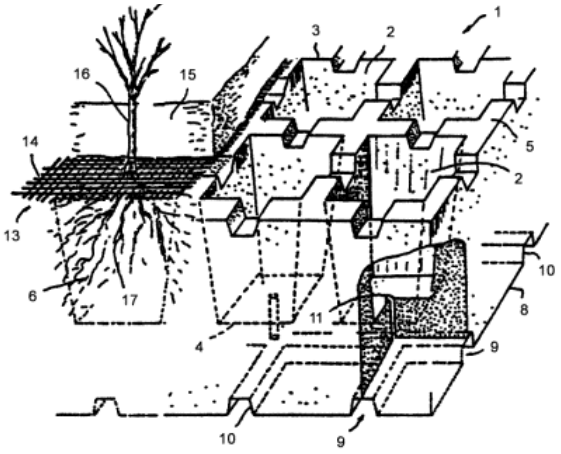

Figure 3. Modular green roof system with the cells: 1 – support; 2 – cell; 3 – upper part; 4 – bottom; 5 – cruciform connection element; 6 – organic base; 7 – base coating; 8 – water isolation layer; 9 – openings in water isolation layer; 10 – edge on water isolation layer; 11 – narrow opening; 12, 13 – layers of textile material; 14 – grating; 15 – soil layer; 16 – plants; 17 – roots.

Based on these considerations, we carried out an analysis of various constructive and technological solutions for green roofs, consisting of the following elements: type of the fastening system and convenience of installation and use (Table 1).

Table 1. The comparative analysis of the green roof systems.

No	Description of the green roof systems	Type of the fastening system	Convenience of installation and use
1	The system provides for a device for independent irrigation, which is located between the waterproofing and the vegetation layer and consists of a canvas and irrigation channels carried out in the canvas or under it.	The fastening system is complex enough to maintain during operation.	The system uses a lightweight independent irrigation system, which allows for ease of installation.
2	The modular green roof system, consists of the cells, which are preferably identical and symmetrical. Each cell is open in its upper part and closed in the lower part by the bottom, which has narrow openings for removing excess water supplied to the panel. The cells are filled with an organic base for feeding the roots of plants planted in a soil layer. The upper part of the panel is insulated from the ground with a layer of textile material.	The system contains a support made of plastic with a low specific weight. This support is a structure that forms a large number of separate cells located side by side.	Installation takes place in several stages, the duration of installation process is longer.
3	The modular green roof system, designed by authors consists of the modules with the ability to integrate devices that convert solar and wind energy.	Simple fastening system, consisting of reinforcing elements with a double-headed arrow, can be easy applied to the building structure.	Installed modules are adapted to be gripped by a person's hand, which allows a person to fast move the module by himself.

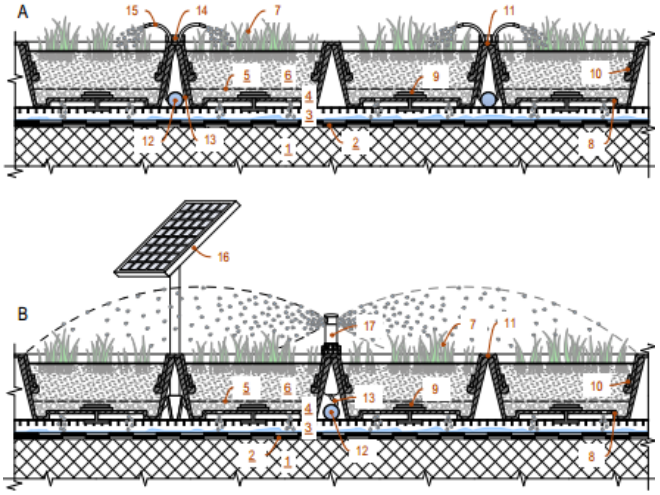

Figure 4. Modular green roof system with the cells: 1 – base coating; 2 – water isolation layer; 3 - grating; 4 – water flow; 5 – drainage layer; 6 - soil layer; 7 – plants; 8 – module; 9 – fastener; 10 – rim; 11 – interlocking apparatus; 12 – hose; 13 – water delivery tubes; 14 – perforated cup; 15 – drip watering tube; 16 – PV module; 17 – sprinkler.

We had evaluated manufacturability of these structural and technological solutions (STS) [16]. Calculation of the coefficient of manufacturability of the device of continuous green roof with devices for independent irrigation $K_{t\ gr}^{1}$ showed that this STS is acceptable:

$$K_{t\,gr}^{1} = \frac{Q_{gr\ k}}{Q_{ml\ i}+Q_{gr\ k}} = 0{,}16 - \ (0{,}1\ldots0{,}2).$$

Calculation of the coefficient of manufacturability of the device modular green roof systems $K_{t\ gr}^{2}$ and $K_{t\ gr}^{3}$ showed that these STS are rational:

$$K_{t\,gr}^{2} = \frac{Q_{gr\ k}}{Q_{ml\ i}+Q_{gr\ k}} = 0{,}04 < 0{,}1.$$

$$K_{t\,gr}^{3} = \frac{Q_{gr\ k}}{Q_{ml\ i}+Q_{gr\ k}} = 0{,}03 < 0{,}1.$$

The most expedient is the solution of the green roof device using modular structures, since with an increase in the complexity of the roof, the total labor intensity of work on the installation of such coatings will be minimal when comparing various options for the device of roofing.

IV. APPLICATION OF INNOVATION GREEN WALL SYSTEM

The great interest is the innovative projects of urban green schools that are being built in San-Francisco and educate children according to a special ecological Curriculum based on the Waldorf pedagogical system. The mission of such green schools is to develop a person who independently chooses paths through life and have imagination, a sense of justice and a sense of responsibility on which the essence of education is based. Green building with a vegetation cover to place of classrooms and the farm where students teach both traditional subjects and acquire behavioral skills, take care of environment, growing zucchini, cabbage, onions and other herbs and vegetables. The unique design is being developed by SWA Landscape, who designed an effective green roof for the building of the California Academy of Sciences in the Golden Gate Park. This building is a tool for teaching in complete harmony with nature. The construction of green rooftops of the building cladding absorbs water, provides thermal insulation and provides a natural habitat for pollinating insects (Figure 5).

Figure 5. Design project of green school in San-Francisco.

Innovative technology for covering of the school buildings and facilities with modular green wall systems is proposed by authors (Figures 6, 7).

Figure 6. The modular green wall system in school buildings and facilities.

Figure 7. The modular green wall system, designed by authors.

The advantages of the system, designed by the authors, emphasizes its unique qualities such as wavy-continued design, pre-vegetated green wall modules, which may be transported to the building, where modules may be arranged in a grid-like fashion to cover one or more walls of the dwelling house or business center. In this manner, the pre-vegetated green wall may be installed in a relatively short period of time.

Many researchers are developing new solutions and researching existing technologies for greening urban areas, the attitudes regarding their application and assessments of manufacturability remains open [17-21].

V. RESULTS

New urbanstyle technology – modular green roof and wall system is developed for use in residential and public buildings. The diversity and multiplicity of modular green system, designed by authors with different configurations and sizes of modules allows to use greening structures in buildings of various functional purposes, including school and preschool education, considering geographic zone and climate characteristics. And it shows interest in installation of this biggest variants of green roofs and walls, their ergonomic design and industrial applicability. It is also important to note that this system, developed by the authors, allows you to integrate devices such as solar panels, micro wind turbines and modern automatic irrigation system, the system also provides trays for filling with water (see Figure 8).

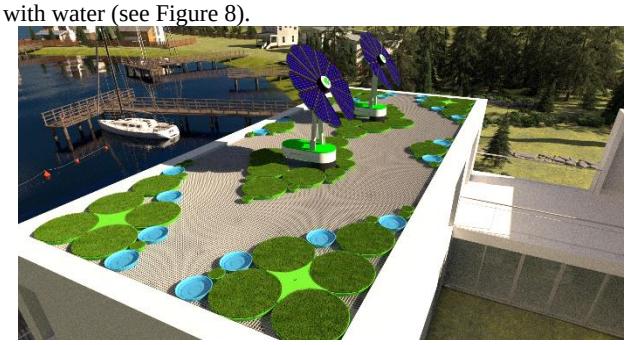

Figure 8. The modular green and blue roof system, designed by authors.

VI. CONCLUSIONS

In this study, we compared the continuous and modular structural and technological solutions of the device green covering systems and concluded that the modular green system is the most applicable since their manufacturability is higher than their counterparts. Assessment was carried out with the method calculation of the coefficient of manufacturability of the device green roof systems.

VII. REFERENCES

[1] Available online: https://www.leonardodicaprio.org/leonardo-delivers-landmark-speech-at-the-united-nations-climate-summit/

[2] P. Bevilacqua, R. Bruno, and N. Arcuri, “Comparing the performances of different cooling strategies to increase photovoltaic modules electric in different meteorological conditions,” Energy, vol. 195, p. 116950, 2020.

[3] P. Bevilacqua, A. Morabito, R. Bruno, V. Ferraro, and N. Arcuri, “Seasonal performances of photovoltaic cooling systems in different weather conditions,” J. Clean. Prod., 2020.

[4] P. Bevilacqua, R. Bruno, and N. Arcuri, “Green roofs in a Mediterranean climate: Energy performances based on in-situ experimental data,” Renew. Energy, vol. 152, pp. 1414–1430, 2020.

[5] M. Shafique, X. Luo, and J. Zuo, “Photovoltaic-green roofs: A review of benefits, limitations, and trends,” Solar Energy. 2020.

[6] D. Chemisana and C. Lamnatou, “Photovoltaic-green roofs: An experimental evaluation of system performance,” Appl. Energy, 2014.

[7] M. Ramshani, A. Khojandi, X. Li, and O. Omitaomu, “Optimal planning of the joint placement of photovoltaic panels and green roofs under climate change uncertainty,” Omega (United Kingdom), 2020.

[8] A. Scherba, D. J. Sailor, T. N. Rosenstiel, and C. C. Wamser, "Modeling impacts of roof reflectivity, integrated photovoltaic panels and green roof systems on sensible heat flux into the urban environment," Build. Environ., 2011.

[9] A. Nagengast, C. Hendrickson, and H. Scott Matthews, "Variations in photovoltaic performance due to climate and low-slope roof choice," Energy Build., 2013.

[10] D. Chemisana and C. Lamnatou, "Photovoltaic-green roofs: An experimental evaluation of system performance," Appl. Energy, 2014.

[11] B. Y. Schindler, L. Blaustein, R. Lotan, H. Shalom, G. J. Kadas, and M. Seifan, "Green roof and photovoltaic panel integration: Effects on plant and arthropod diversity and electricity production," J. Environ. Manage., 2018.

[12] L. Blank and Y. Carmel, "Woody vegetation patch types affect herbaceous species richness and composition in a Mediterranean ecosystem," Community Ecol., 2012.

[13] M. J. van Zonneveld, J. R. Gutiérrez, and M. Holmgren, "Shrub facilitation increases plant diversity along an arid scrubland-temperate rain forest boundary in South America," J. Veg. Sci., 2012.

[14] F. Valladares, "Light Heterogeneity and Plants: from Ecophysiology to Species Coexistence and Biodiversity," 2003.

[15] T. Baumann, H. Nussbaumer, M. Klenk, A. Dreisiebner, F. Carigiet, and F. Baumgartner, "Photovoltaic systems with vertically mounted bifacial PV modules in combination with green roofs," Sol. Energy, 2019.

[16] *Korol E.A., Shushunova N.S.* Processability of the device of exploited roofs with greening systems. IOP Conference Series Materials Science and Engineering 869:022009 DOI: 10.1088/1757-899X/869/2/022009

[17] Bruno R, Bevilacqua P, Longo L, Arcuri N 2015 Small Size Single-axis PV Trackers: Control Strategies and System Layout for Energy Optimization Energ. Procedia vol 82 pp 737-743

[18] *Korol, S.P., Shushunova, N.S., Shushunova, T.N.* Innovation technologies in Green Roof systems // Matec Web of Conferences.2018. Volume 193, 04009. https://doi.org/10.1051/matecconf/201819304009

[19] *Korol E.A., Shushunova N.S., Mayilyan A.L.* Organizational and Technological Procuring of Roofing Devices with Greening Systems. IOP Conference Series Materials Science and Engineering. 2020. Volume 753, 32059. DOI: 10.1088/1757-899X/753/3/032059

[20] Bevilacqua P, Mazzeo D, Bruno R and Arcuri N 2017 Surface temperature analysis of an extensive green roof for the mitigation of urban heat island in southern mediterranean climate. Energy and Buildings.Vol 150 pp 318-327. https://doi.org/10.1016/j.enbuild.2017.05.081

[21] Carbone M, Garofalo G, Nigro G et al. 2015 Green Roofs in the Mediterranean Area: Interaction between Native Plant Species and Sub-Surface Runoff. Applied Mechanics and Materials, vol 737 pp 749-753. DOI: 10.4028/www.scientific.net/AMM.737.749

Exploring the sustainability of cable lines in fire case

1st Tatiana Eremina
Institute of Integrated Safety in Construction
Moscow State University of Civil Engineering
Moscow, Russia
main@stopfire.ru

2nd Dmitry Korolchenko
Institute of Integrated Safety in Construction
Moscow State University of Civil Engineering
Moscow, Russia
da-vip@mail.ru

Abstract

This paper presents a statistical analysis of the fire hazard of cable lines. Basic properties of cable lines of different types in a fire are specified. Factors affecting the sustainability of cable lines in the event of a fire are identified. An assessment of the sustainability of cable lines in fire conditions in accordance with GOST IEC 60331-21-2011 and GOST IEC 60332-3-22-2011 was made. The results are used for provision of fire safety in buildings and facilities during their operation.

Keywords: fire danger of cable lines; fire resistance; limit state of the cable; fire spread; fire influence.

I. INTRODUCTION

The sustainability of cable lines in a fire depends upon various factors. Cables utilize combustible materials (electrical insulation, cable sheaths, etc.) and intrinsic heat sources (thermal emission of conductor cores, provoking de-stabilization with subsequent flames proliferation) [1-3]. For example, cables with rubber sheath, with PVC sheaths, with PE sheath demonstrate different resistance under fire conditions. The multitude of insulation types of cable lines stipulates the demand for comparative studies of their behavior in a fire.

Based on statistical data for the past 10 years, it is apparent that 20-25% of fires annually occurring in Russia cause de-stabilization of electric installations, whereas 50-60% of fires occurring in electric installation proper are caused by the insulation of the cable lines.

Cabling utilities of complex topology are distinguished not only by high combustible loads (insulation of the cables), but also by fire proliferation hazards and emissions of gaseous combustion products into the air of the buildings and facilities.

It is well-known that cable sheaths are made of polymer insulation compounds which emit chlorine, bromine, fluorine, sulfur dioxide, etc. which build in combination with water vapor acids and alkalies causing corrosion of metal structures and equipment.

As a consequence of that, studies of sustainability of cable lines in a fire obtain one of the highest priorities in the sphere of fire safety.

II. METHODOLOGICAL BASIS FOR THE RESEARCH

Due to the high intensity of the technical progress, the scale of cable lines is increasing along with the growth of industrial facilities requiring enhanced sustainability under fire conditions. Traditionally, different types of fire-resistant cables are utilized [4-7].

In accordance with Russian codes [8], the following utilities shall retain their functionality in a fire within the time required for their intended performance and escape of people to a safe area: cable lines and wiring of fire-protection systems, of facilities for firemen support, of fire detection systems, of fire annunciation and escape management, of emergency lighting in escape routes, of emergency ventilation and smoke protection, of automatic fire-righting systems, of the internal fire-fighting water pipeline, of emergency lifts for firemen in building and facilities; the power supply lines of the premises of buildings and facilities shall feature emergency trip devices preventing fire occurrence; the installation rules and the specifications of the emergency trip devices shall be selected under consideration of fire safety requirements.

It is well-known that the proliferation of the fire is dependent not only on the cable quantity, but also on the arrangement of the cables in the conduit space.

As an example, Fig. 1 demonstrates that five cables of VVG and NRG type, in most cases, contribute to fire proliferation at vertical samples arrangements. Thereby, stable flame proliferation will be observed when these cables are arranged in a bundle with a gap (Fig. 1). In this connection, all contemporary cable types being fire-retardant in a bundle (non-flammable) shall be tested in bundles of combustible materials with or without a gap, dependent upon the type and the arrangement method thereof in conduit facilities.

IEECP'21, July 29-30, 2021, Silicon Valley, San Francisco, CA – USA

D!f: https://sci-index.com/DAI/2021.99101/IEECP/14526951

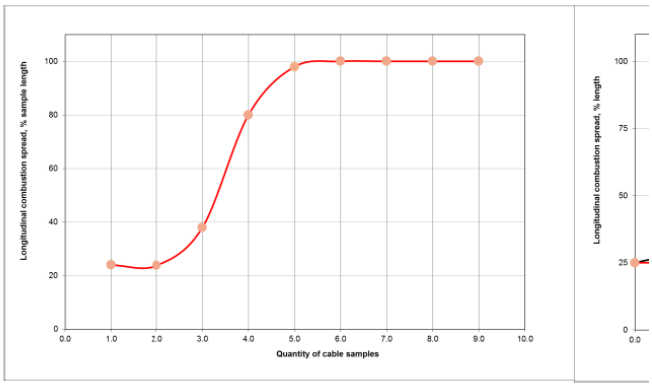

Figure 1. Flame proliferation dependent on cables arrangement.

It is known, that if, during the operation, electrical or optical wires or cables are subject to joint conduit installation, then, the combustion proliferation test results must be obtained exactly for bundles. A bundle is a group of parallel cables clamped together in a single conduit.

During bundle operation, the following distinctive features shall be considered:

- The biggest quantity of combustibles (cable insulation), experiencing the impact of an external fire source, as well as of the fire occurring when cables are burning;
- Joint arrangement of cables during the installation;
- The temperature of the gaseous combustion products emitted by a cabling bundle is considerably higher than that of a single cable;
- Increased emission of gaseous combustion products by a cable bundle at a certain increased temperature;
- Cable design, e.g. armored or armor-free, multi-core or single-core.

III. EXPERIMENT

The fire resistance of the cable is evaluated in accordance with Standard [9] "Fire-exposure testing of electrical and optical cables. Retaining of functionality". The sustainability assessment of a vertically arranged cable bundle is performed in accordance with [10] "Cable lines. Retaining of functionality under fire conditions. Test method".

Based on the applicable testing method, a sample is bundled in the lab imitating a joint installation. The number of the cable sections in the sample is dependent on the quantity and the density of non-metallic cable material. Cables and wires labeled as "НГ" (Russian for "fire-retardant") are subject to mandatory fire-safety tests. The essence of the method is that cable sections are bundled on a test rack and put vertically into a combustion chamber and exposed to flames. Upon finishing the test, the smoldering cable shall get extinguished by itself. The length of the charred cable section shall not extend beyond 2.5 meters. Such cable is deemed to have passed the test.

Based on the requirements to such tests [11], the sample shall contain several cable sections of at least 3.5 m each sampled from one reel.

The number of the cable sections in the section shall be selected in a manner that the rated volume of non-metallic materials is finally equal to 7 liters per 1 running meter of the sample length.

The cable section constituting the sample shall be tempered prior to the test commencement at (20±10) °C for at least 16 hours. The cable sections under test shall be dry.

Such experimental studies were conducted with the following samples:

1) KG 3x50+16-0.66 cable with rubber sheath;
2) AAShv 3x120-10 cable with PVC sheath;
3) Cable with PE sheath. TPPeP 50x2x0.4.

These samples consisted of three bundles of cable sections, each one of at least 3.5 m each.

The proliferation of the flames is determined on the length of the damaged cable section. The present test can be a proof of limited flame proliferation along the cable.

The experimental procedure is as follows:

- three bundles of three types of cables are fastened to the rack;
- the bundles are exposed to flames within 40 minutes;
- the air flow velocity through the test chamber is maintained till the flames go totally out;
- after the exposure to the flames is finished, the sample is carefully wiped. Soot on the sample is admissible if its surface is undamaged; softening or deformation of non-metallic material of the sample is admissible, too. As flames proliferation value, the length of the damaged section is taken (in meters, from the bottom of the burner to the end of the charred section), and it is determined as follows: pressure is exerted on the cable with a sharp tool like a knife blade; the elastic-to-brittle transition place on the sample surface is considered to be the end of the charred section;
- the exposure to the flame in the test chamber is stopped in 28 min 54 seconds due to the fact that the fire has reached the middle of the bundle of cable sections;

Experimental results:

- the charred section of the cable bundles of KG 3x50+116-0.66 rubber-coated cable was 2.5 m;
- the charred section of the bundle of AAShv 3x120-10 cable with PVC sheath was 2.3 m;
- the charred section of the cable section bundles of TPPeP 50x2x0.4 Polyethylene-coated cable was 2.2 m.

The length of the charred cable section measured from the bottom of the burner shall not exceed 2.5 m.

The recommended requirement to the assessment of the results corresponds to the obtained experimental value recorded in the technical report [12].

The results demonstrate that these cables have passed the tests.

IV. CONCLUSION

Studies of the specifics of the sustainability of cable lines under fire conditions demonstrate dependence on the insulation of the cable lines, on the cable types and on the installation method.

The safety of cable lines is indispensable for integrated safety of buildings and facilities, as well as for their further operation.

The results of the study described herein can be taken for the design of cable lines and electrical installations, compilation of technical document packages and specifications.

The studies are financially supported by the Ministry of Science Higher Education of the Russian Federation (Project: Theoretical and experimental design of new material compositions for provision of operational safety in buildings and facilities in accordance with specified conditions).

V. ACKNOWLEDGMENTS

This work was financially supported by the Ministry of Science and Higher Education of the Russian Federation (Project: Theoretical and experimental design of new composite materials to ensure safety during the operation of buildings and structures under conditions of technogenic and biogenic threats #FSWG-2020-0007).

VI. REFERENCES

[1] S. L. Barbot'ko. Combustion process modeling of materials under heat emission assessment test // Fire and explosion safety. — 2007. — V.16 Issue 3. — pp. 10-24.

[2] Huiqing Zhang. Fire-Safe Polymers and Polymer Composites // Technical Report DOT/FAA/AR-04/11. Federal Aviation Administration, William J. Hughes Technical Center Airport and Aircraft Safety, 2004. — 209 p.

[3] Smith E. E. Measuring rate of heat, smoke and toxic gas release // Fire Technology. —1972. — Vol. 8, Issue 3. — P. 237-245. DOI: 10.1007/bf02590547.

[4] G. I. Smelkov. Fire safety of electric wiring [text]/ G.I. Smelkov — M.: "KABEL" LLC, 2009. — 328 p.

[5] G. G. Orlov, L. A. Korol'chenko, A. V. Lyapin Optimization of requirements to design, space and layout solutions during the design of buildings and facilities for explosion-hazardous manufacturing facilities // Fire and explosion safety. — 2014. — Issue 11. — pp. 67-74

[6] Yu. Polandov, D. Korol'chenko. Consideration of turbulence influence on gas explosion expansion in non-closed areas. MATEC Web of Conferences, 2017, vol. 106, article number 01040, 8 p. DOI: 10.1051/matecconf/201710601040

[7] National Standard of Russian Federation 53307–2009. Elements of civil structures. Fire-resistant doors and gates. Fire resistance test method. Moscow, Standartinform Publ, 2009 (in Russian).

[8] Technical Regulations on Fire Safety Requirements No. 123-FZ dd. 22.07.2008 (with amendments No. 117-FZ dd. 10.07.2012, No. 185-FZ dd. 02.07.2013)

[9] GOST IEC 60331-21-2011 "Testing of electrical and optical cables under exposure to flames. Retaining of functionality".

[10] GOST R 53316-2009 "Cable lines. Retaining of functionality under fire conditions. Test method".

[11] GOST R IEC 60332-3-22-2005 NATIONAL STANDARD OF THE RUSSIAN FEDERATION "Testing of electrical and optical cables under exposure to flames". Part 3-22. PROLIFERATION OF FLAMES ALONG VERTICALLY ARRANGED BUNDLES OF WIRES AND CABLES.

[12] IEC/TR2 60332-3(1992) Electrical cables. Inflammability testing. Part 3: Testing of bundled wires or cables.

Bio-hydrogenated diesel production from palm oil with process integration of hydrogen production and hydro-processing

Chaiwat Prapainainar
Department of Chemical Engineering
King Mongkut's University of Technology North Bangkok
Bangkok, Thailand
chaiwat.r@eng.kmutnb.ac.th

Suwimol Wongsakulphasatch
Department of Chemical Engineering
King Mongkut's University of Technology North Bangkok
Bangkok, Thailand
suwimol.w@eng.kmutnb.ac.th

Suttichai Assabumrungrat
Department of Chemical Engineering
Chulalongkorn University
Bangkok, Thailand
suttichai.a@chula.ac.th

Paweena Prapainainar
Department of Chemical Engineering
Kasetsart University
Bangkok, Thailand
fengpwn@ku.ac.th

Abstract

Bio-hydrogenated diesel (BHD) or green diesel is a second generation liquid fuel that can be synthesized through hydrodeoxygenation reaction of fat and its derivatives. It has been expected to replace petroleum diesel and biodiesel due to structure stability and low sulphur. Nevertheless, BHD production still has limitation on the ground of high price for hydrogen feed. Thus, this study report feasibility study of an integrated process of hydrogen production and hydro-processing. The integrated process used refined bleached deodorized palm oil (RBDPO) as a feed. RDBPO was hydrolyzed to produce palm fatty acid (PFA) and glycerol. Glycerol was then fed to sorption-enhanced steam reforming to generate hydrogen gas. After that, bio-hydrogenated diesel was synthesized through hydro-processing between palm fatty acid and hydrogen. The simulation model using ASPEN Plus predicted 57.8 wt.% of overall yield of BHD generated and the integrated process can be self-reliable in hydrogen production without using hydrogen from external sources. Subsequently, production cost and economic profitability of the integrated process were estimated to determine the attractiveness on investment. It was found that total capital investment (TCI) of the production plant was M$25.87 and cost of production $0.52 per litre of BHD. Sensitivity analysis of net present value was conducted after that using three variables, namely RBDPO price, BHD price, and gasoline price. This process was compared with BHD synthesized from fatty acid methyl ester, FAME. At an equivalent capacity, BHD produced from PFA was inferior in term of overall yield, energy consumption and environmental impact.

Keywords: *Bio-hydrogenated diesel, hydro-processing, sorption-enhanced steam reforming*

IEECP'21, July 29-30, 2021, Silicon Valley, San Francisco, CA – USA

D!f: *https://sci-index.com/DAI/2021.99101/IEECP/14526948*

Carbene Based Materials for Organic Solar Cells

Gergana Kostadinova
Faculty of Chemistry and Pharmacy
Sofia University
Sofia 1164, Bulgaria
gergana_kostadinova26@abv.bg

Rumen Lyapchev
Faculty of Chemistry and Pharmacy
Sofia University
Sofia 1164, Bulgaria
rlorgchem@gmail.com

Joanna Stoycheva
Faculty of Chemistry and Pharmacy
Sofia University
Sofia 1164, Bulgaria
stoycheva.joanna@gmail.com

Julia Romanova
Faculty of Chemistry and Pharmacy
Sofia University
Sofia 1164, Bulgaria
jromanova@chem.uni-sofia.bg

Alia Tadjer
Faculty of Chemistry and Pharmacy
Sofia University
Sofia 1164, Bulgaria
tadjer@chem.uni-sofia.bg

Abstract

Successful strategies for the modelling of singlet fission chromophores – highly efficient organic materials in solar cells, will be demonstrated on a series of theoretically designed NHC-carbene dimers. All compounds are synthetically feasible and thus suitable for practical application. They differ in topology, conformation, and type of substituents, which allows us, using quantum-chemical methods, to reveal the intimate correlation between structure and excited state properties. Several potential candidates for singlet fission chromophores were discovered in the series. The relationship between molecular conformation and singlet fission propensity is demonstrated for the first time.

Keywords: *singlet fission, excited states, photovoltaics, quantum-chemistry*

IEECP'21, July 29-30, 2021, Silicon Valley, San Francisco, CA – USA

DAI : ***https://sci-index.com/DAI/2021.99101/IEECP/14526957***

Interplay Bewteen Diradical Character and Stability in Singlet Fission Chromophores

Vaska Petakova
Faculty of Chemistry and Pharmacy
Sofia University
Sofia 1164, Bulgaria
vaska.petakova@abv.bg

Joanna Stoycheva
Faculty of Chemistry and Pharmacy
Sofia University
Sofia 1164, Bulgaria
stoycheva.joanna@gmail.com

Alia Tadjer
Faculty of Chemistry and Pharmacy
Sofia University
Sofia 1164, Bulgaria
fhat@chem.uni-sofia.bg

Julia Romanova
Faculty of Chemistry and Pharmacy
Sofia University
Sofia 1164, Bulgaria
jromanova@chem.uni-sofia.bg

Abstract

It was recently demonstrated that molecules with low to intermediate diradical character are good candidates for singlet fission chromophores and are therefore promising for photovoltaics application. On the other hand, the diradical character can also be associated with low stability and high reactivity – undesired molecular features for practical utilization. Therefore, in order to reveal the relationship between diradical character – stability – singlet fission propensity, we have performed quantum-mechanical calculations on a series of *o*- and *p*-quinone methides. Most of the investigated compounds are reported in the literature and data on their stability and reactivity are available. The study allows us to conclude on the impact of molecular stability on the excited state properties and to explore the compromise between diradical character and singlet fission propensity from stability perspective.

Keywords: *computational modelling, excited states, photovoltaics*

IEECP'21, July 29-30, 2021, Silicon Valley, San Francisco, CA – USA

DAI : *https://sci-index.com/DAI/2021.99101/IEECP/14527008*

Unlocking New Opportunities for the Photovoltaic Materials Market

Joanna Stoycheva
Faculty of Chemistry and Pharmacy
Sofia University
Sofia 1164, Bulgaria
stoycheva.joanna@gmail.com

Alia Tadjer
Faculty of Chemistry and Pharmacy
Sofia University
Sofia 1164, Bulgaria
fhat@chem.uni-sofia.bg

Julia Romanova
Faculty of Chemistry and Pharmacy
Sofia University
Sofia 1164, Bulgaria
jromanova@chem.uni-sofia.bg

Abstract

Singlet fission (SF) is a photophysical process, occurring in organic materials and having the potential to boost the solar cells' efficiency. Our study aims at guiding the way for molecular design of compounds, capable of SF. Doping of quinoid structures with Se or/and N-atoms turns out to be a productive strategy for that. Through functionalization and pH modulation, we succeeded to establish rules that link the molecular characteristics to the SF proclivity. Quantum chemical calculations at an appropriate level of theory show that all modelled structures satisfy the conditions, required for a successful fission of singlet excitons.

Keywords: *singlet fission, organic photovoltaics, quantum chemistry, materials*

IEECP'21, July 29-30, 2021, Silicon Valley, San Francisco, CA – USA

D!f: *https://sci-index.com/DAI/2021.99101/IEECP/14526987*

A comparative study of Li-ion batteries thermal behavior with different geometries,capacities,cathode materials

Khalid ZIAT
Normandy university
LUSAC Laboratory
Saint-Lo, France
khalid.ziat@unicaen.fr

Hasna LOUAHLIA
Normandy university
LUSAC Laboratory
Saint-Lo, France
Hasna.louahlia@unicaen.fr

Hamid GUALOUS
Normandy university
LUSAC Laboratory
Saint-Lo, France
Hamid.gualous@unicaen.fr

Abstract

Li-ion batteries are nowadays widely used in electric vehicles, portable devices and smart grids. They are commercialized in different geometries, capacities and serval technologies depending on users' requirements. During operating time, heat is generated inside Li-ion batteries due to chemical reactions which causes temperature rise. Non-controllable thermal behavior of these batteries may lead to the deterioration of their performance and may also cause a thermal runaway. In this study, A comparison of the thermal behavior of five li-ion batteries is performed. Used batteries are: LFP (lithium iron phosphate) prismatic (72Ah,60Ah,20Ah), NMC (Nickel Manganese Cobalt) prismatic (53Ah) and NMC cylindrical (3Ah). All batteries are tested under different climate conditions (0°C,10°C,20°C,30°C) and consecutive charge/discharge cycles were applied. The application of consecutive charge/discharge cycles aims to describe the temperature profiles and difference with the ambient in quasi-stationary regime. Constant current was used during each charge/discharge cycle, maximum and minimum voltage recommended by manufactures were chosen as cut-off voltage. T-type thermocouples are used to measure the temperature. The results show a 'V' shape during a cycle in quasi-stationary regime for all tested batteries. Moreover, the temperature difference increases for decreasing ambient temperature. The batteries specific heat capacity and thermal conductivities were experimentally measured. The results show a linear increase of the specific heat capacity for increasing ambient temperature while no dependency of thermal conductivity to ambient temperature was observed.

Keywords: Li-ion batteries, Battery surface temperature, Charge/Discharge cycle.

I. INTRODUCTION

Recently, many studies have been focusing on enhancing the efficiency of the use of electric energy storage systems and electric engines used in transport sector [1,2]. these studies aim to introduce novel solutions based on clean energies sources to ensure reducing the world global emissions of CO_2 of which 24% is caused by transport sector [3] and to limit the dependency of this sector to fossil fuels [4]. One of the markets which is strongly progressing in last decades is the Li-ion batteries industries. Many electric vehicles and hybrid electric vehicles are using Li-ion batteries as energy source systems such as Nissan Leaf and Mitsubishi iMiev [5]. Nevertheless, many technical issues may damage the Li-ion batteries and lead to their ignition [6]. The thermal behavior of Li-ion batteries depends on many factors such as applied current, climate conditions and the used chemistries. Arsri et al. [7] proved in their study the obtention of higher battery temperature for higher discharge current. Furthermore, Schuster et al. [8] experimentally studied the effect of increasing charge and discharge from 5A to 40A on a 40Ah battery. The measured battery temperature rise was from 3°C to 11°K for a half cycle. Moreover, Panchal et al. [9] tested a 20Ah battery under different discharge current (1C and 3C) for different external ambient conditions (5°C,15°C,25°C,35°C). Their results show when increasing ambient temperature from 5°C to 35°C the battery average surface temperature rise from 10.1°C to 35.9°C for an applied current of 1C. While, for an applied current of 3C, the average surface temperature rises from 15.7°C to 40.3°C. In another side, the effect of battery internal chemistry on its thermal behavior was also studied by several researchers, Goutam et al. [10] studied the temperature profile for three different commercialized pouch batteries (20Ah NMC type, 14Ah LFP, 5Ah LTO). Same current rates were applied. The result show higher obtained temperature during charge compared to discharge. Moreover, NMC battery type temperature was the highest compared to the two other tested batteries.

The studies performed on batteries thermal behavior are supplied by the characterization batteries thermal parameters as they explain the thermal behavior. Madani et al. [11] reviewed experimental and analytical methods to determine internal resistance and entropic heat coefficient reacting inside the battery and affecting internal heat generation amounts and also battery specific heat and thermal conductivity. Murashko et al. [12] proposed a novel method to determine the specific heat of a pouch LTO battery cell. Results show no dependency of the specific heat to the battery SOC. Loges et al. [13] experimentally studied 7 commercialized cells manufactured with different chemistries. The results show a linear increase of specific heat capacity with ambient temperature. Moreover, a slight dependence to SOC lower than 2.5%. Al-zareer et al. [14] proposed a novel method to characterize the specific heat and thermal conductivities of three cylindrical batteries of different chemistries (NCA, NMC, LCO). Experimental measurements of voltage and temperature was used to determine battery internal heat

IEECP'21, July 29-30, 2021, Silicon Valley, San Francisco, CA – USA

D!f: https://sci-index.com/DAI/2021.99101/IEECP/14526966

generation and the inverse method was applied to determine the thermal properties. The obtained results show a specific heat of (1046 J. Kg^{-1}. K^{-1}, 1002J.Kg^{-1}. K^{-1}, 958.2J. Kg^{-1}. K^{-1}) for respectively the (NMC, LCO, NCA) batteries.

In the present paper, both a thermal behavior study and thermal parameters characterization were performed for different applied ambient temperature. Consecutive charge discharge cycles were applied on five li-ion batteries tested on a climate chamber to ensure same climate conditions. The effect of ambient temperature on batteries thermal behavior was investigated then measurements of battery thermal parameters were carried out to explain the thermal behavior.

II. Experimental setup

The charge and discharge experimental cycles were conducted using Chroma 17020 test bench. It is equipped with 8 charge/discharge chains with a maximum power and current of (1200W,60A) in each chain. Figure 1 illustrates the used test bench and the five Li-ion batteries tested in this research. Moreover, Table 1 summarize the tested batteries. Two different batteries chemistries were chosen LFP and NMC, this choice is justified by their wide use as energy storage systems in electric vehicles. All batteries were tested under their 1C-rate and consecutive charge discharge cycles were applied. The voltage cut-off of each battery is determined by the recommendation of its manufacture. T-type thermocouples were inserted in each battery and an average battery surface temperature is then determined to enable the comparison with other batteries. The chroma 17020 was connected to Battery pro graphical interface permitting the system control and data acquisition. To ensure same climate condition all batteries were tested inside a climatic chamber Weiss Technik. 4 different temperature (0°C,10°C,20°C,30°C) were tested to enable performing a comparative study of the effect of climate conditions on tested batteries thermal behavior.

Figure 1. Experimental setup and tested batteries inside the climate chamber

Table 1. Tested batteries.

Cathode material	Geometry	Capacity (Ah)	Voltage range (V)
LFP	Prismatic	72	(2.6-3.6)
LFP	Prismatic	60	(2.6-3.6)
LFP	Prismatic	20	(2.7-3.7)
NMC	Prismatic	53	(2.9-4.3)
NMC	Cylindrical	3	(2.6-4.1)

The measurement of batteries specific heat capacity and thermal conductivities were performed using a heat flow meter (Net-zsch HFM446) illustrated in Figure 2 this test bench gives the possibility to test samples with a maximum size of (203 mm, 203mm, 51mm). and applied temperature range varies from -20°C to 90°C. A high accuracy of measurement is ensured by the used heat flow meter lower than 2% as given by its manufacture.

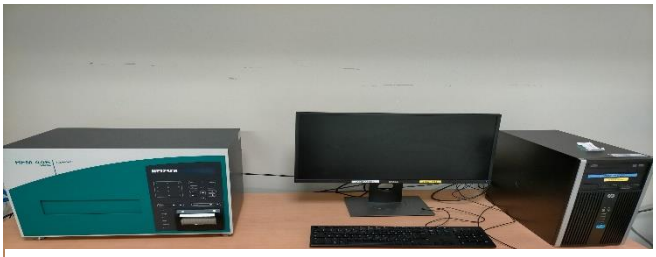

Figure 2. Heat Flow Mete test bench

III. Results analysis

A. Consecutive charge/discharge cycles

Figure 3 illustrates the results of the average temperature measured on battery surface for four batteries (LFP 72 Ah, LFP20 Ah, NMC 53 Ah, NMC 3Ah) and each battery was tested for different ambient temperatures (30°C,20°C,20°C,0°C). 1C-rate was applied on each battery and consecutive charge/discharge cycles were performed. the purpose is to characterize thermal regimes existing for all tested batteries. During the first charge cycle, the temperature of the 20Ah LFP battery rise strongly until attending a temperature of 5°C then the measured temperature is quietly constant during the rest of the test. Moreover, the temperature of the 72Ah battery rise strongly during all first charge cycle time and reaches a temperature of 19°C. Furthermore, the temperature of the 3Ah battery rise slightly first during the first charge cycle, then it decreases slightly. The temperature of the 53 Ah NMC battery rises strongly during the first half of the first charge cycle then slightly decreases until reaching 34°C in the end of the cycle. The batteries temperature rises during operating time because heat is generated inside them. Two main heat types could be defined. Reversible heat which depends to battery entropy and irreversible heat which is related to the battery internal resistance and proportional to the square of current [15]. The obtained experimental results show for the tested batteries the existence of a transient thermal regime in the first charge cycle followed by a quasi-stationary regime. This regime is characterized by a non-constant temperature during either charge or discharge cycle in a side and in another side the temperature profile is repetitive in each cycle. This phenomenon is due to the amount of internal heat generated in each cycle which could be considered approximately equals as same charge and discharge current are applied. Furthermore, this variation of temperature profile in the quasi-stationary regime is caused by the variation of battery entropy for each state of charge.

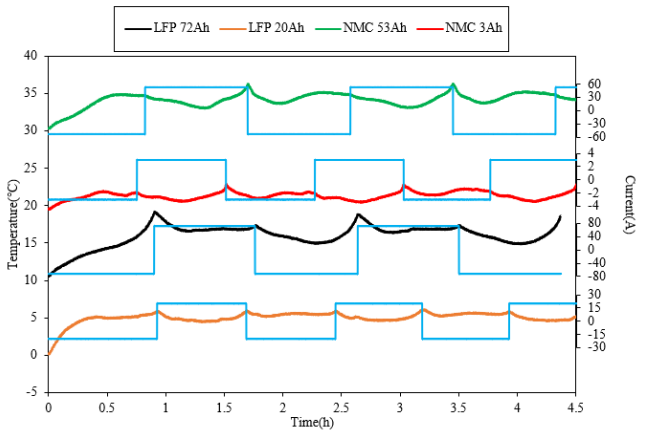

Figure 3. consecutive charge/discharge cycles applied for different ambient temperature and different battery chemistries.

thermal behavior

The effect of ambient temperature on battery temperature during quasi-stationary regime for 60Ah battery is presented in Figure 4 Same temperature profile was obtained for all tested ambient temperatures. The results show lower battery surface temperature rise for higher ambient temperature. In the beginning of charge cycle temperature decreases slightly then increases until the end of the cycle. Temperatures in the starting instant of the charge cycle obtained for ambient temperature of (0°C, 10°C, 20°C and 30°C) are respectively (6.87°C ,6.08°C, 4.36°C and 3.43°C) while in the end of the cycle are (6.40°C,5.36°C, 4.32°C and 3.31°C). The temperature profile in discharge cycle has same "V" shape profile as charge cycle. Nevertheless, the minimal temperature rise obtained in discharge cycle is slightly lower than the obtained in charge cycle. This is caused mainly by the difference of entropy coefficient during charge and discharge cycle [16].

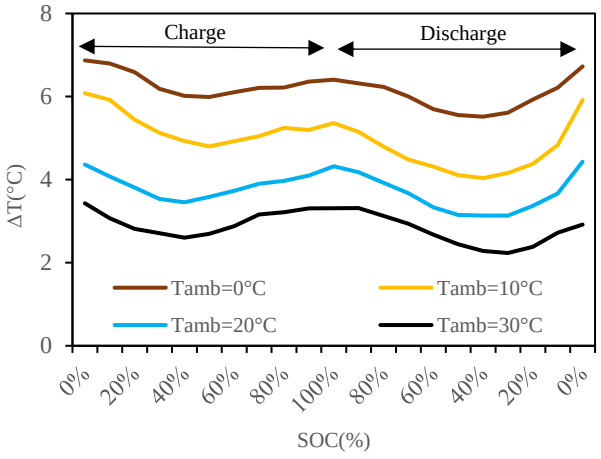

Figure 4. Effect of temperature on 60Ah battery temperature rise.

A comparison of temperature profile for three different batteries (NMC 53Ah, LFP 20Ah, NMC 3Ah) tested under a temperature of 10°C is shown if Figure 5. the decrease of temperature in the beginning charge cycle is related directly to the endothermic part of the entropic heat coefficient for a SOC of charge lower than 40% followed by an exothermic stage [17]. The slight difference between temperature profile in charge and discharge cycles is due mainly to the difference between the entropic coefficient during charge and discharge studied for three different batteries' chemistries (NCA, LCO, LFP) in [18]. their results prove a hysteresis of the entropy coefficient and higher entropy during charge compared to discharge which explain our experimental results showing the difference in temperature profile. Moreover, even though all the three batteries were tested under 1C-rates different temperature rise were obtained. This is justified by the difference of applied current on each battery. The NMC 53Ah battery's temperature is the highest as the applied current for this battery is the highest.

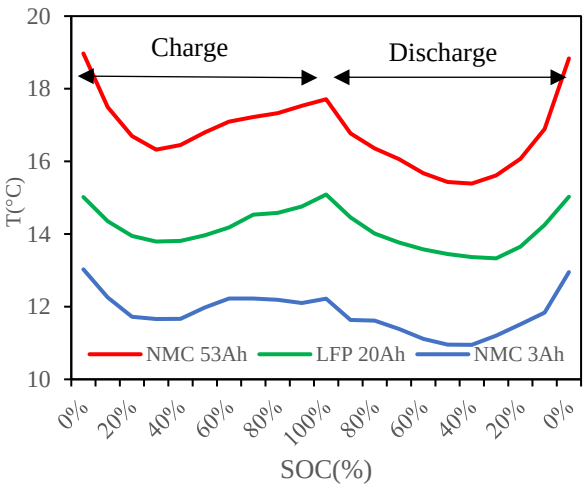

Figure 5. Comparison of temperature profile of different batteries in quasi-stationary regime Tamb=10°C.

Figure 6 illustrates the maximum temperature rise obtained for the five tested batteries and for 4 different applied ambient temperature (0°C,10°C,20°C,30C). For all tested batteries the temperature shows strong dependency to ambient temperature. The temperature of batteries rises basically due to internal heat generation, as the applied current is same in all ambient temperature for each battery. The dependency of battery temperature to environmental temperature could be explained by a change in the battery thermal properties. The internal resistance of battery tested by Wu et al. [19] was found to be dependent to ambient temperature. It decreases for increasing ambient temperature, this decrease is about 25% for an applied temperature ranging from 0°C to 25°C. The effect of ambient temperature was investigated on the battery entropy. The experimental study conducted by Bazinski et al. [20] show no dependency of the battery entropy to the ambient temperature. Additionally, the temperature obtained for the three LFP batteries was higher for higher battery capacities. Besides, the temperature of the NMC 53Ah battery was found to be higher than tested LFP batteries even if the ones who have higher capacity. This is

due mainly to the strong thermal stability of LFP batteries comparing to NMC batteries [21].

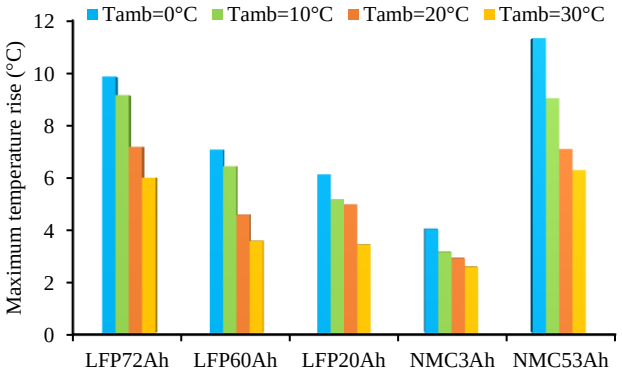

Figure 6. Different batteries maximum temperature rise for different ambient temperatures.

C. Measurement of specific heat capacity

In the previous section, five li-ion batteries thermal behavior was investigated for different climate conditions. A strong dependency of battery temperature to climate conditions was proven. This dependency is justified by the dependency of battery thermal parameters to environmental conditions. In this section the specific heat is measured for three batteries (LFP 60Ah, LFP 72Ah, NMC 53Ah). Figure 7 presents the applied cycles of temperature on each battery using the HFM 446 heat flow meter. Same applied battery thermal behavior ambient temperatures were applied to measure the battery specific heat capacity.

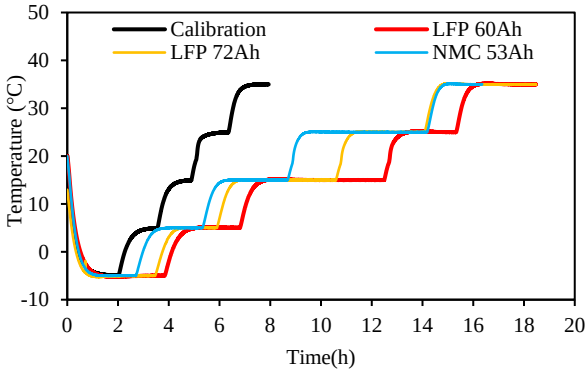

Figure 7. applied cycles to measure batteries specific heat capacity.

The results shown in Figure 8 present the specific heat capacity of three batteries versus temperature. A linear increase of the specific heat is obtained for increasing temperature. This result may give an appropriate explanation to the thermal behavior. For higher applied environmental temperature, the battery heat store capacity rise. Lower heat is dissipated via battery surface which explains the lower temperature rise.

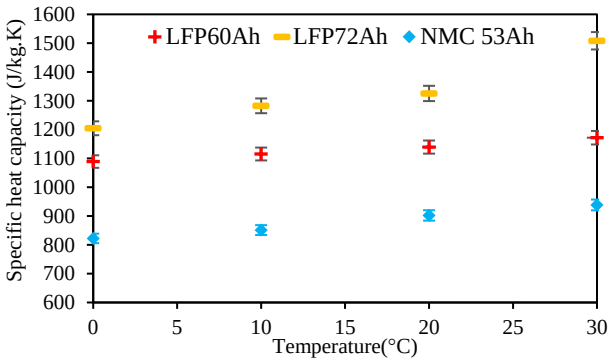

Figure 8. Measured specific heat capacity versus temperature.

D. Measurement of thermal conductivity

In this section, the thermal conductivity of tested batteries is discussed. The effect of temperature on battery thermal conductivity is illustrated in Figure 9 Three ambient temperatures were applied (10°C, 20°C, 30°C). Obtained experimental result show no dependency of thermal conductivity to ambient temperature.

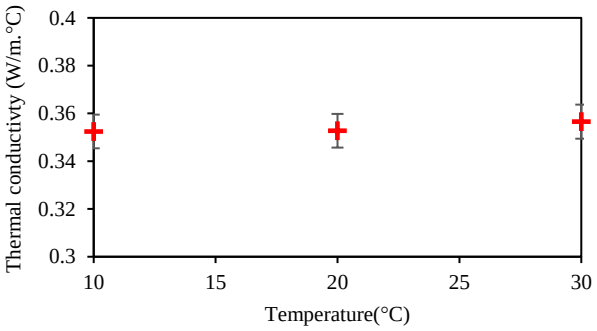

Figure 9. Measured thermal conductivity of the 60Ah LFP battery.

Figure 10 shows the results of the thermal conductivity measurement for three batteries under a temperature of 20°C. The LFP 60Ah has a low thermal conductivity comparing to the LFP 72Ah and NMC 53Ah. This is due basically to the effect of external shell which is made from plastic material.

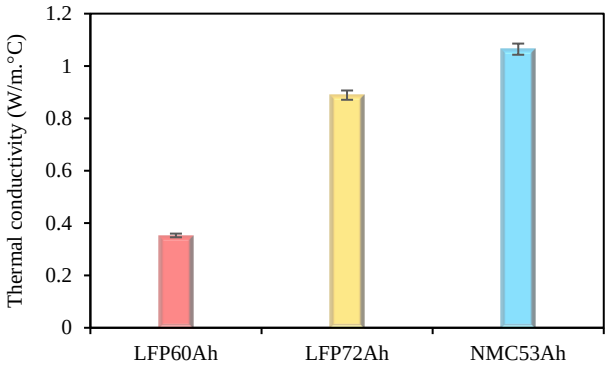

Figure 10. Comparison of the measured thermal conductivity of different batteries.

IV. Conclusion

The thermal behavior of five li-ion batteries is investigated for different ambient temperatures. The chemistries of the used batteries are LFP/graphite and NMC/graphite, two geometries were chosen prismatic and cylindrical. Each battery was tested under 1C rate and consecutive charge and discharge cycles were applied in similar climate conditions in each test to enable an accurate comparison of the results. During operating time, the temperature of all batteries rises due to internal heat generation. It reaches after cycling a quasi-stationary state in which the temperature is not constant, but it presents a repetitive profile in each one of the charge and discharge cycles. The profile of temperature in quasi-stationary regime has a "V" shape due to the strong dependency of the battery entropy to the SOC. The battery temperature depends strongly to applied climate conditions, Lower battery temperature rise is measured for higher ambient temperature. This phenomenon is due mainly to the influence of ambient temperature on the internal chemical compositions of batteries which causes a change of battery thermal parameters. Finally, the battery specific heat capacity and thermal conductivity were experimentally measured. Obtained results show a linear increase of battery specific heat capacity for increasing applied temperature while no dependency of thermal conductivity to the ambient conditions was noticed.

V. REFERENCES

[1] Vazquez, S., Lukic, S. M., Galvan, E., Franquelo, L. G., & Carrasco, J. M. (2010). Energy storage systems for transport and grid applications. IEEE Transactions on industrial electronics, 57(12), 3881-3895.

[2] Furfari, S. (2016). Energy efficiency of engines and appliances for transport on land, water, and in air. Ambio, 45(1), 63-68.

[3] International Energy Agency. CO2emissions from fuel combustion: overview (2017 edition). 2017.

[4] International Energy Agency. World energy balances. 2015.

[5] Pollet, b. G., staffell, i., & shang, j. L. (2012). Current status of hybrid, battery and fuel cell electric vehicles: from electrochemistry to market prospects. Electrochimeica acta, 84, 235-249.

[6] Associated Press 2011 New post-accident Chevy Volt engine fires prompt investigation J. Fox News

[7] Arsri, S. W., Anwar, M., Farisi, F. A., Pratama, J. A., Iftadi, I., Kaleg, S., ... & Diharjo, K. (2020, April). Analytical study of temperature effect on current and voltage of battery at charging and discharging condition on electric vehicle. In AIP Conference Proceedings (Vol. 2217, No. 1, p. 030068). AIP Publishing LLC.

[8] Schuster, E., Ziebert, C., Melcher, A., Rohde, M., & Seifert, H. J. (2015). Thermal behavior and electrochemical heat generation in a commercial 40 Ah lithium ion pouch cell. Journal of Power Sources, 286, 580-589.

[9] Panchal, S., Dincer, I., Agelin-Chaab, M., Fraser, R., & Fowler, M. (2016). Experimental and theoretical investigation of temperature distributions in a prismatic lithium-ion battery. International Journal of Thermal Sciences, 99, 204-212.

[10] Goutam, S., Timmermans, J. M., Omar, N., Bossche, P. V. D., & Van Mierlo, J. (2015). Comparative study of surface temperature behavior of commercial li-ion pouch cells of different chemistries and capacities by infrared thermography. Energies, 8(8), 8175-8192.

[11] Madani, S. S., Schaltz, E., & Knudsen Kær, S. (2018). Review of parameter determination for thermal modeling of lithium ion batteries. Batteries, 4(2), 20.

[12] Murashko, K. A., Mityakov, A. V., Pyrhönen, J., Mityakov, V. Y., & Sapozhnikov, S. S. (2014). Thermal parameters determination of

[13] [illegible] specific heat capacities of Li-ion cell components and their influence on thermal management. Journal of Power Sources, 336, 341-350.

[14] Al-Zareer, M., Michalak, A., Da Silva, C., & Amon, C. H. (2021). Predicting specific heat capacity and directional thermal conductivities of cylindrical lithium-ion batteries: A combined experimental and simulation framework. Applied Thermal Engineering, 182, 116075.

[15] Bai, Y., Li, L., Li, Y., Chen, G., Zhao, H., Wang, Z., ... & Zhou, J. (2019). Reversible and irreversible heat generation of NCA/Si–C pouch cell during electrochemical energy-storage process. *Journal of Energy Chemistry*, *29*, 95-102.

[16] Ahmadou Samba, A., Omar, N., Gualous, H., Van den Bossche, P., Van Mierlo, J., & Boubekeur, T. I. (2013). Development of 2D thermal battery model for Lithium-ion pouch cells. World Electric Vehicle Journal, 6(3), 629-637.

[17] Damay, N., Forgez, C., Bichat, M. P., & Friedrich, G. (2016). A method for the fast estimation of a battery entropy-variation high-resolution curve–Application on a commercial LiFePO4/graphite cell. Journal of Power Sources, 332, 149-153.

[18] Schmidt, J. P., Weber, A., & Ivers-Tiffée, E. (2014). A novel and precise measuring method for the entropy of lithium-ion cells: ΔS via electrothermal impedance spectroscopy. Electrochimica Acta, 137, 311-319.

[19] Wu, X., Chen, Z., & Wang, Z. (2017). Analysis of low temperature preheating effect based on battery temperature-rise model. Energies, 10(8), 1121.

[20] Bazinski, S. J., & Wang, X. (2013). The influence of cell temperature on the entropic coefficient of a lithium iron phosphate (LFP) pouch cell. Journal of The Electrochemical Society, 161(1), A168.

[21] Zheng, G., Zhang, W., & Huang, X. (2018). Lithium‐Ion Battery Electrochemical‐Thermal Model Using Various Materials as Cathode Material: A Simulation Study. ChemistrySelect, 3(41), 11573-11578.

Study of CZTSSe based solar cells with different ETMs by SCAPS

Lhoussayne Et-taya
LM3ER-OTEA Department of physics,
Faculty of Sciences and Techniques
Moulay Ismail University of Meknes
Errachidia, Morocco
l.ettaya@edu.umi.ac.ma

Touria Ouslimane
LM3ER-OTEA Department of physics,
Faculty of Sciences and Techniques
Moulay Ismail University of Meknes
Errachidia, Morocco
ouslimanetouria@gmail.com

Abdellah Benami
LM3ER-OTEA Department of physics,
Faculty of Sciences and Techniques
Moulay Ismail University of Meknes
Errachidia, Morocco
a.benami@fste.umi.ac.ma
https://orcid.org/0000-0001-5516-5660

Abstract

Third-generation thin-film solar cells based on CZTSSe are highly promising because of their excellent optoelectrical properties, earth-abundant, and non-toxicity of its constituent elements. In this work, the performance of CZTSSe based solar cells with TiO2, CdS, and ZnSe as electron transporting materials (ETMs) was numerically investigated using the Solar Cell capacitance Simulator (SCAPS). The effect of the active layer's thickness and electron affinity, different buffer layers and the contour plot of the operating temperature versus thickness of the CdS buffer layer were studied. The results show that the optimum power conversion efficiency for CdS, TiO2 and ZnSe, as the ETMs, is 23.16%, 23.13%, and 22.42%, respectively.

Keywords: CZTSSe, Third-generation thin-film, SCAPS, efficiency, ETMs.

I. INTRODUCTION

Photovoltaic cells are used to convert large amounts of sunlight to electricity directly. Many studies have recently been conducted to improve the efficiency of thin-film solar cells (TFSCs). Because of their extraordinary properties, TFSCs based on CZTSSe and related materials have attracted increased interest as an absorber layer in third-generation photovoltaic devices. CZTSSe is a p-type conductivity semiconductor with a tunable direct bandgap of 0.95-1.5 eV, a large absorption coefficient of over $10^4 cm^{-1}$, a low cost (earth-abundant), and non-toxic element composition [1]. The certified power conversion efficiency (PCE) of CZTSSe was reported to be up to 12.62%, which is lower than that of CIGS and CdTe (23.4% and 22.1%, respectively). It should be improved for large-scale photovoltaic applications to overcome the scarcity of In, Ge, and Te, as well as the toxicity of Cd [2-5].

There has been lots of research into replacing toxic ETM (CdS) with alternative materials in CZTSSe-based TFSCs. As a result, we propose and simulated three device structures with buffer layers of CdS, TiO_2, and ZnSe using SCAPS-1D software. The effect of several parameters on device performance (V_{oc}, J_{sc}, FF, and PCE) was investigated, including thickness, electron affinity, various buffer layers, and temperature.

II. Methodology

The schematic cross-section of the TFSC structure used in this study is shown in Fig. 1. The device under investigation consists of a Mo back contact that serves as the positive terminal, the p-CZTSSe active layer in which electron-hole pairs are generated after absorption of incident photons. Following that, CdS, TiO2, or ZnSe ETM was used to align the absorber and the window layer. The buffer layer is then stacked with i-ZnO, which is capped by a ZnO: Al window layer that acts as a transparent conductive oxide (TCO) to collect charges.

SCAPS is a program developed at the University of Gents in Belgium [6]. It is widely used for the simulation of various types of TFSCs. The SCAPS simulation results have been reported to agree well with the corresponding experimental results, which provides a convincing reason to use them in this study [4]. The software is based on solving the fundamental semiconductor equations ((1), (2), and (3)), namely the Poisson equation and the hole and electron continuity equations. It computes the band diagram in a steady-state, the recombination profile, and carrier transport in one dimension. The equations are shown below [4,7,8].

$$\frac{\partial^2 \Psi}{\partial x^2} + \frac{q}{\varepsilon}\left[p(x) - n(x) + N_D - N_A + \rho_p - \rho_n\right] = 0 \quad \textbf{(1)}$$

$$\frac{1}{q}\frac{dJ_p}{dx} = G_{op}(x) - R(x) \quad \textbf{(2)}$$

$$\frac{1}{q}\frac{dJ_n}{dx} = -G_{op}(x) + R(x) \quad \textbf{(3)}$$

Here q is the electron's charge, ε is the dielectric constant, Ψ is the electrostatic potential and, N_A (N_D) is the density of acceptor-like (donor-like). p (n), ρ_p (ρ_n), and J_p (J_n) are hole (electron) concentration, hole (electron) density, electron distribution, and hole (electron) current density, respectively. R is the net recombination from direct and indirect recombination, and G_{op} is the optical generation rate.

The values of the device and material parameters used in this study are taken from the literature, experimental, theory, and reasonable estimation [7,8,10] and are summarized in Table 1.

The device was illuminated with an AM 1.5 spectrum with a light power of 1000 W/m^2. This study's shunt and series resistances were 600 Ω/cm^2 and 1.5 Ω/cm^2, respectively [4].

IEECP'21, July 29-30, 2021, Silicon Valley, San Francisco, CA – USA

D!f: *https://sci-index.com/DAI/2021.99101/IEECP/14546610*

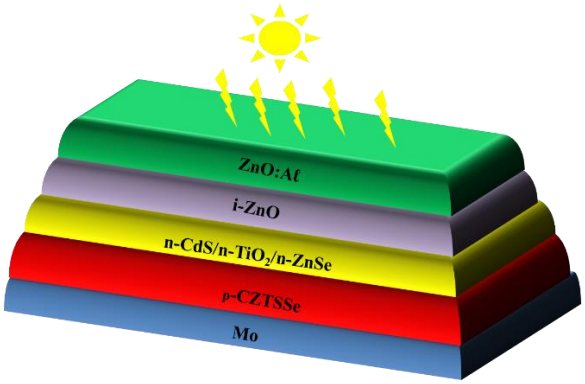

Fig.1. Structure of CZTSSe cell

Table.1 Parameters used in the simulation [7,8,10]

Parameters	ZnO:Al	i-Zno	n-TiO_2	n-ZnSe	n-CdS	p-CZTSSe
d (nm)	200	50	50	50	Variable	Variable
E_g(eV)	3.3	3.3	3.26	2.90	2.4	Variable
χ (eV)	4.4	4.4	4.2	4.02	4.2	Variable
ε (eV)	9	9	10	10	10	13.6
N_c (cm^{-3})	$2.2x10^{18}$	$2.2x10^{18}$	$2.2x10^{18}$	$2.2x10^{18}$	$2.2x10^{18}$	$2.2x10^{18}$
N_v (cm^{-3})	$1.8x10^{19}$	$1.8x10^{19}$	$1.8x10^{19}$	$1.8x10^{19}$	$1.8x10^{19}$	$1.8X10^{19}$
V_{th} e^- (cm/s)	10^7	10^7	10^7	10^7	10^7	10^7
V_{th} p (cm/s)	10^7	10^7	10^7	10^7	10^7	10^7
μ_n(cm^2/Vs)	10^2	10^2	10^2	25	10^2	10^2
μ_h (cm^2/Vs)	25	25	25	100	25	25
N_D (cm^{-3})	10^{20}	10^{19}	10^{18}	10^{18}	10^{17}	0
N_A (cm^{-3})	0	10^{19}	0	0	0	10^{18}
α (cm^{-1})	[4]	[4]	[10]	[10]	[4]	[4]

d: Thickness, Eg: Bandgap, χ: Electron Affinity, ε: Dielectric permittivity, Nc: Density of states in CB, Nv: Density of states in VB, Vth e^-: Thermal velocity of electron, Vth p: Thermal velocity of hole, μn: Electron mobility, μh: Hole mobility, N_D: Donor density, N_A: Acceptor density, α: Absorption coefficient

III. Results and discussion

A. Effect of the CZTSSe absorber layer's thickness

The absorber layer is crucial in enhancing device efficiency. In this context, simulations with CdS, TiO_2, and Znse buffer layers were used to examine the solar cell's performance in terms of the CZTSSe absorber layer. The thickness of the CZTSSe the absorber layer varied from 500 nm to 3000 nm, with a fixed ETM thickness of 50 nm. As the thickness of the CZTSSe absorber layer increases, more photons are absorbed, resulting in more electron-hole pairs [10]. Fig.2. depicts the variation of photovoltaic parameters (V_{oc}, J_{sc}, FF, PCE) as a function of CZTSSe absorber layer thickness, in which the result is in good agreement with Beer-Lamberts law. Table 2 summarizes the changes in all device parameters caused by various ETMs for absorber thicknesses of 500 nm and 3000 nm.

Table. 2 The effect of the ETM layer on the photovoltaic parameters for absorber thicknesses of 500 nm and 3000 nm.

Buffer layer	CZTSSe thickness (nm)	Voc (V)	Jsc(mA/cm^2)	FF (%)	PCE (%)
CdS	500	0,6708	29,55026	74,78	14,82
	3000	0,7245	42,6436	74,96	23,16
TiO_2	500	0,6706	29,37618	74,7	14,72
	3000	0,7245	42,6101	74,93	23,13
ZnSe	500	0,6703	29,45534	70,24	13,87
	3000	0,7243	42,58405	72,68	22,42

B. Effect of the electron affinity of the absorber layer

Figure 3 depicts the effect of absorber layer CZTSSe electron affinity on photovoltaic cell performance. The electron affinity of the absorber layer varied from 4,35 eV (CZTSe) to 4,5eV (CZTS) as extracted from the reference [4]. We can see that VOC, FF, and PCE values increase until a maximum value of χ=4,41eV is reached, then decrease with further increase of χ. On the other hand, Jsc decreases linearly with the electron affinity. Because increasing the absorber layer's electron affinity reduces the number of photons reaching the absorbing layer, the amount of current generated, and the short circuit current decreases.

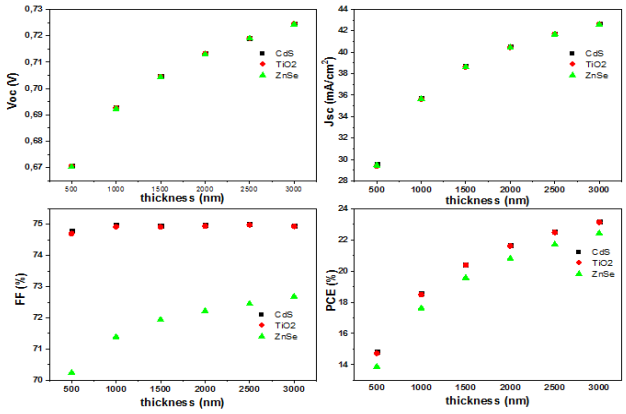

Fig.2. Effect of various thickness of CZTSSe absorber layer with the different buffer layers

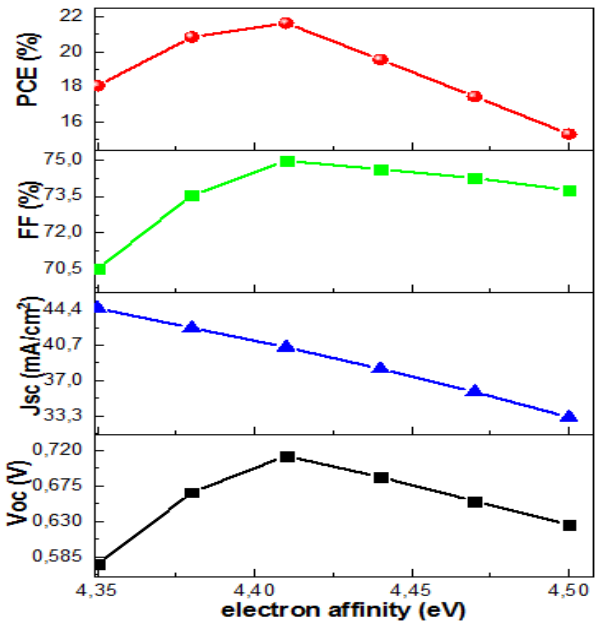

Fig.3. Variation of PCE, FF, Jsc, and Voc as a function of CZTSSe electron affinity

C. Impact of the CdS buffer layer thickness and Temperature contour plot

The buffer layer and operating temperature are well known to affect the performance of solar cells. As a consequence, the CdS buffer layer thickness and operating temperature have been increased to improve performance, from 30 nm to 70 nm and from 240 °C to 320°C, respectively. As shown in Fig. 4, the all-output parameters are not affected by the thickness of CdS. On the other hand, the increase in temperature induces a decrease in PCE, FF, and V_{oc}; this decrease was significant from the ambient temperature of 300°C. However, J_{sc} rises as the temperature rises.

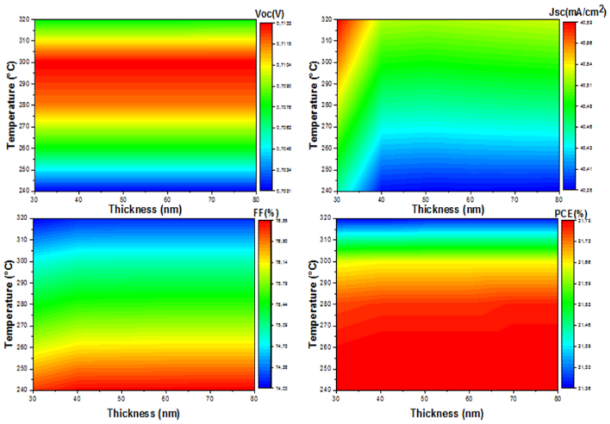

Fig.4: Contour plot of solar cell output as a function of the CdS buffer layer thickness and operating temperature.

IV. Conclusion

In this paper, numerical simulations of CZTSSe-based TFSCs were performed using the SCAPS-1D software. Three different solar cells with buffer layers of CdS, TiO_2, and ZnSe were investigated in order to find a safe alternative to the toxic CdS. Maximum PCE of CZTSSe solar cells with CdS, TiO2, and ZnSe buffer layers was predicted to be 23.16%, 23.13%, and 22.42% at ambient temperature and 3000 nm active layer, respectively. As a result, TiO_2 may be a viable choice for producing and manufacturing low-cost, high-efficiency Cd-free CZTSSe heterojunction solar cells.

V. ACKNOWLEDGMENTS

The authors are very much grateful to Dr Burgelman for providing SCAPS-1D software.

VI. REFERENCES

[1] G. Altamura, J. Vidal, Chem. Mater. 28 (2016) 3540–3563.
[2] S. Enayati Maklavani, S. Mohammadnejad, Opt. Quantum Electron. 52 (2020)
[3] G.K. Gupta, A. Dixit, Opt. Mater. (Amst). 82 (2018) 11–20
[4] L. Et-taya, T. Ouslimane, A. Benami, Sol. Energy 201 (2020) 827–835
[5] A.E. Benzetta, M. Abderrezek, M.E. Djeghlal, J. Nano- Electron. Phys. 10 (2018) 6–10
[6] M. Burgelman, K. Decock, S. Khelifi, A. Abass, Thin Solid Films 535 (2013) 296–301
[7] A. Benami, J. Energy Power Eng. 13 (2019) 32–36
[8] T. Ouslimane, L. Et-taya, L. Elmaimouni, A. Benami, Heliyon 7 (2021) e06379
[9] M. Atowar Rahman, Sol. Energy 215 (2021) 64–76
[10] H. Fujiwara, R.W. Collins, Spectroscopic Ellipsometry for Photovoltaics, 2018
[11] F.A. Jhuma, M.Z. Shaily, M.J. Rashid, Mater. Renew. Sustain. Energy 8 (2019) 1–7
[12] N. Cheng, W. Li, S. Sun, Z. Zhao, Z. Xiao, Z. Sun, W. Zi, L. Fang, Mater. Sci. Semicond. Process. 90 (2019) 59–64

Thermodynamic study of a membraneless electrochemical process for the hydrogen and oxygen high-pressure generation

Andrii Shevchenko
Hydrogen Energetics Department
A.M. Pidhorny Institute of Mechanical Engineering Problems of NASU,
Kharkiv, Ukraine
shevchenkoandrii84@gmail.com
ORCID: 0000-0002-6009-2387

Nguyen Tien Khiem
Vietnam Academy of Scienceand Technology,
Hanoi, Viet Nam
ntkhiem@imech.vast.vn
ORCID: 0000-0001-5195-2704

Bui Dinh Tri
Vietnam Academy of Scienceand Technology,
Hanoi, Viet Nam
bdtri@vast.vn

Anatolii Kotenko
Hydrogen Energetics Department
A.M. Pidhorny Institute of Mechanical Engineering Problems of NASU,
Kharkiv, Ukraine
kotenko19580820@gmail.com
ORCID: 0000-0003-2715-634X

Abstract

The article presents the results of the thermodynamic analysis of the electrochemical process of hydrogen and oxygen high-pressure generation. This process can improve the energy efficiency of the membraneless electrolysis method.

The method is based on the use of a gas-absorbing electrode with a highly developed contact surface of the electrode material with the electrolyte. The electrochemical activity of the gas-absorbing electrode material (Fe(g)) is higher in its characteristics than that of platinum-coated electrodes and exceeds them in the efficiency of the electrolysis process. The electricity consumption required for the production of hydrogen and oxygen is in the range of 3.95 kWh/m^3 to 4.16 kWh/m.^{3} It should also be noted that this process is cyclic, consisting of a half-cycle of hydrogen evolution and a half-cycle of oxygen evolution. The distribution of the energy consumption by half-cycles is 0.88 kWh/m^3 per H_2 ↑; 3.28 kWh/m^3 on O_2 ↑ respectively. The material of the gas-absorbing electrode (Fe (g)) chemically binds the oxygen when it acts as the anode, while the hydrogen is evolved at the cathode (Ni). The reverse of the polarity allows the hydrogen to be chemically bound by the cathode material (Fe (g)) and the oxygen gas to be evolved at the anode (Ni). The cyclic operation of the electrochemical cell makes it possible to stop the usage of proton-exchange membranes, which results in a significant increase in the operating pressure of the generated gases (up to P = 20.0 MPa). This pressure is achieved not because of the use of compressor equipment, but due to the isochoric process of electrochemical production of high-pressure hydrogen and oxygen. The above advantages contribute to the successful implementation of an innovative electrolyzer as an element of a buffer storage system for a secondary energy carrier (hydrogen) in energy technology complexes using alternative energy sources.

Keywords: electrolyzer, anode, cathode, hydrogen, oxygen, high-pressure, alternative energy sources.

I. INTRODUCTION

Hydrogen (H_2) is a gas with a very low density of 0.0813 g/l under normal conditions (at 248 K and 0.1 MPa) [1] and therefore there are many difficulties in the development of efficient and compact storage of H_2. The low efficiency of mechanical compressors for hydrogen (15-45%) and oxygen (13-17%) leads to an additional increase (by 10-15%) in the unit cost of electricity for the production and storage of gases [2]. When the hydrogen is compressed to P = 70.0 MPa, its bulk density of the stored energy is $\rho V(H_2)$ = 5.6 MJ/L (40 g H_2/L) [3]. Therefore, the development of electrochemical technologies for generating hydrogen under high operating pressure and minimal power consumption is promising and relevant for hydrogen power engineering [4].

Distinctive features of water electrolysis from the other methods of hydrogen production are: simplicity of the technological scheme, availability of water as a feedstock, easiness of maintenance of the electrolysis installations, high reliability of the operation. All these make it possible to successfully combine the given method with the usage of other renewable energy sources (sun, wind, etc.) [5, 6]. The main disadvantage of the electrochemical method for producing hydrogen is its high energy consumption.

The authors of the article have developed and successfully tested the technology for the production of high-pressure hydrogen both in laboratory and field conditions [7, 8]. The main difference of the technology compared to the traditional electrolysis technologies is the usage of variable valence metals as materials of electrodes [9].

The technological and design features of this electrolysis technology make it possible to successfully use it as a buffer energy storage in an energy-technological complex using alternative energy sources [10].

II. PURPOSE AND OBJECTIVES OF THE STUDY

The main goal of the study is to determine the regularities of the redox reactions of the cyclic process of the gas-absorbing electrode. The process understanding makes it possible to secure the membraneless production of high-pressure hydrogen and oxygen. The determination of the electric potential of chemical reactions and the overvoltage of gas evolution at the cathode and anode allows composing the energy balance of a membrane-less electrolysis process. Thermodynamic analysis reveals the main distinguishing features of the standard and the proposed electrolysis system. Based on the results of the analysis, it is possible to develop a set of methods for reducing irreversible losses and increasing the energy efficiency of the cyclic method for

IEECP'21, July 29-30, 2021, Silicon Valley, San Francisco, CA – USA

DAI: https://sci-index.com/DAI/2021.99101/IEECP/14527140

the electrochemical production of high-pressure hydrogen and oxygen.

Optimization of the electrochemical system operation modes, the development of design and technological solutions aimed to reduce the energy consumption of the hydrogen and oxygen production process without the use of compression devices can be implemented as follows:
- selection and optimization of the structure of electrode materials;
- selection of electrode material with low gas evolution potential;
- optimization of the algorithm of operation and temperature conditions;
- optimization of the design of the main elements of the electrolysis system.

III. ELECTROCHEMICAL PROCESSES ON THE ELECTRODE ASSEMBLY USING A GAS-ABSORBING ELECTRODE

The authors of the article have developed an innovative membraneless electrochemical method for the decomposition of a liquid alkaline electrolyte. The method is based on the use of a gas-absorbing substance with a highly developed contact surface of the electrode material with the electrolyte.

The use of sponge iron as the oxygen-bonding electrode material is consistent with the reaction:

$$Fe + 2OH^- <=> Fe(OH)_2 + 2e \quad (1)$$

With the prolonged operation of the active mass of the electrode, deeper oxidation of Fe occurs:

$$Fe(OH)_2 + OH^- <=> Fe(OH)_3 + e \quad (2)$$

The electrochemical production of hydrogen and oxygen on the half-cycle of H_2 evolution corresponds to the transition of Fe (II) to Fe (III), and the half-cycle of O_2 evolution corresponds to the electrochemical reduction of Fe (Fig. 1).

The material of the gas-absorbing electrode (Fe (g)), in a state of the anode, chemically binds oxygen, while hydrogen is freely released on the other electrode, the cathode (Fig. 1 a). The reverse of the polarity allows the hydrogen to be bound at the cathode (Fe (g)) and the oxygen to be released at the anode (Fig. 1 b).

$Fe(OH)_2$ retains a spongy structure and has an expansive contact surface with the electrolyte. Polarization during the oxidation of the electrode active mass is caused by a slowdown in the diffusion of OH^- ions. The diffusion rate decreases with an increase in the thickness of the reacted Fe-layer.

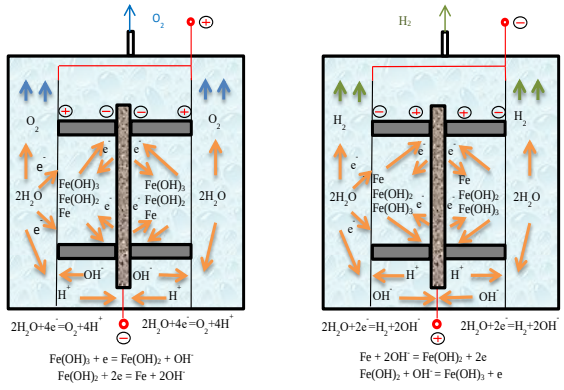

(a) (b)

Figure 1. Diagrams of electrochemical processes occurring on electrode assemblies with a gas-absorbing electrode: a - half-cycle of oxygen evolution; b - half-cycle of hydrogen evolution.

The evolution of gaseous hydrogen occurs at the passive electrode (cathode) (Fig. 1 a). It is advisable to use Fe or Ni as a passive electrode. The overvoltage of hydrogen evolution on Ni is 210 mV, and on Fe is 80 mV (see Table 1).

Table 1. Overvoltage of hydrogen and oxygen evolution [11]

Electrode material	Overvoltage, mV	
	H_2	O_2
Pt (platinized)	0	250
Fe	80	250
Pt (smooth)	90	450
Ni	210	60

The low overvoltage of hydrogen and oxygen evolution at the passive Ni-electrode allows obtaining these gases directly from the very beginning of the electrochemical decomposition of the water (current density from 200 A/m^2 to 600 A/m^2).

IV. ANALYSIS OF THERMODYNAMIC PROCESSES OF LIQUID ELECTROLYTE DECOMPOSITION IN ELECTROCHEMICAL SYSTEMS FOR PRODUCING HYDROGEN AND OXYGEN

The energy assessment is based on the description of a unified hydrogen production model. It consists of stationary balances of energy, entropy and mass, as well as the ideal gas equation. Based on this, reversible energy demand is used to identify internal thermodynamic losses. Additional consideration of the irreversibility allows determining the loss of efficiency, taking into account the specific characteristics of the device.

The basis for the energy balance of a standard electrolysis system is the irreversible energy loss when current passes through the electrolyte Fig. 2 [12].

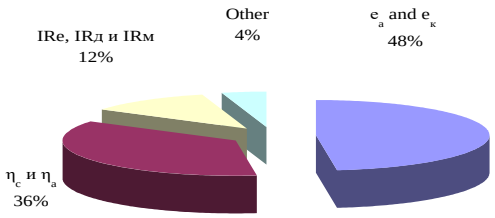

Figure 2. Voltage Distribution on Electrodes in the Electro-Chemical Cell.

The energy balance of the electrolysis system can be written as an equation:

$$E = e_a + e_c + \eta_c + \eta_a + e_{cp} + e_d + IR_e + IR_m + IR_c \quad (3)$$

where: e_a and e_c – reversible thermodynamic potentials of anode and cathode; η_c и η_a – overvoltage of the release of hydrogen on the cathode and oxygen on the anode; e_{cp} и e_d – concentration and diffusion polarizations; I – current; R_e, R_m и R_c – resistance of the electrolyte, metal conductors and contacts in the cell.

The thermodynamically reversible potentials of the anode and cathode are determined from the formula:

$$e_{a(c)} = \Delta H^0_{298\ (reaction)} / nF \quad (4)$$

where: $\Delta H^0_{298(reaction)}$ – enthalpy of reaction J·mol^{-1}; n – the amount of a substance involved in the reaction; F – Faraday number 96570 A·s.

The free energy and the enthalpy are calculated for conditions with temperatures of 298 K and pressure of 101.3 kPa. The enthalpy of reaction (1) at the active electrode is defined as:

$$\Delta H^0_{298}(1) = \Delta H^0 Fe(OH)_2 - 2\Delta H^0 OH^- \quad (5)$$

and is 104.315 kJ mol^{-1}, and the enthalpy of the reaction (2) is determined as:

$$\Delta H^0_{298}(2) = \Delta H^0 Fe(OH)_3 - \Delta H^0 Fe(OH)_3 - \Delta H^0 OH^- \quad (6)$$

and is 36.267 kJ·mol^{-1}.

Table 2 shows the calculated values of the free energy ΔG^0 and the enthalpy ΔH^0 of the reaction components at the gas-absorbing electrode.

Table 2. Free energy and enthalpy of reactions

The chemical compound	Free energy ΔG^0, J•mol^{-1}	Enthalpy ΔH^0, J•mol^{-1}
OH^-	157360	228850
H_2 (gas)	0	0
O_2 (gas)	0	0
$Fe(OH)_2$	480008	562015
$Fe(OH)_3$	700050	827132

The voltage of the active mass oxidation reaction at the anode e_a is determined following equation (4) and for the reaction (1) is 0.54 V, and for the reaction (2) is 0.19 V.

The voltage E of the half-cycle of hydrogen evolution (see Fig. 2), considering the active mass oxidation reaction at the anode and the evolution of hydrogen at the cathode, is determined according to equation (3) and for the reaction (1) is 0.33 V, and for the reaction (2) it is 0.52 V.

The thermoneutral voltage is equal to the cell voltage in a hypothetical isobaric-isothermal process, in which there is no heat and mass exchange with the external environment and all the energy required for the reaction (the sum of the required heat and work) is supplied in the form of electricity.

The thermoneutral voltage Eq is practically constant. Considering the heat of evaporation, it is equal to Eq'= 1.481 V, and during the electrolysis of water vapor it is Eq"= 1.25 V [13].

The share of the work required for water decomposition in relation to the total energy consumption in the electrochemical process ή is equal to the E_T / Eq ratio. Since E_T for water decreases with increasing temperature (at atmospheric pressure $dE_T / dT = -0.25$ mV·K^{-1}), then as the temperature rises, the share of the heat increases, and at T = 5000 K. Practically all the energy required for water decomposition is used in the form of heat (ή ≈ 0).

The dependences of E_T and other reaction parameters on the temperature are given in Table 3,

Table 3. Theoretical values of EMF and energy consumption in the reaction of water decomposition (14.7 psi.)

Reaction parameter	Temperature K							
	298	353	423	473	573	773	1273	2272
E_T. V	1.23	1.18	1.15	1.10	1.04	0.95	0.80	0.50
ή	0.83	0.80	0.92	0.88	0.83	0.76	0.64	0.40
$W_T^{electric}$, kWh.m^3	2.94	2.82	2.75	2.63	2.49	2.27	1.91	1.20
W_T^{heat}, kWh.m^3	0.60	0.72	0.24	0.36	0.5	0.72	1.08	1.79

where the theoretical values of $W_T^{electric}$ are determined from the equation [14]:

$$W_T^{electric} = 2.394 E_T = 2.394\ Eq\acute{\eta}. \quad (7)$$

The theoretical values of W_T^{heat} are obtained from the formula [14]

$$W_T^{heat} = 2.394\ (Eq - E_T) = 2.394 Eq\ (1 - \acute{\eta}). \quad (8)$$

The decrease in the voltage value of the electrochemical decomposition of a liquid alkaline electrolyte (equation 3) in the proposed method for the hydrogen and oxygen generation was achieved due to:

- the exclusion of the voltage drop across the proton exchange membrane IRm, due to its absence from the energy balance (equation 3);
- the reduction of the overvoltage values of the hydrogen evolution at the cathode and oxygen evolution at the anode ηκ and ηa, since gas evolution occurs only at one of the electrodes.

V. EXPERIMENTAL STUDY OF ELECTROCHEMICAL ACTIVITY AND ELECTROCHEMICAL CHARACTERISTICS OF ELECTRODE MATERIALS

A laboratory setup has been created in order to simulate the processes in an electrochemical cell for experimental studies of the electrochemical activity and electrochemical characteristics of electrode materials in cathode-anode systems.

Fig. 3 shows a functional diagram of the developed laboratory setup, which consists of: a reactor, main pipelines, separators, a tank with distilled water, a monitoring and control power supply unit, and a system for measuring the flow characteristics of the generated gases (Fig. 3 a.)

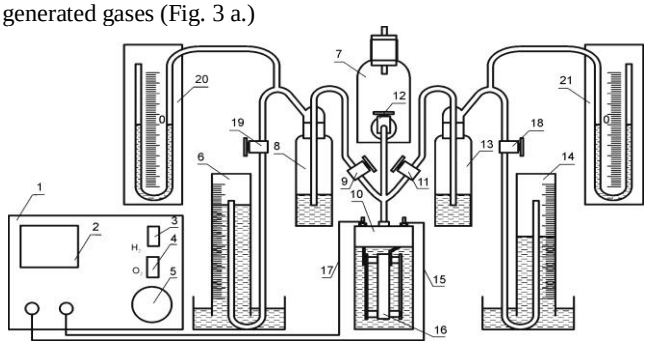

(a)

(b)

Figure 3. Functional diagram of a laboratory setup with an electrochemical cell: 1- a monitoring and control power supply unit; 2 - digital indicator IC 412.3; 3 –power switch; 4 - hydrogen and oxygen half-cycle power switch; 5 - current control handle; 6 - oxygen measuring vessel; 7 - buffer tank H_2O; 8 - oxygen separator; 9 - oxygen line valve; 10 - electrolysis cell; 11 - hydrogen line valve; 12 - valve for filling the hydraulic system with electrolyte; 13 - hydrogen separator; 14 - hydrogen measuring vessel; 15, 17 - electric wires; 16 - electrode assembly; 18, 19 - shut-off valves for hydrogen and oxygen lines; 20, 21 - U-shaped

differential pressure gauges for oxygen and hydrogen lines; a - laboratory setup diagram; b –photo of an electrochemical cell.

In the upper part of the reactor, there are power supply terminals, a fitting for an electrolyte inlet to the reaction zone and a gas outlet fitting, above which there is a three-way valve for dividing the gas-liquid channel into oxygen and hydrogen mains (Fig. 3 b). The electrode assembly is located in the internal section of the reactor; the reactor is filled with a 25% aqueous solution of KOH with the electrolyte density of 1.21 mg/l [15].

The diagram of the main elements and the design of the experimental sample of the electrode assembly are shown in Fig. 4.

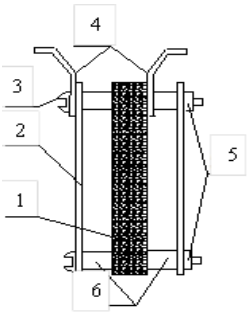

(a)

(b)

Figure 4. Schematic and experimental sample of the electrode assembly: 1- gas absorbing electrode (active); 2 - gas evolving electrode (passive); 3 - screws; 4 - current leads; 5 - screw-nut; 6 - spacer dielectric sleeves; a - electrode assembly diagram; b - experimental sample.

The three pairs of electrodes were defined for the experimental studies: 1 – Fe(g)-X18H15; 2 – Ft(g)-Fe; 3 – Fe(g)-Ni (Fig. 5).

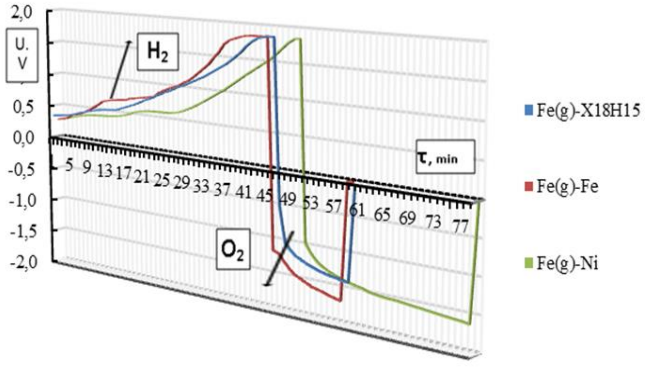

Figure 5. The sequence diagram of the change in the voltage of hydrogen and oxygen release during electrolysis with electrode combinations: 1. Fe(g)-X18H15; 2. Fe(g)-Fe; 3. Fe(g)-Ni.

A comprehensive experimental study was carried out in two stages.

The first stage of the experimental study was aimed to determine the voltage threshold value for the point when the gas began to evolve from two electrodes at the same time. On the half-cycle of the hydrogen evolution, this value was 1.8 V, and on the half-cycle of the oxygen evolution, it corresponded to 1.7 V (at the operating current density J = 0.02 A/cm^2, or 200.0 A/m^2), for the selected pairs of electrodes (Fe(g)-X18H15; Fe(g)-Fe; Fe(g)-Ni). Figure 6 shows the results of the first stage of the experimental study.

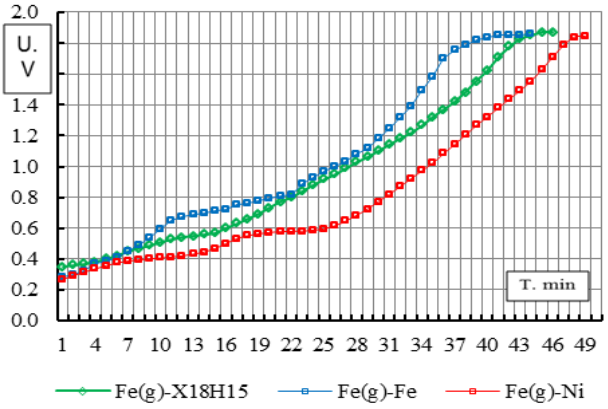

(a)

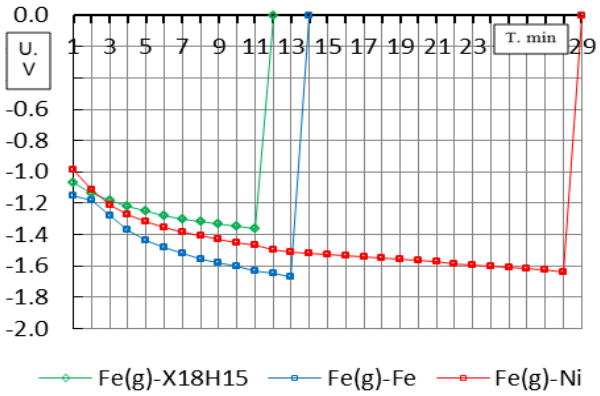

(b)

Figure 6. The sequence diagram of the voltage change of the membraneless high-pressure hydrogen generator, at J = 0.02 A/cm^2 with the electrode twins: 1. Fe(g)-X18H15; 2. Fe(g)-Fe; 3. Fe(g)-Ni: (a) - the half-cycle of H_2 generation; (b) - the half-cycle of O_2 generation.

The analysis of the study results has shown that on the hydrogen half-cycle (Fig. 6 a), the voltage of the onset of hydrogen evolution was 1.8 V and did not depend on the electrode materials (Fe(g)-X18H15; Fe(g)-Fe; Fe(g)-Ni), although it depended on the operating current density J = 0.02 A/cm^2. On the half-cycle of oxygen evolution (Fig.6 b), the voltage of the onset of the oxygen evolution was 1.7 V, and the half-cycle time depended on both the electrode materials and the operating current density.

The second stage of the experimental study was aimed to prevent the simultaneous release of hydrogen and oxygen. The half-cycle termination voltage threshold has been limited. The equilibrium potential values for the cathodic and anodic processes e_k and e_a were optimized by limiting the voltage of the reaction on the electrodes (Fig. 7).

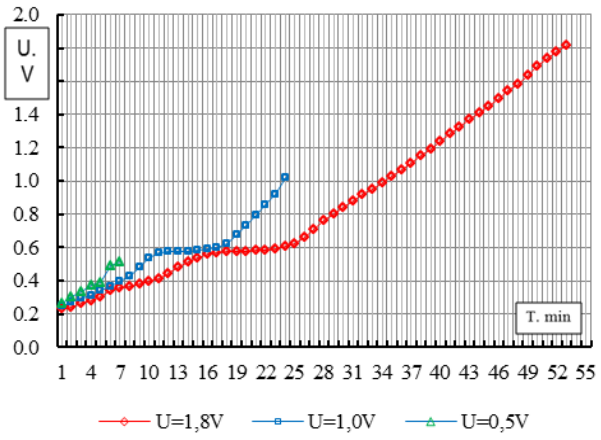

(a)

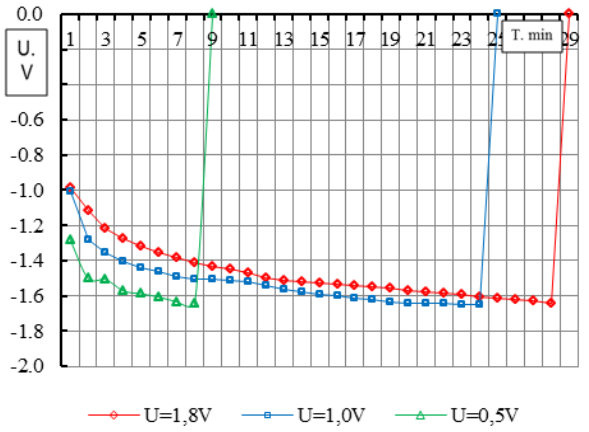

(b)

Figure 7. The cyclogram of the voltage change of the high-pressure hydrogen generator with a voltage limitation from 1.8 V to 0.5 V at J = 0.02 A/cm^2 with the electrode twins Ni - Fe (g): (a) - the half-cycle of H_2 generation; (b) - the half-cycle of O_2 generation.

Fig. 7 shows that the voltage limiting of the reaction on the electrodes affects the half-cycle of hydrogen evolution (Fig. 7 a) and, accordingly, the half-cycle of oxygen evolution (Fig. 7 b). At the same time, the amount of H_2 and O_2 released and the dynamics of the releases were measured (Fig. 8).

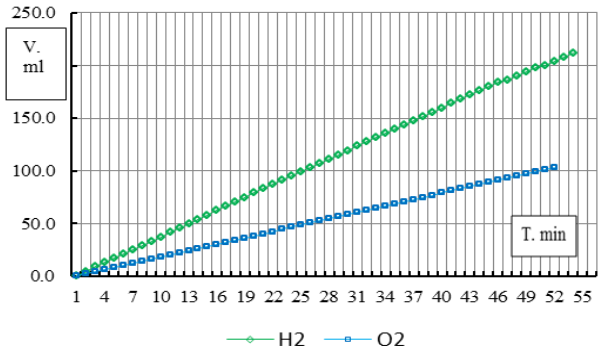

Figure 8. The dynamics of hydrogen and oxygen generation: - limiting the voltage of the reaction from 0.5 to 1.8 V; - current density I = 0.02 A/cm^2; - electrode twins Ni – Fe(g).

As it is seen from Fig. 8, the dynamics of hydrogen and oxygen evolution is preserved and does not depend on the limitation of the voltage of the reaction at the electrodes. Half-cycles have shortened in time, but the number of half-cycles has increased.

The experimental results have shown that the electrochemical activity of the gas-absorbing electrode material (Fe(g)) is higher in its characteristics than that of platinum-coated electrodes, and exceeds them in the efficiency of the electrolysis process. Thus, the electricity costs for hydrogen and oxygen production are in the range from 3.95 kW·h/m^3 to 4.16 kW·h/m^3. It should also be noted that this process is cyclic, consisting of a half-cycle of hydrogen evolution and a half-cycle of oxygen evolution [16]. The energy consumption on the half-cycle of the hydrogen generation is 0.88 kW·h/m^3, and for the oxygen half-cycle is3.28 kW·h/m^3

VI. DISCUSSION OF RESEARCH RESULTS

With the cyclic operation, there is no need to use proton exchange membranes. This makes it possible to significantly increase the operating pressure of the generated gases up to P = 20.0 MPa and higher. Compressor equipment is used to achieve this level of operating pressure in standard electrolysis systems for producing hydrogen. This limits the common use of these systems at present [17]. Such equipment has several disadvantages: special requirements for maintenance, low efficiency (from 16 % to 30 %), high cost [18]. The absence of gas compressors in the technological scheme makes it possible to successfully use the high-pressure electrochemical hydrogen generator as a buffer energy storage in the energy-technological complexes with alternative energy sources.

The advantage of the described membraneless method of hydrogen production lies in the ability to control the reaction rate (by regulating the current), and, consequently, the consumption of electricity for its generation. This is especially important when using renewable types of energy (sun, wind) as primary energy carriers [19], characterized by inconsistent energy supply [20], as well as in joint operation with power units of thermal power plants and nuclear power plants for smoothing loads during the period of peak energy consumption [21].

Based on the obtained experimental data, the fully functional experimental electrolysis installation for the hydrogen and oxygen high-pressure generation EHP - 0.02 - 150 was manufactured (Fig. 9).

(a)

(b)

Figure 9. Experimental electrolysis installation EHP - 0.02 - 150: (a) - view from the side of the reactor compartment; (b) - view from the side of power electronics, control and monitoring systems.

The external view of the reactor compartment with executive devices is shown in Fig. 9 a. The main controls are displayed on the control panel. A smart relay "Zelio Logic" from Schneider Electric was used. This is the relay with the ability to program relay logic [22], time delay, pulse counting, processing signals from both discrete and analog sensors. The ability to transmit data via the SR2 USB01 cable for connection to a USB port [23], via Ethernet protocols and using a GSM modem made it possible to eliminate the need for an operator to stay in the EHP area and ensure high reliability and safety of operation [24].

VII. CONCLUSIONS

The choice of a gas-absorbing electrode made of a structured material, which is a metal with variable valence, and a gas-evolving electrode with a low reversible potential of cathodic and anodic processes, which does not include expensive platinum group metals, gave the following results:

1. The high reactivity of hydrogen and oxygen evolution using galvanic Ni as a passive electrode indicates a decrease in the overvoltage on the corresponding half-cycles. The low overvoltage of the release of H_2 (0.21 V) and O_2 (0.06 V) at the passive electrode makes it possible to obtain these gases directly from the very beginning of the water electrochemical decomposition (Fig. 3).

2. The reactivity of H_2 (O_2) evolution using the X18H15 – Fe(g) electrode assembly occupies an intermediate position between Ni-Fe (g) and Fe–Fe (g), which makes it possible to reduce the cost of the electrode system.

3. Optimization of operating modes by limiting the threshold values of the voltage of the electrochemical reaction (in the range of 0.5 - 1 V) makes it possible to minimize the specific energy consumption for the process of H_2 (O_2) release.

4. Specific electricity consumption in hydrogen and oxygen half-cycles was respectively - 0.88 kWh/m^3 per H_2↑ and - 3.28 kWh/m^3 per O_2↑. The total specific electricity consumption for the production of these gases does not exceed 4.16 kWh/m^3.

5. The considered technology for producing hydrogen and oxygen makes it possible to exclude the consumption of electrical energy associated with a voltage drop across the proton exchange membrane IRm, due to its absence. This ensures the generation of H_2 (O_2) under high working pressure up to P = 20.0 MPa.

VIII. ACKNOWLEDGMENTS

This work was completed with financial supports from Vietnam Academy of Science and Technology under project of Number:QTUA-0101/18e20**.**

The research was conducted according to projects No. 13-20 "Metal hydride batteries for systems that supply hydrogen to fuel cells". The research was made within the framework of scientific projects of the target program of scientific research of the National Academy of Sciences of Ukraine: "Development of scientific bases of production, storage, and use of hydrogen in autonomous power supply systems".

IX. REFERENCES

[1]. D.R. Lide, "CRC Handbook of Chemistry and Physics", 88th ed., CRC Press, 2007. http://refhub.elsevier.com/S1002-16)30324- sbref7

[2]. Jensen, J. O., Vestbø, A. P., Li, Q., & Bjerrum, N. J.. "The energy efficiency of onboard hydrogen storage." Journal of Alloys and Compounds, 2007, 446, pp. 723-728. http://www.intechopen.com/books/show/title/energy-efficiency

[3]. E.W. Lemmon, M.L. Huber, M.O. McLinden, "NIST Stand." Ref. Database 23 Ref. Fluid Thermodyn. Transp. Prop. REFPROP, 2013.

[4]. Nikolic, V. M., Tasic, G. S., Maksic, A. D., Saponjic, D. P., Miulovic, S. M., & Kaninski, M. P. M. "Raising efficiency of hydrogen generation from alkaline water electrolysis–energy saving." International Journal of Hydrogen Energy, 2010, vol. 35, no. 22, pp. 12369-12373.

[5]. Bard, A. J., & Fox, M. A.. "Artificial photosynthesis: solar splitting of water to hydrogen and oxygen." Accounts of Chemical Research, 1995, vol. 28, no. 3, pp. 141-145.

[6]. Iordache, I., Bouzek, K., Paidar, M., Stehlík, K., Töpler, J., Stygar, M., & Zgonnik, V. "The hydrogen context and vulnerabilities in the central and Eastern European countries." International Journal of Hydrogen Energy, 2019, vol. 44, no. 35, pp. 19036-19054. https://doi.org/10.1016/j.ijhydene.2018.08.128.

[7].Solovey, V.V., Shevchenko, A.A., Zipunnikov, M.M., Kotenko, A.L., Nguyen Tien Khiem, Bui Dinh Tri, &, Tran Thanh "Development of high pressure membraneless alkaline electrolyzer." International Journal of Hydrogen Energy. 2021. https://doi.org/10.1016/j.ijhydene.2021.01.209

[8]. Solovey, V. V., Zipunnikov, M. M., Shevchenko, A. A., Vorobjova, I. O., & Kotenko, A. L. "Energy effective membrane-less technology for high pressure hydrogen electro-chemical generation." French-Ukrainian Journal of Chemistry, 2018, vol. 6, no. 1, pp. 151–156. https://doi.org/10.17721/fujcV6I1P151-156.

[9].Shevchenko, A.A., Zipunnikov, M.M., Kotenko, A.L., Vorobiova, I.O., Semykin, V.M..(2019) "Study of the influence of operating conditions on high pressure electrolyzer efficiency." Journal of Mechanical Engineering,, vol. 22, no. 4, pp. 53-63. https://doi.org/10.15407/pmach2019.04.053

[10].Shevchenko, A. "Creation of autonomous and network energy-technological complexes with a hydrogen storage of energy." Vidnovliuvana Energetika, 2020, vol. 61, no. 2, pp. 18-27. https://doi.org/10.36296/1819-8058.2020.2(61).18-27.

[11]. Yakimenko, L. M. "Elektrodnyye materialy v prikladnoy elektrokhimii [Electrode materials in applied electrochemistry]". Moscow: Khimiya, 1977, 264 p. (in Russian).

[12]. Sukhotin, A. M. "Spravochnik po elektrokhimii [Handbook of electrochemistry]". Leningrad: Khimiya, 1981, 488 p. (in Russian).

[13]. Spielrain, E. E., Malyshenko, S.P., Kuleshov. G.G. "Introduction to hydrogen energy". M.: Energoatomizdat, 1984, - 264 p. (in Russian).

[14]. Tomilov, A. P. "Prikladnaya elektrokhimiya [Applied electrochemistry]": A textbook. Moscow: Khimiya, 1984, 520 p. (in Russian).

[15]. Solovey, V., Zipunnikov, M., & Semikin, V. "Method for Calculating the Feed Water Replenishment Parameters under Electrolysis Process in Electrolyzer " French-Ukrainian Journal of Chemistry, 2020, vol. 8, no. 2, pp. 168-175. https://doi.org/10.17721/fujcV8I2P168-175

[16]. Solovey, V. V., Zipunnikov, N. N., & Shevchenko, A. A. "Issledovaniye effektivnosti elektrodnykh materialov v elektroliznykh sistemakh s razdelnym tsiklom generatsii gazov [Research of the efficiency of electrode materials in electrolysis systems with a separate cycle of gas generation]." Problemy mashinostroyeniya – Journal of Mechanical Engineering, 2015, vol. 18, no. 1, pp. 72–76 [in Russian].

[17]. Akbar Dadkhah, Dimitar Bozalakov, Jeroen D.M. De Kooning, Lieven Vandevelde. "On the optimal planning of a hydrogen refuelling station participating in the electricity and balancing markets. International Journal of Hydrogen Energy, 2021, vol. 46, no. 2, pp. 1488-1500. https://doi.org/10.1016/j.ijhydene.2020.10.130

[18]. Buttner, W., Rivkin, C., Burgess, R., Hartmann, K., Bloomfield, I., Bubar, M., & Moretto, P. "Hydrogen monitoring requirements in the global technical regulation on hydrogen and fuel cell vehicles." International journal of hydrogen energy, 2017, vol. 42, no. 11, pp. 7664-7671.

[19]. Chang, W. J., Lee, K. H., Ha, H., Jin, K., Kim, G., Hwang, S. T., & Hong, J. S. "Design principle and loss engineering for photovoltaic–electrolysis cell system." ACS Omega, 2017, vol. 2, no. 3, pp. 1009-1018.

[20] M. Reuß, J. Reul, T. Grube, M. Langemann, S. Calnan, M. Robinius, R. Schlatmann, U. Rau and D. "Solar hydrogen production: a bottom-up analysis of different photovoltaic– electrolysis pathways." Stolten,Sustainable Energy Fuels, 2019, Advance Article, https://doi.org/10.1039/C9SE00007K

[21]. Shevchenko, A. A., Zipunnikov, M. M., Kotenko, A. L. "Adaptation of the high-pressure electrolyzer in the conditions of joint operation with TPP and NPP power-generating units." Scientific Bulletin of National Mining University, 2020, vol. 6. pp. 76 – 82. https://doi.org/10.33271/nvngu/2020-6/076

[22]. Smart relay SR3B261BD. Retrieved from: https://www.se.com/id/en/product/SR3B261BD/modular-smart-relay-zelio-logic---26-i-o---24-v-dc---clockdisplay/

[23]. SR2USB01 : USB PC connecting cable - for smart relay Zelio Logic. Retrieved from: https://www.mejrubiop.com/index.php?main_page=product_info&products_id=204852

[24]. Modem interface - GSM - for communication interface SR2COM01.Retrieved from: https://www.se.com/id/en/product/SR2MOD02/modem - interface---gsm for-communication-interface-sr2com01/

Description of Colombian Electricity Pricing Derivatives

Dr. S Prabakaran,
Associate Professor,
School of Economics and Business Administration,
Department of Accounting & Finance,
Pontificia Universidad Javeriana Cali. Cali, Colombia.
Email – jopraba@gmail.com

Abstract

Electricity markets are becoming a popular field of research amongst academics because of the lack of appropriate models for describing electricity price behavior and pricing derivatives instruments. Models for price dynamics must consider seasonality and spiky behavior of jumps which seem hard to model by standard jump process. Without good models for electricity price dynamics, it is difficult to think about good models for futures, forward, swaps, and option pricing. In this paper, we attempt to introduce an algorithm for pricing derivatives to intuition from the Colombian electricity market. The main ambition of this study is fourfold: 1) First we begin our approach through to simple stochastic models for electricity pricing. 2) Next, we derive analytical formulas for the prices of electricity derivatives with different derivatives tools. 3) Then we extent short of the model for price risk in the electricity spot market 4) Finally we construct the model estimation under the physical measures for the Colombian electricity market. And this paper ends with a conclusion.

Key Words - Electricity markets, Energy Derivative, Option, and Forward Contract.

I. INTRODUCTION

Deregulation of electricity markets has led to a substantial increase in risk borne by market participants. The often unexpected, extreme spot price changes range even two orders of magnitude and can cause severe financial problems to the utilities that buy electricity in the wholesale market and deliver it to consumers at fixed prices. The utilities and other power market companies need to hedge against this price risk. A straightforward way to do it is to use derivatives, like forwards and options.

Here, we use the latter approach and describe the spot price dynamic models to review the electricity pricing with details of how to implement the pricing of the electricity market an After specifying a model we have to choose for derivatives pricing methodology. However, such an approach fails in the case of electricity due to extremely limited storage possibilities. Therefore, instead of using a discrete-time model approach we employ a concept of the risk premium/market price of risk and find such a pricing measure that yields the observed forward market prices. With such methodology, we can derive forward prices from the spot price model and to find explicit formulas for premiums of European options written on spot, as well as, on forwarding prices.

Over the last two decades, the electricity industry worldwide has undergone a profound restructuring process. Particularly in Colombia, laws 142 and 143 of 1994 in addition to later reforms, opened up an intensive reorganization of the electricity market, like the creation of the wholesale electricity market (MEM) in 1995 simultaneously to the vertical unbundling of the generation, transmission, distribution, and retail activities, seeking to improve the efficiency and quality of the electricity industry. Under this new framework, the power generation and retail businesses could be competitive deregulated markets, whereas the remaining two, transmission and distribution, were established as regulated activities.

Colombia has a hydro-dominated electricity market. Roughly 80% of its energy comes from hydro resources, 67% of its capacity, and 50% of its firm energy—energy in an exceptionally dry period. The cornerstones of the wholesale electricity market in Colombia are the spot energy market and the firm energy market. The spot energy market is a single-zone hourly market that determines the spot energy price in every hour as well as the efficient dispatch of resources.

This paper aims to introduce pricing electricity derivatives to the Colombian market with an alternative formalism.

II. STOCHASTIC MODEL FOR ELECTRICITY PRICING DERIVATIVES

In the last few years, there has been a rapidly increasing literature on stochastic models for the prices of electricity and other commodities. Many researchers have observed that the models typically used in financial markets are inappropriate due to the special features of commodity prices and especially of electricity prices as described in the introduction.

In this section, we will give a short evaluation of some of the models considered so far in the literature and compare them with our approach.

The choice of the stochastic model for electricity prices depends on the time granularity that needs to be reflected in the model. Liquidly traded futures and forward contracts typically have full months, quarters, or years as delivery periods, either as base load or peak load. Price quotes for single hour deliveries are in most cases only available as day-ahead prices from the spot market. However, many structured OTC products, such as swing options, are strongly influenced by the hourly price behavior. Since due to the non-storability of electricity, spot products cannot be used for hedging purposes, the electricity market is a highly incomplete market and pure arbitrage option pricing methods fail for most structured products. Previous work has been focused mainly on either of the two following approaches:

- Market models for futures prices: Instead of modeling the spot price and deriving futures prices, the futures prices themselves are modeled. This approach goes back to Black's model [1], where a single futures contract is considered. Ideas from the

IEECP'21, July 29-30, 2021, Silicon Valley, San Francisco, CA – USA

DAI : https://sci-index.com/DAI/2021.99101/IEECP/14735834

Heath-Jarrow-Morton theory for interest rates [2] are used in [3], [4], [5] and [6] to model the dynamics of the whole futures price curve. Such models have the advantage that the market can be considered as being complete and standard risk-neutral pricing may be used. Risk-neutral parameters can often be implied from traded options on futures prices. The disadvantage of such approaches is that futures prices do not reveal information about price behavior on an hourly or even daily time scale.

- Spot price models: This class of models aims at capturing the hourly price behavior by fitting their model to historical spot price data. Since there is no arbitrage relation between spot prices and futures prices, additional assumptions have to be made to use this model for pricing derivatives. Usually, this is done either by assuming the rational expectation hypothesis

$$F_{t,T} = \mathbf{E}\left[S_T \mid F_t\right], \tag{1}$$

As done e.g. in [7] to price generation assets, or by calibrating a market price of risk for each factor and then changing to an equivalent martingale measure P^* under which the relation $F_{t,T} = \mathbf{E}^*\left[S_T \mid F_t\right]$, holds.

Most models for the spot market employ at least two risk factors: one factor capturing the short-term hourly price dynamics characterized by mean reversion and extremely high volatility, and the other factor representing long-term price behavior observed in the futures market. Since there are no liquidly traded derivatives on a daily or hourly time scale that have a strong dependence on the short-term risk factor, it is exceedingly difficult to estimate the short-term market price of risk.

Through this paper, we will denote S_t the spot market price at time *t*. Since are working in a deterministic interest rate framework, we will not distinguish between forward and futures prices. Therefore, single hour futures prices at time *t* for delivery at time *T* are conditional expectations under the equivalent martingale measure

$$F_{t,T} = \mathrm{E}^*\left[S_T \mid F_t\right], \tag{2}$$

Where $F_t = \sigma\left[S_s : \mathrm{s} \le \mathrm{t}\right]$, is the natural filtration generated by the price process?

Future prices for power delivery over a period $S_t = (\ )\left[T_1, T_2\right]$ are given by

$$F_{t,T_1,T_2} = \mathrm{E}^*\left[\frac{1}{T_2 - T_1}\int_{T_1}^{T_2} S_T\, dT \,\middle|\, F_t\right] = \frac{1}{T_2 - T_1}\int_{T_1}^{T_2} F_{t,T}\, dT, \tag{3}$$

Or, in a discrete time setting by

$$F_{t,T_1,T_2} = \mathrm{E}^*\left[\frac{1}{T_2 - T_1}\sum_{T=T_1}^{T_2 - 1} S_t \,\middle|\, F_t\right] = \frac{1}{T_2 - T_1}\sum_{T=T_1}^{T_2 - 1} F_{t,T}. \tag{4}$$

The simplest model considering mean-reverting behavior is given by an Ornstein- Uhlenbeck process. Here the price process S_t is a diffusion process satisfying the stochastic differential equation

$$dS_t = -\left(S_t - a\right)dt + \sigma dW_t, \tag{5}$$

Where (W_t) is a standard Brownian motion, σ the volatility of the process, and λ the velocity with which the process reverts to its long term mean *a*.

In electricity markets, prices show strongly mean-reverting behavior so that estimates λ are quite large. Typical characteristic times for mean reversion are within a few days. Therefore, this model has the major drawback that futures prices are nearly constant over time, since under the assumption of (5) the futures price is given by

$$F_{t,T} = \mathrm{a}\left(1 - e^{0-\lambda(T-t)}\right) + S_t e^{-\lambda(T-t)} \tag{6}$$

For this reason, several authors suggest a two-factor model, see e.g. [8], [9] and [10]. In [9] a model of the form

$$dS_t = -\lambda\left(S_t - Y_t\right)dt + \sigma dW_t \tag{7}$$

is suggested, where Y_t is a Brownian motion. A similar model is given in [10], where commodity prices are described in the form

$$S_t = \exp\left(X_t + Y_t\right), \tag{8}$$

where (X_t) is an Ornstein-Uhlenbeck process responsible for the short-term variation and (Y_t) is a Brownian motion describing the long-term dynamics. The model we will introduce in and can be considered as an extension of the ideas of [10].

All models considered so far did not consider seasonality. Some authors simply neglect this serious difficulty. Others propose to use deterministic seasonality described by sinusoidal functions, see [11], [12], [13] and [10]. In [14] it is suggested to use equation (5) with a long-run mean a_t describing the seasonal patterns. A general deterministic seasonality is proposed in [14] and [15]. Here, the spot price is modeled as

$$S_t = f(\mathrm{t}) + X_t \ \text{or}\ S_t = \exp\left(f(\mathrm{t}) + X_t\right) \tag{9}$$

with an arbitrary deterministic function $f(t)$ and a mean-reverting stochastic process X_t

In our approach, the deterministic component $f(t)$ is specified by the load forecast `t and additional stochastic behavior is introduced by the use of SARIMA models for the time series of load and prices.

There are also different attempts to account for price spikes. One possibility to cope with spikes is the introduction of jump terms, see [4], [14], and [17]. The main criticism for these models is that under the typical assumption of a jump-diffusion model a large upward jump is not necessarily followed by a large downward jump. Therefore, some authors suggest hidden Markov models, also known as Markovian regime-switching models, where it is guaranteed that upward jumps are followed by downward jumps. Such models have been considered e.g. in [18, [19], [20], [21] and [22]. Regime-switching models are very intuitive candidates for electricity price models since there are some clear physical reasons for switches of regimes such as forced outages of important power plants. On the other hand, it seems to be difficult to combine regime-switching with seasonality.

Another approach is motivated by the economic background for price spikes. Prices are determined mainly by supply and demand (load). Therefore, the non-linear relation between load and price should be taken into account in the model. This non-linear transformation is called the 'power stack function' in [23] and [24]. They suggest an exponential function for that purpose. A similar model for spot prices has recently been considered in [1], where the relation

$$S_t = f\left(X_t\right) \tag{10}$$

is suggested with X_t being an Ornstein-Uhlenbeck process, and f a power function. We also prefer an approach based on the power stack function, since there is a natural interpretation of this non-linear transform in terms of the merit order curve.

III.ELECTRICITY DERIVATIVE PRICING

A. Electricity Options

The power industry had been utilizing the idea of options through embedded terms and conditions in various supply and purchase contracts for decades, without explicitly recognizing and valuing the options until the beginning of the electricity industry restructuring in the U.K., the U.S. and the Nordic countries in the 1990s. The emergence of the electricity wholesale markets and the dissemination of option pricing and risk management techniques have created electricity options not only based on the underlying price attribute (as in the case with plain vanilla electricity call and put options), but also other attributes like volume, delivery location and timing, quality, and fuel type.

A counterpart of each financial option can be created in the domain of electricity options by replacing the underlying of a financial option with electricity [25] for introduction to various kinds of financial options). Here, we describe a sample of electricity options that are commonly utilized in risk management applications in the generation and distribution sectors. These options usually have short- to medium maturity times such as months or a couple of years. Options with maturity times longer than 3 years are usually embedded in long-term supply or purchase contracts, which are termed as structured transactions.

Now, we turn to the pricing of a European call option written on the electricity spot price. Recall, that a European option is a contract that gives the buyer the right to buy/sell the underlying commodity at some future date t (called maturity) at a certain price K (called the strike price). First, we find the pricing measure Q^{λ}. Like Merton (1976) in the context of jump-diffusion processes, we assume that the dynamics of spikes and drops are the same in the actual and pricing measures. We start with finding the spot price dynamics under λ parameterization.

Let $\lambda(u)$ be a deterministic function square-integrable on $u \in [0, T_{\max}]$, where $T_{\max}$ is a time horizon long enough to contain all maturities of derivatives quoted in the market, and introduce a new process W_t^{λ}:

$$W_t^{\lambda} = W_t + \int_0^t \frac{\lambda(u)}{\sigma_b} du, \tag{11}$$

where σ_b is the volatility of the base regime. From the Girsanov theorem, we have that W_t^{λ} is a Wiener process under a new measure Q^{λ} defined as

$$\frac{dQ^{\lambda}}{dQ} = \exp\left[-\int_0^{T_{\max}} \frac{\lambda(u)}{\sigma_b} dW_u - \frac{1}{2}\int_o^{T_{\max}} \left(\frac{\lambda(u)}{\sigma_b}\right)^2 du \right] \tag{12}$$

with the filtration F_t^W, being the natural filtration of the process W_t .Now, the base regime process $X_{t,b}$ can be rewritten as:

$$dX_{t,b} = [\alpha - \lambda(t) - \beta X_{t,b}]dt + \sigma_b dW_t^{\lambda} \tag{13}$$

and the expected future spot price is given by:

$$E^{\lambda}(P_t \mid F_0) = p_{bb}^{(t)} \begin{bmatrix} X_0 e^{-\beta t} + \frac{\alpha}{\beta}\left(1 - e^{-\beta t}\right) \\ -\int_0^t e^{-\beta(t-u)} \lambda(u) du \end{bmatrix} + p_{bs}^{(t)} \left(e^{\mu_s + \frac{1}{2}\sigma_s^2} + c_s \right) p_{bd}^{(t)} \left(-e^{\mu_d + \frac{1}{2}\sigma_d^2} + c_d \right) + g_t \,. \tag{14}$$

The function $\lambda(t)$ can be calibrated to the market forward prices so that $E^{\lambda}(P_t \mid F_0) = f_0^t$, e.g. by using some fitting procedure (like the least-squares minimization). Alternatively, one can find the risk premium and then use the relation between the market price of risk $\lambda(t)$ and the risk premium:

$$p_{bb}^{(t)} \int_0^t e^{-\beta(t-u)} \lambda(u) du = RP(t) \,, \tag{15}$$

which is a simple consequence of the fact that $RP(t) = E(P_t \mid F_0) - E^{\lambda}(P_t \mid F_o)$, formula (15) and Ito's lemma.

Now, the price of a European call option written on the electricity spot price can be derived.

Option price formula. If the electricity spot price P_t is given by the MRS model then the price of a European call option written on P_t with strike price K and maturity T is equal to:

$$C_T(K) = e^{-rT} \begin{bmatrix} p_{bb}^{(T)} C_{T,b}(K) + \\ p_{bs}^{(T)} C_{T,s}(K) + p_{bd}^{(T)} C_{T,d}(K) \end{bmatrix} \tag{16}$$

Where

$$C_{T,b}(K) = \frac{s}{\sqrt{2\pi}} \exp\left(-\frac{(K' - m)^2}{2s^2} \right) + (m - K')\left[1 - \Phi\left(\frac{K' - m}{s} \right) \right] \tag{17}$$

$$C_{T,s}(K) = \mathrm{II}_{\{K' > C_s\}} \begin{Bmatrix} \exp\left(\mu_s + \frac{\sigma_s^2}{2} \right) \\ \left[1 - \Phi\left(\frac{\log(K' - c_s) - \mu_s - \sigma_s^2}{\sigma_s} \right) \right] \\ -(K' - C_s)\left[1 - F_{LN(\mu_s, \sigma_s^2)}(K' - c_s) \right] \end{Bmatrix} + \mathrm{II}_{\{K' \le c_s\}} \left[\exp\left(\mu_s + \frac{\sigma_s^2}{2} \right) + c_s - K' \right] \tag{18}$$

and

$$C_{T,d}(K) = \mathrm{II}_{\{k'<c_d\}} \begin{Bmatrix} -\exp\left(\mu_d + \frac{\sigma_d^2}{2}\right)\Phi \\ \left[\frac{\log(c_d - K') - \mu_d - \sigma_d^2}{\sigma_d}\right] + \\ (c_d - K')F_{LN(\mu_d,\sigma_d^2)}(c_d - K') \end{Bmatrix} \quad (19)$$

Further, $K' = K - g_T, m = X_0 e^{-\beta T} + \frac{\alpha}{\beta}\left(1 - e^{-\beta T}\right) -$ and $F_{LN(\mu,\sigma^2)}$ is $\int_0^T e^{-\beta(T-u)}\lambda(u)du$, $s^2 = \frac{\sigma_b^2}{2\beta}\left(1 - e^{-2\beta T}\right)$ the cumulative distribution function of the log-normal distribution with parameters μ and σ^2.

Here, we assume that the option is settled in an infinitesimal period $[T, T+\Delta]$. However, in practice, the electricity spot price usually corresponds to delivery during some period (e.g. an hour, a day) and, hence, the maturity of the option should be specified on the same timescale. On the other hand, the analyzed spot price quotations usually represent some delivery period. For instance, if the considered data is quoted daily, then the maturity of the option would be also given in daily timescale and would correspond to daily delivery.

B. Electricity Forwards

Electricity forward contracts represent the obligation to buy or sell a fixed amount of electricity at a pre-specified contract price, known as the forward price, at certain time in the future (called maturity or expiration time). In other words, electricity forwards are custom-tailored supply contracts between a buyer and a seller, where the buyer is obligated to take power and the seller is obligated to supply. The payoff of a forward contract promising to deliver one unit of electricity at price F at a future time *T* is:

Payoff of a Forward Contract $(S_T - F)$

Where S_T is the electricity spot price at time *T*. Although the payoff function (1) appears to be the same as for any financial forwards, electricity forwards differ from other financial and commodity forward contracts in that the underlying electricity is a different commodity at different times. The settlement price S_T is usually calculated based on the average price of electricity over the delivery period at the maturity time *T*.

Probably, the most popular electricity derivatives are the forward contracts. Recall that a forward contract is an agreement to buy (sell) a certain amount of the underlying (here MWh of electricity) at a specified future date. The settlement of the contract can be specified in two ways: with the physical delivery of electricity or with only financial clearing. Both types of settlements are in the following called delivery. Denote the price at the time t of a forward contract with delivery at the time T by f_t^T. Since the cost of entering a forward contract is equal to zero, the expected future payoff under the pricing measure should fulfill:

$$E^{\lambda}\left(P_T - f_t^T \mid F_t\right) = 0, \quad (20)$$

what implies that $f_t^T = E^{\lambda}\left(P_T \mid F_t\right)$. (21)

Observe, that now we define the price of a forward contract at any future date t. This is motivated by the fact that the valuation at time 0 of an option written on a forward contract requires the knowledge about the forward price dynamics at the option's maturity t.

Forward price formula. If the electricity spot price P_t is given by the MRS model, then the price at the time t of a forward contract written on P_t with delivery at the time T is given by the following formula

$$f_t^T = P\left(R_{[T]} = b \mid F_t\right)\left[\begin{array}{l} E^{\lambda}\left(X_{t,b} \mid F_t\right)e^{-\beta(T-t)} + \\ \frac{\alpha}{\beta}\left(1 - e^{-\beta(T-t)}\right) - \\ \int_t^T e^{-\beta(T-u)}\lambda(u)du \end{array}\right] +$$
$$P\left(R_{[T]} = s \mid F_t\right)\left(e^{\mu_s + \frac{1}{2}\sigma_s^2} + c_s\right) + \quad , \quad (22)$$
$$P\left(R_{[T]} = d \mid F_t\right)\left(c_d - e^{\mu_d + \frac{1}{2}\sigma_d^2}\right) + gt$$

where $P\left(R_{[T]} = i \mid F_t\right) = \sum_{j\in\{b,s,d\}} P\left(R_{[T]} = i \mid R_{[t]} = j\right)\mathrm{II}_{\{R_{[t]}=j\}}$ Note that in the above formula $E^{\lambda}\left(X_{t,b} \mid F_t\right)$ is used, since this expectation depends on the state process value at a time t. Namely, if $R_t = b$ then $E^{\lambda}\left(X_{t,b} \mid F_t\right) = X_{t,b} = X_t$. On the other hand, if at time t a spike or a drop occurred then $E^{\lambda}\left(X_{t,b} \mid F_t\right) = E^{\lambda}\left(X_{t,b} \mid F_{t-1}\right)$ and again this expectation is dependent on R_{t-1} value.

When deriving the forward price dynamics, we must remember that the properties of the obtained model should comply with the observed market prices. One of the most pronounced features of the market forward prices is the observed term structure of volatility, called the Samuelson effect. Precisely, the volatility of the forward prices is quite a law for distant delivery periods, however, it increases rapidly with approaching maturity of the contracts. Here, the forward price volatility is described by the part $P\left(R_{[T]} = b \mid F_t\right)E^{\lambda}\left(X_{t,b} \mid F_t\right)e^{-\beta(T-t)}$ of the formula (22). Hence, it is specified by the volatility of the spot price base regime scaled with $e^{-\beta(T-t)}$ and the corresponding probability of switching to the base regime. Observe that the scaling factor $e^{-\beta(T-t)}$ exhibits the Samuelson effect as it increases too 1 with t approaching maturity time T. Moreover, the forward price volatility, again due to the scaling factor, is lower than the spot price volatility. This is following the behavior of the market spot and forward prices.

Electricity forward contracts listed on energy exchanges are usually settled during a certain period (a week, a month, a year, etc.). Denote the price at the time t of a forward contract settled during the period $[T_1, T_2]$ $f_t^{[T_1,T_2]}$. The latter is the mean price of forwarding contracts with delivery during the period $[T_1, T_2]$, namely:

$$f_t^{[T_1,T_2]} = \int_{T_1}^{T_2} w(T_1,T_2,T)\, f_t^T dT \quad , \quad (23)$$
$$= \int_{T_1}^{T_2} w(T_1,T_2,T)\, E^{\lambda}\left(P_T \mid F_t\right)dT$$

where $w(T_1,T_2,T)$ is the weight function representing the time value of money. The form w depends on the contract specification. For contracts settled at maturity, we have $w(T_1,T_2,T) = \frac{1}{T_1 - T_2}$, while for instant settlement $w(T_1,T_2,T) = \frac{re^{-rT}}{e^{-rT_1} - e^{-rT_2}}$, where $r > 0$ is the interest rate (Benth et *al.*, 2008a). The price $f_t^{[T_1,T_2]}$ can be obtained from formulas (22) and (23). Indeed, we have:

$$f_t^{[T_1,T_2]} = E^{\lambda}\left(X_{t,b} \mid F_t\right)\int_{T_1}^{T_2} \frac{w(T_1,T_2,T)}{P\left(R_{[T]} = b \mid F_t\right)} e^{-\beta(T-t)}dt + \int_{T_1}^{T_2}\left[\frac{\alpha}{\beta}\left(1 - e^{-\beta(T-t)}\right) - \int_t^T e^{-\beta(T-u)}\lambda(u)du\right]dT + \left(e^{\mu_s+\frac{1}{2}\sigma_s^2} + c_s\right)\int_{T_1}^{T_2} w(T_1,T_2,T)\, P\left(R_{[T]} = s \mid F_t\right)dT + \left(c_d - e^{\mu_d+\frac{1}{2}\sigma_d^2}\right)\int_{T_1}^{T_2} w(T_1,T_2,T)\, P\left(R_{[T]} = d \mid F_t\right)dT + \int_{T_1}^{T_2} w(T_1,T_2,T)\, g_T dT \quad (24)$$

C. Options Written on Electricity Forward Contracts

Finally, we find an explicit formula for a European call option written on a forward contract delivering electricity during a specified period. Observe, that the forward price $f_t^{[T_1,T_2]}$ depends on the spot price at the time t and, as a consequence, also on the state process value at the time t.

We consider an option written on an electricity forward contract with settlement during a specified period, as it is the most popular specification of electricity options on energy exchanges. For example, in the EEX market, there are options written on forwarding contracts with monthly, quarterly, and yearly settlement periods. The maturity of such options is set to the fourth business day before the beginning of the underlying contract's settlement period.

Price formula for an option written on a forward contract. The price of a European call option with strike price K and maturity t written on a forward contract with delivery during the period $[T_1,T_2]$ is equal to:

$$Cf_t^{[T_1,T_2]}(K) = e^{-rt}\left\{A_0(b)C_{t,b}\left(\frac{K - B_0(b)}{A_0(b)} + g_t\right) P\left(R_{[t]} = b \mid R_0 = b\right) + \sum_{i\in\{s,d\}}\sum_{k=1}^{[t]}\left[A_k(i)C_{[t]-k+1,b}\left(\frac{K - B_k(i)}{A_k(i)} + g_{[t]-k+1}\right) \times P\left(R_{[t]} = i, R_{[t]-1}1b,\ldots,R_{[t]-k} = b \mid R_0 = b\right)\right]\right\} \quad (25)$$

Where

$$A_k(i) = \int_{T_1}^{T_2} \frac{w(T_1,T_2,T)}{P\left(R_{[T]} = b \mid R_{[t]} = i\right)e^{-\beta(T-[t]+k-1)}dT}, \quad (26)$$

$$A_0(b) = \int_{T_1}^{T_2} \frac{w(T_1,T_2,T)P}{\left(R_{[T]} = b \mid R_{[t]} = b\right)e^{-\beta(T-t)}dT}, \quad (27)$$

$$B_k(i) = \int_{T_1}^{T_2} w(T_1,T_2,T)\, P\left(R_{[T]} = b \mid R_{[t]} = i\right)\times \left[\frac{\alpha}{\beta}\left(1 - e^{-\beta(T-[t]+k-1)}\right) - \int_{[t]-k+1}^{T} e^{-\beta(T-u)}\lambda(u)du\right]dT + \left(e^{\mu_s+\frac{1}{2}\sigma_s^2} + c_s\right)\int_{T_1}^{T_2} w(T_1,T_2,T)\, P\left(R_{[T]} = s \mid R_{[t]} = i\right)dT + \left(c_d - e^{\mu_d+\frac{1}{2}\sigma_d^2}\right)\int_{T_1}^{T_2} w(T_1,T_2,T)\, P\left(R_{[T]} = s \mid R_{[t]} = i\right)dT + \int_{T_1}^{T_2} w(T_1,T_2,T)\, g_T dT \quad (28)$$

$$B_0(b) = \int_{T_1}^{T_2} \frac{w(T_1,T_2,T)\, P\left(R_{[T]} = b \mid R_{[t]} = b\right)}{\left[\frac{\alpha}{\beta}\left(1 - e^{-\beta(T-t)}\right) - \int_t^T \frac{\alpha}{\beta}\left(e^{-\beta(T-u)}\lambda(u)du\right)\right]dT + \left(e^{\mu_s+\frac{1}{2}\sigma_s^2} + c_s\right)\int_{T_1}^{T_2} w(T_1,T_2,T)\, P\left(R_{[T]} = s \mid R_{[t]} = b\right)dT + \left(c_d - e^{\mu_d+\frac{1}{2}\sigma_d^2}\right)\int_{T_1}^{T_2} w(T_1,T_2,T)\, P\left(R_{[T]} = d \mid R_{[t]} = b\right)dT + \int_{T_1}^{T_2} w(T_1,T_2,T)\, g_T dT} \quad (29)$$

And $C_{t,b}(K)$ is the "base regime part" of the price of a European call option written on the electricity spot price with maturity t and strike K, see equation (29) with $T = t$.

IV. PRICE RISK MODEL

Electricity has proven to be the most volatile commodity, and it is not the exception in the Colombian competitive electricity market. It makes it compulsory to develop appropriate risk management to maximize agents' benefits and minimize the corresponding uncertainty upon them. Among the risks that firms have to handle, are a macroeconomic risk, price risk, market risk, credit risk, regulatory risk, country risk, and quantity risk. The last one is a non- tradable risk, and an implicit feature of electricity, which has to do with the amount of energy that will be demanded in the future, which follows a stochastic process as well as the spot price. This situation directly impacts the firm's revenues and makes it necessary to include it when designing the hedging portfolio.

Financial theory has developed research studies to find how to address this problem. In [26] electricity risk management is handled by a multi-market trading approach, while other references like [27] get to focus on best risk management trough forward on-peak and off-peak contracts. Nevertheless, the electricity derivatives are increasingly studied and used around the world to manage the financial risks and resource adequacy of power markets, like it is advocated in [28]. Particularly [29] proposed a financial call option to hedge against critic hydrologic scenarios in the Colombian electricity system by ensuring generation adequacy.

Further, derivative instruments have been developed to also handle the quantity risk, like swing options, weather derivatives, interruptible contracts, among other instruments named in [30]. The features of these derivative products make

them be usually traded over the counter (OTC); therefore, they are low liquidity instruments, which is why they are not regarded in this paper. However, references [31] and [32] study quantity risk.

Oum, Deng, and Orean [33] deal with the static hedging problem of an LSE who has to serve an uncertain electricity demand q at a regulated fixed price r in a single period from 0 to 1. Besides, the LSE procures the electricity to serve his customers, from the wholesale market at a spot price p. Hence the profit of the LSE would be:

$$y(p,q) = (r-p)\cdot q \quad (30)$$

To protect himself against price risk, the LSE can take a long position in q^{-9} forwarding contracts at a fixed forward price F. However, the LSE will face another risk that arises from the fact that demand $\bar{q}$ may vary from the expected value at time 0 to the actual realized value at time 1. Then, if the actual demand realized by the retailer agent is $\bar{q}+\Delta q$, then, the share of the profit in (28), that is at risk is: $(r-p)\cdot\Delta q$, where Δq could be different to zero (gains/losses).

To deal with this hedging problem, the authors derive the optimal hedging portfolio as a function of the spot price p. That is:

$$Y(p,q) = (r-p)q + x(p) \quad (31)$$

where $x(p)$ is the optimal hedging portfolio as a function of the spot price p.

Regarding the LSE's preferences and risk aversion profile, it is necessary to identify its utility function U over total profit Y. In turn, because of the positive correlation between price and demand, which will be evident later in the paper for the Colombian electricity market, there exists a joint probability function $f(p,q)$ defined on the probability measure P, which characterizes the behavior of p and q at time 1. On the other side, Q is a risk-neutral probability measure by which the hedging instruments are priced and $g(p)$ is the probability density function of p under Q. Keeping this in mind, the optimization problem is formulated as follows:

$$\max_{x(p)} E\left[U\left(Y(p,q)\right)\right] \quad (32)$$

$$\text{s.t. } E^{Q}[x(p)] = 0 \quad (33)$$

where $E[\cdot]$ and $E^{Q}[\cdot]$ denote expectations under probability measures P and Q, respectively. In (30) the constraint implies that the hedge portfolio $x(p)$ is self-financing, that is, the LSE can borrow funds in the money market, to purchase the derivative instruments needed to obtain the maximum expected utility over the total profit $Y(p,q)$. This constraint also means that there are no arbitrage opportunities through this hedging portfolio, under a constant risk-free rate. The optimization process yields as a result of the optimal payoff function $x^{*}(p)$.

Through an extension of the fundamental calculus theorem, it is demonstrated that any twice continuously differentiable function can be written as follows, for fixed value F:

$$x(p) = x(F)\cdot 1 + x'(F)\cdot(p-F) + \int_0^F x''(K)\cdot(K-p)^{+}\,dK + \int_F^{\infty} x''(K)\cdot(p-K)^{+}\,dK \quad (34)$$

The expression $(.)^{+}$ in the above equation is equivalent to the function $max(\cdot,0)$. It is important to note that in the expressions above 1, $(p-f)$, $max(K-p,0)$, $max(p-K,0)$ correspond to the payoff profile of a bond, forward contract, put option, and call option, respectively. In this sense, and remaining the LEGO© approach theory presented, with $x(F)$ units in bonds, $x'(F)$ units of forwarding contracts, $x''(K)dK$ units of put options with the strike price $K(K<F)$, and $x''(K)dK$ units of call options with the strike price $K'(K'>F)$, it is possible to replicate the resultant optimal hedging portfolio $x^{*}(p)$ from the optimization process. This financial derivative has an underlying asset the electricity spot price.

Viewed from this angle, to replicate the optimal function $x^{*}(p)$, the equation (34) implies that it is necessary to have a set of continuum strike prices for both put and call options. Since markets are incomplete, there are no markets with that amount of strike prices on board, and assuming that there is only n put options and m call options available in the market, Oum, Deng, and Orend proposed a portfolio compounded by $x(F)$ units of bonds, $x'(F)$ units of forwarding contracts, $\frac{1}{2}(x'(K_{i+1})-x'(K_{i-1}))$ units of put options with strike prices $K_i, i=1,...,n$ and $\frac{1}{2}(x'(K_{j+1})-x'(K_{j-1}))$ units of call options with strike prices $K_j, i=1,...,m$. The errors of this replicating strategy are calculated depending on the range in which spot price is realized at time 1.

V. MODEL ESTIMATION UNDER THE PHYSICAL MEASURE

The non-storability feature of electricity along with the steeply rising supply and the inelastic demand curve, both schematically represented in Figure 1, makes the electricity price p and the electricity demand q to be positively correlated. It happens in this way in the Colombian electricity market, since the dispatch is carried out in order of merit, so, when demand rises during on-peak hours, it forces the system to put in operation a more expensive generation resource, increasing the spot price as well.

Additional to the fact explained above, throughout summer seasons, the hydropower plants which are technologies with

lower variable costs, reduce their power production due to natural water inflows shortages and of course to a diminishment in water reserves into reservoirs. This turns out in a higher marginal system cost, so an increment in demand translates into an increase in the spot price. This increment in the spot price reaches larger values during summer seasons than during winter seasons. Therefore, the correlation between p and q is bigger during dry periods in the Colombian wholesale electricity market.

The earlier reasons justify the usage of the price-quantity hedging strategy presented, to design suitable derivative instruments to be used by the agents of the electricity market.

It is clear that the advantage offered by the financial derivative products arises from the fact that is likely to achieve the maximum expected value of total profit $Y(p,q)$, together with the minimum deviation of this profit (which means less uncertainty over LSE's total profit), after building a hedging portfolio with those instruments.

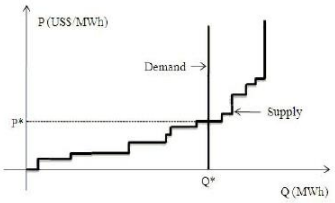

Figure 1: Supply and demand equilibria at Colombian electricity market.

To do so, a utility function to represent the risk aversion preferences of the agents like a mean-variance utility function is a good candidate to accomplish both goals at the same time. Here it is utilized the same mean-variance utility function which has been used in financial hedging literature to deal with non-tradable risk:

$$U(Y) = Y - \frac{1}{2}a\left(Y^2 - E[Y]^2\right) \tag{35}$$

where a represents the agent's risk aversion coefficient. Certainly, maximizing the expected value of the utility function in (33) $\left(E[U(Y)] = E[Y] - \frac{1}{2}aVar(Y)\right)$ is equivalent to maximize the expected value of $Y(p,q)$ and also to minimize the variance of (33), which is the advantage provided by a price-quantity hedging portfolio.

In equation (33) it is presented the optimal hedging function constrained to the mean-variance utility function. The arithmetic procedure to find this expression is developed.

$$x^*(p) = \frac{1}{a}\left(1 - \frac{g(p)/f_p(p)}{E^Q\left[g(p)/f_p(p)\right]}\right) - E\left[y(p,q)\,|\,p\right] + \tag{36}$$

$$E^Q\left[E\left[y(p,q)p\right]\right]\frac{g(p)/f_p(p)}{E^Q\left[g(p)/f_p(p)\right]}$$

where $f_p(p)$ is the marginal density function of p under the probability measure P.

From the perspective of a clearinghouse or a market maker, who is willing to design the most adequate hedging instruments for all the participants in the market, the goodness of this model, is that equation (36) can be used to calculate the optimal payoff function for each retailer, which will determine the optimal hedging instruments needed by each particular retailer. Once this task is undertaken, and seeking to find the optimal hedging instruments for all of them jointly interacting in the market, here it is proposed to estimate a weighted average market payoff function $\bar{x}(p)$ as presented in equation (36), which will represent the joint needs of all the agents and could be used to determine general hedging instruments -suitable for all-, by no favoring big or small agents and giving to each of them the same hedging opportunities.

$$\bar{x}(p) = \sum_{i=1}^{N} w_i x_i^*(p) \tag{37}$$

Where, $$w_i = \frac{\int_0^S x_i^*(p)dp}{\sum_{i=1}^{N}\int_0^S x_i^*(p)dp} \tag{38}$$

The variable S corresponds to a price-cap value defined under the market maker or clearinghouse criteria. Within the Colombian framework, this variable could be interpreted as the scarcity price associated with the firm energy market described above, since hedging above this price already exists given the call options related to that market.

After calculating $\bar{x}(p)$, the replicating methodology suggested is used to find the right number of bonds, forward contracts, put and call options needed to best describe the behavior of $\bar{x}(p)$.

Some of these financial instruments are currently available in the Colombian market, except the financial options. The simplest of them, bonds, can be found available in the stock market; forward contracts needed to replicate the function $x^*(p)$, could be either the current bilateral contracts (not suggested), the forward contracts that are planned to be included in MOR proposal, or even better, future contracts which are quite possibly to be launched the next year by a central chamber of counter-party risk (CRCC) to be established soon in Colombia. Since there are no financial options to replicate the optimal hedging function on the current electricity market.

Now, for the empirical analysis and the estimation procedure we use data from the Colombian electricity markets daily market representative rate value (in Colombian Pesos) the period from January 1, 1995, to December 2 2013 with 6853 observations. The fig 2 time series of the resulting price for the above Colombian electricity daily price.

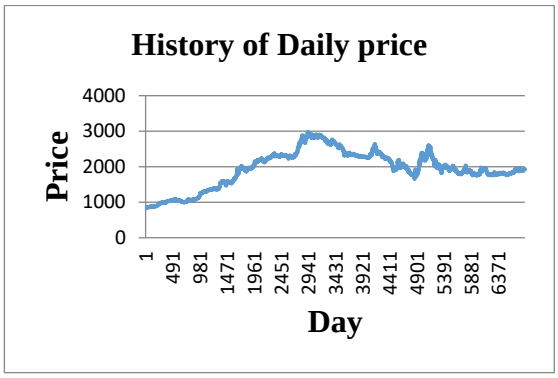

Figure 2: History of Daily price

The fig 3 gives the QQ plot for electricity daily price.

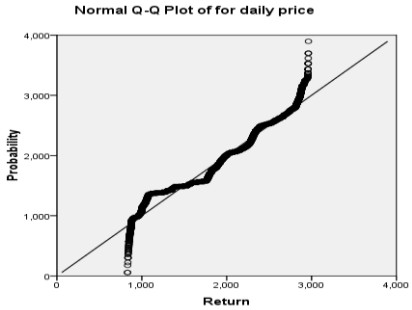

Figure 3: Normal QQ plot.

VI. CONCLUSION

From the above discussion, in this paper, we attempted to introduce an algorithm for pricing derivatives to intuition from the Colombian electricity market. Initially, we started our approach through simple stochastic models for electricity pricing. And, we derived analytical formulas for prices of electricity derivatives with different derivatives tools. 3) Then we extended short of the model for price risk in the electricity spot market. Finally, we constructed the model estimation under the physical measures for the Colombian electricity market. And this paper ends with a conclusion.

VII. REFERENCES

1. F. Black, The Pricing of Commodity Contracts, Journal of Financial Economics 3 (1976), 167 - 179.
2. D. Heath, R. Jarrow, A. Morton, Bond pricing, and the term structure of interest rates: a new methodology, Econometrica 60 (1992), 77 - 105.
3. L. Clewlow, C. Strickland, Valuing Energy Options in a One Factor Model Fitted to forwarding Prices, Working Paper, University of Sydney, April 1999.
4. G.E.P. Box, G.M. Jenkins, Time Series Analysis: Forecasting and Control, (Revised Edition) Holden-Day, San Francisco, 1976.
5. S. Koekebakker, F. Ollmar, Forward curve dynamics in the Nordic electricity market, Preprint, Norwegian School of Economics and Business Administration, 2001.
6. M. Manoliu, S. Tompaidis, Energy Futures Prices: Term Structure Models with Kalman Filter Estimation, Applied Mathematical Finance 9 (2002), 21 - 43.
7. C. L. Tseng, G. Barz, Short-term Generation Asset Valuation: a Real Options Approach, Operations Research 50 (2002), 297 - 310.
8. R. Gibson, E.S. Schwartz, Stochastic convenience yield and the pricing of oil contingent claims, Journal of Finance 45 (1990), 959 - 976.
9. D. Pilipovic, Energy Risk: Valuing and Managing Energy Derivatives, McGraw-Hill, New York, 1998.
10. E. Schwartz, J.E. Smith, Short-Term Variations, and long-term dynamics in commodity prices, Management Science 46 (2000), 893 - 911.
11. M.T. Barlow, A diffusion model for electricity prices, Mathematical Finance 12 (2002), 287-298.
12. R. J. Elliott, G.A. Sick, M. Stein, Modelling Electricity Price Risk, Preprint, University of Calgary 2003.
13. H. Geman, A. Roncoroni, A Class of Marked Point Processes for Modeling Electricity Prices, Preprint, ESSEC Business School, Cergy-Pontoise 2003.
14. S. Knittel, M. Roberts, An Empirical Examination of Deregulated Electricity Prices, Boston University, POWER Working Paper PWP-087, 2001.
15. R. Gibson, E.S. Schwartz, Stochastic convenience yield and the pricing of oil contingent claims, Journal of Finance 45 (1990), 959 - 976.
16. A. C. Harvey, Forecasting, Structural Time Series Models and Kalman Filtering, Cambridge University Press, 1989.
17. D. Heath, R. Jarrow, A. Morton, Bond pricing, and the term structure of interest rates: a new methodology, Econometrica 60 (1992), 77 - 105.
18. C. De Jong, R. Huisman, Option formulas for mean-reverting power prices with spikes, Working Paper, Erasmus University Rotterdam, 2002.
19. S. Deng, Stochastic Models of Energy Commodity Prices and Their Applications: Mean-reversion with Jumps and Spikes, Working paper, Georgia Institute of Technology, 2000.
20. R. J. Elliott, G.A. Sick, M. Stein, Modeling Electricity Price Risk, Preprint, University of Calgary 2003.
21. R. Huisman, R. Mahieu, Regime Jumps in Electricity Prices, Working Paper, Erasmus University Rotterdam, 2001.
22. V.A. Kholodnyi, The Stochastic Process for Power Prices with Spikes and Valuation of European Contingent Claims on Power, Preprint, TXU- RAG-01/00, July 2000.
23. Eydeland, H. Geman, Fundamentals of Electricity Derivatives, in Energy Modeling and the Management of Uncertainty, (pp. 35{43), Risk Books, London, 1999.
24. P. Skantze, A. Gubina, M. Ilic, Bid-based stochastic model for electricity prices: The impact of fundamental drivers on market dynamics Report, MIT Energy Laboratory (2000).
25. Hull J. Options, Futures, and other derivative, 4th Edition, Prentice-Hall, Englewood, NJ, 2000.
26. M. Liu, F. Wu, Risk management in a competitive electricity market, Electrical Power and Energy Systems Vol. 29 (2007) pp. 690 - 697.

27. R. Huisman, R. Mahieu, F. Schlichter, Electricity portfolio management: Optimal peak / off-peak allocations, Research in Management.
28. H. Chao, R. Wilson, Resource adequacy, and market power mitigation via options contracts, POWER Ninth Annual Research Conference.
29. J. Villareal, C. Soto, Ensuring generation adequacy with firm energy call options: A case study for the hydro - dependent Colombian system.
30. S. Deng, S. Oren, Electricity derivatives and risk management, Energy Vol. 31 (2006) pp. 940 - 953.
31. Y. Oum, S. Oren, S. Deng, Hedging quantity risks with standard power options in a competitive wholesale - electricity market, Special Issue on Applications of Financial Engineering in Operations, Production, Services, Logistics, and Management, Naval Research Logistics Vol. 53 (2006) pp. 697 - 712.
32. M. Prokopczuk, S. Rachev, G. Schindlmayr, S. Truck, Quantifying risk in the electricity business: A RAROC - based approach, Energy Economics Vol. 29.
33. Y. Oum, S. Oren, Optimal static hedging of volumetric risk in a competitive wholesale electricity market, Management Science (in press).

ETHANOL DEMAND IN BRAZIL: A CONTRIBUTION TO A BETTER ESTIMATE

1st Anderson Luís da Silva
Paulista School of Politics, Economics and Business
Federal University of Sao Paulo
Osasco, Brazil
alsi@outlook.com.br

2nd Juan Castañeda-Ayarza
Economic and Management Center
Pontificia Universidade Católica
Campinas, Brazil
juan.arturo@puc-campinas.edu.br

Abstract

Through the GMM method, this work proposes to advance the modeling of demand for anhydrous ethanol and hydrated ethanol in Brazil. Several previous studies with the same objective brought relevant contributions to estimate the demand for biofuels better. The models present in this article gathered those contributions that were previously seen in isolation. Further, new advances have been made. The results generated by this model have proven to be significant. This paper also identified contributions that could be relevant to further modeling demand for anhydrous and hydrated ethanol, but which are not possible given the limited data.

Keywords: *Fuel ethanol demand, GMM, Economic analysis*

I. INTRODUCTION

The first fifteen years of the 21st century were characterized by global concerns about energy supply and the acceptance of the need to address the effects of climate change [1]. These factors have aroused interest and significant investments in renewable energy by the international community. However, the global energy matrix is still composed almost entirely of fossil carbon sources - about 81% - while those of renewable energy represents only 14% of the total [2].

Because of high oil prices (fossil carbon source represents 33% of the global energy matrix and is the primary fuel source [2]), particular emphasis has been placed on liquid biofuels. They are direct substitutes for oil and allegedly contribute to rural development, emission reductions in the transport sector, and reduced oil imports [3].

Brazil, in addition to standing out from other countries for having the most sustainable energy matrix - renewable energy sources representing about 43.5% of the entire national energy matrix [2] - is also the third-largest producer and consumer of biofuels in the world, behind only the United States and China. However, unlike other countries, Brazil can increase biofuel production without causing apparent food supply damage [4].

Studies conducted by the Brazilian Sugarcane Industry Association (Unique, 2016) have shown that no country in the world produces ethanol with the same efficiency as Brazil due to the quality of the raw material and suitable weather conditions [4].

The sector's success has come from improvements in technology, the state incentive to increase renewable energy, and the introduction of flex-fuel vehicles in 2003. All of this gave a new boost to the sugar-alcohol industry and the reduction in production costs (around 70%), in addition to constant increases in the price of oil, which ended up making this biofuel highly competitive in the domestic and foreign markets [5].

The demand for ethanol fuel, produced from renewable resources, has increased considerably in Brazil in recent years. The projection of the Brazilian Energy Research Company (EPE, 2018), considering a high growth scenario, is that the demand for ethanol fuel in Brazil will reach 50 billion liters in 2030, meaning an increase of 87% compared to current consumption [6].

This heated scenario for the Brazilian ethanol industry demonstrates the importance of studies on fuel demand behavior. There are several papers on this subject, such as Buonfiglio and Bajay (1992) [7], Tokgoz and Eleboid (2006) [8], Junior et al. (2010) [9], Serigati et al. (2010) [10], Freitas and Kaneko (2011) [11] and Randow et al. (2013) [12] (Table 1).

Table 1. Precedents of demand modeling to Brazilian biofuel

Author	Keyword	Biofuel Demand Estimation
Junior et al. (2010)	Simple model	$D_e = f(P_e, P_g, Y)$
Buonfiglio and Bajay (1992); Serigati et al. (2010)	Complementary Good	$D_e = f(P_e, P_g, F, Y)$
Freitas and Kaneko (2011)	Seasonality	$D_e = f(P_e, P_g, F, Y, dummies)$
Tokgoz and Elobeid (2006)	Aspects of fleet	$D_{ae} = f(P_{eh}, P_g, Interaction, Blend, Y)$ $D_{he} = f(P_{eh}, P_g, Interaction, FF, Y)$

IEECP '21, July 29-30, 2021, Silicon Valley, San Francisco, CA – USA

DAI : *https://sci-index.com/DAI/2021.99101/IEECP/14905224*

	compositio n

About Brazilian ethanol, the simplest regression model found for this fuel was as seen in Junior et al. [9], which therefore took into consideration only the variables ethanol price, gasoline price, and consumer income. Buonfiglio and Bajay [7] and Serigati et al. [10], when estimating a demand model for Brazilian ethanol, in addition to the explanatory variables found in the simplest regression models, also considered it essential to include a new variable in the model, the 'fleet' variable (F), represented by the number of vehicles in circulation in the country.

Freitas and Kaneko [11] differentiated themselves from the former by taking into account in their ethanol demand model the seasonality in price and consequently in ethanol consumption.

Due to the non-existence of sugarcane stock (as it is a highly perishable agricultural good that cannot be stored), Brazilian mills have an average idleness per year of four months in biofuel production. In this interval, which corresponds to the inter-harvest period between November and March, the mills present a significant drop in ethanol supply, which leads to an increase in final consumer prices and lower fuel consumption [11, 15].

Therefore, Freitas and Kaneko [11] included in their model a dummy variable containing an observation for each month analyzed, which is intended to contribute to the discernment of the magnitude of the seasonal effects on ethanol consumption in Brazil.

Tokgoz and Elobeid [8], in their estimation model for the demand for ethanol in Brazil, trying to treat the fleet variable (F) in a certain way that aspects of it are considered. Their first contribution to a better estimation of ethanol demand in the country is that it is divided between the demand for anhydrous ethanol and hydrous ethanol. Hydrated ethanol is extracted in the distillation process. It is used by vehicles powered only by alcohol and by flex-fuel vehicles. Simultaneously, anhydrous ethanol derived from hydrated ethanol after the dehydration process is contained by state imposition in gasoline. It is used in vehicles powered only by gasoline and flex-fuel vehicles.

Thus, it is assumed that the demand for each type of ethanol responds to different incentives, so they should not be considered in the same equation. While anhydrous ethanol consumption is directly proportional to the gasoline price, hydrous ethanol has an inverse relationship.

The behavioral equation proposed by Tokgoz and Elobeid [8] for anhydrous ethanol consumption includes, in addition to the price of anhydrous ethanol and the price of gasoline, the imposition of blending, since anhydrous ethanol is used only as a blend at the level of imposition. The variation in this percentage of imposition influences the consumption of anhydrous ethanol. For the hydrated ethanol equation, the variable FF is added, representing the number of flex-fuel vehicles in the vehicle fleet since hydrated ethanol is used in these vehicles at any level. For both equations, a term of interaction is also included, which equals the price of gasoline times the ratio of flex vehicles in the total fleet of vehicles. According to the authors, this interaction term captures the higher sensitivity of demand for flex-fuel vehicles in gasoline prices.

With the increase in the flex-fuel fleet, demand for anhydrous and hydrous ethanol tends to become more sensitive to changes in gasoline prices. In the case of anhydrous ethanol demand, with the increase in gasoline prices, demand for ethanol declines as consumers who own flex-fuel vehicles replace gasoline blended with anhydrous ethanol with hydrous ethanol, so the coefficient of interaction in this equation is negative.

On the other hand, demand for hydrated ethanol increases if the price of gasoline increases, as consumers of flex-fuel vehicles prefer the use of hydrated ethanol over gasoline that has anhydrous blended. Thus, the interaction coefficient in the hydrous ethanol equation is positive.

Tokgoz and Elobeid [8] chose not to put the price of anhydrous ethanol in their model. In addition to being integrated with the price of gasoline, anhydrous ethanol has a high correlation with the price of hydrated ethanol and the fact that the cost of dehydration is constant.

However, these papers intersect to some extent. They have different and isolated contributions on the subject. This article aims to contribute to the advancement of ethanol demand modeling in Brazil by estimating one or more models that bring together these different contributions in the literature and beyond, from them also propose advances.

II. METHOD

Using the free software of RStudio integrated development environment, the regression of the models with multiple variables proposed by this work, which gathers the different contributions present in the existing literature, will be performed using the GMM econometric technique (Generalized method of moments). The data present in the models comprise the monthly period that goes from May 2013 to April 2020; this one is due to data limitation regarding the variables that consider the vehicle fleet that started to be separated by fuel only in May 2013.

As seen in Hayashi (2000) [13], the generalized method of moments (GMM) is a generalized form of estimation that equals a moment to a given value, which is nothing more than satisfying a sample mean. Taking two random variables z_t e m_t the generalized estimator of moments can be expressed as follows:

$$\hat{\beta}_1 = \frac{\sum_{t=1}^{T}\sum_{t=1}^{T} y_t x_j (m_t m_j + z_t z_j)}{\sum_{t=1}^{T}\sum_{t=1}^{T} x_t x_j (m_t m_j + z_t z_j)}$$

(1)

The estimator has asymptotic properties, and it is expected that the instruments generated and the additional moments have no correlation with the error term.

The regression models for anhydrous ethanol demand and hydrated ethanol demand were estimated in the log-log functional form to obtain coefficients that can be interpreted as the variables' elasticity.

$$\log C_{eh_t} = \beta_{0_t} + \beta_1 \log \mathrm{P_{eh_t}} + \beta_2 \log \mathrm{P_{gc_t}} + \beta_3 \log \mathrm{It_t} + \beta_4 \log \mathrm{AF} + \beta_5 \log \mathrm{Y}$$

(2)

$$\log C_{ea} = \beta_0 + \beta_1 \log \mathrm{P_{eh}} + \beta_2 \log \mathrm{P_{gc}} + \beta_3 \log \mathrm{It} + \beta_4 \log \mathrm{HF} + \beta_4 \log \mathrm{HBlend} + \beta_5 \log \mathrm{Y}$$

(3)

The variables present in the above models refer to: Ceh (hydrated ethanol consumption); Peh (the price of hydrated ethanol); Pgc (the price of C gasoline); It (term of interaction that is equal to the ratio of the fleet of flex-fuel vehicles times the price of gasoline, which aims to capture the consumer preference of the flex-fuel fleet between gasoline and ethanol); AF (Anhydrous fleet; Y (GDP); Cea (consumption of anhydrous ethanol); HF (Hydrated Fleet); and Blend = Levels of the imposition of blending of anhydrous ethanol in gasoline.

III. RESULTS AND DISCUSSION

The models proposed in this work, based on the researched literature, are presented below:

$$D_{ae} = f(P_{eh}, P_g, Interaction, Blend, AF, Y, Seasonality)$$

$$D_{he} = f(P_{eh}, P_g, Interaction, HF, Y, Seasonality)$$

For the anhydrous ethanol demand equation, it essential to include the variable 'Anhydrous Fleet' (AF), equivalent to the fleet of vehicles using anhydrous ethanol, being composed of the fleet of vehicles powered by gasoline plus the fleet of flex-fuel vehicles, and for the hydrous ethanol equation, in place of the variable FF (Flex Fleet), the inclusion of the variable 'Hydrated Fleet' (HF), composed of the fleet of vehicles powered by hydrous ethanol, equivalent to the fleet of vehicles powered by alcohol, and the fleet of flex vehicles.

Table 2. Model 1 results from GMM regression

Variable	Coefficient	Std. Error	t-test	p-value
LNCEH	0,48	0.047	10.288	0.0000
LNPEH	-1,83	0.32	-5.7137	0.0000
LNPGC	1,19	0.36	3.3089	0.0014
LNIT	0,69	0.28	2.4358	0.0172
LNHF	0,22	0.98	0.9840	0.3282
LNY	0,96	0.14	6.6558	0.0000
R-square		0.93	J-test	13.56427
Adjusted R-square		0.93	Prob. (J).	0.258048

The R square of the regression was very high (Table 2), showing that the instrumentalized variables explain the model well. Except for ln Hydrated, all variables were statistically significant, at least 5%. Ethanol demand presents an expected variation of -1.83% when Ln Peh increases by 1%. The other interpretations are analogous.

The GMM minimizes a function representing the conditions of duly weighted moments. If these moment conditions are correct, they will average 0. It leads to a super-identification test using the minimized value of the function; this is the J test, which has the moment conditions correct when the null hypothesis. As shown in Table 3, the test was not rejected.

The rejection of the test represents moments that are not equal to zero; that is, one rejects the model because the condition of moments is not valid. That is, the instruments were not valid. What was not the case, the instruments were valid.

Table 3. Model 2 results from GMM regression

Variable	Coefficient	Std. Error	t-test	p-value
LNCEA	0,42	0.095	4.436274	0.0000
LNPEH	0.99	0.16	5.975518	0.0000
LNPGC	-1,68	0.35	4.699009	0.0014
LNIT	0,83	0.33	2.482698	0.0172
LNBLEND	2,27	0.23	9.721190	
LNAF	-1,49	0.33	-4.4325	0.3282
LNY	1,6	0.12	13.72629	0.0000
R-square		0.74	J-test	17.14020
Adjusted R-square		0.72	Prob. (J).	0.103796

The interpretation of results is similar to the previous one. All coefficients were statistically significant, and the J statistic was not rejected.

IV. LIMITATIONS

As noted by Randow et al. (2013) [12], although the available supply and transportation structure allows ethanol to be sold at all service stations in the country, Brazil's fuel market is relatively concentrated.

Given the concentration of production, the vast distance between most Brazilian states and the largest ethanol producers, the consequently high costs of transaction of ethanol produced, and the poor conditions of Brazilian roads, ethanol's price in most Brazilian states is very high. It exceeds 70% of the price of gasoline [12].

Sugarcane ethanol-producing states present different climatic conditions. Due to these different climatic conditions, the sugarcane harvest and consequently the idleness in ethanol production in these states is not homogeneous either.

While the interstate sugarcane harvest and the idle production of mills in the center-south region occur between November/December and March/April, in the northeastern region, they are seen between April/May and August/September [14].

We point out that ethanol prices and their consumption are not homogeneous because of the fuel production seasonality. However, the only way to consider such heterogeneity in a model is to observe each Brazilian state. Beyond that, these observations need to be monthly, which cannot yet be done due to limited information.

After consulting several databases about proxy data for consumer income, such as GDP, per capita GDP, average household income, disposable income, and energy consumption, although monthly data are available, data from each state or even municipality were not founded.

V. CONCLUSION

Two models for Brazilian ethanol demand were proposed. These models and their variables were based on the combination of antecedents re-search.

This work is the first that brought together different and relevant contributions in a single model and is the first that for each ethanol demand function, in the variable that refers to the vehicle fleet, only the vehicles that use that fuel was taken into consideration. The results returned by regression using the GMM method show that this estimate's models are generally significant.

It is concluded that more comprehensive and analytical modes of national ethanol demand would be possible. Both dependent and independent variables were based on observation for each Brazilian state instead of a single national observation. However, these advances are not possible due to data limitations.

VI. ACKNOWLEDGMENTS

This study was financed in part by the Fund for Scientific Initiation (FAPIC) from the Pontifical Catholic University of Campinas, Brazil.

VII. REFERENCES

[1] Castañeda-Ayarza, J.A. et al (2017). Final and B molasses for fuel ethanol production and some market implications, *Renewable and Sustainable Energy Reviews*, vol. 70, n. 1, p.1059-1065.

[2] EPE – Energy Research Company. ABCDEnergy: Energy and Eletric Matrix, acessed *on-line* in 20/06/2019, available at <*http://epe.gov.br*>.

[3] Silva, F.B. (2017). *Feasibility analysis of corn-based ethanol: a comparative study*, Undergraduated Thesis, Rio Verde University, Rio Verde, GO, Brazil.

[4] Miotello, W.; Hoffmann. W. A. M. (2010). Apontamentos de estudos sobre Ciência, Tecnologia & Sociedade, Pedro e João Editores, 431 p.

[5] Leite, R.C. Cortez. L. A. B. E. Ministério das Relações Exteriores (MRE), acessed *on-line* in 12/07/2019, available at <*http://www.agencia.cnptia.embrapa.br/Repositorio/etanol3_000g7gq2cz702wx5ok0wtedt3xdrmftk.pdf*>.

[6] EPE – Energy Research Company. Cenários de Oferta de Etanol e Demanda do Ciclo Otto, acessed *on-line* in 13/05/2019, available at <*http://epe.gov.br*>.

[7] Buonfiglio, A. Bajay, S. V. (1992). As demandas do álcool e da gasolina no Brasil, *Revista Brasileira de Energia*, vol. 2, n. 2.

[8] Tokgoz, S, Elobeid. A. E. (2006). Na analysis of the link betwenn Ethanol, Energy and Crop Markets, *CARD Working Papers*, vol. 06.

[9] Junior, L. J. C. et al (2010). Análise da demanda brasileira de cana-de-açúcar, etanol e açúcar, *Marinha em Revista*, vol. 2.

[10] Serigati, F. C. et al. *Impacto dos veículos flex-fuel sobre o mercado de combustíveis no Brasil*. In: XLVIII Congresso da SOBER, 2010, Campo Grande-MS. Anais do XLVIII Congresso da SOBER, 2010

[11] Freitas, L. C., Kaneko, S. (2011). Ethanol demand under the flex fuel technology regime in Brazil, *Energy Economics*, vol. 33, n. 6, p.1146-1154.

[12] Randow B. M. V. (2013). Os determinantes da oferta e da demanda de etanol nos estados brasileiros, *Revista Brasileira de Energia*, vol. 19, n. 2, p.287-319.

[13] Hayashi, F. (2000). *Econometrics*, Princeton University Press, New Jersey, USA.

[14] Banco Nacional do Desenvolvimento Econômico. Centro de Gestão e Estudos Estratégicos. Sugarcane-based bioethanol: energy for sustainable development. 1st ed. Rio de Janeiro: Banco Nacional de Desenvolvimento Econômico e Social, 2008. 300 p.

[15] Azevedo R. G. N. G. (2018). Análise econômica da produção de etanol pela integração do milho nas usinas flex e full no estado do Mato Grosso. Undergraduate thesis, Universidade Federal do Paraná, Brazil.

Identification of wind energy deployment determinants: Fuzzy cognitive map-based method

Sara Ghaboulian Zare
Industrial Engineering department,
Sadjad University of Technology,
Mashhad, Iran
s.ghaboolian25@gmail.com

M. Alipour
School of Engineering and Built Environment,
Griffith University,
Southport, QLD 4222
Australia
Mohammad.alipour@griffithuni.edu.au

R. Parsaei Tabar
Faculty of Economics and Administrative Sciences,
Ferdowsi University
Mashhad, Iran
Reza.parsa.d@gmail.com

Mehdi Hafezi
School of Engineering and Built Environment,
Griffith University,
Southport, QLD 4222 Australia
mehdi.hafezi@griffithuni.edu.au

Abstract

Wind energy is undoubtedly an essential generation source required to achieve a transformative renewable energy supply portfolio. However, long-term sustainable wind energy deployment faces various challenges due to various complex interconnected impediment factors. These inherent endogenous and exogenous uncertainties preclude obtaining an accurate future trend, which complicates the design of a good policy. This study seeks to critically identify all the involved parameters that contribute to the future of wind energy in Iran. In doing so, the research employs Fuzzy Cognitive Maps to analyse the relationship and role of each determined element within the system. The research outcome revealed 26 influential factors shaping the dynamics of the system in six main categories (PESTEL). The findings demonstrated that Iran's wind sector is predominated by economic and political drivers with strong interconnections. Five key concepts, including two economic, one legal, and two political, were ascertained that contribute to the system's stability.

Keywords: Wind Energy; Fuzzy Cognitive Map; Renewable Energies

I. INTRODUCTION

The roller-coaster of Iran's international policy is rolling fast fuelled by nuclear matters with big world powers participation. The resulting governmental changes over the past years have been dramatic in the country's energy sector. Privatization and economic reformations have postponed at the expense of these disruptions. The reliance on oil and gas exports is at 60% of total revenue and 80% of export earnings [1] Sufficient sources of renewable energies (REs) relying financially on fossil fuel exports have been more defenceless yet less prioritized sectors. In recent years, wind energy has consistently been one of RE's fastest-growing sources. Onshore and offshore wind energy globally account for more than 19.1% (or 622,408 MW) of the total electricity generation by REs, which is just a piece of the total capacity (1,263,914 GWH) [2]. Despite the significant production capacity (i.e., 39,420 GWH) in Iranian wind farms, the sector is vulnerable and overly exposed to the mentioned factors. Under the current inconsistent positions, the industry ability to achieve intentions set has remained an open question. To address this gap, the FCM approach investigates the characteristics, communications, and influences of concepts. The FCM-based framework is built in a participatory workshop and is bolstered throughout a survey. This study seeks to promote wind energy in Iran and enrich the burgeoning literature by using FCM in the RE sector to identify the most critical factors influencing the expansion of this industry and design strong strategic decisions.

II. Fuzzy Cognitive Mapping Procedure

FCM is a mapping and qualitative simulation method used to visualise dynamic multidimensional models by providing causation and modelling input values to simulate variations of a complicated system. For the researchers who use this method, the key considerations are the structural analysis and description of a system in terms of the causal system's components [3]. This method's results are accomplished by identification and development steps. FCM modelling can provide a cross-network of significant variables and components. The FCM technique determines the need to describe the entire system's scope and limits and quantify the relation between the system components [4]. The FCM analysis yield the following results in this study: (1) Identify and classify system variables into different categories, including economic, environment, legal, political, social, and technological. (2) Evaluating concepts based on their impact on other variables; (3) Draw the parameters' interrelationships according to the specialised knowledge.

Principally, cognitive maps are directed diagrams which have two major components: (1) variables (known as nodes) to describe the system components and behaviours, and (2) links (known as edges) to represent the links and interrelationships between the nodes. Links between the nodes are assigned weights to quantify the strength of their causal associations. The fuzzy logic added to cognitive maps demonstrates the degree of uncertainty involved in human thought. The addition of fuzzy numbers enables highlighting the level of influence and impact that concepts have on other concepts and the system, resulting in higher investigation efficiency. In an FCM, concepts take the fuzzy values in the range between (0,1) (or (-1,1) [5]) and weights of the arcs/interconnections belong to the

IEECP'21, July 29-30, 2021, Silicon Valley, San Francisco, CA – USA

DAI : https://sci-index.com/DAI/2021.99101/IEECP/14527164

interval (-1,1) [6]. This presents vague degrees of causality between hazy casual concepts. There are three different types of possible causalities (R_{ij}) between every pair of concepts C_i and C_j:

$R_{ij}>0$: positive causality, where C_i casually increases C_j,

$R_{ij}<0$: negative causality, where C_i casually decreases C_j, and

$R_{ij}=0$: no causality between C_i and C_j.

The logic of an FCM developed upon dynamic feedbacks refers to forward iterations. A mathematical formulation is designated to measure the values of the corresponding variables for each concept. Typically, an FCM of n concepts could be represented mathematically by a n state vector: (A) which gathers the concept's values and by a n×n weight matrix (W). Having assigned values A_i to the concepts C_i and weight among concepts, the FCM converges to an equilibrium point using below calculation rule:

Rescaled-Kosko interference:

$$A_i^{(s+1)} = f\left((2 \times A_i^s - 1) + \sum_{j=1, j\neq i}^{n} w_{ji} \times (2 \times A_j^s - 1)\right) \quad (1)$$

Kosko [7] has introduced an iterative equation which was further developed by Papageorgiou [8] to calculate the values of the concepts at each iteration (Eq. 1). This equation is known as rescaled-Kosko interference. Where s is the interaction index an every simulation step; $A_i^{(\kappa)}$represent the value of concept C_i at the simulation step s ; and w_{ij} illustrates the weight of the interconnection between concept C_i and concept C_j. The simulation process is initiated by assigning values to nodes to be transformed through the simulation process. Accordingly, fuzzy values are assigned to concepts, and, as a result, all concepts store specific numeric values. Necessarily, transformation functions are required to retain fuzzy causal edges between -1 to +1. Generally, there are four most commonly used transformation functions: hyperbolic tangent, trivalent, and linear Sigmoid [9]. Linear Sigmoid function (Eq. 2) was selected in this study as the transition function due to its reliability and accuracy [10].

Linear Sigmoid: $f(x) = \frac{1}{1+e^{-\lambda \times x}}$ (2).

III. Research Methodology

The FCM method was a progressive procedure with two main steps (Figure 1): (I) recognition of concepts, (II) FCM expansion and analysis. The first stage included a literature review, surveys, compiling the outcome of the surveys, and lastly, finalising the picked concepts. Upon defining the study's purpose and scope, a preliminary list of influential parameters in the wind sector was initially identified from the literature review. The overall trend of wind energy deployment refers to the electricity generated by turbines in onshore wind farms.

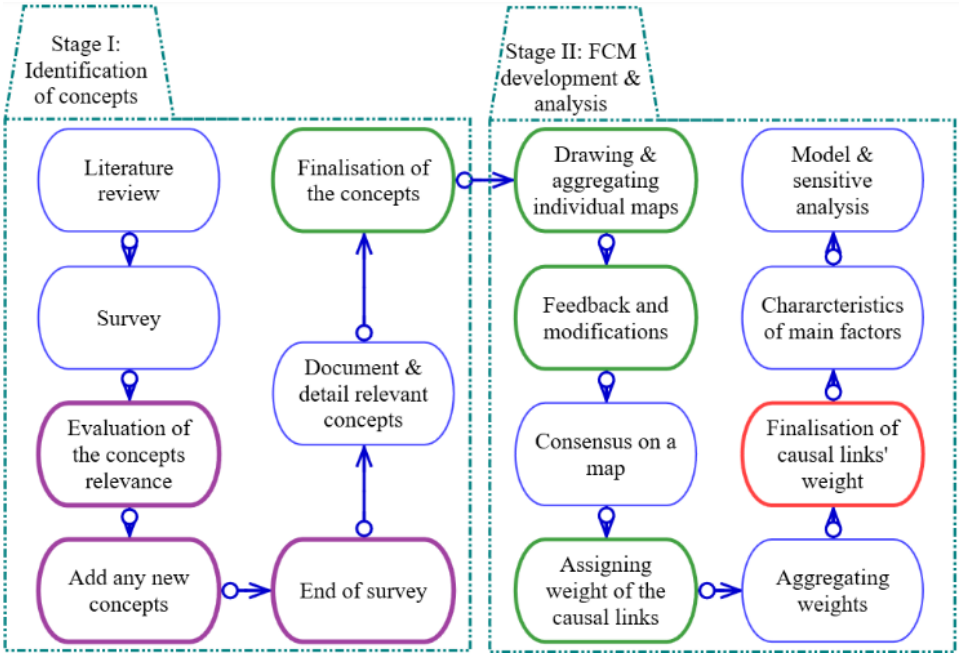

Figure 1.Proposed framework. Blue cells: Authors activity; Purple cells: Questionnaire surveys; Green cells: Expert engagements; Red cell: Expert group consultation.

The discovered variables were grouped into six main categories of the PESTEL framework [11]: political, economic, social, technological, environmental, and legal. These concepts were then given to respondents through a questionnaire survey to estimate their relevance. This categorisation strived at (1) improving the weights assigned, (2) helping the respondents of the questionnaires to find any lost concepts within each category, and (3) gaining some impressive generalised results. One hundred and forty postgraduate students in energy engineering and foresight from top-ranked universities of Iran were asked through email to evaluate the association level between 36 parameters and the object by a 7-point bipolar Likert scale and add any missed variable with its connection degree at the end of each main section. The response rate was 26.4% (37 replies). The collected values of each concept were accumulated. Those rated as 'moderate connection' or above were given to the experts in the last step of stage I (finalisation of the concepts).

A group of 15 expert stakeholders firstly were familiarised with the case and the FCMs. Next, the ascertained factors were distributed to the professionals for further estimation. The factors were discussed, modified, merged, and filtered to ultimately reach 26 concepts (72.2% of the initial concepts; Table 1).

Table 1. Main categories and concepts

Main factor	#	Concept
Economic	EC_1	Economic stagnation*
	EC_2	Electricity demand
	EC_3	Operating expenses
	EC_4	Electricity price
	EC_5	Investment risk
	EC_6	Return on investment
	EC_7	Budget provision
	EC_8	Exchange rate
	EC_9	Electricity export
	EC_{10}	Energy price liberalization
	EC_{11}	Private sector disengagement*
Environment	EN_1	Environmental regulations
	EN_2	Environmental concerns
Legal	LE_1	Market regulations
	LE_2	Government supports*
	LE_3	Guaranteed electricity purchase
	LE_4	Disruption of administrative
Political	PO_1	Unstable relations with the U.S.*
	PO_2	Unstable relations with EU
	PO_3	Sanctions*
	PO_4	Regional & domestic instability
Social	SO_1	Population growth
	SO_2	Public knowledge
Technological	TE_1	Technology maturity
	TE_2	Local technical development
	C_{26}	Deployment of wind energy

* Key concepts

After agreement on the concepts, they were requested to draw individual maps. The personal maps were assembled, and a preliminary cognitive map depicting the consensus viewpoint was presented. The aggregated map was declared to the panel to obtain feedback and possible changes to gain consensus on the map. Then stakeholders weighted the causal links conveniently using either (1) numerical coding using values within the range of -1 (most significant negative) and +1 (most significant positive) or (2) linguistic terms that indicate the identical quantitative values. The gathered assessments were combined by averaging the causal weights. The aggregated weights were used (the red cell in Figure 1) in an online meeting with the entire expert stakeholder group to finalise the links and arrive at an agreement on the final cognitive map. Finally, various aspects of the developed FCM were investigated, and the properties of the main categories and model structure were analysed, and the sensitivity of the key concepts was measured.

A. Revealing Key Concept

Narrowing the variables to the most central and uncertain items sets value on the analysis when there are too many parameters with a minor role in the system's dynamics. In identifying key concepts, the experts' viewpoints are consolidated into the model's characteristics. Three indices obtained from the FCM highlight these characteristics: in-degree, outdegree, and centrality. These indexes were measured to define the concept's role in the model. The first two indicate the weight of the inbound and outbound links. They are recognised as the driver (influential or active) and receiver (dependent or passive). Centrality measures the overall importance of a concept to the causal flow on the cognitive map by calculating the absolute sum of interactions between concepts [7]. Concepts with the highest centrality after experts' approval were elected as key concepts. More information and characteristics of the model are presented as following.

IV. RESULTS

The main factors features, model structure, and sensitivity analysis of the key concepts are presented in the following sections.

A. Analysis of the PESTEL Factors

The main factors outline particular features when studying the aggregate value of their corresponding concepts. While they were not employed in the FCM simulations, they do provide dominant penetrations toward two overall trends: First, the central aspects of the main factors (Figure 2), and second, the macro connection that exist between them (Table 2. Twenty-eight interlinkages between the PESTEL factors.).When self-loops are included, social and environmental factors have the most negligible impact on the system, while legal, economic, and political categories are the most influential with the highest centrality (6.4, 6.39 6.13, respectively) (Figure 2). The technological aspect will play a limited role (2.65) in the growing wind energy, as expected. The political factor is more of a transmitter than a receiver (5.03 > 1.10), in contrast to the economic factor's passive role. When exogenous dynamics are excluded, wind energy expansion is dominated by legal and technological categories, which have the highest centrality (5.1 and 4.8, respectively). As the least active and most influential factors (0.05 and 3.98), political parameters fall to the third level. A large proportion of economic factors are self-loops (52%) as they become more receivers than transmitters (2.11 > 1.23), and social and environmental categories are the two lowest rated with the lowest centrality.

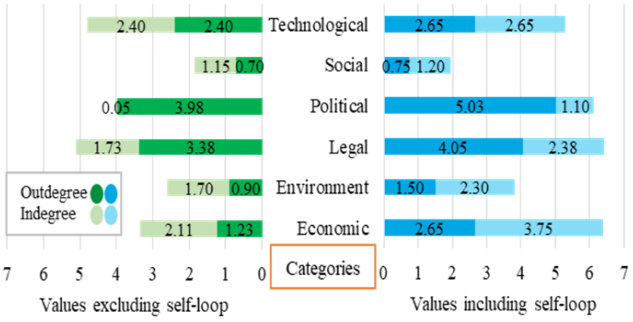

Figure 2. Outdegree and in-degree values of the PESTEL categories, including and excluding self-loops.

Concepts within all groups associate with others, meaning there is no solely dependent category (Table 2). As the most active group, the economic factor is a significant receiver concerning the political and legal considerations (12.1 and 9.5, respectively). This indicates that political and legal variations powerfully shape the financial determinants. The political factor influences two other variations, environment and legal, while playing a minor role as a receiver from the economic factor (0.2). The legal factor does not direct the political elements, but it changes technological and social variables. The synergy between the environment category and four others designates its almost active role in the system.

Table 2. Twenty-eight interlinkages between the PESTEL factors.

Categories	Economic	Environment	Legal	Political	Social	Technological
Economic	15.3	1.6	4.4	0.20	0.5	2.8
Environment	0.1	1.2	0.1		1.0	0.6
Legal	9.5	0.4	2.6		0.7	1.4
Political	12.1	0.8	1.9	4.20		
Social	0.6	0.6	0.2		0.1	
Technological	3.5		0.3		0.1	0.5

B. Model Structure

The FCM model (Figure 3) involves 26 concepts and is arranged into six PESTEL categories. Around 42% of concepts refer to the economic group, while the legal, social, and technological factors possess the lowest share (8%). There are 185 linkages among concepts, including three positive self-loops in the economic and social categories. Environmental and social indicators do have a direct influence on goal whilst nine economic concepts, three political and legal, and two technological concepts directly impact the goal. Deployment of wind energy only transforms electricity exports directly. Experts opted for five key concepts amongst seven parameters with the highest centralities that significantly impact the system. Two come from the economic category (EC1 and EC11), one is legal (LE2), and the other two are political (PO1 and PO3). Within the FCM model, private sector disengagement has the most control over other concepts (7.7), whereas government support and sanctions are strongly influenced by other determinants (9.2 and 7.5, respectively). The highest centrality and outdegree among all concepts belong to the government support that proves the government's fundamental influence on wind energy spread. Unstable relations with the U.S. was preferred by the specialists for their significant influence on the system (7.30), although budget provision and investment risk had higher centrality (8.1 and 7.8). All concept types are ordinary (no being isolated concept), which means they are in relation to at least one concept in the network.

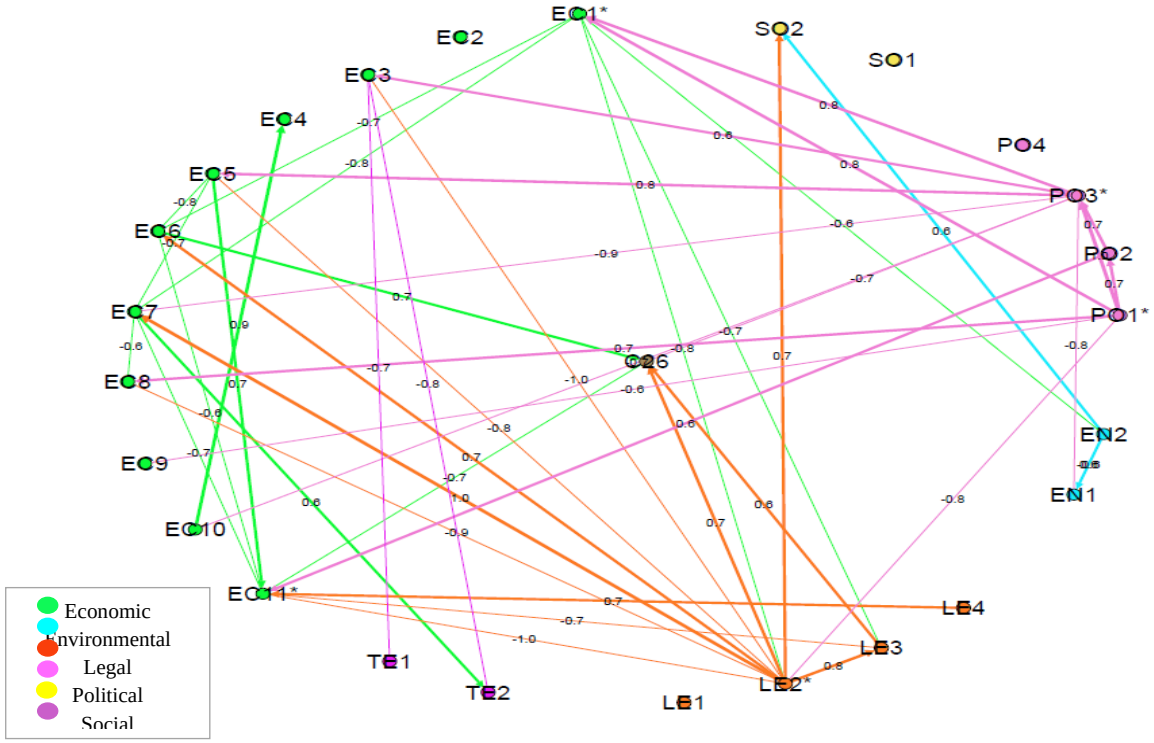

Figure 3. The finalised FCM visualised by Gephi, illustrating only nodes with the weights >= 0.5 (+/-).

Three useful guides promote the perception of the performance of the network and its concepts. Closeness centrality calculates the distances from a vertex to the other concepts [12]. The eigenvector centrality measures the impact of a concept in a network as the extension of the degree centrality, and harmonic centrality assesses the average distance of a concept to other connected or unconnected nodes. As Figure 4 demonstrates, the network connections indicate that the concepts' harmonic and closeness centrality are approximately equal. It confirms the connectivity of the network. Economic stagnation (EC_1), which has the greatest harmonic and closeness centrality, is actively correlated to other concepts while its eigen centrality is lower than 0.1. The highest eigen centrality level for private sector disengagement (EC_{11}) displays its meaningful impression on the system. High closeness and harmonic centrality for both unstable relations with the U.S. and sanctions (PO_1 and PO_3) explain their dynamic cooperation with the system's other components.

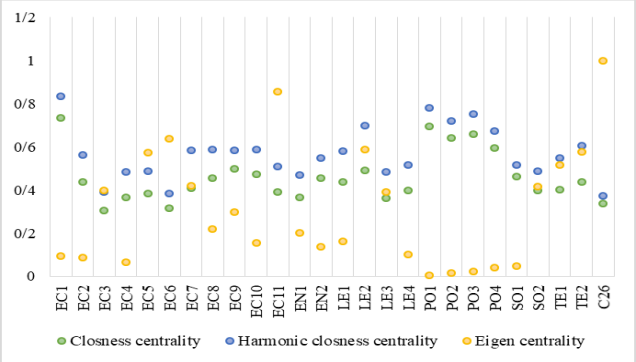

Figure 4. Analysis of the concepts' performance using three network indices.

C. Sensitivity Analysis

The sensitivity of the model is checked here to assess the consequences of a key concept's modifications on the system and goal. For this purpose, the model is run to create the initial steady state. Its results of no intervention with a starting vector at one were reached after less than 25 iterations. Key concepts sensitivity was then derived by analogising the relative variations between the obtained steady state and a new one.

To better appreciate the concepts' respond to the changes, the impact of each key variable alteration on the system in isolation is considered (Figure 5). The highest qualification level is observed when sanctions, unstable relations with the U.S., and economic stagnation values are clamped to 0. A reduction in economic stagnation generates a sizeable relative increase in the return on investment and operating expenses (+46% and -34%, respectively). Sanctions and unstable relations with the U.S. shift the value of 14 and 18 variables (> 5 %), respectively. Such key concepts adversely influence EC_{11} and EC_5 by almost identical values. These changes are nearly correlated to the return on investment rise and the economic stagnation fall. The lack of government support leads to a rise in private sector disengagement and investment risk of about 9%. When clamping private sector disengagement to 0, concepts profoundly stabilized except for budget provision and local technical development. Private sector disengagement is also most stimulated by EC_1, PO_1, and PO_3 at around -39%, -36%, and -40%, respectively.

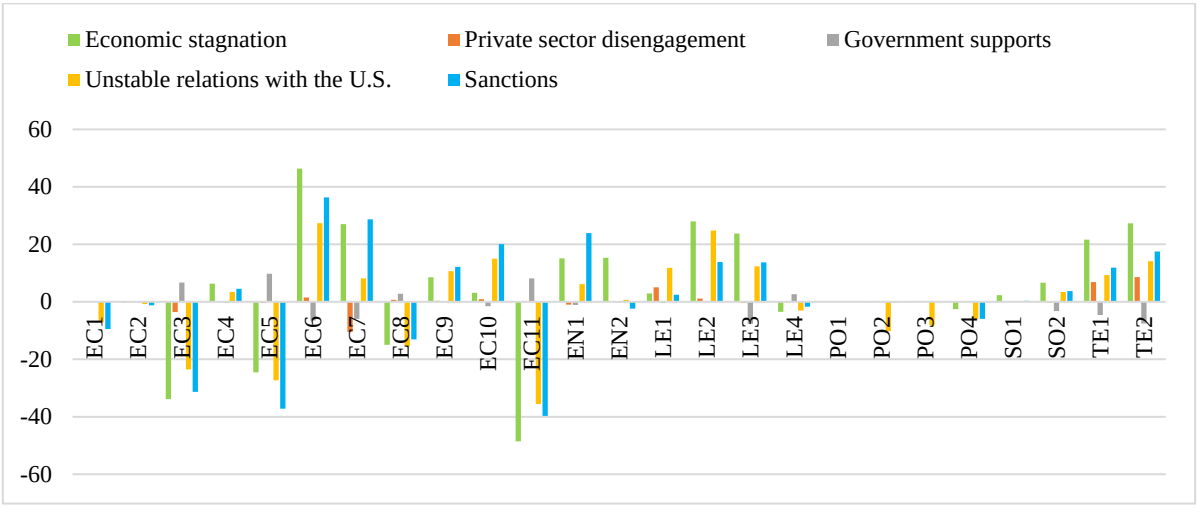

Figure 5. The comparison between steady-state and change rate of 25 concepts by clamping each key concept to 0.

The target variable's fluctuation is compared to its steady-state value when the key concepts reach 0 (Table 3). Wind energy usage is reduced to zero with a 90% reduction in government support, and its significant performance in the system is marked. On the contrary, the general orientation shows that sanctions and recession control the dynamics of the main concept by providing an ideal value of +68%. The slight positive effect of private sector disengagement improves the wind energy situation to + 33%, and promotion in relations with the U.S. will expand wind energy by 55% in the country.

Table 3. The sensitivity of the goal (C26) by clamping each key concept from 1 to 0.

Key concepts	Value of goal (C26) when a key concept is clamped from 1 to 0										
	1	0.9	0.8	0.7	0.6	0.5	0.4	0.3	0.2	0.1	0
Economic stagnation	-0.09	0.02	0.13	0.24	0.33	0.42	0.50	0.56	0.61	0.64	0.68
private sector disengagement	-0.10	-0.06	-0.01	0.04	0.08	0.13	0.17	0.21	0.25	0.29	0.33
Government supports	0.65	0.61	0.56	0.50	0.42	0.33	0.22	0.10	-0.03	-0.15	-0.26
Unstable relations with the U.S.	-0.26	-0.20	-0.13	-0.05	0.03	0.12	0.22	0.31	0.40	0.49	0.55
Sanctions	-0.08	0.02	0.13	0.23	0.33	0.41	0.49	0.55	0.60	0.64	0.67

V. DISCUSSION and CONCLUSION

An FCM method was applied to investigate the specifications and predictable future of the wind sector in Iran. Thirty-six concepts that may influence was derived from the literature review to develop the map. The recognised concepts relationship was examined in an online survey before being confirmed by specialists' opinions. Twenty-six concepts were finalised and divided into the six PESTEL categories. Results determine that the country's wind energy development is dominated by economic and legal concepts with robust interconnections. Conversely, social and environmental concepts are the least authoritative operators. Five key factors are two political (sanctions, unstable relations with the U.S.) and one economic (economic stagnation) concepts that dominate the system's maturity.

In selecting the FCM technique, diverse criteria were regarded: (1) handling a complicated issue at a strategic level that was intermingled with macro determinants, (2) dealing with a non-linear problem, (3) modelling a proper long-term issue with high uncertainty, and (4) delivering meaningful outcomes without widespread data. Energy systems' investigation was administered through a broad spectrum of mathematical and statistical approaches [13, 14]. Absolute mathematical methods cannot obtain uncertainties and are more beneficial for short-term evaluations [15]. Energy system models are proper for long-term assessments but only when there are large data from several sectors. These methods concentrate on the final foresight results using quantified parameters while their causality and evolvements are not into account. Simulation modelling procedures address the system's feedback dynamics and have been well studied in the energy domain [14, 16-18]. FCM is helpful in scientific data shortage, and the concepts are holistic and unintelligent. The simple nature of this method is easily user-friendly for politicians, but it is powerful for magnifying to obtain high abstraction of complex issues. Although the result of its simulation is useful for understanding and insight into the system, the diversity of views of mental models provides a sufficient future trend (s). As an emerging tool in this field, further research can demonstrate the applicability of FCM.

This research did not investigate the next decision-making process that could effectively handle and counterbalance the uncertainties. Finding strong beneficial policies will not be an easy assignment as the majority of the uncertainties are exogenous. The scenarios facing the Iranian wind industry concerning various economic, political and social conditions that were identified as the most important indicators have not been studied in this paper, and can be discussed as an important issue in future research to familiarise politicians with the possible conditions of this industry. What politicians of the RE sector can realistically discover and pursue hidden connections and gaps between economic and legal determinants. In doing so, it is essential to focus on long-term contracts and legal obligations that guarantee financial benefits to private businesses. Another solution to the natural uncertainty that minimizes political change's engagement is transforming the cash flow by finding alternative and more sustainable case sources.

Finally, two observations can be obtained from the developed model. The two-stage process to recognise the concepts aimed to identify all aspects related to the main issue. However, the concentration on macro behaviours at the top layer inevitably neglected possible micro-and meso-level connections and their interlinkages with the economic and private sectors. This was inevitable to maintain the same level of investigation for all parameters. Future studies can outline more sub-maps that consider these missing links and combine them into a multi-layer map correlating micro-, meso- and macro-level analyses. Future work could also focus more attention on the critical exogenous economical-political elements.

VI. REFERENCES

[1] Alipour M, Hafezi R, Ervural B, Kaviani MA, Kabak Ö. Long-term policy evaluation: Application of a new robust decision framework for Iran's energy exports security. Energy. 2018;157:914-31.

[2] IRENA. Available from: https://www.irena.org/Statistics/View-Data-by-Topic/Capacity-and-Generation/Statistics-Time-Series. 2019.

[3] Papageorgiou E, Kontogianni A. Using Fuzzy Cognitive Mapping in Environmental Decision Making and Management: A Methodological Primer and an Application. 2012.

[4] Felix G, Nápoles G, Falcon R, Froelich W, Vanhoof K, Bello R. A review on methods and software for fuzzy cognitive maps. Artificial Intelligence Review. 2019;52:1707-37.

[5] Groumpos PP. Fuzzy Cognitive Maps: Basic Theories and Their Application to Complex Systems. 2010. p. 1-22.

[6] Mourhir A, Papageorgiou EI, Kokkinos K, Rachidi T. Exploring Precision Farming Scenarios Using Fuzzy Cognitive Maps. Sustainability. 2017;9.

[7] Kosko B. Fuzzy cognitive maps. International journal of man-machine studies. 1986;24:65-75.

[8] Papageorgiou EI. A new methodology for decisions in medical informatics using fuzzy cognitive maps based on fuzzy rule-extraction techniques. Applied Soft Computing. 2011;11:500-13.

[9] Hafezi M, Giffin AL, Alipour M, Sahin O, Stewart RA. Mapping long-term coral reef ecosystems regime shifts: A small island developing state case study. Science of The Total Environment. 2020;716:137024.

[10] Papageorgiou EI, Poczęta K, Laspidou C. Application of Fuzzy Cognitive Maps to water demand prediction. 2015 IEEE International Conference on Fuzzy Systems (FUZZ-IEEE). p. 1-8.

[11] Song J, Sun Y, Jin L. PESTEL analysis of the development of the waste-to-energy incineration industry in China. Renewable and Sustainable Energy Reviews. 2017;80:276-89.

[12] Rochat Y. Closeness Centrality Extended to Unconnected Graphs: the Harmonic Centrality Index. 2009.

[13] Jebaraj S, Iniyan S. A review of energy models. Renewable and sustainable energy reviews. 2006;10:281-311.

[14] Swan LG, Ugursal VI. Modeling of end-use energy consumption in the residential sector: A review of modeling techniques. Renewable and sustainable energy reviews. 2009;13:1819-35.

[15] Amer M, Daim TU, Jetter A. A review of scenario planning. Futures. 2013;46:23-40.

[16] Ahmed A, Khalid M. A review on the selected applications of forecasting models in renewable power systems. Renewable and Sustainable Energy Reviews. 2019;100:9-21.

[17] Baur L, Uriona M. Diffusion of photovoltaic technology in Germany: A sustainable success or an illusion driven by guaranteed feed-in tariffs? Energy. 2018;150:289-98.

[18] Zhao J, Mazhari E, Celik N, Son Y-J. Hybrid agent-based simulation for policy evaluation of solar power generation systems. Simulation Modelling Practice and Theory. 2011;19:2189-205.

Research on Mud Loss Prevention and Control for Deep Wells with Complex Pressure System in Mingebrak Oilfield, Uzbekistan

1st Wanjun Li
Engineering Technology R&D Company Limited
lChina National Petroleum Corporation
Beijing, China
liwanjundri@cnpc.com.cn

2nd Qi Liu
Engineering Technology R&D Company Limited
China National Petroleum Corporation
Beijing, China
liuqidr@cnpc.com.cn

3rd Huifeng Liu
Engineering Technology R&D Company Limited
China National Petroleum Corporation
Beijing, China
lhfdri@cnpc.com.cn

4th Jun Yan
China National Oil and Gas Exploration and Development Company Ltd
China National Petroleum Corporation
Beijing, China
yanjun@cnpcint.com

5th Yong Wang
China National Oil and Gas Exploration and Development Company Ltd
China National Petroleum Corporation
Beijing, China
wangyong@cnpcint.com

6th Shujiu Feng
China National Oil and Gas Exploration and Development Company Ltd
China National Petroleum Corporation
Beijing, China
Fengshujiu@cnpcint.com

7th He Ba
Engineering Technology R&D Company Limited
China National Petroleum Corporation
Beijing, China
bahedr@cnpc.com.cn

8th Yue Xiao
Engineering Technology R&D Company Limited
China National Petroleum Corporation
Beijing, China
xiaoyuedr@cnpc.com.cn

Abstract

Reservoirs at Mingebrak Basin in Uzbekistan are characterized by big burial depth (5200-6500m), high temperature (150-200℃), high pressure (pressure coefficient 2.08-2.41), high salt content (220000mg/l), and high H2S content (5~6%) in the formation fluid. The Musgothic formation is especially complex because it contains different pressure systems. Leakage and blowout are easy to occur during well drilling and the average drilling period is 732 days. The data of well drilling history have been analyzed and the causes of the long drilling period have been detected. The results showed that the drilling problems in the Musgothic formation was the main cause of the non-drilling time because leakage and overflow occurred frequently and time was consumed in dealing with leakage and overflow. Three methods have been taken to conquer the drilling problems: finding out the setting positions and improving the wellbore structure; selecting the organic salt drilling fluid and optimizing the formula of it through experiments; developing different lost circulation materials to bridge different types of leakage. Leakage prevention and control technologies have been worked out through analysis and experiments. Firstly, the mudstone at the top of Musgothic and the high-pressure formation at bottom of Musgothic were taken as setting positions respectively and the wellbore structure was improved from three-hole structure to four-hole or five-hole structure. Secondly, an organic salt drilling fluid formula with temperature resistance of 180℃, salt contamination resistance of 30%NaCl and 1% gypsum, and 93.48% recycle rate was developed. Thirdly, three types of loss control materials: return loss control materials, fracture loss control materials, and permeable leakage control materials were developed to deal with different types of formation leakage. The three methods, five-hole wellbore structure, high temperature organic salt drilling fluid and 840 m3 loss control materials have been successfully used in an exploration well M15 in Mingebrak Oilfield, and the drilling period was only 390 days, only about a half of the average drilling period in this area. The study of the mud loss prevention and control technologies of this paper is significant for reducing the drilling period in Mingebrak Oilfield, Uzbekistan. Their successful application in well M15 set a good example for safe and fast drilling of deep wells in this oilfield and the technologies will be popularized for application in other wells of this area.

Keywords: HT/HP; High Salt; High H2S; Deep Well; Mud Losses

IEECP'21, July 29-30, 2021, Silicon Valley, San Francisco, CA – USA

DAI : https://sci-index.com/DAI/2021.99101/IEECP/14527263

I. INTRODUCTION

Central Asia is one of the five strategic cooperation zones of PetroChina Overseas. The oil and gas reservoirs in this area usually have deep burial, high bottom hole temperature, high pressure, high acid gas content, and high salt content, which puts forward higher requirements for drilling engineering[1-3]. Among them, the Mingebrak structure of Uzbekistan is one of the most representative blocks, and the pressure system in the regional interval is complicated. The drilling fluid exhibits a narrow density window[4-6]. When the density is high, it will cause serious lost circulation[7-8], and when the density is low, high-pressure brine gushing will occur[9-10]. In the past, 15 wells were drilled in this area with an average drilling period of 732 days. 9 wells experienced serious lost circulation during the drilling process, 3 wells experienced blowout accidents, and 7 wells were scrapped due to leakage and other reasons. Leak prevention and control during the drilling process has become the key technology to achieve the successful completion of complex deep wells and the exploration and development of such oil and gas blocks[11-13].

II. Analysis of the Causes of Frequent Drilling Loss

Mingebrak Oilfield has developed relatively complete strata, with Quaternary, Neogene, Paleogene, and Cretaceous in sequence from top to bottom. The stratigraphic sequence is shown in Table 1.

Table 1. The stratigraphic sequence division table of typical wells in Mingebrake block

Stratigraphic division			Section m		Complex display of past drilling
Pleistocene		Q	0-345		/
Pliocene	Bucktree	N_2	345-3440		M10 has serious leakage in the 940-2800m well section; M14 has leakage in 3200m
Miocene	Mascot	N_1	BPC	3440-5097	The M13 pipe string broke at 3900m, accompanied by leakage. Salt water intrusion occurred when M222 drilled to 3450m, then gas intrusion and leakage occurred
			KKC	5097-5533	M10 and M222 were accompanied by severe leakage and formation fluid intrusion during drilling in this interval. M9 has strong oil and water invasion in this interval. M5 leaks at 5237 meters at the bottom of the well
Oligocene	Sumsar	E_3		5533-5655	M9 experienced water and salt invasion at 5180-5505m
	Rishtan			5655-5717	M13 expands and shrinks in diameter of gypsum rock at 5700 and 5900m
Eocene	Turkistan	E_2		5717-5766	M6 is attacked by hydrogen sulfide at 5897-5901m
	Alai			5766-5844	M13 contains a lot of hydrogen sulfide gas when conduct open hole test at 5710-5735m
Paleocene	Buhar	E_1		5844-5918	

Based on the statistics of the historical data of drilling wells in Mingebrak Oilfield, it is found that the loss of drilling occurred concentratedly in the Bucktree and Mascot stages of the Neogene. The specific data are shown in Table 2.

The depth range from 345-3440m is Bucktree Stage, and the lithology is mainly conglomerate, sandstone, and siltstone. The thin layer of conglomerate is loosely cemented and is prone to lost circulation.

The depth range from 3440-5533m is the Mascot stage. The upper part is the Bredrosov Formation, with a depth from 3440-5097m. The lithology is mainly sandstone and siltstone, which is characterized by strong homogeneity and high permeability, and mud loss is prone to occur during drilling. The depth of 5097-5533m is the Kopicenokrasni Formation, which is dominated by multiple sets of reservoirs caprock sandstone and multiple sets of limestone reservoirs. The range of its pressure coefficient fluctuates greatly, a large section of salt-gypsum layer is developed, and it contains a high-pressure salt water layer with a pressure coefficient of up to 2.30, which is prone to complicated situations such as lost circulation and kick.

Table 2. Statistics of leakage data in Mingbulak block

Well No.	Leakage times	Typical leakage interval	Depth (m)	Leakage rate (m^3/h)	Leakage (m^3)
M3	28	Mascot	5413	38.1	342.9
M5	25	Bucktree	3255	16.8	33.4
		Mascot	5370-5372	44.5	449.34
M5	33	Bucktree	2999	9.4	70.9
M7	14	Mascot	5313	31.7	261.68
M9	24	Mascot	5251	34.3	193.7
M10	16	Mascot	5315	42.9	362.2
M12	15	Mascot	5228-5265	30	288.3
M14	19	Bucktree	3276-3651	8.9	251
		Mascot	5273-5283	18.2	177.4
M222	25	Mascot	4714	12.5	99.2
		Mascot	5355-5370	35.8	298.6

Historical data statistics show common characteristics: the Mascot stage is prone to leakage, and it shows the characteristics of large leakage and fast leakage. The data of past leakage is shown in Figure 1. The main reason is that the gypsum rock layer developed in the Mascot, the abnormally high-pressure layer and the atmospheric layer coexist, the formation pressure system is complicated, and the on-site drilling operation is difficult to control[14], resulting in multiple losses.

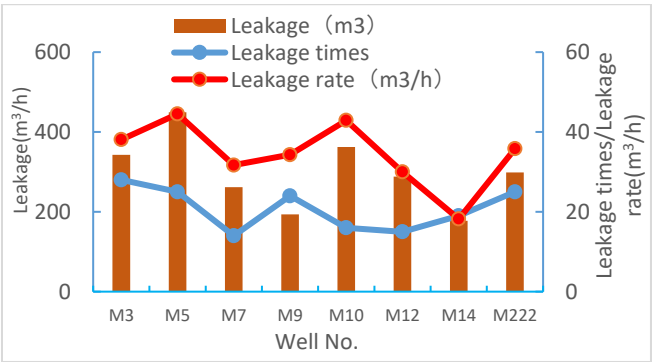

Figure 1. Statistics of Leakage Data of Mascot in Mingebrak Block.

III. Optimized design of anti-leakage well structure

Analyze the structural complexity of the Minggebulak block, draw formation pressure maps, and combine the problems encountered in the past drilling process to summarize the risks and difficulties of drilling through the four sets of strata from top to bottom.

Combining with drilling difficulties, the well structure is designed as a 4th spud structure, with 5th spud structure as an alternative. The purpose is to solidify the Quaternary shallow conglomerate layer, the middle and lower Bucktree and the high mudstone layer on the top of the Mascot, the Mascot high-pressure reservoir and the Paleogene high H_2S layer.

IV. Optimization of lost circulation drilling fluid system

Mingebrake block is characterized by deep burial, high temperature and high pressure and large fluctuation of gypsum pressure[15-16]. Under the condition of high temperature and high salinity, due to high solid content and less free water, with the accumulation of solid content or mixing with plugging materials, the viscosity of drilling fluid increases, the rheological property decreases, and the annular pressure loss increases, which is easy to induce lost circulation.

Organic salt drilling fluid technology has advantages in high temperature resistance, good fluidity, strong inhibition, good lubricity, and strong anti-pollution ability, which is suitable for drilling in formations prone to leakage, especially for keeping low viscosity and shear at high temperature.

A. Optimization of Organic Salt System

Organic salt drilling fluid system is mainly composed of fluid loss reducer, plugging and anti-sloughing agent, inhibiting lubricant, organic salt water soluble weighting agent, and the most important is compounded with strong inhibiting and high-density organic salt water solution.

The density of organic salt drilling fluid can be adjusted from 1.10 g /cm^3 to 1.52g/cm^3 through the optimization of weighting agent and ratio of drilling fluid, as shown in Table 3. In addition, by adding activated barite and iron ore powder into the drilling fluid formulation, the drilling fluid density is increased to 2.5g/cm^3, which meets the requirements of high-pressure formation drilling with pressure coefficient of 2.41 in Mingebrak oilfield.

Through optimization, the final formula was obtained as follows: clear water + 0.3% sodium carbonate + 3% polyol anti sloughing agent + 1.5% static shear strength improver # 1 + 5% fluid loss additive # 1 + 4% polyol resin + 3% fluid loss additive # 2 + 3% asphalt powder + 1% inhibition lubricant + 50% organic salt water soluble weighting agent # 1 + 30% organic salt water soluble weighting agent # 2 + activated barite + iron ore powder.

Table 3. Relationship between Weighting Agent Dosage and Drilling Fluid Density

B / A	10	20	30	40	50	60	70	80	90
10	1.10	1.14	1.18	1.21	1.23	1.26	1.29	1.32	1.34
20	1.15	1.18	1.21	1.24	1.26	1.29	1.32	1.34	1.34
30	1.19	1.22	1.25	1.27	1.30	1.32	1.34	1.36	1.36
40	1.24	1.26	1.28	1.30	1.33	1.35	1.37	1.39	1.40
50	1.27	1.29	1.32	1.35	1.37	1.38	1.40	1.40	1.40
60	1.30	1.32	1.35	1.37	1.38	1.40	1.40	/	/
70	1.32	1.35	1.37	1.39	1.41	1.42	1.42	/	/
80	1.37	1.38	1.40	1.43	1.44	1.44	1.44	/	/
90	1.39	1.42	1.43	1.44	1.45	1.45	1.46	/	/
100	1.42	1.44	1.45	1.46	1.48	1.48	/		//
110	1.44	1.46	1.46	1.49	1.49	/	/	/	/
120	1.47	1.48	1.49	1.50	/	/	/	/	/
130	1.49	1.50	1.50	1.51	/	/	/	/	/
140	1.51	1.52	1.52	/	/		/	/	/

Note: A-Weighting Agent 1(%), B-Weighting Agent 2(%).

B. Evaluation of organic salt drilling fluid system

1) High Temperature Resistance Evaluation Test

180 ℃ high temperature evaluation experiment was carried out for the optimized organic salt system and the results show that the formula has good high temperature stability and rheology (Table 4.)

Table 4. Experimental Data of Drilling Fluid Thermal Rolling at 180 ℃

Formula	T ℃	ρ g/cm^3	AV	PV	YP Pa	Gel Pa/Pa	FL	HTHP$_{FL}$
			MPa.s				ml	
After heating	180/24h	2.30	81.5	76	5.5	1.0/1.5	2.0	8
After heating	180/48h	2.30	86	81	5	1.0/3.5	0	9.2
After heating	180/72h	2.30	63	61	2	1.0/2.5	2.4	16

2) Evaluation of Drilling Fluid Inhibition

Drilling fluid cuttings recovery experiment: take the formation outcrop cuttings, use clean water, Bantu mud, bentonite slurry and composite salt mud to do the recovery experiment. The recovery rates of clean water, composite salt mud and organic salt mud are 7.04%, 71.04% and 93.48% respectively.

The calcareous soil is weighed and compacted. After soaking in organic salt mud for 8 hours, the expansion is only 0.253 mm. Compared with the expansion of 4.676 mm after soaking in clean water for 8 hours, the linear expansion is reduced by 94.59%. Thus, the organic salt drilling fluid shows good inhibition.

V. Research and development of plugging agent

Based on the analysis results of formation coring data, the argillaceous sandstone and fine sandstone in the lost circulation section have loose cementation, developed fractures, mainly filled with salt paste, some fractures have a width of 1cm, and most of them extend vertically and obliquely [17-18].

According to the amount and speed of leakage, the average particle size of plugging material is usually 1 / 3-1 / 2 of the diameter of pore throat. The plugging material is assembled and filled in the fracture to block the large channel formed by the fracture, so as to reduce the drilling fluid leakage.

Through the core laboratory test and plugging agent evaluation experiment[19-20], the plugging agent formula for the large fracture and large channel leakage, the fracture leakage at the interface of mudstone and sandstone, and the permeability leakage in the formation with micro fracture and pore development are obtained. The formula and applicable conditions are shown in Table 5, which meet the requirements of Mingebrak area Block site plugging requirements.

Table 5. Formula Data of Plugging Agent

Formula	Applicable leakage type	Leakage characteristics
Formula of lost circulation plugging agent Water +3-5% Asphalt +2-4%QS-2+0.3-0.5%XC+BaSO4+3-5%TP-2+2-3%ZSQD-98+3-5%ZYD+4-6% Vermiculite +4-6% Mica +2-3% Leite plugging agent +2-3%GDJ-V+1-2% Walnut shell	Loss circulation caused by large cracks and large channels	No drilling fluid returned from wellhead
Formula of plugging agent for fractured leakage Water +3-5% Asphalt +2-3%QS-2+0.3-0.5%XC+$BaSO_4$+5-8%TP-2+2-3%ZSQD-98+3-5% Vermiculite +2-3% Mica +3-5%GDJ-V+3-5% Sawdust	the interface of mud sandstone, and the filling (sodium chloride, etc.) in the fracture is dissolved, and the leakage point is formed	The initial leakage is large, then gradually constant to 15-30m^3/h
Formula of permeable plugging agent Water +4-7% Asphalt +3-5%QS-2+0.3-0.5%XC+$BaSO_4$+5-8%TP-2+2-3%ZSQD-98+3-5%DF-1+3-5% Sawdust	Microfracture and pore formation	The leakage rate is generally 2-10m^3/h

VI. Field Application and Effect Evaluation

Well M15 is a key exploration well in Mingebrak oilfield (design depth is 5918m), with The of long fractures distribution length and complex formation pressure system. In addition, leakage and overflow are easy to occur in drilling process, indicating high well control risk and operation difficulties.

In view of the above risk prediction, a series of deep well leakage prevention and control technology concepts was applied to the drilling design of well M15: the fifth-spud wellbore structure was used to seal the necessary points, the organic salt drilling fluid system was selected as the main drilling fluid of the reservoir section, and the plugging agent was chosen on site to ensure the smooth completion of the well.

According to the post drilling evaluation, the fifth spud wellbore structure of the well is well matched with the actual drilling (Figure 2), and all the necessary sealing points of the formation are sealed from top to bottom. The organic salt drilling fluid system has a wide range of density, which balances the formation pressure in the whole drilling process, ensures the wellbore safety and protects the oil and gas reservoir to the maximum extent, and plays a certain role in preventing leakage and blowout.

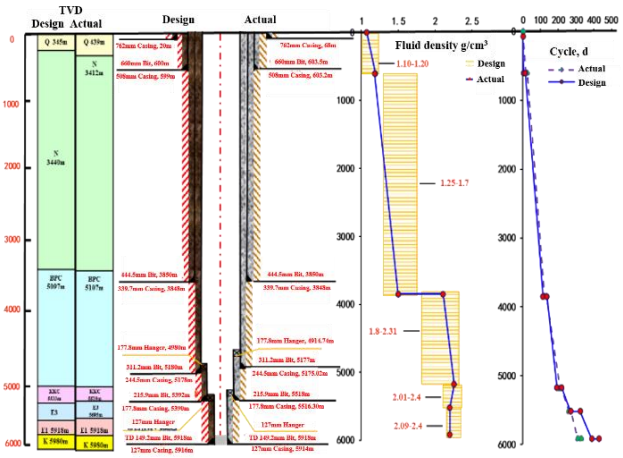

Figure 2. Comparison between actual drilling parameters and design parameters of M15 well.

Although the wellbore structure and drilling fluid have played a role in the prevention and control of the lost circulation, the lost circulation still occurred when the well was drilled in the fourth to fifth spudding section of Musgotian stage, with 34 lost circulation layers and 2800m^3 of drilling fluid.

The site accurately judges the type of leakage by the factors such as leakage rate and leakage amount, and selects the appropriate plugging agent for different types of leakage. Through plugging while drilling combined with bridge plug composite plugging technology, 53 times of plugging agent injection are implemented, and a total of 836.1m^3 of each type of plugging agent is put into the well, which improves the success rate of plugging and ensures the smooth completion of drilling construction.

The drilling cycle of M15 well is 390 days and the completion cycle is 430 days. Compared with the average completion cycle of 15 wells in the early stage of 732 days, it saves 302 days and increases the drilling speed by 41%.

VII. Conclusions

(1) The lack of understanding of formation pressure system in Mingebrake structure leads to the poor adaptability of well structure design and drilling fluid system, resulting in frequent leakage and overflow during drilling, which is one of the main reasons for the extension of drilling cycle.

(2) The optimization of wellbore structure effectively reduces the drilling difficulty of different pressure systems in the process of complex deep well drilling, and reduces the risk of vicious blowout accident in the formation with complex pressure system of Musgotian stage.

(3) Organic salt drilling fluid has the advantages of good inhibition, low solid content, strong anti-pollution ability and easy rheology

control, which has gradually become the preferred drilling fluid formula in Mingebrak oilfield.

(4) A variety of lost circulation agents are developed for different types of lost circulation mechanism, such as lost circulation, fracture and permeability, which effectively improve the adaptability of lost circulation in different formations and lithology of deep wells, and become an effective measure of lost circulation control.

(5) The successful application of leakage prevention technology in complex deep wells solves the drilling problems such as leakage and overflow caused by complex drilling fluid pressure system in Mingebrake block, reduces well control risk and ensures the success rate of drilling.

VIII. REFERENCES

[1] Wang Wenqiang, Xue Weiqiang, Zhan Ning, Chen Jun and Zhang Zhongliang. Drilling Technologyof Ming 15 Ultra-deep Well[J]. Petrochemical Industry Technology,2019,26(08):45+50.

[2] Li Kexiang. Practical well completion engineering[M].Petroleum Industry Press,2002.12.

[3] Ma Hongyan, Zheng Bangxian, Chen Jingwang, Guo Jinsong, Song Xiaojian and Li Heqing. Optimized, safe and fast drilling technologies used in the ultra deep and high temperature wells in Yangshuiwu buried hill[J].OIL Drilling & Production Technoly,2020,42(05):573-577.

[4] Wang Meidong. A Search of Tarim oilfield, North Tarim Block Drilling Speed [D].Supervisor: Zhu Liang;Wang Fuhe.Yangtze University,2020.

[5] Liu Yaxin. Research on casing leakage prevention technology under narrow safety density window in ultra-deep Tarim well[D]. Supervisor ：Guo Xiaoyang Southwest Petroleum University,2019.

[6] Wang Zhongliang,Wang Wenqiang,Xue Weiqiang,Tang Jiang and Li Gaogang.Application of narrow density window drilling technology in well Ming15[J].Chemical Enterprise Management,2019,(24):173-174.

[7] Guo Yuhua, Li Laihong, Li Shiwen, Cai Dongsheng and Ma Hongliang. Present situation and development trend of drilling fluid technology[J]. Petrochemical Industry Technology,2019,26(10):251-252.

[8] Lin Yongxue, Wang Weiji and Jin Junbin. Key Drilling Fluid Technology in the Ultra Deep Sectionof Well Ying-1 in the Shunbei Oil and Gas Field[J].Petroleum Drilling Techniques,2019,47(03):113-120.

[9] Chang Shengli and Wang Wenqiang. Development and application of compound organic salt test solution[J].Chemical Engineering and Equipment,2020,(10):164-165.

[10] Kang Yili, Wang Kaicheng, Xu Chengyuan, You Lijun, Wang Limin, Li Ning and Li Jiaxue. High temperature aging property evaluation of lost circulation materials in deep and litra-deep well drilling[J].ACTA Petrolei Sinica,2019,40(02):215-223.

[11] Peng Zhenbin. Trends in the development of loss control technology[J] Petroleum drilling technology, 1989,17(2): 65-69.

[12] He Sai. The Mechanism of Lost Circulation and Plugging Technology for Deep Fractured Reservoir [J]. Petrochemical Industry Technology,2020,27(02):28-29.

[13] Duan Guangliang. Current situation, challenge, demand and development trend of drilling fluid technology [J]. Chemical Engineering&Equipment,2017,(08):235-237.

[14] Dong Meng. Research and application of drilling speed raising measures in salt paste layer of Kelasu structure [D]. Supervisor : Fan Xiangyu;Yu Kebin.Southwest Petroleum University,2017.

[15] Gai Jing'an,Chang Shengli,Zhang Zhongliang,Liu Guiming, Fang Zheng and Tang Jian. Pollution and treatment of CO_3~(2-) and HCO~(3-) ions in well Ming 15, Uzbekistan [J]. Western Exploration Project,2018,30(08):64-66+70.

[16] Gai Jing'an, Li Xicheng, Xue Weiqiang, Lyu Xiaoping, Xiao Bin, Zhao Chen and Liu Xiumei. Drilling Fluid Technology for Well Ming-15 in Mingbulak Oilfield, Uzbekistan[J].Drilling Fluid&Completion Fluid,2019,36(02):202-207.

[17] Chang Shengli , Wang Hongzhi , Chen Jun , Gai Jing'an Liang Zhiyin and Gao Bowen.Fractured Leakage Plugging While Drilling and Bridge Plug Pressure Plugging Technology in Ming 15 Well [J]. Petrochemical Industry Technology,2019,26(10):75+80.

[18] Gai Jingan , Wang Zhenyu , Wang Duoxia , Lv Xiaoping , Hui Yushe and Zhao Chen. Leakage prevention and plugging technology of Ming 15 well in Wuguomingmingbulak block[J]. Petrochemical Industry Technology,2019,26(08):106+105.

[19] Wu Xiubin,Ma Wenying and Wang Fuyin. Research and application of the composite high strength plugging technology[J]. Drilling Fluid & Completion Fluid, 2002,19(6):101-103.

[20] Guo Baoli and Yuan Menglei. The novel lost circulation simulator[J]. Drilling Fluid & Completion Fluid, 2003,20(4): 47-51.

Optical-Electronic Matrix System for the monitoring of nocturnal migration of birds

Alexandra Sinelschikova
St.Petersburg State University
Zoological Institute of the RAS
St.Petersburg, Russia
Sinelsch@mail.ru

Mikhael Vorotkov
Pulkovo Observatory
St.Petersburg, Russia
biser_gao@mail.ru

Victor Bulyuk
Biological Station "Rybachy"
Zoological Institute of the RAS
St.Petersburg, Russia
victor.bulyuk@mail.ru

Abstract

This paper is dedicated to a new technique for advances in the study of the main parameters of flight and monitoring of nocturnal migration of birds. The Optical-Electronic Matrix System allows us to detect and record aerial targets in the night sky of a size greater than 5 cm and at an altitude of 100 to 1000 meters a.g.l. The principal design features are: (1) An optical device for receiving images of flying targets on three high-sensitivity CCD matrices when illuminated by infrared light from searchlight beams; and (2) Instantaneous parallactic computation enabling the distance from the device to target to be accurately measured, and sequential images of each target to be recorded to a computer. The device has been tested on songbirds during seasonal nocturnal migration and provides accurate image details of important target flight parameters including altitude, linear size (wingspan and body length), the direction of flight – track, the orientation of the body axis – heading, groundspeed, airspeed, wing-beat frequency, number of beats in each series of wing-beats, duration of the pause between series of wing-beats, and type of flight trajectory (straight or curved). Special attention was given to one of the major difficulties in research of bird migration – the potential for the identification of individual species of birds flying in the night sky by the combination of the recorded flight parameters. There are also potential practical applications for aviation bird-strike at night as well as the remote monitoring of insects, bats, and other targets of natural and artificial origin.

Keywords: optical-electronic device, monitoring, nocturnal migration, birds

1. INTRODUCTION

Ecological monitoring of bird migration involves both diurnal and nocturnal field observations. More than half of the species nesting in North America and Europe migrate nocturnally [1] and are difficult to record in the dark. They form from 63 to 85% of the total (day plus night) stream of passage [2]. Migration at night is typical for many waterfowl, waders, and especially passerine birds with a size range of 10 - 50 cm [3]. They fly at altitudes of 1-3 km and airspeeds of 5-20m/s [4,5]. The task is to solve the problem of detection and identification of the small size targets moving in darkness at a considerable distance from the observer and to capture their visual images. Monitoring of migration is not only a quantitative estimation of the stream of birds but also their identification and collective flight parameters. Because the flow of migrants usually consists of dozens of species that may exhibit different migratory directions, altitudes, flight abilities, and migratory strategies it is an advantage to be able to distinguish particular species or groups of species that are similar in their taxonomy and ecology. The study of the nocturnal migration of birds under natural conditions is limited by the possibilities of the methods used for observation and identification of targets in the sky at different altitudes. There are numerous current techniques for the detection of birds flying at night and observing their flight characteristics. Ornithologists have traditionally used the following methods: moon-watching, i.e. observing by telescope birds crossing the moon disc [6], the infrared thermal camera which generates an image of the warm part of the body of a warm-blooded animal flying at considerably low altitude [7], weather surveillance radars which are excellent for broad front bird survey and migration forecasts in real-time [8] and tracking pencil-beam radars [5]. These methods are applied to gather information on the numbers, flight directions, speeds, and altitudes of birds aloft. But they do not provide real images of the flying object and solve the main problem of nocturnal migration research - species identification. Visualization of the target, the shape of its silhouette, and measurements are important for bird species identification and discrimination between birds, large insects, and bats, all of which may be numerous in some regions [7]. Presented here are the results of five years of joint experimental research work of ornithologists and engineers, culminating in the design and testing of a new Optical-Electronic Matrix System (OEMS) for the detection and recording of nocturnal aerial targets. The images and the significant parameters obtainable using this equipment we believe will contribute a significant step forward in bird migration research.

2. REQUIREMENTS FOR THE DEVICE

The following requirements for further advances in this field of biological research have influenced our design during the development of this device:

I. To create a clear image of a flying target to ensure adequate accuracy of measurement of its linear size.

II. To collect and store statistically representative data.

III. To monitor continuously the migratory activity through a series of complete nights at frequent sample dates throughout the migration seasons.

IEECP'21, July 29-30, 2021, Silicon Valley, San Francisco, CA – USA

DAI : *https://sci-index.com/DAI/2021.99101/IEECP/14527269*

IV. To catalog the following main flight parameters for each recorded bird: a) altitude; b) linear size (body length and wingspan); c) direction of flight (track); d) orientation of the body axis (heading); e) ground speed and airspeed; f) wing-beat frequency and its variation; g) the number of beats in each series of wing-beats; h) duration of the pause between each series of wing-beats; and i) type of flight trajectory.

The principal system design used to meet these requirements is a parallactic computation of the distance from the device to the target. This enables subsequent calculation of the target linear size from a known distance and its angular dimensions; the ground speed from the angular displacement for a known time interval; and the dynamic characteristics of the target and its orientation in space from the pattern of trajectory with a sequence of the instantaneous images. The main concern was to overcome the contradiction between the need for a high angular resolution to ensure the required accuracy of measurements on the one hand and the need for a wide field of vision on the other to achieve a statistically representative sample of targets and to consider trajectory type.

3. DESIGN SOLUTIONS FOR THE DEVICE

The device consists of two main components: the recording unit (electronic-optical system) and the illumination system, separated from each other at the locating distance of 5 m.

3.1 The Recording Unit.

The image of an object, under the artificial illumination of infrared light, is received on three high-sensitivity CCD matrices. The optical system consists of three channels with parallel optical axes; the twined channels are separated from the third one at the locating distance by 1 meter (see Figure 1). Each channel includes a high-quality objective lens, a heating anti-condensation system, an image precise focusing unit, and a CCD matrix camera. The objective lenses have different focal distances. In this project we used three lenses with the following parameters: F (focal length)=50 mm (6°FoV), S (focal length/aperture)=1.7; F=86 mm (3.5°), S=1.5; F=120 mm (2.5°), S=1.8. Their different combinations determine the angular resolution and field of vision of the channels. The scales of the fields of vision differ by a factor of 1.5–2.5. Their centers are accurately superimposed by the laser beam. During the exposure time (0.3–1.5 seconds) a target usually passes an angular distance of 0.25–5 degrees depending on its altitude. One channel is equipped with an obturator (rotating) shutter which breaks the track of an object into 10–50 instantaneous and sequential images within one frame. The obturator shutter is servo-controlled by an independent computer which allows the setting of an accurate speed of rotation and required time interval between separate images with a duration of exposure of 18–25milliseconds. The speed of rotation is optimized and governed on the assumption that the most probable speed of a bird at the moment of observation varies between 5 and 20 m/sec, with an average of about 10 m/s [5]. Modern CCD matrix cameras allow us to use an electronic shutter and program a high frame rate (75-100 f/s) and set a short exposure (we used 5 milliseconds). The electronic shutter has several advantages. It is convenient to operate and makes it possible to generate up to 50 silhouettes of the bird on one saved image with an exposure of 1sec. Program subtraction of noise and background flare provides high contrast of a series of sequential silhouettes generated on one image. The channel with a wide field of vision works without a shutter and forms the image as a target track of variable width and brightness. Besides the frame, each file saves information on the moment of time of exposure on the matrix, exposure sequence, and other parameters of the obturator, which are required for subsequent processing. Average volume per night is about 50,000 files with a total volume of 25 Gb. To provide uninterrupted monitoring, the system works continuously throughout the night. Further data analyses are performed after the raw data collection.

3.2 The Illumination System.

The flying targets were illuminated from the ground by a narrow faint beam from searchlights. Nocturnal migrants can be attracted by white light which changes their natural behavior [9]. Our previous investigation showed that such attraction is typical of nights with rain, drizzle, high air humidity, and lower cloud cover [10]. We rejected the use of a white searchlight beam and switched to infrared (IR) light panels instead, composed of IR light-emitting diodes (in total 600 x 3W LEDs, with 5° FoV) with a wavelength of 805 nm. This wavelength is invisible to birds [11]. Adjustment to the searchlights is a critical technique that requires preliminary computer simulation depending on the current weather conditions. To improve this procedure an additional adjusting searchlight was used which formed a reference grid in the night sky using three needle-shaped beams. After adjusting this grid, white lights were switched off in order not to attract birds.

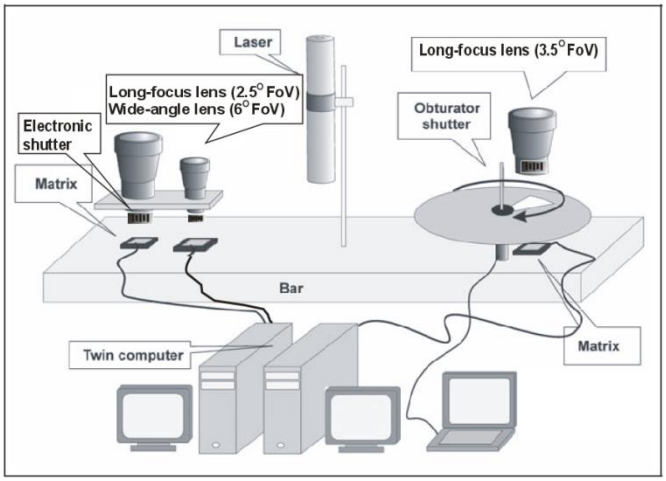

Figure 1. The Recording Unit. The objective lenses of 3.5°/ 6° and 2.5° are separated from each other at the locating distance by 1 m.

4. COMPUTATION OF FLIGHT PARAMETERS

4.1 Altitude of flight

The altitude of flight was calculated by a parallactic computation of the distance from the OEMS to the target simultaneous observed from two points separated from each other at a fixed distance. A locating distance of 1 m provides an error of altitude measurement of about ±50 m. The results of our observations have shown that small objects (birds of wingspan up to 20 cm) are recorded regularly at the range of 650 m and relatively large objects (birds with a wingspan of 30 cm and more) – at 800-1000 m. The illumination system of the OEMS allows the recording of targets within an altitudinal range of 100–1000 m. Birds flying higher have low-quality silhouettes and maximum error of estimation of their size is over 30%–40%. In the lowlands of Europe and North America, passerine birds may fly at altitudes up to 2000–3000 m a.g.l. during their seasonal migrations. Nevertheless, the bulk of passerines (70%–80%) fly below 1000 m [4,7].

4.2 Linear size of birds

No technical system is currently available which allows measurement of the real size of birds flying at night. The linear

size, i.e. wingspan and body length, is measured on the basis of angular size and distance to the bird (see Figure 2). The margin of error in the measurements obtained from high-quality silhouettes (about 80% of received images) is 3%–10% depending on the altitude of the bird.

4.3 Flight direction (track) and Heading (axis of body)

Tracks and headings often may not coincide especially when the bird is subjected to wind displacement and tries to compensate for lateral drift. The clear image of the silhouette for the first time made it possible to measure an angle between the track direction and the heading. The accuracy of measurement was about 3°. We were surprised to find that in most of the birds (75%) the headings and track directions deviated by more than 5°. Long tracks (>30 m) were recorded in 37% of birds. A straight shape trajectory over the whole visible length of track was recorded in 80% of tracks.

4.4 Ground speed and air speed

Ground speed can be calculated by two methods: 1. From the duration of the exposure of one frame via any channel. In each frame during exposure time a bird passes a certain path. The exposure duration is known. The path is calculated relative to the altitude of the bird. The ground speed of a bird is calculated on basis of the length of its path and duration of exposure. 2. In some cases the beginning or the end of track are cut off by the edge of the screen. This is typical for the tracks of low flying birds. In these cases we can calculate the ground speed by the frame rate of an electronic shutter or frequency of rotation of an obturator shutter on the channels with fragmented tracks. The frame rate (or frequency of rotation of an obturator shutter) is known and the time interval between the sequential silhouettes of a bird can be calculated. Like in previous case knowing the altitude of the bird we easily can calculate the average ground speed for the fragmented track.

The vector of ground speed of a bird (direction of this vector is the track direction; its length is the ground speed value) is a sum of the vector of airspeed (direction of this vector is heading; its length is the airspeed) and the vector of wind (wind direction; wind velocity). Using wind profiling data at the altitude of a bird's flight there is no problem in calculating its airspeed.

4.5 Wing beat pattern (WBP) and its characteristics

WBP assumes the following characteristics: 1 Actual wing beat frequency within each cycle of beats (beats/sec) (in passerine birds the cycles are usually separated by pauses); 2 Effective wing beat frequency [12] – an average frequency during the whole track, including cycles of beats and pauses; 3 Pause duration between the cycles of beats (sec); 4 Proportion of pauses (%) during the whole track; 5. A number of beats in each cycle. Most of these characteristics can be calculated only for long tracks (at least 20 m) with several wing beat cycles and pauses present. The proportion of such tracks in our monitoring was about 60%.

The OEMS was tested and applied for data collecting at the Curonian Spit of the Baltic Sea at the Rybachy Biological Station (55°05´ N, 20°44´ E) during 2013 - 2019. Species identification was possible only in a few species by the silhouette, linear size, wing-beat pattern, and phenology. But accurate classification of the bird order was possible for 95% of images. In total, over 4000 birds were recorded and 477 of them were identified as the Song Thrushes (*Turdus philomelos*), the common nocturnal migrants in the Baltic region [13].

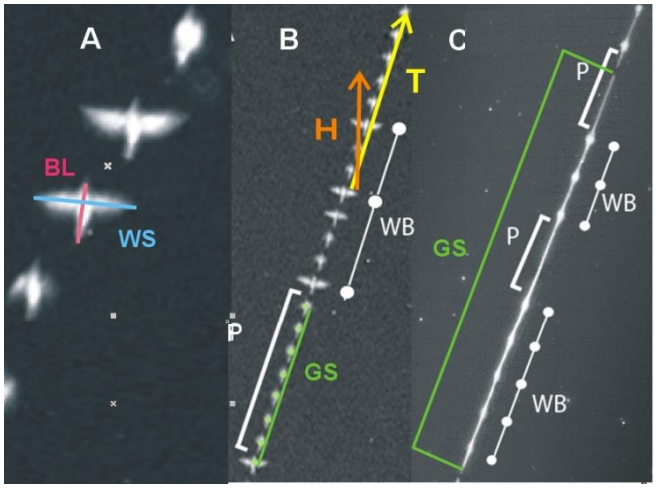

Figure 3. The images of the same bird identified as a Song Thrushes captured on three channels simultaneously. A) objective lens with the field of vision 2.5°; B) objective lens with the field of vision 3.5°;and C) objective lens with the field of vision 6°. Parameters: altitude-270m agl, track direction (T)-29°, heading direction (H)-11°, wingspan (WS)-37cm, body length(BL)-23cm, ground speed(GS)-14.9m/s, pause duration (P)-0.23s, wing beat frequency (WB)-9.9beats/s, 3-4 flaps in one cycle of beats.

5. ACKNOWLEDGMENTS

The authors are grateful to anonymous referees and the editor for critical comments. We also thank Lyndon Roberts for the language review. This study was financially supported by the Russian Foundation for Basic Research (no. 19-44-390002p-a) and Zoological Institute RAS (registered research project No AAAA-A19-119021190073-8).

REFERENCES

[1] W. K. Taylor, "Analysis of Ovenbirds killed in central Florida," Bird Banding, vol. 43, No. 1, 1972, pp. 15-19.

[2] M. Zalakevicius, S. Svazas, V. Stanevicius, and G. Vaitkus, "Bird Migration and Wintering in Lithuania," vol. 2: A Monograph, Inst. of Ecol., Vilnius, 1995.

[3] G. R. Martin, "Understanding bird collisions with man-made objects: a sensory ecology approach," Ibis, vol. 153, 2011, pp. 239–254.

[4] B. Bruderer, D. Peter, and F. Korner-Nievergelt, "Vertical distribution of bird migration between the Baltic Sea and the Sahara," J. Ornithology, vol. 159, 2018, pp. 315–336.

[5] B. Bruderer and A. Bold, " Flight characteristic of birds: I. radar measurements of speed," Ibis, vol. 143, 2001, pp. 178–204.

[6] F. Liechti, "Calibrating the moon-watching method – chances and limits," Avian Ecol. and Behav., vol. 7, 2001, pp. 27-40.

[7] S.A.Jr. Gauthreaux and J.W. Livingston, "Monitoring bird migration with a fixed-beam radar and a thermal-imaging camera," J. Field Ornithology, vol. 77, No. 3, 2006, pp. 319–328.

[8] P. B. Newcombe, C. Nilsson, T.-Y. Lin, K. Winner, G. Bernstein, S. Maji, D. Sheldon, A. Farnsworth, and K. G. Horton, "Migratory flight on the Pacific Flyway: strategies and tendencies of wind drift compensation," Biol. Lett.15 20190383. 2019 http://doi.org/10.1098/rsbl.2019.0383

[9] S. R. Loss, T. Will, and P. P. Marra, "Direct human-caused mortality of birds: improving quantification of magnitude and assessment of population impact," Front. Ecol. Environ., vol. 10, 2012, pp. 357-364.

[10] C. V. Bolshakov, V. N Bulyuk, A. Sinelschikova, and M. Vorotkov, "Influence of the vertical light beam on numbers and flight trajectories of night-migrating songbirds," Avian Ecol. Behav., vol. 24, 2013, pp. 35–49.

[11] N. S. Hart, "The visual ecology of avian photoreceptors," Prog. Retin. Eye Res., vol. 20, No. 5, 2001, pp. 675–703.

[12] B. Bruderer, D. Peter, A. Boldt, and F. Liechti, "Wing-beat characteristics of birds recorded with tracking radar and cine camera," Ibis, vol. 152, No. 2, 2010, pp. 272–291.

[13] A. Sinelschikova, M. Vorotkov, V. Bulyuk, and C. Bolshakov, "Compensation for wind drift in the nocturnally migrating Song Thrushes in relation to altitude and wind," Behavioural Processes, vol. 177, 2020, 104154, ttps://doi.org/10.1016/j.beproc.2020.104154.

In situ FTIR studies for photocatalytic reduction of CO_2 by TiO_2 nanotubes

H.-H. Chang
[1]*Department of Environmental Engineering*
National Cheng Kung University
Tainan 70101, Taiwan
wanghp@mail.ncku.edu.tw

H.-Y. Chang
[1]*Department of Environmental Engineering*
National Cheng Kung University
Tainan 70101, Taiwan
wanghp@mail.ncku.edu.tw

H.-P. Wang
[1]*Department of Environmental Engineering*
National Cheng Kung University
Tainan 70101, Taiwan
wanghp@mail.ncku.edu.tw

Abstract

A better understanding of CO_2 adsorption on the one-dimensional TiO_2 nanotube (TiNT) is of great importance for improving its photocatalytic reduction ability. In this work, adsorption and photocatalytic reduction of CO_2 on the TiNT was studied by *in situ* FTIR. The IR absorbance features at 1303 and 1393 cm^{-1} are associated with carbonate species, e.g., bidentate carbonate on the TiNT. Complete desorption of CO_2 from the TiNTs may occur at T>418 K. The *in situ* FTIR studies indicate bidentate carbonate and carboxylate species on the TiNTs, which may conduct the surface reactions enhanced by UV/Vis light to yield of low carbon fuels or chemicals.

Keywords: *In situ FTIR, photocatalytic reduction of CO_2, TiO_2 nanotubes*

IEECP'21, July 29-30, 2021, Silicon Valley, San Francisco, CA – USA

DAI : ***https://sci-index.com/DAI/2021.99101/IEECP/14548371***

Photocatalytic Reduction of CO_2-to-C_1 by Dual Photoelectrode Reactor

H.-Y. Chang
[1]*Department of Environmental Engineering*
National Cheng Kung University
Tainan 70101, Taiwan
wanghp@mail.ncku.edu.tw

L.-W. Wei
[1]*Department of Environmental Engineering*
National Cheng Kung University
Tainan 70101, Taiwan
wanghp@mail.ncku.edu.tw

H.-P. Wang
[1]*Department of Environmental Engineering*
National Cheng Kung University
Tainan 70101, Taiwan
wanghp@mail.ncku.edu.tw

Abstract

Global warming has been proved to be caused by the excessive emissions of CO_2 from the usage of fossil fuels. Therefore, promoting carbon mitigation strategies and energy transition are of increasing importance. Reduction of CO_2 to C_1 fuels by solar energy like artificial photosynthesis is thus environmentally attractive and close the carbon cycle. There are still major challenges such as low conversion efficiency and high recombination of electron-holes during photocatalytic reduction of CO_2. We have developed novel perovskite quantum dots (PQDs) encapsulated within metal organic frameworks (MOFs) (PQD@MOF) composite for dual photoelectrodes to proceed the high-efficiency photocatalytic reduction of CO_2. By the PQD@MOF under visible-light irradiation, about 500 μmol C_1/mgCat/h were obtained. It is apparent that the novel PQD@MOF photocatalysts are chemically feasible for solar-driven CO_2 reduction to C_1 fuels.

Keywords: *photocatalytic reduction of CO_2, perovskite, metal organic frameworks, reactor design*

IEECP'21, July 29-30, 2021, Silicon Valley, San Francisco, CA – USA

DAI : *https://sci-index.com/DAI/2021.99101/IEECP/14546700*

Electrokinetic Remediation of Arsenic in a Gold Tailing Studied by *in situ* EXAFS

1st C.Y. Peng
Department of Water Resources and Environmental Engineering
Tamkang University
Taipei, Taiwan
cypeng@gms.tku.edu.tw

2nd P.-A. Chen
Department of Environmental Engineering
National Cheng Kung University
Tainan, Taiwan
a1005231@gmail.com

3rd P.-C. Chang*
Department of Environmental Engineering
National Cheng Kung University
Tainan, Taiwan
wanghp@ncku.edu.tw

4th H. Paul Wang*
Department of Environmental Engineering
National Cheng Kung University
Tainan, Taiwan
wanghp@ncku.edu.tw

Abstract

The tailings of arsenic-containing gold ores have caused a serious environmental problem in the north of Taiwan. Electrokinetic remediation (EKR) is one of the feasible methods for *in situ* soil decontamination. Although EKR has been proven to be very feasible in laboratory- and bench-scale experiments and small-scale field tests, an understanding of the complex arsenic involved in the EKR is of great importance. Thus, the main objective of this work was to track the fate of arsenic in the gold tailing by *in situ* EXAFS spectroscopy. By XRD, it is clear that As_2O_3 is the main arsenic compound in the gold tailing. After EKR, the arsenic concentration near the anode is greater than that near the cathode in the arsenic-containing tailing. The first derivative feature of XANES spectra appeared at 11870 eV indicates the existence of As_2O_3 that is the main arsenic compound in the arsenic-containing gold tailing. Prolonging the EKR contact time to 90 min, the bond distances of As-O (1st shell) and As-As (2nd shell) are increased slightly, that is attributed to the perturbation by the electric field. Note that the dissolved $H_2AsO_3^-$ is accumulated near the anode. The amount of As_2O_3 (dissolved as $H_2AsO_3^-$) in the tailing is increased significantly after EKR for 60 min. However, when the EKR time was prolonged to 90 minutes, the amount of $H_2AsO_3^-$ is decreased, suggesting the migration of arsenic to the anode and eventually accumulated near the anode. This work illustrates the usefulness of EXAFS and XANES for revealing speciation of arsenic embedded in the complex matrix of a gold tailing in the EKR process.

Keywords: *Arsenic, electrokinetic remediation, in situ EXAFS, XANES, gold tailing.*

IEECP'21, July 29-30, 2021, Silicon Valley, San Francisco, CA – USA

DAI : *https://sci-index.com/DAI/2021.99101/IEECP/14546727*

Capacitive deionization of salt water using thin stainless steel and graphite collectors in the FdCDI process

1st C.-H. Wu
Department of Environmental Engineering
National Cheng Kung University
Tainan, Taiwan
chk587423@yahoo.com.tw

2nd P.-A. Chen
Department of Environmental Engineering
National Cheng Kung University
Tainan, Taiwan
a1005231@gmail.com

3rd P.-C. Chang
Department of Environmental Engineering
National Cheng Kung University
Tainan, Taiwan
jack19680312@gmail.com

4th H. Paul Wang*
Department of Environmental Engineering
National Cheng Kung University
Tainan, Taiwan
wanghp@ncku.edu.tw

Abstract

While the global water resource is very limited, the rapid population growth and urbanization have caused an added demand for fresh water. The developing capacitive deionization (CDI) method has gained extensive attention mainly due to its high energy-efficiency, environmental friendly, and low cost for desalination. To improve the benefits of flow-electrode CDI (FCDI) and the simplicity of the traditional flow-by CDI methods, a novel fluidized CDI (FdCDI) has been developed**.** In this work, a feasible study for FdCDI of saltwater using the thin stainless steel (SS) as the current collectors was investigated. The less resistance graphite current collectors for the FdCDI electrodes without activated carbon (AC) coating have a greater salt adsorption capacity than that of the SS ones. Moreover, the graphite current collectors possess a nearly ideal capacitor behavior and allow the ions in the solution to be more efficiently electrosorbed by the electric double layer of flow electrodes. Nevertheless, the cyclic voltammetry (CV) curves of the AC-coated SS and graphite electrodes have a near rectangle shape for the charge/discharge process, which can be regarded as supercapacitors at a scan rate of 5-25 mV/s. The shape of the curve is similar, indicating that less resistance causes the ions to transport fast in the microporous electrodes. The thin SS become a better current collector simply due to the fact of the more feed rates (by +85%) can be achieved for FdCDI.

Keywords: *Capacitive deionization, stainless steel, graphite, fluidized capacitive deionization.*

IEECP'21, July 29-30, 2021, Silicon Valley, San Francisco, CA – USA

DAI : *https://sci-index.com/DAI/2021.99101/IEECP/14546745*

Enhanced extraction of PAHs from fly ashes with variable dielectric-constant supercritical fluids

1st K.-A. Hsueh
Department of Environmental Engineering
National Cheng Kung University
Tainan, Taiwan
iomikilove@gmail.com

2nd Y.-C. Tsai
Department of Environmental Engineering
National Cheng Kung University
Tainan, Taiwan
jack1998870308@gmail.com

3rd T.-E. Wu
Department of Environmental Engineering
National Cheng Kung University
Tainan, Taiwan
emily2738tw@gmail.com

4th I.-H. Chen
Department of Environmental Engineering
National Cheng Kung University
Tainan, Taiwan
hermosa2336@gmail.com

5th Y.-J. Tuan
Department of Environmental Engineering
National Cheng Kung University
Tainan, Taiwan
eugenet@ncku.edu.tw

6th H.-P. Wang
Department of Environmental Engineering
National Cheng Kung University
Tainan, Taiwan
wanghp@ncku.edu.tw

Abstract

There is a lack of quality data on the levels of polycyclic aromatic hydrocarbons (PAHs) in incineration fly ashes primarily due to the conventional Soxhlet extraction fails by the recovery of PAHs during the process. To better understand the hindered PAH finger-print patterns in the fly ashes, extractions with supercritical fluids (SCFs) such as dichloromethane (SDCM) (T_c=333 K and P_c=248 bar), water (SCW) (T_c=673 K and P_c=240 bar), and CO_2 ($SCCO_2$) (T_c=333 K and P_c=248 bar) were studied. By adjusting the dielectric constant (ε) of the supercritical fluids and mixtures, moderate-to-low polarity PAHs in the fly ashes can be extracted. Virtually most of PAHs hindered in fly ashes can be quantitatively extracted with the supercritical fluids at a wide range of ε. Moreover, the adjustable-ε SCF method developed in this work may have promising applications in the analysis of deuterated-PAHs embedded in interplanetary dusts.

Keywords: *PAHs, supercritical dichloromethane, supercritical water, supercritical fluids.*

IEECP'21, July 29-30, 2021, Silicon Valley, San Francisco, CA – USA

DAI : *https://sci-index.com/DAI/2021.99101/IEECP/14547594*

High-temperature desulfurization by ZnO/Raney CuO absorbents

1st T.-C. Wang
Department of Environmental Engineering,
National Cheng Kung University
Tainan, Taiwan
P56094157@gs.ncku.edu.tw

2nd T.-E. Wu
Department of Environmental Engineering,
National Cheng Kung University
Tainan, Taiwan
emily2738tw@gmail.com

3rd Y.-C. Tsai
Department of Environmental Engineering,
National Cheng Kung University
Tainan, Taiwan
jack1998870308@gmail.com

4th Y.-J. Tuan
Department of Environmental Engineering,
National Cheng Kung University
Tainan, Taiwan
eugenet@ncku.edu.tw

5th H. Paul Wang
Department of Environmental Engineering,
National Cheng Kung University
Tainan, Taiwan
wanghp@ncku.edu.tw

Abstract

Desulfurization of syngas containing H_2S at high temperatures for integrated gasification combined cycle is gaining momentum as a commercially viable source of clean energy. Thus, a feasibility study for hot-gas (1% H_2S) desulfurization by ZnO on skeletal Raney CuO (ZnO/R-CuO) absorbent was carried out. The degree of the hot-gas desulfurization by ZnO/R-CuO was 90.0% at 873 K and decrease to 46.5% as the temperature raised to 1073 K. The rate constant (k) for the desulfurization by ZnO/R-CuO at 873 K was 8.35×10^4 cm^3/min g with the activation energy (Ea) of 114.8 kJ/mol. Speciation of zinc and CuO in the ZnO/R-CuO for the hot-gas desulfurization was also studied by synchrotron X-ray absorption near edge structure (XANES) spectroscopy. Mainly Zn(II) and Cu(II) were found in the ZnO/R-CuO. By EXAFS, in the 2nd shells, a decrease of Cu-Cu bond distance in ZnO/R-CuO was observed during desulfurization. However, an increase in Zn-Zn bond distance was observed after desulfurization. It is apparent that hot-gas desulfurization by ZnO/Raney CuO absorbent is chemical feasible.

Keywords: *Raney CuO, ZnO, hot-gas desulfurization, EXAFS.*

IEECP'21, July 29-30, 2021, Silicon Valley, San Francisco, CA – USA

D!f: *https://sci-index.com/DAI/2021.99101/IEECP/14547723*

Photocatalytic reduction of CO_2 to C_1 fuels by (Ni/ZnO)@C nanoreactors

1st M.-L. Liu
Department of Environmental Engineering
National Cheng Kung University
Tainan, Taiwan
morning.liu@aiesec.net

2nd L.-W. Wei
Department of Environmental Engineering
National Cheng Kung University
Tainan, Taiwan
wei3532607@gmail.com

3rd H.-P. Wang
Department of Environmental Engineering
National Cheng Kung University
Tainan, Taiwan
wanghp@ncku.edu.tw

Abstract

The (Ni/ZnO)@C core-shell nanoparticles were prepared by carbonization of Ni^{2+}- and Zn^{2+}-cyclodextrin complexes at 723 K for 2 h. ZnO and Ni encapsulated in carbon-shell were etched partially to form the (Ni/ZnO)@C yolk-shell nanoreactors for photocatalytic reduction of CO_2 to C_1 fuels. By XRD, it is clear that ZnO is the main zinc crystallite in the nanoreactors, and its nanoparticle size is between 10-20 nm. The TEM images of the nanoreactors indicate that Ni and ZnO having the nanosizes of 5-30 nm are capsulated in the porous carbon-shell that allows molecules to diffuse in and out for photocatalytic reduction of CO_2 to C_1 fuels. It is worth noting that ZnO in the (Ni/ZnO)@C yolk-shell nanoreactor plays the main photoactive role in photocatalytic degradation of methylene blue. However, excess Ni encapsulated in carbon-shell leads to a de-activity in photocatalytic degradation of MB and reduction of CO_2. By *in situ* FTIR spectroscopy, the disappearance of CO_2 is at the expense of formation of species containing CH and carbonyl groups, possibly related to yields of C_1 species such as HCOOH.

Keywords: *CO_2 reduction, photocatalysis, nanoreactors, yolk-shell, methanol.*

IEECP'21, July 29-30, 2021, Silicon Valley, San Francisco, CA – USA

DAI : *https://sci-index.com/DAI/2021.99101/IEECP/14550426*

In situ EXAFS studies of photoelectrocatalytic reduction of gold and lanthanum ions recycled from E-wastes

1st T.-E. Wu
Department of Environmental Engineering,
National Cheng Kung University
Tainan, Taiwan
emily2738tw@gmail.com

2nd Y.-C. Tsai
Department of Environmental Engineering,
National Cheng Kung University
Tainan, Taiwan
jack1998870308@gmail.com

3rd Y.-J. Tuan
Department of Environmental Engineering,
National Cheng Kung University
Tainan, Taiwan
eugenet@ncku.edu.tw

4th H. Paul Wang
Department of Environmental Engineering,
National Cheng Kung University
Tainan, Taiwan
wanghp@ncku.edu.tw

Abstract

Recycling of rare precious metals (RPMs) from E-waste by traditional methods such as pyrometallurgy and hydrometallurgy are generally high energy consumption, cost, and risk of environmental pollution. In this study, fluid capacitive deionization (FdCDI) process was used to concentrate the RPMs from a wastewater. The solar-driven photoelectrocatalytic (PEC) reduction of RPM ions (such as Au^{3+} and La^{3+}) to metals was investigated. Electrons jumped to an excited state by solar energy can be transferred to photocathode through the external circuit to generate electricity in the PEC-I. In the solar-driven PEC-II on the photoanode, the photo-generated electrons can cause the reduction of RPM ions to metals. The speciation of gold and lanthanum during the FdCDI processes was determined by X-ray absorption near structure (XANES) spectroscopy for a better understanding of their electronic structure and oxidation states during photoelectrocatalysis, their synchrotron extended X-ray absorption fine structure (EXAFS) spectra were also determined for an improvement of the photoelectrocatalysts.

Keywords: *photoelectrolysis, FdCDI, RPMs, XANES, EXAFS.*

IEECP'21, July 29-30, 2021, Silicon Valley, San Francisco, CA – USA

DAI : *https://sci-index.com/DAI/2021.99101/IEECP/14547738*

Photocatalytic reduction of CO_2 to methanol by Cu_2O/TiO_2 heterojunctions

1st S.-P. Cheng
Department of Environmental Engineering
National Cheng Kung University
Tainan, Taiwan
pingc2102@gmail.com

2nd L.-W. Wei
Department of Environmental Engineering
National Cheng Kung University
Tainan, Taiwan
wei3532607@gmail.com

3rd H.-P. Wang
Department of Environmental Engineering
National Cheng Kung University
Tainan, Taiwan
wanghp@ncku.edu.tw

Abstract

Conversion of CO_2 to low-carbon fuels using solar energy is considered an economically attractive and environmental friend route. The development of novel catalysts and the use of solar energy via photocatalysis is the key to achieve the goal of chemically reducing CO_2 under mild conditions. Thus, in this study, the novel Cu_2O/TiO_2 heterojunctions were used for CO_2-to-low-carbon fuels. The p-n heterojunction is able to enhance the separation of photogenerated electron-hole pairs. By UV-vis diffuse reflection absorption spectroscopy, it is clear that Cu_2O coupled with TiO_2 causes a red-shift to the visible light range. Under a 6-h UV-vis irradiation, 12.4-70.6 μmol methanol/g-catalyst can be generated by the Cu_2O/TiO_2 heterojunctions. However, excess Cu_2O in the Cu_2O/TiO_2 heterojunctions may cause less absorption of UV-vis light and decrease the excited electrons from TiO_2, which may obstruct the photoactivity for reduction of CO_2.

Keywords: *photocatalysis, CO_2, Cu_2O, TiO_2, p-n heterojunction, methanol.*

IEECP'21, July 29-30, 2021, Silicon Valley, San Francisco, CA – USA

DAI : *https://sci-index.com/DAI/2021.99101/IEECP/14546643*

Low-cost $FeNi_3$@C for DSSC counter electrodes

C.-C. Chen
Department of Environmental Engineering, National Cheng Kung University
Tainan, Taiwan
a91030310@yahoo.com.tw

Y.-F. Liou
Department of Environmental Engineering, National Cheng Kung University
Tainan, Taiwan
star.ryf127@gmail.com

L.-W. Wei
Department of Environmental Engineering, National Cheng Kung University
Tainan, Taiwan
wei3532607@gmail.com

H. Paul Wang
Department of Environmental Engineering, National Cheng Kung University
Tainan, Taiwan
wanghp@ncku.edu.tw

Abstract

To reduce the cost of a dye-sensitized solar cell (DSSC), noble metal platinum (Pt) on the counter-electrode has been replaced with relatively cheap metals, i.e., photo-activity-designable bimetal core-shell nanoparticles. In present work, nickel and iron encapsulated within carbon-shell ($FeNi_3$@C) nanoparticles were prepared by carbonization of Ni^{2+} and Fe^{3+}-β-cyclodextrin at 673 K for the DSSC counter-electrode. By component fitted X-ray absorption near-edge structure (XANES) spectroscopy, metallic nickel (Ni) and iron (Fe (73%) and Fe_3O_4 (27%)) are observed in the $FeNi_3$@C. The $FeNi_3$@C nanoparticles are deposited on a conductivity glass recovered from thin film transistor (TFT) liquid crystal display wastes for the counter-electrode of a DSSC. The DSSC having the $FeNi_3$@C nanoparticles coated counter-electrode has the conversion efficiencies of 3.1%. In addition, the cost of the DSSC using the reccycled conducing glass and cheaper nanostructured $FeNi_3$@C electrode can be reduced by at least 38%.

Keywords: *Dye-sensitized solar cells, FeNi3@C, DSSC counter-electrode.*

IEECP'21, July 29-30, 2021, Silicon Valley, San Francisco, CA – USA

DAI : *https://sci-index.com/DAI/2021.99101/IEECP/14549037*

Solar-driven H_2O-to-H_2O_2 by NiP/BiOI-gC_3N_4 composites

Y.-F. Liou
Department of Environmental Engineering,
National Cheng Kung University
Tainan, Taiwan
star.ryf127@gmail.com

L.-W. Wei
Department of Environmental Engineering,
National Cheng Kung University
Tainan, Taiwan
wei3532607@gmail.com

H. Paul Wang
Department of Environmental Engineering,
National Cheng Kung University
Tainan, Taiwan
wanghp@ncku.edu.tw

Abstract

Water splitting to hydrogen and oxygen through a four-electron transport route has been widely studied for hydrogen energy. Alternatively, H_2O can photocatalytically yield H_2 and H_2O_2 ($2H_2O \rightarrow H_{2(g)} + H_2O_{2(aq)}$) through a two-electron reaction that is more kinetically feasible. The naturally separated H_2O_2 aqueous solution from gaseous H_2 can be directly utilized in oxidation of organic pollutants in wastewater. In this work, NiP dispersed bismuth oxyiodide (BiOI) and graphite carbon nitride (gC_3N_4) composites were prepared for photoelectrodes to yield H_2O_2. And other transition metal phosphide such as CoP with BiOI-gC_3N_4 was also used to enhance the solar driven H_2O-to-H_2O_2 reactivity. As the NiP and CoP dispersed BiOI-gC_3N_4 composite are very effective for H_2O_2 yields, it would be very useful for the feed of a H_2O_2 fuel cell for electricity.

Keywords: *Hydrogen peroxide, bismuth-based catalyst, NiP*

IEECP'21, July 29-30, 2021, Silicon Valley, San Francisco, CA – USA

DAI : *https://sci-index.com/DAI/2021.99101/IEECP/14549358*

Selective extraction of cobalt from spent lithium-ion batteries

1st Y.-C. Tsai
Department of Environmental Engineering
National Cheng Kung University
Tainan, Taiwan
jack1998870308@gmail.com

2nd T.-E. Wu
Department of Environmental Engineering
National Cheng Kung University
Tainan, Taiwan
emily2738tw@gmail.com

3rd I-H. Chen
Department of Environmental Engineering
National Cheng Kung University
Tainan, Taiwan
hermosa2336@gmail.com

4th Y.-J. Tuan
Department of Environmental Engineering
National Cheng Kung University
Tainan, Taiwan
eugenet@ncku.edu.tw

5th H. Paul Wang
Department of Environmental Engineering
National Cheng Kung University
Tainan, Taiwan
wanghp@ncku.edu.tw

Abstract

Lithium-ion battery (LIB) are widely used in electronic products and electric vehicles largely due to the advantages of low price, low memory effect, high power efficiency, and long life cycle. In recent years, an increasing amount of end-of-life LIBs are to be recycled. Extraction of spent LIB has been carried out for recycling of valuable metals such as cobalt. Environmental friendly organic acids such as citric acid was used to selectively extract cobalt. For a better understanding of the cobalt speciation during extraction, in situ synchrotron extended X-ray absorption fine structure (EXAFS) spectra at 323-363 K. Specifically, H_2O_2 (0-1%) was added during the extraction to obtain desired Co^{3+}/Co^{2+} ratios that also facilitate the extraction efficiency.

Keywords: *lithium ion battery, cobalt, extraction, citric acid, EXAFS*

IEECP'21, July 29-30, 2021, Silicon Valley, San Francisco, CA – USA

D!f: *https://sci-index.com/DAI/2021.99101/IEECP/14547603*

Examination of nuclear and renewables potentials in Malaysia

Pei Jia Pok
Department of Nuclear and Quantum Engineering
KAIST
Daejeon, South Korea
peijiapok@kaist.ac.kr

Man-Sung Yim
Department of Nuclear and Quantum Engineering
KAIST
Daejeon, South Korea
msyim@kaist.ac.kr

Abstract

Malaysia relies heavily on fossil fuels such as coal and natural gas as its main source for electricity generation. Decades of exploitation and usage of these materials had not only caused contamination and depletion but also contributed to the large amount of carbon dioxide emission in the country. In 2015, Malaysia has signed the Paris Agreement and vowed to achieve the reduction of carbon dioxide emission by 45% per GDP to the level of 2005 by 2030. Prior to the Fukushima accident that happened in 2011, Malaysia has had plan to own a 2GW nuclear power plant by 2030. However, this plan was then delayed and now cancelled after the Fukushima accident. The importance of this research is to examine the changes in the environment and economy of Malaysia by adding nuclear power and renewables into its energy mix. Carbon dioxide emission trend will be determined and an economic analysis will be conducted. This research intends to draw a best-fit scenario for Malaysia to have a new energy mix that can achieve in the 45% carbon dioxide reduction. This research will be helpful for the Malaysia government as a reference to plan for its future energy production system**.**

Keywords: *Malaysia; Optimization; Nuclear energy; Renewable energy*

IEECP'21, July 29-30, 2021, Silicon Valley, San Francisco, CA – USA

DAI : *https://sci-index.com/DAI/2021.99101/IEECP/14546706*

Dechloriation of incineration fly ash by fluidized capacitive deionization for utilization

P.-C. Chang
Department of Environmental Engineering,
National Cheng Kung University,
Tainan 70101, Taiwan
jack19680312@gmail.com

P.-A. Chen
Department of Environmental Engineering,
National Cheng Kung University,
Tainan 70101, Taiwan
a1005231@gmail.com

H. Paul Wang*
Department of Environmental Engineering,
National Cheng Kung University,
Tainan 70101, Taiwan
wanghp@ncku.edu.tw

Abstract

Most of non-recyclable municipal solid wastes have been treated by incineration for energy recovery and stabilization. However, the fly ash (FA) discharged from air pollution control devices contains toxic metals and chlorides as well as leachable dioxins that make it considered as hazardous wastes. Chlorides in FA that was washed with water can be removed by electrosorption using the new fluidized capacitive deionization (FdCDI) method. Ions including Cl^- in water can be stored in the electrical double layer (EDL) of electrodes, and deionized water (<50 mg/L) can be recycled and reuse under low voltages (0.8-1.2 V). Note that the regeneration of FdCDI can be achieved by applying a zero or reversed voltage. In the FdCDI process, no chemical is needed, resulting no sludge to be discharged and treated. In addition, the effects of Cl^- counter ions during FdCDI was also studied. The Cl^- removal efficiency (51% approximately) with the salt adsorption capacity of 10 mg /g was obtained in the FdCDI process. This work illustrates that fly ash can be dechlorided by the FdCDI method for utilization such as civil engineering fillers.

Keywords: *Municipal solid waste incinerator fly ash, fluidized capacitive deionization, water washing, chloride electrosorption, zero waste*

IEECP'21, July 29-30, 2021, Silicon Valley, San Francisco, CA – USA

DAI : *https://sci-index.com/DAI/2021.99101/IEECP/14551164*

Liquefaction of scrap tires for recycling of fuel oils

H.-A. Lee
Department of Environmental Engineering,
National Cheng Kung University,
Tainan 70101, Taiwan

P.-C. Chang
Department of Environmental Engineering,
National Cheng Kung University,
Tainan 70101, Taiwan

P.-A. Chen
Department of Environmental Engineering,
National Cheng Kung University,
Tainan 70101, Taiwan

H. Paul Wang*
Department of Environmental Engineering,
National Cheng Kung University,
Tainan 70101, Taiwan
wanghp@ncku.edu.tw

Abstract

Scrap tires containing metal wires, fibers, carbon black, and poor thermal conducting rubbers, are far more difficult to be treated effectively. Million fuel oil equivalent are discarded every year through the disposal of scrap tires. Recycling of scrap tires is of increasing importance as incineration and landfilling becomes expensive, and the acceptance of these methods is decreasing. The feasibility for recycling of product oils, metal wires, and carbon black from liquefaction of scrap tires was thus investigated in the present work. The liquefaction process involves contacting the scrap tires (5-15 cm pieces) with hot used motor oil in an inclined screw reactor. Liquefaction of scrap tires at 643 K for 20 min yielded approximately oils (90%), non-condensable gases (5%), and non-liquefiable solid residues (metal wires and fibers) (5%). In the liquefaction process, ZnO (original in tire rubber) could be sulfurized with the tire rubber cross-linked sulfur, and a significant decrease of the sulfur concentration in the product oil and flue gas streams was found. Fuel oils, clean metal wires and fibers, and dry carbon black were recycled. In addition, the flue gas was used for keeping the circulated hot motor oil at 643 K. The bench-scale inclined screw liquefaction reactors suggest that the tire liquefaction process is technically feasible.

Keywords: *Liquefaction, scrap tires, pyrolysis*

IEECP'21, July 29-30, 2021, Silicon Valley, San Francisco, CA – USA

DAI : *https://sci-index.com/DAI/2021.99101/IEECP/14551170*

Numerical simulation of highly-efficient lead free tin-based perovskite solar cell with Sb_2S_3 as novel hole transport layer

Most. Marzia Khatun
Department of Electrical, Electronic and Communication Engineering, Pabna University of Science and Technology,
Pabna 6600, Bangladesh.
mmarzia.pust@gmail.com

Sabrina Rahman
Department of Electrical, Electronic and Communication Engineering, Pabna University of Science and Technology,
Pabna 6600, Bangladesh.
srmithila@gmail.com

Adnan Hosen
Department of Electrical, Electronic and Communication Engineering, Pabna University of Science and Technology,
Pabna 6600, Bangladesh.
adnan_hosen@yahoo.com

Md. Nur Hossain Riyad
Department of Electrical, Electronic and Communication Engineering, Pabna University of Science and Technology,
Pabna 6600, Bangladesh.
nurhossain.eece@gmail.com

Adil Sunny
Department of Electrical, Electronic and Communication Engineering, Pabna University of Science and Technology,
Pabna 6600, Bangladesh.
adilsnn@gmail.com

Sheikh Rashel Al Ahmed*
Department of Electrical, Electronic and Communication Engineering, Pabna University of Science and Technology,
Pabna 6600, Bangladesh.
rashel@pust.ac.bd
*Corresponding author

Abstract

This work reports the performance enhancement of lead free perovskite solar cell (PSC) with Sb_2S_3 as a novel hole transport layer (HTL) numerically by using Solar Cell Capacitance Simulator in One Dimensional (SCAPS-1D). Three different HTLs such as Sb_2S_3, Spiro-OMeTAD, and CuI are introduced into the conventional $CH_3NH_3SnI_3$-based solar cell configuration consisting of Al/FTO/WS_2/$CH_3NH_3SnI_3$/Sb_2S_3 or Spiro-OMeTAD or CuI/Ni. The photovoltaic performances of the lead free perovskite solar cells with the proposed HTLs are evaluated extensively and compared using the SCAPS-1D simulation tool. The impacts of thickness, defect density, acceptor density of perovskite absorber and valance band offset at HTL/perovskite interface on the device performance parameters are analyzed. The variation of working temperature on the PSC outputs is also investigated to realize the stability of the proposed PSC with Sb_2S_3 HTL. The thicknesses of the WS_2 electron transport layer (ETL), $CH_3NH_3SnI_3$ absorber, and Sb_2S_3 HTL are optimized to be 0.05 μm, 0.7 μm, and 0.1 μm, respectively. The improved power conversion efficiency is achieved to be 27.29% for the optimized solar cell structure of Al/FTO/WS_2/$CH_3NH_3SnI_3$/Sb_2S_3/Ni, while the efficiencies of 25.65% and 21.21% are obtained for the lead free the PSCs with Spiro-OMeTAD and CuI HTLs, respectively. Based on the overall investigation and simulation results of the proposed device, it is predicted that WS_2 as ETL and Sb_2S_3 as HTL would be very promising for enhancing the performance of the lead free tin-based PSC, and it would provide constructive research opportunities for the designers to fabricate low-cost lead-free PSCs.

Keywords: Tin-based perovskite, lead free, HTL, Sb_2S_3, performance enhancement

IEECP'21, July 29-30, 2021, Silicon Valley, San Francisco, CA – USA

DAI : *https://sci-index.com/DAI/2021.99101/IEECP/14546793*

I. INTRODUCTION

Hybrid inorganic-organic PSCs have recently emerged as rising star PV technology to the research community worldwide because of high efficiency and significantly lower cost with simple processing techniques [1,2]. The best power conversion efficiency of approximately 25% has been achieved for the PSC having $CH_3NH_3PbI_3$ as active layer [3]. This $CH_3NH_3PbI_3$ perovskite absorber contains toxic lead (Pb) which is a matter of concern for human safety as well as instability under long term environmental issues such as temperature and incident solar radiation [4]. Many researches have been conducted to find alternate perovskite absorber materials [2,5,6] for the PSCs. Among them, tin-based perovskite absorber has been considered as one of the most promising materials due to its non-toxicity, high mobilities, and chemical stabilities in PSCs [7,8]. The attractive features of the $CH_3NH_3SnI_3$ material such as suitable band gap ~1.3 eV [9], high absorption coefficient (10^5 cm^{-1}), and excellent optical properties along with high mobility and small effective mass make it possible alternative to $CH_3NH_3PbI_3$ for photovoltaic (PV) applications [10]. However, tin-based PSCs still face some challenges to achieve superior performances because Sn^{2+} ion gets easily oxidized into Sn^{4+} by exposed with air [11], and thus the overall PV performances of the devices would be affected [12]. In this regard, effective advancement can be made to prevent tin from oxidation by adding SnF_2, $SnCl_2$ and SnI_2 to suppress self-doping [13].

The basic structure of PSC is ETL/perovskite/HTL where perovskite layer acts as absorber to absorb incident photons and the functions of ETL and HTL are to extract the light-generated carriers from the absorber to respective electrodes. ETL and HTL play significant roles by decreasing recombination losses at the interfaces and the net outcome is improved cell performance

and stability [14]. Most commonly used ETL and HTL in PSCs are TiO_2 [10] and Spiro-OMeTAD [15]. However, TiO_2 requires high temperature processing and also it has poor electron mobility and charge transport quality [14–16]. On the other hand, the smooth transportation of holes from the absorber to back contact is restricted by the higher potential barrier generated at the Spiro-OMeTAD HTL/$CH_3NH_3SnI_3$ interface. Therefore, the improper selection of ETL and HTL resulting misaligned band structure with enhanced recombination at the ETL/Perovskite and Perovskite/HTL interfaces results in the low conversion efficiency of $CH_3NH_3SnI_3$-based solar cell.

In the previous work, the excellent photovoltaic efficiency of the $CH_3NH_3SnI_3$-based PSC with alternative WS_2 as ETL has been reported to be 19.84% [17]. Thus, the WS_2 material as ETL having spike-type conduction band offset (CBO) at the WS_2/$CH_3NH_3SnI_3$ interface is used in this work. The organic HTLs including Spiro-OMeTAD have low chemical stability and need expensive synthesis process. Due to these disadvantages of organic HTLs in the PSCs, inorganic p-type materials such as NiO_x, CuI, Cu_2O, and CuSCN as HTLs have much attracted for the low-cost and stable PSC applications [18]. Unfortunately, the PV performances of the PSCs with mentioned HTLs severely degrade due to high recombination rate and photocorrosion [19–21].

To enhance the PV performances of $CH_3NH_3SnI_3$-based PSC, in this study, the Sb_2S_3 material as a novel HTL is proposed between the perovskite absorber and back contact. A comparative study is carried out among Spiro-OMeTAD, CuI, and Sb_2S_3 HTLs in the Al/FTO/WS_2/$CH_3NH_3SnI_3$/HTL/Ni structure using the SCAPS-1D simulator.

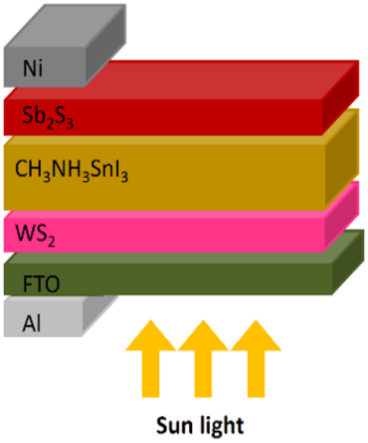

Figure 1. Schematic diagram of the proposed $CH_3NH_3SnI_3$-based PSC.

II. DEVICE STRUCTURE AND SIMULATION PARAMETERS

To analyze the performance of the proposed PSC, the numerical simulation has been carried out by using the one dimensional solar cell device simulator, namely SCAPS-1D program (version 3.3.01), developed by University of Gent [22]. The SCAPS-1D software performs the simulation by resolving the Poisson's equation, the carrier continuity equation, and the drift-diffusion equation. Figure 1 shows the schematic diagram of the lead free tin-based perovskite heterojunction solar cell having the configuration of Al/FTO/WS_2/$CH_3NH_3SnI_3$/Sb_2S_3/Ni. In the designed structure, WS_2 has been employed as electron transport layer with fluorine doped tin oxide (FTO) as transparent conducting oxide (TCO) layer and Sb_2S_3 as hole transport layer into the conventional $CH_3NH_3SnI_3$-based PSC. For metallic electrodes, Aluminum (Al) and Nickel (Ni) have been utilized as the front and back contacts, respectively. Figure 2 represents the energy level diagrams of the PSCs. The simulation approach includes the effects of thickness, doping concentration, and bulk defect density of absorber layer on the solar cell outputs. Table 1 shows the physical parameters used to conduct the simulation. The validation of the parameters has been accomplished by choosing them carefully from the previously reported experimental and theoretical researches [9,10,23–27]. All the simulations have been conducted under illumination of 100 mW/cm^2 and AM1.5G light spectrum at operating temperature 300K. The thermal velocities of electrons and holes are assumed to be approximately 10^7 cm/s [27], while the trap capture cross-sections are kept fixed at 10^{-15} cm². The surface recombination velocity for both electrons and holes are fixed at 10^7 cm/s [27]. The interface defects at ETL/perovskite and perovskite/HTL interfaces have also been introduced to understand the realistic solar cell outputs. Table 2 represents the parameters of the interface defect adopted for the simulation.

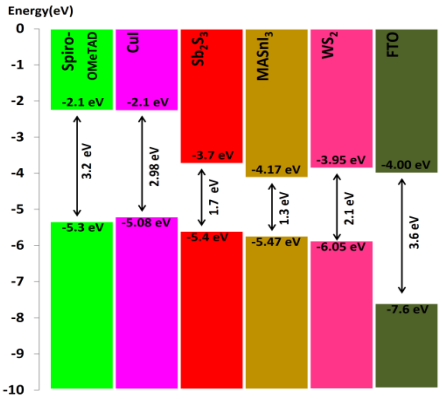

Figure 2. Energy level diagrams of the $CH_3NH_3SnI_3$-based PSCs.

Table 1. Simulation parameters used in the proposed $CH_3NH_3SnI_3$ PSC with different HTLs.

Parameter (unit)	TCO FTO	ETL WS_2	MA-SnI_3	HTL Sb_2S_3	HTL Spiro-OMeTAD	HTL CuI
W (μm)	0.05	0.05	0.7*	0.1	0.1	0.1
E_g (eV)	3.6	2.1	1.3	1.7	3.2	2.98
χ (eV)	4	3.95	4.17	3.7	2.1	2.1
ε_r	9	13.6	8.2	7.08	3	6.50
N_C (cm^{-3})	2.2 ×10^{18}	2 ×10^{18}	10^{18}	2 ×10^{19}	2.5 ×10^{18}	2.8 ×10^{19}
N_V (cm^{-3})	1.8 ×10^{19}	2 ×10^{18}	10^{18}	10^{19}	1.8 ×10^{19}	10^{19}
μ_e (cm^2/V-s)	100	100	1.6	9.8	2×10^{-4}	100
μ_h (cm^2/V-s)	25	25	1.6	10	2×10^{-4}	43.9
N_D (cm^{-3})	10^{18}	10^{17}	0	0	0	0
N_A (cm^{-3})	0	0	10^{16}*	10^{18}	10^{18}	10^{18}
Defect type	-	SA	Neutral	SD	SD	SD
N_t (cm^{-3})	-	10^{15}	10^{15}*	10^{15}	10^{15}	10^{15}

Note: * is a variable field

W: Thickness; E_g: Energy band gap; χ: Electron affinity; ε_r: Relative permittivity; N_c: Conduction band density of states; N_v: Valance band density of states; μ_n: Electron mobility; μ_p: Hole mobility; N_D: Donor concentration; N_A: Acceptor concentration; SA = Single-Acceptor; SD = Single-Donor; N_t: Defect density; MA= CH_3NH_3

Table 2. Defect parameters at the ETL/perovskite and perovskite/HTL interfaces.

Parameters (unit)	ETL/perovskite interface	perovskite/HTL interface
Defect type	Neutral	Neutral
Capture cross-section of electrons and holes (cm^2)	10^{-16}	10^{-16}
Reference for defect energy level E_t	above the highest E_v	above the highest E_v
Energy with respect to Reference (eV)	0.6	0.6
Total density (cm^{-2})	10^{10}	10^{10}

III.RESULTS AND DISCUSSION

A. Impact of HTL on solar cell outputs

Figure 3(a) shows the current density-voltage (J-V) characteristics of the PSCs with different HTLs. The impact of the HTLs in the $CH_3NH_3SnI_3$-based PSCs on the output performances is evaluated. As can be seen in the Figure 3(a), the enhanced PV performance is achieved for the tin-based PSC with the Sb_2S_3 HTL. The PV device with CuI HTL provides open circuit voltage (V_{oc}) of 0.841 V and conversion efficiency of 21.21%. The V_{oc} and photovoltaic efficiency of 0.960 V and 25.65% are estimated for the PSC with Spiro-OMeTAD HTL. On the other hand, the $CH_3NH_3SnI_3$-based PSC having Sb_2S_3 HTL results the best power conversion efficiency of 27.29% including V_{oc} of 0.971 V, J_{sc} of 33.98 mA/cm^2, and FF of 82.69 %. Figure 3(b) demonstrates the external quantum efficiency as a function of the wavelength for the $CH_3NH_3SnI_3$-based PSCs with three different HTLs. It is also observed that the enhanced quantum efficiency can be obtained for the solar cell with Sb_2S_3 HTL at long wavelengths. Therefore, it is revealed that the overall device performances of the PSCs can be enhanced by introducing Sb_2S_3 HTL at the back contact.

The energy band diagram of the $CH_3NH_3SnI_3$-based solar cells with different HTLs is depicted in Figure 3(c). The energy band alignment at the perovskite/HTL and ETL/perovskite interfaces is very crucial to explain the transportation of photo-generated carriers from the absorber to the respective electrodes. V_{oc} of the PSCs with HTLs is improved by the high built-in electric field induced at the back side along the perovskite absorber. J_{sc} is also incremented due to smooth collection of photo-induced electrons and holes by the respective metal electrode. To fabricate more efficient PSC, the CBO at perovskite/HTL should be positive and the VBO ought to be close to zero or negative so that the holes are collected from the absorber easily, while the electrons are blocked by the HTL to reduce interface recombination. The CBOs of 2.07 eV for Spiro-OMeTAD, 2.07 eV for CuI, and 0.47 eV for Sb_2S_3 are found, respectively. On the other hand, the VBO values of Spiro-OMeTAD, CuI, and Sb_2S_3 are determined to be 0.17 eV, 0.39 eV, and 0.07 eV, respectively. The VBO at the $CH_3NH_3SnI_3/Sb_2S_3$ interface is nearly zero and thus holes get transported to the HTL from the absorber with more ease contributing to more photo-current density. On the other hand, as the VBO is largely positive introducing other two HTLs, holes get restricted due to large barrier which resulted in poorer J-V characteristics than the PSC with Sb_2S_3. It can be seen that the energy band diagram for Al/FTO/WS_2/$CH_3NH_3SnI_3$/Sb_2S_3/Ni is properly aligned, thus resulting in better device performance with reduced recombination owing to more hole collection at the back contact. According to the simulation results, in this work, the inorganic material Sb_2S_3 as a novel HTL into the $CH_3NH_3SnI_3$-based PSC is selected to understand the device performances in the next sections.

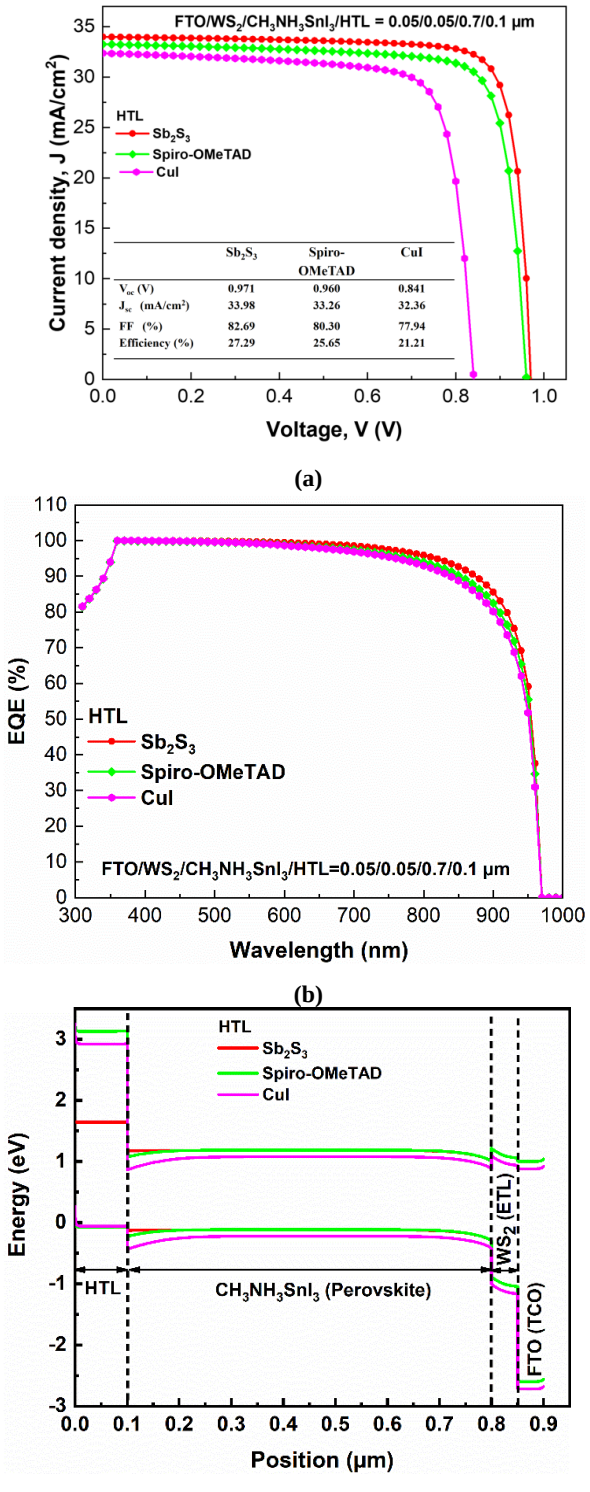

Figure 3. Simulated a) J-V characteristics, b) spectral response, and c) energy band diagram of the $CH_3NH_3SnI_3$-based solar cells.

B. Impact of absorber thickness on solar cell outputs

Figure 4 shows the performance parameters of PSC configuration with Sb_2S_3 with the variation of absorber layer thickness. The absorber thickness is varied from 0.05 to 2 µm, while the other parameters for ETL and HTL as well as the absorber are fixed. The J_{sc} rises rapidly with increasing thickness due to the incremented rate of photo-generated charge carriers. A thinner absorber leads to poor light absorption hence results in lower J_{sc} and efficiency, while a thicker absorber causes high recombination as the electric field becomes weak enough to separate charge carriers. The V_{oc} and FF are diminished slightly with increased thickness because of the enhanced recombination and series resistance. In Figure 4, the power conversion efficiency is increased up to the absorber thickness of 0.7 µm, and then is almost saturated. Therefore, the optimum absorber thickness of the proposed PSC is found to be 0.7 µm.

The best conversion efficiency of 27.29% with V_{oc} of 0.971 V, J_{sc} of 33.98 mA/cm^2, and FF of 82.69% is determined at the optimized thicknesses of 0.05 µm for WS_2, 0.7 µm for $CH_3NH_3SnI_3$ absorber, and 0.1 µm for Sb_2S_3 HTL, respectively.

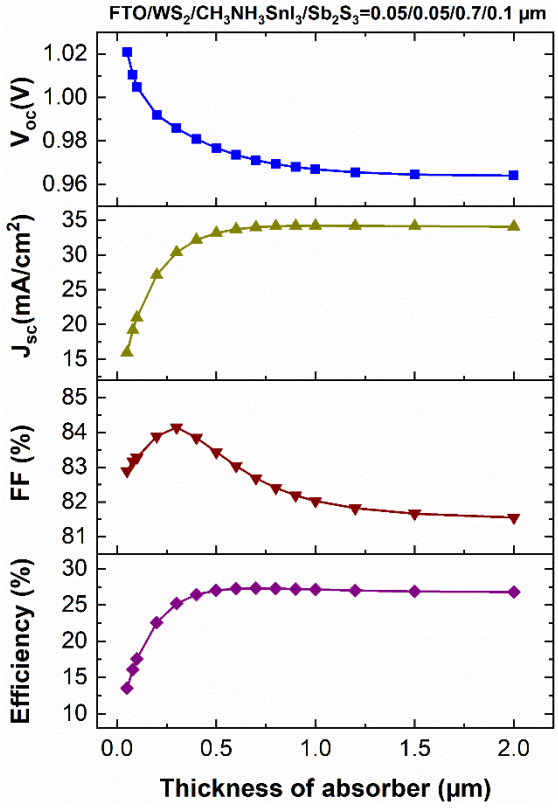

Figure 4. Performance parameters of PSC configuration with Sb_2S_3 with the variation of absorber layer thickness.

C. Impact of doping density in absorber on solar cell outputs

To investigate the performance of the solar cell, the doping density of the absorber layer is varied from 1×10^{12} to 1×10^{18} cm^{-3} with 0.7-µm-thick $CH_3NH_3SnI_3$ absorber layer, 0.1-µm – thick Sb_2S_3 HTL (Doping : 1×10^{18} cm^{-3}) and 0.05-µm-thick ETL (Doping : 1×10^{17} cm^{-3}). Figure 5 illustrates the photovoltaic parameters such as V_{oc}, J_{sc}, FF, and efficiency as a function of the $CH_3NH_3SnI_3$ absorber doping density. From the Figure 5, it is found that the V_{oc} increased from 0.93 V to 1.09 V with the increase of doping density. The J_{sc} remained almost constant up to 1×10^{15} cm^{-3} and then diminished linearly when the density is further increased. It is also seen that both FF and efficiency noticeably increased from 78.95 to 85.45% and 25.11 to 27.53%, respectively, when the doping concentration expanded from 1×10^{12} to 1×10^{18} cm^{-3}. Increasing the acceptor density in absorber layer acts as a contributing factor to the generation of more charge carriers which results in the improvement of the performance of the solar cell, thus the efficiency is enhanced. For further investigation, the acceptor density of the absorber layer is optimized at 1×10^{16} cm^{-3}.

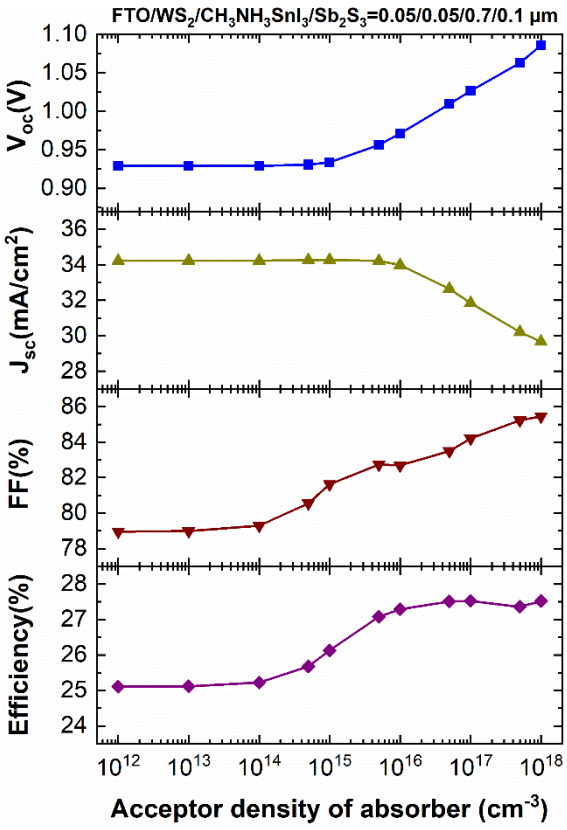

Figure 5. Photovoltaic parameters such as V_{oc}, J_{sc}, FF, and efficiency as a function of the $CH_3NH_3SnI_3$ absorber doping density.

D. Impact of defect density in absorber on solar cell outputs

The impact of defect density in absorber layer on the PV performance is analyzed by varying the defect from 1×10^{12} to 1×10^{17} cm^{-3} with 0.7 µm $CH_3NH_3SnI_3$ absorber layer, 0.1 µm HTL and 0.05 µm ETL, respectively. A graphical representation of the performance parameters of the proposed tin-based PSC with Sb_2S_3 HTL as a function of absorber defect density is presented in Figure 6. It is evident from the Figure 6 that all the performance parameters are reduced linearly with the increment of the defect density. Increasing the defect density in the absorber layer leads to elevate the charge-carrier recombination rate which negatively affects the performance of the cell by diminishing the overall power conversion efficiency from 32.61 to 15.38%. To optimize the output results, the defect density has been selected to be 1×10^{15} cm^{-3}.

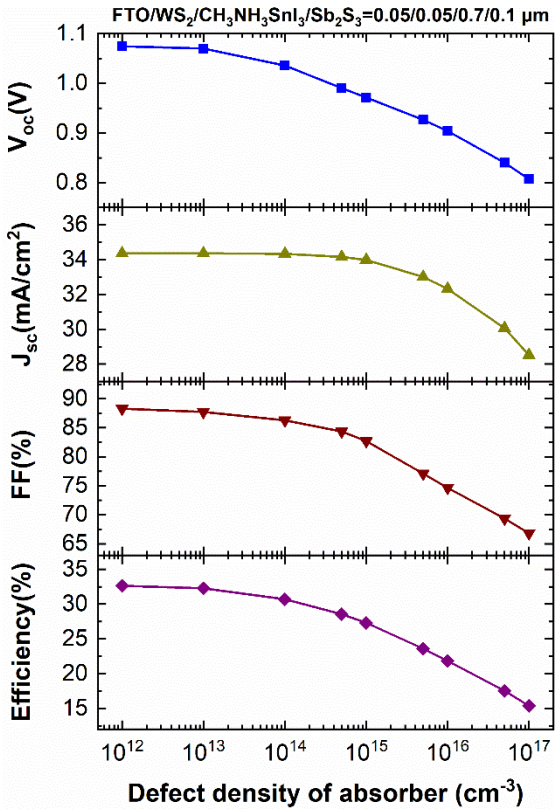

Figure 6. Performance parameters of the proposed tin-based PSC with Sb_2S_3 HTL as a function of absorber defect density.

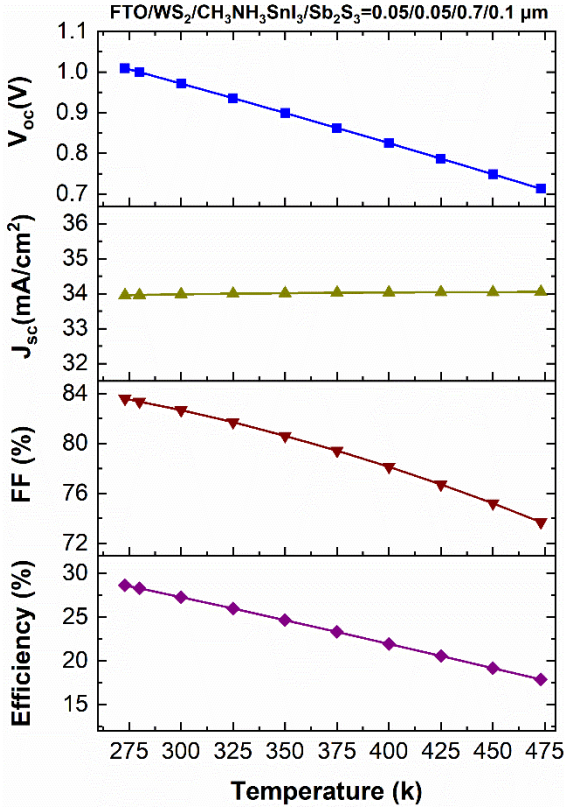

Figure 7. Effect of temperature on the PV performances of the proposed tin-based PSC.

E. Impact of operating temperature on solar cell outputs

The stability of the proposed PSC is also investigated by varying the operating temperature. Figure 7 shows the effect of temperature on the PV performances of the proposed tin-based cell PSC. The operating temperature is varied from 273 to 473K. All the solar cell outputs except the J_{sc} are degraded as the increase of temperature. The V_{oc} is the most affected parameter decreasing from 1.009V to 0.713V by increasing the operating temperature. This is attributed to enhancement of the reverse saturation current [27]. J_{SC} is almost remained constant. FF is deteriorated significantly from 83.59 to 73.71% as it is directly related to V_{oc} and J_{sc}. The efficiency from 28.64 to 17.88% at the temperature of 273K and 473K is estimated. The reduction of energy band gap of the semiconductor materials may results in the degradation of the overall conversion efficiency of the proposed PV device [28].

IV. CONCLUSIONS

In this work, the numerical investigation of lead-free tin-based perovskite solar cell with different HTLs has been performed to observe the behavior of the PV device. A new $CH_3NH_3SnI_3$-based perovskite solar cell with the structure of Al/ FTO/WS_2/$CH_3NH_3SnI_3$/Sb_2S_3/Ni has been designed and studied by SCAPS-1D program. To improve the photovoltaic performance, WS_2 as ETL and Sb_2S_3 as HTL have been proposed, respectively. A comparative study for different HTL materials including CuI and Spiro-OMeTAD into the conventional $CH_3NH_3SnI_3$-based PSC has also been presented to substantiate the performance of the proposed solar cell. The solar cell has been optimized at 0.7 µm CH_3NH_3SnI absorber, 0.1 µm HTL, and 0.05 µm ETL, respectively. Furthermore, the impact of doping concentration and bulk defect density of absorber layer on the PV output parameters have been evaluated. The optimum doping concentration of the absorber layer is also obtained to be 1×10^{16} cm^{-3}. It is revealed that the conversion efficiencies of 21.21% and 25.65% with FF values of 77.94% and 80.33% have been obtained for the CuI and Spiro-OMeTAD HTLs, respectively. On the other hand, the enhanced power conversion efficiency of 27.29% with V_{oc} of 0.971 V, J_{sc} of 33.98 mA/cm^2 and FF of 82.69% has been achieved for the proposed structure. Therefore, this study leads to suggest that considering the proposed cell as an encouraging guideline, it is feasible to design a new environmentally efficient and cost effective tin-based perovskite solar cell with better performance.

V. ACKNOWLEDGMENTS

The authors would like to thanks Dr. Marc Burgelman and his colleagues at the Department of Electronics and Information Systems (ELIS), University of Gent, Belgium for providing the SCAPS simulation package.

VI. REFERENCES

[1] A. Bag, R. Radhakrishnan, R. Nekovei , and R. Jeyakumar, “Effect of absorber layer, hole transport layer thicknesses, and its doping density on the performance of perovskite solar cells by device simulation,” Sol. Energy, vol. 196, pp. 177–182, January 2020.

[2] K. Kumari, A. Jana , A. Dey, T. Chakrabarti, and S. K. Sarkar, “Lead free $CH_3NH_3SnI_3$ based perovskite solar cell using ZnTe nano flowers as hole transport layer,” Opt. Mater., vol. 111, January 2021.

[3] M. A. Green, E. D. Dunlop, J. H. Ebinger, M. Yoshita, N. Kopidakis and A. H, Baillie, “Solar cell efficiency table

(Version 55)," Prog. Photovolt., vol 28, pp. 3–15, January 2020.

[4] G. Niu, W. Li, F. Meng, L. Wang, H. Dong, and Y. Qiu, "Study on the stability of $CH_3NH_3PbI_3$ films and the effect of post-modification by aluminum oxide in all-solid-state hybrid solar cells," J. Mater. Chem. A., vol. 2, pp. 705–710, January 2014.

[5] W. Zhou, Y. Zhao, X. Zhou, R. Fu, Q. Li, Y. Zhao, K. Liu, D. Yu and Q. Zhao, "Light independent ionic transport in inorganic perovskite and ultrastable Cs-based perovskite solar cells," J. Phys. Chem. Lett., vol. 8, pp. 4122–4128, August 2017.

[6] T. Krishnamoorthy, H. Ding, C. Yan, W. L. Leong, T. Baikie, Z. Zhang, M. Sherburne, S. Li, M. Asta, N. Mathews and S. G. Mhaisalkar, "Lead-free germanium iodide perovskite materials for photovoltaic applications," J. Mater. Chem. A, vol. 3, pp. 23829–23832, October 2015.

[7] P. Roy, N. K. Sinha, and A. Khare, "An investigation on the impact of temperature variation over the performance of tin-based perovskite solar cell: A numerical simulation approach," Mater. Today, vol. 39, pp. 2022–2026, 2021.

[8] C. C. Stoumpos, C. D. Malliakas and M. G. Kanatzidis, "Semiconducting tin and lead iodide perovskites with organic cations: Phase transitions, high mobilities and near- infrared photoluminescent properties," Inorg. Chem., vol. 52, pp. 9019–9038, July 2013.

[9] M. Kumar, A. Kumar, A. Raj, P. C. Sati, M. Sahni, and A. Anshul, "Organic-inorganic perovskite-based solar cell designs for high conversion efficiency: A comparative study by SCAPS simulation," Mater. Today, in press, December 2020.

[10] I. Alam, and M. A. Ashraf, "Effect of different device parameters on tin-based perovskite solar cell coupled with In_2S_3 electron transport layer and CuSCN and Spiro-OMeTAD alternative hole transport layers for high efficiency performance," Energy Sources, Part A: Recovery, Utilization, and Environmental Effects, pp. 1–17, September 2020.

[11] S. Abdelaziz, A. Zekry, A. Shaker and M. A. Ebrahim, "Investigating the performance of formamidinium tin-based perovskite solar cell by SCAPS device simulation," Opt. Mater, vol. 101, pp. 109738, March 2020.

[12] Y. Takahashi, H. Hasegawa, Y. Takahashi and T. Inabe, "Hall mobility in tin iodide perovskite $CH_3NH_3SnI_3$: Evidence for a doped semiconductor," J. Solid State Chem., vol. 205, pp. 39–43, September 2013.

[13] J. T. Lin, Y. K. Hu, C. H. Hou, C. C. Liao, W. T. Chuang, C. W. Chiu, M. K. Tsai, J. J. Shyue and P. T. Chou, "Superior stability and emission quantum yield (23% ± 3%) of single layer 2D tin perovskite TEA_2SnI_4 via thiocyanate passivation," Small, vol 16, pp. 2000903, April 2020.

[14] A. Ahmed, K. Riaz, H. Mehmood, T. Tauqeer and Z. Ahmed, "Performance optimization of $CH_3NH_3Pb(I_{1-X}Br_X)_3$ based perovskite solar cells by comparing different ETL materials through conduction band offset engineering," Opt. Mater., vol. 105, pp. 109897, July 2020.

[15] X. Zhao, and M. Wang, "Organic hole-transporting materials for efficient perovskite solar cells," Mater. Today Energy, vol. 7, pp. 208-220, March 2018.

[16] F. Anwar, R. Mahbub, S. S. Satter and S. M. Ullah, "Effect of different HTM layers and electrical parameters on ZnO nanorod-based lead-free perovskite solar cell for high efficiency performance," Int. J. Photoenergy, vol. 2017, pp. 9846310, November 2017.

[17] A. Kumar and S. Sing, "Numerical modeling of lead-free perovskite solar cell using inorganic charge transport materials," Mater. Today, vol. 26, pp. 2574–2581, 2020.

[18] B. Gil, A. J. Yun, Y. Lee, J. Kim, B. Lee, and B. Park, "Recent Progress in Inorganic Hole Transport Materials for Effcient and Stable Perovskite Solar Cells," Electron. Mater. Lett., vol. 15, pp. 505–524, September 2019.

[19] P. P. Zhang, Z. J. Zhou, D. X. Kou, and S. X. Wu, "Perovskite Thin Film Solar Cells Based on Inorganic Hole Conducting Materials," Int. J. Photoenergy, vol. 2017, pp. 6109092, May 2017.

[20] J. Li, Z. Mei, L. Liu, H. Liang, A. Azarov, A. Kuznetsov, Y. Liu, A. Ji, Q. Meng, and X. Du, "Probing Defects in Nitrogen-Doped Cu_2O," Sci. Rep., vol. 4, pp. 7240, November 2014.

[21] C. Y. Toe, Z. Zheng, H. Wu, J. Scott, R. Amal, and Y. H. Ng, "Photocorrosion of Cuprous Oxide in Hydrogen Production: Rationalising Self-Oxidation or Self-Reduction," Angew. Chem. Int., vol. 57, pp. 13613–13617, October 2018.

[22] M. Burgelman, K. Decock, A. Niemegeers, J. Verschraegen, S. Degrave, SCAPS Manual (version: 3.3.07). Department of Electronics and Information Systems, University of Gent, Belgium, http://scaps.elis.ugent.be (accessed: January, 2021).

[23] V. Odari, R. Musembi, and J. Mwabora, "Device Simulation of Sb_2S_3 Solar Cells by SCAPS-1D Software," Afr. j. phys. sci., Vol. 3, pp. 39–54, February 2019.

[24] Y. Xiao, H. Wang, and H. Kuang, "Numerical simulation and performance optimization of Sb_2S_3 solar cell with a hole transport layer," Opt. Mater., vol. 108, pp. 110414, October 2020.

[25] A. A. Kanouna, M. B. Kanounb, A. E. Merada , and S. G. Said, "Toward development of high-performance perovskite solar cells based on $CH_3NH_3GeI_3$ using computational approach," Sol. Energy, vol. 182, pp. 237–244, April 2019.

[26] K. Sobayela , M. Shahinuzzamand , N. Amin , M.R. Karim, M.A. Dar , R. Gul , M.A. Alghoul , K. Sopian , A.K.M. Hasan , and Md. Akhtaruzzaman, "Efficiency enhancement of CIGS solar cell by WS_2 as window layer through numerical modelling tool," Sol. Energy, vol. 207, pp. 479–485, September 2020.

[27] S. R. A. Ahmed, A. Sunny, S. Rahman, "Performance enhancement of Sb_2Se_3 solar cell using a back surface field layer: A numerical simulation approach," Sol. Energy Mater. Sol. Cells, vol. 221, March 2021.

[28] P. Singh, N.M. Ravindra, "Temperature dependence of solar cell performance-an analysis," Sol. Energy Mater. Sol. Cells, vol. 101 pp. 36–45, June 2012.

Improving Energy Performance and Thermal Comfort for Heritage Buildings: A Case Study Murabaa Palace

Abobakr Al-Sakkaf
Department of Building, Civil, and Environmental Engineering
Concordia University
Montréal, Canada
abobakr.alsakkaf@concordia.ca

Sherif Ahmed Mahmoud
Department of Architecture Engineering
Military Technical College
Cairo, Egypt
sherif_ahmed@mtc.edu.eg

Eslam Mohammed Abdelkader
Structural Engineering Department, Faculty of Engineering
Cairo University
Giza, Egypt
eslam_ahmed1990@hotmail.com

Abstract

Heritage Buildings are significant of their historical and architecture added value, which require in deep and precise preliminary brainstorming when considering upgrade or retrofitting of these valuable buildings. This study opts to spotlight on some passive design architecture interventions to improve the thermal comfort and the required cooling energy for the building. The Murabaa Palace in Riyadh was selected as a case study. The design builder software was used to evaluate the energy performance of four passive architectural design alternatives. The results show that using Low-E double glass in addition to applying double wall with polystyrene thermal insulation can enhance the thermal comfort inside the building and reduce the energy performance and CO_2 emissions to 17% and 9% respectively.

Keywords: Heritage buildings, passive design, energy conservation, and reduction of CO_2 emissions.

I. INTRODUCTION

Heritage buildings are integral parts of modern life, in which they gain their significance from their historical, archeological, and cultural added value [1; 2; 7; 13]. Therefore, improving the energy performance and indoor thermal comfort of an as built building with minimum interventions and preserving its heritage value is a dilemma. This is the role of introducing passive architectural design by precise choice of building materials and additions [9; 14; 18]. Accordingly, this research aims to spotlight on some passive architectural alternatives that can enhance indoor thermal comfort, reduce energy required for cooling and in turn minimize the CO_2 emissions.

Moreover, heritage buildings inherited from the past are a crucial component of our modern society. Heritage included those buildings, structures, artifacts, and areas that are historically, aesthetically and architecturally significant. Figure 1 below shows the number of world heritage properties inscribed each year per region. As of July 2019, a total of 1,121 World Heritage Sites located in167 States around the globe. Additionally, three key factors determine whether a property worth to be listed as heritage are: historic significance, historic integrity, and historical context. Historic significance is related to how valuable the property to the history, archaeology, engineering or culture of a community. This includes any heritage building that is associated with a past event or an important person in addition to those building that has a distinctive physical characteristic. Historic integrity is relevant to the authenticity of the building identity with existing evidence of its unique physical characteristics during the building's historic period [5].

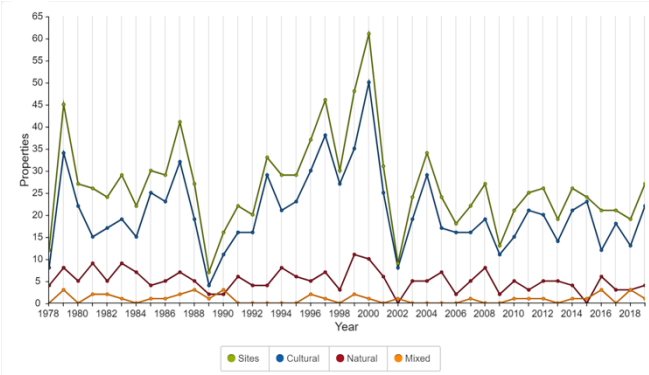

Figure 1. The number of world heritage properties inscribed each year per region [5].

According to Al-Sakkaf et al. [3; 4] the trends of protection and use of heritage buildings and cultural heritage components testify to increasing attention in the study of heritage and legacy. Studies have shown that project life cycle phases have been developed to evaluate the performance of buildings in general. Nevertheless, heritage buildings and their need were not considered. In heritage buildings projects there are six life cycle phases include: a) planning, b) manufacturing, c) transportation, d) construction, e) operation and f) maintenance phases. In addition, there is a lack of

IEECP'21, July 29-30, 2021, Silicon Valley, San Francisco, CA – USA

D!f: *https://sci-index.com/DAI/2021.99101/IEECP/14546634*

a comprehensive rating system that could assess the heritage buildings elements and to study the possibility of passive design architecture interventions to evaluate the thermal comfort interims of energy for heritage buildings. Furthermore, this paper will assist facility managers in their rehabilitation decisions. Therefore, study opts to spotlight on some passive design architecture interventions to improve the thermal comfort and the required cooling energy for the building Accordingly, the case study is applied in this research MP in Saudi Arabia.

Heritage buildings require reliable restoration, preservation procedures and evaluate the performance of heritage building interims of thermal comfort and user satisfaction. Therefore, it is essential to develop a sustainability rating system that accounts for socio-economic factors, to manage the maintenance of heritage buildings. In the Middle East, for instance, BREEAM and LEED rating systems cannot be employed because of different climatic conditions and local contexts [4; 16]. A sustainability rating tool can be defined as a systematic methodology to examine the overall sustainability assessment of a whole building. This includes economic, environmental, social, cultural, and value-based aspects. Thus, the outcome of such a tool can be used as a means of comparison with other buildings [2]. Around the globe, many rating systems pertain to different areas of sustainable development. By March 2010, there were 382 registered building software tools for sustainability development [3]. Nevertheless, only a few systems are well established and recognized by the World Green Building Council. This comprises Green Globes, Green Building Index, Green Building Program (GBP), Green ship Indonesia, Green Globes, BREEAM, LEED, etc.

Another important aspect that affects building performance is orientation. Building orientation can maximize opportunities for passive solar heating when needed, solar heat gain avoidance during cooling time, natural ventilation, and day lighting throughout the year. For example, southern exposure is the key physical orientation feature for passive solar energy in the northern hemisphere. In general, a south-facing orientation within 30º east or west of true south will provide around 90% of the maximum static solar collection potential. The optimum directional orientation depends on site specific factors and on local landscape features such as trees, hills, or other buildings that may shade the sunspace during certain times of the day. Rectangular buildings should be oriented with the long axis running east-west, so the east and west walls receive less direct sun in the summer. In the winter, passive solar heat gain occurs on the south side of the building [3; 15].

Besides, this research will follow various steps starting with a brief introduction describing the problem statement and the aim. Then the methodology that shows the case study data, the design builder simulation software calibration and data entry, and passive design alternatives and data entry. Ending this research with results and final conclusion.

II. LITERATURE REVIEW

Several previous models were reported in the literature that managed to assess energy consumption in residential buildings, office buildings and commercial buildings. Fayaz et al. [10] utilized back propagation artificial neural networks for the prediction of household energy consumption. They utilized some pre-processing procedures of data normalization and statistical moments for data cleaning and filtering. Results demonstrated that the filtering stages could enhance the prediction accuracies, such that the developed model achieved mean absolute error, mean absolute percentage error and root mean squared error of 4.32, 11.96% and 5.46, respectively. Mohamed Abdelkader et al. [16] studied the implementation of a set of machine learning models in the emulation of heating and cooling loads in residential buildings. The input variables encompassed surface area, roof area, wall area, glazing area, glazing area distribution, overall height and relative compactness. The utilized machine learning models were back propagation artificial neural network, generalized regression neural network, radial basis neural network, radial kernel support vector machines and ANOVA kernel support vector machines. It was argued that radial basis neural network performed better than other machine learning models obtaining mean absolute percentage error, mean absolute error and root mean squared error of 1.01%, 0.53 and 0.21, respectively.

Gassar et al. [12] introduced a set of data-driven models for the sake of simulating electricity and gas consumption in residential buildings in London at the lower supper output areas and middle supper output areas. Their study included the use of multi-layer neural network, multiple regression, random forest and gradient boosting. The input parameters involved average number of rooms per house, number of buildings, household spaces, land area, number of households, population, median house price and annual median household income. It was highlighted that multi –layer neural network outperformed other machine learning models at both levels of lower supper output areas and middle supper output areas yielding a correlation coefficient more than 99%. Gao et al. [11] studied the utilization of a set of machine learning paradigms for designing energy efficient residential buildings. This comprises elastic net, Gaussian process regression, least median of squares regression, multi-layer perceptron, radial basis function regression and others. The outputs of the model were the amounts of heating and cooling loads and they were calculated based on a set of building characteristics. It was inferred that random forest, rules decision table, alternating model tree, lazy k-star yielded less prediction error than other machine learning models.

Turhan et al. [17] compared the results of an energy simulation software called “KEP-IYTE-ESS” and artificial neural network in forecasting heating loads of buildings. The input variables of the developed artificial neural network model were width\length ratio, area/volume ratio, wall overall height transfer coefficient, total external surface area, and total window area/total external surface area ratio. Simulation results showed good similarity between the predicted and observed predicted values. In this regard, the developed artificial neural network attained mean absolute percentage error of 5.06% and successful predication rate of 97.7%. Amber et al. [6] compared the prediction capabilities of five intelligent techniques for forecasting electricity consumption in an administrative building. The deployed artificial intelligence models were artificial neural network, deep neural network, support vector machines, genetic programming and multiple regression. The electricity consumption was simulated according to the solar radiation, temperature, wind speed, humidify and weekly index. It was stated that the developed artificial neural network surpassed other artificial intelligence models accomplishing mean absolute percentage error of 6%.

Chae et al. [19] proposed artificial neural network model for emulating sub-hourly electricity consumption in commercial buildings. The input predictors were environmental, operational and time factors. The environmental factors included sky condition, wind speed, rain indicator, precipitation probability, outdoor relative humidity and outdoor dry-bulb temperature. The developed Bayesian regularized neural network with Levenberg–Marquart back propagation algorithm was found to provide a good predictive model that can minimize energy costs in buildings. Yu et al. [21] employed decision tree for simulating future building energy demand. The predicted loads were obtained according to annual average air temperature, house type, construction type, floor area, heat loss equivalent, equivalent leakage area, number of occupants, space heating, hot water supply and type of kitchen. It

was projected that the developed decision tree model could accomplish accuracies of 93% and 92% for the training and testing datasets, respectively.

Jovanovic et al. [20] studied the implementation of an ensemble of artificial neural networks in forecasting heating energy consumption. This encompassed feedforward backpropagation neural network, radial basis function network and adaptive neuro-fuzzy interference system. The input parameters involved mean daily outside temperature, mean daily wind speed, total daily solar radiation, minimum daily temperature, maximum daily temperature, relative humidity, day of the year, month of the year and heating consumption of the previous day. Results showed that the three different types of artificial neural networks accomplished a perfect agreement between the actual and predicted values. In the view of the above, it can be derived that most of the reported models evaluate energy consumption in typical residential, office and commercial buildings. In this context, the literature lacks models which can look at the energy consumption of heritage buildings, and the environmental implications of their different architectural design alternatives.

III. METHODOLOGY

The methodology of this research that was followed to enhance the energy performance of the Murabaa palace heritage building is divided into two main parts as will be described below in detail: 1) the case study description; 2) Design Builder software calibration and data entry; and 3) Passive design alternatives and energy simulation.

A. Case Study Data

Murabba Palace is in Riyadh, Kingdom of Saudi Arabia. It was built around 150 years ago. Murabba Palace is one of the most popular historic buildings in the Kingdom with an area of 9,844.64 m^2. The building gets its name from its square shape. It is one of the museums in the city and is comprised of 12 designated areas with conference rooms, meeting rooms, and administrative offices. The main materials used in its construction were bricks, indigenous stones, tamarisk trunk and palm-leaf stalks. The walls of the building were built using straw reinforced adobe with engraved ornaments on coating as shown in Figure 2.

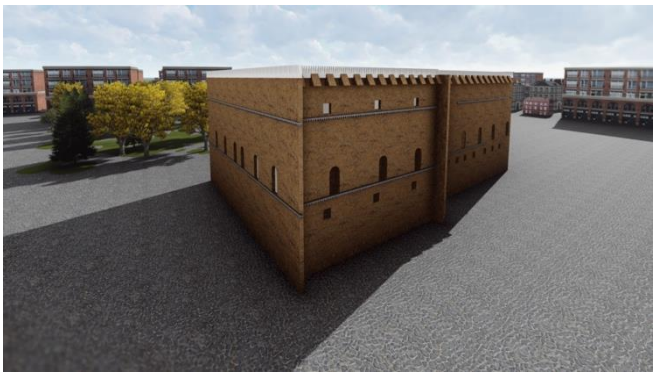

Figure 2. 3 D model for Murabaa Palace.

B. Design Builder Calibration and Data Entry

Design Builder software [8] version 4.5.0.148 was utilized to perform the energy simulations for the selected passive design insulation retrofitting for the Murabaa Palace. The location of the building is Riyadh and the selected weather data form the software template is SAU_RIYADH_IWEC. The activity template was set to Generic Office Area. The building has no lighting control. The used HVAC system is central unit VAV Air cooled chiller. The mechanical ventilation is turned on. No heating system is utilized. Moreover, natural ventilation and mixed mode are both set in action in the software. The windows in the building are composed of single layer 6mm clear glass.

The construction material data entry was divided into four categories: 1) roof floor layers; 2) ground floor layers; 3) typical floor levels; and 4) external wall layers. As shown in Figure 3, the roof comprises 15-20 cm diameter wooden athel beam, 3 cm palm bot layer, 1cm date palm leaves, non-woven layer, 20 cm stabilized soil layer. Furthermore, the ground floor consists of compacted filling material, polyethylene layer for thermal insulation, 10 cm reinforced concrete, 2 cm cement mortar, 6 cm Riyadh stone stones as shown in Figure 4. Additionally, as shown in Figure 5, the first-floor layers are divided into 15 cm wooden athel tree trunk beam, 3 mm palm bot, 1 cm palm leaves layers, non-woven polyester layer, 10 cm mud soil and 10 cm stabilized earth. Finally, the external wall is 40 cm stabilized earth bricks with 3 cm thick external and internal stabilized earth render. The total U-values for roof floor, ground floor, first floor, and external wall layers are 0.441 W/m^2.K, 0.779 W/m^2.K, 0.406 W/m^2.K, and 1.737 respectively.

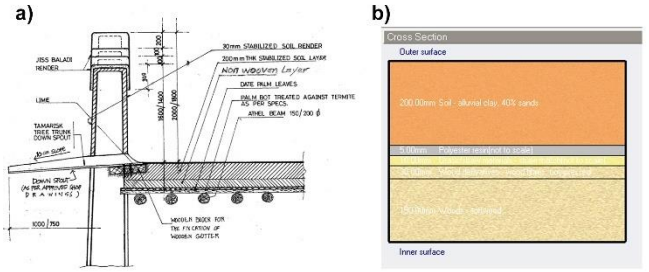

Figure 2. Roof floor layer: a) as built detail, b) design builder data entry roof layer.

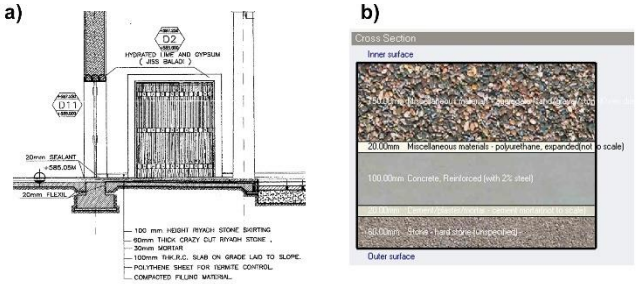

Figure 3. Ground floor layer: a) as built detail, b) design builder data entry ground layer.

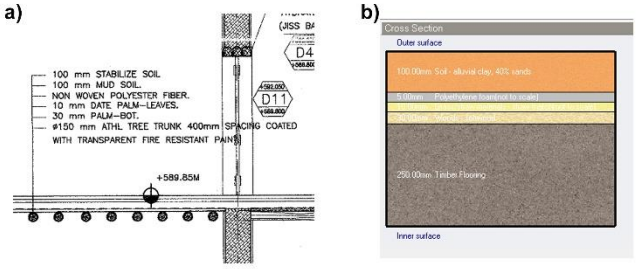

Figure 4. First floor layer: a) as built detail, b) design builder data entry ground layer.

C. Passive Design Alternatives and Energy Simulations

According to the heritage character of the building, the selected passive interventions were taken place to improve the energy performance of the building and the indoor thermal comfort with minimum intervention and retrofitting actions to preserve the heritage entity of the building exterior shape and the internal character of the building as much as possible. There are four scenarios that were utilized as follows: 1) replacing the existing single glass with double reflected glass with 13 mm gas filled gap that decreases the U-value from 5.360 W/m^2.K, as in the base case, to be 2.294 W/m^2.K; 2) replacing the existing single glass with double reflected glass with 13 mm gas filled gap that decreases the U-value from 5.360 W/m^2.K to be 1.622 W/m^2.K; 3) using the loE-glass as in the second scenario in addition to 5 cm air-gap and 12 cm rammed earth brick that makes the U-value 1.614 W/m^2.K as shown in Figure 5 (a); and 4) using the loE-glass as in the second scenario in addition to 5 cm expanded polystyrene thermal insulation and 12 cm rammed earth brick which achieves U-value 0.568 W/m^2.K as shown in Figure 5 (b).

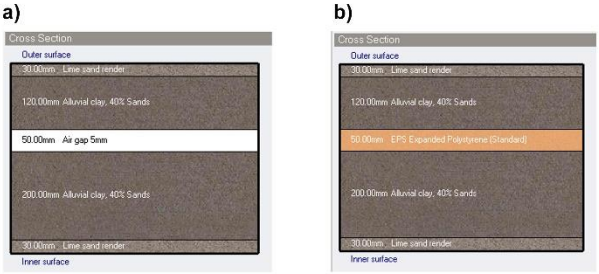

Figure 5. Proposed double wall layers: a) double wall with air-gap, b) double wall with polystyrene.

IV. RESULTS AND DISCUSSION

According to the simulations performed using design builder software the fourth case (low E double glass with double wall enclosing thermal insulation) achieves the minimum cooling energy consumption of 96779 Wh/m^2 annually, which is attributed to the minimum U-value. The other three cases consume 112129 Wh/m^2, 114908 Wh/m^2, 112718 Wh/m^2 respectively as illustrated in Table 1. Hence, the four cases achieve reduction in cooling energy consumption than the base case as follows: (case_1) 4%; (case_2) 2%; (case_3) 4%; and (case_4) 17%. Moreover, although the annual cooling energy consumption in case of using reflective glass case is lower than that when applying double wall with air cavity, but in the summer peak months (June, July, August, and September) it can be recognized, based on Table 1, the double wall achieves more reduction than using reflective glass only.

Accordingly, the carbon emissions inherit the same reduction characteristics in the four passive intervention cases as shown in table 2. Using double reflective glass possesses 132176 Kg CO_2 equ that represents 2% reduction than the base case. Applying double low-E glass emits 132532 Kg CO_2 equ, which is equal to 1.8% reduction than the base case. Utilizing both double low-E glass and double wall with air gap represents 1% reduction with 133860 Kg CO_2 equ. Finally, applying both double low-E glass and double wall with thermal insulation emits 122873 Kg CO_2 equ, which is equal to 9 % reduction than the base case.

The predictive mean value (PMV) is a metric used to indicate the degree thermal comfort achieved in a certain space. The value of this metric ranges from value of 3 to -3, and improvement in this metric takes place when its value tends to zero. Therefore, based on Table 3 and Figure 6, case 4 has the best PMV values than the other three cases and it improves the indoor thermal comfort than the base case through the twelve months of the year. Moreover, it can be recognized that applying double low-E glass achieves more improvement than using double reflective glass in the winter months.

Table 1. Monthly and annual cooling electricity.

	As Built	Case1 Wh/m^2	Case2 Wh/m^2	Case3 Wh/m^2	Case4 Wh/m^2
January	51	44	70	77	129
February	535	504	587	598	687
March	1692	1635	1813	1835	1994
April	6958	6704	7061	7020	6556
May	15711	15151	15482	15201	12929
June	17362	16699	16961	16579	13824
July	21015	20151	20441	20000	16619
August	20596	19798	20033	19577	16190
September	16924	16310	16623	16253	13648
October	11370	10973	11377	11158	9788
November	3976	3848	4105	4059	3988
December	323	312	356	360	428
Total	116513	112129	114908	112718	96779

Table 2. Monthly and annual CO_2 emissions equivalent.

	As Built	Case1 Kg equ.	Case2 Kg equ.	Case3 Kg equ.	Case4 Kg equ.
January	5680	5676	5696	5691	5727
February	5246	5227	5284	5277	5338
March	6208	6173	6295	6281	6391
April	9623	9469	9661	9686	9379
May	15170	14831	14861	15031	13484
June	15462	15060	14987	15219	13317
July	18384	17861	17769	18036	15720
August	17897	17414	17279	17556	15227
September	15430	15057	15023	15247	13444
October	12539	12299	12411	12543	11581
November	7583	7505	7633	7661	7590
December	5612	5605	5634	5631	5675
Total	134833	132176	132532	133860	122873

Table 3. Monthly Fanger PMV.

	As Built	Case1	Case2	Case3	Case4
January	-1.02	-0.99	-0.88	-0.85	-0.60
February	-0.57	-0.55	-0.46	-0.44	-0.30
March	-0.10	-0.09	-0.02	-0.02	0.04
April	-0.32	-0.33	-0.27	-0.27	-0.34
May	0.38	0.35	0.39	0.37	0.13
June	0.82	0.78	0.81	0.78	0.45
July	0.76	0.72	0.75	0.72	0.38
August	0.88	0.83	0.86	0.83	0.47
September	0.67	0.63	0.67	0.64	0.34
October	0.74	0.73	0.76	0.75	0.63
November	0.17	0.17	0.22	0.22	0.20
December	-0.68	-0.64	-0.56	-0.55	-0.34

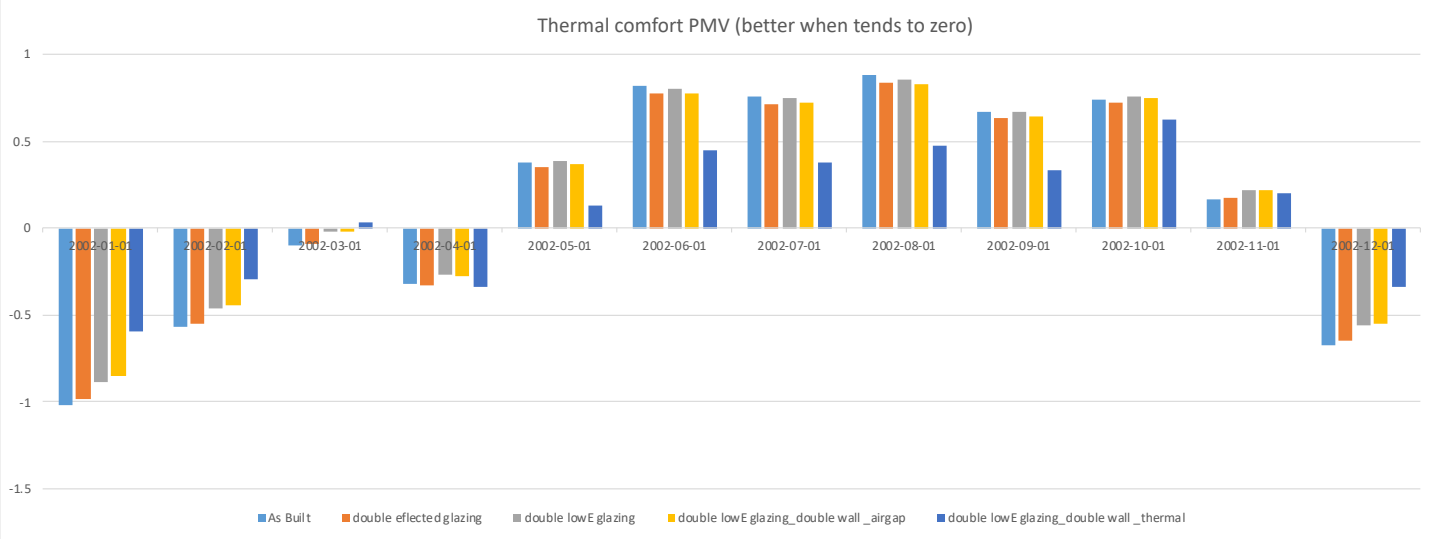

Figure 6. Fanger PMV thermal comfort.

V. CONCLUSION

As the heritage buildings has their significant character and added value to our today's architecture, also as the whole world stands hand in hand to achieve sustainability through our daily practices especially in building sector, the heritage buildings possess certain difficulties when they are required to conserve energy and enhance their indoor thermal comfort while preserving their architecture materials and character. Accordingly, this research introduced few passive architecture treatments to enhance the indoor thermal comfort, reduce energy consumption and minimize CO_2 emission. The four selected alternatives are 1) using double reflective glass, 2) using double low-R glass, 3) using double low-E glass with double wall and air gap, and 4) using double low-E glass with double wall and thermal insulation. The fourth alternative was able to achieve reduction in both required cooling energy and CO_2 emissions with percentages 17% and 9% better than the as built base case. However, these findings should be require in deep life cycle cost analysis to stand for the economic worth of these passive designs compared to the improvements in energy and thermal comfort.

VI. REFERENCES

[1] Al-Sakkaf, A., Zayed, T., Bagchi, A., Mahmoud, S., & Pickup, D. (2020). Development of a sustainability rating tool for heritage buildings: future implications. Smart and Sustainable Built Environment.

[2] Al-Sakkaf, A., Zayed, T. &, Bagchi, A. *"A Review of Definition and Classification of Heritage Buildings and Framework for their Evaluation"* The 2nd International Conference on New Horizons in Green Civil Engineering (NHICE-02), Victoria, British Columbia, Canada, August, 2020.

[3] Al-Sakkaf, A., Mohammed Abdelkader, E., El-Zahab, S., Zayed, T. & Bagchi, A. (2021) *"The Holistic Framework of Heritage Buildings Life Cycle Phases"*, The 1st International Conference on Fundamental, Applied Sciences and Technology (ICoFAST 2021).

[4] Al-Sakkaf, A., Zayed, T. &., Bagchi, A., & Abdelkader E. "Sustainability Rating Tool and Rehabilitation Model for Heritage Buildings", CSCE Annual Conference, Laval, Canada, 2019.

[5] Central Public Works Department (2013). *Handbook of Conservation of Heritage Buildings*, 104.

[6] Amber, K. P., Ahmad, R., Aslam, M. W., Kousar, A., Usman, M., & Khan, M. S. (2018). Intelligent techniques for forecasting electricity consumption of buildings. *Energy*, *157*, 886–893.

[7] DAWOUD, M.M. and ELGIZAWY, E.M., 2018. The correlation between art and architecture to promote social interaction in public space. In *Cities' Identity Through Architecture and Art*.

[8] DESIGNBUILDER, 2018. *DesignBuilder [Online], Available: http://www.designbuilder.co.uk. Accessed 21/4/2018.*

[9] FAHMY, M., M. MAHDY, and NIKOLOPOULOU, M., 2014. Prediction of future energy consumption reduction using GRCenvelope optimization for residential buildings in Egypt. *Energy and Buildings 70*, 186-193.

[10] Fayaz, M., Shah, H., Aseere, A., Mashwani, W., & Shah, A. (2019). A Framework for Prediction of Household Energy Consumption Using *Feed Forward Back Propagation Neural Network. Technologies*, 7(2), 1-16.

[11] Gao, W., Alsarraf, J., Moayedi, H., Shahsavar, A., & Nguyen, H. (2019). Comprehensive preference learning and feature validity for designing energy-efficient residential buildings using

machine learning paradigms. *Applied Soft Computing Journal*, 84, 1-23.

[12] Gassar, A. A. A., Yun, G. Y., & Kim, S. (2019). Data-driven approach to prediction of residential energy consumption at urban scales in London. *Energy*, 187, 1-13.

[13] JOKILEHTO, J., 2006. Considerations on authenticity and integrity in world heritage context. *City and time 2*, 1, 1-16.

[14] MAHMOUD, S., FAHMY, M., MAHDY, M., ELWY, I., and ABDELALIM, M., 2020. Comparative energy performance simulation for passive and conventional design: a case study in Cairo, Egypt. *Energy Reports 6*, 699-704.

[15] Mirrahimi, S., Mohamed, M. F., Haw, L. C., Ibrahim, N. L. N., Yusoff, W. F. M., & Aflaki, A. (2016). The effect of building envelope on the thermal comfort and energy saving for high-rise buildings in hot–humid climate. Renewable and Sustainable Energy Reviews, 53, 1508-1519.

[16] Mohammed Abdelkader, E., Al-Sakkaf, A., & Ahmed, R. (2020). A comprehensive comparative analysis of machine learning models for predicting heating and cooling loads. D*ecision Science Letters*, 9(3), 409–420.

[17] Turhan, C., Kazanasmaz, T., Uygun, I. E., Ekmen, K. E., & Akkurt, G. G. (2014). Comparative study of a building energy performance software (KEP-IYTE-ESS) and ANN-based building heat load estimation. *Energy and Buildings*, 85, 115–125.

[18] UNESCO, 2018. *World heritage statistic.* UNESCO.

[19] Chae, Y. T., Horesh, R., Hwang, Y., & Lee, Y. M. (2016). Artificial neural network model for forecasting sub-hourly electricity usage in commercial buildings. *Energy and Buildings*, *111*, 184–194.

[20] Jovanović, R., Sretenović, A. A., & Živković, B. D. (2015). Ensemble of various neural networks for prediction of heating energy consumption. *Energy and Buildings*, *94*, 189–199.

[21] Yu, Z., Haghighat, F., Fung, B. C. M., & Yoshino, H. (2010). A decision tree method for building energy demand modeling. *Energy and Buildings*, *42*(10), 1637–1646.

Integration of vanadium redox battery with PV systems: Modeling and simulation of Vanadium Redox flow batteries based on MATLAB/Simulink

Mohamed-Amine BABAY
Industrial engineering laboratory
Faculty of Science and Technologies,
Sultan Moulay Slimane University
Beni Mellal, Morocco
mdamine.babay@gmail.com

Mustapha ADAR
Industrial engineering laboratory
Faculty of Science and Technologies,
Sultan Moulay Slimane University
Beni Mellal, Morocco
Adar.mustapha@gmail.com

Mustapha MABROUKI
Industrial engineering laboratory
Faculty of Science and Technologies,
Sultan Moulay Slimane University
Beni Mellal, Morocco
Mus_mabrouki@yahoo.com

Abstract

Several models have been developed and they are now providing a good understanding of how VRB works. This knowledge is very important to evaluate its performance when applied in an electrical system. This article presents a new VRB model based an electrical equivalent model of VRFB, the effect of flow rate and pump power losses has been considered in modeling the VRFB. The VRFB is connected to a resistive variable load, for discharging and a system PV for charging. A control method for State of Charge (SOC) estimation is also proposed as it plays an important role in over-charge/discharge of VRFB. An equivalent electrical model of PV system including a VRB was implemented in MATLAB/Simulink environment to analyze the operational performance of the proposed system.

Keywords: Energy storage system, Vanadium Redox Flow Battery, State of Charge, Battery modeling, Solar PV, Flow rate

I. INTRODUCTION

Since the early 1970s, redox batteries have been extensively researched and several different redox pairs have been studied and reported in the literature. Only three of these systems have undergone some commercial development, namely the all-vanadium system (via VRB-ESS), the bromine-polysulphide system (RGN-ESS) and the zinc-bromine system (Powercell).

The vanadium bromine system has a high energy density so it can replace the all-vanadium system and can be used as an energy storage system for electric vehicles. Other redox flow battery systems due to slow electrochemical kinetics of redox torque, membrane fouling, cross contamination, high cost (mainly due to the membrane and battery design low efficiency), poor sealing, loss of bypass current and low and problematic energy capacity (due to the use of aqueous electrolytes). To date, one of the main factors limiting the further development of redox batteries is the high cost associated with ion exchange membranes.[1]

Alotto et al. [2]conducted a detailed study of the redox battery and described its development and future technical level. The first VRB model [3] parameterized the battery voltage, voltage loss, parasitic current loss, etc. [2]–[4]. But each of these studies is not effective in modeling the transient response, or is more complicated in the extended measurement of the parameters.

D'Agostino et al [5] tried to include the operating mode and start time in their VRB model and suggested that efficient management of electrolyte pumps would minimize losses and increase efficiency. Ontiveros and Mercado [6] proposed a new stacking model for VRB, which includes stacking efficiency and mechanical model to improve the accuracy of the VRB model and understand its operation. This paper implements a simplified VRB model that includes parasitic losses and takes into account the estimated voltage and state of charge of the battery in the solar system. The future energy system must be carefully designed to ensure energy reliability and security without being affected to insure the dynamic sustainability of the grid system.

Due to the intermittent nature of renewable systems, increasing permeability poses a huge challenge to the operation of the power grid.

However, due to growing global awareness of pollution and ozone depletion, most countries have chosen green energy policies, forcing technology providers to seek options for using and managing renewable energy without compromising grid supply and security.

The Energy Storage System (ESS) has become an indispensable partner for renewable energies, as it enables energy to be stored when it is available and supplied when the load requires it.

Many forms of energy storage have been developed, but the Battery Energy Storage System (BESS) is the most mature and developed technology in decades [7].

IEECP'21, July 29-30, 2021, Silicon Valley, San Francisco, CA – USA

DAI : ***https://sci-index.com/DAI/2021.99101/IEECP/14546805***

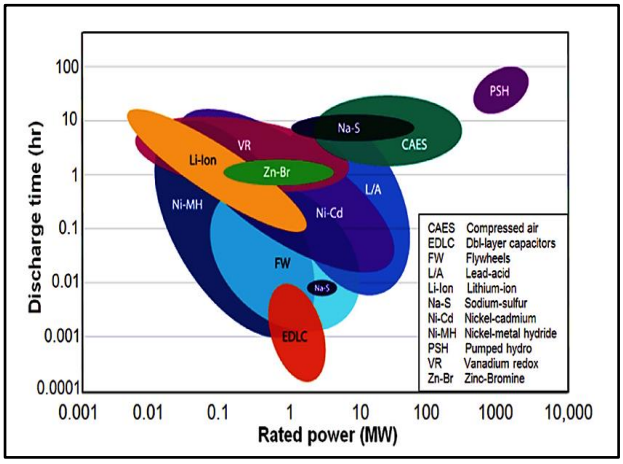

Figure 1:Power ratings and discharge times of various energy storage technologies. Reproduced by permission from American Chemical Society Z. Yang, J. Zhang, M.C. Kintner-Meyer, X. Lu, D. Choi, J.P. Lemmon, J. Liu, Chemical Reviews 111 (2011) 3577e3613. Copyright

The latest developments in battery technology have led to the development of flow batteries, which utilize features such as scalability and modularity in conventional electrochemical storage technologies. By storing the liquid electrolyte in a separate container outside the battery, they provide a better way to manage its energy capacity. If necessary, the electrolyte must be pumped into the battery containing the electrodes.

Therefore, this allows the system to have a large energy capacity independent of the power capacity of the battery module.

Further, advantages of VRFB are that they can operate over a wide range of power inputs and outputs; furthermore, VRFB can be completely discharged without damaging the battery [1], [8].

Beside the positive characteristics of the VRFB, electrochemical side reactions can occur during long-term operation leading to capacity fade due to diffusion, gas evolution, and air oxidation [9]. The capacity fade due to diffusion of vanadium ions through the membrane can simply be overcome by remixing the electrolyte in order to rebalance the ion concentrations [9].

Nevertheless, in terms of long-life cycle, the VRFB has an advantage due to the fact that the energy carrier, the electrolyte, can be restored and the peripheral components must be replaced after obsolescence. Over the last years, several VRFB models have been presented in the literature.

A detailed 2-D model of a single-cell battery based on mass, charge, and momentum laws is proposed by Shah et al. [10], to investigate the effects of variation ion concentration, electrolyte flow rate, and electrode porosity. This model is further extended to consider the evolution of oxygen and hydrogen [11], and to observe the effect of current density, electrode porosity, and local mass transfer coefficient on the cell performance [10]. Tang et al. [9] proposed a dynamic model of a single-cell battery to describe the capacity loss caused by diffusion and side reactions.

Such detailed models provide important insights for the development and improvement of the core components of VRFB, but they require more computational resources and may not be practical for long-term simulations at system level. At this level, models can be applied to optimize the battery design and fabrication as the model presented in [12] or to focus more on the application of VRFB in interaction with other energy systems [13].The two other side reactions cause a permanent imbalance of the electrolyte, which requires chemical or electrochemical rebalancing methods to restore the capacity.

Different types of flow batteries are now available, such as redox batteries, non-membrane batteries and hybrid batteries [14].

As the name suggests, the redox battery is characterized by the simultaneous redox reactions occurring in the electrodes of the battery cells. Many redox batteries have been developed, such as iron-chromium flow batteries, vanadium flow batteries, zinc bromide flow batteries, etc.

The redox battery is characterized by the simultaneous redox reactions occurring in the electrodes of the battery cells. In this study, the vanadium redox battery (VRB) was chosen because it is the most promising of all long-life redox batteries and offers considerable energy capacity without any heating problems.

Tableau 1:General comparison of static battery, redox flow cells and fuel cells [8]

Electrochemical device	Site of reactants/products	Electrolyte conditions	Separator
Static battery	Active electrode material	Static and held within cell	Microporous polymer separator
Redox flow cell	Aqueous electrolytes in reservoirs	Electrolyte-recycles through the cell	Ion-exchange membrane (cationic or anionic)
Fuel cell	Gaseous or liquid fuel plus air	Solid polymer or ceramic acts as solid electrolyte within cell	Ion-exchange membrane polymer or ceramic

The advantages of redox flow cells can be summarized in four features: moderate cost, modularity, transportability and flexible operation. Due to their modular design its construction and maintenance costs could be the lowest of any of the storage systems mentioned above. The redox flow batteries are well-suited for transmission and distribution deferral applications, where batteries might be transported from substation to substation or load center in order to provide local capacity needed to defer expensive upgrades [8] .

Tableau 2:Advantages and disadvantages of storage systems compared to redox flow cells[8]

Battery energy storage system	Advantages	Disadvantages	Redox system
Conventional systems	Well-known technology Low maintenance Low size	Frequent maintenance Heavy High construction cost Not portable Expensive technology	Flooded lead-acid battery Valve-regulated lead-acid (VRLA)
Developmental systems	Transportability High energy (charging) efficiency Flexible operation	Thermal management Difficult maintenance	Sodium/sulfur battery Zinc/bromine redox flow cell
Redox flow cells	Low cost Modularity Transportability Flexible Operation High efficiency Large scale	Newer technology	Bromine/polysulfide redox flow cell Vanadium redox flow cell Iron/chromium redox flow cell Zinc/cerium redox flow cell

II. VANADIUM REDOX FLOW BATTERY (VRFB)

The vanadium redox flux (VRB) battery is an electrochemical energy storage system based on a reversible chemical reaction in a sealed electrolyte. VRB are essentially comprised of two key elements: the cell stacks, where chemical energy is converted to electricity in a reversible process, and the tanks of electrolytes where energy is stored [6].

It consists of two electrolyte tanks, containing sulfuric acid electrolyte with active vanadium species in different oxidation states: $\mathbf{V_4}$ / $\mathbf{V_5}$ redox couple (positive) and $\mathbf{V_2}$ / $\mathbf{V_3}$ redox couple (negative).

Both electrolytes are circulated through the cell stack by pumps. The stack consists of many cells, each of which contains two half-cells that are separated by a proton exchange membrane (PEM)[6].

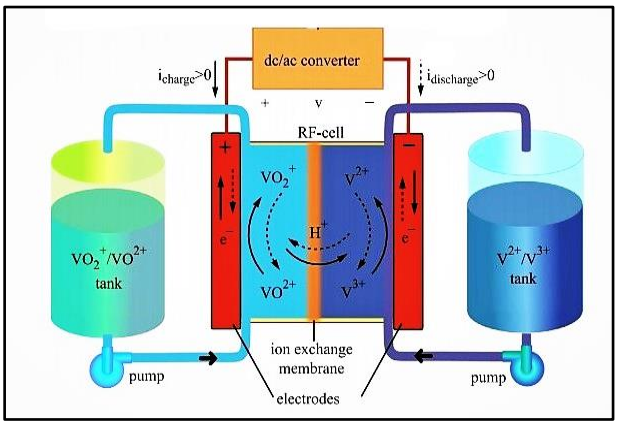

Figure 2:General Scheme of a Vanadium Redox Flow [2]

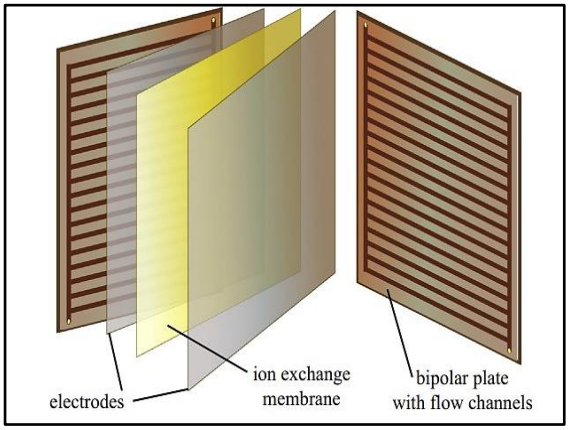

Figure 3:Typical configuration of a classical all-vanadium redox flow battery single cell [2]

In the half-cells the electrochemical reactions take place on inert carbon felt polymer composite electrodes from which an external direct current is used, in order to charge or discharge the battery. During discharge, electrons are removed from the negative electrode electrolyte (anolyte) and transferred to the positive electrode electrolyte (positive electrolyte) via an external circuit.

The flow of electrons is reversed during charging. Reduction occurs in the anolyte, while oxidation occurs in the catholyte [15].

The nominal potential produced by a single cell is about 1.35 V, depending on the concentration of vanadium. The terminal voltage is obtained by connecting several batteries in series in a "cell". The energy available is related to the battery voltage and the current density established by the battery and the energy available depends solely on the supply of electrolyte charged in the battery. Therefore, the power rating and stored energy can be easily increased by adding or reducing the battery and the electrolyte reservoir, respectively.

III. MODELING OF VRFBS: A NEW MODEL OF THE VRB STACK

A. Electrical Equivalent model of VRFB

The charging and discharging of VRFB involves chemical reactions in positive and negative half cells where the four electro-active states of Vanadium (V^{2+}, V^{3+}, V^{4+}, V^{5+}) are reversibly exchanged through oxidation and reduction process. During charging in the positive side, the V^{4+} (Basically oxide VO_{2+}) is converted into V^{5+} (Basically Oxide VO_{2+}) by oxidation and in the negative side V^{3+} is converted into V^{2+} by reduction reaction. The whole process takes place by exchange of proton through ion exchange membrane and subsequent removal of water molecule.

To estimate the electrode potential the of the two sides, VRFB positive half-cell equilibrium potential and negative half-cell equilibrium potential are considered as E^{0+} = 1.182 V [30] and E^{0-} = -0.207 V [16] at SHE (Standard Hydrogen Electrode) [17].

Thus, the cell equilibrium potential becomes E^0= 1.39 V [16] which is calculated by the difference between the equilibrium cell potentials of the two electrodes (positive and negative) expressed in Eq1:

$$E^0 = E^{0+} - E^{0-} \quad (1)$$

In the Nernst equation, SOC is the initial State of Charge which is defined as the capacity of energy stored in the electrolytes divided by the energy rating, n is the number of cells in the stack,

- V equilibrium is equal to the cell voltage at 50% SOC,
- F is the Faraday constant with the value of 96485C/mole,
- R is the universal gas constant with the value of 8.3145J/(K. mole),
- T is the temperature in the Kelvin scale.

Both parameters $R_{Reaction}$ and $R_{Resistive}$ compose the internal losses, which electrically reflect reaction kinetics, mass transport resistance, membrane resistance, solution resistance, electrode resistance and bipolar plate resistance.

The parasitic losses are presented by a constant resistance $R_{fixedloss}$ and a controlled current source I pump, which stands for the power consumption of the re-circulation pump, system controller, and power loss from cell-stack by-pass.

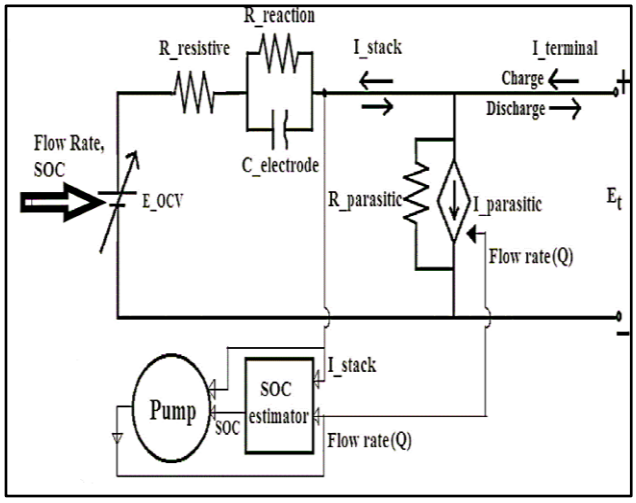

Figure 5: Faunctional schematic of the electrical equivalent model of a practical VRFB

In this model, the pump and the associated controller circuit losses (parasitic losses) are represented as a combination of controlled current source ($I_{Parasitic}$) and a shunt resistor ($R_{Parasitic}$) in the VRFB electrical equivalent model. Similarly, the self-discharge loss of VRFB is also represented in the model.

To understand the electrical equivalent circuit of a practical VRFB system, a schematic diagram is developed as shown in Fig. 5 where the electrical RC equivalent model is represented by typical Randles equivalent circuit. Based on the proposed schematic in Fig.5, an electrical characteristics model of VRFB system is developed in MATLAB/ Simulink environment as shown in Fig. 4.

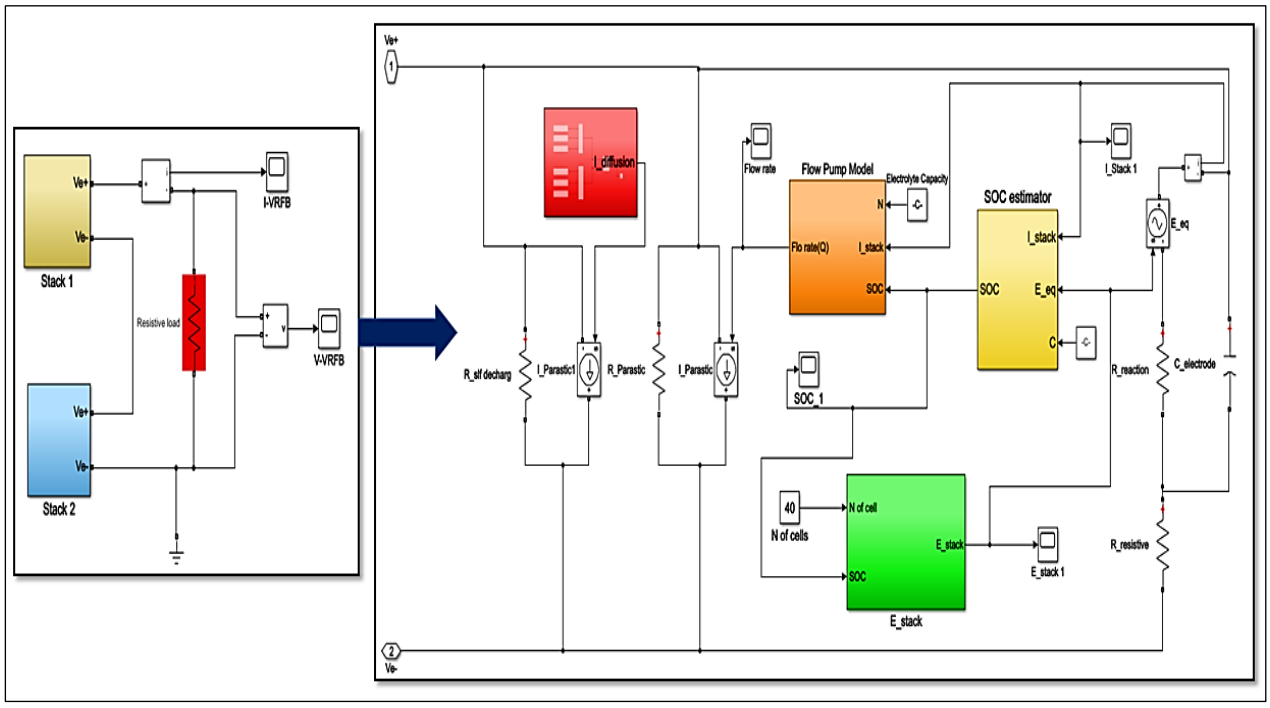

Figure 4:Generalised electrical characteristics model of a VRFB in MATLAB/Simulink

To analyze the whole model of the VRFB system it has been divided into three major subsystems namely

- E_{Stack} Estimator
- SOC Estimator and Stack Voltage estimation
- Flow Pump model

The proposed model has been constructed based on the following assumptions:

- Positive and negative side electrolytes are in chemically balanced condition.
- The pumps are not operational during the period when the battery is in the open circuit mode.
- VRFB Stack temperature and electrolyte temperature are almost constant (29–31C).

B. VRFB storage modeling

The VRFB stores chemical energy and generates electrical energy through redox reactions between vanadium ions dissolved in the electrolyte. The most important feature of the VRFB is its modularity of power (Watt) and energy (Watt-hour), which are independent of each other, so that they can be expanded independently depending on the PV solar energy and load capacity.

1) E_{Stack} Estimator

The basic idea of the VRFB stack estimation model is obtained from the Nernst potential equation. In equation (1) in section 1, the cell equilibrium potential was discussed on the basis of the two half-cell potentials (positive and negative).

To develop a model for estimating the open-circuit voltage of a battery, the equation Eq can be used. Calculate in more detail using the following equation (1).

In the positive electrode side:

$$E^{+} = E^{0+} - \frac{RT}{F}\ln\left\{\frac{[VO^{2+}]}{[VO_2^{+}][H^{+}]^2}\right\} \quad (2)$$

In the negative electrode side:

$$E^{-} = E^{0-} - \frac{RT}{F}\ln\left\{\frac{[V^{2+}]}{[V^{3+}]}\right\} \quad (3)$$

Where:

E^{+} = Positive electrode potential (Volts)

E^{-}= Negative electrode potential (Volts)

R = Universal gas constant (8.3144J K^{-1}. mol^{-1})

T = Ambient temperature (K)

$[VO^{2+}]$= Concentration of VO^{2+} (mol.L^{-1})

$[VO_2^{+}]$ = Concentration of VO_2^{+} (mol.L^{-1})

$[V^{2+}]$ = Concentration of V^{2+}(mol.L^{-1})

$[V^{3+}]$ = Concentration of V^{3+} (mol.L^{-1})

Now taking H^{+} concentration to be constant (Corcuera et al. [18] have assumed $[H^{+}]$ as 1 mol to eliminate its effect on the Nernst Potential).

According to the above assumptions, Eq (2) can be replaced by;

$$E^{+} = E^{0+} - \frac{RT}{F}\ln\left\{\frac{[VO^{2+}]}{[VO_2^{+}]}\right\} \quad (4)$$

Eq (2-4), the relation between Vanadium Concentration with the SOC is established to design a competitive model of cell equivalent voltage estimation.

During charging, the SOC increases with time and during discharging the reverse happens. Inside the positive half-cell the $[VO_2^{+}]$ increases during charging whereas $[VO^{2+}]$ reduces due to oxidation and inside the negative half cell the $[V^{2+}]$ increases during charging whereas $[V^{3+}]$ reduces due to reduction process.

During the discharge process, an inverse phenomenon occurs inside the two half-cells. Therefore, we can deduce the following relationship from the above phenomenon[18], [19] :

- Positive Half Cell:

$$[VO_2^{+}] = K * SOC[V] \text{ and } [VO^{2+}] = K * (1 - SOC)\,[V] \quad (5)$$

- Negative Half Cell:

$$[V^{2+}] = K * SOC[V] \text{ and } [V^{3+}] = K * (1 - SOC)[\,V] \quad (6)$$

Where:

k is proportionality constant and [V] is the total Vanadium concentration (mol.L^{-1})

From the Eqs. (5) and (6) we can finally establish the mathematical relationship between SOC and the equivalent cell Potential E_{Stack}:

$$E_{cell,eq} = E^{+} - E^{-} \quad (7)$$

$$E_{cell,eq} = E^{0+} - \frac{RT}{F}\ln\left\{\frac{1-SOC}{SOC}\right\} - E^{0-} - \frac{RT}{F}\ln\left\{\frac{SOC}{1-SOC}\right\} \quad (8)$$

$$E_{cell,eq} = E^{0+} - E^{0-} + \frac{2RT}{F}\ln\left\{\frac{SOC}{1-SOC}\right\} \quad (9)$$

Then the VRFB stack open circuit potential is calculated by:

$$E_{stack} = n * \left\{E_{cell,eq(at\ 50\%\ SOC)} + \frac{2RT}{F}\ln\left(\frac{SOC}{1-SOC}\right)\right\} \quad (10)$$

Where:

The cell equilibrium potential $E_{cell,eq}$= 1.39 V as mentioned in [18].

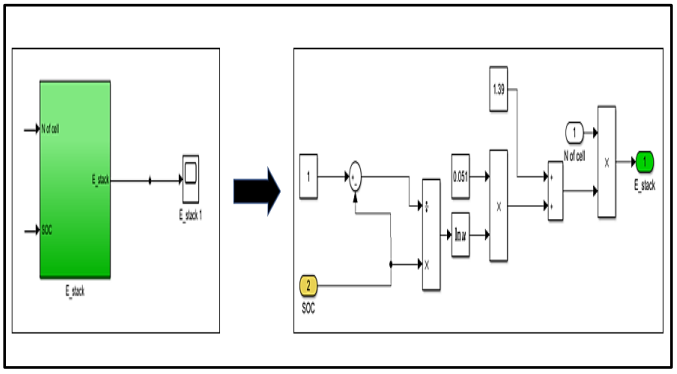

Figure 6: E_{stack} Schematics in Matlab/Simulink

2) Flow Pump model

The most important parameter to model the flow pump is the electrolyte flow rate (Q). The flow rate again depends on three factors namely Stack current (I_{Stack}), SOC (estimation model will be discussed) and electrolyte capacity (N).

The flow rate is directly proportional to Stack current (I_{Stack}) and inversely proportional to SOC and electrolyte capacity (N). The mathematical expression of flow rate (Q) based on which the pump has been modelled is given in Eq. (2):

$$Q = \frac{I_{Stack}}{N * SOC}\ cm^3 sec^{-1} \quad (11)$$

The electrolyte capacity (N) is also dependent upon some chemical parameters [20]expressed as :

$$N = n_e * c * F\ A\ s\ cm^{-3} \quad (12)$$

Where:

n_e = No. of electron transferred/mol

c = Vanadium concentration in the electrolyte (mol L^{-1})

F = Faraday's constant (96,485 C mol^{-1})

Here the total vanadium concentration (mol L^{-1}) is assumed to be constant as 1.6 mol L^{-1} for simulation.

Considering the pressure drop in flow pipes and the stack, head loss and finally the mechanical power consumption of the pump is calculated based on the equations and assumptions of Zhang et al.

The pump power loss and the pump controller circuit [21] losses are represented by a controlled current source ($I_{Parasitic}$) and a shunt resistance ($R_{Parasitic}$).

The pump internal resistance and the auxiliary control circuit resistance are clubbed into a single resistance which is approximated as 13.889V based on the literature of Barote et al. [22], [23].

The relation between the variables ($I_{Parasitic}$with I_{stack} and SOC) involved in the flow pump model subsystem is shown in Fig. 4.

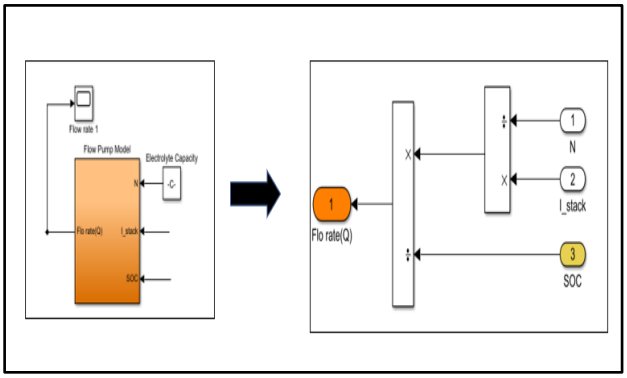

Figure 7:Flow Pump Model Schematic in Matlab/Simulink

3) State of Charge model (SOC)

The State of Charge of the Battery VRF is estimated by dynamically updating its value for every time step. The SOC of the system can be defined as seen in Eq. 13

$$SOC = \frac{\text{Current Energy in Battery}}{\text{Total Energy Capacity}} \quad (13)$$

SOC is changed based on the power delivered/absorbed by the cell stack. So, each time step the SOC is tracked it can use the previous SOC obtained to determine the future SOC value. The change in SOC is implemented as seen in [14, Eq. (14-16)].

$$SOC(t+1) = SOC(t) + \Delta SOC \quad (14)$$

$$\Delta SOC = \frac{\Delta E}{E_{capacity}} = \frac{I_{stack} * V_{stack} * t}{P_{rating} * t_{rating}} \quad (15)$$

$$\Delta SOC = I_{stack} * V_{stack} * C \quad (16)$$

The inputs are two variable parameters (I_{stack}; V_{stack}) and one constant block (C). With the help of a discrete time–integrator block in Matlab the SOC of the battery is accumulated and thus it is computed at each cycle based on the previous SOC, depending on the input values.

An important issue in battery modeling is transient behavior. The ability of the system to respond quickly to fast changes is especially important for power smoothing applications. In a VRB battery, the transient effects are related to electrode capacitance

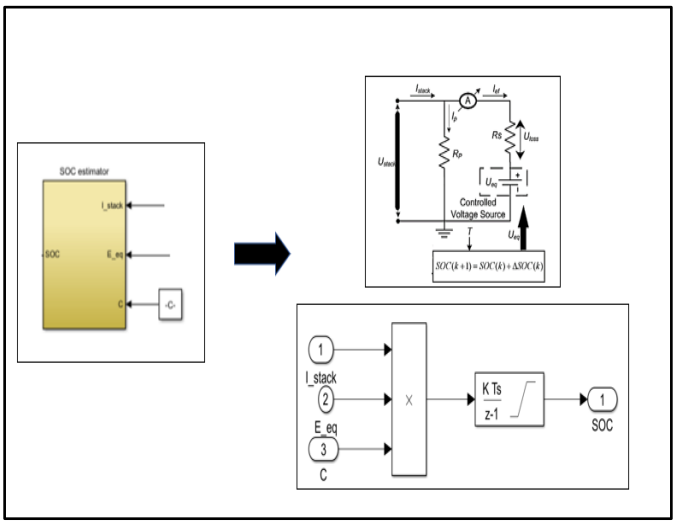

Figure 8:SOC Estimator Schematics in Matlab/Simulink

IV. SYSTEM CONFIGURATION

A. Model description

The proposed system model includes three main subsystems: solar PV panels, MPPT controller and DC-DC boost converter, VRFB storage.

1) Assumptions for Vanadium Redox Flow Battery

- Energy storage system has capacity of 10 kWh. The system contains two stacks with power rating of 1 kW each. Stack output voltage is 48 V
- Single cell voltage is 1.0 V, current density is at 0.1 A cm^{-1}, the bipolar plate thickness is 0.6 cm, and the end plate thickness is 10 cm.
- The cell voltage-current relationship is based on Nernst equation and the cell internal resistance. No activation over-potential and concentration over-potential are taken into consideration.

2) Battery Power Density and Energy Density

First, the stack volume was calculated. We assume a 10 kWh energy storage battery contains two stacks. Two stacks (N_{stack}=2) have power rating (P_{stack}) of 1 kW. Voltage of each stack (E_{stack}) is 48 V. Two stacks are connected in series. The stack current (I_{stack}) is:

$$I_{stack} = \frac{P_{stack}}{E_{stack} * N_{stack}} = \frac{1000}{48 * 2} = 10.4A \quad (17)$$

If the cell voltage of a single cell (E_{cell}l) is 1.0 V, then the number of cell (N_{cell}) in a stack to produce stack voltage of 48 V is:

$$N_{cell} = \frac{E_{stack}}{E_{cell}} = 48 \quad (18)$$

We assume the thickness of a bipolar plate is 0.6 cm and the thickness of endplate is 10 cm, then the stack length L_{stack} is:

$$L_{stack} = \left[L_{bipolar} * (N_{cell} + 1)\right] + \left(2 * L_{endplate}\right) \quad (19)$$

$$L_{stack} = 50\ cm \quad (20)$$

If the cell is operated at current density (i_{cell}) of 0.1 A cm^{-2}, then the cell cross section area (A_{stack}) is:

$$A_{stack} = \frac{I_{stack}}{i_{cell}} * 1.4 = 146\ cm^2 \quad (21)$$

Stack volume (V_{stack}) is:

$$V_{stack} = L_{stack} * A_{stack} = 7\ Liter \quad (22)$$

Total Volume of two stacks is 14 Liters.

The volume of electrolyte storage is calculated as follows. For a 100% discharge- charge battery, the volume of electrolyte ($V_{electrolyte}$) for positive electrode or for negative electrode can be calculated from equation (23).

$$C * V_{electrolyte} = \frac{I_{stack} * t_{charge}}{n_{rxn} * F} \quad (23)$$

Here "C" is the reactant concentration, "t_{charge} " is the charge time in seconds, "n_{rxn} " is the equivalent of reaction (n_{rxn}=1), and "F" is Faraday constant (96500 Coulomb/equivalent). For C = 2 M, the volume of electrolyte needed for 10 hr charge-discharge is 187 liters and the total electrolyte volume is 374 liters.

The volume of the stack is about 3.6% of the system. Majority of the battery volume is electrolyte. For a 10 kWh energy storage and 1 kW stack, the stack power density is 69 W/L and battery power density is 2.6 W/L. The battery energy density is 26 Wh/L.

3) PV PLANTS DESCRIPTION

A. Meteorological conditions

Fig. 9 shows the monthly ambient temperature and the monthly horizontal solar radiation. The reported average annual ambient temperature is 19.11°C. The recorded maximum value of temperature is 29.21 in July and the lowest value was 9.24°C in January. The monthly global horizontal irradiance ranged from 98.9 kWh/m^2 in January to 240.4 kWh/m^2 in July.

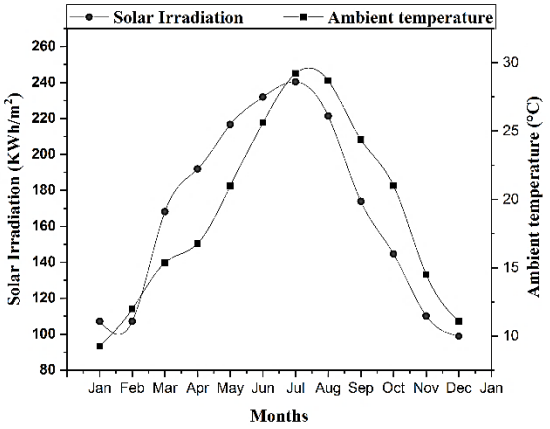

Figure 9: The monthly ambient temperature and horizontal solar radiation

The photovoltaic system was installed on the rooftop (Fig.10) of the Faculty of Science and Technology, Beni Mellal, Morocco. It consisted of three mini-stations of 2kWp photovoltaic for each one, distinguished by the three silicon technologies: Monocrystalline (mc-si), Polycrystalline (pc-si) and Amorphous (a-si). Each mini-station of both monocrystalline and polycrystalline types formed by eight panels of Sunmodule plus SW 255 Wp from Solarworld. The modules, which are included 60 solar cells connected in series, have a yield of 15% under standard test conditions [24].

Every string is connected to the 3-phase Sunny Boy 2500HF inverter. The Amorphous Silicon mini-station consists of 12 panels of NEXPOWER NT_155AF 155 Wp forming two strings joined in parallel. Each string is formed by connecting 6 modules in series. Both strings are linked to a 3-phase Sunny Boy 2500HF inverter. The unshaded modules were fixed with a tilt angle of 30°, facing south at an azimuth angle of 0°. [25]

More details can be illustrated in Table.3

Figure 10:The three PV plant

Tableau 3:Electrical characteristics

Modules	*mc-si*	*pc-si*	*a-si*
Module nominal power (W)	255	255	155
Module nominal open circuit voltage (V)	37.8	38	85.5
Module nominal voltage at maximum power (V)	31.4	30.9	65.2
Module nominal short circuit current (A)	8.66	8.88	2.56
Module nominal current at maximum power (A)	8.15	8.32	2.38
Temperature coefficient of power (per K)	-0.450%	-0.410%	-0.280%
Temperature coefficient open circuit voltage (per K)	-0.300%	-0.310%	-0.320%
Temperature coefficient short circuit current	0.004%	0.051%	0.070%

Tableau 4: Geographic coordinates, mean temperature and global horizontal irradiation

	Beni Mellal
Latitude	32°20' North
Longitude	6°21' West
Average temperature	23,47
Overall horizontal irradiation (kWh/m² /year)	2392,87

To extract maximum power from the solar PV array, Perturb and Observe algorithm is used for its simplicity in implementation. The algorithm performance is tested under a practical irradiance profile. A suitable DC-DC boost converter is designed in MATLAB/Simulink to track the maximum power from the solar PV array. The aim of maintaining high dc link voltage at the PCC (point of common coupling) is to minimize losses. The MATLAB/Simulink model of the DC-DC boost converter is shown in figure 11.

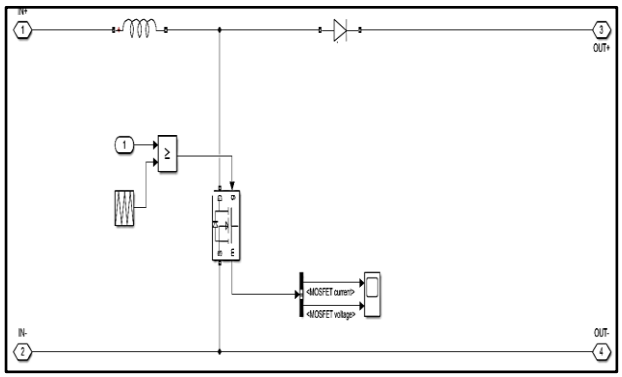

Figure 11:MATLAB/Simulink model of DC-DC boost converter

V. SIMULATION RESULTS AND DISCUSSION

The initial value of SOC of the battery was set to 90% as shown in figure 12. Since the battery is discharging through a 2.6 kW resistive load the SOC was dropped from 0.9 (initial set value) to 0.898 in a time interval of 2 sec.

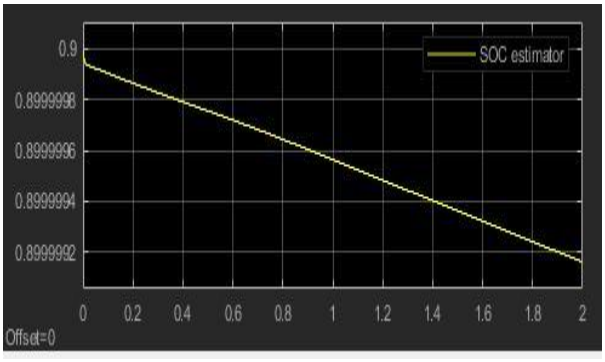

Figure 12:SOC of the VRF battery

At 90% SOC, the calculated stack1 voltage of the VRF battery from Eq. 10 was found to be 30.04 V which is same as shown in figure 8 and the stack1 voltage is discharged to a value of 30.01 V at 0.898 SOC as from the Eq.10.

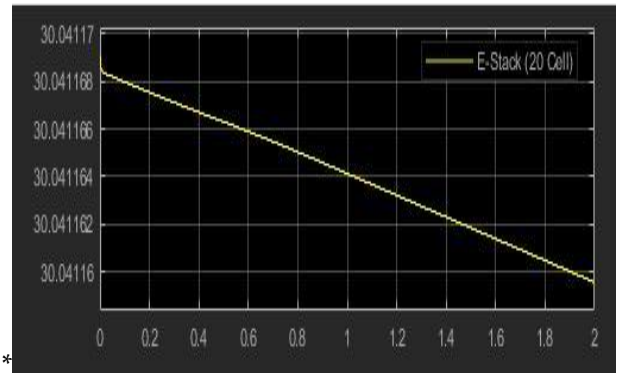

Figure 13: Stack Voltage of VRF Battery

The output voltage from the VRF battery is shown in figure 14. Its average value was found to be 28.217V.

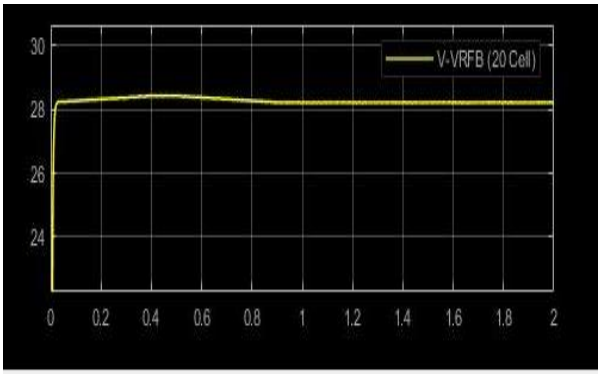

Figure 14: Output voltage of the VRF Battery

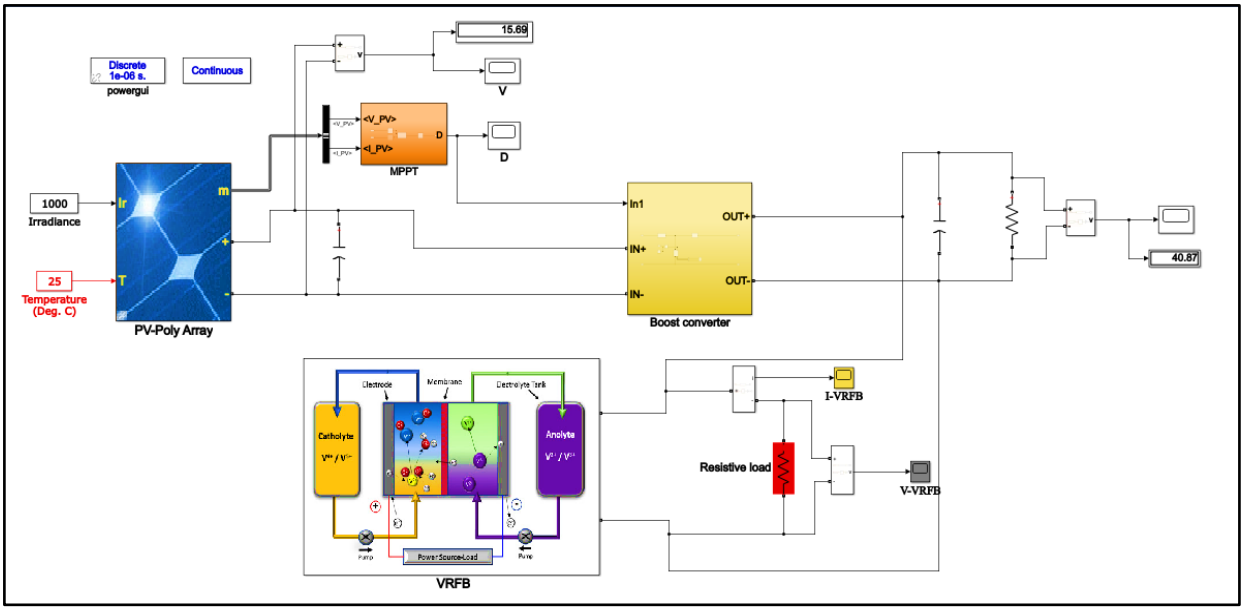

Figure 15:Schematic Schematic of the proposed system in MATLAB/Simulink

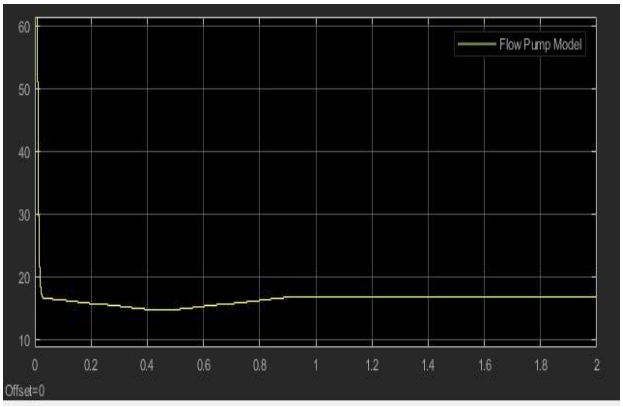

Figure 16:Flow rate pump

From the flow rate calculated from the flow pump model, the current absorbed by the current control source (I_parasitic) of stack 1 was found to be 0.23 A (calculated from Eq. 11) and the value of flow rate is 16.98 as shown in figure 16.

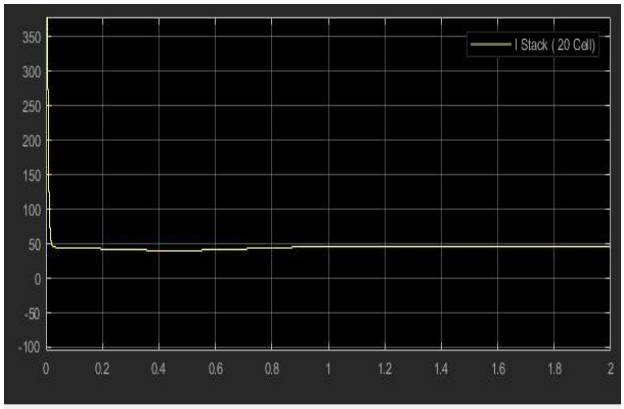

Figure 17:Load current of the VRF Battery

The VRF battery is discharged to supply 2.6kW power to the resistive load with a load current of 45.7A as shown in figure 17.

VI. CONCLUSION

The proposed work has demonstrated the performance of VRFB storage. The VRFB storage state of charge (SOC) is kept within an operating limit of 10% to 90% to avoid deep discharge and thus lengthening the battery lifetime.

This paper has successfully established a VRFB model in Matlab / Simulink environment considering the influence of flow rate, flow pump loss and parasitic loss. A SOC estimation technique for dynamic updating of the VRFB is proposed. The simulation results show that the VRFB can deliver 2.6 kW - 3.4 kW of active power to the resistive loads with a deviation of 0.063%. The simulated value matches the calculated value. The discharge characteristics of the VRFB, such as a decrease in SOC and the battery voltage transition over time, were also observed.

Resistive Load	N of Cell	I VRFB	V VRFB	E Stack	I Stack	Flow Rate pump
2.6 kW	10	14.8	14.23	15.02	19.76	7.318
	20	29.34	28.21	30.04	45.7	16.93
	30	43.91	42.23	45.06	70.9	26.26
	40	58.49	56.24	60.08	96.09	35.59
	50	73.06	70.25	75.1	121.3	44.92
3.4 kW	10	18.99	13.97	15.02	26.38	9.77
	20	37.66	27.69	30.04	58.83	21.79
	30	56.36	41.44	45.06	90.55	33.54
	40	75.06	55.19	60.08	122.3	45.28
	50	93.76	68.94	75.1	154	57.03

VII. ACKNOWLEDGMENTS

This work is supported by CNRST.

VIII. REFERENCES

[1] M. H. Chakrabarti, S. A. Hajimolana, F. S. Mjalli, M. Saleem, and I. Mustafa, "Redox Flow Battery for Energy Storage," *Arab. J. Sci. Eng.*, vol. 38, no. 4, pp. 723–739, 2013.

[2] P. Alotto, M. Guarnieri, and F. Moro, "Redox flow batteries for the storage of renewable energy: A review," *Renew. Sustain. Energy Rev.*, vol. 29, pp. 325–335, 2014.

[3] F. T. Wandschneider *et al.*, "Model of a vanadium redox flow battery with an anion exchange membrane and a Larminie-correction," *J. Power Sources*, vol. 272, pp. 436–447, 2014.

[4] M. H. Li, T. Funaki, and T. Hikihara, "A study of output terminal voltage modeling for redox flow battery based on charge and discharge experiments," *Fourth Power Convers. Conf. PCC-NAGOYA 2007 - Conf. Proc.*, pp. 221–225, 2007.

[5] R. D'Agostino, L. Baumann, A. Damiano, and E. Boggasch, "A Vanadium-Redox-Flow-Battery Model for Evaluation of Distributed Storage Implementation in Residential Energy Systems," *IEEE Trans. Energy Convers.*, vol. 30, no. 2, pp. 421–430, 2015.

[6] L. J. Ontiveros and P. E. Mercado, "Modeling of a Vanadium Redox Flow Battery for power system dynamic studies," *Int. J. Hydrogen Energy*, vol. 39, no. 16, pp. 8720–8727, 2014.

[7] A. H. Fathima and K. Palanismay, "Modeling and Operation of a Vanadium Redox Flow Battery for PV Applications," *Energy Procedia*, vol. 117, pp. 607–614, 2017.

[8] C. Ponce de León, A. Frías-Ferrer, J. González-García, D. A. Szánto, and F. C. Walsh, "Redox flow cells for energy conversion," *J. Power Sources*, vol. 160, no. 1, pp. 716–732, 2006.

[9] A. Tang, J. Bao, and M. Skyllas-Kazacos, "Dynamic modelling of the effects of ion diffusion and side reactions on the capacity loss for vanadium redox flow battery," *J. Power Sources*, vol. 196, no. 24, pp. 10737–10747, 2011.

[10] N. Gurieff, D. F. Keogh, V. Timchenko, and C. Menictas, "Enhanced reactant distribution in redox flow cells," *Molecules*, vol. 24, no. 21, 2019.

[11] A. A. Shah, H. Al-Fetlawi, and F. C. Walsh, "Dynamic modelling of hydrogen evolution effects in the all-vanadium redox flow battery," *Electrochim. Acta*, vol. 55, no. 3, pp. 1125–1139, 2010.

[12] A. Tang, J. Bao, and M. Skyllas-Kazacos, "Thermal modelling of battery configuration and self-discharge reactions in vanadium redox flow battery," *J. Power Sources*, vol. 216, pp. 489–501, 2012.

[13] B. Turker, S. Arroyo Klein, E. M. Hammer, B. Lenz, and L. Komsiyska, "Modeling a vanadium redox flow battery system for large scale applications," *Energy Convers. Manag.*, vol. 66, pp. 26–32, 2013.

[14] A. Z. Weber, M. M. Mench, J. P. Meyers, P. N. Ross, J. T. Gostick, and Q. Liu, "Redox flow batteries: A review," *J. Appl. Electrochem.*, vol. 41, no. 10, pp. 1137–1164, 2011.

[15] C. Blanc and A. Rufer, "Optimization of the operating point of a vanadium redox flow battery," *2009 IEEE Energy Convers. Congr. Expo. ECCE 2009*, pp. 2600–2605, 2009.

[16] M. Skyllas-Kazacos and M. Kazacos, "State of charge monitoring methods for vanadium redox flow battery control," *J. Power Sources*, vol. 196, no. 20, pp. 8822–8827, 2011.

[17] A. Bhattacharjee and H. Saha, "Design and experimental validation of a generalised electrical equivalent model of Vanadium Redox Flow Battery for interfacing with renewable energy sources," *J. Energy Storage*, vol. 13, pp. 220–232, Oct. 2017.

[18] S. Corcuera and M. Skyllas-Kazacos, "State-of-Charge Monitoring and Electrolyte Rebalancing Methods for the Vanadium Redox Flow Battery," *Eur. Chem. Bull.*, vol. 1, no. 12, pp. 511–519, 2012.

[19] C. Blanc and A. Rufer, "Understanding the Vanadium Redox Flow Batteries," *Paths to Sustain. Energy*, no. November 2010, 2010.

[20] C. Blanc, "Modeling of a vanadium redox flow battery electricity storage system," Jan. 2009.

[21] T. A. Nguyen, M. L. Crow, and A. C. Elmore, "Optimal sizing of a vanadium redox battery system for microgrid systems," *IEEE Trans. Sustain. Energy*, vol. 6, no. 3, pp. 729–737, 2015.

[22] C. Blanc *et al.*, "Modeling and Operation of a Vanadium Redox Flow Battery for PV Applications," *J. Power Sources*, vol. 13, no. 2, pp. 607–614, 2015.

[23] L. Barote and C. Marinescu, "A new control method for VRB SOC estimation in stand-alone wind energy systems BT - 2009 International Conference on Clean Electrical Power, ICCEP 2009, June 9, 2009 - June 11, 2009," no. 22134, pp. 253–257, 2009.

[24] M. Adar, Y. Najih, M. Gouskir, A. Chebak, M. Mabrouki, and A. Bennouna, "Three PV plants performance analysis using the principal component analysis method," *Energy*, vol. 207, 2020.

[25] M. Adar, H. Bazine, Y. Najih, C. Bahanni, M. Mabrouki, and A. Chebak, "Simulation study of three PV systems," *Proc. 2018 6th Int. Renew. Sustain. Energy Conf. IRSEC 2018*, 2018.

Vibration Characterizations of motor-gear-rotor system with considering the lateral-torsional-axial coupling effect

Wenyu Bai
College of Mechanical Engineering
Zhejiang University of Technology
HangZhou,PR China
bauyo@zjut.edu.cn

Hongyu Xi
College of Mechanical Engineering
Zhejiang University of Technology
HangZhou,PR China
15157655293@163.com

Xiaohang Zhang
College of Mechanical Engineering
Zhejiang University of Technology
HangZhou,PR China
1277574786@qq.com

Zhouxin Wu
College of Mechanical Engineering
Zhejiang University of Technology
HangZhou,PR China
WZX16JY@outlook.com

Linbin Zhang
College of Mechanical Engineering
Zhejiang University of Technology
HangZhou,PR China
lbz@zjut.edu.cn

Abstract

To investigate the dynamic responses of high-speed motor-gear transmission system in the electric vehicle, the non-linear coupled lateral-torsional-axial vibration model of motor-gear-rotor coupling system is developed based on the engagement of gears under various excitations. Firstly, the electromagnetic radial and tangential forces of the permanent magnetic synchronous machine are analyzed by finite element method, and the influences of the extracted electromagnetic radial and tangential force with considering the slot effect and magnetic saturation effect is presented. Furthermore, the dynamic characteristics of the motor-gear-rotor coupling system with the effects of the time-varying mesh stiffness, electromagnetic excitations and gear eccentricity are analyzed. The simulation results reveal the phenomenon that torsional vibration displacements are larger than those in lateral and axial directions, which is more obvious than the model without motor coupling. Meanwhile, the vibrations due to the time-varying mesh stiffness, gear eccentricity, slot effect and magnetic saturation effect are distinguished at different operation speed. Additionally, nonlinear motions are observed due to the electromagnetic excitations, including limit cycles and jumping phenomena for the motor rotor and gears. The research results lay a foundation for dynamic characteristics and fault diagnosis of the high-speed motor-gear transmission system for the electric vehicle.

Keywords: Motor-gear-rotor system; Electromagnetic excitations; Time-varying mesh stiffness; Dynamic vibrations

Introduction:

Permanent magnet synchronous motors (PMSM) have been widely used in electric vehicles (EV) because of its inherent quietness and high efficiency. The NVH problem of electric vehicles includes not only the Permanent magnet synchronous motors, but also the gearbox. The powertrain of an electric vehicle is shown in Figure 1, And a mechanism diagram suitable for electric vehicle powertrain is shown in Figure 2. The fixed coordinate system Ai-xiyizi(i=1,2) is established in the ideal center Ai of the driving and driven gear, and the fixed coordinate system Bi-xiyizi(i =1~4) is established in the ideal center Bi of the bearing. The rotation center coordinates of the main and driven gears are O1(x1, y1, z1) and O2(x2, y2, z2) respectively, and the centroid coordinates are G1(x_{g1}, y_{g1}, z_{g1}) and G2(x_{g2}, y_{g2}, z_{g2}). And the dynamic meshing model of the gear rotor system is shown in Fig. 3.

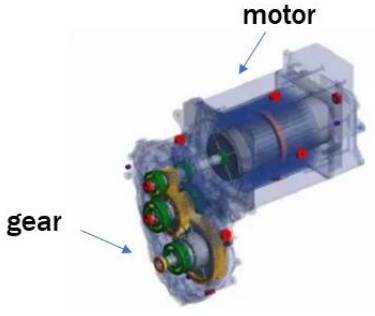

Fig. 1. Structure of the electric powertrain.

IEECP'21, July 29-30, 2021, Silicon Valley, San Francisco, CA – USA

D!f: https://sci-index.com/DAI/2021.99101/IEECP/14737983

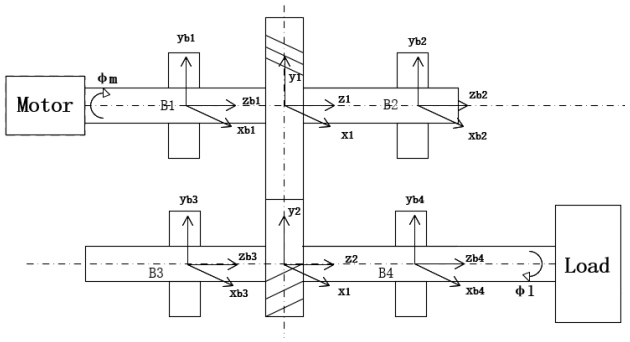

Fig. 2. Gear - rotor transmission system static model.

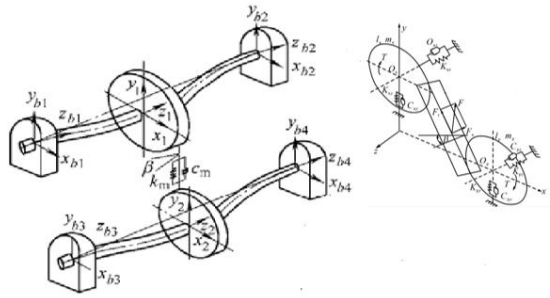

Fig. 3. Dynamic model of gear-rotor transmission system.

Results:

1.Using JMAG-Designer 2D finite element simulation, the torque curve of motor is extracted, as shown in Figure 1. And the extracted torque will act on the non-linear coupled lateral-torsional-axial vibration model, the subsequent simulation will also confirm the coupling effects between motor and gear.

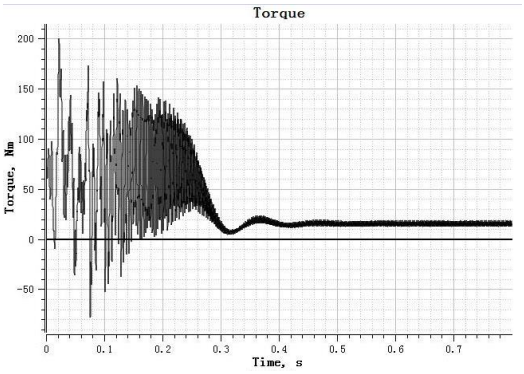

Fig. 4. Motor torque curve.

2. In this paper, the vibration response of the system is preliminarily calculated when the speed of the driving gear is n1=1485r/min. The motor - gear coupling effects are the most obvious on bearing b1, and the vibration displacements in three directions of bearing b1 are analyzed here. Fig. 5, Fig. 6 and Fig. 7 respectively show the displacements in X, Y and Z directions.

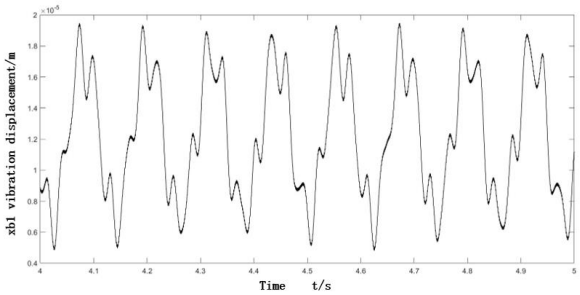

Fig. 5. No1 bearing displacement curve in X direction.

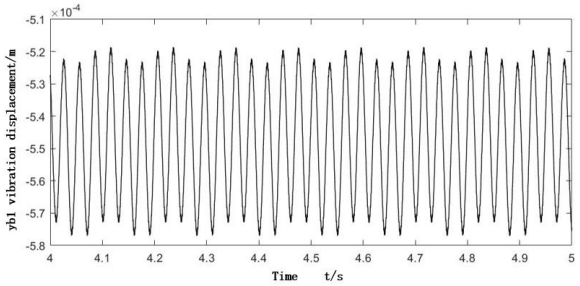

Fig. 6. No1 bearing displacement curve in Y direction.

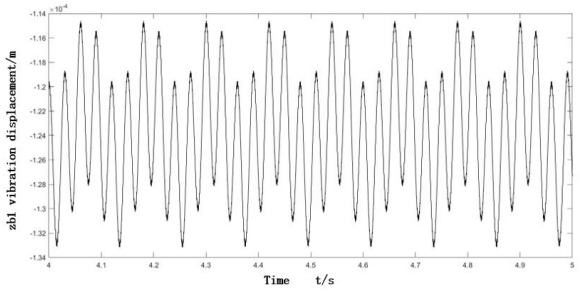

Fig. 7. No1 bearing displacement curve in Z direction.

3. Limit cycles and jump phenomena for the motor rotor and gears are analyzed in this paper. Due to the coexistence of electromagnetic excitations and bearing excitations, jump phenomena will appear. As the non-linear coupled lateral-torsional-axial vibration model is a nonlinear system, the motion characteristics of drive shaft gear center is shown in Fig. 8, the driving gear vibration are clearly dominated by the nonlinear limit cycle motion induced by the magatic motor forces and bearing excitations.

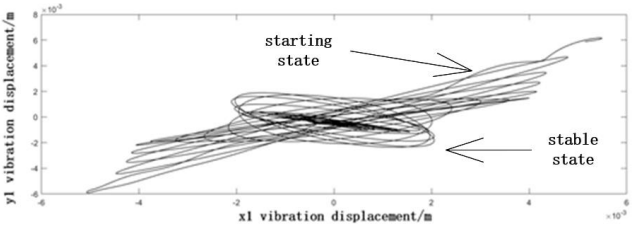

Fig. 8. Limit cycle motion.

Conclusion:

1. Compared with other models, the non-linear coupled lateral-torsional-axial vibration model takes more

nonlinearity factors into account. Due to the lateral-torsional coupling effects of helical gear system, the torsional vibration displacement in the transmission system is obviously larger than the lateral and axial vibration displacement. With the increasing of speed, the vibration displacement increases significantly, and the frequency amplitude fluctuates obviously.

2. Nonlinear motions are observed due to the electromagnetic excitations, including limit cycles. Limit cycle vibrations occur in this model, the results due to the dominance of the tangential component of the dynamic magnetic force over the bearing damping.

3. Further research will be conducted of the nonlinear phenomena of the electric driving system, and the corresponding results of this research can be applied to electric driving system of vehicles.

Highlights：

1. The influences of the extracted electromagnetic radial and tangential force with considering the slot effect and magnetic saturation effect is presented.
2. The dynamic characteristics of the motor-gear-rotor coupling system with the effects of the time-varying mesh stiffness, electromagnetic excitations and gear eccentricity are analyzed by the new coupling model.
3. Nonlinear motions are observed due to the electromagnetic excitations, including limit cycles and jumping phenomena for the motor rotor and gears.
4. The results of this research can be applied to electric vehicles.

First Author

Wenyu Bai is currently a lecturer at the college of mechanical engineering, Zhejiang University of Technology, Hangzhou, China. He received his B.S. degree, M.S. degree and Ph.D. degree of mechanical engineering from Chongqing University, China. From 2016 to 2018, he was a visiting Ph.D. student at the University of Cincinnati and the University of Texas at Arlington, USA sponsored by China Scholarship Council. His research interests include, electric drive system design, manufacturing and dynamics analysis.

RESEARCH OF THE PURCHASING ABILITY POPULATION OF THE KYRGYZ REPUBLIC IN PURCHASING POWER PLANTS BASED ON RENEWABLE ENERGY SOURCES

Kenzhaev Idirisbek Gulamovich
doctor of technical sciences, professor,
Osh State University, Kyrgyz Republic, Osh
e-mail: kenjaevig@rambler.ru

Sultanov Sayit Kozhonovich
candidate of technical sciences, docent,
Osh State University, Kyrgyz Republic, Osh
e-mail: sait65@rambler.ru

Tursunbaev Zhanbolot Zhanyshovich
candidate of technical sciences, docent ,
Osh State University, Kyrgyz Republic, Osh
e-mail: janbolot.72@rambler.ru

Mendibaev Damirbek Abiybillaevich
teacher,
Osh State University, Kyrgyz Republic, Osh
e-mail: damirbekmd@gmail.com

Abstract: *The problem of the purchasing power of the population plays a dominant role in the economy of the republic as a factor influencing the number of important indicators of the country. The results of this work are given in this work. authors of studies on the definition of the dynamics of development of the living standards of the population of the Kyrgyz Republic for the last 20 years. It is clear that under the conditions of a low level of national income per capita, a large value has a reduction in the cost of impact on energy installations. It is also established that the main criterion for the wide realization of energy installations among the population is an increase in the share of energy produced by installations based on renewable energy sources in the overall energy balance.*

Keywords: budget, income, power plants, energy, renewable energy sources, life level.

1. INTRODUCTION

The National Development Program of the Republic of Kyrgyzstan provides for an increase in the level and quality of life of citizens by ensuring sustainable economic growth leading to the creation of conditions for full employment of the population, receiving high and stable incomes, the availability of a wide range of social services, compliance with high living standards in a favorable health and environment [1-3].

The most important indicator characterizing the state of living standards of the population and the labor market is wages. In 2020 the average monthly nominal wage increased by 4.9 percent compared to the previous year. Real wages in 2020 compared to 2015 increased by 20.1 percent, with an increase in the average monthly nominal wages for this period by almost 1.3 times. According to the results of an integrated sample survey of household budgets and labor force, annually conducted in all regions of the republic, in 2020. monetary incomes per capita in nominal terms were 1.4 times higher than in 2015. As in previous years, the most important source in the formation of monetary income is income from labor activity, both in urban settlements (77.9 percent) and in rural areas (65.3 percent). The second most important source in the income formation of the population living in rural areas was income from the sale of products of personal subsidiary plots, the share of which decreased from 21.9 percent in 2015 to 15.2 percent of all income in 2020. The share of social transfers in the structure of the population's income decreased from 16.2 percent in 2015. up to 15.8 percent - in 2019. The share of consumer spending in the structure of cash expenditures in 2019 accounted for 84.5 percent, payment of taxes - 8.6 percent, other expenses - 6.9 percent. These data were obtained through an integrated sample survey of household budgets of Kyrgyzstan.

Over the past five years in the social sphere of the state, there has been a noticeable increase in the main indicators of the standard of living of the population. So, in 2015-2020 per capita money income of the population of Kyrgyzstan, according to a sample survey of household budgets, increased 1.4 times.

Kyrgyzstan belongs to the developing countries, i.e. reducing property inequality is one of the most important areas for improving the standard of living, since at present in the republic there is a high level of stratification of the population by property and social characteristics. Over the past five years, the number of the poor in the republic has decreased from 50% in 2003 to 25.6% in 2018. This trend is encouraging to move towards progress.

The standard of living of the population of the Kyrgyz Republic over the years of sovereignty has been characterized ambiguously [1]. The general standard of living of the population is influenced by the gross domestic product per capita, the consumer price index, the deficit (surplus) of the state budget and their dynamics (table 1).

Table 1. Ratio of growth (decline) rates of gross domestic product, consumer price index and budget deficit (surplus) of the Kyrgyz Republic

№	Indicators	1995	2000	2005	2010	2015	2020
1	Growth (decline) in gross domestic product per capita	12	9,5	10,0	-0,5	5,1	5,6
2	Consumer goods and services price index	76	101,8	95,8	101,7	106,5	101,5
3	Deficit (surplus) of the budget	-	-	0,86	18,5	4,8	4,2

DAI : *https://sci-index.com/DAI/2021.99101/IEECP/14737980*

Along with the purchasing power of the population, the standard of living also depends on the level of poverty of the population. At present, poverty is not amenable to precise definition; a family lives in poverty when its basic needs exceed the means available to meet its needs. In recent years, there has been some progress in overcoming poverty.

Unfortunately, the growth of incomes of the population does not yet provide normal standard consumption. In this regard, it would be advisable to find new non-traditional ways to improve the standard of living, based on real and substantiated principles of improving the social situation of the population.

The minimum consumer budget for a month, established by the Decree of the Government of the Kyrgyz Republic dated August 30, 2018, was 7492.6 soms per person, while per capita income in the same year was 4739.4 soms, i.e. the lack of the size of the consumer budget per capita indicates the need to increase the level of consumption (in prices of the National Bank of the Kyrgyz Republic as of April 15, 2021 at the rate of $ 1 = 84.80 soms). The main welfare of the population is housing and providing it with vital equipment.

In rural areas, more than 90% of families live in separate apartments or single-family houses. At the same time, the quality of living conditions in most settlements does not correspond to modern requirements, i.e. low level of arrangement of utilities (hot water supply, electrification, gasification, untreated drinking water, etc.).

In raising the standard of living of the population, an important place is given to employment and the reduction of unemployment. Employment is the provision of work for the able-bodied population, the creation of an opportunity to earn a living and the maintenance of the labor initiative of citizens, assistance and encouragement in the development of their ability to productive creative work.

The state of employment directly affects the income of the population, the structure of which, depending on the type of activity of people, can change (wages, income from entrepreneurial activity, social transfers, receipts from the sale of agricultural products, feed, livestock, income from property and other cash receipts). According to the data of the National Statistical Committee of the Kyrgyz Republic, the average per capita income in households is shown in table 2.

Table 2. The structure of workers 'and employees' incomes in 1995-2020 (in %)

Income indicators	1995	2000	2005	2010	2015	2020	2020 by 1995, in %
Cash income	100	100	100	100	100	100	100
including:							
1. Remuneration	42,1	39,5	61,0	61,4	64,9	69	164,3
2. Social transfers	18,4	8,3	9,4	13,6	16,2	16,4	89,1
3. Property income	1,5	1,5	-	-	0,6	0,5	33,3
4. Income from the sale of agricultural products	37,4	50,2	19,7	17,3	14	10	26,7
5. Others	0,6	0,5	9,9	7,7	4,3	4,1	683

As you can see from the table. 2, in recent years, income from labor activity has grown 1.6 times, and other incomes - 6-7 times.

Cash income of the population is spent mainly (about 80%) on consumer spending - the purchase of food, industrial goods and payment for services, tax. The rest of the costs are distributed between the costs of purchasing livestock, poultry, agricultural implements, fodder and other means for running a personal subsidiary farm.

Consequently, in the current prevailing socio-economic conditions, the involvement of renewable energy sources in the overall balance of energy consumption is of great economic and social importance for Kyrgyzstan.

However, for these reasons, the widespread implementation of expensive metal installations and a tangible solution on this basis to energy, economic and social problems in Kyrgyzstan is impossible.

2. METHODOLOGICAL BASIS OF RESEARCH

Analysis of the data shows that the level of well-being of the population is also characterized by the provision of durable items for cultural and household and economic purposes. This indicator indirectly reflects the level of well-being of the household and its cash income for a certain period of time. According to the survey, in 2020. on average, there were 111 televisions, 92 refrigerators, 79 washing machines, 14 tape recorders and 39 electric vacuum cleaners per 100 households. On average, each household had two cell phones and one in four had a car. Half of all items of cultural, household and economic purposes were things with a service life of up to 10 years, which include computers, television and radio equipment and electrical household appliances. Durable items such as furniture and vehicles had a lifespan of more than 10 years.

The above data allows us to conclude that the population of Kyrgyzstan is able to purchase and use for economic needs power plants of small capacities operating on renewable energy sources.

Therefore, the development of inexpensive installations based on renewable energy sources and their widespread implementation among the population is of great importance.

As you know, the annual energy demand (E) of the country can be estimated by the expression [2]

$$E = E_o N \quad (1)$$

where $E_o -$ is the average energy consumed by one person; N - is the number of inhabitants of the country.

The average energy consumed by one person here includes the energy needed in the production sector, in the service sector and in everyday life. The standard of living in the country, which obviously depends on the average energy consumed by one person, can be, as a first approximation, estimated by the value of the national income (S) per capita:

$$S = f_1 E_o \quad (2)$$

where f_1 - is a coefficient, a non-linear function of many parameters. It can be seen as the efficiency of using energy for the production of living goods. Therefore, it is desirable that its value be as large as possible.

From (1) and (2) we get:

$$E = \frac{1}{f_1} SN \quad (3)$$

The above expression refers to energy derived from conventional sources.

When using renewable energy sources along with traditional sources, the consumed energy consists of energy from traditional sources E_{tr} (electricity, coal, oil products, natural gas, etc.) and from renewable sources E_v (solar, wind energy, biomass energy, etc.) [4-13]

$$E = E_{tr} + E_v \quad (4)$$

In turn, E_v can be considered as the energy generated by the used installations on renewable sources:

$$E_v = nE_u \quad (5)$$

where n - is the total number of used (sold) installations on renewable sources; E_u- average (conditional) energy generated by one conditional installation.

If C_o is the cost of one conventional installation on renewable sources, which generates a conventional value of energy E_u, then the total cost of all installed installations will be nC_o.

Obviously, the total number of implemented installations is also proportional to the national income:

$$nC_o = f_2 S \quad (6)$$

$$n = f_2 \frac{S}{C_o} \quad (7)$$

where f_2- is a coefficient, also a non-linear function of many parameters and depending on the popularity of solar power plants among consumers, their competitiveness with devices based on traditional energy sources. Then

$$E_v = f_2 \frac{S}{C_o} E_u \quad (8)$$

So, the total amount of energy consumed by the country will be equal to

$$E = E_{tr} + E_v = \frac{1}{f1} SN + f_2 \frac{S}{C_o} E_u$$

$$E = S\left(\frac{1}{f1} N + f_2 \frac{1}{C_o} E_u\right) \quad (9)$$

Expression (9) considers the cost of power plants installed in renewable energy sources, as well as the possibility of population settlements in the acquisition of these facilities for household needs.

3. EXCLUSIONS

Thus, from this expression, we can draw the following conclusion that in conditions when the level of national income per capita S is low, it is of great importance to reduce the cost of solar plants C_o in order to make them widely sold among the population and increase the share of energy generated by renewable sources E_v in the overall balance of energy consumption.

4. GRATEFULNESS

The authors express their gratitude to the National Statistical Committee of the Kyrgyz Republic for the results of statistical analysis, which were used in the performance of current work and reviewers for their positive assessment.

5. REFERENCES

[1]. The standard of living of the population of the Kyrgyz Republic. National Statistical Committee of the Kyrgyz Republic. Annual publication, Bishkek - 1995-2020.

[2]. Medvedev V.A., Abalkin L.I., Ozherelyev O.I. and others. Political economy: Textbook for universities - M.: Politizdat, 1990. - 735 p.

[3]. Avezov R.R., Orlov A.Yu. Solar heating and hot water systems. - Tashkent :, Fan, 1988 .- 288 p.

[4]. Sultanov S.K. Economic aspects of the use of renewable energy sources in Kyrgyzstan. Science, education, technology. No. 1-2, 2003, pp. 174-177.

[5]. Bayramov R.B., Ushakova A.D. Solar water heating installations. - Ashgabat: Ylym Publishing House, 1987. p. 157.

[6]. Ismanzhanov A., Rasakhodzhaev B.S., Sultanov S.K. Combined solar installation for electricity and hot water supply for individual farms in mountainous and rural areas. Collection of articles of the International Scientific Conference "Innovation-2012", October 18-19, 2012, Tashkent State Technical University, Tashkent, "El-Press", 2012, 315 p., pp. 128-129.

[7]. Ismanzhanov A., Sultanov S.K, Ryskulov R. Research of technical and economic indicators of a mobile solar water heating installation. Science and new technologies. Republican scientific and theoretical journal. Bishkek. No. 2, 2015, 115 p., pp. 34-35.

[8]. Ismanzhanov A., Sultanov S.K. Study of tne technical end economic characteristics of solar water-heating installations made from alternative materials. Applied Solar Energy, Vol. 35, No. 4, 1999. pp. 9.

[9]. Ismanzhanov A., Sultanov S.K., Rasakhodjaev B.S. Influence of renewable energy resources on the energy balance of the socio-economic situation in Kyrgyzstan. "Challenges of the modern world" Proceedings of the international scientific-practical conference, Novosibirsk State University of Economics and Law. Novosibirsk, September 24-25, 2013 P.323. pp. 155-159.

[10]. Ismanzhanov A., Sultanov S.K., Rasakhodjaev B.S. The problem of operation of solar water heaters in mountainous areas. "Fundamental and applied questions of physics" Collection of abstracts of reports of the Republican conference, dedicated to the 100th anniversary of Academician S.A. Azimova, Tashkent, November 6, 2014. pp. 203-205.

[11]. Kenzhaev, I.G., Trukhov, V.S., Tursunbaev, I.A., Lezhebokov, A.I. Energy balance of autonomous solar power plant with the stirling engine. Applied Solar Energy (English translation of Geliotekhnika), 1997, 33(1), pp.17–23.

[12]. Kenjaev I.G., Osmonov O.M. Ismanjanov A.L. Analyze of process of gas fuel in furnace and burning unit of energetic unit with Stirling engine.// Proceedings of the in Central Asia and Europe. 5-6 November, 2004, Tashkent. pp.159-162.

[13]. Kenzhaev I.G., Klychev Sh.I., Bahramov SA, Bagyshev AS. Thermal losses of two-layer ball batteries heat solar installations. Geliotekhnika, 2020, Vol. 56, №1, pp. 315-222.

GENERATION OF HYDROGEN AND OXYGEN FROM WATER BY SOLAR ENERGY CONVERSION

Yu.A. Shapovalov
Center of physical-chemical methods of research and analysis
Al-Farabi Kazakh National University
Almaty, Republic of Kazakhstan
yu.shapovalov@mail.ru

R.R Tokpayev
Center of physical-chemical methods of research and analysis
Al-Farabi Kazakh National University
Almaty, Republic of Kazakhstan

T.N. Khavaza
Center of physical-chemical methods of research and analysis
Al-Farabi Kazakh National University
Almaty, Republic of Kazakhstan

Abstract

The Sun is the main source of energy on our planet. For several billion years, biological systems have acquired the unique ability to efficiently convert energy from the sun through photosynthesis. The study of photosynthesis is a topical area of scientific research that will make it possible to solve the problem of obtaining environmentally friendly energy from water.

In photosynthesis, the source of electrons is water, the oxidation of which produces electrons, protons and molecular oxygen. Oxidation of water takes place in photosystem II (PS-II). X-ray structural studies showed that the PS-II molecule consists of one or two subunits. The latter includes 108 electro-photoactive molecules, has 2 clusters with a spatial configuration in the form of a “chair”, the chemical composition is Mn_4CaO_5. Manganese and calcium atoms in the cluster do not interact with each other, forming chemical bonds only with oxygen. The Mn_4CaO_5 cluster contains 4 water molecules, two molecules each of Mn in position 4 and Ca, forming a complex as $Mn_4O_5Ca(H_2O)_4$. Analysis of the PS-II structure indicates that the components of the enzyme molecule form charge-transfer complexes (CTC) with each other and form a semiconductor structure that performs light-harvesting and electron transport functions.

Based on the structure of PS-II, the mechanism of the generation of H+, O2 ↑ , e^- ions from water as a result of photoenzymatic reaction can be described with a high degree of certainty. The energy of light from light harvesting molecules and their complexes migrates along the semiconductor structure of PS-II into the active center of the biocatalyst. This is accompanied by conformational changes in $Mn_4O_5Ca(H_2O)_4$ cluster, the consequence of which is the breaking of chemical bonds of water and the formation of atomic oxygen and 2 protons. Atomic oxygen in an aqueous medium forms hydrogen peroxide. Catalytic oxidation of hydrogen peroxide by the Mn^{4+} ion leads to the formation of oxygen, hydrogen ions, and heat is released in the reaction $H_2O_2 - 2e^- \rightarrow O_2 \uparrow + 2H^+ + 23.5$ kcal. Mn^{4+} is reduced to Mn^{2+} and then oxidised to Mn^{4+} by transferring the reducing equivalents of PS-I. Two protons in water form hydroxonium ions by the reaction $H^+ + H_2O \rightarrow H_3O^+$, which are electrochemically reduced to molecular hydrogen by the scheme $2H_3O^+ + 2e^- \rightarrow 2H_2O + H_2 \uparrow$. Thus, the PS-II cluster is the key structural formation providing water splitting and hydrogen and oxygen production by solar energy conversion. In addition, it was found that PS-II cluster, as a crystal, does not lose its ability to split water under the action of light quanta. It should be added that a catalyst of similar qualitative composition $Ca(MnO_4)_2$, is used for hydrogen peroxide decomposition in space jet technology.

Keywords: *photosynthesis, photosystem II, cluster, semiconductor, CTC.*

DAI : *https://sci-index.com/DAI/2021.99101/IEECP/14810250*

OPTIMIZATION OF PROCESS PARAMETERS FOR THE OPERATION OF A FLOW-THROUGH SUPERCRITICAL UNIT

R.R. Tokpayev, T.N Khavaza, Yu A. Shapovalov, M.K. Nauryzbayev
Center of physical-chemical methods of research and analysis al-Farabi Kazakh National University
Almaty, Republic of Kazakhstan
yu.shapovalov@mail.ru

F.M.Gumerov, S.V.Mazanov, S.A. Soshin
Department of "Theoretical Foundations of Heat Engineering" Kazan National Research Technological University
Kazan, Russian Federation

Abstract

Biodiesel (BD) is an environmentally friendly, alternative energy source. It has a number of advantages over petroleum diesel: it is fire-safe, has a higher flash point, and has minimal toxic emissions during combustion.

It is most promising to produce BD in supercritical (SC) conditions, above the critical point of methanol or ethanol. A mobile flow-through SC unit was designed, which included tanks for initial product, flow-through reactor (FTR) with a heating element, cooler, separator, high pressure pump, control unit, pressure regulator, FTR made of thick-walled stainless-steel tube bent in the form of a spiral. A gas burner was used as the heating element and was controlled by an HMI PLC SCADA automation system. HMI PLC SCADA system was used to input technological parameters, as well as to provide acquisition and processing of data of peretherification reaction. A significant advantage of the developed mobile flow-through SC unit was its small size, high capacity and environmental safety.

Investigations were conducted on optimization of technological parameters of OB production flow-through SC unit operation. At the description of processes occurring in an FTR, the kinetic model which included a number of assumptions has been accepted. As a model isothermal ideal displacement reactor (IDR) was considered as a model in which the volume of the reaction mixture did not vary along the entire length of the flow reactor and there was no reverse and radial transfer of substances. The substance flow in the IDR only proceeded in the longitudinal direction, similar to a piston. The residence time of all components of the reaction mixture in the IDR was constant. The simplified kinetic model did not take into account the formation of intermediate compounds. The reaction order in terms of alcohol pressure was taken as 1, and the transesterification process was described by one irreversible reaction of the first order.

As a result of calculations values of effective rate constants of transetherification reaction depending on molar ratio of alcohol to oil were obtained. The rate constant of reaction was determined by the method of least squares, by comparing experimental data on oil conversion with calculated data. Values of effective rate constants of reaction depending on temperatures in the interval 320-380 °C were used for determination of activation energy E_a of supercritical transetherification of oil at various ratios of mixture - ethanol/oil, using Arrhenius equation. It is obtained that the system has to overcome an energy barrier beyond which an increase in the reaction rate constant occurs. The reaction rate constant increased by a factor of 85 when the temperature was raised from 200°C to 350 °C. Thus, a high temperature was necessary to overcome the energy barrier. It was obtained that the rates of the transesterification reaction under subcritical conditions were two orders of magnitude lower than under supercritical parameters.

Keywords: *biodiesel fuel, supercritical unit, flow-through reactor.*

IEECP'21, July 29-30, 2021, Silicon Valley, San Francisco, CA – USA

DAI : *https://sci-index.com/DAI/2021.99101/IEECP/14810268*

Evaluation of the failure modes of the finger-jointed timber species for utilization of waste timber

C. K. Muthumala
Research, Development and Training Division
State Timber Corporation
Colombo, Sri Lanka
ck_muthumala@yahoo.com

Sudhira de Silva
Dept. of Civil & Environmental Engineering
Faculty of Engineering
University of Ruhuna
Galle, Sri Lanka
yasapriya@gmail.com

K.K.I.U. Arunakumara
Dept. of Crop Science
Faculty of Agriculture
University of Ruhuna
Mapalana, Sri Lanka
kkiuaruna@crop.ruh.ac.lk

P.L.A.G. Alwis
Dept. of Agric. Engineering
Faculty of Agriculture
University of Ruhuna
Mapalana, Sri Lanka
plagalwis@gmail.com

Abstract

Off-cut wood pieces are often dumped by sawmills as they are considered to be wastes in the wood industry. A certain portion of timber has to be removed also due to inadequate length of sawn timber material. Finger jointing technique is used to eliminate wood defects which weaken the strength of sawn wood plank and unused short pieces can even be used for obtaining defect free longer lengths of timber. A study was undertaken to evaluate the tensile strength performance and major failure modes of the finger-jointed productions. A finger profile of 13 mm finger length, 4 mm pitch and 1 mm tip width were used in the study. The sections were joined using PVAc adhesive. BS 373: 1957 and BS EN 15497:2014 were used as standards for tests. The test for tensile properties were performed using Universal Testing Machine (UTM 100 PC) with loading plate moving speed of 01mm/min. Load vs. displacement variation was obtained and maximum load was identified to calculate ultimate tensile strength for evaluating the major failure modes. Density and major finger joint failure modes were also investigated.

The major failure mode of the finger- jointed seven timber species subjected to a tensile test was mainly due to glue line failure (47.14%), followed by wood grain failure (24.28 %) and fiber failure(15.71%). The least failure mode was recorded as weak finger joint (12.85 %). The highest mean finger joint strength was obtained from Grandis (50.23 N/mm^2) timber species and least mean finger joint strength was recorded in Kumbuk (16.88 N/mm^2) timber species. There is no considerable relationship between Density and the failure occurrence of finger-jointed timber species. This results would be benefited for finger-jointed furniture manufacturing industry for sustainable use of wood waste.

Keywords: Finger joint, tensile strength, Failure mode, Glue line failure

I. INTRODUCTION

Timber is an excellent material for use in roofs and other construction works, furniture, interior decorations, doors, window frames, paneling, partition boards, floorings, wood carvings and musical instruments etc [1]. Nearly 450 species of wood are found in the forests in Sri Lanka, and the timber made from this wood is used in both structural and non-structural applications.

Timber is a renewable natural resource, which can effectively reduce climate change. Timber processing generates enormous amounts of timber residues and these timber residues can be used to lessen the effects of climate change [2]. Trees sequester carbon during their life, pulling carbon dioxide (CO_2) from the atmosphere and storing it in their mass. For every kilogram of wood grown, 1.5 kg of CO_2 is removed from the atmosphere [3]. Storing CO_2 in wood could therefore be considered as an effective means of mitigating climate change, though wood also releases CO_2 when they used t as fuels [4]. Quantitative characteristics and behavior of timber are determined by its mechanical properties. These mechanical properties are important because they can significantly influence the performance and strength of the timber used in structural applications [5]. The strength of wood used for timber depends on the species of the wood and the effects of some of the growth characteristics of the wood [6].

Off-cut wood is currently one of the wastes dumped by sawmills and as they failed to fully utilize the wood supply. Waste sawn timber material of furniture factory and short length of sawn timber are also big problem in timber industry. However, some of this wasted wood is already being used as fuel wood for boilers in sawmills and also for bread baking. To further suggest ways to minimize the waste, by applying a jointing system, this utilizes the finger- jointed techniques. Using this method, waste timber planks, trimmings and edgings can be used as Finger- jointed boards and furniture in sustainable way.

Finger joint is a sustainable, eco-friendly and economically viable concept for furniture industry. It ensures the sustainable utilization of small wood cut pieces which removed as waste [7]. Engineered wood, including finger joint lumber, can meet the new demands and is recognized as providing a high quality, dependable and cost-effective alternative to traditional building products [8].

IEECP'21, July 29-30, 2021, Silicon Valley, San Francisco, CA – USA

D!f: *https://sci-index.com/DAI/2021.99101/IEECP/14810304*

The finger joint timber manufacturing is considered to be a viable solution for minimizing the waste generation in furniture manufacturing activities. Type of glues applied for the joining process of finger joint is one of the key factors which determine the strength of the product.
This study was undertaken to determine the major failure modes of the finger- jointed timber species under tensile test. Finger length of 13 mm is commonly used finger type in Sri Lankan furniture manufacturers.

MATERIALS AND METHODS

For the experimental tests, samples made of timber that is commonly used in Sri Lanka and collected from the southern and central provinces of Sri Lanka were made from the following species of wood (Table 1).

Table 1. Wood species selected for the study

Common name	Botanical name
Grandis	*Eucalyptus grandis*[1]
Jack	*Aartocarpus heterphyllus*[2]
Kumbuk	*Terminalia arjuna*[2]
Mahogany	*Swietenia macrophylla*
Pine	*Pinus caribaea*[1]
Satin	*Chloroxylon swietenia*[2]
Teak	*Tectona grandis*[2]

1-Central Province, 2-Southern Province

Finger- jointed samples were prepared from defects free sawn wood timber to calculate tensile strength properties. Finger joint specimens were made at finger joint factory at Boossa in the State Timber Corporation (STC). Finger-jointed timber specimens were made with constant finger geometry as 13 mm Finger Length, 1 mm Tip width, Tp gap 0.5 mm and 4 mm finger pitch. Finger joint geometry is shown in Figure 1.

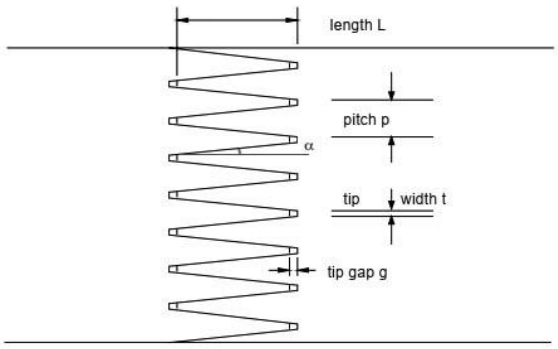

Figure 1. Geometric parameters of finger joint

(L is the finger length, B is the tip thickness, S is the tip gap, P is the pitch, α is the slope, and H is the finger depth).

The highest mean tensile strength was obtained from PVAc-SWR glue type used in finger joint production in Sri Lanka. [9,10]. Glue was applied in one face of joint. Thus, polyvinyl acetate (PVA) adhesive was used as bonding agent (Glue type) for finger- jointed samples. Assembling pressure of 6 MPa was used in this study according to recent finger joint study by Min-ChyuanYeh et al.(2011) and Juvonen [11,12].

The specimens were prepared defects free heart wood sawn woods and dimensions of the sample prepared for tensile tests shown in Figure2.

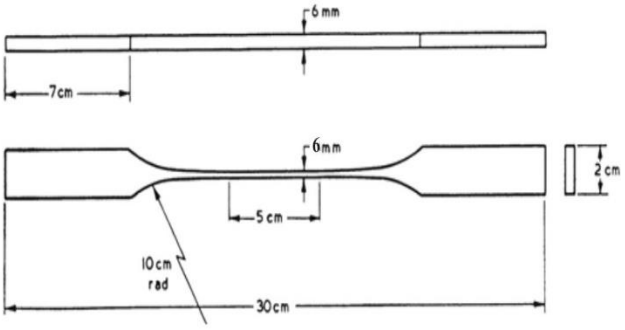

Figure 2. The dimensions of the samples prepared for tension test.

The density values were calculated for seven timber species using following equation (Eq. 01). Dry weight of the timber samples was taken by placing in 105^0C at the electric oven for period of 48 hours [13].

$$\text{Density} = \frac{\text{Weight of oven dry wood (kg)}}{\text{Volume of wood (m}^3\text{)}} \qquad \text{(Eq – 01)}$$

Determination of basic density was done based on the green volume and oven-dry weight using a water displacement method. Moisture contents were measured using moisture meter.

Ten replicates were made for each timber species. Samples which were placed in normal room temperature conditioned showed good structural performance compared to hot and wet conditioned [14]. BS 373: 1957 and BS EN 15497:2014 were used as standards for tests. [13,15]. The test for tensile strength were performed by Universal Testing Machine (UTM 100 PC) Experimental setup was shown in Figure 3.

Figure 3. Experimental set-up of tensile test

Determination of the Tensile strength

Maximum load act in timber section was taken into calculation. Equation 2 was used to calculate the Tensile strength.

Tensile strength of timber

$$= \frac{\text{Maximum Load}}{\text{Average cross section area of specimen}} \text{N/mm}^2 \qquad \text{(Eq – 02)}$$

RESULTS AND DISCUSSION

Table 2 presents the Density values of seven timber species at 12 % moisture content level.

Table 2. Dry density values of timber species

Timber species	Density (kg/m^3)
Grandis	570 ± 5
Jack	645 ± 3
Kumbuk	750 ± 4
Mahogany	570 ± 3
Pine	460 ± 2
Satin	975 ± 5
Teak	720 ± 5

The average densities of the seven species of wood in their descending order were 975 kg/m^3 for Satin; 750 kg/m^3 for Kumbuk ; 720 kg/m^3 for Teak ;645 kg/m^3 for Jack, 570 kg/m^3 for Grandis ; 570 kg/m^3 for Mahogany and 460kg/m^3 for Pine.

The failure modes of the finger-jointed timber species subjected to the tensile test were placed into 4 categories in this study; Finger broken, Glue line failure, wood grain failure and fiber failure.

Table 3. Failure occurrence of finger-jointed timber species

Timber species	Finger broken %	Glue line failure %	Wood grain failure %	Fiber failure %	Mean Strength (N/mm^2)
Grandis	10	40	50	-	50.23
Jack	20	30	20	30	36.06
Kumbuk	30	-	60	10	16.88
Mahogany	-	50	10	40	35.77
Pine	20	70	-	10	17.04
Satin	10	80	10	-	21.13
Teak	-	60	20	20	36.48
Total %	12.85	47.14	24.28	15.71	

The highest mean tension strength was Grandis, significantly lower than all other species. Grandis finger joint specimen shows the highest average tensile strength followed by Teak, Jack, Mahogany, Satin, Pine, while the lowest was the Kumbuk. It was also noted that finger-jointed Kumbuk samples failed in tension not due to in glue line failure but also other failure modes: 60 % wood grain failure, 30 % finger broken failure and 10 % fiber failure. The major reasons for failure of Satin finger-jointed samples were glue line failure (80 %). Singh et al (2016) was conducted research, to assess the tensile strength of finger jointed sections of *Eucalyptus spp.* and average value of maximum tensile stress of finger jointed samples is 23.5 N/mm^2 [16]. But present study shows average value of maximum tensile stress of finger jointed Grandis is 50.23 N/mm^2. Similar trends was reported by Awan et al.(2012) as maximum tensile stress value for *E. camaldulensis* was 59.93 N/mm^2 [17].

According to Table 3, finger-jointed timber specimens failed in tension with different modes depending on the wood species. There were 47.14 % of finger-jointed specimens that failed due to glue line failures (Figure 4) followed by 24. 28 % of wood grain failure and 15.71 % of fiber failure and 12.85 % of finger broken failure. The major reasons for failure of finger-jointed timber species were glue line failure except, Kumbuk.

Figure. 4. Glue line failure of the finger-jointed specimen under tensile test

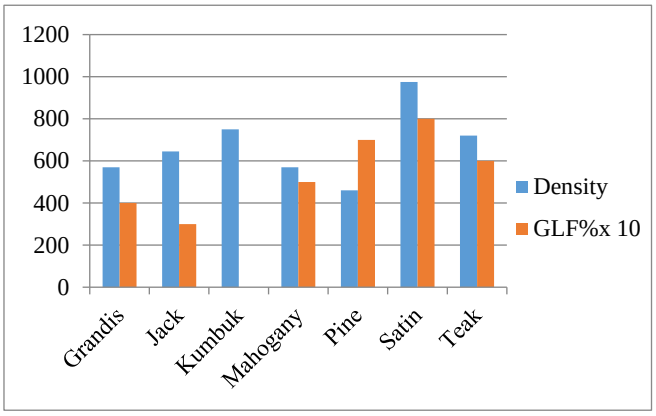

Figure. 5. Relationship between Density and the Glue line failure (GLF) %

Relationship between density and the glue line failure is shows in Figure 5. According to the Fig. 4, there is no considerable relationship between Density and the failure occurrence of finger-jointed timber species. A previous research study revealed that denser woods have more fibers per unit area, but the influence of other natural or anatomical characteristics of the wood can interfere, in order it's not possible to say that relationship between density of the piece influences on tensile strength is a rule for all wood species [18]. The another previous research study was done by Min-Chyuan Yeh et al. (2011) based on the broken-finger failure mode, emphasized that there was no difference between horizontal and vertical joint formation of finger-jointed lumber [11]. To minimize glue line failure, usage of sharp saw blades and remove dust from joint surfaces can be used, because precise and clear finger cuts are very important for finger joint production.

CONCLUSIONS

According to the results following conclusion can be drawn from this study.

The major failure mode of the finger- jointed seven timber species subjected to a tensile test was mainly due to glue line failure (47.14%), followed by wood grain failure (24.28 %) and fiber failure (15.71 %). The least failure mode was weak finger joint (12.85 %).

The highest mean finger joint strength was obtained from Grandis (50.23 N/mm^2) timber species and least mean finger joint strength was recorded in Kumbuk (16.88 N/mm^2) timber species. This results will find of this study useful for industrial application and help to produce high quality finger joint production using waste timber planks.

It is suggested that usage of sharp saw blades and remove dust from joint surfaces is necessary to improve the structural performance of the finger-jointed lumber, because precise and clear finger cuts are very important for high strength and quality finger joint production.

ACKNOWLEDGMENTS

The authors would like to thank staff of the Wood Laboratory of the State Timber Corporation of Sri Lanka for their assistance during this research work.

REFERENCES

[1] C. K. Muthumala, De Siva Sudhira, K.K.I.U. Arunakumara and P.L.A.G. Alwis, "Identification of joint efficiencies in 13 mm finger jointed timber species used in Sri Lanka", ICSBE 2018. LNCE 44 Springer nature.pte, ltd. Singapore. 2020.pp.261-267.

[2] E . Bernard, "Maximizing wood residue utilization and reducing its production rate to combat climate change", Res.art. International Journal of Plant and Forestry Science, Vol 1, No.2, 2014, pp-1-12.

[3] ASCE, "Sustainability Guidelines for the Structural Engineer", D. Kestner, P.E.; J. Goupil, P.E.; and Emily Lorenz, P.E. **https://materialspalette.org/wood/** (Accessed: 30 , May 2019).

[4] L . Philippe, "Wood preservation (carbon sequestration) or wood burning (fossil-fuel substitution), which is better for mitigating climate change" . Annals of Forest Science (2014) 71:117–124, https://hal.archives-ouvertes.fr/hal-01098394/document (Accessed: 30 May 2019).

[5] J. E. Vinandy, "Effects of long-term elevated temperature on CCA-treated Southern Pine lumber". Forest Products Journal. 44(6), 1994, pp 49–55.

[6] D. Yeomans, "Strength Grading Historic Timbers." Cathedral Communications Limited 2010 Retrieved from http://www.buildingconservation.com/ articles/grading timbers /grading timbers.ht , 2003.

[7] A.L. Sandika, G.D.P.S. Pathirana and C. K. Muthumala, "Finger joint timber products for effective utilization of natural resources: An analysis of physical properties, Economic factors and Consumers' perception". International Symposium on Agriculture and Environment, University of Ruhuna, Sri Lanka, 2017, pp 109-111.

[8] C.W. Alex and R. B. Miller, USDA. Forest Service, Forest Products Laboratory, Madison, WI. 2005.

[9] C. K. Muthumala, M.W.T.C. Dulanjalee, De Siva Sudhira, P. L. A. G. Alwis and K. K. I. U. Arunakumara, "Factors affecting the glue strength of finger joints in commonly used timber species in Sri Lanka. Res.Pap. International Symposium on Agriculture and Environment, University of Ruhuna, Sri Lanka.2018, pp. 126-128.

[10] C. K. Muthumala, De Siva Sudhira, K. K. I. U. Arunakumara and P. L. A. G. Alwis , "Investigate the most suitable glue type for finger-joints production in Sri Lanka". Research journal of Agriculture and Forestry Sciences. Res Pap ISCA. India. 6(11) Nov. p.6-9., 2018.

[11] Min-ChyuanYeh,Yu-Li Lin, Yung-Chin Huang, "Evaluation of the Tensile Strength of Structural Finger-Jointed Lumber". Taiwan J For Sci 26(1), 2012,pp.59-70 www.airtilibrary.com

[12] R. Juvonen , " End pressure for finger-jointing. Seminar on the production, marketing and use of finger-jointed sawn wood" - Hamar , Norway. 1980.

[13] British Standards Institution , BS 373: 1957. Methods of testing small clear specimens of timber. British Standards Institution. London, 1957.

[14] S. Vievek S, De Silva S, De Silva S. and C. K. Muthumala, "Finger joint and their structural performance in different exposure conditions". International Conference on Sustainable Build Environment, Kandy, Sri Lanka, 2016.

[15] British Standards Institution , BS EN 15497:2014. Structural finger jointed solid timber-Performance requirements and minimum production requirements. European Committee for Standardization. B 1000 , Brussels, 2014.

[16] C. P. Singh, V. S. Kishan Kumar and Sachin Gupta. "Maximum Tensile Stress of Eucalyptus Sections Finger Jointed with PVA Adhesive". International Science Community Association, Research Journal of Agriculture Vol. 4(8), 2016, 10-13, www.isca.in

[17] A. R. Awan, M. I. Chughtai., M. Y. Ashraf , K. Mahmood , M. Rizwan, M. Akhtar , M. T. Siddiqui and R. A. Khan "Comparison for physico-mechanical properties of farm-grown eucalyptus camaldulensis dehn, With conventional timbers". Pak. J. Bot., 44(6), 2067-2070., R.A. 2012.

[18] C. P. M. Marcos, C. N. Carlito, H. I. Felipe and C. J. Carlito ," Evaluation of Tensile Strength of a *Eucalyptus grandis* and *Eucalyptus urophyla* Hybrid in Wood Beams Bonded Together by Means of Finger Joints and Polyurethane-Based Glue. *Materials Research*. 2016; 19(6): 1270-1275 DOI: http://dx.doi.org/10.1590/1980-5373-MR-2016-0072, 2016.

Effect of surfactants on morphology and textural parameters of silica nanoparticles derived from paddy husk and their efficient removal of methylene blue

Himasha Gunathilaka
School of Science and Education, Faculty of Humanities and Sciences,
Sri Lanka Institute of Information Technology,
Malabe, Colombo, Sri Lanka
himasha.g@sliit.lk

Charitha Thambiliyagodage
School of Science and Education, Faculty of Humanities and Sciences,
Sri Lanka Institute of Information Technology,
Malabe, Colombo, Sri Lanka
charitha.t@sliit.lk

Leshan Usgodaarchchi
Department of Materials Engineering, Faculty of Engineering,
Sri Lanka Institute of Information Technology,
Malabe, Colombo, Sri Lanka
leshan.u@sliit.lk

Sajeevan Angappan
Department of Materials Engineering, Faculty of Engineering,
Sri Lanka Institute of Information Technology,
Malabe, Colombo, Sri Lanka
sajeevanangappan@gmail.com

Abstract

Effective removal of textile dyes is important in environmental remediation especially for decontamination of wastewater. Herein, we report the synthesis of mesoporous silica nanoparticles (MSNs) from paddy husk with varying concentrations of surfactants, Cetyltrimethylammonium bromide (CTAB), and Polyethyleneglycol (PEG) by sol-gel synthesis method. Ratios of the surfactants CTAB: PEG were varied as 2:0 (MSN1),1:1 (MSN2), 0:2 (MSN3). MSNs were characterized by scanning electron microscope (SEM), Brunauer-Emmett-Teller surface area analyzer (BET), Thermogravimetric analyzer (TGA), and X-ray diffractometer. According to the SEM images, MSNs of all the combinations were aggregated with spherical and irregular shaped nanoparticles. MSNs synthesized with a 1:1 surfactant ratio showed more spherical nanoparticles. BET surface areas of MSN1, MSN2, and MSN3 are 468.35, 95.94, 177.46 m2/g, respectively. TGA curve indicated that desorption of the physisorbed water was completed at 125 °C. The effect of dye removal by the MSNs was studied on the adsorption of methylene blue (MB). Effect of dye concentration (5-30 mg/l), adsorbent dosage (5-20 mg), pH of the medium (2-10), ionic strength of the medium (0-6g/l NaCl), presence of a heavy metal (Pb2+- 0-500 mg/l) and temperature (25-55 °C) on MB adsorption was studied. At all the varied parameters, the adsorption efficiency of MB varied as MSN1> MSN3> MSN2, being similar to the trend of the surface area. The percentage of MB adsorption decreased with increasing MB concentration while it increased with increasing adsorbent dosage. The highest efficiency of MB adsorption was obtained at pH 10 and it decreased with increasing ionic strength and increasing concentration of heavy metal ions. The maximum percentage of MB adsorption resulted at 55 °C. Therefore, it can be concluded that the MSNs synthesized using only CTAB as the surfactant is an effective adsorbent in removing textile dyes from wastewater.

Keywords: Silica nanoparticles, Cetyltrimethylammonium bromide, Polyethyleneglycol, Methylene blue

I. INTRODUCTION

Pollutants are being released into the water reservoirs causing serious problems. Pollutants such as heavy metals, pesticides, fertilizers, hydrocarbons, biphenyls, detergents, oils, greases, pharmaceuticals etc.[1], [2] are released due to rapid industrialization. Among them, the release of dye molecules has critically impacted aquatic ecosystems as well as human health by causing allergies, neurological disorders, hypertension, cardiovascular diseases, and pulmonary diseases once absorbed through various pathways [3]–[5]. Dyes that are not readily biodegradable are released to water reservoirs by the runoffs from various industries such as textile, pharmaceutical, paper, plastic, food, pulp, etc. One of the main sources of dye waste is the textile industry. Many methods including Adsorption[6], coagulation/flocculation [7], Ion exchange [8], electrochemical processes [9], advanced oxidation processes [10], and bacterial biodegradation [11] have used to remove the dyes from wastewater. Adsorption is a promising wastewater treatment method as it could be applied to remove almost all the pollutants, and the method is

IEECP'21, July 29-30, 2021, Silicon Valley, San Francisco, CA – USA

DAI : *https://sci-index.com/DAI/2021.99101/IEECP/14904873*

inexpensive and easy to operate. In general, adsorption is the process where the substances are accumulated at a surface or an interface. Activated carbon (AC) is widely used to remove heavy metal ions and organic pollutants due to the high surface area resulted from the large micropore and mesopore volumes.[12], [13] In addition to AC adsorbents like carbon nanotubes,[14] zeolite,[15] sawdust,[16] seed shells,[17] maghemite nanoparticles,[18] clay material,[19] etc. have been used for wastewater purification. However, the blockage of micropores of activated carbon by macro dye molecules makes it more difficult for large dye molecules to diffuse into the internal pore structure of activated carbon, limiting its applicability [20]. Mesoporous silica is a porous material that has been used as an absorbent due to its unique surface and pore properties such as high surface area and high pore volumes [21]. In this study, we report the synthesis of mesoporous silica nanoparticles (MSN) using paddy husk which is an agricultural waste product. MSNs have been synthesized by the sol-gel method by using CTAB and PEG as the surfactants. Synthesized MSNs were used to remove methylene blue from artificial wastewater is also studied.

II. Methodology

Paddy husk were washed with water to remove the impurities. They were treated in 2 M Sulfuric acid for 3 hours at 110 °C under refluxing conditions. Acid treated paddy husk were washed with an abundant volume of DI water until a neutral pH is achieved. They were heated in a muffle furnace at 600 °C for 5 hours. Obtained white colour silica was treated with 4M KOH for 5 hours at 80 °C. The obtained solution was filtered and surfactants (CTAB and/or PEG) were added to the filtrate as tabulated below in table 1. The mixture was stirred for 30 minutes and 0.5 M sulfuric acid was added dropwise till pH reached 4. Obtained gel was aged for 8 hours and was washed with DI water until the washings are negative for Cl^- ions. The precipitate was dried and calcined at 600 °C for 5 hours.

Table 1. Surfactant/s added for the synthesis

Sample	% CTAB	% PEG
MSN1	2	0
MSN2	2	2
MSN3	0	2

Effect of the pH (2-10), dye concentration (5-30 mg/l), adsorbent dosage (5-20 mg), temperature (25-55 °C), ionic strength (NaCl, 2-6 g/l) and presence of heavy metal (Pb^{2+}, 100-500 mg/l) on adsorption of MB to the synthesized MSNs were determined. Generally, a known weight of MSN was shaken in a 25 ml of desired concentration of MB for one hour at room temperature.

III. RESULTS AND DISCUSSION

A. Morphological analysis

Morphology of the synthesized mesoporous MSNs (MSN1 – MSN3) was studied by SEM and TEM (Figure 1). SEM images show that spherical and irregular shaped nanoparticles are much aggregated and are in the range of 220 – 415 nm. MSNs of the MSN2 sample (Figure 1 (c)) are more spherical compared to the others. This observation is also supported by the TEM images where the TEM image of MSN1 (Figure 1 (e)) show more irregular shaped NPs, and the TEM image of MSN2 (Figure 1 (f)) show more spherical NPs. Therefore, it is evident that when CTAB and PEG are mixed in a 1:1 ratio more spherical NPs have resulted. Positively charged surfactant (CTAB) readily form interactions with the negatively charged silica. Neutral surfactant (PEG) forms hydrogen bonds with the hydroxyl groups on the silica surface [22]. Hence, by the action of both surfactants in equal proportions, NPs are located well apart from each other producing more spherical NPs. However, with other surfactant mixtures with different proportions more irregular shaped NPs have produced indicating that the NPs were not well separated and during calcination, at higher temperatures, they were aggregated due to Oswald ripening producing larger and irregular nanoparticles. However, the used surfactant concentrations are insufficient to produce well-dispersed uniform NPs.

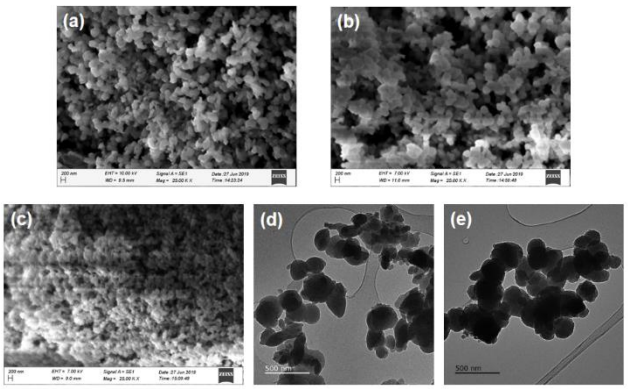

Figure 1. SEM images of (a) MSN1 (b) MSN2 (c) MSN3 TEM images of (d) MSN1 (e) MSN 2

B. FT-IR analysis

FT-IR spectra were acquired to study the bonding nature of the MSNs and effective surface functionalization by the surfactants (Figure 2). The bands at 1050 and 800 cm-1 is attributed to the Si-O-Si stretching and Si-O bending frequencies. The band at 460 cm-1 is assigned to Si-O out of plane deformation [23], [24]. The band at 1620 cm-1 corresponds to C=O vibration of carboxyl, lactonic and anhydride groups [25]. The peak at 2950 cm-1 is attributed to the C-H stretching frequency, indicating the presence of CH_2 group suggesting that the MSN surface has been functionalized by PEG and CTAB used for particle dispersion [26]. A broad band at 3400 cm-1 is assigned to the O-H stretching indicating the presence of H_2O as moisture [24].

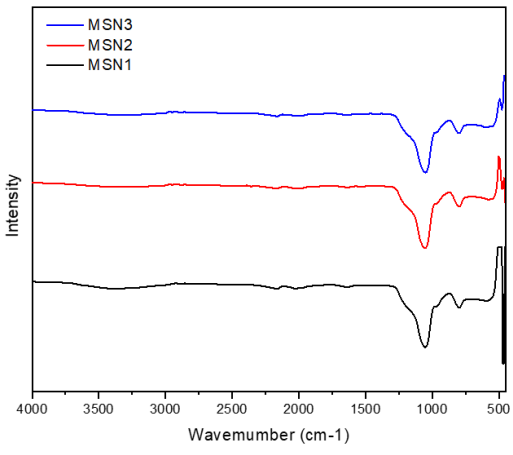

Figure 2. FT-IR spectra of the synthesized MSNs.

C. XRD analysis

XRD pattern (Figure 3) shows a broad peak centered at $2\theta = 21.5°$ indicating the amorphous nature of the synthesized MSNs. Further, any peaks correspond to crystalline silica were not present suggesting that during acid leaching of paddy husk metal ions

associated such as Ca, Mg, K, Fe, Mn have been leached out preventing the formation of crystalline silica. On the other hand, calcined temperature (550 °C) is insufficient to produce crystalline silica.

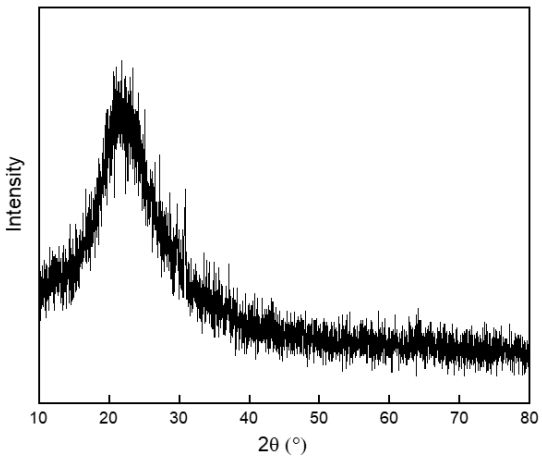

Figure 3. XRD pattern of MSN1

D. Surface area analysis

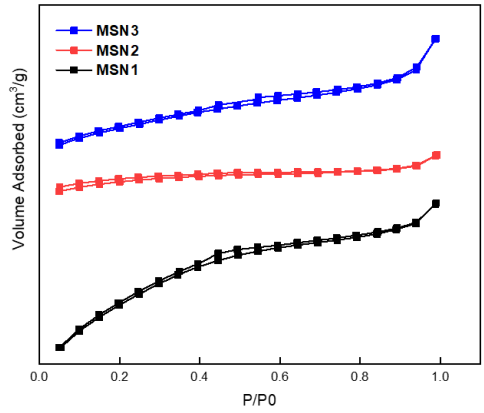

(a)

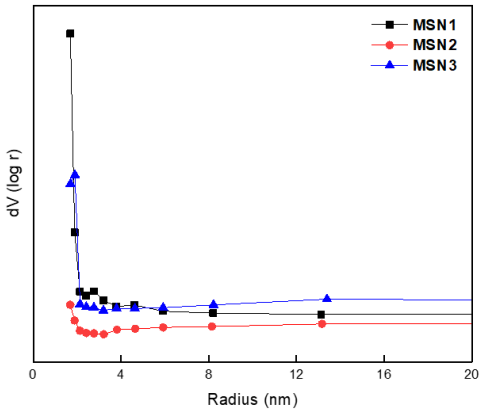

(b)

Figure 4. (a) BET isotherms (b) BJH Pore size distribution curves of MSNs

BET adsorption-desorption isotherms and BJH pore size distribution curves were collected to study the textural properties including surface area, total pore volume and average pore size. All three BET adsorption and desorption isotherms (Figure 4(a)) belong to the type V with H2 hysteresis loop indicating the presence of disordered mesopores where the distribution of pore size and shape is not well defined. BJH pore size distribution curves (Figure 4 (b)) also support this observation where the board pore size distributions have resulted. The surface area of the MSNs vary in the order of MSN1> MSN3> MSN2 of which the highest surface area (468.35 m2/g) was obtained in MSN1 and the least (95.94 m2/g) resulted in MSN2. The total pore volume of MSNs varied as MSN1> MSN3> MSN2 as tabulated in Table 1. Hence, it is evident that with equal proportions of the surfactants (MSN2) pore network has not been established properly resulting in low surface area and pore volumes. Surfactants exist as monomolecular at lower concentrations but at higher concentrations, they tend to form micelles to decrease the system entropy. Surfactants driven porous structure is determined by the concentration of the surfactant, length of the hydrophobic chain, hydrophilic head group, and the counter ion in the case of ionic surfactants. Here, in this study, two different surfactants (CTAB and PEG) with different properties were used. CTAB is a cationic surfactant and PEG is a neutral surfactant. CTAB interacts with silica via Coulombic attractions and PEG interacts via Hydrogen bonds with silica surface hydroxyl groups. CTAB has a hydrophilic group at the end of the CTAB chain. This end interacts with the silica surface. CTAB chain is long and CTAB hydrophobic chains repel each other separating MSNs effectively. At calcination, CTAB molecules removed creating a well-established porosity and hence a high surface area as obtained for MSN1 in this study. Each hydrophilic group of PEG lies in between two -CH2- groups. This makes the PEG molecules diffuse faster and form the directional alignment on the surface rather than forming a micelle structure. Adsorbed PEG molecules on the silica surface could hinder the growth of the particles through steric hindrance or could lead to the formation and large silica clusters. Here as PEG 6000 was used agglomeration effect has taken place rather than the steric hindrance effect due to high molecular weight. This has led to low surface area in MSN3 compared to MSN1. CTAB on MSNs is not closely arranged as they repel each other. PEG molecules easily get inserted into the loosely adsorbed CTAB layers due to the hydrophobic effect and dipole –ion interactions that may have generated between two surfactants. Hence, the repulsive forces between the same charged particles are reduced and the density of the hydrophobic chains are increased. Further, oxygen entities of the PEG could get positively charged due to the interactions with H^+ in water. Therefore, this creates a repulsive force with the CTAB molecules and hence as a consequence surfactant mixtures disperse the MSNs well forming more spherical NPs as shown in SEM and TEM images [27]. However, the coexistence of two surfactants affects the development of the porous structure leading to lower surface area (MSN2) compared to the MSNs where only one surfactant was used (MSN1 and MSN3).

Table 2. Textural parameters of the synthesized MSNs

Sample	BET Surface area (m^2/g)	Total pore volume (cc/g)	Average pore size (nm)
MSN1	468.35	0.332	1.42
MSN2	95.94	0.076	1.60
MSN3	177.46	0.189	2.13

E. Effect of different parameters

Effect of pH, dye concentration, adsorbent dosage, ionic strength, presence of a heavy metal (Pb^{2+}), and temperature on percentage removal of MB was studied (Figure 5). It could be seen that the highest % removal was obtained by MSN1, while the least by MSN2 for all the parameters tested. The obtained trend of data variation is consistent with the pattern of surface area and total pore volume

variation resulted in surface area analysis. MSN1 has the highest surface area and total pore volume while MSN2 has the least. Hence, MSN1 has a high number of active sites for adsorption compared to MSN2 and MSN3 and the activity of MSN3 is greater than that of MSN2 due to the same reason. The highest percentage removal of MB was obtained at pH 10 and the % removal increased with increasing pH. At pH 2 only 13.55% of MB was removed and 80.94% was removed at pH 10 by MSN1. MSN2 and MSN3 also show the same trend with varying pH. MB molecules are positively charged and has a high affinity to the negatively charged silica surfaces. However, at low pH values H^+ ions also readily adsorb to the silica surface. Therefore, at low pH values, there is a competition between H^+ and MB molecules. Adsorption of H^+ ions is high compared to the MB as the H^+ readily adsorb due to their small size and occupy the adsorption surface and due to the steric hindrance adsorption of MB molecules is less. However, at high pH values adsorption of MB is high because the abundant positively charged species is MB.

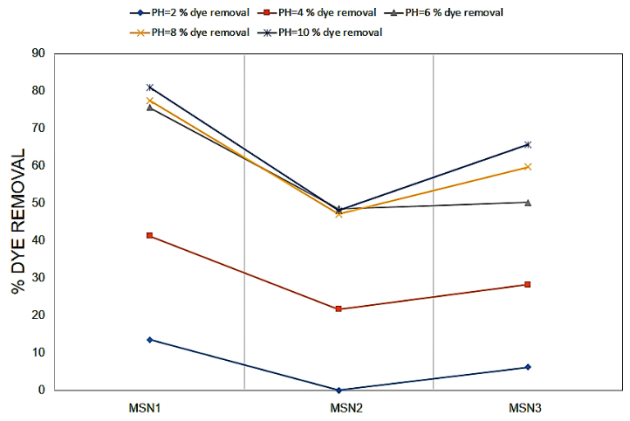

Figure 5. Effect of pH on dye removal by MSNs

Effect of dye concentration on % removal was determined in a concentration range of 5-30 mg/l (Figure 6). MSN1 was capable of removing 73.64% of 5 ppm MB in one hour while only 32.82% was removed by when 30 mg/l of MB was used.% removal of MB decreased with increasing dye concentration by all synthesized MSN. As the weight of the adsorbent is constant, the number of adsorption sites is the factor that limits the adsorption. Therefore, at high dye concentrations though more dye molecules are present sufficient number of adsorption sites are not available for adsorption resulting in low % removals.

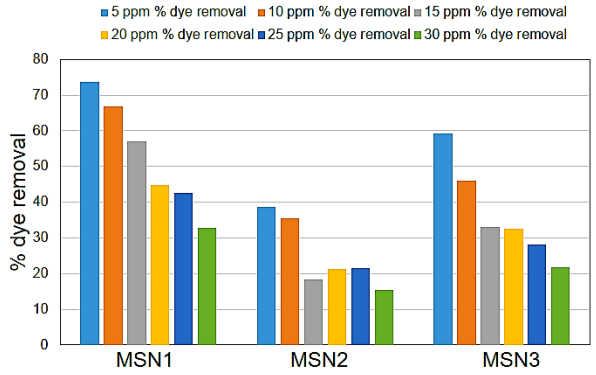

Figure 6. Effect of dye concentration on dye removal by MSNs

Adsorbent dosage was varied in the range of 5-20 mg to determine the effect of the weight of the adsorbent on the % removal of MB (Figure 7). The percentage removal of 86.47% was obtained by using 20 mg and only 57.14% removal was resulted with 5 mg of MSN1. With increasing, adsorbent dosage % removal of MB increased as high adsorbent weights of all three MSN due to the presence of more adsorption sites.

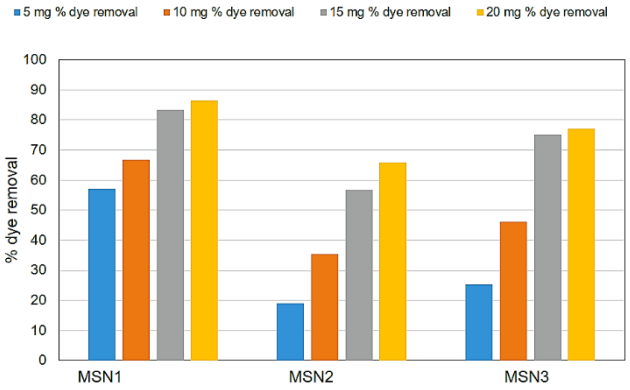

Figure 7. Effect of adsorbent dosage on dye removal by MSNs

The presence of ionic salts affects the adsorption of MB to silica surface where reduced adsorption was obtained with NaCl in the medium (Figure 8). Ionic salts interfere with the adsorption process in two mechanisms. According to the first mechanism, Na^+ compete with positively charged MB molecules to the adsorption sites resulting in low adsorption of MB due to the steric hindrance. The second mechanism explains that an increased ionic strength compress the double electric layer and lead to electrostatic repulsion of MB from the surface [28]–[30]. MSN1 has removed 66.80% of MB without added NaCl but with 6 g/l NaCl in the medium only 53.23 % of MB has been removed. Similarly, the % removal of MB has decreased with increasing NaCl concentration in all MSNs studied.

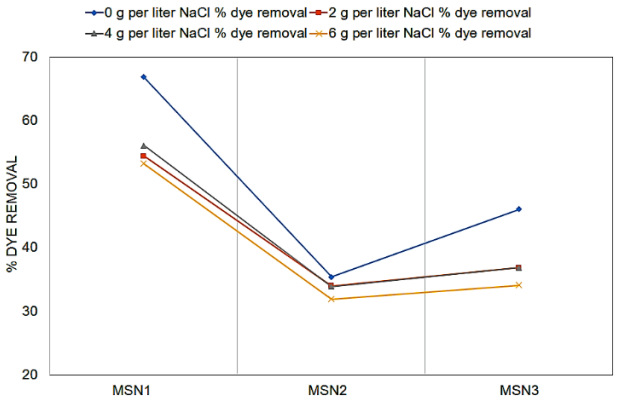

Figure 8. Effect of ionic strength on dye removal by MSNs

The effect of the presence of heavy metal on the removal of MB by MSN has been tested by using Pb^{2+} as the heavy metal ion (Figure 9). Positively charged metal ions and MB compete to the silica surface available and as Pb^{2+} are small in size compared to MB, more Pb^{2+} adsorb to the negatively charged silica surface and MB shows comparatively less adsorption due to the steric hindrance. The percentage of dye removal decreased with increasing Pb^{2+} concentration in all MSNs studied. The percentage removal of 66.80 % of MB was achieved by MSN1 in the absence of Pb^{2+}, with 100 mg/l Pb2+ in the medium 51.19 % MB was removed and 38.84% was removed in the presence of 500 mg/l Pb^{2+} in the medium.

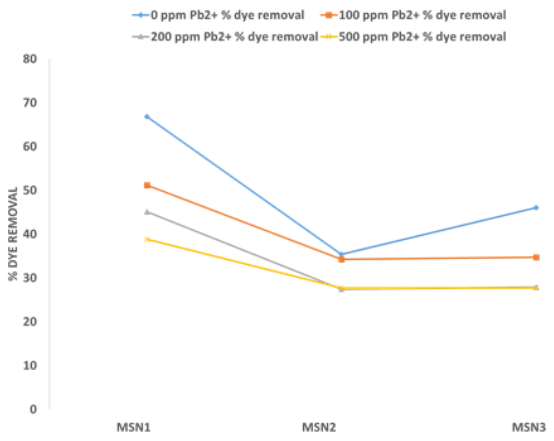

Figure 9. Effect of heavy metals on dye removal by MSNs

Adsorption of MB to silica is also affected by temperature. The effect of temperature was determined at different temperatures (25 - 55 °C) (Figure 10). MSN1 was capable of removing 60% of MB at 25 °C, while 74.52% of MB was removed at 55 °C. Percentage removal increased with increasing temperature in all the MSNs synthesized. Kinetic energy and the velocity of the dye molecules increase with increasing temperature. Therefore, the percentage of molecules with sufficient energy to reach the adsorbent surface at a given time is high at higher temperatures. This results in higher % removal of MB at high temperatures.

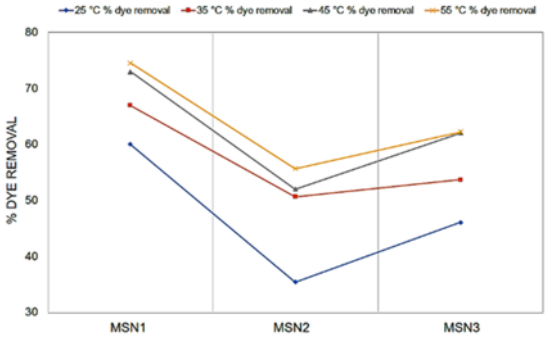

Figure 10. Effect of temperature on dye removal by MSNs

F. CONCLUSIONS

MSNs were successfully synthesized by the sol-gel method using paddy husk as the raw material using CTAB and/or PEG as the surfactants. Synthesized MSN were effective in removing MB. MSN1 showed the highest activity on removing MB followed by MSN3. MSN2 exhibited the least activity. Surface area and total pore volume were high in MSN1 followed by MSN3 and MSN2. Dye adsorption was maximum with 5 ppm MB, 20 mg of adsorbent, pH 10 and at 55 °C. The presence of NaCl and Pb2+ retarded the adsorption of MB.

IV. ACKNOWLEDGMENTS

Authors acknowledge Sri Lanka Institute of Information Technology for the financial support and Sri Lanka Institute of Nanotechnology for providing the instrument facilities.

V. REFERENCES

[1] "Low cost adsorbents for the removal of organic pollutants from wastewater," J. Environ. Manage., vol. 113, pp. 170–183, Dec. 2012, doi: 10.1016/J.JENVMAN.2012.08.028.

[2] M. Nageeb, "Adsorption Technique for the Removal of Organic Pollutants from Water and Wastewater," in Organic Pollutants - Monitoring, Risk and Treatment, InTech, 2013.

[3] H. M. Salem and A. A. Elfouly, "Minerals Reconnaissance at Saint Catherine Area, Southern Central Sinai, Egypt and their Environmental Impacts on Human Health."

[4] G. Bringmann and R. Kühn, "Comparison of the toxicity thresholds of water pollutants to bacteria, algae, and protozoa in the cell multiplication inhibition test," Water Res., vol. 14, no. 3, pp. 231–241, Jan. 1980, doi: 10.1016/0043-1354(80)90093-7.

[5] W. Guo, X. Liu, Z. Liu, and G. Li, "Pollution and potential ecological risk evaluation of heavy metals in the sediments around Dongjiang Harbor, Tianjin," in Procedia Environmental Sciences, Jan. 2010, vol. 2, pp. 729–736, doi: 10.1016/j.proenv.2010.10.084.

[6] M. T. Yagub, T. K. Sen, S. Afroze, and H. M. Ang, "Dye and its removal from aqueous solution by adsorption: A review," Advances in Colloid and Interface Science, vol. 209. Elsevier, pp. 172–184, Jul. 01, 2014, doi: 10.1016/j.cis.2014.04.002.

[7] S. Sadri Moghaddam, M. R. Alavi Moghaddam, and M. Arami, "Coagulation/flocculation process for dye removal using sludge from water treatment plant: Optimization through response surface methodology," J. Hazard. Mater., vol. 175, no. 1–3, pp. 651–657, Mar. 2010, doi: 10.1016/j.jhazmat.2009.10.058.

[8] S. Raghu and C. Ahmed Basha, "Chemical or electrochemical techniques, followed by ion exchange, for recycle of textile dye wastewater," J. Hazard. Mater., vol. 149, no. 2, pp. 324–330, Oct. 2007, doi: 10.1016/j.jhazmat.2007.03.087.

[9] C. A. Martínez-Huitle and E. Brillas, "Decontamination of wastewaters containing synthetic organic dyes by electrochemical methods: A general review," Applied Catalysis B: Environmental, vol. 87, no. 3–4. Elsevier, pp. 105–145, Apr. 2009, doi: 10.1016/j.apcatb.2008.09.017.

[10] S. H. S. Chan, T. Yeong Wu, J. C. Juan, and C. Y. Teh, "Recent developments of metal oxide semiconductors as photocatalysts in advanced oxidation processes (AOPs) for treatment of dye waste-water," J. Chem. Technol. Biotechnol., vol. 86, no. 9, pp. 1130–1158, Sep. 2011, doi: https://doi.org/10.1002/jctb.2636.

[11] A. Khalid, M. Arshad, and D. E. Crowley, "Biodegradation potential of pure and mixed bacterial cultures for removal of 4-nitroaniline from textile dye wastewater," Water Res., vol. 43, no. 4, pp. 1110–1116, Mar. 2009, doi: 10.1016/j.watres.2008.11.045.

[12] A. Jusoh, L. Su Shiung, N. Ali, and M. J. M. M. Noor, "A simulation study of the removal efficiency of granular activated carbon on cadmium and lead," Desalination, vol. 206, no. 1–3, pp. 9–16, Feb. 2007, doi: 10.1016/J.DESAL.2006.04.048.

[13] P. G. González and Y. B. Pliego-Cuervo, "Adsorption of Cd(II), Hg(II) and Zn(II) from aqueous solution using mesoporous activated carbon produced from Bambusa vulgaris striata," Chem. Eng. Res. Des., vol. 92, no. 11, pp. 2715–2724, Nov. 2014, doi: 10.1016/J.CHERD.2014.02.013.

[14] H. Wang, A. Zhou, F. Peng, H. Yu, and J. Yang, "Mechanism study on adsorption of acidified multiwalled carbon nanotubes to Pb(II)," J. Colloid Interface Sci., vol. 316, no. 2, pp. 277–283, Dec. 2007, doi: 10.1016/J.JCIS.2007.07.075.

[15] R. Apiratikul and P. Pavasant, "Sorption of Cu2+, Cd2+, and Pb2+ using modified zeolite from coal fly ash," Chem. Eng. J., vol. 144, no. 2, pp. 245–258, Oct. 2008, doi: 10.1016/j.cej.2008.01.038.

[16] F. Kaczala, M. Marques, and W. Hogland, "Lead and vanadium removal from a real industrial wastewater by gravitational settling/sedimentation and sorption onto Pinus sylvestris sawdust," Bioresour. Technol., vol. 100, no. 1, pp. 235–243, Jan. 2009, doi: 10.1016/J.BIORTECH.2008.05.055.

[17] O. S. Amuda, F. E. Adelowo, and M. O. Ologunde, "Kinetics and equilibrium studies of adsorption of chromium(VI) ion from industrial wastewater using Chrysophyllum albidum (Sapotaceae) seed shells," Colloids Surfaces B Biointerfaces, vol. 68, no. 2, pp. 184–192, Feb. 2009, doi: 10.1016/J.COLSURFB.2008.10.002.

[18] *,†,‡ Mélanie Auffan et al., "Enhanced Adsorption of Arsenic onto Maghemites Nanoparticles: As(III) as a Probe of the Surface Structure and Heterogeneity," 2008, doi: 10.1021/LA702998X.

[19] G. McKay, M. S. Otterburn, and J. A. Aga, "Fuller's earth and fired clay as adsorbents for dyestuffs," Water. Air. Soil Pollut., vol. 24, no. 3, pp. 307–322, Mar. 1985, doi: 10.1007/BF00161790.

[20] X. Zhuang, Y. Wan, C. Feng, Y. Shen, and D. Zhao, "Highly efficient adsorption of bulky dye molecules in wastewater on ordered mesoporous carbons," Chem. Mater., vol. 21, no. 4, pp. 706–716, Feb. 2009, doi: 10.1021/cm8028577.

[21] C. H. Huang, K. P. Chang, H. De Ou, Y. C. Chiang, and C. F. Wang, "Adsorption of cationic dyes onto mesoporous silica," Microporous Mesoporous Mater., vol. 141, no. 1–3, pp. 102–109, May 2011, doi: 10.1016/j.micromeso.2010.11.002.

[22] R. L. Derosa and J. A. Trapasso, "Poly(ethylene glycol) interactions with alumina and silica powders determined via DRIFT," J. Mater. Sci., vol. 37, no. 6, pp. 1079–1082, Mar. 2002, doi: 10.1023/A:1014328716329.

[23] C. J. Thambiliyagodage, V. Y. Cooray, I. N. Perera, and R. D. Wijesekera, "Eco-Friendly Porous Carbon Materials for Wastewater Treatment," in Lecture Notes in Civil Engineering, vol. 44, Springer, 2020, pp. 252–260.

[24] B. Shokri, M. A. Firouzjah, and S. I. Hosseini, "FTIR analysis of silicon dioxide thin film deposited by metal organic-based PECVD," in Proceedings of 19th international symposium on plasma chemistry society, 2009, vol. 2631, pp. 26–31.

[25] F.-N. Allouche, N. Yassaa, and H. Lounici, "Sorption of Methyl Orange from Aqueous Solution on Chitosan Biomass," Procedia Earth Planet. Sci., vol. 15, pp. 596–601, Jan. 2015, doi: 10.1016/j.proeps.2015.08.109.

[26] B. Lin and S. Zhou, "Poly(ethylene glycol)-grafted silica nanoparticles for highly hydrophilic acrylic-based polyurethane coatings," Prog. Org. Coatings, vol. 106, pp. 145–154, May 2017, doi: 10.1016/j.porgcoat.2017.02.008.

[27] D. Liu, L. Fang, and F. Cheng, "Bisurfactant-assisted preparation of amorphous silica from fly ash," Asia-Pacific J. Chem. Eng., vol. 11, no. 6, pp. 884–892, Nov. 2016, doi: 10.1002/apj.2022.

[28] P. Pimol, M. Khanidtha, and P. Prasert, "Influence of particle size and salinity on adsorption of basic dyes by agricultural waste: dried Seagrape (Caulerpa lentillifera)," J. Environ. Sci., vol. 20, no. 6, pp. 760–768, Jan. 2008, doi: 10.1016/S1001-0742(08)62124-5.

[29] C. H. Weng, Y. T. Lin, and T. W. Tzeng, "Removal of methylene blue from aqueous solution by adsorption onto pineapple leaf powder," J. Hazard. Mater., vol. 170, no. 1, pp. 417–424, Oct. 2009, doi: 10.1016/j.jhazmat.2009.04.080.

[30] C. E. de F. Silva, B. M. V. da Gama, A. H. da S. Gonçalves, J. A. Medeiros, and A. K. de S. Abud, "Basic-dye adsorption in albedo residue: Effect of pH, contact time, temperature, dye concentration, biomass dosage, rotation and ionic strength," J. King Saud Univ. - Eng. Sci., vol. 32, no. 6, pp. 351–359, Sep. 2020, doi: 10.1016/j.jksues.2019.04.006.

Effect of Banana fibers on the enhancement of compressive toughness of Reinforced Concrete Columns –A Review

1st Muhammad Abrar
Department of Civil Engineering
Capital University of Science and Technology
Islamabad, Pakistan
abrar19125@gmail.com

2nd Majid Ali
Department of Civil Engineering
Capital University of Science and Technology
Islamabad, Pakistan
professor.drmajid@gmail.com

Abstract

Fibers have been used in concrete by different researches since a few decades. Natural fibers are widely used as additive material in concrete to enhance the strength and mechanical properties of concrete. It has been observed that by using fiber reinforced composite (FRC), the weight and manufacturing cost can be reduced. The purpose of this study is to find out the flaws in reinforced concrete (RC) columns regarding compressive toughness and their remedial measures. This paper includes the state of the art review of behavior of RC columns under compressive load, role of toughness and available measure to increase compressive toughness (CT). Analysis of chemical, mechanical and physical properties of banana fiber is done for choosing it as suitable fiber. Usage of banana fiber in different proportions in concrete and its effect towards enhancing the compressive toughness is also studied. The compressive strength of concrete by using FRC is reduced in most of the cases but ability to absorb energy is increased. There are a very less number of experimental studies present in literature regarding use of banana fiber in FRC so there is a need of a lot of work on it. Banana fibers can be used in future studies to enhance plasticity of concrete and its fire resistance.

Keywords: Banana fiber, Compressive toughness (CT), Fiber reinforced composites (FRC).

I. INTRODUCTION

Since past century, concrete has been used as primary engineering material in construction industry [1]. The concrete with combination of steel reinforcement is called reinforced concrete (RC) to withstand whole loads of structure. It is not necessary that the reinforced concrete structures having high strength always show a good structural performance. On the other hand, a material having higher energy absorption (toughness) provides higher structural performance when undergoes to failure due to certain reasons. Ductility is the count of a material that how much it deforms plastically before happening of fracture. The materials with low ductility and low strength have low energy absorption whereas the materials with high ductility and high strength have more ability to absorb energy. Hence, the materials with later described properties are more useful for structures [2]. In reinforced concrete structures, columns as compressive members transfers vertical load to foundation. Due to increase in axial stresses than capacity of column, it will fail in compression. There are many types of failures that can be minimized or controlled by enhancing ability of energy absorption (toughness) of columns. So there is need to study behavior of concrete under low toughness and techniques of enhancement of toughness to increase overall performance and durability of RC structures.

There are many reasons for applying natural fibers in concrete. Natural fibers are nature friendly and usually obtained from plants and trees. They are cheaper and have good mechanical properties i.e. tensile strength, flexural strength and compressive strength. The cost of replacement is very low as compared to other concrete materials. So, they have become popular among researchers. Many types of natural fibers are present and easily available. Coir, bamboo, rise husk, banana and jute fibers are some examples of natural fibers. Concrete columns when undergoes compressive load, a resistance is present to withstand this load and resist against cracking and failure. At a point, column starts cracking and then deforms completely. According to British standard BS EN 12390-3:2019, the concrete can withstand the strain of 0.0035 and the steel present in RC structures starts yielding at a strain of 0.002 that can increase than concrete. When axial stress value exceed the certain limit then it causes increase in strain limit of concrete. Hence, as a result of this, concrete will fail suddenly by sudden crushing of concrete. If this particular section is properly reinforced it will provide warning before failure phenomenon. Sometimes columns due to eccentric moments caused by unbalanced loads are subjected to bending moments along with axial forces. Axial compressive stress and bending stress act, by adding the effect resulting final stress in that particular section. Failure of column due to these additive stresses will happen as explained earlier. The designers should keep in mind the load combinations and possible alternative loading effects. We need to be alert while having deviations in span.

IEECP 21, July 29-30, 2021, Silicon Valley, San Francisco, CA – USA

DAI : *hhttps://sci-index.com/DAI/2021.99101/IEECP/14899311*

The flaws of columns under compressive loads can be overcome by using appropriate fiber materials as additive for enhancing overall structural compressive member's strength and toughness [3]. Columns may take an extra time in fracture as fiber can take load while experiencing compressive load. The purpose of this study is to analyze the behavior of RC columns under axial loads and the available ways to increase compressive toughness by taking into count the state of the art literature. Chemical, physical and mechanical properties of banana fibers are studied to choose banana fiber as suitable fiber. The feasibility and existing studies related to the usage of banana fiber in RC columns and expected performance due to banana fiber reinforced RC columns and improved toughness is also discussed.

II. FLAWS IN RC COLUMNS REGARDING COMPRESSIVE TOUGHNESS

Concrete is a brittle material and have lower ductility in comparison with steel [4]. Column is compression member of RC structure which transfers load to foundation. Axial load of structure is applied on column, eccentric moments also join and transformation of combined effect happens [5]. Corrosion in RC columns results in reduction of performance degradation in member strength and ductility. The un-retrofitted eroded columns failure mode is converted from flexure failure to shear compression failure [6]. When column experiences compression load the concrete cover spalls out resulting in reduction of durability and toughness [7]. By the consequences of this phenomenon, durability and performance is compromised in long terms in worse conditions [8] [9] [10]. Concrete and reinforcement withstands stresses when columns are axially loaded. In unfortunate conditions, if the area of cross-section of column is less as compared to the loads, the column can be failed without going any lateral deformation. As steel of column and concrete has reached the yield stress. This failure is due to the crushing effect of material.

Vertical elements like columns are subjected to cyclic loading. In the compression members, the higher stresses are generated near connections. The lack of links in the areas where shear stresses are high cause failure of columns. If toughness of the column which is under cyclic load is less, then it will suddenly collapse. Columns are usually designed against considering the effect of shear, axial and bending forces but sometimes due to irregularities in structure, effect of torque can be observed. Columns have reinforcement around the section and considered as rigid. However, if torsional effect crosses the limits then columns can collapse. Low toughness will cause sudden deformation while collapsing. The engineered cementious composites (ECC) behavior was determine under pure compression load by testing. Results were combined in terms of load deformation curves, ductility and toughness. It was observed that the failure mode was sudden due to low toughness but toughness can be increased by using ECC skin [11].

III. AVAILABLE MEASURES TO ENHANCE COMPRESSIVE TOUGHNESS

The effect of content of fiber on flexural and compressive strength by appropriate tests was found. It was observed that the mechanical properties were enhanced along with first crack and failure strength by enhancing the amount of fiber in concrete mixture. Concrete has brittle nature and this nature induces micro cracking, due to penetration of intruding agents the service live of concrete may be reduced causing durability issues. Carbon nanotubes result in reduction of micro cracking by enhancing cement paste matrix. Hence it increases the toughness and durability resistance [12]. Recycled aggregate has been used along with fibers by researchers to check the properties of concrete made by recycled aggregate. For this purpose recycled aggregate (RA) was used from 0% to 100% and fiber 0% to 1%. Results revealed that the hardened properties of this concrete were somehow less than the conventional concrete that can be due to presence of old mortar in RA. On the other hand, compressive strength increased marginally but the split tensile strength increased by 43-52% and flexural strength 35-44%. There was a considerable increase in compressive toughness of concrete [15].

The stress-strain graph by varying content of RA and fibers is shown in figure 1. It was observed that the failure in graph for the concrete without fibers is sudden and post-peak toughness is little. However, the failure in concrete that has fiber content is gradual with significant amount of toughness [14] [15]. It was concluded that the addition of fibers enhanced the peak stress ration from 1.091 to 1.112 and peak strain ratio from 1.49 to 1.56. The overall value of peak strain ratio was increased by 50-60% and peak stress ratio is increased by 9-11%. It is clear from table 1 that the compressive toughness (total energy absorbed) is considerably increased [13]. This Toughness can be increased by using fibers in concrete. So, the structure will show gradual failure pattern instead of sudden failure. [16] Conducted a

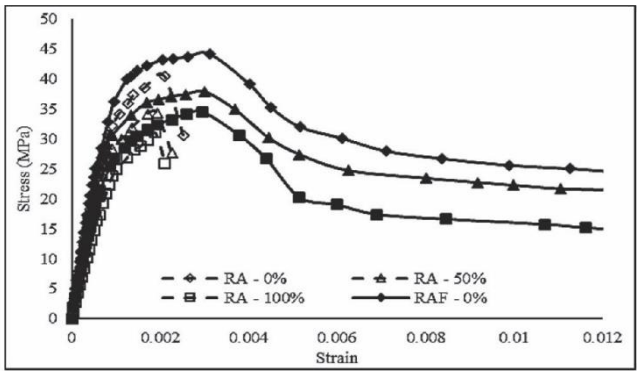

Figure 1. Stress-strain graph of recycled aggregate (RA) with and without fiber [13].

study one the effects of fiber towards the enhancement of compressive toughness. This study concluded that by the addition of fibers there was a slight increase in compressive load but post-peak compressive ductility was greatly enhanced. The compressive toughness values were calculated for 0.5% and 0.75% addition of fibers. Compressive toughness increased by three to six times. The increased compressive toughness was due to the bridging effect of fibers towards micro-cracking. Due to the bridging effect of fibers, propagation of micro-cracking to macro-cracking reduced. Hence, material withstand more load instead of sudden deformation and ability to absorb energy and toughness increased.

Table 1. Toughness index with and without fibers [13]

Specimen ID	Total Energy (KJ/m^3)	Toughness index
RA-0%	76.23	5.04
RAF-0%	384.34	-
RA-50%	57.52	5.74
RAF-50%	330.17	-
RA-100%	44.85	5.73
RAF-100%	257.10	-

IV. SELECTION OF SUITABLE FIBER

Many kind of natural and artificial fibers are present for use during construction. Each fiber has own characteristics. Fibers are usually use to enhance the properties of concrete. At one side if fibers enhance properties of concrete, it's not necessary to enhance all properties. Some properties remains same and some properties are enhanced considerably to take desired results. Natural fibers increase tensile and flexural strength of concrete. It has been observed that compressive strength is reduced by usage of natural fibers in most of the cases. There is an important factor of absorbing

energy is increased by natural fibers [16]. As a result of this the plasticity of concrete is enhanced. Concrete takes more fracture time as compared to the normal concrete made by simple mixture of cement, sand, aggregates and water. The Mechanical properties of Banana Fiber-reinforced virgin and recycled High-Density Poly Ethylene (HDPE) were determine in terms of tensile and flexure properties. During this study results concluded that the improvement occurred in tensile modulus and reduction in tensile strength. Furthermore, the reasonable increase in flexural strength and flexural modulus was observed [17].

Natural fibers are divided into two major categories the one is animal fibers and other is plant fibers. Chicken feathers, cocoon silk, spider silk and wool are some examples of animal fibers and used for biomedical applications. Composites prepared by natural fibers are eco-friendly, light in weight with considerable strength. The important factors that make natural fibers superior to artificial fibers are minimal health hazards during preparation, low cost, good thermal and acoustic insulation, biodegradable, good specific strength and modulus and ease of availability. Fibers are sometimes treated with different chemicals to obtain better strength results [18]. Plant fibers contain jute, coir, banana, bamboo and coconut etc. Banana fiber is natural fiber with good mechanical properties [19]. It has good thermal conductivity and thermal resistance [20]. It has strong moisture absorption and light in weight. Table 2 contains the chemical properties of banana fiber. Table 3 shows the mechanical and physical properties of banana fiber [22] . It has been observed that the treatment of banana fibers with 6% NaOH concentration for optimum treatment and immersion time is 2 hours. This process yields the 12.45 GPa tensile modulus whereas 371 MPa tensile strength and 3.96 MPa interfacial shear strength. As concentration of NaOH increases the tensile strain also increases. Mechanical properties of banana fiber deteriorate significantly when concentration of NaOH increases beyond 6% [22].

Table 2. Chemical properties of banana fiber [22]

Sr. No	Constituents	Banana Fiber
1	Cellulose (%)	63-64
2	Hemi cellulose (%)	6-9
3	Lignin (%)	5-10

Table 3. Mechanical and physical properties of banana fiber [22]

Sr. No	Mechanical and Physical Properties	Banana Fiber
1	Density (g/m^3)	1.25-1.35
2	Tensile Strength (MPa)	529-914
3	Tensile Modulus (GPa)	24-32
4	Elongation (mm)	2-2.5
5	Fiber Diameter (m^{-4})	50-250

Different natural fibers and their properties are present in Table 4. The low density and higher tensile strength of banana fiber make it superior than other described fibers. Because concrete is weak in tension and strong in compression. The usage of banana fiber may provide better strength properties as well as compressive toughness.

Table 4. Comparison of mechanical properties of different plant fibers [30]

Sr. No	Natural Fibers	Density (g/cm^3)	Tensile Strength (MPa)
1	Jute	1.35-1.45	393-773
2	Pineapple	1.44-1.56	170-727
3	Banana	1.30-1.35	503-790
4	Cotton	1.50-1.60	287-587

V. EXPECTED FEASIBILITY, USABILITY AND PERFORMANCE

Due to the increase of environmental, social and economic issues, there is need for sustainable and low cost construction. Dumping of agricultural waste like banana fiber is a matter of concern and it may cover large part of agricultural land. The other way which is often adopted is burning of agricultural waste, which is also not a healthy practice [24]. It causes global warming. The utilization of this agricultural waste (banana fiber) can enhance the properties of concrete and ability to absorb energy is also increased. Banana fiber is feasible to be used in concrete because it has no impacts on human and environment. Hence, it is a sustainable light weigh material for cleaner production and sustainable development. Banana fibers can be used in reinforced concrete columns to enhance their compressive toughness and other properties [25]. It changes the brittle nature of concrete to ductile behavior [26]. Micro-cracking is one of the major flaw in concrete [26]. Micro-cracks under the application of loads are converted to macro-cracks. So, the structure fails. Micro-cracking can be bridge by usage of banana fibers in concrete. Varied

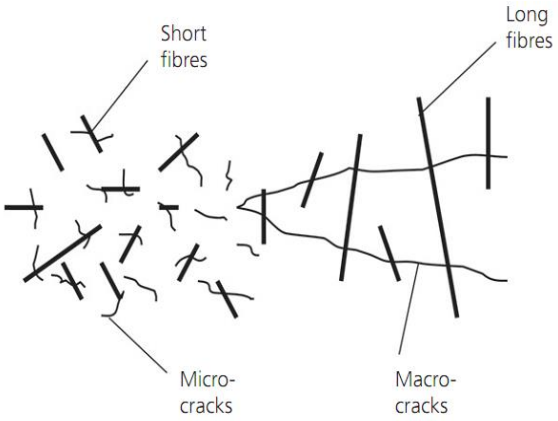

Figure 1. Crack bridging mechanism of natural fibers used in concrete [28].

length banana fibers can be used to bridge micro as well as macro-cracking in concrete as shown in figure 2. Due to addition of fibers in concrete, the stresses may transfer to upper and lower portion of crack surface in concrete. So, there can be reduction of stress in cracks tip. By this phenomenon, the cracks propagation to macro-cracking can be controlled up to some extent. Concrete will withstand more load [27]. Hence, the ability to absorb energy and finally the toughness will increase.

Concrete spalls out under the effect of elevated temperatures and failure of concrete columns may happen. Usage of fibers in concrete RC columns may lead to decrease in spalling phenomenon up to some extent [29]. The overall performance of concrete depends upon the compressive, tensile and flexural strengths of concrete. It has been observed that utilization of natural banana fibers lead to increase in all strength parameters with reduction of cement content which is not environment friendly. Performance of concrete is also

enhanced by fibers and adverse ecological effects are also minimized. This is the need with the growing age to find out new materials which are sustainable, enhance performance without compromising strength properties. Natural fibers are more feasible than artificial fibers like steel fiber because they are easy to mix and handle. Natural fibers are fire resistant and found useful to earthquake prone area. Because they have good response under seismic loadings. Concrete columns made up of reinforced concrete and banana fiber may provide better properties than simple RC columns with less ecological effects and cleaner production.

VI. CONCLUSIONS

Fibers have great influence on the properties of concrete columns. Flaws in concrete and ways of improvement are studied. Analysis of banana fiber's mechanical chemical properties is done for choosing it as a suitable fiber in this study. The expected feasibility of RC columns made up of fibers and their expected performance is also taken into count. By conducting this study following conclusions can be drawn:

- By addition of fibers, compressive strength may be compromised but considerable increase in compressive toughness is observed.
- The specimen without fiber content showed sudden failure with small value of post-peak toughness. On the other hand, specimen of concrete with fiber exhibited a significant post-peak toughness and a gradual failure.
- The overall value of peak strain ratio is increased by 50-60% and peak stress ratio is increased by 9-11% by addition of fiber.
- Due to the use of banana fibers in concrete columns, micro-cracking can be reduced along with propagation of micro-cracks towards macro-cracks, toughness can be increased and material can continue to withstand load.
- Toughness can be increased by using ECC skin.

The above outcome is favorable indicating the enhancement of performance of concrete columns. Banana fibers can be used to increase the toughness of RC columns and as a result of this overall durability can be enhanced.

VII. ACKNOWLEDGMENTS

The authors would like to thank all who has helped in this research, especially Engr. Blawal Hasan. The careful reviews and constructive suggestions by anonymous reviewers are gratefully acknowledged.

VIII. References

[1] H. Tiana, Z. Zhou, Y. Zhang, Y. Wei, "Axial behavior of reinforced concrete column with ultra-high performance concrete stay-in-place formwork," Engineering Structures, 2020.

[2] M. A. Mosaberpanah, Ozgur Eren, "Relationship between 28-days compressive strength and Compression toughness factor of Ultra High Performance Concrete using design of experiments," in International Conference on Sustainable Design, Engineering and Construction, 2016.

[3] A. G. Adeniyi, A. S. Adeoye, J. O. lghalo, D. V. Onifade, "FEA of effective elastic properties of banana fiber-reinforced polystyrene composite," Mechanics of Advanced Materials and Structures, 2020.

[4] M. Khubaib, I. Khan, M. M. Rana, Y. Zhang, C. K. Lee, "Behaviour of engineered cementitious composite-encased stub concrete columns under axial compression," Magazine of Concrete Research, pp. 984-1005, 2020.

[5] G. Lin, J. J. Zeng, J. G. Teng, L. J. Li, "Behavior of large-scale FRP-confined rectangular RC columns under eccentric compression," Engineering Structures, 2020.

[6] Y. Zhou, X. Chen, X. Wang, L. Sui, X. Huang, M. Guo, B. Hu, "Seismic performance of large rupture strain FRP retrofitted RC columns with corroded steel reinforcement," Engineering Structures, vol. 216, 2020.

[7] Z. Huang, X. Huang, W. Li, L. Mei, J. Y. R. Liew, "Experimental behavior of VHSC encased composite stub column under compression and end moment," Steel and Composite Structures, pp. 69-83, 2019.

[8] J. Caiab, J. Pana, X. Li, "Behavior of ECC-encased CFST columns under axial compression," Engineering Structures, pp. 1-9, 2018.

[9] J. Cai, J. Pan, C. Lu, "Mechanical behavior of ECC-encased CFST columns subjected to eccentric loading," Engineering Stuctures, pp. 22-28, 2018.

[10] J. Cai, J. Pan, H. Su, C. Lu, "Experimental study on the hysteretic behavior of ECC-encased CFST columns," Engineering Structures, pp. 107-121, 2018.

[11] M. K. I. Khan, M. M. Rana, Y. X. Zhang, C. K. Lee, "Compressive behaviour of engineered cementitious composites and concrete encased steel composite columns," Journal of Constructional Steel Research, 2020.

[12] A. J. Khan, L. A. Qureshi, M. N. A. Khan, A. Gul, M. Umar, A. Manan, Y. I. Badrashi, A. Abbas, U. Javed, R. Farooq, "Axial Compressive Behavior of Reinforced Concrete (RC) Columns Incorporating Multi-Walled Carbon Nanotubes and Marble Powder," Crystals, 2021.

[13] Y. Paluri, S. Mogili, H. Mudavath, V. Noolu, "Effect of fibres on the strength and toughness characteristics of recycled aggregate concrete," Materials Today: Proceedings, pp. 2537-2540, 2021.

[14] H. H. Kasagani, S. R. Ravi, T. Prathipati, C. Butchi, K. Rao, "Influence of graded glass fibres on strain hardening and strain softening behaviour of CGGF under uniaxial stress," Magazine of Concrete Research, 2021.

[15] S. Abdallah, W. A. David, " Concretes, Comparisons Between Pull-Out Behaviour of Various Hooked-End Fibres in Normal–High Strength," *International Journal of Concrete Structures and Materials*, 2019.

[16] K. H. Mo, K. K. Q. Yap, U. J. Alengaram, M. Z. Jumaat, "The effect of steel fibres on the enhancement of flexural and compressivetoughness and fracture characteristics of oil palm shell concrete," Construction and Building Materials, 2014.

[17] J. E. Rivera, R. Eid, P. Paultre, "Influence of synthetic fibers on the seismic behavior of reinforced-concrete circular columns," Engineering Structures, 2021.

[18] B. K. Singh, U. K. Komal, Y. Singh, S. S. Banwait, I. Singh, "Development of banana fiber reinforced composites from plastic waste," Materials Today, 2021.

[19] N. M. Nurazzi, M. R. M. Asyraf, A. Khalina, N. Abdullah, H. A. Aisyah, S. A. Rafiqah, F. A. Sabaruddin, S. H. Kamarudin, M. N. F. Norrrahim, R. A. Ilyas, S. M. Sapuan, "A Review on Natural Fiber Reinforced Polymer Composite for Bullet Proof and Ballistic Applications," Polymers, 2021.

[20] J. Kenned, K. Sankaranarayanasamya, J. S. Binoj, S. K. Chelliah, "Thermo-mechanical and morphological characterization of needle punched non-woven banana fiber reinforced polymer composites," Composites Science and Technology, vol. 185, 2020.

[21] K. Muthukumar, R. V. Sabariraj, S. D. Kumar, T. Sathish, "Investigation of thermal conductivity and thermal resistance analysis on different combination of natural fiber composites of Banana, Pineapple and Jute," Materials Today: Proceedings, 2020.

[22] P. V. Badyankala, T. S. Manjunathab, B. G. Vaggara, K. C. Praveen, "Compression and water absorption behaviour of banana and sisal hybrid fiber polymer composites," Materials Todays: Proceeding, pp. 381-386, 2021.

[23] A. Parrea, B. Karthikeyana, A. Balajib, R. U. Dhayasankar, "Investigation of chemical, thermal and morphological properties of untreated and NaOH treated banana fiber," Materials Today: Proceedings, pp. 347-352, 2020.

[24] I. O. Adejumo, O. A. Adebiyi "Agricultural Solid Wastes: Causes, Effects, and Effective Management," In Solid Waste Management. IntechOpen.

[25] N. K. Krishna, M. Prasanth, R. Gowtham, S. Karthic, K. M. Mini, "Enhancement of properties of concrete using natural fibers," Materials Today:PROCEEDINGS, 2018.

[26] R., P. S. Sarvesh, "An Experimental study on Crushed Stone Dust as Fine Aggregate in Cement Concrete," Materials Today: Proceedings, 2018.

[27] J. B. Sajin, P. B. Aurtherson, J. S. Binoj, N. Manikandan, M. S. Senthil Saravanan, T.M. Haarison, "Influence of fiber length on mechanical properties and microstructural analysis of jute fiber reinforced polymer composites," Materials Today: Proceedings, 2021.

[28] M. Khan, M. Cao, "Effect of hybrid basalt fibre length and content on properties of cementitious composites," Magazine of Concrete Research, 2021.

[29] D. Zhang, G. Y. Tan, K. H. Tan, "Combined effect of flax fibers and steel fibers on spalling resistance of ultra-high performance concrete at high temperature," Cement and Concrete Composties, 2021.

[30] D.U. Shah, Developing plant fibre composites for structural applications by optimising composite parameters: a critical review, Journal of materials science. 48 (18), 2013

THE EFFECTS OF THE TRANSIENT AND PERFORMANCE LOSS RATES ON PV OUTPUT PERFORMANCE

Chibuisi C. Okorieimoh
School of Electrical & Electronic Engineering
Dublin Energy Lab
Technological University Dublin
Dublin, Ireland
chibuisi.okorieimoh@tudublin.ie

Brian Norton
School of Electrical & Electronic Engineering
Dublin Energy Lab
Technological University Dublin
Dublin, Ireland
brian.norton@tudublin.ie

Michael Conlon
School of Electrical & Electronic Engineering
Dublin Energy Lab
Technological University Dublin
Dublin, Ireland
michael.conlon@tudublin.ie

Abstract

Solar photovoltaic (PV) panels experience long-term performance degradation as compared to their initial performance, resulting in lower like-per-like efficiencies and performance ratios. Manufacturers of solar photovoltaic modules normally guarantee a lifespan of more than 20 years. To meet such commitments, it is important to monitor and mitigate PV module degradation during this period, as well as beyond, to recognize maintenance and repair needs. Solar PV modules degrade over time, becoming less effective, less reliable, and eventually unusable. The effects of transient and performance loss rates on the output performance of polycrystalline silicon (p-Si) solar PV modules are the focus of this study. PV modules' electrical performance and solar energy conversion efficiency change as solar irradiance and ambient temperature change. A rise in ambient temperature or a decrease in solar irradiance, for example, all result in a reduction in performance.

Large variations in operating conditions due to uncontrollable external parameters such as cloud movement and wind velocity, as well as changes in factors external to PV systems such as unexpected shading, inverter problems, and control failures, may trigger transient performance changes on PV modules output. The data used in this analysis were from the Warrenpoint site location of the Electric Supply Board (ESB) for the years 2016-2020. Clear days in winter, spring, summer, and autumn were caused by a rise in daily sunshine hours in February, May, June, and September, according to the output performance. Due to the highest amount of solar irradiation at the site location, these days saw an increase in PV output generation. According to the performance loss rates, the median degradation rates in 2016 (4.5%/year to 14%/year) and 2017 (0.1%/year to 5.2%/year) are 8.40%/year and 3.87%/year, respectively. This means that the degradation rate is greater than 1%/year, the hazardous probability is between 90% and 100%, and a severity of 10 is given (With an associated failure of corrosion in solder bonds). 2018 (-7.5%/year to 2.5%/year), 2019 (-16%/year to -23%/year), and 2020 (-5.1%/year to -10% /year) had median degradation rates of -2.75%/year, -18.23%/year, and -5.2%/year, respectively. This shows that the degradation rates are less than 1% per year, and their hazardous probabilities range from severity rank 9 to 1, or 80% to 70% to 0% safety risk. All of these factors have a negative impact on PV output performance.

Keywords: *Transient, Performance loss rates, PV output performance, Degradation rates.*

INTRODUCTION

Solar PV panels experience long-term performance degradation resulting in lower like-per-like efficiency and performance ratios when compared with their initial performance [1]. Also, there are some transient effects (such as PV ambient temperature, wind velocity, shade, and dust particles) that reduce the output performance of the solar PV panels [2]. Reducing rates of PV module degradation aims to maintain the efficiency of solar PV systems [3]. As manufacturers usually guarantee the life span of PV modules for more than 20 years [3], it is, therefore, necessary to track and mitigate the degradation of PV modules over this period both during and beyond this period knowing degradation behavior is essential for operation, maintenance, and repair [1]. Most significantly, many PV module failures and, performance losses are caused by the gradual accumulation of damaged PV modules due to long-term outdoor exposure in harsh environments. This outdoor environmental stress is known as weathering [4]. To put a check on the outdoor installed PV modules, there is a need for accelerated tests. Outdoor testing of PV modules may take a longer time to be accomplished and it is impossible to wait up to 20-25 years to introduce a new PV module. Hence, it is important to develop and use accelerated tests to quantify or measure up the new PV modules [5]. Such accelerated stress tests are thermal cycling, humidity-freeze, damp heat, mechanical load (both static and dynamic), and ultraviolet exposure [5]. When a PV module fails to generate power, such failure will be seen as a reliability issue while a decrease in output of a PV module is caused by environmental degradation such as corrosion and it is classified as a durability issue. Therefore, the durability and reliability issues may eventually lead to PV module failure [4].

IEECP'21, July 29-30, 2021, Silicon Valley, San Francisco, CA – USA

DAI : *https://sci-index.com/DAI/2021.99101/IEECP/14736087*

A. *PV Durability and Reliability Issues*

The best way to deal with the PV reliability issues is by the use of the bathtub reliability curve (see Figures 1 (a) and 1 (b)) to find the physics of failure for each mode [6]. The bathtub reliability curve of a PV module is a graphical model made to represent the failure rate of a group of PV modules over some time. The curve helps the PV manufacturers to predict when failures occur on the PV module and possibly identify the root causes of the failure and possible ways of preventing them [4]. The bathtub reliability curve describes the failure rate of the PV module as a function of in-service life. Therefore, the curve consists of three essential parts, namely: Failure mode A (infant mortality), failure mode C (normal life), and failure mode B (end of life wear-out).

Failure mode A: Failure mode A is the early life failure (also, known as infant mortality) that normally occurs in the first 1-2 years of a PV module's life. Failure mode A occurs at the initial stage of the module's life cycle. The cause of failure mode A may be due to fundamental design faults, processing issues, errors in manufacturing, or inappropriate installation [4]. Therefore, Passing IEC 61215 or 61646 qualification tests are not proof that a PV module has been tested and shown to be durable and reliable rather the IEC environmental stress test protocols are designed primarily to test the period of early life failures (infant mortality) (see Figure 1 (b)) [6].

Failure mode C: Failure mode C is the constant (random) failures (also, known as normal life). This is the second part of the failure mode that occurs within the lifespan of the PV module. It is called the "constant (random) failures" because the failures in this mode are usually predictable and homogeneous. This failure mode usually occurs within this period when the stresses of the module have exceeded the strength of its weakest component. The cause of this failure mode is a result of unexpected environmental stress or load issues. For instance, when a PV module exceeds its capabilities it can suffer from a normal life failure (failure mode C).

Failure mode B: Failure mode B is the last part of the curve known as the end of life for the PV module (also, known as the end of life wear-out). In this failure mode, the curve rises steeply as many of the PV modules simply reach the point where they failed due to simple age or wear and tear. Failures of this kind are reasonably predictable.

B. *Distinguishing Transient Performance changes from longer-term degradation*

PV module output varies with solar irradiance and module temperature. It is also affected by shading, rain, and dust [7],[8]. All these variations are transient on a variety of timescales and/or reversible. Degradation refers to the loss of output due to physical degradation or damage to the PV cell, the effects are not reversible [1]. It refers to effects that will ultimately require the replacement of a PV cell for the system to return to its initial performance. The transient effect caused by an increase in PV cell ambient temperature can lead to reductions in output and efficiencies [2]. Degradation is measured by changes in mean efficiency and/or performance ratio over the long term as illustrated indicatively in Figure 2 [1]. It can also be observed in perturbation caused by cell failure in the current-voltage (I-V) curves for an array [1].

Individual module degradation can be attributed to intrinsic property changes in the PV materials caused by external effects such as:

- Potential induced degradation (PID) [9]; and
- Light-induced degradation (LID) [10].

The outdoor operation of cells as part of a module in an array means mechanisms external to the solar cell such as corrosion in interconnections and solder bonds play a significant role in performance degradation [3]. This makes it important to determine the degradation rates under outdoor operational conditions rather than indoor testing of isolated modules. [3], classified the major difficulties in evaluating degradation rates of PV modules from real operational data into:

- Large fluctuations of the operational data due to uncontrollable external parameters such as weather conditions like solar radiation, rain, cloud movement, wind velocity, and ambient temperature together with unexpected changes of factors external to PV systems such as unexpected shading, inverter problems, and control failures.
- systematic 'degradation' in the measurement of PV module operational performance caused by control sensor drifting with time as a result of electronic aging of components such as the drifting of irradiance sensors. The energy output of a PV system depends on weather conditions [11], [12], [3]. The degradation rate of silicon PV modules is around -0.7% per year of maximum power rating [11]. Reducing rates of PV module degradation aim to maintain the efficiency of solar PV systems [3]. As manufacturers usually guarantee the life span of PV modules for more than 20 years [3], it is, therefore, necessary to track and mitigate the degradation of PV modules over this period. Both during and beyond this period knowing degradation behavior is essential for operation, maintenance and repair.

C. *Degradation Rates of Photovoltaic Modules*

The study of annual degradation rates of recent crystalline silicon PV modules was carried out by Tetsuyuki and Atsushi [13]. Six crystalline silicon PV modules connected to an electric power grid were analyzed. Three indicators were used for the annual degradation rates of the different crystalline silicon PV: energy yield, performance ratio, and indoor power. The performance of the module was evaluated from electricity output measurements taken over 3 years. The following trends were found in the three indicators; energy yield: 0.0, -0.4% per year, 0.0, 0.1% per year, 1.5% per year and 0.5% per year, performance ratio: 0.0, -0.4% per year, -0.1% per year, 0.0, 1.4% per year and 0.5% per year and indoor power: 0.1% per year, -0.3% per year, 0.2% per year, 0.0, 0.7% per year and 0.6% per year were similar. The performance of the newly installed PV modules was found to decrease by over 2% as a result of initial light-induced degradation (LID) after installation [13].

The power output of an outdoor PV module has been shown to reduce as a result of thermal cycling causing crack formation between solders and metals [14]. Dunlop and Halton [7] studied the degradation of PV modules in outdoor conditions for 22 years. They monitored the electrical power outputs of monocrystalline silicon (m-Si), polycrystalline silicon (p-Si), and amorphous silicon (a-Si) modules. They found an 8% to 12% decrease in maximum power output of the PV modules (P_{max}) after 20 years of outdoor exposure. Their research showed that about 80% of the reduction was due to corrosion and the remaining 20% was attributed to dust accumulating on the PV modules. An experimental study of degradation modes and their effects on the PV module was conducted after 12 years of field operation [15]. Their investigation found that degradation led to annual reductions in output power ranging between 2.08% and 5.2%. Short circuit current (I_{sc}) is reduced by between 2.75% and 2.84% annually. The open-circuit voltage (V_{oc}) was found to be the least affected, with annual reductions ranging between 0.01% and 4.25%. The existence of only one highly degraded PV module in a PV system reduces daily output from Takatoshi et al, [16]:

i. 19.8 kWh to 18.7 kWh during sunny days;
ii. 11.3 kWh to 10.8 kWh during partly cloudy sunny days; and
iii. 5.5 kWh to 5.3 kWh during cloudy days.

D. *Analysis of Risk Priority Number (RPN) on the Severity of PV Failure Modes*

Failure Modes and Effects Analysis (FMEA) finds the effect of each failure mode and its causes on the system, according to the severity (S), occurrence (O), and detect-ability (D) [17]. The IEC 60812 standard has assumed a different range of S, O, and D for a PV system, which is helpful to identify the particular single failure mode based on RPN for the particular PV system and operating environment conditions [17]. A measurement of RPN is therefore expressed in (1) [17]:

$$RPN = S \times O \times D \quad (1)$$

Where:
S is the severity, which is a non-dimensional number. Severity determines the single failure mode, which strongly affects the PV system performance.
O is the occurrence, which depends on the probability of occurrence of a defect in the PV system during the exposure time.
D is the detection, which technology or instrument can identify the failure modes in a PV system during its exposure time.
The severity rank of failure mode depends on the degradation rate per year and safety issues. It is very difficult to find out the severity rank of a particular failure mode, as the degradation of a PV module is a cumulative sum of many factors [18],[19]. The highest rank in the severity given according to the safety issue probably insulation resistance failure, de-lamination, and burn mark occurs in the PV module, it is a threat or hazard to person or either property [17]. The severity number from 9 to 10 related to safety issues and the highest degradation factor, whereas the numbers from 8 to 1 depending on the performance degradation factor. In the present study, the severity rank performs according to References [20],[21]. The rank of severity has been given by Pramod et al [17] in Table 1.

MATERIALS AND METHODS

A. *Site Location and Climate Description*

The location chosen for this study is based on the Electricity Supply Board ESB) site located at Upper Dromore Road, Warrenpoint, Northern Ireland at 54.115551ºN latitude and 6.263654ºW longitude. The City of Warrenpoint acquires its power from the ESB public grid, which is shared with other residential and industrial consumers.
(https://www.google.com/maps/place/Newry+BT34+3PN,+UK/@54.1132142,-6.2642131,248a,35y,44.92t/data=!3m1!1e3!4m5!3m4!1s0x4860da664698253b:0xd3507b57cb2eea3!8m2!3d54.1150048!4d-6.2630492)is used to identify the site location.

B. *System Monitoring and Data Acquisition*

The data acquisition system used in this research consists of two SMA STP-20000TL-30 inverters each with a 20 W sensor box and a data logger. The sensor box measures the total solar radiation on the solar PV modules in-plane. The sensor box and the inverter have been connected to the data logger and the power injector. The data recording was set at 15 minutes (quarter-hour) intervals in the data logger and was extracted directly from the Excel spreadsheets to the computer and then analyzed using the MATLAB and Excel software tools.

RESULTS

A. *Transient (Partial Shading) Effect in Solar Cells*

I. *Description of System*

In this study, a system description of distributed circuit simulations of a PV module under partial shading conditions is presented. The PV module is connected to a variable DC voltage source converter (VSC) to quantify the I-V and P-V characteristics curves. A MATLAB SIMULINK is used to model the circuit: (i) as three strings of 20 series-connected cells parallel to bypass diodes which allow current flow when cells are shaded or damaged with a standard irradiance of 1 kWm^{-2} applied to String 1 (cells 1-20) while (ii) partial shading is applied to String 2 (cells 21-40) with an irradiance of 0.3 kWm^{-2} and (iii) String 3 (cells 41-60) with an irradiance of 0.6 kWm^{-2} as shown in Figure 4.

II. *Simulation Process*

The model is therefore simulated and at the end of the simulation, the I-V and P-V characteristics curves were plotted. When the PV module is connected to the voltage-sourced converter (VSC) it makes it difficult for the Maximum Power Point Tracking (MPPT) algorithm to converge at the highest peak. The global maximum power point (GMPP) indicated in the red circle of Figure 5 is 334 W at the maximum current of 5.29 A. The resultant characteristics of the PV array are shown in Figure 5. The P-V curves generate three peaks under partially shaded conditions (see Figure 5).

III. *Simulation Results*

Figure 6 shows the variation in the solar PV cell string and bypass diode used to reduce the shading effect. In string 1 (i.e., cells 1-20), the bypass diode (with blue color) has zero current. This is because string 1 solar cells do not have any shading effects. While in String 2 (i.e., 21-40 cells) and String 3 (i.e., 41-60 cells) solar cells had shading effects. It is noticed that the current flow is above zero. This shows that the bypass diode works.

B. *Inverter Percentage Conversion Loss*

When the inverter converts the DC energy from the solar PV system to AC energy, some energy is lost, which could be due to the cable, PV module, or inverter. As shown in Table 2, this is estimated as inverter percentage conversion loss using equation (2) and the values vary according to the number of energy losses from the inverter given by (3).

$$\text{Inverter percentage conversion loss} = \frac{DC\ Energy - AC\ Energy}{DC\ Energy} \times 100\% \quad (2)$$

$$\eta_{inverter} = \frac{E_{AC}}{E_{DC}} \times 100\% \quad (3)$$

Where: $\eta_{inverter}$ is the inverter efficiency that is the ratio of output energy (AC energy) to input energy (DC energy) multiply by 100%.

C. *Yields, Array Capture, and System Losses*

Table 3 displays the daily DC array, AC final, and reference yields, DC array capture, and AC system losses of the PV system as measured at quarter-hourly intervals using the ESB Warrenpoint system. These were obtained from the system measurement and analyzed using (4), (5), (6), (7), and (8). In December and May, the monthly daily DC array, AC final, and reference yields, DC array capture, and AC system losses ranged from 0.46 to 4.72 h/day, 0.45 to 4.63 h/day, 5.2 to 16.41 h/day, 4.74 to 11.69 h/day, and 0.01 to 0.09 h/day, respectively. The average annual daily DC array, AC final, and reference yields, DC array capture, and AC system losses were 2.32 hours per day, 2.30 hours per day, 8.83 hours per day, 6.51 hours per day, and 0.02 hours per day, respectively. Figures 7 (a) and 7 (b) show the DC array, AC final, and reference yields of a monthly daily PV system as obtained from the ESB Warrenpoint

system, as well as the AC system loss. The DC array capture loss could be due to transient effects (such as shading, dust, wind velocity, ambient temperature, or module temperature) [2], corrosion of solar cell connections, or degradations.

$$Y_{A,day} = \frac{DC\ Energy\ (\frac{kWh}{kWp})}{Total\ number\ of\ days\ in\ operation} \quad (4)$$

$$Y_{F,day} = \frac{AC\ Energy\ (\frac{kWh}{kWp})}{Total\ number\ of\ days\ in\ operation} \quad (5)$$

$$Y_{R,day} = \frac{Solar\ Irradiation\ (\frac{kWh}{m^2})}{\frac{G_{STC}(kWm^2)}{Total\ number\ of\ days\ in\ operation}} \quad (6)$$

$$Lc_{,day} = Y_{R,day} - Y_{A,day} \quad (7)$$

$$Ls_{,day} = Y_{A,day} - Y_{F,day} \quad (8)$$

Where:

- $Y_{A,day}$: daily array yield, that is, the ratio of the DC output energy (kWh) to its module capacity (kW_P) from a solar PV array over a total number of days in operation [22].
- $Y_{F,day}$: daily final yield, that is, the ratio of the AC output energy (kWh) to its module capacity (kWp) from a solar PV array over a total number of days in operation [23].
- $Y_{R,day}$: daily reference yield, that is, the ratio of total daily in-plane solar irradiation (kWh/m^2) its reference solar irradiance (G_{STC}).
- $Lc_{,day}$: daily DC array capture loss, that is, the difference between the DC array yield ($Y_{A,day}$) and the reference yield ($Y_{R,day}$).
- $Ls_{,day}$: daily AC system loss, that is, the difference between the final yield ($Y_{F,day}$) and array yield ($Y_{A,day}$).

DC array yield and AC final yield are plotted as a function of solar irradiance in Figure 8 (a-b) using quarter-hourly (15-minute) interval data. Figure 8 (c-d) shows that the DC array yield and AC final yield are both linearly proportional to solar irradiance. Figure 8 (a-b) depicts sublinear behavior caused by a transient effect like shade/shadow cast, overcast period, or average inverter efficiency loss (about 0.6%) over the PV field. As a result, at low solar irradiance levels, both DC array and AC final yields are either zero or very low due to inverter losses as well as PV generator low irradiance losses.

D. Measurement of Solar Irradiance

Figures 9 and 10 depict various views of the ESB Warrenpoint site solar irradiance, as well as a solar power calendar based on the plane of array solar irradiance averaged for each quarter-hourly period between March and May 2016. March and May were chosen because of their peak clearness indices. It has been observed that March 13, 14, and 22 and May 13, 16, 27, and 31 are clear days, whereas other days such as March 9, 10, 11, 12, 15, 16, 17, 18, and 22, and May 8, 12, 14, 17, 23, 24, 29, and 30 are partly cloudy, and other days such as May 1, 2, 3, 4, 5, 6, 7, 9, 10, 11, 15, 18, 19, 20, 21, 25, 26, and 28, and March 1, 2, 3, 4, 5, 6, 7, 8, 10, 19, 20, 21, 23, 24, 25, 26, 27, 28, 29, 30, and 31 are overcast. As a result of the peak daily clearness index found in May, there are clearer days in May than in March.

E. Measurement of Output Performance

The daily incident solar radiation for any given location is determined by the sun's path across the sky and the amount of cloud cover in the area (Trueblood et al., 2013[46]). Figure 11 (a-d) depicts daytime power profiles at quarter-hourly (15-minute), half-hourly (30-minute), and hourly (60-minute) intervals for three days in each season: a clear day, an overcast day, and a middle day. The clear day, as defined here, is the day of the season with the greatest amount of solar irradiation, resulting in a parabolic curve (see Figure 11 (a-d)); the overcast day is a day with the least amount of solar irradiation, resulting in distortions from perfect parabolic shapes (see Figure 11 (a-d)); and a middle day is a day with the median amount of solar irradiation, resulting in partial parabolic curves. The chosen days of power profiles span the months of each of the four seasons (winter, spring, summer, and autumn) (see Figure 12). Figure 12 shows that the clear days (as seen in Figure 11 (a-d)) in winter, spring, summer, and autumn were caused by an increase in daily sunshine hours in February, May, June, and September. Because of the highest amount of solar irradiation at the site location, these days were generally characterized by an increase in PV output generation. The median increase in daily sunshine hours occur in January, April, July, and October during the winter, spring, summer, and autumn. As a result, PV output generation was moderately high. The overcast day was generally characterized by low solar irradiation due to a decrease in daily sunshine hours, as seen in December, March, August, and November (see Figure 12). As a result, the overcast day generates less PV output. The autumn and winter daily profiles, on the other hand, are more extended, with higher output generation at midday, but they have fewer total hours than the summer and spring profiles, which have more hours of daylength. Because PV panels are more efficient at lower temperatures, output generation is higher during clear days in the spring than during clear days in the summer [24]. The middle day demonstrates that PV output generation can vary throughout the day, owing to cloud movement.

F. Performance Variations

I. Weather-Corrected Performance Ratio (PR)

The performance ratio (PR) is a metric used to evaluate solar photovoltaic installations. PR normalizes the output of the PV system to its installed capacity and the available solar irradiance at the site of installation, allowing a comparison of the performance of systems with different installed capacities in different geographical locations [25]. 3-5 years of data are required to capture seasonal variations [25]. Because the performance ratio is affected by the module and ambient temperature of the system's site location due to variation with changes in meteorological conditions, it is important to measure or quantify this variation and show how it can be removed or reduced by using the two methods described below [26], [27]:

- Traditional calculation of PR (uncorrected PR) using equation (9):

$$PR_{uncor\ r} = \frac{\sum P_{AC\_t}}{\sum_t [P_{STC}(\frac{G_{POA}}{G_{STC}})]} = PR_{Syst.} = \frac{Y_F}{Y_R} \times 100\% \quad (9)$$

- Modifications of uncorrected PR through temperature normalization to produce a temperature-corrected PR to become a weather-corrected PR using (10):

$$PR_{corr} = \frac{\sum P_{AC\_t}}{\sum_t [P_{STC}(\frac{G_{POA}}{G_{STC}})(1+\frac{\delta}{100}(T_{cell\_avg} - T_{ref}))]} \quad (10)$$

$$R_D = \frac{m \times 12}{c} \times 100\% \quad (11)$$

$$\%T_{Losses} = PR_{uncorrected} - PR_{corrected} \quad (12)$$

Where: PR_{uncorr}: uncorrected performance ratio; PR_{corr}: corrected performance ratio; P_{AC}: measured AC electrical generation (W); P_{STC}: summation of installed modules (49920 W_p);

G_{POA}: measured plane of array (POA) irradiance (W/m^2); t: data collection time (15 mins.); G_{STC}: irradiance at standard test conditions (STC) (1000 W/m^2); T_{ref}: reference temperature (25°C);T_{ref}: reference temperature (25°C); δ : Temperature coefficient for power (-0.4%/°C);

R_D: Degradation rates (%); $\%T_{Losses}$: Percentage temperature losses; m and c are the slope and vertical intercept of the linear trend line of the PR versus time (months) plot respectively.

As a result, the weather-corrected PR from 2016 to 2020 is analyzed using the annual PR regression method, and performance data is

sorted for solar irradiance levels greater than 700 Wm^{-2}, as proposed by Quansah and Adaramola in their works [25]. (11) Is used to compute the degradation rates (R_D) [25].

Figures 13-17 show annual PR regression graphs for five years (2016-2020) for both temperature-corrected PR and uncorrected PR. Table 4 and Figure 18 show the annual uncorrected system PR, temperature-corrected system PR, degradation rates, and percentage of temperature losses from 2016 to 2020. Figure 17 depicts a decrease in PV power output over time due to the performance loss rate or degradation rate. It can be seen using error bars and the Severity ranking of failure mode proposed by Pramod et al [17]. According to Figure 17 and Table 4.

The median degradation rates in 2016 (4.5% /year to 14%/year) and 2017 (0.1% /year to 5.2%/year) are 8.40% /year and 3.87%/year, respectively. This demonstrates that the degradation rate is greater than 1% per year, and the hazardous probability is between 90% and 100%. [17]. This is assigned a severity of 10 (with an associated failure of corrosion in solder bonds) [28] and a severity of 10 (with an associated failure of EVA discoloration) [29].

The median degradation rates in 2018 (-7.5%/year to 2.5%/year), 2019 (-16%/year to -23 %/year), and 2020 (-5.1%/year to -10%/year) are -2.75%/year, -18.23%/year, and -5.2%/year, respectively. This demonstrates that the degradation rates are less than 1%/year and that their hazardous probabilities range from severity rank 9-1 or 80% - 70% to 0% safety hazard [17]. EVA discoloration, metallization of the front side grid, de-lamination between EVA and solar cell, glass weathering, de-lamination between EVA and solar cell, oxidation of antireflecting coating, cell metallization and hotspot, surface soiling, corrosion in solder bond, and de-lamination, junction box degraded could all be associated failures here [17].

CONCLUSIONS

Since environmental factors such as humidity, dust accumulation, and wind velocity are agents of transient and performance loss rates, it is important to minimize or reduce these effects by inspecting the proposed geographical location before the installation of solar PV systems. Because of the diversity of climates, it is essential to broaden the optimization considerations to achieve a more significant result. Instead of using standard methods for installing a solar PV system, it is important to consider dominant factors such as wind directions and speeds, which have transient effects on solar PV system output performance. Since solar cell output performance degrades as cell temperature rises due to thermal degradation, it's critical to maintain the surface of a solar panel at a temperature that doesn't exceed its standard test conditions (25ºC). Air- or water-cooling techniques may help to alleviate the problem of overheating caused by an increase in solar irradiance and high temperatures on a solar panel. Therefore, using the characteristics of an anti-reflecting material to increase the output performance of a solar PV panel is recommended.

Figure 1 (a): Using Bathtub curve to explain PV Durability and Reliability Issues [4].

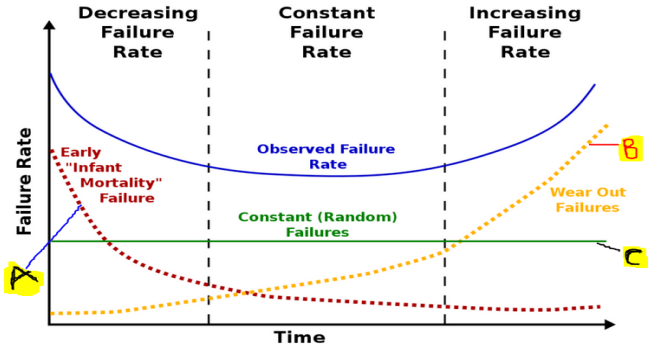

Figure 1 (b): Multiple failure modes overlap of solar PV modules [4].

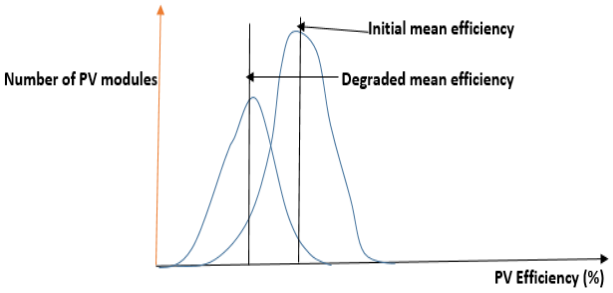

Figure 2: Degradation of Solar PV system [1].

Figure 3: Location and Satellite view of ESB site situated at Upper Dromore Road, Warrenpoint, Northern Ireland, UK (https://www.google.com/maps/place/Newry+BT34+3PN,+UK/@54.1132142,-6.2642131,248a,35y,44.92t/data=!3m1!1e3!4m5!3m4!1s0x4860da664698253b:0xd3507b57cb2eea3!8m2!3d54.1150048!4d-6.2630492).

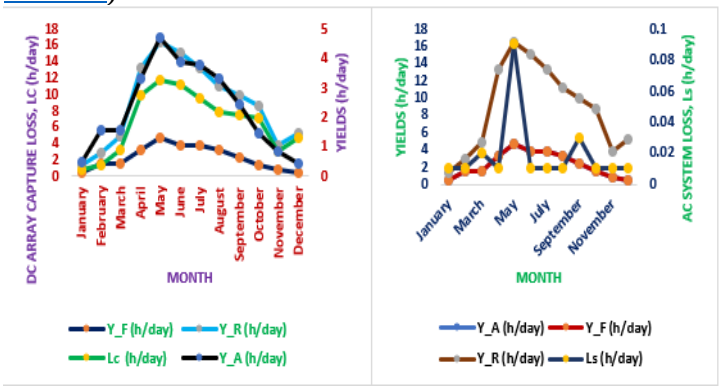

a. b.

Figure 7: Monthly daily yields, DC array capture, and AC system losses of ESB Warrenpoint system.

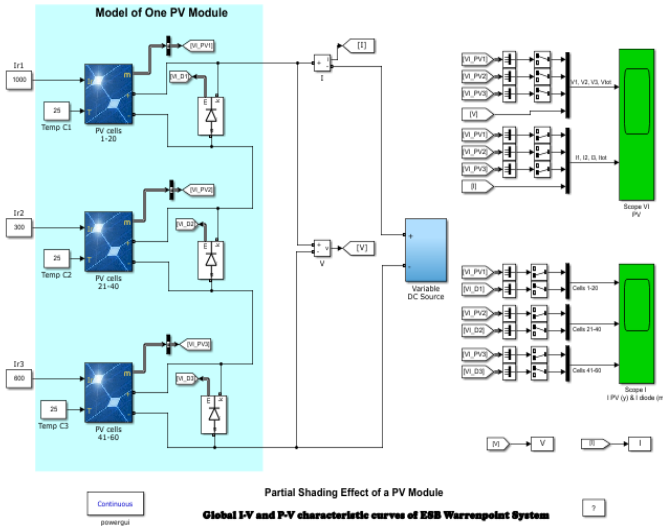

Figure 4: PV module connected to a variable DC voltage source converter (VSC) (https://uk.mathworks.com/help/physmod/sps/ug/partial-shading-of-a-pv-module.html;jsessionid=9479da359d71d0f731ea5a9a6d64)

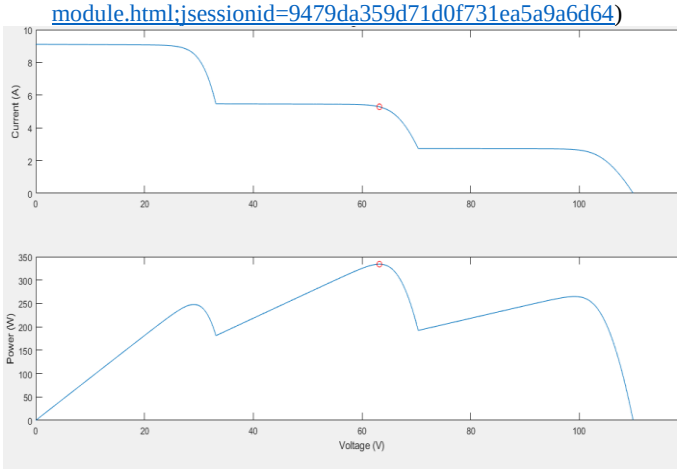

Figure 5: I-V and P-V characteristics curves of a PV system

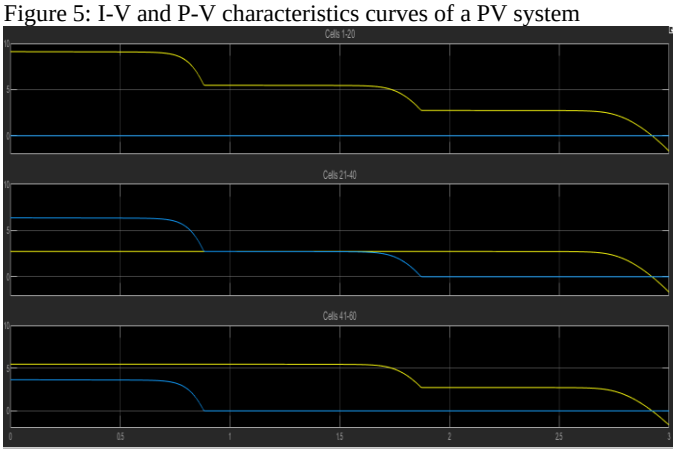

Figure 6: Shading effect of PV current (with yellow color line) and diode current (with blue color).

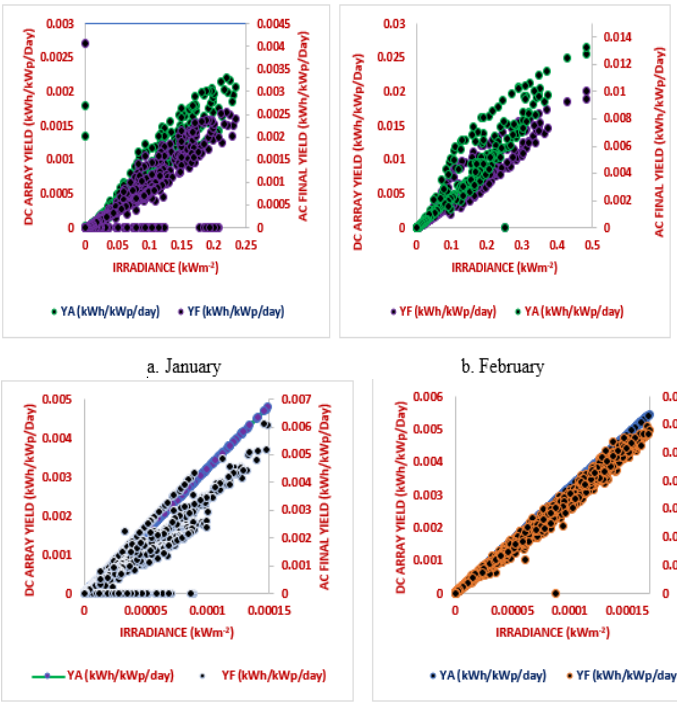

Figure 8: Quarter-Hourly data for AC Final yield and DC Array yield.

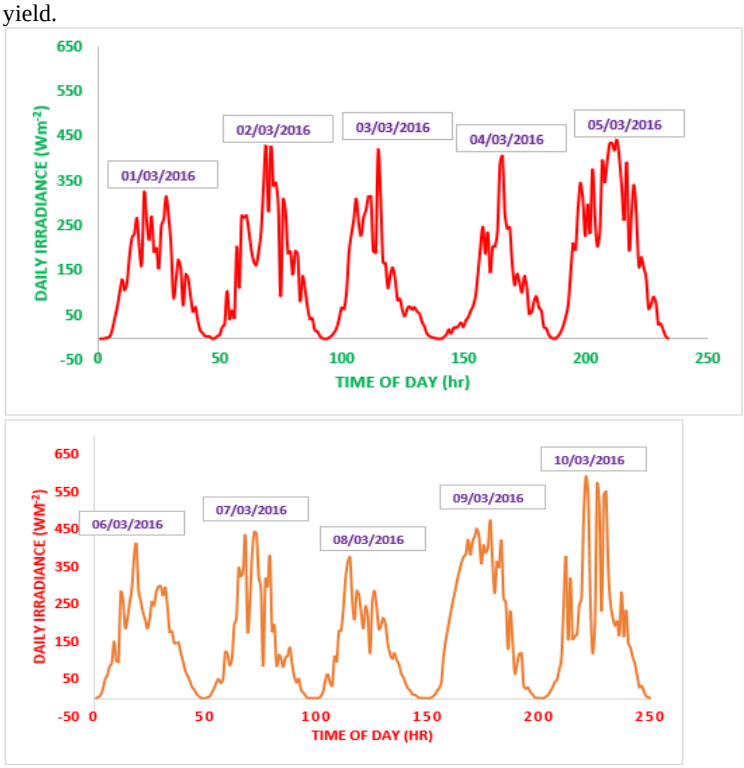

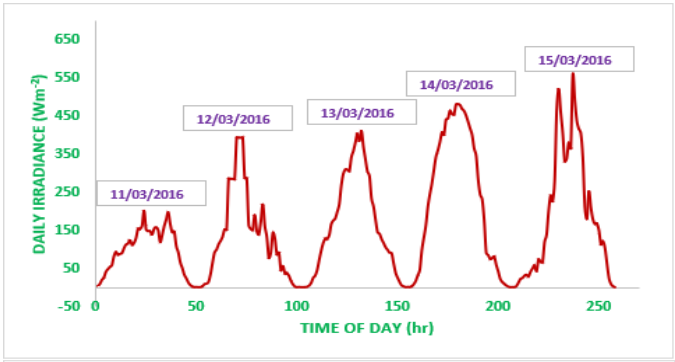

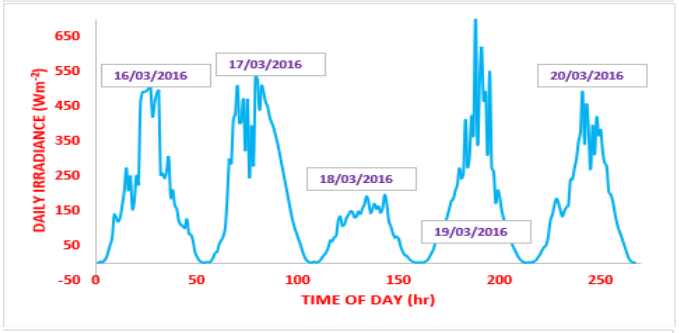

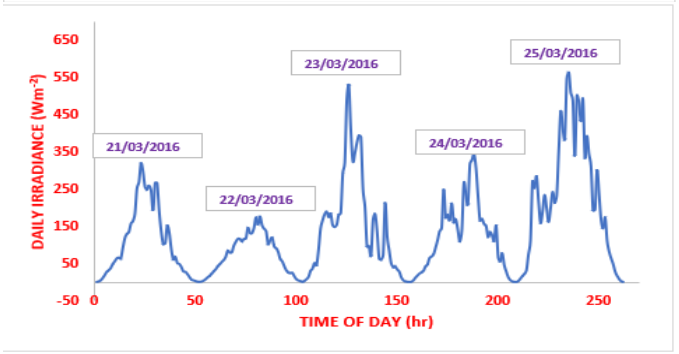

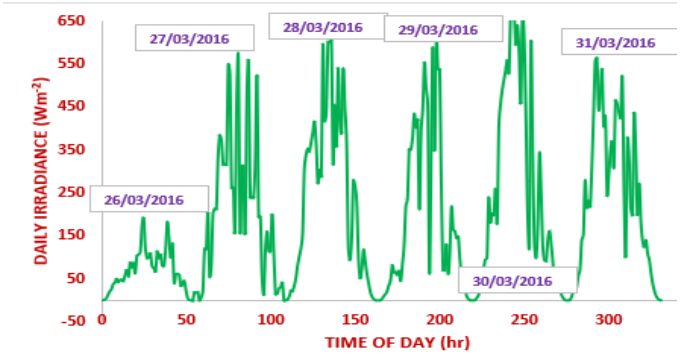

Figure 9: Measured solar irradiance profiles for each day in March 2016.

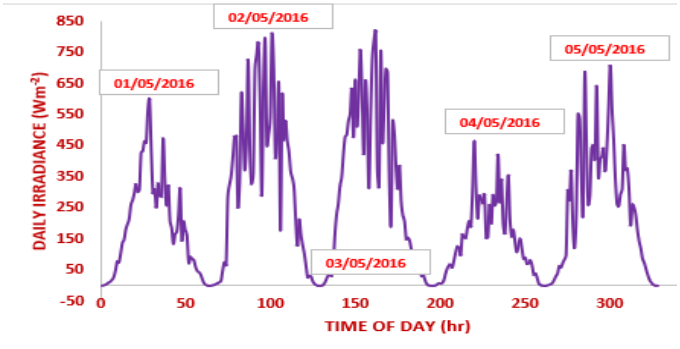

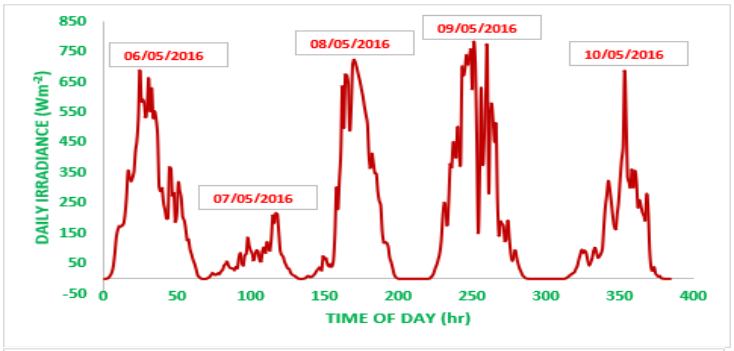

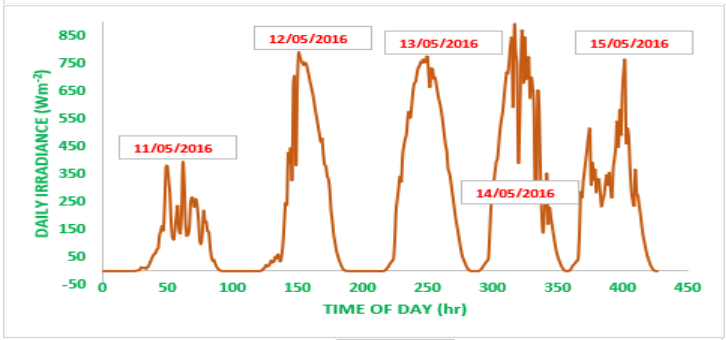

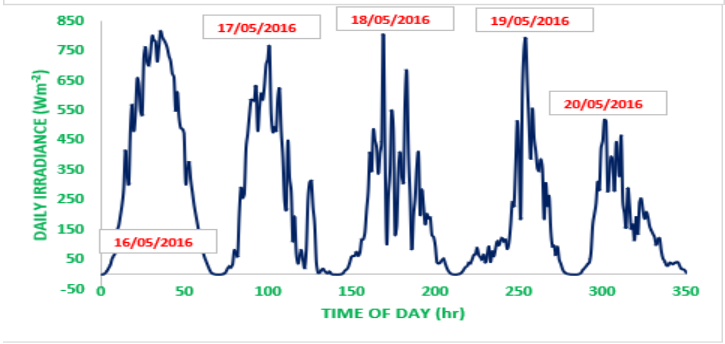

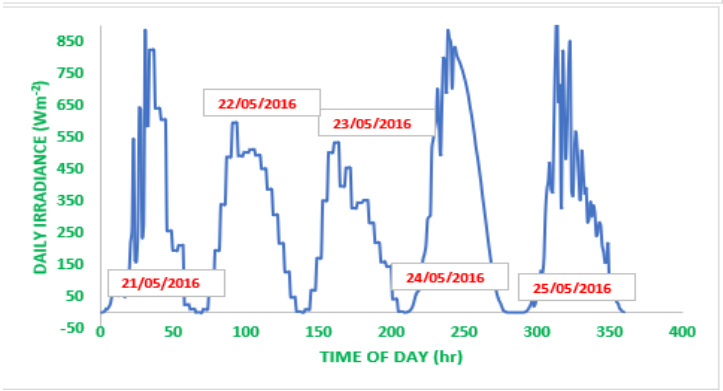

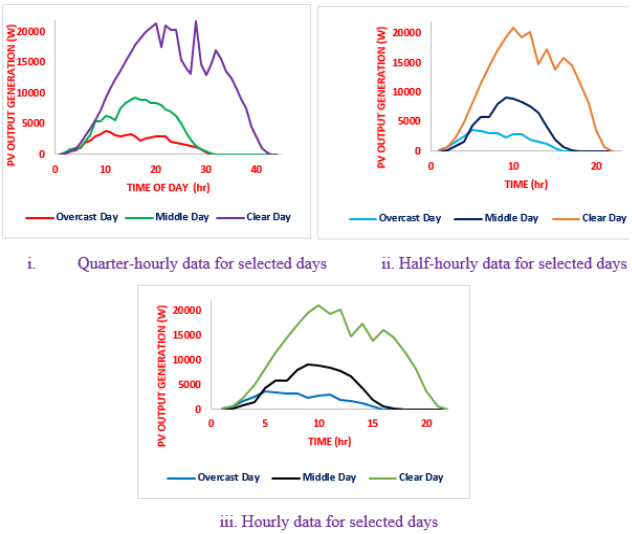

Figure 11 (a): Power output profiles of selected days during the winter season.

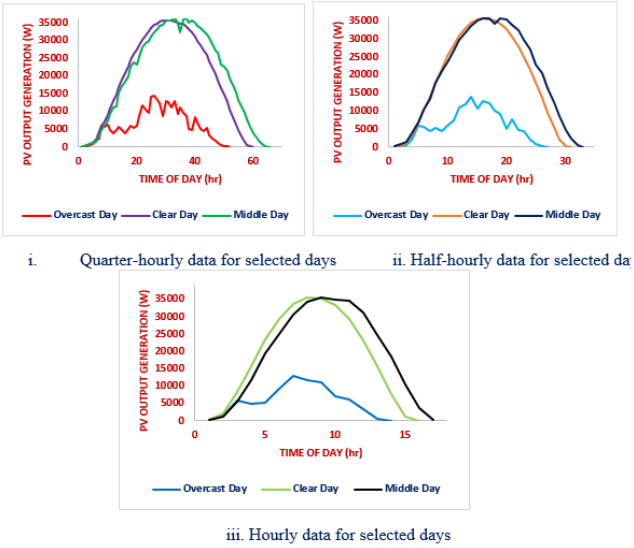

Figure 11 (b): Power output profiles of selected days during the spring season.

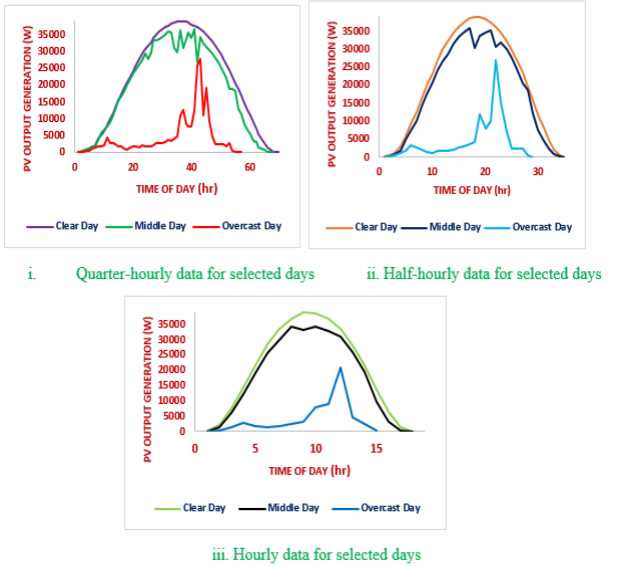

Figure 11 (c): Power output profiles of selected days during the summer season.

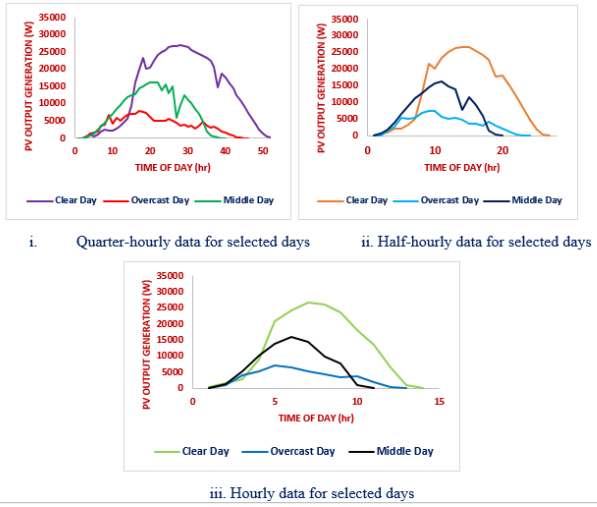

Figure 11 (d): Power output profiles of selected days during the autumn season.

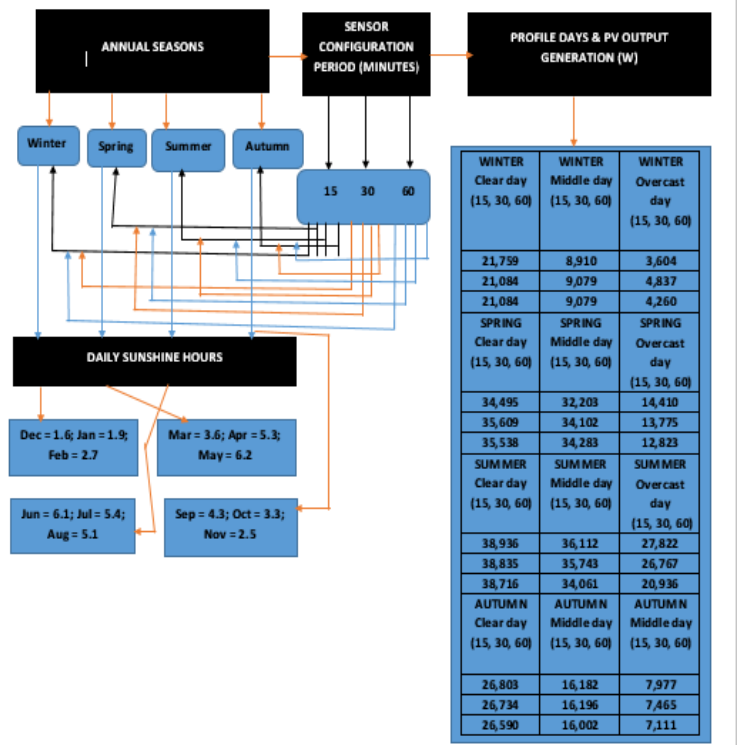

Figure 12: A chart showing power profiles of selected days in winter, spring, summer, and autumn in 15 minutes, 30 minutes, and 60 minutes sensor configuration period of ESB Warrenpoint system.

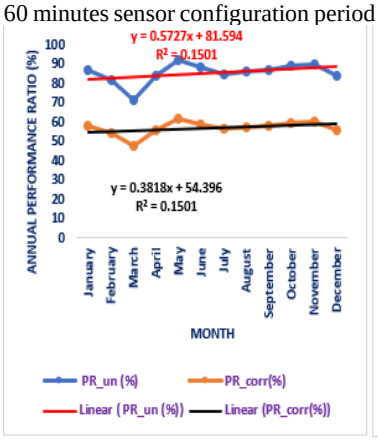

Figure 13: Annual System PR for 2016

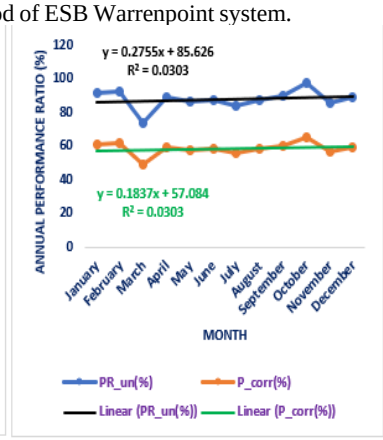

Figure 14: Annual System PR for 2017

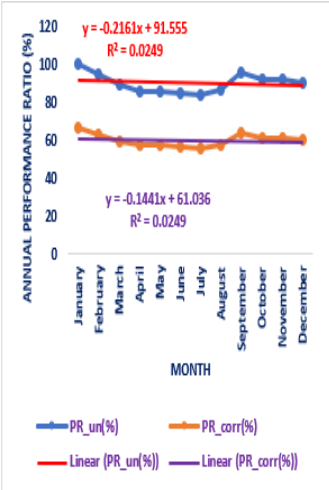

Figure 15: Annual System PR for 2018

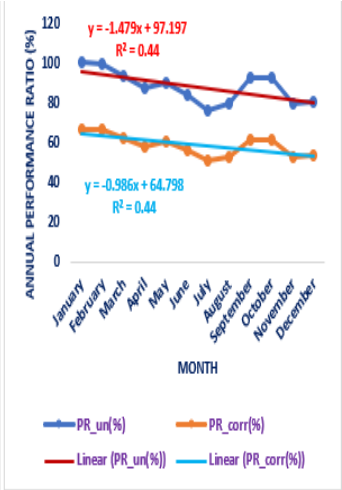

Figure 16: Annual System PR for 2019

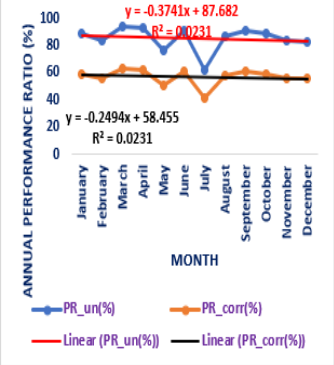

Figure 17: Annual System PR for 2020

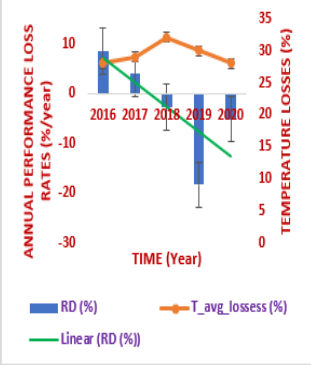

Figure 18: Annual Performance Loss Rates (%/year)

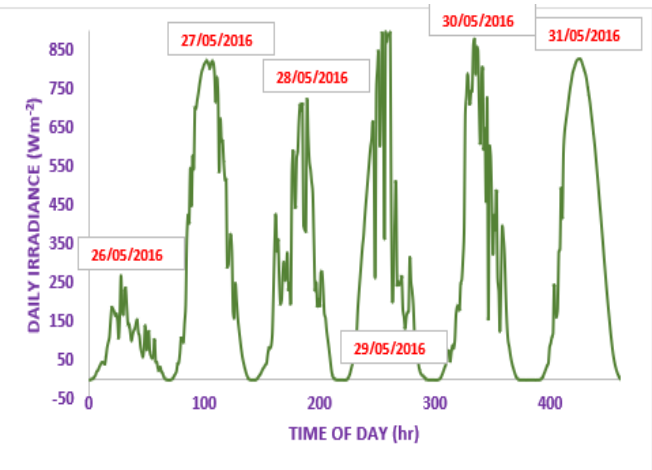

Figure 10: Measured solar irradiance profiles for each day in May 2016.

Table 1: Severity ranking of failure mode [17].

S/N	Severity	Rank
1.	Degradation rate should be >1.0%/year with safety, hazardous probability in the range <90−100>%	10
2.	Degradation rate should be <0.9–1.0>%/year with safety, hazardous probability in the range <80–90>%	9
3.	Degradation rate should be in the range <0.8–0.9>%/year with safety, hazardous probability in the range <70–80>%	8
4.	Degradation rate should be in the range <0.7–0.8>%/year with safety, hazardous probability in the range <60–70>%	7
5.	Degradation rate should be in the range <0.6–0.7>%/year with safety, hazardous probability in the range <50–60%> %	6
6.	Degradation rate should be in the range <0.5–0.6>%/year with safety, hazardous probability in the range <40–50> %	5
7.	Degradation rate should be in the range <0.4–0.5>%/year with safety hazardous probability in the range <30–40>%	4
8.	Degradation rate should be in the range <0.3–0.4>%/year with safety hazardous probability in the range <20–30>%	3
9.	Degradation rate should be in the range <0.2–0.3>%/year with safety hazardous probability in the range <10–20>%/	2
10.	The degradation rate should be <0.1–0.2>%/year with no safety hazard	1

Table 2: Monthly DC Energy and AC Energy, inverter efficiency, and percentage conversion loss of quarter-hourly system measurement obtained from the ESB Warrenpoint System.

Month	DC Energy [MJ]	AC Energy [MJ]	Inverter Efficiency (η) (%)	Inverter Percentage Conversion Loss (%)
January	2763	2720	98.40	1.6
February	1978.6	1975.3	99.80	0.17
March	8640.2	8543.1	98.90	1.12
April	17810.3	17802.16	99.95	0.046
May	26092	25595	98.10	1.51
June	20628	20606.5	99.90	0.104
July	20980	20940	99.81	0.191
August	18320	18291	99.84	0.158
September	12990	12838	98.82	1.17
October	8121	8062	99.27	0.73
November	4540	4531	99.80	0.2
December	2540	2526	99.45	0.55
Total	145,403.1	144,430.1		
Average	12,116.9	12,035.8	99.42	0.629

Table 3: DC array, AC final, and reference yields, DC array capture, and AC system losses of quarter-hourly measured ESB Warrenpoint system.

Month	Y_A (h/day)	Y_F (h/day)	Y_R (h/day)	$L_{C,day}$ (h/day)	$L_{S,day}$ (h/day)
January	0.5	0.49	1.39	0.89	0.01
February	1.59	1.58	2.94	1.35	0.01
March	1.56	1.54	4.81	3.25	0.02
April	3.33	3.32	13.31	9.98	0.01
May	4.72	4.63	16.41	11.69	0.09
June	3.86	3.85	15.12	11.26	0.01
July	3.8	3.79	13.31	9.51	0.01
August	3.31	3.3	11.09	7.78	0.01
September	2.43	2.4	9.88	7.45	0.03
October	1.47	1.46	8.66	7.19	0.01
November	0.85	0.84	3.87	3.02	0.01
December	0.46	0.45	5.2	4.74	0.01
Average	2.32	2.30	8.83	6.51	0.02

Table 4: Annual uncorrected system PR, temperature-corrected system PR, degradation rates, and percentage of temperature losses from 2016-2020.

Year	R_D (%/year)	$PR_{uncorrected}$ (%)	$PR_{corrected}$ (%)	$T_{avglosses}$ (%)
2016	4.5 to 14	86.5	58	28.5
2017	0.1 to 5.2	91	61	30
2018	-7.5 to 2.5	99.8	67	32.8
2019	-16 to -23	100	67	33
2020	-5.1 to -10	89	59	30

ACKNOWLEDGMENTS

Our thanks go to the Fiosrai Research Fund of Technological University Dublin, Ireland for funding this research work. We also thank the Electric Supply Board (ESB) of Ireland for permitting us to use data from their solar plant to carry out this research study.

REFERENCES

[1] C.C. Okorieimoh, B. Norton, and M. Conlon, "Long-Term Durability of Solar Photovoltaic Modules" In Scott L., Dastbaz M., Gorse C. (eds) Sustainable Ecological Engineering Design. Springer, Cham, 2020, pp. 317-325. https://doi.org/10.1007/978-3-030-44381-8_24.

[2] C.C. Okorieimoh, B. Norton, and M. Conlon, "Effect of transient performance changes on photovoltaic modules output" Poster. 10TH Annual GRS Symposium, 2019, 10.13140/RG.2.2.28516.94083.

[3] X.Y. Li, "Degradation analysis of photovoltaic modules based on operational data: effects of seasonal pattern and sensor drift", IOP Conf. Series: Earth and Environmental Science, 2016, Vol. 40, pp. 012063. DOI:10.1088/1755-1315/40/1/012063.

[4] F.Z. Allen, and P.D. David, "Photovoltaic Module, Weather Durability and, Reliability" "Will my module last outdoors?". Solar Energy Competence Centre, Atlas Material Testing Technology LLC, 2015. www.atlas-mts.com.

[5] J. Wohlgemuth, "Reliability of PV Systems, Reliability of Photovoltaic Cells, Modules, Components, and Systems", Proc. of SPIE, 2008, Vol. 7048, pp. 704802-1.

[6] Z. Allen, "PV Durability and Reliability Issues. Atlas Material Testing", Journal of Renewable Energy World, 2009, Vol. 1, Issue 5.

[7] E.D. Dunlop, and D. Halton, "The performance of crystalline silicon photovoltaic solar modules after 22 years of continuous outdoor exposure. Prog Photovoltaics", 2006, Vol.14, Issue 1, pp.53–64. DOI: 10.1002/pip.627.

[8] G.N. Tiwari, R.K. Mishra, and S.C.Solanki "Photovoltaic modules and their applications: A review on thermal modeling", Applied Energy, 2011, Vol. 88, pp. 2287-2304.

[9] S. Pingel, O. Frank, M. Winkler, S. Daryan, T. Geipel, H. Hoehne, and J. Berghold, "Potential induced degradation of solar cells and panels", Proc. 35th IEEE Photovolt. Spec. Conf., 2010, pp. pp. 2817-22.

[10] B. Sopori, P. Basnyat, S. Shet, V. Mehta, J. Binns, and J. Appel, "Understanding light-induced degradation of c-Si solar cells", Proc. IEEE Photovolt. Spec. Conf., 2012, pp. 5200-54200.

[11] C.R. Osterwald, A. Anderberg, S. Rummel, and L. Ottoson, "Degradation analysis of weathered crystalline-silicon PV modules," Proc. 29th IEEE Photovolt. Spec. Conf., 2002, pp. 1392-5.

[12] G.N. Tiwari, R.K. Mishra, and S.C. Solanki, "Photovoltaic modules and their applications: A review on thermal modeling", Applied Energy, 2011, Vol. 88, pp.2287-2304.

[13] I. Tetsuyuki, and M. Atsushi, "Annual degradation rates of recent crystalline silicon photovoltaic modules", Progress in photovoltaics: Research and Applications, 2017, Vol. 25, pp. 953-967. DOI: 10.1002/pip.2903.

[14] P. Nochang, J. Jaeseong, and H. Changwoon, "Estimation of the degradation rate of multi-crystalline silicon photovoltaic module under thermal cycling stress. Microelectronics Reliability", 2014. DOI: http://dx.doi.org/10.1016/j.microrel.2014.03.021

[15] M. Saadsaoud, A.H. Ahmeda, Z. Er, and Z. Rouabah, "Experimental study of degradation modes and their effects on the reliability of photovoltaic modules after 12 years of field operation in the steppe region", Special issue of the 3rd International Conference on Computational and Experimental Science and Engineering (ICCESEN 2016), Journal of Acta Physica Polonica A, 2017, Vol. 132, pp.3-11. DOI: 10.12693/APhysPolA.132.930.

[16] H. Takatoshi, N. Tomoya, T. Tadashi, and I. Yoshitaka, "Influence of degradation in units of PV modules on the electric power output of PV system", Journal of International Council on Electrical Engineering, 2018, Vol. 8, No. 1, pp.118–126. DOI: https://doi.org/10.1080/22348972.2018.1477095

[17] R. Pramod, M. Maria, M.K. Nallapaneni, O.S. Sastry, and G.N. Tiwari, "Risk priority number for understanding the severity of photovoltaic failure modes and their impacts on performance degradation," Case Studies in Thermal Engineering, 2019, Vol. 16. https://doi.org/10.1016/j.csite.2019.100563

[18] S. Chattopadhyay, R. Dubey, V. Kuthanazhi, J.J. John, C.S. Solanki, A. Kottantharayil, B.M. Arora, K.L. Narasimhan, V. Kuber, J. Vasi, A. Kumar, and O.S. Sastry, "Visual degradation in field-aged crystalline silicon PV modules in India and correlation With electrical degradation", IEEE J. Photovolt., 2014, Vol 4, pp. 1470-1476.

[19] S. Kumar, S. Roy, and R. Gupta, "Comparison of reliability tests by characterization of degradation in photovoltaic modules", MOJ Sol. Photoenergy Syst., Article 00006, 2017. 10.15406/mojsp.2017.01.00006

[20] D.C. Jordan, T.J. Silverman, J.H. Wohlgemuth, S.R. Kurtz, and K.T. VanSant, "Photovoltaic failure and degradation modes", Prog. Photovolt. Res. Appl., 2017, Vol. 25, pp. 318-326.

[21] J. Kuitche, R. Pan, and G. Tamizhmani, "Investigation of dominant figures modes for field-aged c-Si modules in desert climatic conditions," IEEE J. Photovolt, 2014, Vol. 4, pp. 814-826.
[22] Sustainable Energy Authority of Ireland (SEAI), Irish energy balances: Statistics publications, 1990-2009, Available: www.seai.ie
[23] J.D. Mondol, Y.G. Yohanis, and B. Norton, "The effect of low insolation conditions and inverter oversizing on long-performance of a grid-connected photovoltaic system," Prog. Photovolt. Res. Appl,2006, Vol. 15, pp. 353-368.
[24] C. Trueblood, S. Coley, T. Key, L. Rogers, A. Ellis, C. Hansen, and E. Philplot, "PV measures up for fleet duty, Data from a Tennessee Plant Are Used to Illustrate Metrics That Characterise Plant Performance". DOI: 10.1109/MPE.2012.2234405.
[25] D.A. Quansah, and M.S. Adaramola, "Assessment of early degradation and performance loss in five co-located solar photovoltaic module technologies installed in Ghana using performance ratio time-series regression," Journal of Renewable Energy, 2019, Vol. 131, pp. 900-910.
[26] S. Kurtz, J. Luis Becerra Cruz, E. Riley, and C. Hansen, "Weather-Corrected Performance Ratio," National Renewable Energy Laboratory Technical Report, NREL/TP-5200-57991,2013.
[27] D.C. Jordan, C. Deline, S.R. Kurtz, G.M. Kimball, M. Anderson, "Robust PV Degradation Methodology and Application", IEEE Journal of Photovoltaics, 2018, Vol. 8, pp. 525-531. DOI: 10.1109/JPHOTOV.2017.2779779.
[28] P. Rajput, G.N. Tiwari, B. Bora, and O.S. Sastry, "Visual and electrical degradation of 22 years field age monocrystalline silicon PV module in the composite climate of India", IEEE, 42nd Photovoltaic Specialists Conference (PVSC), 2015, pp. 1-3.
[29] D. Berman, and D. Faiman, "EVA browning and the time-dependence of I-V curve parameters on PV modules with and without mirrors-enhancement in a desert environment", Sol. Energy Mater. Sol. Cells, 1997, Vol. 45, pp. 401-412.

Bio-oil production using sawdust of *Triplochiton scleroxylon* in microwave pyrolysis

BADZA Kodami
Department of Applied Chemistry
ENSAI
Ngaoundere, Cameroun
badzakodami@gmail.com

KOM REGONNE Raïssa
Department of Applied Chemistry
ENSAI
Ngaoundere, Cameroon
rkregonne@yahoo.fr

NGASSOUM Martin Benoit
Department of Applied Chemistry
ENSAI
Ngaoundere, Cameroon
ngassoum@yahoo.fr

Abstract

Biomass conversion into bio-oil by pyrolytic technology is one of the most promising alternative to convert the biomass into useful products and energy. The development of bio-oil from biomass has attracted a great deal of interest not only because of the environment pollution but also because of the rapid depletion of the fossil fuel reserves. In the present work a microwave pyrolysis of *Triplochiton scleroxylon* sawdust commonly name *Ayous* is used for bio-oil and biochar production. Several power varying from 500-650 Kw, reaction time in the range 15-25 min and the amount of Wave absorber values from 10 to 30% were considered. The response surface methodology (RSM) combined with Central Composite design (CCD) is used for modeling and optimizing both the process bio-oil and biochar yield. The results show that the optimum conditions are obtained for a reaction power 576.27 Kw, a reaction time of 28.07 min and an absorption intake 3.19%. Under these conditions, the predicted bio-oil yield is around 44.8% with good pH (6.06 ± 0.4) but a very high-water content 25 ± 1.2%. Whereas the biochar 39.44% is obtained under the conditions: Power 448.8 kw, an time of 12 min and an absorption intake of 17.11%. The identification of compounds by GC/MS has identified the con families of alkanes, esters, alcohols and phenolic compounds at low and high molecular weights. A global view of these results makes it possible to say that *Ayous* bio-oil can be used as biofuel, however processing operations must be carried out in order to reduce the water content and its acidity. The biochar can be directly used as a soil amendment.

Keywords : *Triplochiton scleroxylon* sawdust, *Bio-oil*, *Biochar*, *Microwave-Pyrolysis*

IEECP'21, July 29-30, 2021, Silicon Valley, San Francisco, CA – USA

DAI : *https://sci-index.com/DAI/2021.99101/IEECP/14810202*

Transforming Granite Wastes into High Performance Hybrid Polymer Composites for Environmental Sustainability and its Comparative Optimization using TOPSIS Technique

Aakash Sharma*
Mechanical Engineering Department
Swami Keshvanand Institute of Technology, Management and Gramothan
Jaipur, India
aakasharma1507@gmail.com

Vikash Gautam*
Mechanical Engineering Department
Swami Keshvanand Institute of Technology, Management and Gramothan
Jaipur, India
gautam.mnitj@gmail.com

Amar Patnaik
Mechanical Engineering Department
Malviya National Institute of Technology
Jaipur, India
apatnaik.mech@mnit.ac.in

M. J. Pawar
Mechanical Engineering Department
K. J. Somaiya College of Engineering
Mumbai, India
manojjpawar@gmail.com

Ashiwani kumar
Mechanical Engineering Department
Feroze Gandhi Institute of Technology
Lucknow, India
Ashi15031985@gmail.com

Vikas kukshal
Mechanical Engineering Department
National Institute of Technology
Uttarakhand, India
vikaskukshal@nituk.ac.in

Abstract

This research work aims to examine the opportunity of re-exploiting granite wastes to get inventive vinyl ester based hybrid polymer composites. The foremost advantage of recycling the granite wastes is low cost and eco-friendly production. Granite wastes generated by stone processing units are generally dumped in open lands, which creates severe environmental complications causing soil, air and water pollution. Hence, the inculcation of such kind of industry wastes into the polymer fabrication process can be a serious solution for sustainable waste utilization. The examined mechanical properties of the fabricated granite dust filled hybrid composites are compared with Titania particulate filled E-glass fiber reinforced polymer composites. Conventional hand layup technique is prominently exploited for the fabrication of composite specimens. The granite dust/titania weight fraction is varied from 5-15 wt. % while keeping bi-directional E-glass fiber weight fraction as constant i.e., 30 wt. %. Density and percentage void content has been determined and also mechanical characterization such as hardness, tensile strength, flexural strength, impact strength and inter laminar shear strength of the produced polymer composite material has been carried out. As far as incorporation of granite dust is concerned, there has been a significant improvement in the physical as well as mechanical characteristics of the fabricated composite material. Also, to determine the best proxy situation from a finite lot of decision proxies in terms of various oppugning criteria, TOPSIS decision making approach is used.

IEECP'21, July 29-30, 2021, Silicon Valley, San Francisco, CA – USA

DAI : ***https://sci-index.com/DAI/2021.99101/IEECP/14737971***

Keywords: Granite dust, Sustainability, Titania, Hand layup, Mechanical characterization, TOPSIS.

I. INTRODUCTION

The development of particle-filled polymer composites reinforced with fibers is the need for structural components that are prone to fracture and cracks by utilization of stone waste such as granite dust. Granite dust would be a solution not only to control health issue but also pollution control such as soil, air with reduction on the dependency on depicted natural resources [1]. Therefore, reusing the waste is considered to be the most important solution in the modern world. For composites, the materials are mixed to reduce shortages and increase characteristic performance of the materials. The overall economy of these composites are found to be very low when industrial waste is added to the matrix as reinforcement [2]. Since, traditional fillers such as metals and ceramic powders possess high cost, it is important to replace traditional composite ceramics with other cheap and abundant wastes such as granite, silica [3] and boron [4] that are available in abundant form without embracing quality. Granite dust is an industrial waste material that can be used as a filler in a polymer matrix [5].

Granite dust is a combination of different oxides with better mechanical and wear properties [6]. Vikash et.al. [7] in their work concluded that with the addition of granite particles, the aluminum alloy composites has improvised hardness and desired strength. Awad et.al. [8,9] studied the influence of particle sizes and % content of marble/granite filler on the physico-mechanical properties and observed that the addition of M/G fillers in the HDPE composites outstripped its thermal and mechanical properties. Similarly, the use of Granite dust [10] along with baggage ash [11] and copper scrap [12] for concrete modification is quite common among the researchers. Also, the influence of

granite dust from the fold and thrust belt [13] on the physico-mechanical properties of mortar is studied and inferred that incorporation of granite powder in mortar leads to an increase in the diffusion properties of fluids due to significant improvement in porosity [14].

In series to this, hybrid polymer composites is prominently a varied kind of composite material consisting of a polymer matrix and two types of reinforcements: fibers and particles. The fiber reinforcement provides rigidity and longitudinal strength, and the particles provides tensile strength and impact resistance. One such work included graphite as a filler and E-glass fibre as a reinforcing material to fabricate hybrid VE based composites [15]. A review has also been performed on the mechanical properties of the polymer composites in terms of hybridization [16] where it was inferred that it possess better strength-to-weight ratio than most of the conventional alloys [17]. Similarly, studies on the mechanical properties of the hybrid polymer composites [18,19] with a dammar based hybrid matrix [20], based on natural fibers [21] such as animal-plant fiber hybrid composites [22] has also been performed.

Along with composite processing and mechanical assessment, optimization of composite criteria is also very important as far as the minimization of experimental setup and identification of parameters that most influence the characterization of the fabricated composites is concerned [23]. In this order, a multi-criteria decision making approach, such as TOPSIS, has been performed by various researchers in their study. This MCDM method is found to be very crucial tool for the decision makers to choose an alternative in discrete problems [24]. Especially, TOPSIS has become much easier for the users with the help of computers. Various articles shows the use of decision making TOPSIS model for finding the optimal reinforcements in CaCO3 and Al2O3 composites [25] and natural fiber composites [26].

In this study, vinyl ester resin was used as the matrix material, granite dust/titania particulate was used as filler, and E-glass fiber was used as a reinforcement to obtain titania/granite dust filled glass fiber reinforced polymer composites. Then characterization of the physico-mechanical behavior of the obtained polymer composite material has been prominently performed using TOPSIS technique.

II. EXPERIMENTAL DETAILS

A. Materials and methodology

In the present study, vinyl ester is used for the preparation of polymer composite filled with granite dust/titania particles and reinforced with E-glass fiber through the conventional hand layup method. Vinyl ester as a matrix material imparts magnificent mechanical properties to the composite material. As a reinforcement, E-glass fiber is used which is predominantly a mixture of different oxides (55%SiO_2, 18%CaO, 11%Al_2O_3, 6%B_2O_3, 5%MgO, and 5% other). Further, titania as a filler material, is an oxide of titanium [27] and granite dust is a combination of different oxides that poses excellent mechanical and wear resistant properties [28]. The notations and chemical compositions of the fabricated vinyl ester composites is shown in table 1.

The composition of vinyl ester is varied in correspondence of the granite dust/titania fillers with three varied weight fractions (5 wt.%, 10 wt.%, 15 wt%) while keeping E-glass fiber weight fraction constant i.e., 30 wt.%. The vinyl ester resin is mixed with its corresponding hardener in 10:1 weight ratio. Silicon mold releasing spray has been applied to remove the composites from a wooden mold of dimension 340*340*40 mm^3 after curing. Before the removal of the composites from the wooden mold, the load of 40 kg is applied for about 24 hours during the curing of the casted composites whereas after the removal of composites from the mold, casted samples are post cured for another 24 hours. The desired size of the specimens for mechanical/physical tests are cut using the diamond cutter.

Table 1. Notations and compositions of the composites

Notations	Compositions (by weight)
EG-0	Glass fibre (30%) + Vinyl ester (70%)
EGG-5	Glass fibre (30%) + Vinyl ester (65%) + Granite (5%)
EGG-10	Glass fibre (30%) + Vinyl ester (60%) + Granite (10%)
EGG-15	Glass fibre (30%) + Vinyl ester (55%) + Granite (15%)
EGT-5	Glass fibre (30%) + Vinyl ester (65%) + Titania (5%)
EGT-10	Glass fibre (30%) +Vinyl ester (60%) + Titania (10%)
EGT-15	Glass fibre (30%) + Vinyl ester (55%) + Titania (15%)

B. Physical Characterization

To examine the composite quality, density and void content has to be investigated for physical assessment of the fabricated specimens. For precision assessment, theoretical density and experimental density are obtained separately using weight proportion method and Archimedes principle respectively. The void content is then calculated using a comparative study between the theoretical and experimental densities. For determining the experimental density using the Archimedes principle, several specimens were taken from the obtained composite material and first weighed in air and then weighed in water using electronic weighing machine. The formula for determining the experimental density is:

$$\rho_c = \frac{Wair}{(Wair - Wwater)} * \rho_{water} \quad \text{..... (1)}$$

Where, ρ_c = density of obtained composite
ρ_{water} = density of water (gm/cc)
W_{air} = weight of the specimen in air (gm)
W_{water} = weight of the specimen in water (gm)

Void content of the composites is calculated by densities based on theoretical calculation and experimental investigation using equation:

$$V_f = \frac{\rho_t - \rho_e}{\rho_t} * 100 \quad \text{..... (2)}$$

Where, V_f = volume fraction of void
ρ_t = Density of the composite (Theoretical)
ρ_e = Density of the composite (Experimental)

C. Mechanical Characterization

In mechanical assessment of the fabricated composites, micro hardness test of the specimen is carried out using 1/16" indenter (steel ball) through the Rockwell hardness testing machine and a preliminary load of 50 kgf. The tensile test has been conducted as per ASTM D3039-3062 using the digital tensometer apparatus. The flexural strength and modulus test has also been carried out for the fabricated granite dust/titania filled vinyl ester based polymers. Inter laminar shear strength of composites based on vinyl ester resin (brittle matrix), is determined using a beam shear test (BST). ASTM D7291 standard has been considered to carry

out inter laminar shear strength test of the obtained vinyl ester based polymer composites on the Materials testing machine. The low speed impact test is also conducted for measuring the damage resistance using the impact tester as per ASTM D256.

D. TOPSIS optimization

TOPSIS (Technique for Order Preference by Similarity to the Ideal Solution) works on the principle of selection of an alternative which should be "closest in terms of distance to the positive ideal solution" and "should be farthest in terms of distance to the negative ideal solution" [29]. This decision making approach has a very straight forwarded, logical and accessible concept which has the inherited function of the relative effectiveness measurement of each option in an understandable mathematical form.

Assume Z = (Zij) be a matrix consisting of "p" proxies and "q" criteria, such that we have $(Zij)_{p*q}$ matrix. This matrix is known as the decision matrix (D). And also let Δ = [Δ1, Δ2... Δn] be a weight vector, where Zij, Δj ∈ R and Δ1 + Δ2 + + Δn = 1

Criteria can be beneficial i.e., higher is better or Non-beneficial i.e., smaller is better.

At this point, the various dimensional attribute are converted to dimensionless attributes so that the criteria can be compared. Because varied criteria are basically measured in different units, there is a need to convert the results in the Z scoring matrix to a standardized scale. These values may be normalized using one of the very well-known standardized expressions. Some of the most commonly used methods for calculating the normalized value of ij n are:

$$N = n_{ij} = \frac{m_{ij}}{\left[\sum_{i=1}^{M}(m_{ij})^2\right]^{1/2}} \quad \text{..... (3)}$$

Weighted normalized matrix (V_{ij}) is the result of multiplying the normalized matrix by its associated weight (Δj) calculated by entropy method.

$$V_{ij} = \Delta_j \times n_{ij} \quad \text{..... (4)}$$

Where, *Δj* is the weight assigned to *j*-th criterion, i.e., Δ1+Δ2…….+Δj = 1.

For determining the positive ideal solution (A^+) and the negative ideal solution (A^-) for the normalized matrix based on weights of the criteria, the following expression holds true:

$$A^+ = (V_1^+, V_2^+ \ldots . V_N^+),$$
$$A^- = (V_1^-, V_1^- \ldots . V_N^-) \quad \text{..... (5)}$$

where,

$$V_j^+ = \begin{Bmatrix} (\min_i V_{ij}), & \text{if j is beneficial criteria} \\ (\max_i V_i^+), & \text{if j is Non-beneficial criteria} \end{Bmatrix} \text{ and}$$

$$V_j^- = \begin{Bmatrix} (\min_i V_{ij}), & \text{if j is beneficial criteria} \\ (\max_i V_i^+), & \text{if j is Non-beneficial criteria} \end{Bmatrix} \text{ for j=1, 2….N}$$

Now, by using these positive ideal and negative ideal solutions, separation measures are to be determined.

For this, the distances measured using Euclid geometry of each of the proxies are calculated in terms of the positive ideal and the negative ideal solution:

$$D_j^+ = \sqrt{\sum_{j=1}^{N}\left(V_i^+ - V_{ij}\right)^2}, \text{ and}$$

$$D_j^- = \sqrt{\sum_{j=1}^{N}\left(V_{ij} - V_i^-\right)^2}, \text{ for i=1, 2….M} \quad \text{..... (6)}$$

Finally, the overall relative closeness of the proxies is calculated and then they are arranged in subside relative to their relative closeness and assigned rankings. The overall relative closeness (Pi^*) of the proxies is calculated as:

$$Pi * = \frac{D_i^-}{D_i^+ + D_i^-}, \text{for } i = 1, 2 \ldots . M \quad \text{..... (7)}$$

III. RESULTS AND DISCUSSION

A. Physical Assessment

In the present study, theoretical and experimental densities of the granite dust/titania filled E-glass fiber reinforced vinyl ester based polymer composites is evaluated and the corresponding weight percentage of void content has been examined and represented in the Table 2.

The incorporation of granite dust particles resulted into the increment in density of the composite, thus, increases the percentage of void content. The similar effect is also shown by the titania filled glass fiber reinforced polymer composites with the incorporation of filler content. The void fraction of composites are evaluated from the difference between the expected and the observed density of each sample. This table clearly depicts that with the incorporation of filler particulates, increasing amount of voids are noticed. This may be because of the inner-fiber spacing been decreased. It is clear that a good composite should have a small void fraction. However, the presence of void is inevitable, especially when fabricated through hand lay-up manual technique.

Since void fraction also depends on type of filler used, granite filled polymer composites show lesser percent of void content than that of titania filled composites.

B. Influence of Particulate on Hardness

The hardness of the polymer composite effectively show an increment trend as the weight fraction of the granite dust and TiO2 particulate increases, as shown in fig. 1. The composites (EGT-5, EGT-10 and EGT-15) with titania particulate content is found to exhibit Rockwell hardness in the strict range of 47 HRB for EGT-5 to 71 HRB for EGT-15 while the composites (EGG-5, EGG-10 and EGG-15) with granite dust content exhibits Rockwell Hardness in the range of 43 HRB for EGG-5 to 61 HRB for EGG-15.

The average hardness of granite and TiO2 powder is usually higher like any other type of oxide ceramic and their incorporation increases the hardness of the composite.The minimum hardness is examined for unfilled composite, i.e., EG-0 and maximum hardness is examined for 15 wt.% TiO_2 particulate filled composite material.

Table 2: Theoretical/Experimental densities and % void content with notations

Notations	Compositions (by weight)	Calculated density (g/cc)	Formulated Density (g/cc)	Voids content (%)
EG-0	Glass fibre (30%) + Vinyl ester (70%)	2.12	2.23	4.93
EGG-5	Glass fibre (30%) + Vinyl ester (65%) + Granite (5%)	2.23	2.35	5.11
EGG-10	Glass fibre (30%) + Vinyl ester (60%) + Granite (10%)	2.32	2.48	6.45
EGG-15	Glass fibre (30%) + Vinyl ester (55%) + Granite (15%)	2.45	2.62	6.49
EGT-5	Glass fibre (30%) + Vinyl ester (65%) + Titania (5%)	2.35	2.52	6.74
EGT-10	Glass fibre (30%) + Vinyl ester (60%) + Titania (10%)	2.48	2.68	7.46
EGT-15	Glass fibre (30%) + Vinyl ester (55%) + Titania (15%)	2.52	2.76	8.70

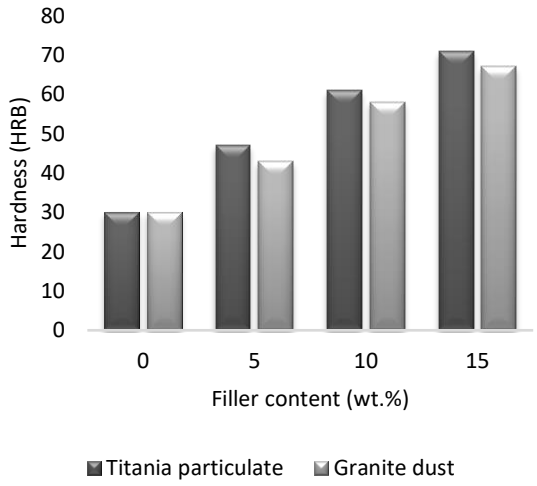

Figure 1 Hardness Variation with filler content

C. Influence of Particulate on Tensile and Flexural Strength

From fig. 2, it is clearly depicted that tensile strength of the hybrid vinyl ester based polymer composites shows a declining trend as far as the incorporation of both titania and granite dust filler is concerned. Such an unexpected behavior of the Bi-directional fiber reinforced composites may be inferred to one of the possible explanation that surface defect and voids have preferably strong impact on the strength of the fabricated composites. The declining trend of the tensile modulus with the incorporation of granite dust/titania particulate in the polymer composites is depicted in the fig. 3. The decrement in the tensile modulus with addition of filler content is may be due of poor adhesiveness of the filler with the matrix material and void formation at the filler – matrix interface.

Fig. 4 prominently indicates that flexural strength of the composites is a function of filler content, i.e., with the addition of the TiO2/granite dust , the flexural strength of the fabricated material composite increases. The formation of micro cracks during the formation of the composites through hand lay-up technique, results in the stress release over a large area provided by the flexural loading, leads to increment in the flexural strength.

The flexural modulus is found to be showing increasing trend with granite dust/titania addition in the vinyl ester produced composites (fig. 5).

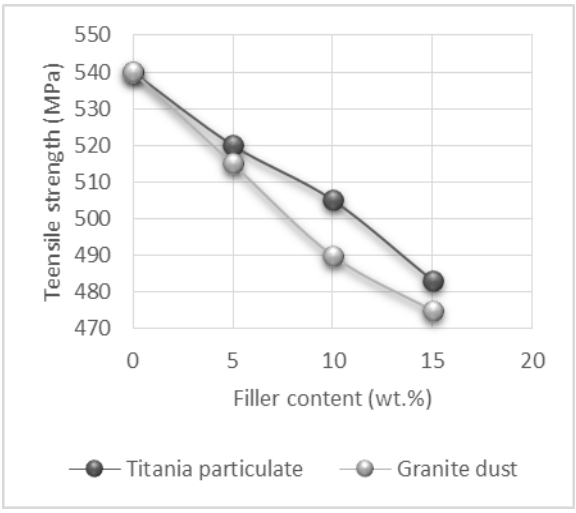

Figure 2 Tensile strength Variation with filler content

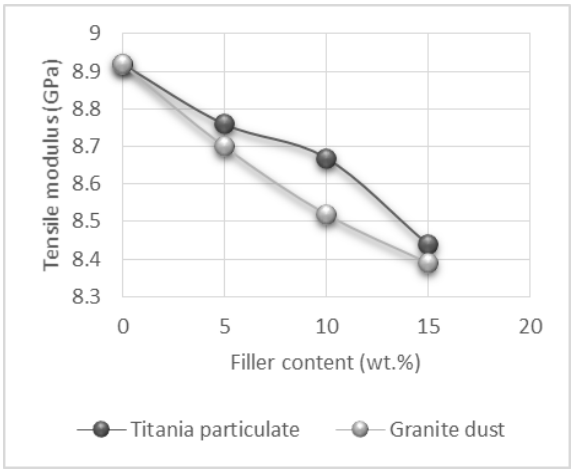

Figure 3 Tensile modulus Variation with filler content

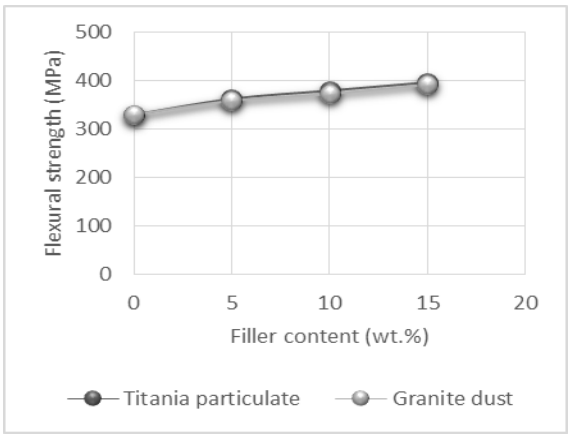

Figure 4 Flexural strength Variation with filler content

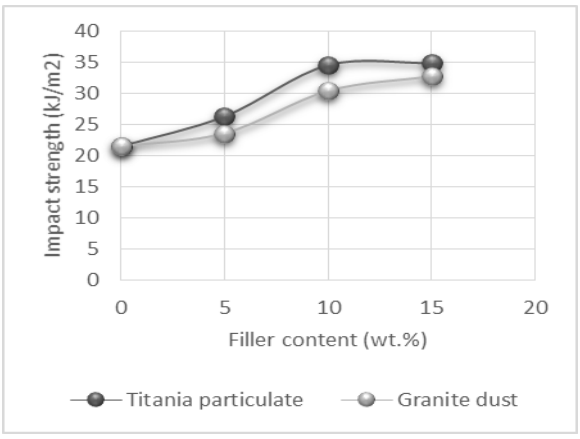

Figure 6 Impact strength Variation with filler

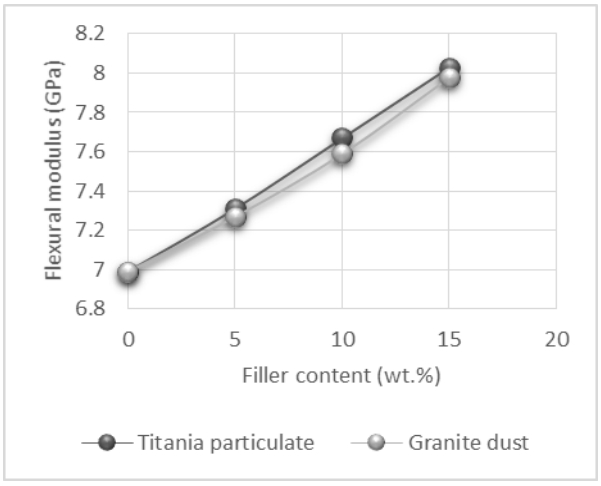

Figure 5 Flexural modulus Variation with filler

D. Influence of Particulate on Impact Strength

The determination of overall energy absorbed during the fracture of the granite dust/titania filled vinyl ester composites is carried out using a low velocity impact tester as per ASTM D256. The outcome of the impact strength test is shown in fig. 6. The graph clearly infer the fact that there is a serious positive change in the damage resistance or impact strength of the fabricated composite with the addition of filler content, i.e., TiO2 particulates as well as granite dust.

It is seen from the test graph that with the incorporation of granite content, the impact strength of the unfilled vinyl ester polymer composite improves effectively by about 10-20% as expected. High deformations loads are required for many structural composite and marine applications. Therefore, the usability of a composite material for such applications must be identified not only by its general design parameters, but also by its energy absorption capacity.

E. Influence of Particulate on ILSS

Laminated composites are most susceptible to stratification between the fiber/matrix interfaces to which a tangential stress is applied. Inter laminar shear stress strongly depends on the matrix prioritized mechanical properties in the construction of laminated composite materials. ILSS shows significant improvement from 14.76 MPa for EG-0 composites to 16.67 MPa and 16.49 MPa for EGT-10 and EGG-10 respectively, and then declines to 15.69 MPa and 15.37 MPa for EGT-15 and EGG-15 composite specimen respectively.

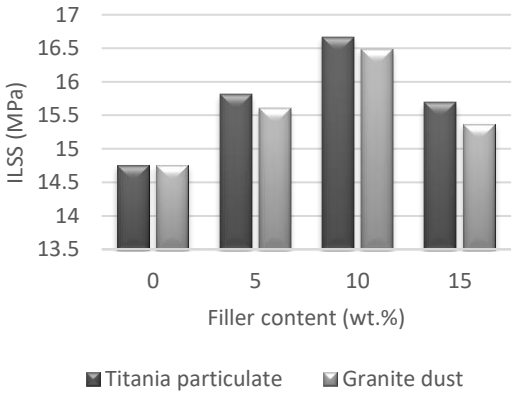

Figure 7 Variation of inter laminar shear strength with filler

The possible reason behind this behaviour can be attributed to high void content for 15 wt.% granite dust/titania powder filled vinyl ester composites. From fig. 7, it is clearly depicted that inter laminar shear strength shows variation for both granite dust/titania particulate in a very identical fashion as reportedly observed by Patnaik et. al. [30] for fly-ash and SiC filled glass reinforced polyester based composites.

F. TOPSIS Optimization Assessment

The TOPSIS method is an empirical and convenient method for selection of alternatives and identification of their respective rankings. Due to the high flexibility of the TOPSIS concept, additional extensions for better choice in different situations is now possible. In fact, TOPSIS is used to solve many theories and the real world issues.

In this work, all the fabricated granite dust filled composite materials are compared with titania particulate filled composites based on TOPSIS technique. For selection of individual alternatives and identification of their rankings, the decision matrix (Table 3), the normalized matrix (Table 4), the weighted normalized matrix (Table 5), positive and negative ideal solutions (Table 6), separation measured values (Table 7), relative closeness values and finally the rankings (Table 8) for the respective alternatives are tabulated below.

Table 3. Decision Matrix (D) Of Fabricated Composites

Composites	Hardness (HRB)	Impact stren. (kJ/m2)	Void con. (%)	Tensile stren. (MPa)	Tensile modu. (GPa)	Flexural stren. (MPa)	Flexural modu. (Gpa)	ILS stren. (Mpa)
0	30	21.51	4.93	540	8.92	330	6.99	14.76
G05	43	23.63	5.11	515	8.7	359	7.27	15.61
G10	58	30.46	6.45	490	8.52	373	7.59	16.49
G15	67	32.81	6.49	475	8.39	392	7.98	15.37
T05	47	26.34	6.74	520	8.76	363	7.31	15.81
T10	61	34.57	7.46	505	8.67	380	7.67	16.67
T15	71	34.91	8.7	483	8.44	397	8.03	15.69

Table 4. Normalized Matrix

Composites	Hardness (HRB)	Impact stren. (kJ/m2)	Void content (%)	Tensile stren. (MPa)	Tensile modu. (GPa)	Flexural stren. (MPa)	Flexural modu. (Gpa)	ILS stren. (Mpa)
0	0.204252	0.274666	0.279596	0.404603	0.39065	0.336044	0.34961	0.353468
G05	0.292761	0.301737	0.289804	0.385872	0.381015	0.365575	0.363615	0.373823
G10	0.394887	0.388951	0.3658	0.36714	0.373132	0.379832	0.37962	0.394897
G15	0.456162	0.418959	0.368068	0.355901	0.367439	0.39918	0.399126	0.368076
T05	0.319995	0.336342	0.382246	0.389618	0.383643	0.369648	0.365615	0.378613
T10	0.415312	0.441433	0.42308	0.378379	0.379702	0.38696	0.383621	0.399208
T15	0.483396	0.445774	0.493404	0.361895	0.369629	0.404271	0.401627	0.375739

Table 5. Weight Normalized Matrix

Composites	Hardness (HRB)	Impact stren. (kJ/m2)	Void content (%)	Tensile stren. (MPa)	Tensile modu. (GPa)	Flexural stren. (MPa)	Flexural modu. (Gpa)	ILS stren. (Mpa)
0	0.097374	0.059151	0.067803	0.005138	0.001147	0.00786	0.005554	0.003709
G05	0.139569	0.064981	0.070279	0.0049	0.001119	0.00855	0.005777	0.003923
G10	0.188256	0.083763	0.088708	0.004662	0.001096	0.008884	0.006031	0.004144
G15	0.217468	0.090225	0.089258	0.00452	0.001079	0.009336	0.006341	0.003863
T05	0.152552	0.072433	0.092697	0.004948	0.001127	0.008645	0.005809	0.003973
T10	0.197993	0.095065	0.102599	0.004805	0.001115	0.00905	0.006095	0.004189
T15	0.230451	0.096	0.119653	0.004596	0.001086	0.009455	0.006381	0.003943

Table 6. Best & Worst Solutions

Solution	Hardness (HRB)	Impact stren. (kJ/m2)	Void content (%)	Tensile stren. (MPa)	Tensile modu. (GPa)	Flexural stren. (MPa)	Flexural modu. (Gpa)	ILS stren. (Mpa)
Positive Ideal Solution(A+)	0.230451	0.096	0.067803	0.005138	0.001147	0.009455	0.006381	0.004189
Negative Ideal Solutions (A-)	0.097374	0.059151	0.119653	0.00452	0.001079	0.00786	0.005554	0.003709

Table 7. Separation Measures of Attributes

Composites	Dj+	Dj-
0	0.138098	0.051853
G05	0.096069	0.065215
G10	0.048661	0.099118
G15	0.025744	0.12773
T05	0.085114	0.062838
T10	0.047597	0.108199
T15	0.051853	0.138097

Table 8. Relative Closeness and Composite Ranking

Composites	Pi*	Rank
0	0.272983	7TH
G05	0.404348	6TH
G10	0.670718	4TH
G15	0.83226	1ST
T05	0.42472	5TH
T10	0.694491	3RD
T15	0.727017	2ND

IV. CONCLUSION

Some of the conclusions were drawn through mechanical experimentation as below:-

1. The granite dust filled E-glass fiber reinforced vinyl ester based polymer composites are fabricated successfully using the hand lay-up fabrication technique and compared with the experimentation results of titania particulate filled E-glass fiber reinforced hybrid polymer composites.

2. It was inferred that with the inclusion/incorporation of granite dust as well as titania particulates in the polymer composites, the mechanical properties, i.e., density and void content, hardness, flexural strength and modulus, impact strength and ILSS shows a significant improvement in the characteristics.

3. Incorporation of granite dust/titania particulate only affected tensile strength and modulus in the negative declining fashion.

4. TOPSIS decision making approach has been predominantly employed to determine the ranking of the fabricated polymer composites and it was inferred that granite dust filled hybrid polymer composite with 15% wt. is ranked 1ST and unfilled polymer composite specimen is ranked 7TH among all the composite specimens.

V. REFERENCES

[1]. P. Bakshi , Asokanpappu , R. Patidar , M. K. Gupta And V. K Thakur "Transforming Marble Waste Into High-Performance, Water-Resistant, And Thermally Insulative Hybrid Polymer Composites For Environmental Sustainability" (2020) Polymers 2020, 12, 1781

[2]. A. H. Awad, W. Ahmed, A. Ghany, A. El-Wahab, R. El-Gamsy and M. H. A. Latif "The Influence Of Adding Marble And Granite Dust On The Mechanical And Physical Properties Of PP Composites" (2019) Journal Of Thermal Analysis And Calorimetry

[3]. Ibrahim Alameri,Meraloltulu Mechanical Properties Of Polymer Composites Reinforced By Silica-Based Materials Of Various Sizes (2020) Applied Nanoscience

[4]. Tayfunuygunoglua, Ibrahim Gunesb, Witoldbrostowc Physical And Mechanical Properties Of Polymer Composites With High Content Of Wastes Including Boron (2015) Materials Research. 2015; 18(6): 1188-1196

[5]. S. K. Nayak and A. Satapathy "Development And Characterization Of Polymer-Based Composites Filled With Micro-Sized Waste Marble Dust" (2020) Polymers And Polymer Composites 1–12

[6]. A. Sharma and V. Gautam "Mechanical and Wear Characterization of Epoxy Resin-Based Functionally Graded Material for Sustainable Utilization of Stone Industry Waste" Advances in Manufacturing Systems: Select Proceedings of RAM 2020 (2021) pp. 303.

[7]. V. Gautam, A. Patnaik and IK Bhat "Utilization of Stone Industry Waste as Filler for Sustainable Development of Aluminum Alloy Composites: A Thermo-Mechanical and Mechanical Characterizations" Advances in Manufacturing Systems: Select Proceedings of RAM 2020 (2021) pp. 109

[8]. A. H. Awad, A. El-Wahab, R. El-Gamsy and M. H. A. Latif "A Study Of Some Thermal And Mechanical Properties Of HDPE Blend With Marble And Granite Dust" (2019) Ain Shams Engineering Journal 10, 353–358

[9]. A. H. Awad, A. Ghany, A. El-Wahab, R. El-Gamsy and M. H. A. Latif "Assessment Of Mechanical Properties Of HDPE Composite With Addition Of Marble And Granite Dust" (2020) Ain Shams Engineering Journal Xxx (Xxxx) Xxx

[10]. Abdelmoaty Mohamed Abdelmoaty "Mechanical Properties And Corrosion Resistance Of Concrete Modified With Granite Dust" (2013) Construction And Building Materials 47 (2013) 743–752

[11]. M. S. Reddy, Dr. Y. Reddy and Gyanentakhelmayum "Evaluation Of Mechanical Properties Of Cement Concrete Pavement Using Granite Dust And Baggage Ash" (2018) International Journal Of Applied Engineering Research, Volume 13, Number 7

[12]. Mathankumar S "Experimental Study on Concrete Adding With Granite Dust And Copper Scrap"(2019) International Research Journal Of Engineering And Technology (IRJET) Volume: 06 Issue: 03.

[13]. J. A. V. Gonçalvesa, Diego Adalbertotelescamposb, Gislane De Jesus Oliveirab, Maria De Lourdes Da Silva Rosac, Marcelo Andrade Macêdoa "Mechanical Properties Of Epoxy Resin Based On Granite Stone Powder From The Sergipe Fold-And-Thrust Belt Composites" (2014) Materials Research.; 17(4): 878-887

[14]. C. Ramadji, Adamahmessan and Elodieprud'homme "Influence Of Granite Powder On Physico-Mechanical And Durability Properties Of Mortar" Materials 2020, 13, 5406.

[15]. V. Gautam, A. Kumar, A. Sharma, D Kumar and A. Kumar "Tribological behaviour of hybrid reinforced vinyl ester based functionally graded materials" Materials Today: Proceedings (2021) 44(6) pp. 4682-4688.

[16]. K. C. Nagaraja, S. Rajanna , G. S. Prakash and G. R. Kumar "Mechanical Properties Of Polymer Matrix Composites: Effect Of Hybridization" 2020 Materials Today: Proceedings Xxx (Xxxx) Xxx

[17]. A. K. Sinha, H. Kumar and N. S. Bhattacharya "Mechanical Properties Of Hybrid Polymer Composites: A Review" (2020) Journal Of The Brazilian Society Of Mechanical Sciences And Engineering, 42:431

[18]. Hadikhoramishad, Mohammad Vahabmousavi "Hybrid Polymer Composite Materials" (2019) AIP Conference Proceedings 2144, 030030

[19]. G€Okhanac¸Ikbas¸Selc¸Uk € Ozcan,Nurcanc¸Alıs¸ Ac¸Ikbas. "Production And Characterization Of A Hybrid Polymer Matrix Composite" (2017) POLYMER COMPOSITES—2017

[20]. Dumitrubolcuand Marius Marinelst˘Anescu A Study Of The Mechanical Properties Of Composite Materials With A Dammar-Based Hybrid Matrix And Two Types Of Flax Fabric Reinforcement (2020) Polymers 2020, 12, 1649

[21]. Wendy Rodriguez-Castellanos And Denis Rodrigue "Production and Characterization of Hybrid Polymer Composites Based on Natural Fibers Composites From Renewable And Sustainable Materials

[22]. A. A. Nair, S. Prakash and Dr. R. C. Paul "Synthesis and Characterization of Hybrid Polymer Composites" (2017) International Journal Of Advanced Engineering Research And Science (IJAERS) [Vol-4, Issue-3

[23]. J. S. Suresh, M. P. Devi, R. Mohammed and C. N. Bhaskar "Processing, Mechanical Characterization And Topsis Ranking of Glass/Particulates Reinforced Epoxy Based Hybrid Composites" (2016) International Journal Of Scientific & Engineering Research, Volume 7 , Issue 5 .

[24]. R. Mohammed, Dr B. R. G. Reddy and N. S. Kumar "Evaluation Of Mechanical Properties Of Epoxy Based Hybrid Composites & MCDM Technique For Composite Selection" (2018) International Journal For Modern Trends In Science And Technology Volume: 04, Issue No: 07.

[25]. K. S. Sravani, B. R. G. Reddy and R. Mohammed "Effect Of Caco3 And Al2O3 Fillers On Mechanical Properties Of Glass/Epoxy Composites" (2017) International Journal For Modern Trends In Science And Technology Volume: 03, Issue No: 06

[26]. Faris M. AL-Oqla, S. M. Sapuan, M. R. Ishak, And Nuraini A. A. "Decision Making Model For Optimal Reinforcement Condition Of Natural Fiber Composites" (2015) Fibers And Polymers 2015, Vol.16, No.1, 153-163

[27]. D Kumar, A. Srivastav and V. Gautam "Investigation on mechanical and thermo-mechanical properties of injection molded PP-TiO2 composites" Materials Today: Proceedings (2021) 44(6) pp. 4607-4611

[28]. V. Gautam, A. Patnaik and IK Bhat "Thermo-Mechanical and Fracture Characterization of Uncoated, Single and Multilayer (SiN/CrN) Coating on Granite Powder Filled Metal Alloy Composites" Silicon (2016), 8(1) pp. 133-143

[29]. Ewaroszkowska, "Multi-Criteria Decision Making Models By Applying The Topsis Method To Crisp And Interval Data Multi-Criteria Decision Making Models", multi-criteria decision making models.

[30]. Pawar, M.J., Patnaik, A., Nagar, R., "Mechanical and thermo-mechanical analysis based numerical simulation of granite powder filled polymer composites for wind turbine blade" (2016) Fibers Polymers 17, 1078]

Sustainability Aspects in Seismic Performance of Confined Masonry Structures: A Review

Sami Ullah
MS Student at Department Civil Engineering
Capital University of Science and Technology
Islamabad, Pakistan
samiullahktk426@gmail.com

Majid Ali
Professor at Department of Civil Engineering
Capital University of Science and Technology
Islamabad, Pakistan
professor.drmajid@gmail.com

Abstract

The brick masonry structures are mostly used in the construction industry for building up to two stories in the world. The unreinforced brick masonry structures performed not well during past earthquakes, which causes economical and human life losses. Confined brick masonry structures are proposed as reinforced brick masonry structures, which are now mostly used in developing countries. The seismic performance of the confined brick masonry structure is very important to withstand the structure while hit by the strong ground motion of earthquakes to reduce the economic losses as well as losses to human lives. The purpose of the work to construct the structures to avoid collapse of the structures during strong ground motion to reduce losses and use proper techniques, material to construct the structures with seismic load resistivity as well as economical. For the seismic performance of confined brick masonry structures, different research papers were studied to understand the effect of the stiffeners on brick masonry structures during strong ground motion. The papers studied including the analytical work on confined brick masonry structure, effects of past earthquakes on unreinforced and reinforced brick masonry structures, and Laboratory testing evaluation of the performance of confined/reinforced brick masonry structures while testing on shaking table by applying strong ground motion. The vertical and horizontal stiffeners used in brick masonry structures show improvement in the strength of the brick masonry structures and enhance the ductility of the brick masonry structures whiles testing on a shaking table with strong ground motion. From studies, it has been concluded that the reinforced concrete stiffeners improved the brick masonry structure's properties like strength, ductility, and avoid collapse of the structure during strong ground motion with peak accelerations. It has been also observed that during the past earthquake the reinforced/confined brick masonry structures performed well as compared to unreinforced brick masonry structures.

Keywords: *Confined brick masonry structures, seismic performance improvement, strength increase, ductility enhancing.*

IEECP'21, July 29-30, 2021, Silicon Valley, San Francisco, CA – USA

D!!: *https://sci-index.com/DAI/2021.99101/IEECP/14737977*

I. INTRODUCTION

The brick masonry structures especially unreinforced masonry structures are commonly used in many developing countries. The unreinforced brick masonry structures cause heavy damages in the past earthquake of the Hindu Kush earthquake 2015 of the magnitude of 7.5, which result in 280 fatalities and substantial damages to 109,123 buildings [Najif]. The failure of the unreinforced masonry structures is due to the seismic force resistance deficiencies, which cause heavy damages to the structures. For improving properties of unreinforced brick masonry structures, French Structural Engineer Paul Cottancin proposed the stiffeners provision method at the end of the 20th century (Edgell, 1985).

Confined masonry structures are widely used in the construction industry in the world, especially in Asia. Confined masonry structures are the basic structure of masonry with the provision of reinforced concrete columns and beam at a proper location like at corners, around openings, intersections, and places whether suitable and required to provide. The basic function of tie-columns in confined masonry structures is basically to improve the strength and ductility of the masonry structure or wall.

The confined masonry structures show better performance instead of masonry structures as observed in past earthquakes of Pakistan, Indonesia, Chili, and Haiti where the losses to property and life were mostly due to the collapse of masonry structures. The masonry structures were mostly used in past because of unawareness of enough knowledge. The provision of reinforcing stiffeners to brick masonry structures made the structures on the safe side to avoid heavy damages during the strong ground motions.

This paper is focusing on the improvement of seismic load resistance of the masonry structures by using different kinds of techniques and materials to enhance the stability of the structure as well as made structures economical. The work on literature review gives different techniques and materials which improve the seismic capacity of the structures. The techniques and materials selecting for confining of the structures must be enhanced the strength or seismic properties of the structures as well as make the structure economical by selecting cheap materials and easy method of construction of the structure.

II. CONCEPT OF CONFINED MASONRY (CM) STRUCTURES

Masonry construction is used for a longer time and still in many developing countries it is using because of the economic construction type. For proper construction of the confined masonry construction, it is necessary to understand the nature of confined masonry structures. To clear the concept about confined masonry structure we will know about what is confined masonry structure

and how it distributed or transfer the load. Masonry structures can be confined in different ways and materials like providing reinforced concrete tie-beams and tie-columns, timber material and can be reinforced by proving reinforcement in hollow bricks and poured with concrete. The most commonly used are tie beams and tie columns. For confining brick masonry structure horizontal and vertical reinforced concrete stiffeners can also be used which variate in size and reinforcement for different seismic zone and soil profile types [*Mehran*].

A. What is Confined Masonry

Confined brick masonry structures are some of the most commonly used structures in America, Europe, and Asia. In a confined brick masonry structure basically, the unreinforced brick masonry structure is confined by the provision of the horizontal and vertical reinforced concrete beams and columns, which is also known as tie-columns and bond beams. These columns and beams have enhanced the ductility of the structure and improve the lateral resistance of the structure to earthquake loadings and hold the brick masonry walls to avoid disintegration of the walls during earthquake lateral forces.

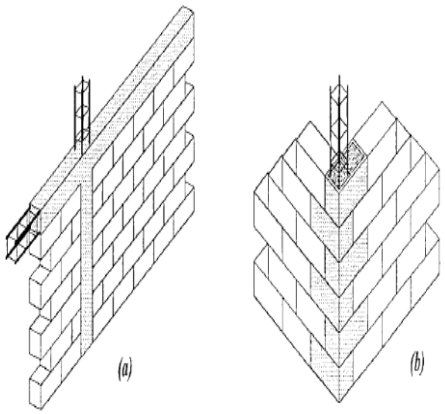

Figure 1. Confined Brick Masonry Walls [*Nasir*]

Confined masonry structure consists of basically the following structural and non-structural elements as given below.

a) Slab

In confined masonry structures, the floor slab and roof slab transferred vertical loads to the masonry walls to be transferred to the foundation properly. In a confined masonry structure, the slab behavior can be considered as a horizontal beam member in the structure.

b) Confining Beams and Columns

The confining elements like tie beams and tie columns provide to masonry walls are avoid disintegration of the masonry walls and withstand the structure vertically during the earthquake.

c) Masonry Walls

Masonry walls in confined brick masonry structures are usually transferred loads from roofs and slabs to the foundation through a plinth beam. Masonry walls behave as a vertical load carry member of the structure as well as resist lateral forces.

d) Plinth Beam or Plinth Band

Plinth beam or plinth band provide below the masonry and walls and above the foundation which transferred the vertical load from masonry walls to foundations.

e) Foundations

The Foundation of the confined brick masonry structure is basically the lowest structure member which transferred the load of the structure from plinth to ground.

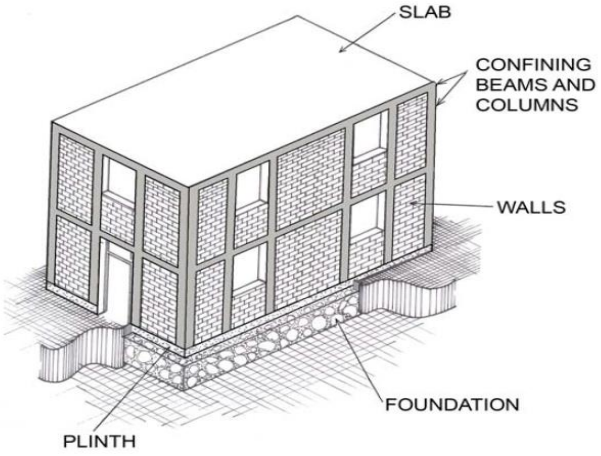

Figure 2. A typical Confined Masonry building of two-story [*Blondet,2005*]

B. How Confined Masonry Structure Different then Reinforced Masonry Structure

In confined brick masonry construction, the reinforcement is provided in confining elements like tie beams and tie columns while in reinforced masonry construction, the reinforcement is provided in brick masonry. For reinforced masonry construction the brick masonry used clay or concrete hollow inside for provision of the reinforcement as can see in figure 3 and figure 4. The confinement of the masonry structure is not only limited to the reinforced concrete stiffeners but also can be used steel, timber, and other similar kind of confining members, but here we are focusing on using reinforced concrete tie-beams and tie-columns as confining element of the masonry structure.

Figure 3. Confined Masonry Structure Construction in Indonesia [*Meisl*]

Figure 4. Reinforced Masonry Structure Construction in Canada [*Bill McEwen*]

C. How Confined Masonry Structure Different then RC Frame Structure

The confined masonry structure is totally different than the reinforced concrete Frame structure because of the construction procedure and transferring the vertical load to the foundation as well as in resisting the lateral seismic load. In confined masonry structure, the seismic lateral load resisting and transferring load to foundation from slab to beams and columns and beams to columns than from columns to foundation, while in confined masonry structure mainly the vertical load from slab transferred to brick masonry walls and from there to the foundation through plinth beam or band. The main differences between confined masonry structures and reinforced concrete frame structures are given in table-01.

Table 1. Comparison between Confined masonry and RC Frames Structures Construction

Types	Confined Masonry	RC-Frames
Load Carrying	In confined Masonry construction the vertical load is basically carrying by masonry walls as well as the lateral load is also carrying by masonry walls.	In RC Frames the vertical load is carrying by Beams and columns from slab to foundation as well as lateral load is also resisting by Frame members.
Foundation Construction	In confined masonry Strip footing and plinth beam or band constructed below the masonry walls	In RC Frames isolated footing, raft/mate, strip footing, pile footing and combined footings are constructing below columns.
Super Structure Construction	1. Construct masonry walls first. 2. Construct vertical tie columns. 3. Then construct tie beams on tie columns and masonry walls. 4. At the end construct the slab and roof.	1. First, construct the columns. 2. Then construct beams and slab/roof. 3. Then construct the masonry walls

III. SEISMIC PERFORMANCE OF CM STRUCTURES

A confined masonry structure is introduced basically for the improvement of a brick masonry structure to avoid disintegration of the masonry walls. The confined masonry structure should perform well during the strong ground motion. Seismic performance is observed in the different past earthquakes which show that confined masonry structure performs well as compared to the unreinforced or unconfined masonry structure.

A. Bam Earthquake

The earthquake occurred in December 2003, which hit the historical city Bam, Iran with a magnitude of M_w 6.7 causes too many losses to the economy and human lives. During the earthquake, most of the buildings collapse due to which approximately forty-five thousand people lost their lives. The brick masonry structures collapses fully while the newly constructed confined and reinforced brick masonry structures perform well and save human lives.

B. Peru Earthquake

The earthquake magnitude of 7.9 hit Pisco, Peru, which causes approximately 519 peoples to death and 1090 injuries. After the earthquake, it was found that confined masonry structures performed well as compared to unconfined masonry buildings. Some confined masonry structures collapse as well due to the soft story effect and also confined masonry building up to six stories performed well. The confined masonry structure which performed well in the earthquake up to six stories may be due to the proper confinement of the brick masonry structures. However, most of the confined masonry structures show better performance with little or no damages [*EERI, 2007*].

C. Central Java Earthquake

Central Java earthquake occurred in May 2006, which hit Java island, Indonesia with a magnitude of 6.3 killed 5,176 peoples and approximately 154,000 houses destroyed completely while 260,000 suffered from damages of different natures. However, the confined masonry structures performed well as compared to unreinforced and partially reinforced structures during the earthquake [*EERI, 2006*].

D. Chile Earthquake

The Chile earthquake occurred in 1985, which caused up to 66,000 buildings to collapse completely and damaged 127,000 houses. 13,500 houses out of 84,000 houses were confined masonry structures from 3 to 5 stories in height. However, the confined masonry building performed well generally as compared to unreinforced masonry buildings during the earthquakes.

E. Pakistan Earthquakes

Pakistan is located in the most active seismic region and hit by different disastrous earthquake-like the Quetta earthquake, Makran earthquake and Azad Kashmir earthquake as shown in table number 02.

Table 02. Major Disastrous Earthquakes in Pakistan

Date	Affected Area	M_w	Depth (km)
12-25-2015	Gilgit Baltistan, Khyber Pakhtunkhwa	6.3	212.5
9-24-2013	Awaran District, Balochistan	7.7	14.8
1-18-2011	Dalbandin, Balochistan	7.7	101
10-8-2005	Azad Kashmir, Balakot	7.6	15
2-27-1997	Balochistan	7	10
12-31-1983	Gilgit-Baltistan	7.2	214
11-28-1945	Makran Coast, Balochistan	8.1	25
5-31-1935	Ali Jaan, Balochistan	7.7	-

All of the earthquakes were disastrous but the Azad Kashmir, Balakot earthquake was the deadliest earthquake of Pakistan which killed more than 79,000 peoples and 65,308 were injured and other extensive damages occurred. At least 32,335 buildings were collapsed and a village in Muzaffarabad completely destroyed while in Uri 80 percent of the town was destroyed [*RPERA*]. These damages occurred due to the unawareness of the proper design guidelines and using of poor construction materials.

F. Comparison

From the seismic performance of the different structures during the past earthquake it has been observed that the places with a large number of unreinforced masonry structures suffered more than the places with a greater number of well-confined masonry structures. This means that the confined masonry structures perform well as compared to the unreinforced masonry structures. As can be seen that the earthquake magnitude of the Chile earthquake was more than the Indonesia earthquake but more losses to the structure have occurred in Indonesia as compared to Chile because of the construction of the well-confined structure in Chile as compared to Indonesia. These studies show that the confining elements like the provision of tie-beans and tie-columns hold the masonry walls in positions and enhanced the lateral resistance of the masonry walls to resist the seismic forces during the earthquake.

IV. SUSTAINABLE BUILDING

Sustainable building is the building that can improve and maintain the quality of life and harmonize within the environment in the region throughout the entire building life-cycle. In developing countries mostly construction is doing to construct economical buildings and the building can sustain itself during the earthquake loading. For sustainable building, research is in progress to use different sustainable techniques and materials to maintain the desired level of quality and performance of the building after seismic loading of earthquakes.

A. Sustainable Techniques

Sustainable techniques are the techniques used to construct the building to make the structures sustainable during earthquake loadings. Different researching techniques were used to enhance the masonry structure properties which contribute to the lateral load resisting capacity of the structures. The most commonly using the technique is the construction of vertical and horizontal columns, which sizes are proposed for different seismic zones and soil profile types to efficiently and economically construct the confined masonry structures [*Mehran, 2020*]. The effect of confining element checked on masonry structures and evaluate the properties of unreinforced and reinforced masonry structures, which shows that confining of masonry structure gives an easy approach to enhance the lateral load resisting properties of masonry structures [*Mehran, 2017*]. So, by using different techniques we can achieve seismically sustainable structures which can resist and withstand earthquake loadings. The most feasible and economical solution is providing the vertical and horizontal stiffeners at the required location of the structures which intern sustainable and economical solution.

B. Sustainable Materials

The seismically sustainable structures cannot be achieved without knowing and using efficient and good quality materials. For making structure seismically sustainable research scholar proposed a different kind of materials to be used to enhance the masonry and confined masonry structures lateral load resisting capacity. For this purpose, plaster with natural fibers used for mortar free interlocking wall, which show improving the lateral resisting of the wall by using a different kind of natural fibers like sisal, rice straw [*Furqan, 2018, 2020*]. Now a days different kinds of natural fibers, synthetic fibers, artificial and industrial fibers are using in concrete to enhance the concrete properties which in result enhancing seismic load resisting properties of structures. The very unique natural coconut fibers and their ropes used in concrete members like beams, columns and mortar free interlocking construction and testing under seismic and dynamic loadings which result very effective for improving the lateral load resisting capacity and can be very useful in the construction of seismic regions [*Majid, 2014, 2016, 2017*]. As these materials are used in concrete which shows a positive response of the structure while testing for the required properties. The plain cement plaster show increase in lateral resistance of the structure than the wall without plaster while the plaster of fiber mixed shows further enlacement in the lateral resistance of the walls. These materials were suggested to use to increase the seismic resistance of the structures and made the construction work economical as well by using local and natural materials for the improvement of structure sustainability. The addition of natural fibers in concrete and plaster enhances the lateral resistance of structure as well as reduces waste material pollution.

V. SUGGESTED IMPROVEMENTS IN CM STRUCTURES CONSIDERING SUSTAINABILITY ASPECTS

The confined masonry structures perform well as compared to unreinforced masonry structures as observed in the past earthquake that occurred in different countries. But it is observed that due to the unavailable of awareness in people of developing countries still people constructing unreinforced masonry structures. For improving the performance of confined masonry structures the following suggestions are given.

1. The proper footing of confined masonry should be constructed.
2. Vertical stiffeners or tie-columns should be provided at each corner of the building and rooms.
3. Tie-columns should be provided around the opening of the doors and windows.
4. Tie beams should be provided above openings of doors and windows.
5. The tie columns and tie beams should be connected and anchored properly.
6. Floor to floor should be properly constructed to avoid soft-story effects.
7. It would be better to limit confined brick masonry construction to the low-rise building of two to three stories.

By following the above steps and suggestions we can avoid the collapse of confined masonry structures and can reduce economic and human life losses. It has been learned from this literature review that we can be reinforced or confined the masonry structures by using different materials like timber, steel, reinforced concrete, and fiber reinforced concrete. The confining of the masonry structure basically enhances the seismic performance of masonry structures to reduce the losses during the earthquake. The reinforced concrete gives more sustainable structures as compared to other materials using for confining of the structures. The study gives us to properly understand of the concept of confined masonry construction and how it different then reinforced and frame structures.

VI. CONCLUSIONS

As in the past earthquake, it has been observed that unreinforced brick masonry structures cause a lot of losses to the economy and human lives due to totally collapsed of the structures while on other hand confined masonry structures and reinforced masonry perform well during the earthquake which reduces the losses to the economy and human lives. As comparing the earthquakes, it seems that the chile earthquake cause little damages to structures as compared to Java, Indonesia earthquake. This is because of the confining structures in Chile and well-designed construction houses while in Indonesia the damage occurred due to unreinforced construction. So, it has been concluded that,

1. The confining and reinforcing of the brick masonry structures enhanced the ductility of the masonry structures and hold the brick masonry wall in position and avoid disintegration of the masonry structures.
2. The confined masonry structures have more lateral resistance to seismic forces as compared to unreinforced masonry structures due to enhancing the lateral resistance

of the masonry structures by providing tie-columns and tie beams.

3. For better performance of the confined masonry structures, the tie-columns should be provided at all intersections of the masonry walls and provided around the openings of the doors and window and similar large openings.
4. Similarly, provide the tie beams at seven feet height of each story or above the opening of doors and windows level throughout the structure's walls.
5. It is concluded as well that the confined masonry shows better performance up to 2 and 3 stories of the buildings.

By following proper design guidelines of confined masonry structures and provide enough reinforcement according to the requirement of the structure we will be able to reduce the effects of the earthquake forces on structures and as a result will be able to reduce economic losses and save human lives.

VII. ACKNOWLEDGMENTS

The authors would like to acknowledge all organizations/persons who have helped in this literature research.

VIII. REFERENCES

[1]. Amjad Naseer, "Performance Behavior of Confined Brick Masonry Buildings under Seismic Demand" Department of Civil Engineering, N. W. F. P University of Engineering and Technology, Peshawar, Pakistan, 2009.

[2]. Blondet, M. (2005). Construction and Maintenance of Masonry Houses – For Masons and Craftsmen. Pontificia Universidad Catolica del Peru, Lima, Peru.

[3]. D. Bernstein, some early reinforced brickwork masterpieces revisited, in: J.A. Wintz, A.H. Yorkdale, Virginia McLean (Eds.), Proc. 5 Th Int. Brick Masonry Conf. (VIBMaC) Held in Washington, DC, 5-10 Oct. 1979, p. 231, 1979.

[4]. EERI (2007). 'Learning from Earthquake: The Pisco, Peru, Earthquake of August 15, 2007' EERI Special Earthquake Report-October 2007.

[5]. EERI (2006), 'The Mw 6.3 Java, Indonesia, Earthquake of May 27, 2006', 2006 August EERI Special Report.

[6]. Furqan Qamar, Terence Thomas, Majid Ali, "Use of natural fibrous plaster for improving the out of plane lateral resistance of mortarless-interlocked masonry walling", Construction and Building Materials, Elsevier, 2018.

[7]. Furqan Qamar, Terence Thomas, Majid Ali, "Improvement in lateral resistance of mortar-free interlocking wall with plaster having natural fibers", Construction and Building Materials, Elsevier, 2020.

[8]. Hamidreza Ramazi, Hussein S. Jigheh, "The Bam (Iran) Earthquake of December 26, 2003: From an Engineering and Seismology Point of View", Journal of Asian Earth Sciences.

[9]. Majid Ali, "Use of coconut fiber reinforced concrete and coconut fiber ropes for seismic-resistant construction", Materiales De Construccion, 2016.

[10]. Majid Ali, "Seismic performance of coconut-fiber-reinforced-concrete columns with different reinforcement configurations of coconut-fiber ropes", Construction and Building Materials, Elsevier, 2014.

[11]. Majid Ali, "Role of Post-tensioned Coconut-fibre Ropes in Mortar-free Interlocking Concrete Construction During Seismic Loadings", Structural Engineering, Springer, 2017.

[12]. Majid Ali, Mawawi Chouw, "Coir Fibre and Rope Reinforced Concrete Beam Under Dynamic Loading", Department of Civil and Environmental Engineering, the University of Auckland, New Zealand.

[13]. Mehran Khan, Majid Ali, "Mehran Khan, Majid Ali, "Earthquake-resistant brick masonry housing for developing countries: An easy approach" NZSEE Conference, 2017.

[14]. Mehran Khan, Majid Ali, "Optimization of Concrete Stiffeners for Confined brick masonry structures" Journal of Building Engineering, Elsevier, 2020.

[15]. Meisl, C.S., Safaie, S., Elwood, K.J., Gupta, R., and Kowsari, R. (2006). Housing Reconstruction in Northern Sumatra after the December 2004 Great Sumatra Earthquake and Tsunami. Special Issue on the Great Sumatra Earthquakes and Indian Ocean Tsunamis of 26 December 2004 and 28 March 2005, Earthquake Spectra, Vol. 22, No S3, pp. S777-S802.

[16]. Miha Tomazevic, Iztok Klemenc, "Seismic Behavior of Confined Masonry Walls", Earthquake Engineering and Structural Dynamics, VOL. 26, 1059-1071 (1997).

[17]. Miha Tomazevic, Iztok Klemenc, "Verification of Seismic Resistance of Confined Masonry Buildings", Earthquake Engineering and Structural Dynamics, VOL. 26, 1073-1088 (1997).

[18]. Mr. N.M.S.I Arambepola, UDRM, ADPC, "Report on Post-Earthquake Rapid Assessment Northern Pakistan-08 October 2005.

[19]. Najif Ismail, Nouman Khattak, "Observed failure modes of unreinforced masonry buildings during the 2015 Hindu Kush earthquake" Earthquake Engineering & Engineering Vibration (2019).

[20]. Seismic Design Guide for Low-Rise Confined Masonry Buildings, Confined Masonry Network A Project of the World Housing Encyclopedia, EERI & IAEE with funding support from Risk Management Solutions.

[21]. Sharon L. Wood, James K. Wight, Jack P. Moehle, "The 1985 Chile Earthquake Observation on Earthquake-resistant Construction in Vina Del Mar" Engineering Studies.

[22]. Smitha Gopinath, C. K. Madheswaran, J. Prabhakar, K.G Thivya Devi & C. Lakshmi Anuhya, "Strengthening of Unreinforced Brick Masonry Panel Using Cast-in-Place and Precast Textile-Reinforced Concrete", Journal of Earthquake Engineering, Taylor and Francis, 2020.

[23]. Vladimir G. Haach, Graça Vasconcelos, Paulo B. Lourenço, "Experimental Analysis of Reinforced Concrete Block Masonry Walls Subjected to In-Plane Cyclic Loading", Journal of Structural Engineering, ASCE, 2010.

Workability of Concrete Having Used Petrol Engine Oil and Banana Fibers

1st Blawal Hasan
Department of Civil Engineering
Capital University of Science and Technology
Islamabad, Pakistan
blawalhasan@gmail.com

2nd Majid Ali
Department of Civil Engineering
Capital University of Science and Technology
Islamabad, Pakistan
professor.drmajid@gmail.com

Abstract

The quality of work and strength factors are directly dependent upon the concrete's property of workability. The objective of this study is to assess the workability of specimens having a 9.4% quantity of used petrol engine oil (UPEO) and varying the proportions (0.0%, 0.5%, 1.0%, 1.5%, 2.0%, and 2.5%) of banana fibers (BF). For this purpose, the slump cone test method is adopted to investigate workability. Proportions for the UPEO and BF are added by taking the mass of cement. The values of the slump of all admixed specimens are compared with normal plain concrete. The addition of UPEO and BF have done by taking the percentage of the mass of cement. It is observed from the results that the addition of UPEO increases the value of slump. On the other hand, the influence caused by the BF is the reduction of the slump value. This study concluded that the workability of concrete depends upon ingredients and admixed additional raw materials which are needed use to achieve the specific property. This study contributes towards the development of sustainable construction material with improved properties of concrete.

Keywords: *Admixture, Banana Fibers, Concrete's Workability, Fiber Reinforced Concrete, Used Petrol Engine Oil*

I. INTRODUCTION

The trend of the addition of natural fibers as reinforcement, to enhance the mechanical properties of the concrete, is increasing in developing countries. This growing interest in the utilization of natural fibers within the concrete is key to an issue which is less workability of concrete [1]. Workability is an important factor that controls the strength and quality of the mix. Workability reduces due to the addition of fiber within the concrete. An increase in the value of lignocellulose natural fibers, like banana fibers (BF), results in an increment in water absorption properties [2]. More water absorption property of fiber within the fresh reduces the slump value of concrete. The addition of all types of agricultural natural fiber significantly may decrease the property of workability [3]. Increase in the quantity of natural fiber within the indicated reduction in the slump of fresh concrete [4]. In the laboratory or at construction sites, the workability of concrete is determined by performing the concrete slump test during the construction work process [5, 6]. The workability property of concrete relies on the slump test and its value. Workability is normally controlled by the raw ingredients and w/c used for the mix design. The addition of natural fiber plays important role in the reduction of the slump of concrete. To overcome this situation, plasticizers and superplasticizers are incorporated to overcome the issue of less workability.

Used petrol engine oil (UPEO) can be used within the concrete, as a chemical admixture. Used engine oil does not leave a significant adverse effect on the load deflection and ultimate load behavior of flexural members [7]. Used engine oil can be added as an air-entraining agent in concrete. Utilization of UPEO did not leave worse the strength of hardened the concrete, but, caused an increase in a slump and air-entrained percentage of the fresh concrete [8]. Used engine oil approximately fulfills all the characteristics of type A water-reducing admixture according to ASTM standard C494 [9]. On the other hand, the researchers investigated the additive influence of agricultural waste/fibers on the properties of composites [10]. By the addition of jute fibers in concrete, resistance against impact loading improved [11]. Now a days, the combination of the fibers and admixture is being used to investigate and improve the properties of the construction materials. It was observed that the strength and ductility with combined addition of fibers and admixture were more than compared to composite prepared by the only addition of admixture [12]. Mechanical properties of cementitious composite enhanced by the addition of nanotube admixture and nano-fibers [13]. Many researchers performed investigations on the fresh properties and observed improvement in the hardened properties of concrete admixing the fibers and admixture simultaneously [14–16]. There are several studies reported on the workability and enhancement of strength and mechanical properties of the concrete by incorporating artificial fibers and admixture during the production of the concrete [17–19]. The toughness index and energy absorption properties were enhanced to resist the cracking with the usage of fibers and admixture in the concrete at the same time [20]. Workability helped in assessing and reducing the risk of segregation of lightweight aggregate concrete having steel and polypropylene fibers [21]. The good mechanical properties can be achieved of composite composed of fiber and mineral admixture by considering the workability property of the fresh concrete [22].

IEECP'21, July 29-30, 2021, Silicon Valley, San Francisco, CA – USA

DAI : *https://sci-index.com/DAI/2021.99101/IEECP/14737965*

Several studies can be found on the workability of artificial fiber reinforced concrete having some amount of admixture. But there is very limited research work on the workability of natural fibers and chemical admixture. This so natural fiber can be affected by chemical fiber due to its acidic/basic properties. To the best of the authors' knowledge, no work has been reported on workability of concrete made by the BF as reinforcement and UPEO as an admixture. As workability plays important role in the hardened properties of concrete. So, it is required to investigate the workability of the concrete made of natural fibers and waste chemical materials as an admixture like UPEO. To evaluate the fresh properties of concrete, different mix designs are casted having the varying proportion of BF and a fixed amount of the UPEO. Both BF and UPEO's contents are added by taking the mass of the cement being used for the production of the composites. A slump test is performed to analyze the workability of the fresh concrete. The undesirable workability of concrete is a deviation from the desired properties of concrete. Other than the basic ingredients can affect the workability of concrete adversely. A low slump means less workable concrete. Less workable concrete cannot be placed and poured into the formwork properly, ultimately leads to a decrease in the strength and improper shape of members. This study will help in controlling the workability while using the fibers and admixture. So, that it cannot be compromised with the desired properties and modeling of the members. It will also help to think about the utilization of waste materials and production of the good mechanical properties by keeping a special focus on the fresh properties of the concrete.

II. METHODOLOGY

A. Raw Materials

Ordinary Portland cement and Margalla crush along with locally available sand were used in the production of normal plain concrete. The maximum size of the aggregate 20 mm used for the manufacturing of both plain concrete and fiber reinforced concrete (FRC). For the preparation of FRC, banana fiber was used. The fixed length of 5 mm of the fiber was used in the preparation of the FRC. UPEO was used within plain concrete to prepare used petrol engine oil plain concrete and FRC. Normal temperature tap water used for preparing the plain concrete (PC), used petrol engine oil plain concrete (PU) and used petrol engine oil and banana fibers plain concrete (PUB). PC and PU are prepared with a 0.5 water cement ratio (W/C) and 0.6 W/C used for the production of all types of PUBs.

B. Mix Design and Concrete Preparation

For the manufacturing of plain concrete, cement, sand and aggregates ratio for mix design 1, 2 and 4, respectively, used with a 0.5 water cement (W/C) ratio. The same mix design is used for producing the used petrol engine oil plain concrete (PU) with a minor change which is the addition methodology of UPEO. After the half time of mixing elapsed, the UPEO is added after stopping the mixture time. To the best of the authors' knowledge, there is no specific or standard method available for the mixing of fiber reinforced concrete, so the layers methodology is used for the production of all PUBs likewise filling of slump cone by layers with a little difference. The W/C ratio is increased from 0.5 to 0.6 for the making of all the PUBs. The increment in the W/C ratio is taken to ensure acceptable compaction with a workable mix to achieve better strength could be achieved. In the methodology of mixing of PUB, 1/3 layer of aggregates is placed following by sand with same, fibers and cement. Then second and third layer is placed in the same manner of placing the first layers. Water is added in portions to avoid the bleeding effect in PUBs. After time elapsed for the mixing, the UPEO is admixed at last. The addition of UPEO is made at last and after spending some time on mixing is just to avoid the sticking of UPEO to a specific portion of the concrete or with its ingredients.

Figure 1. Measuring the value of slump of PUB.

C. Workability Test

The slump cone test is used to investigate the workability or consist of the manufactured PC. The slump test for the PC, PU and PUB is always performed before the pouring in molds. According to ASTM standard C143/C143M-15a, a slump cone test is performed to evaluate the workability of the fresh concrete [23]. Slump cone of a bottom diameter of 200 mm (8 in), bottom diameter of 100 mm (4 in) and height of 300 mm (12 in) is used to perform the test. The cone mold should be non-absorbent. Temping rod is hemispherical from both ends with a diameter of 16 mm (5/8 in) and length not more than 600 mm (25 in). The cone is filled with three equal volumetric layers of concrete. After placing the first 1/3 layer, compaction is done by a total of 25 times randomly dropping temping rod on the surface of the layer from a height of 25 mm (1 in). Similarly, further two layers of the cone are filled and compacted with the help of temping rod. Removed the extra amount of concrete by striking off the temping rod and made it smooth by screeding and rolling the rod over it. Later, the slump cone is lifted vertically upward. The cone is placed upside down beside the concrete of the slump cone's mold. Temping rod is placed over the up-turned slump cone in such a way that its length could reach over the slumped concrete as shown in [Figure 1]. With help of the ruler, the value of the slump is measured carefully. As per the best of the authors' knowledge, there is no such standard test is available to find out the workability of fresh UPEO-PC and UPEO-BFRC. Hence, the same procedure and test standard are used for the determination of the workability of PU and PUB.

III. RESULTS AND ANALYSIS

A. Slump of Fresh Concretes

The values of slump of PC, UPEO-PC and all UPEO-BFRCs is shown in the fifth column of Table 1. It can be observed clearly that a 9.4% addition of the UPEO content in the pc caused an increment in the slump value of the mix [Figure 2]. Even the water cement ratio (W/C) is kept same for the both PC and PU mix. The value of slump of PC and PU 36 mm and 40 mm, respectively. As expected, the addition of UPEO resulted in increment of 11.1% in the value of slump than the value of PC. These slumps of PUBs are less than the slumps of PC and PU. The 0.5% addition of BF has reduced significantly value of slump within the PC. The w/c is increased from 0.5 to 0.6 for the manufacturing of the all PUBs. The slump of the PUBs having fiber content 0.5%, 1.0%, 1.5%, 2.0% and 2.5%

are 23 mm, 19.5 mm, 17 mm, 13 mm and 10.5 mm, respectively. The slump of the is decreased as much the value of the BF is increased within the mix [Figure 2].

Table 1. Water cement ratio (W/C) and slump of PC, PU and all type of PUBs.

Mix	UPEO's addition (%)	BF's addition (%)	W/C (ratio)	Slump (mm)
PC	0	0	0.5	36
PU	9.4	0	0.5	40
PUB_1	9.4	0.5	0.6	23
PUB_2	9.4	1.0	0.6	19
PUB_3	9.4	1.5	0.6	17
PUB_4	9.4	2.0	0.6	13
PUB_5	9.4	2.5	0.6	10

The increase or decrease in optimum length (5 cm) of fiber was lead to a reduction in the slump of the FRC [24]. It can be observed that the incorporation of UPEO content enhances the value of slump PU in comparison with the slump of PC. This indicates the addition of UPEO can lead to the reduction of the water content (W/C ratio).

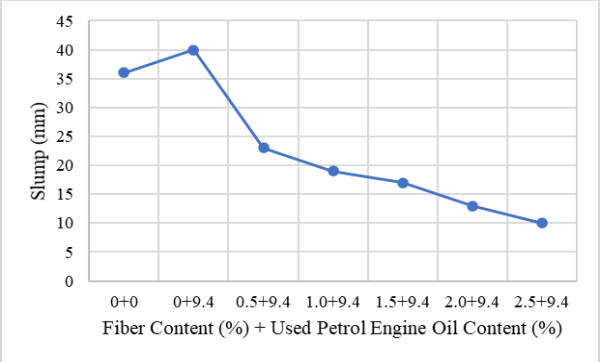

Figure 2. Influence of B.F and UPEO contents on slump

B. Ease with Concrete Handling

The ease with concrete handling means easy to place and transport the concrete, depends upon the workability of the concrete. Generally, it depends upon the W/C ratio of concrete and the size of the aggregate. Compared to PC, it is noticed that PU is more workable and easier to handle having the same w/c ratio. This is due to the increased slump of the PU. The slump value is affected by the addition of UPEO in the concrete mix. It is discovered that placing the PUBs is a little hard than the PC. The ease of handling of PUB is reduced after the incorporation of the fibers. The handling of the PUB became difficult as time passed than the PC. This difficulty is observed due absorption property of the fiber. Handling PUB_5 is much harder than PUB_1. This phenomenon has shown that the incorporation of fiber within the mix has made it harder to handle, place and transport. This is all due to the reduction in the slump caused by the increasing value of fiber in the mix. In general, admixing of natural fibers resulted in the reduction of the slump value of the mix. The values of PUBs were 10-23 mm. Despite these low values of the slump, the PUBs were workable, easy to place and transport and easy with the handling of the concrete but a little hard to handle than PC. It is experienced that the concrete should be poured into molds as soon the mixing is done for ease with concrete handling. As the time duration increased after the mixing, the handling of concrete becomes difficult. Due to less workability, difficulty was faced during the compaction. Ultimately, improper compaction can lead to the opposite direction to the achievement of desired properties of the composite.

IV. SUSTAINABLE CONSTRUCTION MATERIALS (USED PETROL ENGINE OIL AND BANANA FIBERS) AS PART OF CLEANER PRODUCTION

In the transportation sector, the use of vehicles increasing day by day. The main part of the vehicle is the engine and needs to be lubrication for good functionality. These lubricants are needed to replace after a specific running of motor/engine. Used petrol engine oil (used engine oil) is more dangerous to the environment than crude oil as it contains contaminated heavy particles [25]. It doesn't only have the contamination of the heavy particle but also polycyclic aromatic hydrocarbons (PAHs) that are insignificant in the unused oil. The used engine oil (or used petrol engine oil) badly affects the male reproductive parameter [26]. As there are tons of waste engine oil available, it cannot be stored. The used engine oil should be controlled and avoided its entrance and mixing with the runoff water. Eventually, it may pollute the river and sea environment and may cause danger to the water living life. The damping or used oil needs special treatments which costly. On the other hand, agricultural waste is growing day by day. It has been observed that about 21% of greenhouse gas is emitted by agricultural waste. The adverse effects of agricultural waste on the eco-system, human health and aquatic life have necessitated the appropriate dumping. Dumping of this waste covers a large part of precious land and also this is dangerous to human health [27]. The other method to dump the agricultural waste is to burn it. When a large amount of the agricultural is burnt up it releases a large amount of heat making which is dangerous to the global environment and can boost the global warming effect.

Many researchers had utilized agricultural waste differently in the research works related to the development of sustainable construction materials. Agricultural wastes, like coconut fibers and ropes made of these fibers, were used to develop a sustainable construction material and cleaner production [28]. This design of utilization of UPEO and BF for the development of construction material is eco-friendly as it helps in the dumping of agricultural waste and engine lubricant waste. The dumping of agricultural waste is a cost-effective task and required a lot of valuable lands. As it cannot be dumped in the sea or river to avoid pollution of the aquatic environment. Normal concrete releases a large amount of heat during the sintering process [29]. This effect can be minimized by the replacement of some amount of cement by UPEO [9]. Improved properties material can be developed by using agricultural waste/fibers in concrete instead of dumping. Seismic performance of FRC with added ropes of coconut fibers (agricultural waste) was improved as compared with the normal plain concrete [30, 31]. It was reported that sustainable concrete developed of agricultural waste, coconut fibers, helped in the reduction of the thickness of road making compared with normal concrete [32]. This made it economical as well as the number of costly materials is reduced due to reduction caused in the volume due to thickness. Fiber reinforced concrete made by natural fibers has comparable properties with synthetic fiber reinforced concrete in terms of strength. It depends upon the properties of fiber, like orientation, size and the manufacturing techniques [33]. This study helped in developing a sustainable construction material by using waste materials as raw materials. The dumping and recycling of mentioned above materials are uneconomical as well. So, the use of these materials as raw materials helped in the development of sustainable construction material and cleaning of the environment from the severe materials and in controlling the economy factor.

V. CONCLUSIONS

Used petrol engine oil plain concrete (PU) and used petrol engine oil and banana fibers plain concrete (PUB) are inspected to evaluate the effects of used petrol engine oil (UPEO) and banana fibers (BF)

on workability. For the making of PU, 9.4% of UPEO content by mass of cement is admixed in ingredients of normal concrete during the time of mixing. And for the production of the PUBs fixed amount of UPEO and varying proportions of fibers are used. The length of fiber is kept 5 cm and the addition of fiber is made on the base of the percentage mass of cement. The workability of concrete helps in its proper placing. Segregation of concrete can decrease the strength of the concrete adversely. A good workable mix also reduces the vulnerability of the segregation of concrete. The following conclusions are drawn:

- By the incorporation of 9.4% of UPEO, increased the slump value by 11.1% as compared to that of PC retaining w/c ratio same.
- Incorporation of banana fiber 0.5%, 1.0%, 1.5%, 2.0% and 2.5% in the mix has shown slumps of 23 mm, 19.5 mm, 17 mm, 13 mm and 10.5 mm respectively.
- An increase in fiber content within the mix causes a reduction in the slump of the PUB.
- Compared to PC, the workability of PUB reduces with an increase in the content of banana fibers.
- As much as the mix is less workable, the concrete handling goes harder.
- With the increase in workability of PU, the handling of mix become easier compared to PC.

From the above-mentioned results, workability highly affects the handling of concrete. The addition and quantity of the natural have shown a significantly adverse effect on the workability of the concrete. The use of the UPEO only has resulted in an increase in workability and concrete handling. So, a less W/C ratio is required to achieve high workability while adding UPEO to the mix.

VI. ACKNOWLEDGMENTS

The authors would like to thank all who has helped in this research, especially Engr. M Abrar and Engr M Sultan Sikander. The careful reviews and constructive suggestions by anonymous reviewers are gratefully acknowledged.

VII. REFERENCES

[1] M. Ali and N. Chouw, "Coir Fibre and Rope Reinforced Concrete Beam Under Dynamic Loading," *Australian Earthquake Engineering Society Conference,"Newcastle Earthquake–20 years on.*, Newcastle, NSW, Australia, 11-13 December 2009, New Castle, Australia. Dec. 11-13. Paper no. 4.

[2] J. Ronald Aseer, K. Sankaranarayanasamy, S. Renold Elsen, and A. K. Thakur, "Experimental studies on water absorption properties of acetic acid treated banana fiber composites," *Materials Today: Proceedings*, 2021, 2021.02.518.

[3] A. Wongsa, R. Kunthawatwong, S. Naenudon, V. Sata, and P. Chindaprasirt, "Natural fiber reinforced high calcium fly ash geopolymer mortar," *Construction and Building Materials*, vol. 241, p. 118143, 2020.

[4] S. Guler, B. Öker, and Z. F. Akbulut, "Workability, strength and toughness properties of different types of fiber-reinforced wet-mix shotcrete," *Structures*, vol. 31, pp. 781–791, 2021.

[5] I.-C. Yeh, "Exploring concrete slump model using artificial neural networks," *Journal of Computing in Civil Engineering*, vol. 20, no. 3, pp. 217–221, 2006.

[6] I.-C. Yeh, "Modeling slump flow of concrete using second-order regressions and artificial neural networks," *Cement and Concrete Composites*, vol. 29, no. 6, pp. 474–480, 2007.

[7] B. S. Hamad and A. A. Rteil, "Effect of used engine oil on structural behavior of reinforced concrete elements," *Construction and Building Materials*, vol. 17, no. 3, pp. 203–211, 2003.

[8] B. S. Hamad, A. A. Rteil, and M. El-Fadel, "Effect of used engine oil on properties of fresh and hardened concrete," *Construction and Building Materials*, vol. 17, no. 5, pp. 311–318, 2003.

[9] Y. L. Yaphary, R. H. W. Lam, and D. Lau, "Reduction in cement content of normal strength concrete with used engine oil (UEO) as chemical admixture," *Construction and Building Materials*, vol. 261, p. 119967, 2020.

[10] M. U. Farooqi and M. Ali, "Contribution of plant fibers in improving the behavior and capacity of reinforced concrete for structural applications," *Construction and Building Materials*, vol. 182, pp. 94–107, 2018.

[11] T. Hussain and M. Ali, "Improving the impact resistance and dynamic properties of jute fiber reinforced concrete for rebars design by considering tension zone of FRC," *Construction and Building Materials*, vol. 213, pp. 592–607.

[12] J. Cao and D. D. L. Chung, "Carbon fiber reinforced cement mortar improved by using acrylic dispersion as an admixture," *Cement and Concrete Research*, vol. 31, no. 11, pp. 1633–1637, 2001.

[13] Z. S. Metaxa, J.-W. T. Seo, M. S. Konsta-Gdoutos, M. C. Hersam, and S. P. Shah, "Highly concentrated carbon nanotube admixture for nano-fiber reinforced cementitious materials," *Cement and Concrete Composites*, vol. 34, no. 5, pp. 612–617, 2012.

[14] J.-Y. Wang, N. Banthia, and M.-H. Zhang, "Effect of shrinkage reducing admixture on flexural behaviors of fiber reinforced cementitious composites," *Cement and Concrete Composites*, vol. 34, no. 4, pp. 443–450, 2012.

[15] D.-Y. Yoo, S.-T. Kang, J.-H. Lee, and Y.-S. Yoon, "Effect of shrinkage reducing admixture on tensile and flexural behaviors of UHPFRC considering fiber distribution characteristics," *Cement and concrete research*, vol. 54, pp. 180–190, 2013.

[16] D.-Y. Yoo, N. Banthia, and Y.-S. Yoon, "Effectiveness of shrinkage-reducing admixture in reducing autogenous shrinkage stress of ultra-high-performance fiber-reinforced concrete," *Cement and Concrete Composites*, vol. 64, pp. 27–36, 2015.

[17] O. Gencel, W. Brostow, T. Datashvili, and M. Thedford, "Workability and mechanical performance of steel fiber-reinforced self-compacting concrete with fly ash," *Composite interfaces*, vol. 18, no. 2, pp. 169–184, 2011.

[18] Q. Cao, Y. Cheng, M. Cao, and Q. Gao, "Workability, strength and shrinkage of fiber reinforced expansive self-consolidating concrete," *Construction and Building Materials*, vol. 131, pp. 178–185, 2017.

[19] C. Li, L. Miao, Q. You, S. Hu, and H. Fang, "Effects of viscosity modifying admixture (VMA) on workability and compressive strength of structural EPS concrete," *Construction and Building Materials*, vol. 175, pp. 342–350, 2018.

[20] M. Khan, M. Cao, and M. Ali, "Cracking behaviour and constitutive modelling of hybrid fibre reinforced concrete," *Journal of Building Engineering*, vol. 30, p. 101272, 2020.

[21] N. A. Libre, M. Shekarchi, M. Mahoutian, and P. Soroushian, "Mechanical properties of hybrid fiber reinforced lightweight aggregate concrete made with natural pumice," *Construction and*

Building Materials, vol. 25, no. 5, pp. 2458–2464, 2011.

[22] A. Nadiger and M. K. Madhavan, "Influence of mineral admixtures and fibers on workability and mechanical properties of reactive powder concrete," *Journal of Materials in Civil Engineering*, vol. 31, no. 2, p. 4018394, 2019.

[23] AMERICAN SOCIETY FOR TESTING AND MATERIALS. ASTM C143, "Standard Test Method for Slump of Hydraulic-Cement Concrete," *Astm C143/C143M-20*, pp. 1–2, 2020.

[24] M. Ali, A. Liu, H. Sou, and N. Chouw, "Mechanical and dynamic properties of coconut fibre reinforced concrete," *Construction and Building Materials*, vol. 30, pp. 814–825, 2012.

[25] US EPA (2000) Office of the Solid Waste, EPA, 530-F-94-008

[26] W. O. Akintunde, O. A.Olugbenga, O. O. Olufemi, "Some adverse effects of used engine oil (common waste pollutant) on reproduction of male sprague dawley rats," Open access *Macedonian journal of medical sciences*, 3(1), 46.

[27] I. O. Adejumo, O. A. Adebiyi "Agricultural Solid Wastes: Causes, Effects, and Effective Management," In *Solid Waste Management*. IntechOpen.

[28] M. Ali, "Use of coconut fibre reinforced concrete and coconut-fibre ropes for seismic-resistant construction," *Materiales de Construcción*, vol. 66, no. 321, p. 73, 2016.

[29] R. Maddalena, J. J. Roberts, and A. Hamilton, "Can Portland cement be replaced by low-carbon alternative materials? A study on the thermal properties and carbon emissions of innovative cements," *Journal of Cleaner Production*, vol. 186, pp. 933–942, 2018.

[30] M. Ali, "Role of post-tensioned coconut-fibre ropes in mortar-free interlocking concrete construction during seismic loadings," *KSCE Journal of Civil Engineering*, vol. 22, no. 4, pp. 1336–1343, 2018.

[31] M. Ali, "Seismic performance of coconut-fibre-reinforced-concrete columns with different reinforcement configurations of coconut-fibre ropes," *Construction and Building Materials*, vol. 70, pp. 226–230, 2014.

[32] M. Khan, A. Rehman, and M. Ali, "Efficiency of silica-fume content in plain and natural fiber reinforced concrete for concrete road," *Construction and Building Materials*, vol. 244, p. 118382, 2020

[33] M. R. Sanjay, P. Madhu, M,, Jawaid, P Senthamaraikannan, S.Senthil, S. Pradeep, "Characterization and properties of natural fiber polymer composites: A comprehensive review," *Journal of Cleaner Production*, 172, 566-581.

A Survey on Deep Learning in Big Data and its Applications

Zair Bouzidi
LIMPAF Laboratory, Computer Science Dept,
Science & Applied Science Faculty,
Bouira University, Bouira, Algeria
zair.bouzidi@gmail.com

Mourad Amad
LIMPAF Laboratory, Computer Science Dept,
Science & Applied Science Faculty,
Bouira University, Bouira, Algeria
zair.bouzidi@gmail.com

Abdelmalek Boudries
Laboratory LMA, Commercial Science Dept, Faculty of Economics, Business & Management, Bejaia University,
Bejaia, Algeria
abdelmalekboudries@gmail.com

Abstract

Individuals can exchange real-time information thanks to the vast spread and reach of social networks. This active participation with the corporate data, as emails, documents, databases, business processor history, etc and content published on the Web, as age and contact details, reviews, comments, photos, images, videos, sounds, texts, famous cookies, or e-commerce transactions, exchanges on social networks, are very important. Data recovery from different sources can be a difficult task. A timely and correct assessment of an event currently under discussion is critical to the effectiveness of the used method. This information, collected in the Web can then be updated. Various ways are developed to automate this necessity, due to the extraction and analysis of correct social media content. Alleviation methods do not adequately incorporate these approaches. It may be necessary to reveal them in order to make further progress, particularly in the areas of energy efficiency and cleaner production.

Keywords: Big data, Clean energy, Cloud computing, Deep learning, Energy efficiency, Smart Data

I. INTRODUCTION

Social media has been increasingly pervasive in our daily lives in recent years. They have emerged as a viable resource for disseminating, detecting, tracking, and extracting information in order to better manage events [1,2]. Because of its ability to deliver a message to a potentially wide audience, social networking is used to acquire and transmit accurate and timely information. However, the massive amount of information provided during times of crisis event can make collecting relevant and actionable information even more challenging.

Recent events have used social media to allow the afflicted public to immediately submit a vast amount of event information, allowing managers to make speedly accurate and judicious decisions. The comparison of all Big Data models is shown in Table I. Using social media to convey timely information during catastrophes has become commonplace in recent years [2]. Major events can result in millions of messages being shared on social media. Researchers are paying more attention to the relation between social media, awareness and resilience [1,3,4]. Numerous studies [3,4] for the automated recognition of various types of social media material have been conducted in recent years.

With the rise of social media, a current event is being debated across all platforms. In order to acquire a complete picture of the event, it's critical to collect data from various sources. The information gathered from various sources has often qualitative variances. When it comes to recovering information published on social media, acquiring reasonable, great, and outstanding situational awareness, and good damage assessment, managers have an enormous problem. On the web, there are various sources of information where a current topic can be debated. Several automated tools [1] have been developed to assist event management in identifying and filtering useful material that has been posted online. Only a few studies have concentrated on warning [1,2], education [5], situational awareness, and assessment, with the great bulk of research focusing on leveraging social networking as a source of information for only a few phases of event management.

Databases, log files, online web applications, and social media networks are just some of the places where data can be found. It can be tough to work with a range of massive data sources and formats, as well as data stored locally. Data ingestion is the process of bringing raw data from several silo databases or files into a data lake on a data processing platform like Hadoop. A data lake is a storage repository for vast amounts of unstructured data in its original format, with data structure and standards defined only after the data is used. As a result, data lakes have a flat architecture and have schema-on-read, unlike data warehouses, which store data in a highly structured repository and employ a relational or dimensional data model. A data warehouse function called schema-on-write determines the data structure before it is stored. As a result, data lakes are more versatile, as data may be quickly updated and rebuilt to fit various research models. For importing various types of data into Hadoop, a number of data ingestion technologies are now available.

II. BIG DATA

TABLE I. COMPARATIVE TABLE OF ALL MODELS USING BIG DATA

Models	***Identification Usage of Big Data***
[6]	Making Sense of Big Data through Human Computing and Machine Learning
[7]	Decision-Making and emerging Big Data
[8]	Social Networking Data Quality in Big Data
[9]	Big Data privacy in public Social Media

IEECP'21, July 29-30, 2021, Silicon Valley, San Francisco, CA – USA

D!f: *https://sci-index.com/DAI/2021.99101/IEECP/14737953*

Big data refers to all the digital data produced by the use of new technologies for personal or professional purposes [10]. This includes corporate data (emails, documents, databases, business processor history, etc.) as well as data from sensors, content published on the Web (age and contact details, reviews, comments, photos, images, videos, sounds, texts, famous cookies), e-commerce transactions, exchanges on social networks, data transmitted by connected objects (electronic labels, smart meters, smartphones, etc.), geolocated data, etc [6,9,10]. Big data makes it possible to meet a huge technological challenge : to store a large amount of data from different channels on a huge hard drive, easily accessible from all corners of the planet. Data stored in a safe place and recoverable at any time in the event of any incident [10]. Massive data duplication is one of the keystones of the big data architecture. Cloud computing and distributed file systems (DFS) are among the main storage models currently available. These data provide very interesting clues about consumer behavior and market trends. Big data makes it possible to know your profile, but also your overall behavior: frequency of use of social networks and of your online purchases, channels used, hours of connection, etc. Table II shows the comparison of all tehnics and methods used in various OSN models.

TABLE II. COMPARATIVE TABLE OF ALL TECHNIQUES AND METHODS (SOCIAL NETWORKING) USED IN VARIOUS MODELS.

Ref	*Identification Methods*	*Used OSN*
[11]	Flood Disaster Game-based Learning	Twitter
[12]	Educational Purposes with Special Reference at the Faculty of Higher Education	Twitter
[13]	Summarization with social-temporal context	Twitter
[14]	Building a Tweet Summarization Dataset with a TREC Track	Twitter
[15]	Semi-automated artificial intelligence-based classifier for Disaster Response	Twitter
[16]	Summarizing situational tweets in crisis scenarios: An extractive-abstractive approach	
[17]	Based on Artificial NN (ANN)	Twitter & Facebook
[18]	Based on Artificial NN (ANN)	All the Web
[5]	Based on FeedForward NN (FFNN)	All the Web

Big data refers to all the digital data produced by the use of new technologies for personal or professional purposes [10,19]. Table III shows the advantages and limitations of Big Data.

TABLE III. BIG DATA ADVANTAGES AND LIMITATIONS

Advantages[1]	*Limitations*
Cost Savings	[20]
Time Reductions [21]	**Need for talented** [21]
Better sales insights	**Incompatible tools** [22]
Control online reputation	**Correlation Errors**
Understand the market conditions	**Costs**
Increased productivity	**Security and Privacy Concerns**
Fraud detection	
Clean energy with Construction of Global Energy Interconnection (GEI) [23]	

Contents were collected from all online channels tracked automatically by the Online Listening Tool [24,25] from websites to social media, such as Twitter, Facebook, LinkedIn, Instagram, Google+, Youtube and so on. Actually, many networking platforms allow access to their data via Application Programming Interface (API) [26].

Big data has opened up new possibilities in a variety of areas, including science, politics, communication, medicine, meteorology, ecology, economics, commerce and energy, to name a few. Researchers, companies and administrations can carry out trend or predictive analysis, draw up profiles, anticipate risks and monitor phenomena in real time, thanks to analytical tools and data modeling.

Big data makes it possible to meet a huge technological challenge, in storing, in a safe place and recoverable at any time in the event of any incident, a large amount of data from different channels on a huge hard drive, easily accessible from all corners of the planet. Big data is an essential tool for BtoB and BtoC companies. The data collected helps them to design personalized marketing campaigns adapted to the needs, preferences and behavior of consumers. This information helps improve the customer experience, attract prospects and retain existing customers. Improved targeting makes marketing campaigns more effective and reaches the desired segment, the one that is most likely to be interested in the company's products and / or services. Big data is also a competitive advantage for professionals who hold a multitude of data, because they can anticipate changes in behavior and better understand why consumers have turned to a particular service provider.

Big data is a valuable tool in vast private and public fields ranging from online sales to scientific research, including culture, politics, transport, insurance, the banking sector, industry and energy. Big data primarily designates masses of data that are too large, complex and heterogeneous or which change too quickly to be able to be analyzed and used correctly and quickly, with current methods of data processing. The smart data goes beyond this simple notion of large quantity data : it designates the useful and quality information obtained from masses of heterogeneous data, and for which we have not only taken into account the technical mastery of the mass of data but also of the quality, security and protection of data and its use. Knowledge is thus generated from the data. The use of this data is based on technologies that make complex processing possible and thus generate knowledge, a source of added value, and which will become the foundation of the new data economy. That's the reason for which big data must be transformed into smart data [27-30].

Big Data, peuvant être structurée, non structurée ou semi-structurée, permet de capturer, stocker, distribuer, gérer et analyser de vastes ensembles de données avec différentes structures à haute vitesse. Les données sont générées à partir de diverses sources et peuvent arriver dans le système à des rythmes différents. C'est grâce au parallélisme qui permet de traiter ces grandes quantités de données et grâce à Hadoop qui permet de structurer Big Data et le rendre utile à des fins d'analyse. Hadoop, étant un logiciel open source permettant le traitement distribué de grands ensembles de données, il est conçu pour passer d'un seul serveur à plusieurs machines, avec une grande tolérance aux pannes [31].

[1] https://www.vapulus.com/en/advantages-and-disadvantages-of-big-data/#:~:text=Big%20data%20is%20a%20term,a%20higher%20false%20discovery%20rate.

A. Smart Data

We produce information every day, in all situations of our life: whether at our workplace, at the doctor, behind the wheel of our car or at the baker, via our smartphone, our smartwatch or our computer. It is textual data, images or sensors. If we consider the fact that this data can be analyzed, processed and used, then we can really speak of it as raw material. Because these masses of data, this big data, contain immense potential. Streaming is a common Internet method of broadcasting and reading streaming content. It differs from a file download, which necessitates recovering all of a file's data. Streaming content, on the other hand, necessitates the use of an internet connection. Smart Data, a different concept of Big Data, is based primarily on real-time data analysis. This is a method of data analysis that analyzes data directly at the source rather than sending it to a centralized system for analysis. Big and smart data are transversal technologies, which will prevail in almost all areas of our life and will change them for the long term. Traditionally, data is first collected, converted, placed in a database, and processed in waves. However, with this approach, data is usually out of date when it is finally analyzed. Table IV shows Smart Data Areas.

TABLE IV. SMART DATA APPLICATION AREAS.

No	*Smart Data application areas*	*Smart Data application application*
1	Financial services	Fraud detection and prevention
2	Retail	Allowing brands to: - Analyzing the sentiment of their customers, - and Offering personalized and contextual promotions
3	Telecommunications industry	Possibility of - Better allocating bandwidth based on real-time needs, and - diagnosing the condition of antennas
4	Manufacturing	Preventive maintenance
5	Healthcare	- Monitoring patient vital signs and - Reducing readmission rates
6	Oil industry	- Proactive repairing infrastructures, and - Balancing the power delivered according to consumption
7	Public sector	- Detecting and preventing intrusion attempts on the network, and - Predicting the risk of epidemics
8	Transport sector	Possibility of detecting risky conduits

While the term Smart Data refers to an approach to data analysis that involves analyzing data directly at the source to enable immediate decisions to be made, without the need to send it to a centralized system. Processing time is reduced to just seconds. The term "*Smart*" refers to the intelligence of this concept, based on the fact that less data is processed, because statistical models are responsible for determining which are the relevant variables, namely the most correlated. For example, an autonomous car cannot wait for the data to be sent to the cloud and the results to be returned to the user. In this case, the data must be gathered directly by sensors so that the processors in the car can analyze it and the results are sent to the actuators that control the brakes and steering wheel of the vehicle. If the data is not analyzed immediately, the consequences can be tragic. Smart Data always combine the analysis of this data with human intelligence to provide you with comprehensive, synthesized and useful information for your business. The objective of Smart Data is first of all to remove uninteresting data for marketing actions, thus making a first cut in the mass of available data. The second step is to check the remaining information to distinguish which is still valid and which is no longer. This action is based on comparisons with data offered. It also involves the identification of data useful for a particular campaign. Finally, It can also be equipped with geographical criteria for sorting information, in order to highlight data that is only relevant in a specific catchment area. The presence and listening to social networks are also essential, because the E-reputation on social networks and the Web in the customer process are inseparable. Unlike Big Data, Smart Data makes it possible to control and qualify data. It is used for the establishment of a coherent marketing strategy. Smart Data can therefore generate leads and increase sales while building customer loyalty by providing them with optimal experience and satisfaction.

III. DEEP LEARNING

In recent years, Deep learning methodologies have achieved impressive results in computer vision [32], speech recognition, image processing, Disaster Management [19] and handwritten recognition of characters, while they is currently in its infancy in fault diagnosis [33]. Even if training appears to have been effective, Generative Adversarial Networks (GANs) with finite size discriminators and generators can struggle with distribution learning. Table V shows the Comparison of Machine Learning Technics.

TABLE V. COMPARING MACHINE LEARNING TECHNICS.

Algo-rithm	*Lear-ning Type*	*Based-Class*	*Limitation*	*Advantage*
K-Nearest Neigh-bor	Superv ised	Instance	Suufering from dimensiona lity curse	Distance-based problems
Naïve Baye-sian Classifi-cation	Superv ised	Probabi-listic	Imputs Independen cies	Positive Probability for all Classes
Hidden Markov	Superv ised	Marko-vian	With Markov Assump-tion	Time Series Data & Memory-less information
SVM	Superv ised	Deci-sion Boun-dary	Definite Distinction between Classifica-tions	Binary Classification
NN	Superv ised	Non Linear Func-tional Approxi-mation	Little Bias	Binary Inputs
Cluster-ing	Unsu-per-vised	Cluste-ring	/	Data Grouping with Distance: Euclidean, Manhatan
Ridge Regres-sion	Super-vised	Regres-sion	Low Limitation	Continus Variables
Filtering	Unsu-per-vised	Feature Transfor mation	/	Data/many variables to use Filtering

Restricted Boltzmann computer is a classifier, regression, subject modeling, collaborative filtering, and feature learning algorithm. RBM is concerned with the fundamental unit of composition, which has evolved into a variety of common architectures and is commonly used in a variety of large-scale industries. Neuroimaging, Sparse image restoration in mine planning, and Radar target recognition are all applications of the Restricted Boltzmann machine.

By using uncorrected label data and its reconstruction errors, RBM overcomes the issue of noisy labels. The unstructured data problem is solved by a feature extractor, which converts raw data into hidden units. The main drawback is that RBMs are difficult to

train since the most common algorithm, Contrastive Divergence, necessitates precision sampling from a Monte Carlo Markov Chain. In addition, the energy of the model has a complicated partition function, making estimating the log likelihood difficult

In an autoencoder, on the other hand, cross entropy may at least be tracked. Figure 1 shows the Classification of Deep Learning.

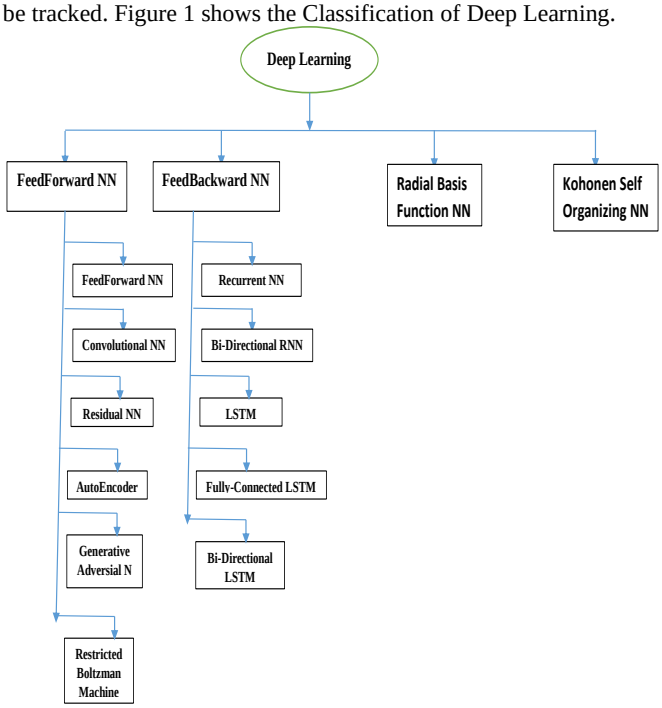

Fig. 1. Classification of Deep Learning

When a deeper feedforward NN is created, it can be giving the model the ability to capture more complex representations, as for Image recognition tasks (convolutional NNs), Natural language processing, Bio-informatics tasks.

If it is tried to create a deep NN to model more simpler phenomena, it is running the risk of over-fitting the data, losing the ability able to generalize to new examples and factoring the amount of resources takes to train a deep neural net.

Deep LSTM (DLSTM) and CLSTM are two LSTM variants that are important. The DLSTM model has a different number of layers than the LSTM model in general. The extraction of well-defined temporal data would be impossible with a single-layer LSTM. By piling more layers, the LSTM model, on the other hand, would be able to achieve better temporal features, making it better suited to capturing motion in the time dimension. To ensure that spatial features are preserved, CLSTM runs the data through convolutional layers first. The LSTM extracts temporal attributes from the Convolutionan NN (CNN) output, allowing the model to capture both spatial and temporal motion. These two variants can also be combined to create a convolutional deep LSTM, in which the outputs of a CNN are fed into a multilayer stacked LSTM, which guarantees a better result at the expense of increased computational complexity [34].

In comparison to RNN, the BRNN can be trained without the restriction of only using input data up to a predetermined future frame. As an example of an unsupervised task, gaps filling in high-dimensional time series with complex dynamics, where unidirectional RNNs have recently been trained successfully to model such time series, but inference in the negative time direction is non-trivial [35].

In a number of speech recognition tasks, both Convolutional NNs (CNNs) and Long Short-Term Memory (LSTM) have outperformed Deep NNs (DNNs). CNNs, LSTMs, and DNNs have complementary modeling capabilities, with CNNs excelling at reducing frequency variations, LSTMs excelling at temporal modeling, and DNNs excelling at mapping features to a more separable space. Combining CNNs, LSTMs, and DNNs into a single unified architecture [36] is an interesting opportunity to carry advantage of their complementarity.

CNNs present some limitations of temporal modeling [37]. The traditional models of Bi-directional Long Short-Term Memory (BLTSM) have encountered some limitations in presentation with multi-level features, but they can keep track of temporal information while allowing deep data representations [37]. Sentiment polarity classification (SPC) on social data is achieved using a Deep Bi-directional Long Short-Term Memory (DBLSTM) architecture with multi-level function presentation. By using DBLSTM, It can exploit more level features than BLTSM, while inheriting its temporal modeling (BLTSM) [37].

The benefits of radial basis function (RBF) networks include ease of design, good generalization, high input noise tolerance, and the ability to learn online.

It's possible that the popularity of Kohonen Self-Organizing NN stems from the fact that it has an easy-to-understand algorithm, is straightforward to use, and generates nice, intuitive results.

Abiodun et al. (2018) [38] recommend that future research can focus on combining various ANN models into a single network-wide application, as needed and depending on the characteristics of the various ANN models.

Neural learning is carried out by Feedforward or Feedback neural network. In Feedforward, we have *supervised learning* such as Feedforward NN itself for classification [5], convolutional NN [39-41] for image recognition/classification or Residual NN (ResNets) [42] for image recognition, *unsupervised learning* such as Autoencoder [36] for Dimensionality reduction and encoding, Generative Adversarial Network [42] network for generating realistic fake data, reconstruction of 3D models or image improvement and *supervised or unsupervised learning* such as Restricted Boltzmann machine [36] for dimensionality reduction, feature learning, topic modeling, classification, collaborative filtering or many body quantum mechanics (See Fig. 1).

In Feedbackward, we have only *supervised learning* such as Recurrent NN [19,34] for sequences recognition as precise timing, Bidirectional Recurrent NN [43] for natural language processing, Long Short-Term Memory [36] for temporal data such as stock market values over a period of time, video frames, Fully Connected-LSTM [44] for learning non-linear and complex processes in hydrological or meteorological modeling and Bi-Directional-LSTM [45] through time-natural language processing and language translation. Neural learning can be trained in either supervised/unsupervised ways by Radial Basic Function Network [46] for M-means clustering, Least square function, function approximation and time series prediction or unsupervised ways by Kohonen Self Organizing Netowork [46] for dimensionality reduction, optimization problems or clustering analysis.

IV. DISCUSSION ABOUT APPLICATIONS OF DEEP LEARNING AND BIG DATA

A. Big Data Application Areas

Smart Data has a wide range of applications (See Table IV). The judicious use of data may help almost every aspect of society and the economy. In banking and marketing, big data technologies are already widely used.

Edge computing and smart data devices are being tested by data scientists, marketers, and manufacturers to create more money, improve decision-making, and detect equipment flaws before they become costly.

When it comes to energy applications, Smart Data can be valuable in a variety of industries. Thanks to big data technologies in supporting Construction of Global Energy Interconnection (GEI) development, clean energy with GEI and its technology innovation

direction uses Big Data for sharing, fusion, and comprehensive application of energy related data all over the world [23].

B. Deep Learning Application Areas

The potential use of industrial data via using Deep Learning algorithms for energy efficiency and greener production goals has been explored in the scientific literature [47].

As the benefits of Artificial Intelligence (AI) and Data Science become more apparent in the energy market, companies are developing an increasing number of apps and solutions that use AI to assist their clients in improving their energy efficiency. Deep Learning analyzes energy usage data to discover consumption trends, calculate the amount of energy utilized by a specific household appliance, and provide individualized recommendations on how to save energy and save money. Artificial intelligence detects equipment failure in the energy business, particularly on coal-fired power plants, potentially causing injuries or even death to workers, by using Deep Learning, sensors, and operational data to forecast when vital infrastructure will break, allowing for prompt maintenance and preventing accidents in power plants and power stations. Deep Learning processes data from smart meters, drones, and sensors installed on energy assets, as well as weather data, to anticipate energy demand, system load, outages, and the amount of renewable energy supplied by solar panels and wind turbines. It aids global power producing and distribution businesses in anticipating outages and boosting power flow through their enormous power networks.

AI-powered real-time management and analysis platforms connected with on-site equipment, as well as creating intelligent adaptive controllers linking with motor and other moving parts of lift systems to deliver both real-time control and maximize production, were developed to decrease expenses for sending people to remote locations for oil exploration and production. Energy businesses might use drone data to conduct virtual inspections of solar and wind installations (both offshore and onshore) and to develop AI-powered software that analyzes system drone imagery and generates actionable reports to track and manage solar asset health.

Deep learning models trained on an increasing number of datasets, satellite imaging, and climate physics can help on both fronts (precise weather and demand forecasts) and help the world achieve carbon neutrality by 2050 (climate neutrality with accurate supply-demand matching)[2].

Researchers employ a mixed architecture consisting of a convolutional neural network (CNN) integrated with an artificial neural network (ANN) to perform French energy demand predictions using weather data [48]. Our entire energy system's efficiency must increase. Blockchain, artificial intelligence, machine learning algorithms, and data software, all of which are critical, have a lot of potential in terms of minimizing the intermittency of some renewable energy sources[3].

V. CONCLUSION AND FUTURE WORKS

The study included a wide range of topics, including disaster management improvements made possible by Big Data and, in particular, Deep Learning. Deep Learning enables the use of Big Data to a variety of fields. Humanitarian operations and crisis management are evolving radically as a result of Big Data and Deep Learning. This paper retains more energy area. This study examines Big Data, Cloud Computing and Deep Learning, finding all of their distinguishing features and classifying Deep Learning architectures. It concludes with a description of all the advancements in the energy sector made possible by Big Data, Cloud Computing and Deep Learning.

Based on the examined literature, certain areas of improvement for additional research and future research development in Big Data, particularly in Deep Learning, can be given to professionals, researchers, and novice researchers.

VI. ACKNOWLEDGMENTS

We acknowledge support of "Direction Générale de la Recherche Scientifique et du Développement Technologique (DGRSDT')". MESRS, Algeria.

VII. REFERENCES

[1] Imran, M., Castillo, C., Lucas, J., Meier, P. & Vieweg, S., (2014), AIDR : Artificial intelligence for disaster response, *Proceedings of the 23rd International Conference on World Wide Web, (ICT-DM), 159-162.* https://doi.org/10.1145/2567948.2577034

[2] Olteanu, A., Vieweg, S., & Castillo, C. (2015), "What to Expect When the Unexpected Happens", Proceedings of the 18th ACM Conference on Computer Supported Cooperative Work & Social Computing - CSCW '15. doi:10.1145/2675133.2675242

[3] Toppel, M., Bartels, M., Nagel, C. and Hahne, M., (2016), "A Social Network to Identify Responsibilities and Expertises in Crisis Scenarios", 3rd International Conference on Information and Communication Technologies for Disaster Management (ICT-DM), 2016

[4] Vulic, I. and Moens, M.-F., (2015), "Monolingual and Cross-Lingual Information Retrieval Models Based on (Bilingual) Word Embeddings", SIGIR'15 Proceedings of the 38th International ACM SIGIR Conference on Research and Development in Information Retrieval, Pages 363-372, Santiago, Chile — August 09 - 13, 2015

[5] Bouzidi, Z., Boudries, A. & Amad, M. (2020). Towards a Smart Interface-based Automated Learning Environment Through Social Media for Disaster Management and Smart Disaster Education. *Advances in Intelligent Systems and Computing. SAI 2020. Vol 1228. Springer, Cham, 443-468.* https://doi.org/10.1007/978-3-030-52249-0_31

[6] Ofli, F. and Meier, P. and Imran, M. and Castillo, C. and Tuia, D. and Rey, N. and Briant, J. and Millet, P. and Reinhard, F. and Parkan, M. and Joost, S., (2016), Combining Human Computing and Machine Learning to Make Sense of Big (Aerial) Data for Disaster Response, Big Data, vol. 4, No. 1

[7] Horita, Flavio E.A. and Albuquerque, Joao Porto (de) and Marchezini, Victor and Mendiondo, Eduardo M., (2017), Bridging the gap between decision-making and emerging big data sources: An application of a model-based framework to disaster management in Brazil, Decision Support Systems, vol. 97, pp. 2-22, doi:10.1016/j.dss.2017.03.001

[8] Immonen, A. and Paakkonen, P. and Ovaska, E., (2015), Evaluating the Quality of Social Media Data in Big Data Architecture, IEEE Access, vol. 3, pp. 2028-2043, doi:10.1109/ACCESS.2015.2490723

[9] Smith, M., Henne, B., Szongott, C. and Voigt, G. von, (2012), Big data privacy issues in public social media, 6th IEEE International Conference on Digital Ecosystems Technologies, pp. 1-6, Doi:10.1109/DEST.2012.6227909

[10] Saranya, M. and Prema, A., (2017), Survey On Big Data Analytcis using Hadoop ETL, International Journal of Computer Trends and Technology (IJCTT), vol. 48, No. 1, doi:10.14445/22312803/IJCTT-V48P105

[11] Zaini, N.A., Noor, S.F.M. & Zailani, S.Z.M. (2020). Design and Development of Flood Disaster Game-based Learning based on Learning Domain. In *International Journal of Engineering and Advanced Technology (IJEAT)*, 9(4), pp. 679-685, DOI:10.35940/ijeat.C6216.049420

[12] Vivakaran, M. V. & Neelamalar, M. (2018). Utilization of Social Media Platforms for Educational Purposes among the Faculty of Higher Education with Special Reference to Tamil Nadu. In *Higher Education for the Future*, 5(1), pp. 4-19, DOI:10.1177/2347631117738638

[13] He, R., Liu, Y., Yu, G., Tang, J., Hu, Q. & Dang, J. (2016). Twitter summarization with social-temporal context. In *World Wide Web*, 20(2), pp. 267-290, DOI:10.1007/s11280-016-0386-0

[14] Dussart, A., Pinel-Sauvagnat, K. & Hubert, G. (2020). Capitalizing on a TREC Track to Build a Tweet Summarization Dataset. In *Text REtrieval Conference*, (TREC'2020)

[2] https://techmonitor.ai/leadership/sustainability/ai-renewable-energy

[3] https://www.electrifying.world/machine-learning-wind-power/

[15] Lamsal, R. & Kumar, T. V. V. (2020). Classifying Emergency Tweets for Disaster Response. In *International Journal of Disaster Response and Emergency Management (IJDREM)*, 3(1), pp. 14-29, DOI:10.4018/IJDREM.2020010102

[16] Rudra, K., Goyal, P., Ganguly, N., Imran, M. & Mitra, P. (2019). Summarizing situational tweets in crisis scenarios : An extractive-abstractive approach. In *IEEE Transactions on Computational Social Systems*, 6(5), pp. 981-993, DOI:10.1109/tcss.2019.2937899

[17] Bouzidi Z., Boudries A. and Amad M., (2018), A New Efficient Alert Model for Disaster Management, Proceedings of Conference AIAP'2018 : Artificial Intelligence and Its Applications, El-Oued, Algeria,

[18] Bouzidi, Z., Amad, M. and Boudries, A., (2019), Intelligent and Real-time Alert Model for Disaster Management based on Information retrieval from Multiple Sources, International Journal of Advanced Media and Communication}, Vol. 7, No. 4, pp. 309-330, doi:10.1145/253260.253325

[19] Bouzidi, Z., Boudries, A. & Amad, M. (2021). Enhancing Crisis Management because of Deep Learning, Big Data and Parallel Computing Environment: Survey. Proceedings of the 3rd International Conference on Electrical, Communication and Computer Engineering (ICECCE), No. 443, 12-13 June 2021, Kuala Lumpur, Malaysia, Accepted

[20] Lefever, S., Dal, M. and Matthiasdottir, A., (2007), Online data collection in academic research : advantages and limitations, Journal British Journal of Educational Technology (BJET) of British Educational Research Association (BERA), vol. 38, No. 4, pp. 574-582, doi:10.1111/j.1467-8535.2006.00638.x

[21] Karma, S., Zorba, E., Pallis, G.C., Statheropoulos, G., Balta, I., Mikedi, K., Vamvakari, J., Pappa, A., Chalaris, M., Xanthopoulos, G. and Statheropoulos, M., (2015), Use of unmanned vehicles in search and rescue operations in forest fires: Advantages and limitations observed in a field trial, International Journal of Disaster Risk Reduction, vol. 13, pp. 307-312, doi:https://doi.org/10.1016/j.ijdrr.2015.07.009

[22] Bello, O. M. and Aina, Y. A., (2014), Satellite Remote Sensing as a Tool in Disaster Management and Sustainable Development : Towards a Synergistic Approach, Procedia - Social and Behavioral Sciences, vol. 120, pp. 365-373, 3rd International Geography Symposium, GEOMED2013, 10-13 June 2013, Antalya, Turkey, doi:10.1016/j.sbspro.2014.02.114

[23] Zhang, D. & Qiu, R. C., (2018), Research on big data applications in Global Energy Interconnection, Global Energy Interconnection, vol 1, No. 3, pp. 352-357, ISSN 2096-5117, doi:10.14171/j.2096-5117.gei.2018.03.006.

[24] Ruggiero, A. and Vos, M., (2014), Social Media Monitoring for Crisis Communication : Process, Methods and Trends in the Scientific Literature, In Online Journal of Communication and Media Technologies, Vol. 4, No. 1

[25] Young, S. D., Rivers, C. and Lewis, B., (2014), Methods of using real-time social media technologies for detection and remote monitoring of HIV outcomes, Preventive Medicine, vol. 63, pp. 112-115

[26] Imran, M., Ofli, F., Caragea, D. & Torralba, A., (2020), Using AI and Social Media Multimodal Content for Disaster Response and Management : Opportunities, Challenges, and Future Directions. *Information Processing & Management, 57(5), 1-9.* http://sci-hub.tw/10.1016/j.ipm.2020.102261

[27] Stillger, M., Lohman, G. M., Markl, V. and Kandil, M., (2001), LEO-DB2's learning optimizer, Very Large DataBases (VLDB), vol. 1, pp. 19-28

[28] Battre, D., Ewen, S., Hueske, F., Kao, O., Markl, V. and Warneke, D., (2010), Nephele/PACTs: a programming model and execution framework for web-scale analytical processing, Proceedings of the 1st ACM symposium on Cloud computing, pp. 119-130

[29] Alexandrov, A., Bergmann, R., Ewen, S., Freytag, J.-C., Hueske, F., Heise, A., Kao, O., Leich, M., Leser, U., Markl, V., Naumann, F., Peters, M., Rheinländer, A., Sax, M. J., Schelter, S., Hoger, M., Tzoumas, K. and Warneke, D., (2014), The stratosphere platform for big data analytics, The VLDB Journal, vol. 23, No. 6, pp. 939-964, Springer Berlin Heidelberg

[30] Carbone, P., Katsifodimos, A., Ewen, S., Markl, V., Haridi, S. and Tzoumas, K., (2015), Apache flink : Stream and batch processing in a single engine, Bulletin of the IEEE Computer Society Technical Committee on Data Engineering, vol. 36, No. 4, IEEE Computer Society

[31] Harshawardhan, S. B. and Devendra, P. G, (2014), A REVIEW PAPER ON BIG DATA AND HADOOP, International Journal of Scientific and Research Publications, vol. 4, No. 10, pp. 756-764

[32] Krizhevsky, A. and Sutskever, I. and Hinton, G., (2012), ImageNet classification with deep convolutional neural networks, Proceedings of Advances in Neural Information Processing Systems, vol. 25, pp. 1090-1098

[33] Bouzidi, Z. Boudries, A. & Amad, M., Deep Learning and Social Media for Managing Disaster: Survey, IntelliSys 2021 Conference, Amsterdam, Accepted

[34] Roshan, S., Srivathsan, G., Deepak, K. and Chandrakala, S., (2020), Violence Detection in Automated Video Surveillance : Recent Trends and Comparative Studies, pp. 157-171, doi:10.1016/B978-0-12-816385-6.00011-8

[35] Berglund, M., Raiko, T., Honkala, M., Karkkainen, L., Vetek, A. and Karhunen, J., (2015), Bidirectional Recurrent Neural Networks as Generative Models, MIT Press, Cambridge, MA, USA

[36] Sainath, T., Vinyals, O., Senior, A. and Sak, H., (2015), Convolutional, Long Short-Term Memory, fully connected Deep Neural Networks, pp. 4580-4584, doi:10.1109/ICASSP.2015.7178838

[37] Khuong, N., Cuong L. and Hong, P., (2016), Deep Bi-directional Long Short-Term Memory Neural Networks for Sentiment Analysis of Social Data, pp. 255-268, doi:10.1007/978-3-319-49046-5_22

[38] Abiodun, O. I., Jantan, A., Omolara, A. E., Dada, K. V., Mohamed, N. A. & Arshad, H. (2018). State-of-the-art in artificial neural network applications : A survey. In *Heliyon*, 4(11), DOI:10.1016/j.heliyon.2018.e00938

[39] Alam, Firoj and Imran, Muhammad and Ofli, Ferda, (2017), Image4Act : Online Social Media Image Processing for Disaster Response, Proceedings of the 2017 IEEE/ACM International Conference on Advances in Social Networks Analysis and Mining, (ASONAM 17), pp. 601-604, doi:10.1145/3110025.3110164

[40] Nguyen, D. T., Al-Mannai, K., Joty, S. R., Sajjad, H., Imran, M. and Mitra, P., (2017b), Robust classification of crisis-related data on social networks using convolutional neural networks, ICWSM, pp. 632-635

[41] Kabir, Md Yasin and Madria, Sanjay Kumar, (2019), A Deep Learning Approach for Tweet Classification and Rescue Scheduling for Effective Disaster Management, Proceedings of the 27th ACM SIGSPATIAL International Conference on Advances in Geographic Information Systems, (SIGSPATIAL'19), pp. 269-278, doi:10.1145/3347146.3359097

[42] He, R., Liu, Y., Yu, G., Tang, J., Hu, Q. & Dang, J. (2016). Twitter summarization with social-temporal context. In *World Wide Web*, 20(2), pp. 267-290, DOI:10.1007/s11280-016-0386-0

[43] Canon, M. J., Satuito, A., Sy, C., (2018), Determining Disaster Risk Management Priorities through a Neural Network-Based Text Classifier, 2018 International Symposium on Computer, Consumer and Control (IS3C), Taichung, Taiwan, 2018, pp. 237-241, doi:10.1109/IS3C.2018.00067

[44] Zhao, J., Deng, F., Cai, Y. and Chen, J., (2018), Long short-term memory - Fully connected (LSTM-FC) neural network for PM2.5 concentration prediction, Chemosphere, vol. 220, doi:10.1016/j.chemosphere.2018.12.128

[45] Kabir, Md Yasin and Madria, Sanjay Kumar, (2019), A Deep Learning Approach for Tweet Classification and Rescue Scheduling for Effective Disaster Management, Proceedings of the 27th ACM SIGSPATIAL International Conference on Advances in Geographic Information Systems, (SIGSPATIAL'19), pp. 269-278, doi:10.1145/3347146.3359097

[46] Pouyanfar, S. and Tao, Y. and Tian, H. and Chen, S.-C. and Shyu, M.-L., (2018), Multimodal deep learning based on multiple correspondence analysis for disaster management, World Wide Web, vol. 22, pp. 1893-1911, doi:10.1007/s11280-018-0636-4

[47] Narciso, D. A. C. & Martins, F.G., (2020), Application of machine learning tools for energy efficiency in industry: A review, Energy Reports, vol. 6, pp. 1181-1199, ISSN 2352-4847, doi:10.1016/j.egyr.2020.04.035.

[48] Real, A. J. d., Dorado F. & Durán, J., (2020), Energy Demand Forecasting Using Deep Learning: Applications for the French Grid, Energies, 13, 2242; doi:10.3390/en13092242 www.mdpi.com/journal/energies

Synthesis, characterization and solution properties of polyacrylamide based ternary copolymerization modified nano silica nanocomposites for EOR

1st Dongyin Wang
College of Science, China National Petroleum Corporation
Nanochemistry Key Laboratory
China University of Petroleum-Beijing
Beijing, China
wangdongyin2019@163.com

2nd Changfeng Chen
College of Science, China National Petroleum Corporation
Nanochemistry Key Laboratory
China University of Petroleum-Beijing
Beijing, China
ccfcup@163.com

3rd Yangchuan Ke
College of Science, China National Petroleum Corporation
Nanochemistry Key Laboratory
China University of Petroleum-Beijing
Beijing, China
key@cup.edu.cn
kyccup@163.com

4th Jixiang Wang
College of Science, China National Petroleum Corporation
Nanochemistry Key Laboratory
China University of Petroleum-Beijing
Beijing, China
jixiangwang2019@163.com

Abstract

In this work, a series of polymer nanocomposites (AAS/KS) of acrylamide (AM)/ acrylic acid (AA)/ sodium p-styrenesulfonate (SSS)/ 3-Methacryloxypropyltrimethoxysilane (KH570) modified nano-silica were successfully synthesized via in situ polymerization. The ^{1}H nuclear magnetic resonance spectroscopy (^{1}H NMR) confirmed the successful synthesis of AAS/KS, the morphology of KH570 modified nano-silica (KS) and AAS/KS polymer nanocomposites were observed by scanning electron microscope (SEM). And thermal gravimetric analysis (TGA) showed that the AAS/2.0 wt% KS had better temperature tolerance than pure polymer (AAS), also the solution properties of temperature-resistance, salt-tolerance, shear resistance and viscoelasticity proved the better oil displacement performance in high temperature and high salt reservoirs. Furthermore, the oil recovery of AAS/2.0 wt% KS is 9.9% higher than that of the water flooding processes during the enhanced oil recovery experiment in laboratory. All results indicated that the AAS/2.0 wt% KS polymer nanocomposite had tremendous potential application for enhancing oil recovery.

***Keywords: Polyacrylamide based ternary polymeride, Modified nano-silica, Nanocomposites, In situ polymerization,* Enhancing oil recovery.**

IEECP'21, July 29-30, 2021, Silicon Valley, San Francisco, CA – USA

DII: https://sci-index.com/DAI/2021.99101/IEECP/14810286

I. INTRODUCTION

In recent years, with the increasing demand for energy, the exploitations of oil resources have drawn more and more attentions. In order to meet the energy needs, various methods of enhancing oil recovery (EOR) have been developed. Chemical enhanced oil recovery (CEOR) is an interesting topic, because it is beneficial to develop heavy oil, unconventional oil and remaining oil [1,2]. Among the CEOR technologies, polymer flooding is widely used at home and abroad. Because the polymer solution with high viscosity can improve the mobility ratio and enlarge the swept volume, thereby the water-soluble polymer have attracted great interest from researchers due to their huge potential properties and wide applications in oil exploitation [3-5].

Among all of the water-soluble polymer systems, the polyacrylamide (PAM) and partially hydrolyzed polyacrylamide (HPAM) are widely used in the polymer flooding technology of oil fields. Due to the water-soluble polymers have a great capability of thickening and increasing the viscosity, which causes a decrease in water/oil mobility ratio, and increasing the sweep area, so as to enhance oil recovery [6-8]. However, many new problems and limitations appears in the application of traditional polyacrylamide in most oil reservoirs of high-temperature and high-salinity conditions [9]. At high temperature, the amide group (-$CONH_2$) is easy to hydrolyze, which leads to the viscosity of polymer decrease rapidly. The hydrolysate usually form precipitates at high salinity, which sharply reduces the viscosity of the polymer [10]. In addition, the interaction of metal ions such as Na^+ and K^+ in the oilfield brines largely shields the mutual repulsion from the carboxylic groups along the HPAM skeleton, leading to the polymer coils to collapse and the hydrodynamic volume to decrease, ultimately lowering the solution viscosity [11,12]. Therefore, various of functional groups were introduced into PAM to obtain excellent performance. Such as

the sulfonic acid group, hydrophobic monomer, organic/inorganic materials, etc. has become a research hotspot [13-15].

Sodium p-styrenesulfonate (SSS) is a special polymer monomer, which shows better temperature resistance and salt resistance. So, SSS is introduced into PAM to enhance the temperature and salt resistance. The poly (vinyl acetate-dibutyl maleate-acyclic acid-sodium p-styrenesulphonate) copolymer emulsion was prepared by Gong et al. [16], which powerfully proved that SSS had great salt tolerance and good thermal resistance. The amphiphilic polymer of sodium p-styrenesulfonate and dodecyl methacrylate with temperature and salt resistance was synthesized by Peng et al. [17]. Bai et al. prepared poly (acrylamide-sodium p-styrenesulfonate-N',N'-dimethyl octadeyl allyl ammonium bromide) to enhance oil recovery in high temperature and high salinity Oilfield [18]. Therefore, the addition of SSS into the acrylamide-based copolymer matrix is beneficial to improve its heat resistance and salt resistance.

As we all know, the application of nano silica in EOR has been paid more and more attention by researchers. Because the nano silica has the very small size, large surface area, high surface energy and the abundant surface hydroxyls. Due to these outstanding properties of nano silica, it is introduced into the polymer to improve its thermal stability, temperature resistance, salt tolerance, viscoelasticity and the capacity of oil displacement, etc. [19-21]. 3-Methacryloxypropyltrimethoxysilane is a silane coupling agent with alkenyl and long alkyl chains. Therefore, the molecule of KH570 can both modify nano-SiO_2, and form water-soluble hydrophobically associating polymer during monomer polymerization. In a word, all the advantages are beneficial to improve the comprehensive properties of the polymer. Consequently, the KH570 modified nano-SiO_2 polymer nanocomposites has a great contribution to EOR.

In this work, we synthesized a novel polymer nanocomposite (AAS/KS) based on acrylamide (AM)/ acrylic acid (AA)/ sodium p-styrenesulfonate (SSS)/KH570 modified nano-silica (KS). The AAS/KS polymer nanocomposite was characterized by ^{1}H nuclear magnetic resonance spectroscopy (^{1}H-NMR), thermal gravimetric analysis (TGA), and scanning electron microscope (SEM). The thickening performance, temperature resistance, salt resistance, shear resistance and viscoelasticity of samples were studied. Also, the oil recovery of AAS/2.0 wt% KS is 9.9% higher than that of the water flooding processes during the enhanced oil recovery experiment in laboratory. All of these outstanding performances proved that AAS/KS polymer composites would be very promising to EOR.

II. EXPERIMENTAL

A. Materials

The unmodified sodium montmorillonite (Na-Mt) with a cationic exchange capacity (CEC) of 100 mmol/100 g was supplied by the Huai An Saibei Technology Co. Ltd., Zhangjiakou, China. Sodium chloride (NaCl, 98%), Calcium chloride ($CaCl_2$, 96%), sodium hydroxide (NaOH, 96%), ammonium persulfate ($(NH_4)_2S_2O_8$, 98%), sodium hydrogen sulfite ($NaHSO_3$, 98%) and absolute ethanol (CH_3CH_2OH, 99.7%) were brought from Tianjin Fuchen Fine Chemical Research Institute, Tianjin, China. Acrylamide (AM, 98%), Acrylic acid (AA, 99%), tetraethyl orthosilicate (Si (OC_2H_5)$_4$, TEOS, 99.5%), acetone (CH_3COCH_3, 99.5%), N, N-dimethylformamide (DMF, 99.5%) were provided by Tianjin Guangfu Fine Chemical Research Institute, Tianjin, China. Ammonia solution (NH_3, 28% aqueous solution) were purchased by Shanghai Aladdin Biochemical Technology Co., Ltd, Sodium p-styrenesulfonate (SSS, 98%) was obtained from Shanghai Macklin Biochemical Co., Ltd., Shanghai, China. N, N'-Methylenebisacrylamide (MBA, 99%), 3-Methacryloxypropyltrimethoxysilane (KH570, 97%) were purchased from Aladdin Biochemical Co., Ltd., Shanghai, China. All of them were analytical grade, and deionized water was used for all experiment.

B. Methods

a) Preparation of SiO_2 nanoparticles and modified by KH570

SiO_2 nanoparticles were prepared by Stöber method[22,23]. The TEOS was added to the mixed solution of ammonia, ethanol and water drop by drop. Then this mixture was reacted at room temperature for 4 hours. After the reaction, it was centrifuged in ethanol for three times and dried in a vacuum oven at 70 ℃ for 24 h.

The previously prepared SiO_2 nanoparticles were added into a three-necked flask (500 mL) which contained the mixture solution of ethanol and water. Then ultrasonic dispersion for 30 min. After, the KH570 was dropped in the flask under continuous vigorous stirring, the catalytic agent of aqueous ammonia was necessary. A molar ration of SiO_2 nanoparticles and KH570 was 18:1. Then the reaction was in nitrogen at 50 ℃ for 12 h. After the reaction, the modified SiO_2 nanoparticles were washed with anhydrous ethanol and dried in a vacuum oven at 50 ℃ for 24 h. The final product was white solid, which was called KS. The synthetic process was showed in Figure 1.

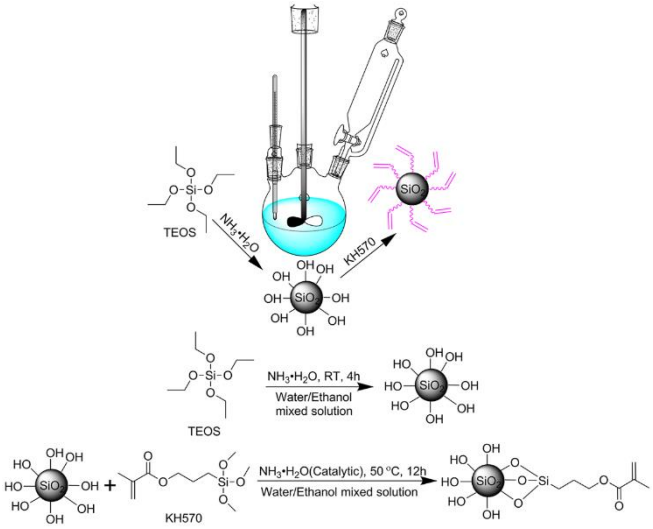

Figure 1. The synthetic process of SiO_2 nanoparticles and modified by KH570.

b) Preparation of AAS/KS nanocomposite

AAS/KS was synthesized by in situ polymerization of aqueous solution. Firstly, a mixture of (0 – 1.000 g) KH 570 modified nano-SiO_2 (KS), 12.532 g AA and 100 g deionized water were added into a 250 mL three neck-flask. Then ultrasonic dispersion for 1h at 50 ℃. After that, put into 18.798 g AM, 1.667 g SSS, 0.333 g MBA and continuously stirring for 1h. Secondly, the pH value of the above mixed solution was adjusted to 8-9 by NaOH solution. Thirdly, a certain amount of $(NH_4)_2S_2O_8$ and $NaHSO_3$ (molar ratio 1:1, 0.3 wt%) as the initiator were dropped into the reaction solution with stirring under nitrogen atmosphere, after further reacted at 50 ℃ for 12 h, the obtained samples were washed with absolute ethyl alcohol and water (volume ratio 9:1) several times to remove residual monomers and initiator. Finally, the gel sample was cut into pieces and dried under vacuous environment at 75 ℃ for 24 h. The final product was ground and sieved with a 200-mesh screen (74 μm eye size), which was called as AAS/x wt% KS (x=1.0, 2.0, 3.0). Pure polymer was prepared by the above process without the presence of

KS, which was called as AAS. The synthetic process of samples was shown in Figure 2.

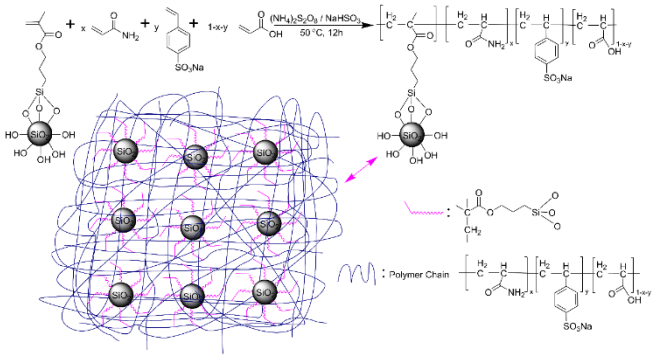

Figure 2. The synthetic process of AAS/modified nano-SiO_2 nanocomposites.

C. Measurements

a) Characterization

The ^{1}H NMR experiment was performed on a Bruker ASCEND-400 NMR spectrometer. The thermal gravimetric analysis was determined by a NETZSCH analyzer (STA409PC, Germany), under a N_2 flow rate of 140 cm^3/min, the samples were heated from 40 ℃ to 900 ℃ with the heating rate of 10 ℃/min. The size and morphologies of nanocomposite samples were obtained by scanning electron microscope (SEM, SU8010, Japan).

b) Viscosity measurement

The viscosities of nanocomposites under different concentration, temperature, salinity were measured with a Brookfield DV-II + Pro viscometer, and the rotor speed was 60 rpm. The shear resistance of samples at 0-1000 s^{-1} and the dynamic rheological behavior at 0-10 Hz were evaluated by HAAKE RS600 controlled rheometer.

c) EOR tests in laboratory

The enhanced oil recovery tests were carried out to verify the effects of the AAS/2.0 wt% KS polymer nanocomposite in enhancing oil recovery. The temperature and the back pressure were maintained at 50 ℃ and 1500 psi, respectively. The detailed experimental procedures were as follows:

(1) The core was saturated with synthetic brine (4973 mg/L) and then crude oil was injected into the core until no water went out from the outlet.

(2) Water flooding was conducted at a flow rate of 0.5 mL/min until the moisture content reached 98%.

(3) 0.2 PV polymer slug was injected into the core, followed by extending water flooding until the moisture content reached 98%.

The artificial sandstone core was employed for the experiments, and the basic parameters were listed in Table 1. Table 2 presented the composition of synthetic brine used in the experiments. The oil recovery ratio was calculated according to the literature [24,25], which was given in equation (1):

$$EOR = E_T - E_W \qquad (1)$$

where EOR was the enhanced oil recovery using polymer solution (%), E_T was the total oil recovery in total flooding process (%), and E_W was the oil recovery of water flooding (%).

Table 1. Basic parameters of artificial sandstone cores.

Core	Length (cm)	Diameter (cm)	Porosity (%)	Permeability (mD)
1#	7.76	3.82	20.64	1121

Table 2. Composition of the brine.

Composition	NaCl	KCl	$CaCl_2$	$MgCl_2{\cdot}5H_2O$	$NaSO_4$	$NaHCO_3$	Total
Concentration (mg/L)	24384	15	55	135	70	2214	4973

III. RESULTS AND DISSCUSSIONS

A. ^{1}H-NMR spectra

The ^{1}H-NMR spectra of AAS/2.0 wt% KS with D_2O as solvent was shown in Figure 3. In the ^{1}H-NMR spectra, the strong peak at 4.70 ppm represented the deuterium in D_2O. The triplet peaks at 1.17-0.95 ppm (2, 7) and double peaks at 2.12-1.90 ppm (1, 6) corresponded to the protons of -CH- and -CH_2- in AM and AA of polymer backbones, respectively. The single peak at 1.50 ppm (12) was the characteristic peak of -CH_3 in tri-polymer. The peaks at 2.30 ppm (11) was attributed to -CH_2- of KH570 in polymer backbones. All the peaks at 3.75-3.24 ppm (15,14,13) were the -CH_2- in the side chain of KH570. The small peak located at 6.81 ppm (3) was due to the proton of -NH_2 in side chain. The chemical shift at 7.61 ppm (10) and 7.25 ppm (9) were attributed to the protons of the benzene backbones, and the peaks at 6.01 ppm (4) and 5.50 ppm (5) were the characteristic peak of -CH_2-, -CH- in the side chain of benzene ring [26]. The weak peak appeared at 8.26 ppm (8) was due to the proton of -COOH of AA. Therefore, the ^{1}H-NMR spectrum further proved that the desired product was successfully prepared.

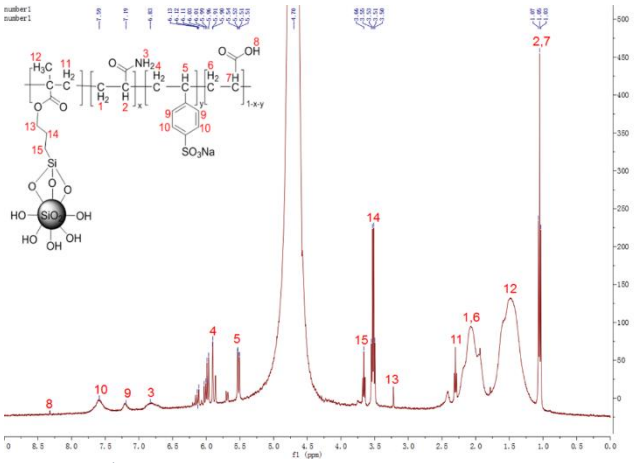

Figure 3. ^{1}H-NMR spectra of AAS/2.0 wt% modified nano-SiO_2 in D_2O.

B. SEM Analysis

The SEM pictures of prepared KS, pure polymer (AAS) and AAS/2.0 wt% KS polymer nanocomposites were shown in Figure 4. It could be seen in the Figure 4 (a) that the average grain diameter of KS is 30 nm. And it was good for spalling crude oil adhered in the micropores of underground strata. It was observed that the two samples presented the perfect network morphology, and the interconnected skeletons and cavities could be seen in the samples. Compared with the pure polymer AAS, the network of AAS/2.0 wt% KS nanocomposite was much more compact. It was obvious that the skeleton was much stronger, the cavities was less and smaller. The compact structure could be ascribed to the introduction of KH570 modified nano-SiO_2. The perfect network structure indicated that the AAS/2.0 wt% KS polymer nanocomposite was robust, and it could exhibit good comprehensive properties, such as viscosity, high temperature-tolerance, great salt-resistance, good shear-resistance and viscoelasticity. Due to these outstanding properties, the AAS/2.0 wt% KS polymer nanocomposite could enhance oil recovery.

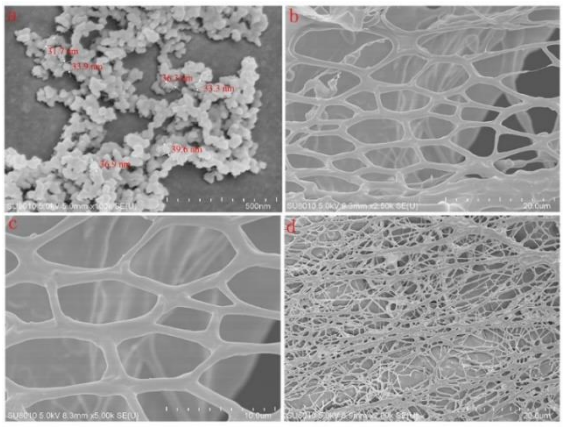

Figure 4. SEM morphologies of (a) KS, (b-c) AAS and (d) AAS/2.0 wt % KS polymer nanocomposite.

C. Thermogravimetric analyses (TGA)

The thermogravimetric analyses curves of pure AAS, AAS/1.0 wt% KS, AAS/2.0 wt% KS, AAS/3.0 wt% KS were showed in Figure 5. From this figure, it could be seen that AAS/2.0 wt% KS presented 10% and 50% weight loss at 262 ℃, 667 ℃, respectively. And, the pure AAS polymer shows 10% and 50% weight loss at 254 ℃ and 473 ℃, AAS/1.0 wt% KS had 10% and 50% weight loss at 256 ℃, 477 ℃, and the AAS/3.0 wt% KS had 10% and 50% weight loss at 299 ℃, 462 ℃. Surprisingly, the temperature of 10% weight loss of AAS/3.0 wt% KS was higher than others. It might be due to the relatively stable intermolecular forces formed by adsorption bridging among the KH570 modified nano SiO_2. However, with the temperature increasing, the intermolecular forces were destroyed. As a result, the weight loss of AAS/3.0 wt% KS decreased rapidly. When the temperature reached 900 ℃, the residual mass of AAS/2.0 wt% KS maintained 35.0%, but the residual mass of AAS/1.0 wt% KS and AAS/3.0 wt% KS were 26.5% and 34.8%, respectively. And pure AAS was only 23.3%. Therefore, under the temperature range of 40-900 ℃, all these results proved that AAS/2.0 wt% KS displayed higher residual mass and better stability. So the AAS/KS polymer nanocomposites could be used to enhance oil recovery in high temperature reservoir.

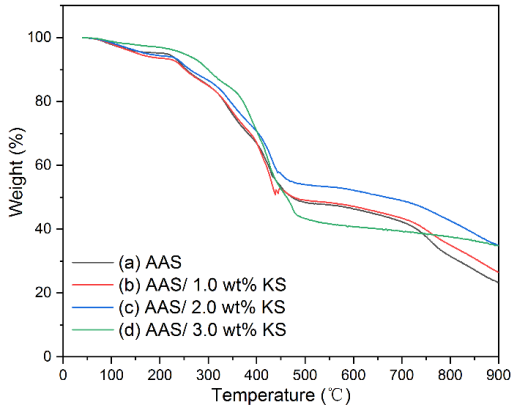

Figure 5. TGA curves of AAS, AAS/1.0 wt % KS, AAS/2.0 wt % KS and AAS/3.0 wt % KS.

Table 3 The thermogravimetric analysis data of samples

	The temperature of 10% weight loss	The temperature of 50% weight loss	The residual mass
AAS	254℃	473℃	23.3%
AAS/1.0 wt% KS	256℃	477℃	26.5%
AAS/2.0 wt% KS	262℃	667℃	35%
ASD/3.0 wt% KS	299℃	462℃	34.8%

D. Viscosification properties of nanocomposites

A certain amount of samples were dissolved into distilled water to obtain different concentrations of sample solutions. Then the apparent viscosity of each sample solution was measured at the temperature of 25 ℃. It was clearly seen from Figure 6 that the apparent viscosity raised with the increase of solution concentration. The concentration of AAS/2.0 wt% KS from 2500 to 12500 mg/L, the apparent viscosity changed from 226 to 1050 mPa.s. At equal temperature, the apparent viscosity of AAS/2.0 wt% KS was significantly higher than that of AAS. The addition of KS could enhance the apparent viscosity of the polymer nanocomposites. Nevertheless, when the addition of KS was 3.0 wt%, the apparent viscosity decreased. It may be that the hydrophobicity of the AAS/3.0 wt% KS increased, resulting in the poor water-solubility. In a word, the viscosification property of AAS/2.0 wt% KS made it have significant application to enhance oil recovery.

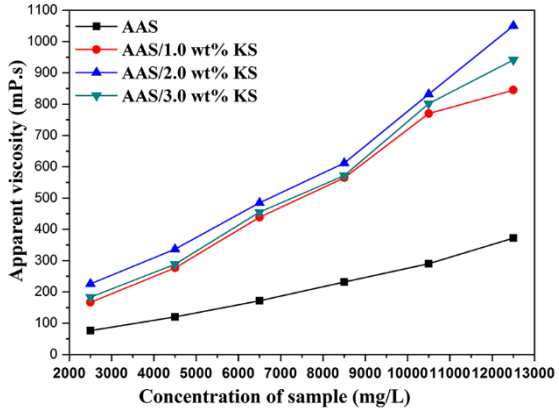

Figure 6. Relationship between apparent viscosity and the concentrations of AAS, AAS/1.0 wt% KS, AAS/2.0 wt% KS, AAS/3.0 wt% KS.

E. Temperature-resistance evaluation

As is known to all, the high temperature could destroy the main chain of polymer and the intermolecular force among polymer chains. Therefore, the molecular framework of polymer was wrecked, resulting in the decrease of apparent viscosity of polymer nanocomposites. The 2500 mg/L of sample solutions were prepared, and the temperature effect on the apparent viscosity of AAS and

AAS/KS solutions could be observed in Figure 7. The results proved that the apparent viscosity of both AAS and AAS/KS solutions decreased with the temperature went up. However, due to the addition of KS made that the polymer nanocomposites exhibited better temperature tolerance. For example, the apparent viscosity of AAS/2.0wt% KS was always higher than other samples under the same conditions. On account of the hydrophobicity of AAS/3.0wt% KS increased, led to the poor water solubility, so the apparent viscosity decreased and the temperature resistance descended. In addition, the SSS with benzene ring was able to resistant high temperature. On the one hand, the benzene ring was the special steady six-membered ring with extremely little ring strain. The decomposition of benzene ring needed enough energy. On the other hand, the steric effect of benzene ring could prevent the rotation of single bond attached to polymer backbone chain. Therefore, the polymer backbone chain was not easy to broken. The AAS/2.0 wt% KS was applied to enhance oil recovery in the oil field, due to its better performance of high temperature resistance.

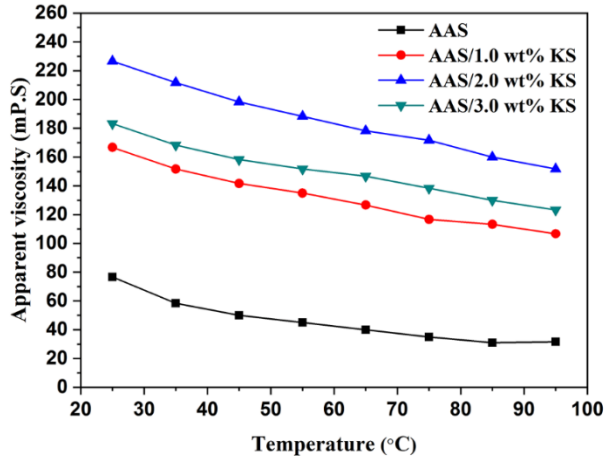

Figure 7. Relationship between apparent viscosity and the temperature-resistance of AAS, AAS/1.0 wt% KS, AAS/2.0 wt% KS and AAS/3.0 wt% KS.

F. Salt-tolerance evaluation

The salt-resistance of polymer nanocomposites was a significant index in polymer flooding to enhance oil recovery. The concentration of sample solutions is 2500 mg/L, the test temperature is 25 ℃, and the results were shown in Figure 8. The apparent viscosity of AAS and AAS/KS solution declined rapidly as the concentration of NaCl or $CaCl_2$ solution increased from 0 to 6000 mg/L. Because the electrolyte ions (Na^+, Ca^{2+}) shielded the effective charge, and then the electric double layer of polymers were compressed by salt ions, resulting in a reduction of hydrodynamic volume. Due to the addition of KS were able to prevent this effect. So the apparent viscosity of AAS/KS was higher than AAS, resulting in better ability in the improvement of oil recovery.

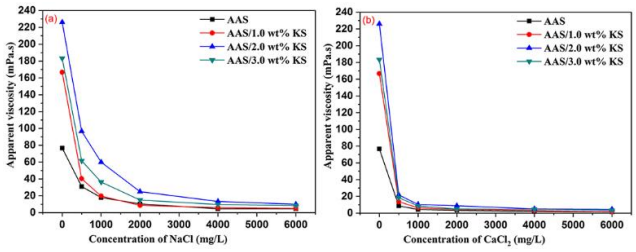

Figure 8. The effect of (a) NaCl solution and (b) $CaCl_2$ solution on apparent viscosity for AAS, AAS/1.0 wt% KS, AAS/2.0wt% KS and AAS/3.0wt% KS.

G. shear resistance evaluation

The shear resistance was a significant performance of polymer nanocomposite in petroleum engineering. In the process of injection and displacement, the shear force from the pump, pipeline, wellbore, bullet hole and porous media greatly reduced the viscosity of polymer solution, and affected the oil recovery [27]. Figure 9 showed the apparent viscosity of AAS, AAS/1.0 wt% KS, AAS/2.0 wt% KS and AAS/3.0 wt% KS under different shear rate. With the increasing of shear rate, the viscosity of AAS/KS decreased, because polymer chains broke down and network structure destroyed. However, the addition of KS, the polymer skeleton became stronger. In the shear rate range of 0-1000 s^{-1}, the apparent viscosity of AAS/2.0 wt% KS was always higher than others. As a result, the optimal addiation of KS in polymer nanocomposites is 2.0 wt%. In short, the AAS/2.0 wt% KS polymer nanocomposite was beneficial to enhance oil recovery.

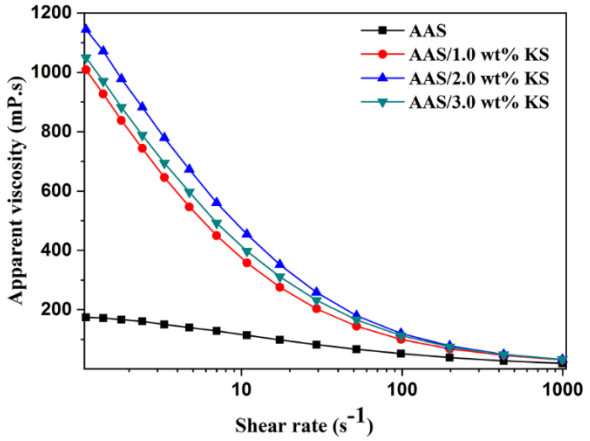

Figure 9. Effect of shear rate on apparent viscosity for prepared sample solutions (solution concentration is 2500 mg/L; T=25 ℃).

H. Viscoelasticity of AAS/KS nanocomposites

Viscoelastic polymer solution could improve the oil-displacement efficiency, thus greatly enhancing the crude oil recovery. Therefore, the dynamic rheology was studied, and the change of storage modulus (G') and loss modulus (G'') with frequency were shown in Figure 10. The G' and G'' of AAS, AAS/1.0 wt% KS and AAS/2.0 wt% KS exhibited an upward tendency along with the increase of frequency. Interestingly, the G' and G'' of AAS/2.0 wt% KS was always higher than those of AAS and AAS/1.0 wt% KS, which indicated that AAS/2.0 wt% KS had better viscoelasticity. The stronger the viscoelasticity, the larger the first normal stress and the dragging force on oil film, and the higher the enhanced oil recovery. While the frequency was less than the characteristic frequency (point of intersection), G'' was higher than G', and the viscidity of nanocomposites was predominant. And when the frequency exceeded the characteristic frequency, G' was greater than G'', and the elasticity play a dominating role. The phenomenon could attribute to the KS interacted with the polymer chains, resulting in the network structure of AAS/KS was reinforced and the elasticity of the polymer composite got more significant. As a result, the AAS/KS could be better applied in EOR.

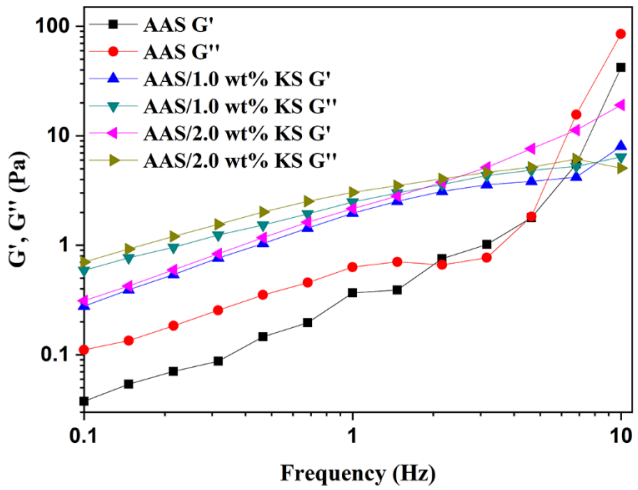

Figure 10. Elastic (G') and viscous (G'') modulus as a function of frequency for AAS, AAS/1.0 wt% KS and AAS/2.0 wt% KS.

I. EOR experiments in laboratory

The EOR capability of AAS/2.0 wt% KS was studied in sandstone cores, and the results were showed in Figure 11 and Table 4. When the moisture content reached 98% in the first water flooding, the oil recovery was E_W (43.8%). As the following water flooding, 0.2 PV polymer flooding and subsequent water flooding could increase the oil recovery to a stable value (E_T= 53.7%). In comparison with the water flooding, the oil recovery increased by 9.9%. The main reason for obtaining higher oil recovery was due to its better temperature-resistance, salt-tolerance, shear resistance and viscoelasticity and so on. All the outstanding properties were attributed to the introduction of KS. All these results showed that AAS/KS nanocomposites had a great potential to enhance oil recovery.

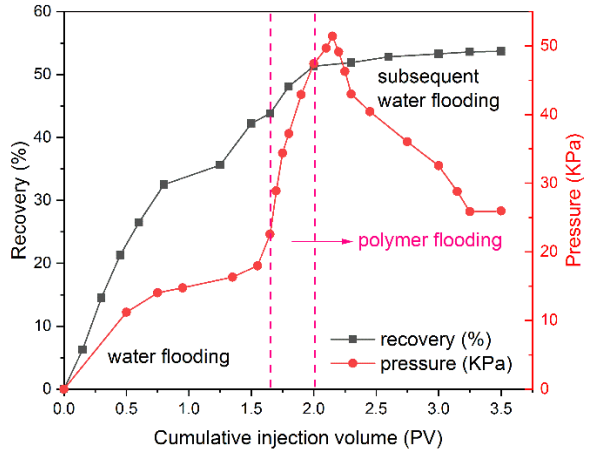

Figure 11. EOR experiments of AAS/2.0 wt% KS in laboratory.

Table 4 EOR of AAS/2.0 wt% KS

Sample	Concentration (mg/L)	E_W (%)	E_T (%)	EOR (%)
AAS/2.0 wt% KS	1000	43.8	53.7	9.9

IV. CONCLUSIONS

A novel of AAS/KS polymer nanocomposites were successfully synthesized by in situ polymerization of AM, AA, SSS, and KH570 modified nano-SiO_2. ^{1}H-NMR analysis determined the successful synthesis of AAS/KS polymer nanocomposites. The results of solution performance tests indicated that the introduction of KS improved the properties of AAS/KS polymer nanocomposites. Compared with pure AAS, the AAS/KS nanocomposites exhibited superior performance on aspects of thermal stability, temperature resistance, salt tolerance, shear resistance and viscoelasticity. Furthermore, the 9.9% oil recovery was increased during the EOR tests in laboratory. These results suggested that AAS/KS nanocomposite had great potential application for EOR in high temperature and high salinity oilfield.

V. ACKNOWLEDGMENTS

This work was financially supported by the National Natural Science Foundation of China (No.51974339; 51674270), National Major Project (No.2017ZX05009-003), and the Research Institute of Petroleum Exploration Development of China National Petroleum Cooperation (HX20201095), CUPB Teaching & Education Projects (XM10720180626: PX-11212308)

VI. REFERENCES

[1] Thomas S, "Enhanced Oil Recovery - An Overview," Oil Gas Sci Technol, vol. 63, pp. 9-19, 2007.
[2] Raffa P, Broekhuis AA, Picchioni F, "Polymeric surfactants for enhanced oil recovery: A review," J Pet Sci Eng, vol. 145, pp. 723-733, 2016.
[3] Sepehri S, Rafizadeh M, Hemmati M, Bouhendi H, "Preparation of acryl amide/2-acryl amido-2-methyl propane sulfonic acid/silane modified montmorillonite water-soluble nanocomposites: study of thermal and rheological properties," J Polym Res, vol. 22, pp. 81, 2015.
[4] Helvacıoğlu E, Aydın V, Nugay T, Nugay N, Uluocak BG, Şen S, "High strength poly(acrylamide)-clay hydrogels," J Polym Res, vol. 18, pp. 2341-2350, 2011.
[5] Yu Y, Zhu C, Liu Y, Zhang E, Kong Y, "Synthesis and Characterization ofN-maleyl Chitosan-Cross-Linked Poly(acrylamide)/Montmorillonite Nanocomposite Hydrogels," Polym Plast Technol, vol. 50, pp. 525-529, 2011.
[6] Abidin AZ, Puspasari T, Nugroho WA, "Polymers for Enhanced Oil Recovery Technology," Procedia Chem, vol. 4, pp. 11-16, 2012.
[7] Zhao T, Xing J, Dong Z, Tang Y, Pu W, "Synthesis of Polyacrylamide with Superb Salt-Thickening Performance," Ind Eng Chem Res, vol. 54, pp. 10568-10574, 2015.
[8] Choi J, Ka D, Chung T, Jung J, Koo G, Uhm T, Jung SH, Park S, Jung H-T, "Evaluation of highly stable ultrahigh-molecular-weight partially hydrolyzed polyacrylamide for enhanced oil recovery," Macromol Res, vol. 23, pp. 518-524, 2015.
[9] R.S. Seright ARC, P.S. Mozley, Peihui Han, "Stability of Partially Hydrolyzed Polyacrylamides at Elevated Temperatures in the Absence of Divalent Cations," SPE Journal, vol. 15, pp. 341-348, 2010.
[10] Zhu D, Wei L, Wang B, Feng Y, "Aqueous Hybrids of Silica Nanoparticles and Hydrophobically Associating Hydrolyzed Polyacrylamide Used for EOR in High-Temperature and High-Salinity Reservoirs," Energies, vol. 7, pp. 3858-3871, 2014.
[11] Alain Zaitoun BP, "Limiting Conditions for the Use of Hydrolyzed Polyacrylamides in Brines Containing Divalent " SPE Journal, vol. 11785, pp. 143-148, 1983.
[12] François J, Truong ND, Medjahdi G, Mestdagh MM, "Aqueous solutions of acrylamide-acrylic acid copolymers: Stability in the presence of alkalinoearth cations," Polymer, vol. 38, pp. 6115-6127, 1997.
[13] Khakpour H, Abdollahi M, "Rheological properties of acrylamide/butyl acrylate/2-acrylamido-2-methyl-1-propane sulfonic acid co- and terpolymers synthesized by heterogeneous and micellar methods," Polym Bull, vol. 74, pp. 5145-5161, 2017.
[14] Zhong C, Zhang H, Feng L, "Solution behavior and associating structures of a salt-tolerant tetra-polymer containing an allyl-capped macromonomer," J Polym Res, vol. 21, pp. 604, 2014.
[15] Maurya NK, Kushwaha P, Mandal A, "Studies on interfacial and rheological properties of water soluble polymer grafted nanoparticle for application in enhanced oil recovery," J Taiwan Inst of Chem E, vol. 70, pp. 319-330, 2017.
[16] Gong W, Li M, Zang Y, Xie H, Liu B, Chen H, "The synthesis of salt-resistant emulsion and its application in ecological sand-fixing of high salt-affected sandy land," Plast, Rubber Compos, vol. 46, pp. 163-172, 2017.

[17] Peng F, Ke Y, Lu S, Zhao Y, Hu X, Deng Q, "Anion amphiphilic random copolymers and their performance as stabilizers for O/W nanoemulsions," RSC Adv, vol. 9, pp. 14692-14700, 2019.
[18] Bai C, Ke Y, Hu X, Xing L, Zhao Y, Lu S, Lin Y, "Preparation and properties of amphiphilic hydrophobically associative polymer/ montmorillonite nanocomposites," R Soc Open Sci, vol. 7, pp. 200199, 2020.
[19] Ji J, Zeng C, Ke Y, Pei Y, "Preparation of poly(acrylamide-co -acrylic acid)/silica nanocomposite microspheres and their performance as a plugging material for deep profile control," J Appl Polym Sci, vol. 134, pp. 45502, 2017.
[20] Lai N, Wu T, Ye Z, Zhou N, Xu Q, Zeng F, "Preparation and properties of hyperbranched polymer containing functionalized Nano-SiO2 for low-moderate permeability reservoirs," Russ J Appl Chem, vol. 89, pp. 1681-1693, 2017.
[21] Yang Y, Li J, "Lipid, protein and poly(NIPAM) coated mesoporous silica nanoparticles for biomedical applications," Adv Colloid Interface Sci, vol. 207, pp. 155-163, 2014.
[22] Werner StÖeber AF, Ernst Bohn, "Controlled growth of monodisperse silica spheres in the micron size range," J Colloid Interface Sci, vol. 26, pp. 62-69, 1968.
[23] Tianbin W, Yangchuan K, "Preparation of silica–PS composite particles and their application in PET," Eur Polym J, vol. 42, pp. 274-285, 2006.
[24] Zhong C, Wang W, Yang M, "Synthesis and solution properties of an associative polymer with excellent salt-thickening," J Appl Polym Sci, vol. 125, pp. 4049-4059, 2012.
[25] M. Izadi SEV, J. F. Zapata Arango, C. Chaparro, J. A. Jimenez, E. Manrique, J. Mantilla, D. E. Dueñas, and O. Huertas, Ecopetrol S.A., "Assessing Productivity Impairment of Surfactant-Polymer EOR Using Laboratory and Field Data," Soc Pet Eng, vol. SPE-190316-MS, pp. 190316, 2018.
[26] Khakpour H, Abdollahi M, "Synthesis, characterization, rheological properties and hydrophobic nano-association of acrylamide/styrene and acrylamide/sodium styrene sulfonate/styrene co- and terpolymers," J Polym Res, vol. 23, pp. 168, 2016.
[27] Vryzas Z, Kelessidis VC, "Nano-Based Drilling Fluids: A Review," Energies, vol. 10, pp. 540, 2017.

Smart grid for power generation from renewable energy resources for sustainable energy development in Kanungu district, Uganda

Jane Rose Atwongyeire
Sustainable Energy Management Program, Faculty of Environmental Management, Prince of songkla Universit, Hat Yai, Songkhla, Thailand
roseatwongyeire@gmail.com

Arkom Palamanit
Energy Technology Program, Department of Specialized Engineering, Faculty of Engineering
Prince of Songkla University
Hat Yai, Songkhla, Thailand
arkom.p@psu.ac.th

Adul Bennui
Southern Regional Center of Geo-Informatics and Space Technology, Faculty of Environmental Management
Prince of Songkla University
Hat Yai, Songkhla, Thailand
adul.b@psu.ac.th

Wathanaporn Kraiwan
Hatyai Technical College, Institute of Vocational Education: Southern region 3, Hat Yai, Songkhla, Thailand
wathanapon.k@gmail.com

Abstract

Development of sustainable energy systems involves many energy aspects such as energy technologies and management, energy security, reliability, and sustainability, as well as energy policy and planning. In that regard, smart energy concepts for sustainable energy development are increasingly being recognized and these include smart grids, Internet of Energy (IoT), blockchain-energy among others. These aim to enable a smooth transition from fossil-based energy to clean alternate energy resources. And also, to play an important role in the power generation and distribution from renewable energy resources (RERs) for universal modern energy access. Thus, this study aimed to demonstrate the inclusion of a smart connective concept (smart grid) in power generation and distribution from solar and small hydropower resources in Kanungu district, Uganda. A GIS-based multi-criteria decision-making method was used in the site selection process based on environmental, economic, and technical factors. And, a final resultant map of smart grid suitable sites for distributed power generation from solar and small hydropower RERs was finally generated using GIS.

Keywords: Multi-criteria decision-making; Power generation; Renewable energy; Smart grid

I. INTRODUCTION

Global energy systems are facing many challenges due to the slow-paced transition from fossil-based energy systems to clean energy systems. Yet, the environmental and health impacts of fossil fuel over dependency remain a serious global concern. With the prevailing concerns, to increase the applications of renewable energy resources (RERs) in the power generation sector is one of the solutions. However, power generation and distribution from RERs has its associated limitations such as low energy density of the source, low energy reliability and security by nature, high implementation costs, etc. To overcome these aspects, modern energy technologies combined with smart energy concepts and energy storage need to be applied and emphasized. In the recent years, several energy concepts have emerged towards sustainable energy systems including smart grids, Internet of energy, blockchain-energy, among others. It is, therefore, important for developing countries like Uganda rich with abundant renewable energy resources to consider such smart energy concepts. Uganda for example, has high potential of RERs for power generation, but the electricity access in the country is still low. Thus, one of the solutions to meet the power demand and sustainably exploit the available resource potentials is power generation from RERs combined with the smart energy concept such as a smart grid. Besides, this implementation not only helps to enhance electricity access, but it is also beneficial for energy planning and policy formulation, leading to sustainable energy development and proper management of the resources [2,3].

Smart grid for example is a connective network that is flexible, reliable, and efficient with the ability to monitor, manage and control the power chain from power generation to distribution. However, development and implementation of such systems differ depending on each country's needs and require strategic planning [2]. Most developing countries including Uganda, have not paid much attention to these smart energy systems because of several factors such as poor electricity access, unreliable infrastructure, etc. Nonetheless, planning and implementation of sustainable energy systems that can both combat issues of electricity access as well as provide sustainable smart solutions in the energy sector is key. Moreover, in the study for energy sufficiency, sustainability, and universal access in the sub-Saharan Africa by Gladkykh et al., (2021), it was reported that renewable energy-based power generation is ideal for sustainable solutions [5]. Therefore, this paper presents a site selection study for power generation from solar and small hydropower energy resources on the basis of a smart connective concept (smart grid). Areas suitable for the application of the smart connective concept in a multi-energy power generation

IEECP'21, July 29-30, 2021, Silicon Valley, San Francisco, CA – USA

DAI: *https://sci-index.com/DAI/2021.99101/IEECP/14905227*

system were selected using a GIS-based multi-criteria decision-making method. This method is known for site selection and energy planning processes especially a combination of GIS and multi-criteria decision-making method such as fuzzy Analytic Hierarchy Process (AHP) [1,8].

II. METHODOLOGY

The study was done based on qualitative and quantitative data. Survey questionnaires were used to obtain qualitative data while quantitative data was obtained both from online portals and governmental institutions. The data collected and used was based on economic, environmental, and technical factors. These factors included respective sub-factors; (a) Under the economic factor, the sub-factors included distance from transmission lines, topography (elevation and slope), and distance to roads; (b) the sub-factors under the environmental factor included land use, sensitive and protected areas; (c) and under the technical factor, the sub-factors included distance from demand centers, available potential energy resources (solar and small hydropower) and climate (rainfall and sunshine). This is because energy planning such as site selection involves a wide spectrum of decision makers, a survey questionnaire designed according to the mentioned factors and literature was distributed to the experts in different energy fields. This was to obtain opinions from the experts in order to make an informed decision. According to the designed questionnaire, experts were required to rate the significancy of each factor according to AHP Saaty's scale of significance (1 to 9). The scores assigned to each factor by the experts were then transformed into equivalent triangular fuzzy numbers (Table 1).

Table 1. Scale of significance [1]

Significance Intensity	Description	Equivalent Triangular Numbers
1	Equal importance	(1.0, 1.0, 1.0)
3	Moderate importance	(2.0, 3.0, 4.0)
5	Strongly higher importance	(4.0, 5.0, 6.0)
7	Very strong higher importance	(6.0, 7.0, 8.0)
9	Extremely high importance	(9.0, 9.0, 9.0)
2	Intermediary importance	(1.0, 2.0, 3.0)
4		(3.0, 4.0, 5.0)
6		(5.0, 6.0, 7.0)
8		(7.0, 8.0, 9.0)

Using fuzzy Analytic Hierarchy Process (AHP), a multi-criteria decision making-method known for solving complex problems, weight values of the factors were calculated following a similar methodology as [1,8]. The calculated weights were firstly used in a GIS-environment to obtain suitable areas potential for solar power generation using the Global Horizontal Irradiance (GHI) data in ArcGIS 10.5. On the other hand, available data for small hydropower potential sites was obtained from Ministry of Energy and Mineral Development (MEMD), Uganda. Potential sites for solar power generation obtained and small hydropower data were then combined in ArcGIS 10.5 to demonstrate a connective power generation system based on a smart grid concept. The study demonstrates possible power generation from multi-energy sources in a smart connective system for distributed energy resources as illustrated in Figure 1. The illustration demonstrates a possible solar and small hydropower multi-energy power generation system interconnected to transmission, distribution, and consumption. The conceptual design shows interflow of information in the power chain that can be defined as an end-to-end relationship of power supply information. The conceptual design consists of:

A. Power generation control areas (PG-CA)

These are power generation control centers (1, 2, 3, …, n) for monitoring power generation from multi-energy power generation sources within approximate area of the power plants. The conceptualized PG-CAs are in charge of forecasted power generation depending on the season. For example, in the rainy season, more power can be generated from small hydropower plants due to limited solar energy while in hot/dry season, more power can be generated from solar plants to have a balanced sustainable power generation as one of the solutions to sustainable energy management and resource exploitation.

B. Main power generation control area (PG-CA-M)

This is a general power generation control center for controlling, regulating, and monitoring power generation based on the information received from the control centers (PG-CA) as well as the demand and supply situation.

C. Control center

The control center is the overall information flow and interaction center to monitor, regulate, and manage the whole power chain including information of power generation, transmission, distribution, and consumption as well as monitoring the behaviors of both the consumer and prosumer in the power supply chain.

D. Transmission, distribution, and consumption

This section of the conceptual design includes information interaction of transmission, distribution, and end-users (consumers and prosumers).

This conceptual design represents an interactive system of information, communication, and technology in a power chain for sustainable energy management and proper resource exploitation. The system can be manipulatively designed according to the needs of each country and set goals. In this study, the focus is on sustainable exploitation of the available resources to enhance electricity access and sustainable energy management for sustainable development in the study area.

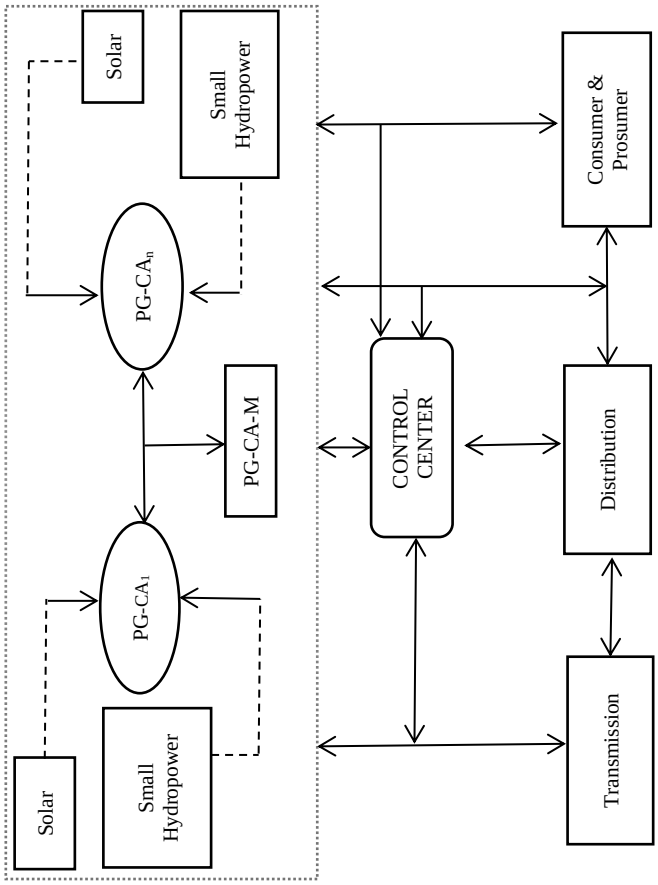

PG-CA Power Generation-Control Area (1,2,3, …n)
PG-CA-M Power Generation-Control Area (Main)

Figure 1. Illustration of a smart connective power system

III. RESULTS AND DISCUSSION: PLANNING A SMART CONNECTIVE POWER SYSTEM

Maier, 2016 reported that in planning an energy system for smart solutions, it is important to integrate energy designs with spatial planning which includes considering factors like system designs, infrastructural and building designs, and evaluation of environmental impacts. And this requires the application of advanced approaches [6]. Several studies have been carried out in the recent years aiming at sustainable energy systems. For example, Stoeglehner, 2011 carried out a study for integrated spatial and energy planning for sustainable energy systems. The author highlighted that some of the important issues to be addressed in planning a renewable energy system on a community scale level is the justification of allocation patterns of energy resources [10]. Gladkykh et al., 2021 carried out a study aiming at the exploration of energy efficiency, sustainability and universal access in sub-Saharan Africa for a social sustainable energy system [5]. Seferlis, 2021 carried out a study for a well sustainably designed and operation energy system to improve power generation and distribution for reduced consumption and emission production [9]. Noorollahi, 2021, carried out a study for renewable energy-based sustainable energy system in Iran contributing to the transition from fossil fuel power generation to renewable energy power generation [7]. Fonseca, 2021 carried out a multi-objective sustainability analysis in designing a distributed energy system focusing on economic, environmental and social aspects [4].

In this study, aiming at sustainable exploitation of energy resources and electricity access, a strategic spatial planning of a smart connective power generation was carried out by selecting suitable sites for a multi-energy resource power generation from solar and small hydropower in Kanungu district, Uganda. As earlier mentioned, suitable sites for power generation from solar were first identified based on the selected factors. Combined with the available data of small hydropower potential sites, suitable areas for a smart connective power generation from both renewable energy resources were obtained. The selection of suitable areas based on a smart connective concept for a smart connective power generation from solar and small hydropower, factors including distance to roads, distance from transmission lines, distance to demand centers and availability of the energy resources were put into consideration. The area consists of four small hydropower feasible sites for power generation which include 0.5 MW Kishamba hydro site, 0.68 MW Birara hydro site, 2.9 MW Mitano hydro site and a 6.7 MW Nengo bridge hydro site according to the data that was obtained from Ministry of Energy and Mineral Development, Uganda. And based on the assumption that 1.4 ha is equal to 1 MW of solar potential, the study area consists of 1,618.95 MW of low suitability, 21,428.08 MW of moderate suitability and 1,350.69 MW of high suitability. As per Figure 2, the resultant map shows suitable areas for smart connective power generation from solar and small hydropower energy resources in Kanungu district, Uganda.

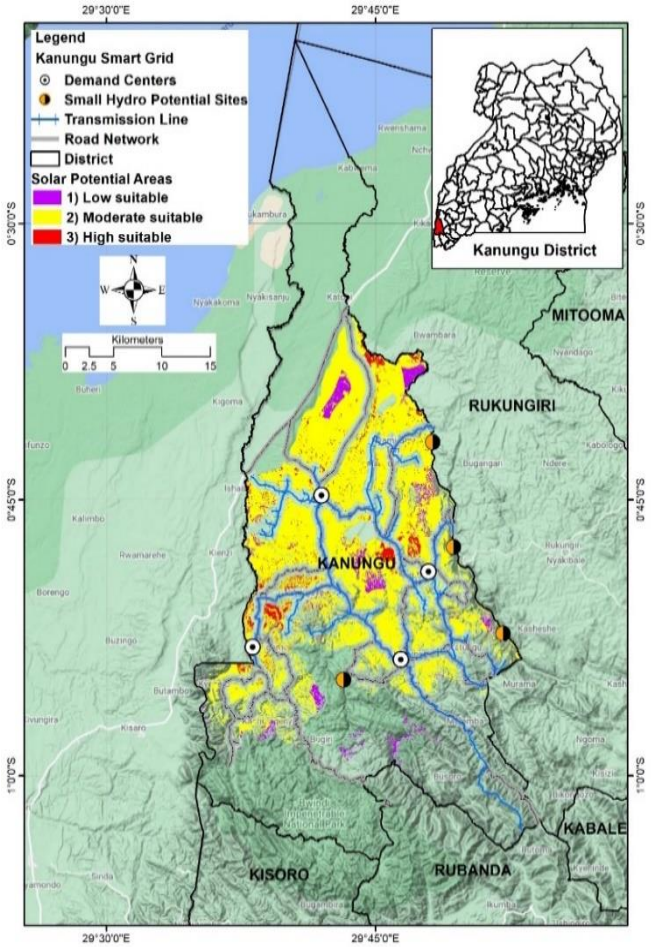

Figure 2. Suitable areas for a multi-energy smart connective power generation system.

IV. CONCLUSION

As the world is moving from fossil-based power generation to clean energy power generation, an emphasis should continue to be put on sustainable, smart, connective, and interactive energy systems. Developing countries like Uganda should consider investing in sustainable smart systems by understanding the need for these smart connective systems. The governments should put in place supportive tools including flexible regulatory frameworks for energy system developments and investments in pilot studies should also be considered for successful implementation of these systems such as smart grids. Most importantly, the countries should make an effort to improve the energy infrastructural systems in order to accommodate the present and future dynamics in the energy sector.

For example, in the case of Kanungu district, Uganda, the study results can be a basis of energy planning, implementation and development in the area for an improved smart connective power generation system.

V. ACKNOWLEDGMENTS

Many thanks to experts, government institutions and researchers for their participation towards the success of this study. And a special appreciation to Thailand International Cooperation Agency (TICA) for the support given to Ms. Atwongyeire Jane Rose during her study in Master of Science in Sustainable Energy Management Program at Faculty of Environmental Management, Prince of Songkla University.

VI. REFERENCES

[1] Abbas Asakereh, Mohsen Soleymani, and Mohammad Javad Sheikhdavoodi. 2017. A GIS-based Fuzzy-AHP method for the evaluation of solar farms locations: Case study in Khuzestan province, Iran. *Sol. Energy* 155, (2017), 342–353. DOI:https://doi.org/10.1016/j.solener.2017.05.075

[2] Paul Basudde. 2020. *Promoting the Transfer and Development of Climate-Smart Energy Technologies in Uganda*. Elsevier. DOI:https://doi.org/10.1016/b978-0-12-409548-9.12401-7

[3] Zenville Erasmus and Antoine Bagula. 2017. Smart renewable energy systems: A great opportunity for developing countries. *2017 IST-Africa Week Conf. IST-Africa 2017* (2017), 1–16. DOI:https://doi.org/10.23919/ISTAFRICA.2017.8102382

[4] Juan D. Fonseca, Jean Marc Commenge, Mauricio Camargo, Laurent Falk, and Iván D. Gil. 2021. Sustainability analysis for the design of distributed energy systems: A multi-objective optimization approach. *Appl. Energy* 290, March (2021). DOI:https://doi.org/10.1016/j.apenergy.2021.116746

[5] Arnaud Gladkykh, Ganna, Diemer. 2021. When justice narratives meet energy system models : Exploring energy sufficiency , sustainability , and universal access in Sub-Saharan Africa. August 2020 (2021). DOI:https://doi.org/10.1016/j.erss.2021.102075

[6] Stephan Maier. 2016. Smart energy systems for smart city districts: case study Reininghaus District. *Energy. Sustain. Soc.* 6, 1 (2016). DOI:https://doi.org/10.1186/s13705-016-0085-9

[7] Younes Noorollahi, Meysam Pourarshad, and Alireza Veisi. 2021. The synergy of renewable energies for sustainable energy systems development in oil-rich nations; case of Iran. *Renew. Energy* 173, (2021), 561–568. DOI:https://doi.org/10.1016/j.renene.2021.04.016

[8] Penjani Hopkins Nyimbili and Turan Erden. 2020. GIS-based fuzzy multi-criteria approach for optimal site selection of fire stations in Istanbul, Turkey. *Socioecon. Plann. Sci.* 71, May (2020), 100860. DOI:https://doi.org/10.1016/j.seps.2020.100860

[9] Panos Seferlis, Petar Sabev Varbanov, Athanasios I. Papadopoulos, Hon Huin Chin, and Jiří Jaromír Klemeš. 2021. Sustainable design, integration, and operation for energy high-performance process systems. *Energy 224*, 120158. DOI:https://doi.org/10.1016/j.energy.2021.120158

[10] Gernot Stoeglehner, Nora Niemetz, and Karl Heinz Kettl. 2011. Spatial dimensions of sustainable energy systems: New visions for integrated spatial and energy planning. *Energy. Sustain. Soc.* 1, 1 (2011), 1–9. DOI:https://doi.org/10.1186/2192-0567-1-2

Energy and Typological Building Characterization of the Social Housing Stock in Southern Spain.

C.M. Calama-González

Á.L. León-Rodríguez
Instituto Universitario de Arquitectura y Ciencias
de la Construcción
Universidad de Sevilla
Sevilla, Spain
calama@us.es; leonr@us.es; rsuarez@us.es

R. Suárez

Abstract

Retrofitting buildings is key for meeting 2030 and 2050 energy efficiency targets, especially for existing residential buildings, which are expected to become a large proportion of the future stock. Prior to promoting energy saving measures, an extensive analysis of the current performance of the stock should be tackled. Thus, building characterization though a statistical approach is a necessary step in order to assess this stock under real variability conditions, instead of considering average fixed values, which has commonly been the approach taken so far. This research statistically analyses the most predominant variability ranges of the residential building stock of southern Spain (Andalusian region), focusing on the H-block, for its building characterization. Results are collected from an extensive database containing information on almost 39,500 dwellings. Conclusions reported may be later implemented into bottom-up building stock modelling approaches for creating real case archetypes to analyze the performance of the stock and provide useful information for policy makers.

Keywords: social housing stock; Mediterranean climate; large database; building characterization; statistical analysis.

I. INTRODUCTION

In the European Union (EU), final energy consumption has been exponentially increasing since the 90s, amounted to almost 940 Mtoe in 2019 [1]. According to the 2020 Global Status Report for Buildings and Construction [2], buildings (35%), industry (32%) and transport (28%) were the three dominant energy consumers in 2019 in EU, among which residential buildings represented 22% of the final energy consumed. The mentioned report also highlighted that the building sector was responsible for 38% of the total global energy-related anthropogenic carbon dioxide emissions, 17% of which were caused by residential buildings.

Cooling energy consumption is expected to noticeably increase in southern Europe due to climate change [3]. A recent study from NASA confirms that nineteen of the warmest years have occurred since 2000, with 1998 as the only exception, and establishes a temperature increase of 1.18 ºC in 2020, compared to 1880 [4]. Thus, global warming may result in a 5 to 10 increased probability in the occurrence of more frequent and severe heatwaves [5], leading to indoor overheating issues in buildings. This is particularly important in the Mediterranean region of southern Europe [6], affecting user's health and the quality of indoor environments.

In this context, energy efficiency has been promoted by regulations and international standards as a key objective for mitigating the effects of climate change in buildings, focusing on a rational use of energy and, subsequently, promoting building decarbonisation [7].

A major challenge of southern Europe in terms of sustainable development is that the aging residential building stock was mainly built prior to the implementation of energy performance regulations [8]. Along with a significantly low building renovation rate [9], current residential buildings are expected to become a large extension of the future stock [10]. For all these reasons, energy retrofitting the residential stock becomes a clear objective for meeting the 2030 and 2050 energy targets.

Assessing the current thermal and energy performance of the building stock is a necessary step prior to any retrofit measure [11]. Besides, in the building retrofit process towards climate change, not only geographical and weather data are relevant, but also building typologies [12] and constructive characteristics [13]. Generally, energy performance of buildings has been assessed at two different scales: macro, which considers the building stock, and micro, which individually assesses buildings. Since applying micro techniques to assess the whole building stock is highly time consuming, building stock modelling has been commonly used to assess large-scale building performance. Since this requires the extensive collection of data (constructive, geometrical, physical and operational variables), a viable stock solution is the development of a bottom-up approach through the definition of building archetypes, grouping buildings with similar parameters [14]. Even though building archetypes are generally used in energy modelling at the urban scale [15], they are developed from national survey databases which provide an overview of the whole national building stock. Thus, they may become invalid at the regional and urban levels [16], since several assumptions have to be made.

IEECP'21, July 29-30, 2021, Silicon Valley, San Francisco, CA – USA

***DAI* : https://sci-index.com/DAI/2021.99101/IEECP/14810292**

Although building stock characterization has been extensively addressed in the literature [17], the case of Spain still requires more extensive research. Monzón-Chavarrías et al. [18] consider a linear block as real case study to analyse multi-family dwellings built in Spain from 1961 to 1980, both prior and after renovation strategies. Nonetheless, to do so these authors consider fixed geometrical, physical and construction characteristics, based on typical solutions of residential buildings. Given that the methodology used is case specific, there is a significant lack of scalability for analysing the stock level. Escandón et al. [19] predict thermal comfort of the housing stock built from 1940 to 1980, through building energy models. In contrast to the previous research, these authors consider a variability range of the main building simulation parameters, generating several building cases representative of the stock. Nonetheless, the analysis is only focused on the linear block typology. Blázquez et al. [20] applied a GIS framework to analyse the residential stock built from 1951 to 1980, at the urban level. Nevertheless, the performance of buildings is individually assessed through an external Energy Certification tool, later transferring the results into the GIS platform, so no building modelling is conducted.

Providing statistical data on the building stock at the regional and urban levels is the basis for developing accurate bottom-up building models for estimating energy performance through building stock modelling. Differently from other works, this research provides a thorough building characterization of the residential building typologies of southern Spain (Andalusia region), analysing a database with exhaustive data (year of construction, building height, number of storeys, average floor area, percentage of glazing surface, etc.) collected of an extensive example of around 39,500 dwellings. Given the typological research gap identified in the literature, efforts are put into analysing one of the most predominant social housing building typologies of southern Spain, the H-block (Figure 1). The objective of this paper is to statistically identify the most representative ranges of building parameters, so future research on this sector may be properly addressed by implementing this information into building performance analysis for building stock modelling, instead of assuming fixed average values. These results would allow generating bottom-up building stock models which will provide useful information to city planners, energy policymakers and key actors in the improvement of sustainable decision-making.

Figure 1. H-typology residential buildings in southern Spain

II. METHODOLOGY

For assessing and characterizing the public social housing stock of southern Spain, the tasks included in Figure 2 were carried out. In task 1, general, typological and morphological data on the social housing stock contained in the public database provided by the Andalusian Agency of House and Retrofitting (AVRA, in Spanish) [21] is compiled and rearranged. The mentioned database includes information on several variables regarding the social housing stock of Andalusia (southern Spain). Specifically, data on cadastral reference, address information, number of dwellings, number of building floors, building height, building typology (single family, multi-family and other), year of construction; year and type of retrofit plan; percentage of glazing surface; type of window frame and glass; cooling and heating annual demand and thermal building systems. This information is obtained from both Execution Projects and Building Evaluation Reports (detailed reports on conservation status, accessibility adaptation and energy efficiency of dwellings). Currently, this database includes information of 39,486 public social dwellings built between 1970-2005.

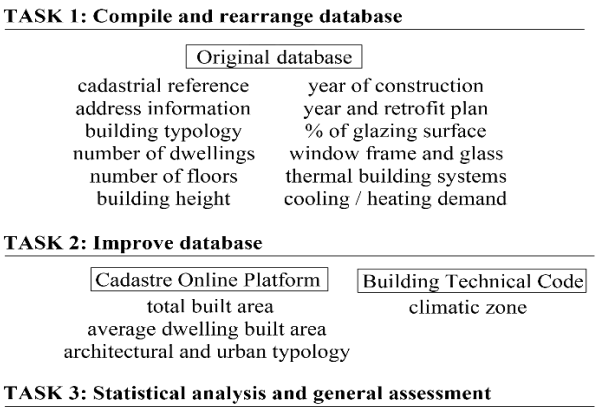

Figure 2. Scheme of the methodology and tasks followed.

In task 2, the original content of AVRA database is expanded through the incorporation of new variables, using public and open access tools. Average floor area per dwelling and building total built surface are collected from the Spanish Electronic Cadastral Platform [22] and included into the database. Likewise, building orientation, architectural typology (linear block, H block, tower block or other) and urban typology (buildings grouped as collective closed blocks, terraced, isolated or irregular) are also collected from the public cadastral online platform and introduced into the database. Finally, the classification of dwellings according to the climatic zone of Andalusia, southern Spain, established by the Spanish Building Technical Code [23] is also incorporated into the analysis. This code classifies the Andalusian territory of southern Spain into several climatic zones by taking into account two indexes (Equations 1 and 2): Climatic Severity in Winter (SCI) and Climatic Severity in Summer (SCV), which depend on the degree-day and solar radiation levels. The SCI is represented by a letter, from A to E, so that "A" defines milder winters and "E" refers to colder winters. SCV is defined by a number, from 1 to 4, so areas identified as "1" have milder summers, while "4" corresponds to warmer summers. In southern Spain, the combination of SCI and SCV defines A3, A4, B3, B4, C3, C4, D2 and D3 climatic zones (Table 1).

$$SCI=a\cdot Ri+b\cdot Gi+c\cdot Ri\cdot Gi+d\cdot Ri^2+e\cdot Gi^2+f \quad (1)$$

$$SCV=a\cdot Rv+b\cdot Gv+c\cdot Rv\cdot Gv+d\cdot Rv^2+e\cdot Gv^2+f \quad (2)$$

Where:

Ri: cumulative average global solar radiation in January, February and December [kWh/m^2]
Gi: average of the degree-day in winter in base 20 for January, February and December. Determined on an hourly basis for each month and divided by 24.
Rv: cumulative average global solar radiation in June, July, August and September [kWh/m^2]
Gv: average of the degree-day in summer in base 20 for June, July, August and September. Determined on an hourly basis for each month and divided by 24.
a to f: specific coefficients included in the Code's appendix.

Table 1. Climatic severity according to the Spanish Technical Building Code.

Climatic severity	Parameter	Range	Climatic zones
SCI	A	SCI≤0.3	A3, A4, B3. B4, C1, C2, C3, C4, D1, D2, D3, E1
	B	0.3<SCI≤0.6	
	C	0.6<SCI≤0.95	
	D	0.95<SCI≤1.3	
	E	SCI>1.3	
SCV	1	SCV≤0.6	
	2	0.6<SCV≤0.9	
	3	0.9<SCV≤1.25	
	4	SCV>1.25	

In task 3, the improved database is statistically analyzed through descriptive techniques, with Microsoft Excel and Matlab, in order to obtain the building parameters' ranges which adequately described the main characteristics of the social housing stock of southern Spain. Even though this study focuses on the characterization of the H-typology, previous results of this stock are available on [24], where data on year of construction, dwellings per block, retrofit year and plan, building systems and energy demand is provided.

III. ANALYSIS AND DISCUSSION

Figure 3 shows the percentage of social dwellings contained in the database, represented per each climatic zone in southern Spain (A3, A4, B3, B4, C3, C4 and others, which represents D2 and D3 zones), classified according to the building typology (single family, multi-family or other, which combines the previous ones). Red dots indicate the percentage of total dwellings per each climatic zone (all three building typologies), which relates to the total number of buildings included on the top of the figure.

It can be seen that 77.5% of the total 39,486 dwellings of the sample correspond to multi-family housing buildings (30,592 dwellings) and are located mainly in B4, A3, B3, C4 and C3 climatic zones. When analyzing single family dwellings, which only represents 16.1% of the total dwellings of the sample, they are located mostly in B4 C3, B3 and C4 zones. Only 6.4% of the sample buildings are categorized as other, which means those buildings include single and multi-family housing dwellings in the same development.

Since multi-family dwellings are predominant in all climatic zones, this building typology has been selected for further analysis. The classification of architectural typologies (H block, linear block, tower block or irregular) is indicated for A3, A4, B4 and C3 climatic zones in Figure 4, where the number of buildings of each architectural typology is also included inside the bars.

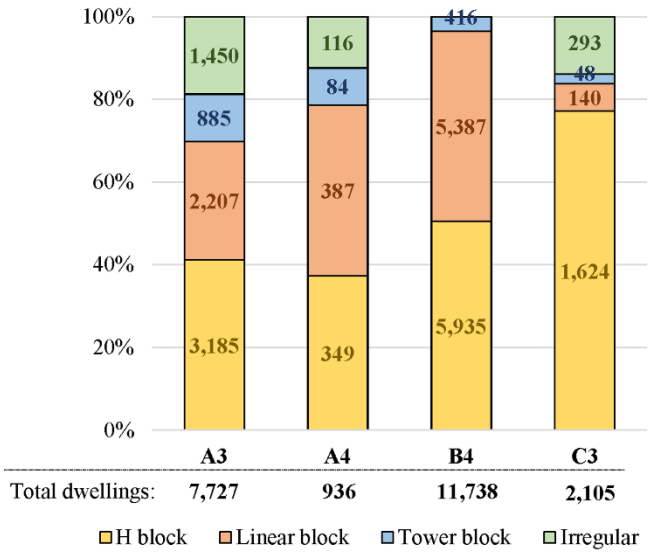

Figure 4. Classification of multi-family dwellings in southern Spain A3, A4, B4 and C3 climatic zones according to the architectural typology. The number of dwellings is also shown.

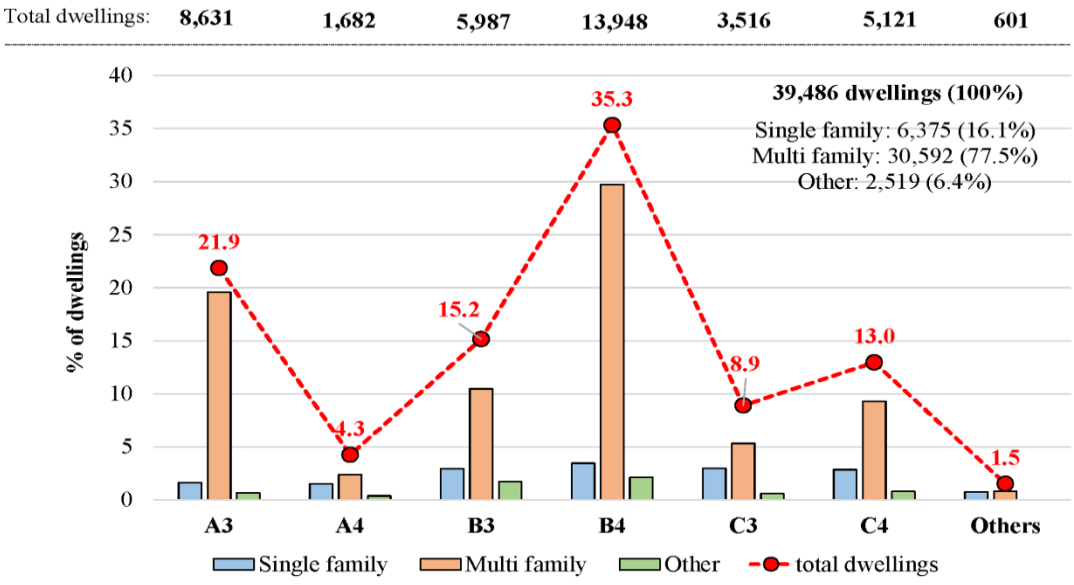

Figure 3. Percentage of single family, multi-family and other dwellings per southern Spain climatic zones. Red values represent the total percentage of dwellings in each climatic zone. Total number of dwellings in shown on the top of the figure.

It can be seen that in almost all four climatic zones, most of the buildings are identified as H block, specifically, 41.2% in A3, 37.3% in A4, 50.6% in B4 and 77.2% in C3. The second rank of typologies correspond to the linear block in A3 and B4 zones (28.6% and 45.9%, respectively). In A4 climatic zone, 41.3% of the total multi-family dwellings are linear blocks, which is only 4.0% higher than the number of H blocks. In C3, the second rank is held by buildings with irregular typologies, corresponding to 14.0% of the total sample. The lowest percentage refers to tower blocks in all zones.

Given the importance of H-blocks in the analyzed social housing stock, as shown in previous figures, and that, as stated in the introduction, most research conducted so far have focused on the linear block, an extensive analysis has been carried out regarding the H-typology. The urban classification of the H-typology multi-family dwellings in A3, A4, B4 and C3 climatic zones has been analyzed, considering the following categories: isolated (single building), terraced (buildings combined with each other leaving an inner courtyard), terraced combined in U-form or as collective closed blocks, terraced (oblique), where buildings are combined forming an oblique line, so there are no inner courtyards, and, finally, irregular typologies, which combine previous ones (Figure 5).

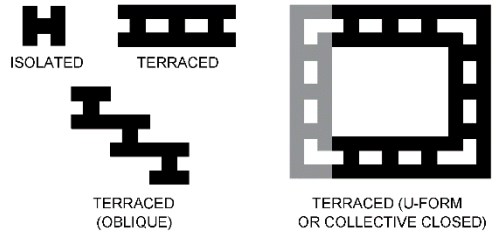

Figure 5. Urban classification considered

Results of these classifications are shown in Figure 6, indicating the total number of dwellings per climatic zone at the bottom of the graphic. All 349 H-blocks in A4 are isolated. In A3 and C3 climatic zones, 85% and 81% of the H blocks are terraced, which represent 2,654 and 1,317 dwellings, respectively. In B4, H blocks are combined in a more diverse way: 44% as terraced oblique (2,606 dwellings), 23% in U-form and collective closed blocks (1,364 dwellings) and 20% as terraced (1,193 dwellings).

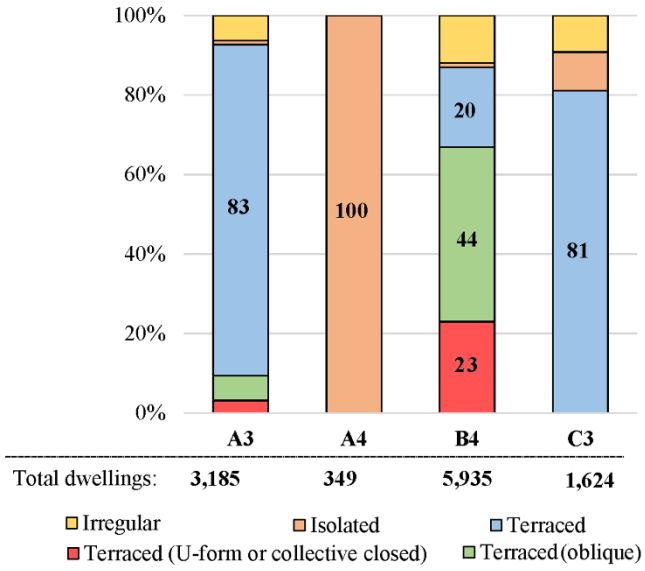

Figure 6. Urban classification of multi-family H-typology dwellings in southern Spain A3, A4, B4 and C3 climatic zones. The number of dwellings is also shown.

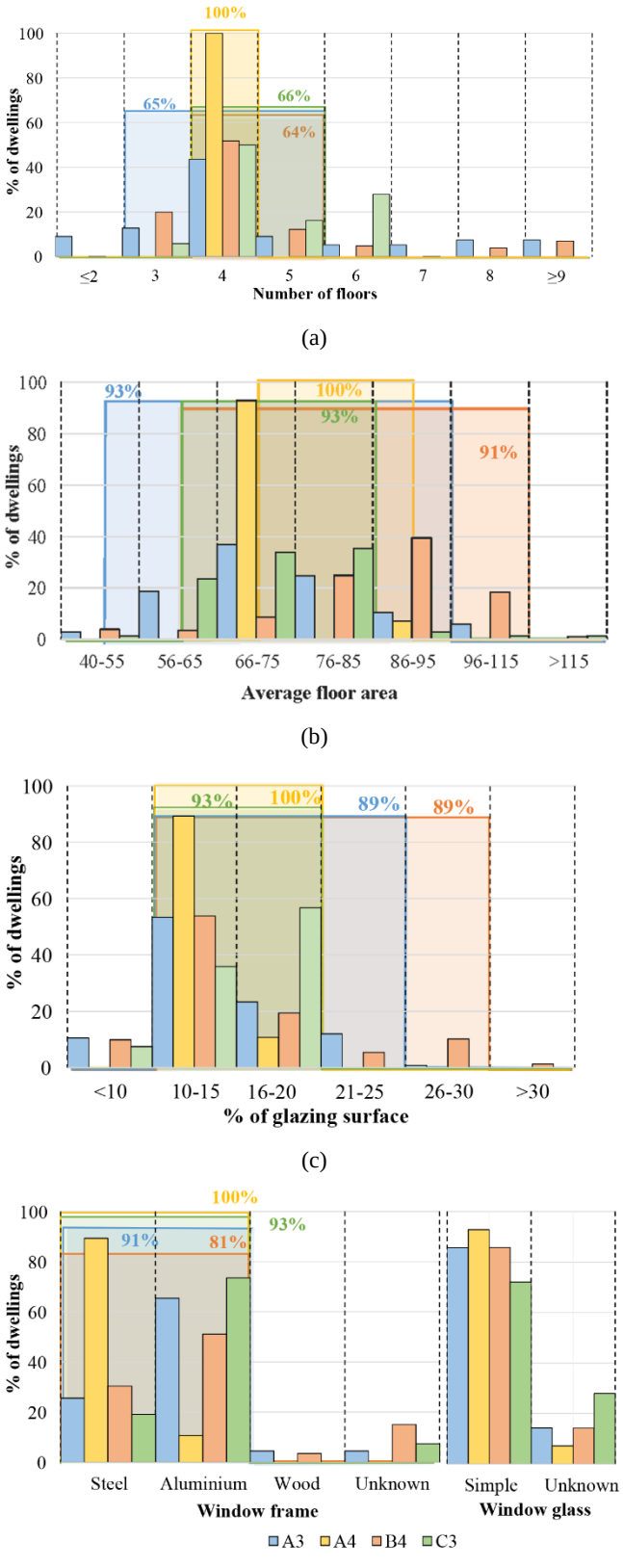

Figure 7. Percentage of H-typology multi-family dwellings classified according to the number of floors of the building, average dwelling floor area, % of glazing surface, window frame and window glass, per each southern Spain A3, A4, B4 and C3 climatic zone. Bold colored numbers indicate the percentage of dwellings represented in the colored ranges.

Building characterization of the H-typology social dwellings of southern Spain is shown in Figure 7, representing several constructive variables per each climatic zone: A3 (blue), A4 (yellow), B4 (orange) and C3 (green).

Firstly, dwellings have been classified according to the number of building floors in Figure 7a, showing the results as percentages of dwellings. In A3, H-blocks have mainly 3 to 5 floors, which refers to 65% of the sampling for this climatic zone. All blocks in A4 climatic zone have 4 floors. Blocks in B4 are mainly 4-storey buildings, but the number of buildings with 3 and 5 floors is also representative. When considered 3 to 5-storey blocks in B4, the percentage of samples analyzed is around 64%. Buildings in C3 are normally 4-storey blocks, but there is also a noticeable percentage of H-typology dwellings with 5 and 6 floors. 66% of the total number of buildings in C3 would be included when 4 to 5-storey blocks are considered. If buildings with 6 floors were also included, it would represent 94% of the dwellings.

The average floor area per dwelling can be seen in Figure 7b. In this case, 93% of the dwellings in A3 climatic zone are between 50 and 95m^2. In A4, 100% of the dwellings are between 70-90m^2. If dwellings between 60-115m^2 were considered, in B4 zone, 91% of the total H-buildings would be represented. Likewise, dwellings with average floor area around 60-85m^2, would represent 93% of the total dwellings in C3 climatic zone. Considering dwellings with floor area equal or less than 55m^2 and over 115m^2 is not representative of the stock since it would only be taken into account 3% of the buildings in A3 climatic zone, 5% in B4 and 2% in C3.

Figure 7c classifies the percentage of H-blocks according to the percentage of glazing surface, per each climatic zone. In A3, A4 and B4, most of the dwellings have a window to wall ratio approximately between 10-15%. While in C3, the percentage of dwellings with a glazing surface between 16-20% is higher. Nonetheless, if a percentage of glazing surface between 10-20% was considered, 93% and 100% of the dwellings would be represented for C3 and A4 climatic zones, respectively. In A3, 89% of the dwellings have a window to wall ratio around 10-25%. The same percentage of dwellings would be analyzed in B4 climatic zone if a glazing surface between 10-30% was considered. If a percentage of glazing surface between 5-10% was considered, that would increase the sampling representativeness by 11% in A3 climatic zone, 9% in B4 and 7% in C3. Considering a window to wall ratio above 20%, would only affect B4 climatic zone, adding 1% of buildings to the sample.

Window frame and glass types are assessed in Figure 7d. In the database, window frame has been divided into four groups: steel, aluminum, wood or unknown. It can be seen that the use of wood frames in the H-typology is quite low when compared to steel and aluminum. In fact, 91% of the dwellings in A3 have frames made of steel and aluminum. Likewise, these materials are represented in 100% of the total dwellings in A4, 81% in B4 and 93% in C3. Thus, considering windows with wood frames would not be representative of the analyzed stock. In parallel, information on the window glass type was classified in the database as simple (single glazing) or unknown, since no double or triple glazing was identified in the stock. Thus, 86% of the buildings in A3 have single glazing surfaces. This occurs in 93% of the cases in A4, 86% of the dwellings in B4 and 72% of the sampling in C3 climatic zone. The percentage of unknown glazing surfaces is higher in C3 climatic zone, when compared to the other zones.

Finally, energy demand and CO_2 emissions of the social H-blocks have been assessed per southern Spain climatic zones (Figure 8). Heating results are indicated in red color, while cooling data is represented in blue. In Figure 8a, it can be seen that in all climatic zones, cooling energy demand is lower than heating demand, which is particularly significant in A4 and C3 zones, where the whiskers of the cooling boxplots are below the ones of the heating boxplots. Heating energy demand of the H-blocks in A3 and B4 climatic zones ranges between approximately 20-80 kWh, 40-60 kWh in A4 and 45-130 kWh in C3. Heating demand of C3 climatic zone is the highest, which is consistent with the winter climatic severity differences between zones. Cooling energy demand of H-typology dwellings in all climatic zones is generally between 5-40 kWh.

CO_2 emissions in the H-blocks (Figure 8b) follow a similar tendency to the energy demands results. The highest carbon dioxide emissions are related to heating systems, which normally consist of electric heat pumps, and are particularly high in C3 climatic zone. In contrast, lowest CO_2 emissions come from H-blocks in A4 climatic zone, where cooling systems are mainly also electric heat pumps.

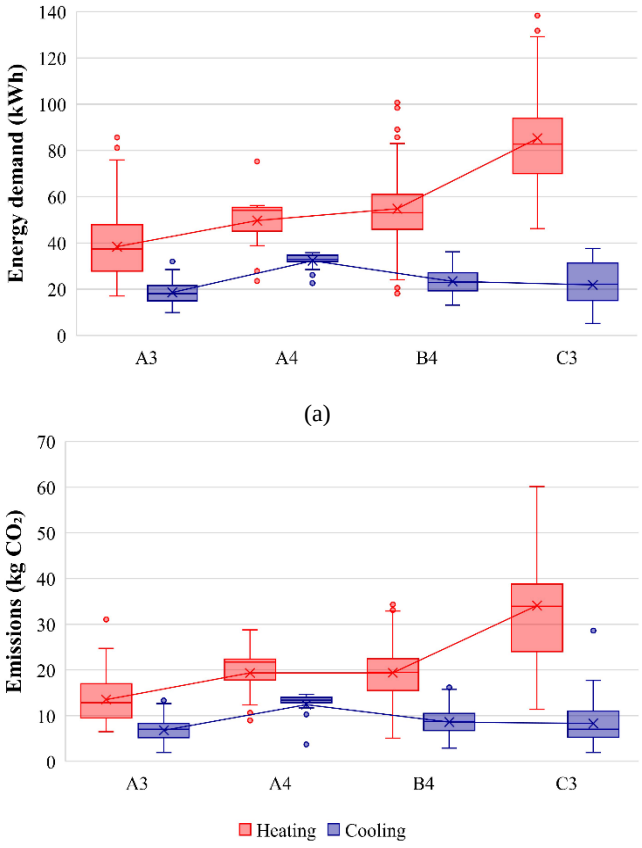

Figure 8. Heating and cooling energy demand and CO_2 emissions of the multi-family H-typology dwellings in southern Spain A3, A4, B4 and C3 climatic zones.

IV. CONCLUSIONS

Prior to any retrofit intervention, it is necessary to assess the energy and thermal performance state of the existing building stock. In this sense, building characterization at the stock level is key to provide large-scale retrofit measures in order to meet future energy targets. This is especially significant in the social residential sector, since a large proportion of these buildings would become the future stock.

In this paper, the social housing stock of southern Spain (Mediterranean area) has been statistically characterized, analyzing morphological, geometrical and constructive aspects of the stock. A large database containing information of up to 39,486 dwellings have been analyzed. Efforts have been put on obtaining the main building parameter ranges which adequately represent the building stock, focusing on the H-typology buildings, since these dwellings have not been normally included in building characterization studies in the Mediterranean area. The final objective of this research is to

provide useful and accurate data on building characterization ranges to be used for future performance analysis through bottom-up stock building modelling, instead of the commonly fixed values approach.

This research has confirmed that 77.5% of the social residential buildings in southern Spain are multi-family buildings, which represent 30,592 dwellings. Among them, the top two building typologies are the H-block (36.3%), with 11,093 dwellings, and the linear block (26.5%), which represents up to 8,121 dwellings. Even though results have been provided for each climatic zone in southern Spain, according to the Spanish Technical Building Code, some general conclusions may be reported. When considering the urban typology of the H-blocks, most of the buildings are isolated and terraced, with a significant number of terraced buildings which are combined forming an oblique line. A high percentage of the H blocks are 3 to 5-storey buildings, with an average floor area between 55-95 m^2. The percentage of the glazing surface of these buildings is normally between 10 and 20%. And a significant number of them have window frames made of steel and aluminum with single glazing windows. Energy heating and cooling demand is around 20-130 kWh and 5-40 kWh, respectively, with higher differences of heating demand according to the climatic severity. Despite of this overall conclusions, as previously stated, this research has also provided parameter ranges of several building variables per each climatic zone for the H-typology dwellings. The percentage of building samples which may be represented in each case according to the variable ranges selected has been also included. This information may be quite useful for the energy performance assessment of the existing stock in the Mediterranean area of southern Spain, providing more accurate results to be used by public stakeholders and energy policy makers in their involvement in decision-making processes.

V. ACKNOWLEDGMENTS

This research was funded by the Spanish Ministry of Economy and Competitiveness and the European Regional Development Fund through the research project "Parametric Optimization of Double Skin Facades in the Mediterranean Climate to Improve Energy Efficiency Under Climate Change Scenarios" (ref BIA2017-86383-R). Calama-González also wishes to acknowledge the financial support provided by the FPU Program of the Spanish Ministry of Education, Culture and Sport (FPU17/01375).

VI. REFERENCES

[1] Energy Statistics: an Overview. Eurostat Statistics Explained. European Commission. https://ec.europa.eu/eurostat/statistics-explained/index.php?title=Energy_statistics_-_an_overview#Final_energy_consumption (accessed May 19, 2021)

[2] 2020 Global Status Report for Buildings and Construction. Towards a zero-emission, efficient and resilient buildings and construction sector. https://globalabc.org/resources/publications/2020-global-status-report-buildings-and-construction (accessed May 19, 2021)

[3] V. Pérez-Andreu, C. Aparicio-Fernandez, A. Martínez-Ibernón and J. L. Vivancos, "Impact of climate change on heating and cooling energy demand in a residential building in a Mediterranean climate", Energy, 165, pp.63-74, 2018, https://doi.org/10.1016/j.energy.2018.09.015.

[4] NASA U.S. National Aeronautics and Space Administration Earth Science Communications Team, Jet Propulsion Laboratory. https://climate.nasa.gov (accessed May 19, 2021)

[5] D. Barriopedro, E. Fischer, J. Luterbacher, R. M. Trigo and R. Garcia-Herrera, "The hot summer of 2010: redrawing the temperature record map of Europe", Science, 332 (6026), pp.220-224, 2011, doi: 10.1126/science.1201224.

[6] E. Rodrigues and M. S. Fernandes, "Overheating risk in Mediterranean residential buildings: Comparison of current and future climate scenarios", Applied Energy, 259, 114110, 2020, https://doi.org/10.1016/j.apenergy.2019.114110.

[7] EN 16798-1:2019. Energy Performance of Buildings – Ventilation for buildings - Part 1: Indoor Environmental Input Parameters for Design and Assessment of Energy Performance of Buildings Addressing Indoor Air Quality, Thermal Environment, Lighting and Acoustics - Module M1–6. Brussels, 2019.

[8] EU energy in figures. Statistical pocketbook 2018, https://op.europa.eu/en/publication-detail/-/publication/99fc30eb-c06d-11e8-9893-01aa75ed71a1/language-en/format-PDF/source-77059768 (accessed May 19, 2021)

[9] Z. Ma, P. Cooper, D. Daly and L. Ledo, "Existing building retrofits: Methodology and state-of-the-art", Energy and buildings, 55, pp.889-902, 2012, https://doi.org/10.1016/j.enbuild.2012.08.018.

[10] T. M. Gulotta, M. Cellura, F. Guarino and S. Longo, "A bottom-up harmonized energy-environmental models for europe (BOHEEME): A case study on the thermal insulation of the EU-28 building stock", Energy and Buildings, 231, 110584, 2021, https://doi.org/10.1016/j.enbuild.2020.110584.

[11] É. Mata, A. Sasic Kalagasidis and F. Johnsson, "Building-stock aggregation through archetype buildings: France, Germany, Spain and the UK". Building and Environment, 2014, https://doi.org/10.1016/j.buildenv.2014.06.013.

[12] K. J. Lomas and R. Giridharan, "Thermal comfort standards, measured internal temperatures and thermal resilience to climate change of free-running buildings: A case-study of hospital wards", Building and Environment, 55, pp.57-72, 2012, https://doi.org/10.1016/j.buildenv.2011.12.006.

[13] A. Mavrogianni, P. Wilkinson, M. Davies, P. Biddulph and E. Oikonomou, " Building characteristics as determinants of propensity to high indoor summer temperatures in London dwellings", Building and Environment, 55, pp.117-130, 2012, https://doi.org/10.1016/j.buildenv.2011.12.003.

[14] G. Dall'O, A. Galante and M. Torri, "A methodology for the energy performance classification of residential building stock on an urban scale", Energy and Building, 48, pp.211-219, 2012, https://doi.org/10.1016/j.enbuild.2012.01.034.

[15] J. Sokol, C.C. Davila and C.F. Reinhart, "Validation of a Bayesian-based method for defining residential archetypes in urban building energy models", Energy and Buildings, 134, pp.11-24, 2017, https://doi.org/10.1016/j.enbuild.2016.10.050.

[16] C.S. Monteiro, A. Pina, C. Cerezo, C. Reinhart and P. Ferrão, "The use of multi-detail building archetypes in urban energy modelling", Energy Procedia, 111, pp.817-825, 2017, https://doi.org/10.1016/j.egypro.2017.03.244.

[17] T. Loga, B. Stein, and N. Diefenbach, "TABULA building typologies in 20 European countries—Making energy-related features of residential building stocks comparable", Energy and Buildings, 132, pp.4-12, 2016, https://doi.org/10.1016/j.enbuild.2016.06.094.

[18] M. Monzón-Chavarrías, B. López-Mesa, J. Resende and H. Corvacho, "The nZEB concept and its requirements for residential buildings renovation in Southern Europe: The case of multi-family buildings from 1961 to 1980 in Portugal and Spain", Journal of Building Engineering, 34, 101918, 2021, https://doi.org/10.1016/j.jobe.2020.101918.

[19] R. Escandón, F. Ascione, N. Bianco, G. M. Mauro, R. Suárez and J. J. Sendra, "Thermal comfort prediction in a building category: Artificial neural network generation from calibrated models for a social housing stock in southern Europe", Applied Thermal Engineering, 150, pp.492-505, 2019, https://doi.org/10.1016/j.applthermaleng.2019.01.013.

[20] T. Blázquez, R. Suárez, S. Ferrari and J. J. Sendra, "Addressing the Potential for Improvement of Urban Building Stock: A Protocol applied to a Mediterranean Spanish Case", Sustainable Cities and Society, 102967, 2021, https://doi.org/10.1016/j.scs.2021.102967.

[21] AVRA Andalusian Agency of House and Retrofitting (Agencia de Vivienda y Rehabilitación de Andalucía, in Spanish), http://www.juntadeandalucia.es/avra (accessed May 19, 2021)

[22] Online Cadastrial Office (Sede Electrónica del Catastro, in Spanish), https://www.sedecatastro.gob.es (accessed May 19, 2021)

[23] Spanish Technical Building Code Basic Document: Energy Savings (Código Técnico de la Edificación. Documento Básico: Ahorro de Energía, in Spanish), 2017 Spanish Government Madrid Spain, https://www.codigotecnico.org (accessed May 19, 2021)

[24] C. M. Calama-González, R. Suárez and Á. L. León-Rodríguez, "Building characterisation and assessment methodology of social housing stock in the warmer Mediterranean climate: the case of southern Spain", IOP Conference Series: Earth and Environmental Science, vol. 410, No. 1, pp.012049, 2020.

Development of Underground transportation Hazard management System (UTHMS) for Indian underground hard rock mines

Dr. Falguni Sarkar
Assistant Professor,
Department of Mining Engineering
National Institute of Technology-Rourkela, India
E-mail: sarkarf@nitrkl.ac.in, falguniind31@gmail.com

Sabyasachi Nayak
Mining Engineer
Founder and Director
Minemagma Pvt. Ltd. Bangalore, India
E-mail: sabyasachi@minemagma.com

Abstract

In present day Indian Mining scenario, the deployment of Heavy Earth Moving Machineries (HEMM) like LHD (Load haul Dump), LPDT (Low Profile Dump Truck), Drill Jumbo, Scissor lifts and passenger carriers etc. in trackless underground mines is very much indispensable requirement for carrying out production, transportation of men and material, manage environmental sustainability and handling emergency situations efficiently. As the HEMM's are exhaustively used to load and haul the mined out materials and also to carry a number of mine workers at a time, occurrence of any accident can give rise to the disastrous consequence. The proactive Safety Management System (SMP) devised and implemented in accordance with Directorate General of Mine safety (DGMS), India, guidelines and Hazard and Operability Analysis (HAZOP) procedure is found inadequate to explore component interaction failure and events involved with operational safety protocol breach in such complex transportation machineries. Therefore, a field experience based hazard management framework namely **Underground transportation Hazard management System (UTHMS)** is proposed in this research for mitigating hazards arises due to contravention of complex human-machine interaction protocols and contemporary health- safety management procedures. The proposed UTHMS will be structured on the basis of **System Theoretic Process Analysis (STPA)**, which will help the mine operators to presume the factors involved in accidents pertaining to transportation system , and formulate effective control structures and OCPs (Operational control Procedure) with clear guidance to control the events leading to the adversity. A digitized platform for monitoring various aspects of UTHMS will be framed and the efficacy of the UTHMS will be tested in selected underground hard mines in India. The brief methodology for establishing UTHMS are explained below:

1. Study on the safety features of various types of HEMMs and construction of a database.
2. Detailed study on the accident/incident scenario pertaining to HEMM, development of Mine Accident Data Analysis (MADA) structure.
3. Evaluation of present safety management system implemented by the mine management to reduce the number of accidents.
4. Establishment of a hazard and failure Analysis Framework for HEMM System Based on STPA.
5. Design of hazard mitigation procedure as per STPA that includes operational control structures, standard operating procedures (SOP), codes of practice (COP) and their monitoring measures.
6. Development of digitized platform to monitor all control procedures, feedback management and record keeping.
7. Implementation of the designed system and analysis of outcomes.

The judicial implementation of the **UTHMS** is expected to reduce maintenance errors and cost of compensations for accidents significantly. Thus, it will help the mining industry to maintain safe and productive work environment.

Keywords: *Heavy Earth Moving Machineries (HEMM), Directorate General of Mine safety (DGMS), Hazard and Operability Analysis procedure (HAZOP), System Theoretic Process Analysis (STPA), Underground transportation Hazard management System (UTHMS)*

DAI : https://sci-index.com/DAI/2021.99101/IEECP/14905209

Effectiveness of Hybrid Fibers in Cementitious Composites Towards Sustainability: A Review

Ali Rehman
Department of civil engineering
Capital university of science and technology
Islamabad, Pakistan
engr.dr.alirehman@outlook.com

Majid Ali
Department of civil engineering
Capital university of science and technology
Islamabad, Pakistan
majid.ali@cust.edu.pk

Abstract

Cementitious composites with less effect on the environment and lower cost are the major components for advanced technology of interest. For concrete composites a lot of negative effects on environment were observed because of the emission of greenhouse gases, deficiency in materials availability, and higher consumption of energy. Hybrid fiber reinforced concrete which is the mixture of different types of fibers in cementitious composites with an enhanced behavior in mechanical properties of cement-based composites as compared to that of single fiber reinforced composites. The incorporation of natural fibers in cementitious composites have relative effects on environment which is one of the major aspects related to sustainability. The overall aim of this research is to explore the behavior of hybrid fiber cement composites towards sustainability and to promote the use of hybrid fibers in composites for improved mechanical properties. The current research is the review of previous studies related to utilization of hybrid fibers in cement composites considering sustainability aspect. In this paper, a review has been done. The purpose of this research is to explore the use of natural fibers hybridization with artificial fibers in cementitious composites for sustainable construction. This paper will provide a brief summary about the benefits of using natural hybrid fibers for sustainable construction. Also, it will promote the potential use of hybrid fibers in cementitious composites. Moreover, the benefits of fiber inclusion in cement composites like enhancement in the mechanical properties of hybrid fibers cementitious composites have increase the demand of these type of composites with introducing the novel principles taking into consideration for sustainability. Thus, addition of natural fibers with artificial/synthetic fibers can be another step toward the sustainability in the concrete industry. This research outcomes would present a valuable reference for both practitioners of industry and research of academia that are interested in the development of sustainable construction materials.

Keywords: Hybrid fiber reinforced concrete, natural fiber, synthetic fiber, mechanical properties, sustainability

IEECP'21, July 29-30, 2021, Silicon Valley, San Francisco, CA – USA

DAI : *https://sci-index.com/DAI/2021.99101/IEECP/14899341*

I. INTRODUCTION

The incorporation of fibers helps the cement based composites to overcome its weaknesses like less tension, higher shrinkage and lower resistance against impact loading [1]. Few of the natural fibers that are utilized in the productions of cement concrete are jute fiber, sisal fiber, hemp fiber, coir fiber, flax fiber and cotton fiber [2, 3]. Worldwide, the local availability of these natural fibers results in no fiber scarceness and available at a low cost. Usually the natural fibers are environmental friendly and nonabrasive material [4]. The natural fiber cement composites have shown favorable properties by using few structural materials, which offers the best application for nanotechnology [5-7]. Numerous natural and artificial fibers (i.e., glass, steel, and synthetic) are available commercially [8-10]. Among the fibers, polypropylene fiber and glass fiber are two excellent micro-reinforcing materials to increase cement concrete's strength properties. Investigations about adding polypropylene fiber and glass in the cement concrete composite have been carried out to improve its mechanical properties. The addition of polypropylene fiber or glass fiber can bridge micro-cracks in the mixture and re-divided stress, and stop stress from growing at the crack location. [11, 12]. Various kinds of fibers like polypropylene fibers, steel fibers, nylon fibers, basalt fibers, and glass fibers are used to produce fiber reinforced concrete. Polypropylene fibers have been an interest of researchers because of their resistivity to shrinkage, higher roughness, and cheap cost [13].

The utilization of fiber in cement composites impacts the environment and industrial pollution; that's why there is an increment in the demand of fiber nowadays. Novel natural materials are used in conventional cement concrete composites to minimize the negative environmental impact [14-16]. The addition of macro synthetic fiber reinforced concrete expanded fast over the past two decades. It was concluded that macro synthetic fiber has better benefits as equated to steel fiber, cheaply available, easily mixed with cement concrete, weight lightness, less corrosive in cement concrete, and give resistance against destructive chemicals [17, 18]. The incorporation of hybrid basalt polypropylene fibers in cement composites is going towards popularity recently. Basalt fiber give superior physical and mechanical properties, stability of higher temperature, excellent tensile strength, incredible resistance to acid alkali, and a strong capacity for plastic deformation, which is a novel variety of environment-friendly, low cost, and green fiber [19, 20]. The addition of recycled aggregates in structural cement concrete composites is a step towards a sustainable solution to minimize the

misuse of natural sources and the adverse ecological impacts of cement concrete waste [21]. Investigators are now exploring the use of recycled materials from damaged vehicle tires, for example, crumb rubber aggregate in cement concrete composites, to overcome the problems generated by waste tires and protect the environment by creating it green and sustainable [22]. Additionally, the investigation stated that the performance of natural coconut fiber and rope with cement concrete reinforced beam under dynamic loading was improved [23]. Moreover, research was conducted on coconut fiber reinforced concrete and coconut fiber ropes utilization to determine the behavior for seismic-resistant construction [24]. The seismic behavior of coconut fiber reinforced concrete columns with various reinforcing arrangements of coconut fiber ropes were studied. This is an innovative material, which is under exploration for the making of safe shelters with cheaper cost in the regions where earthquakes occur [25]. Another research was carried out on the determination of post-tensioned coconut fiber ropes to control uplifts of interlocking blocks for mortar-free construction throughout seismic loadings [26].

The significance of the present research is to review the behavior of hybrid fiber reinforced concrete in the light of sustainability. In this study, different hybridization of artificial and natural fibers together is reviewed for the mechanical properties of cement composites. In addition, the effect of hybrid fibers reinforced concrete on environment is also studied. In this paper, a review has been done. The purpose of this research is to explore the use of natural fibers hybridization with artificial fibers in cementitious composites for sustainable construction. This paper will provide a brief summary about the benefits of using natural hybrid fibers for sustainable construction. Also, it will promote the potential use of hybrid fibers in cementitious composites.

II. CONCEPT OF HYBRID FIBERS

In the concrete industry, hybrid fiber reinforced concrete has been of great importance. When the combination of two or more fibers are used in cement concrete composites, then, as a result, a hybrid fiber reinforced concrete is obtained. Each fiber that is used in hybrid fiber-reinforced cement concrete shows their promising effects on composites [23]. The system of fiber hybridization needs a mixture of various kinds of fibers to produce a synergic impact and improve the cement composite behavior for properties of the fresh state and hardened state [24]. Steel with polypropylene hybridization has been getting popularity amongst different hybrid fiber reinforced combinations. Although concrete develops shrinkage and internal stresses, the hybrid steel polypropylene fiber reinforced cement composites have the ability to divide stresses in every direction over millions of polypropylene fibers available in the mixture [25]. On the other hand, the benefit of utilizing a hybrid fiber in concrete is that it minimizes the structure's dead load because of the low density of the polypropylene fibers as compared to that of steel fibers.

III. BEHAVIOUR OF HYBRID FIBER REINFORCED COMPOSITES

Synthetic fibers, like polypropylene fibers, have recently attracted a lot of attention. For the better mechanical properties of cement concrete reinforced with various kinds of hybrid fibers, the mono-fiber is generally preferred to cement concrete reinforcement. It is strongly recognized that thick and longer fibers restrict the spreading of macro cracks and increase the toughness at the region of post cracking [27]. Whereas micro and shorter fibers bridge the micro cracks, which results in improving the peak strength of composites [28]. Accordingly, the investigators usually select the mixture of fibers with various lengths, diameters, and elastic modulus [29], [19]. Moreover, fiber reinforced cement concrete composites also provide significant obstruction to the development and spreading of cracks [30]. After a detailed study, it is summarized that polypropylene fiber and steel fiber are used frequently in composites. A vital role was played by the aspect ratio and content of fibers in composites for enhancing multiple properties of cement composites. Fibers start sustaining the load during the occurrence of cracks. The fibers start transferring more stresses to the composites while increasing the load on specimens. Fiber fracture or pull-out of the fiber was observed during these stresses that pass the bond strength among the matrix and the fiber [31]. Compared to ordinary and single-length fiber reinforced mortar, the combination of basalt fiber with four various lengths incorporating in cementitious based composites enhanced mechanical performance [32]. In order to get superior structural strength, it is essential to include fibers in ordinary cement mortar [33]. Due to its bridging action, the incorporation of recycled nylon fibers in cement mortar reduces the number and width of cracks [34, 35].

Figure 2 represents a schematic diagram to demonstrate fiber's primary bridging mechanism for cement concrete reinforced with hybrid polypropylene and steel fibers under flexure loading. Many internal macro or micro-cracks develop at the start of loading because of the inherent shortcomings and composites shrinkage; meanwhile, the major surface crack has not appeared. Although, individually dispersed fibers could bridge the cracks, reducing the stress from the composites. So, the polypropylene fiber has the ability to counter the small micro-cracks propagation due to its weak bond with the mixture and more vulnerable tensile properties (i.e., the pull-out load is very low). While the loading raises, the major crack gradually produces, and the fiber tie together presents a crucial act in enhancing the flexure behavior. The slippage of fiber and less bonding can take place, whereas low interaction among mixture and fiber. And probably increase at the interface of polypropylene fiber and the mix. Fiber fracture occurs when the concentrated stress reduces the fiber reinforcement boundary; however, the fiber has completely adhered to the mixture; it was also noticed at the interface of recycled tire steel fiber and the mix. Both phenomenon's showed enrichment of post-cracking achievement, particularly energy absorption capacity, so as the value of energy absorption is altered by multiple factors like the number of fiber and the spacing of fibers nearby a specific crack [36].

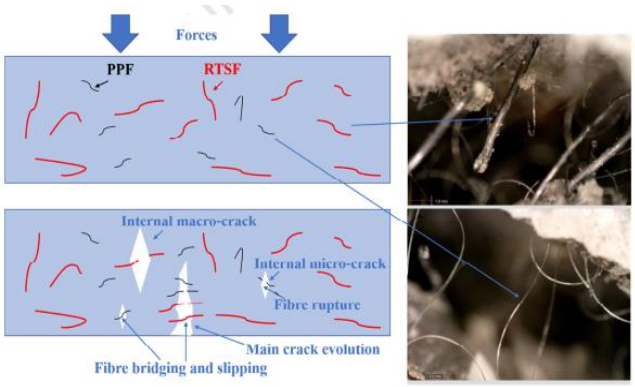

Figure 1. Hybrid fiber reinforced concrete bridging mechanism under flexural loading [36].

IV. HYBRIDIZATION WITH ARTIFICIAL AND NATURAL FIBERS

Experimental research has been taken to assess the enhancement in mechanical properties of interlocked masonry walling without mortar by incorporating natural fibers such as sisal fibers and rice straw used in the mixture of plaster. The terminology for increment in failure loads across non-plastered columns was noticed up to 5 times for control mix and up to 21 times for plaster mix with fibers [37]. Further experimental research was conducted to evaluate shear strengths, and residual compressive strengths for new coconut fiber reinforced concrete interlocking blocks. After sustaining a set of

dynamic loading, the increment up to 3.2% and 5.7% for in-plane strength and compressive strength was observed. This enhancement represents the merits of earthquake loading on structures without mortar [38]. Another study was carried out on the addition of natural plant fibers, i.e., wheat straw, to increase the performance and potential of reinforced concrete for structural applications. Experimental results revealed an improvement of 7.5% for flexure strength, 30.4% for energy absorption, 11.1% for toughness indices, and a good crack arresting mechanism by utilizing wheat straw in fiber reinforced concrete. Moreover, rigid concrete pavement having wheat straw has an equivalent design with a seeming more sustainable and more long-lasting structure [39]. The performance of jute fiber reinforced concrete composites is explored practically under impact and dynamic loading conditions. The resistivity against impact loading by the jute fiber reinforced concrete composites is improved up to 6 times compared with normal concrete. The 100% damping ratio and 68% dynamic young's modulus were also improved. The improvement in splitting tensile strength was 8%, while the flexure strength was 20% observed. According to the results, short jute fibers in cement concrete composites may minimize steel reinforcement of slabs by roughly 28% [40]. Furthermore, the reinforcing index and constitutive modeling are explored for normal concrete, single fiber reinforced cement concrete, two-hybrid fibers reinforced concrete, and multi-scale hybrid fibers reinforced cement concrete containing various basalt fiber dosage. It is reported that the optimal mechanical properties for multi-scale hybrid fiber reinforced cement concrete was noticed with 0.8% basalt fiber dosage, calcium carbonate whisker of 1%, and steel fiber of 0.25% dosage [41].

The findings showed that if the mass ratio of polypropylene fiber to basalt fiber is 2:1 and the total mass is 6 kg/m^3, the favorable hybrid effect is more remarkable for both compressive test and splitting tensile test. Compared to the concrete with exclusion fibers, the splitting tensile strength was risen by 24%, while the compressive strength was risen by 14%. Micro basalt fiber and macro polypropylene fiber fracture resistance could not be exchanged. Fibers with various dimensions and elastic modulus perform vital roles in varying states of composites. Using hybrid basalt polypropylene fibers in cement concrete composites showed an improvement in compressive strength and splitting tensile strength [42]. The hybrid fiber reinforced cement concrete was composed by adding sisal fiber, polypropylene fiber, and banana fiber to investigate the durability and mechanical properties of cement concrete composites. Enhancement was observed by 24.3% and 14.9% for compressive strength of M3 mix when comparison with normal cement concrete composites at the curing age of 28 days. Similarly, an increment was recorded 47.54% and 37.19% of splitting tensile strength for M3 mix when compared with normal cement concrete composites at the curing age of 7 and 28 days, respectively. Also, improvement was observed with the maximum value of 5.58 N/mm^2 and 10.9 N/mm^2 of flexure strength for M3 mix when compared with normal cement concrete composites at the curing age of 7 and 28 days, respectively [43]. Polypropylene, carbon, and aramid fibers can efficiently increase the initial mechanical properties of hybrid fiber reinforced cement concrete composites, particularly for the flexure and tensile strengths. Although the enrichment in tensile strength was associated with the polypropylene fiber aspect ratio, on the other hand, the aspect ratio of aramid fiber contributed to improving the flexural and compressive behaviors. A minor effect of fibers aspect ratio was reported concerning to the initial phase of hybrid fiber reinforced cement concrete composites. Meanwhile, tensile strength is almost 15 times the compressive strength, which is equivalent to plain concrete having 28 days curing age [44]. It was concluded from the results of an experimental study that there was a direct effect of volume content of the fibers on tensile and flexure strength and improvement in the strength of first cracks due to the inclusion of fibers was observed. All other combinations of steel-polypropylene hybrid fiber reinforced cement concrete composites showed effective synergy to the strengths of splitting tensile and flexure strength. Therefore, hybridization of polypropylene/steel is more beneficial for introducing the reinforcement in the structural elements [45]. Table 1 is the representation of raw material, mix proportion and increased strengths of hybrid fiber reinforced concrete.

Table 1. Raw material, mix proportion, studied properties and increased strengths of HFRC [22], [46], [44], [47].

Sr. No.	Raw material	Mix proportion	Strength increment
1	Cement, Sand, Aggregate, Silica Fume, Fly Ash, Slag, Water, Polypropylene (P-P), Steel (S) fiber and Crumb Rubber (C-R).	1: 1.68: 1.15: 0: 0: 0 & w/c ratio 0.45. P-P-F length = 3 mm. S-F length 21 mm. Hybrid Fiber (H-F) = (P-P+S) content = (0+1, 0.1+0.9, 0.175+0.825, 0.25+0.75, 1+0 %). C-R = 20%. Total volume fraction = (1 %). By volume of PC.	C-S = Increased 48.02 MPa with 0.1+0.9 % H-F content as per PC. C-S = Increased 33.94 MPa with 0.1+0.9 % R-H-F content as per R-C. S-T-S= Increased 5.09 MPa with 0.1+0.9 % H-F content as per PC.
2	Cement, Sand, Aggregate, Silica Fume, Fly Ash, Slag, Water, Macro Polypropylene (M-P-P) and Basalt (B) fiber.	1: 2.34: 3.09: 0: 0: 0 & w/c ratio 0.68. 1: 0.96: 2.21: 0: 0: 0 & w/c ratio 0.44. M-P-P-F length = 60 mm. B-F length = 20mm. M-P-P-F content = (0, 0.3, 0.7, 0.1 %). Hybrid Fiber (H-F) = (P-P+B) content = (0+0.1, 0.3+0.1, 0.7+0.1, 0.1+0.1 %). By volume of PC.	C-S = Increased 10%. F-S = Increased 20%.
3	Cement, Sand, Aggregate, Silica Fume, Fly Ash, Slag, Water, Polypropylene (P-P), Carbon (C), and Aramid (A) fiber.	1: 1.12: 2.27: 0: 0: 0 & w/c ratio 0.39. P-P-F length = 9, 12, 18 mm. C-F length = 1.7 mm. A-F length = 5, 7, 9 ,11 mm Hybrid Fiber (H-F) = (P-P+C+A) content = (0.04+0.04+0.04 %). By volume of PC.	C-S = Increased 18.3%. F-S= Increased 38.7%. S-T-S= Increased 40.8%. With H-F content as per PC.
4	Cement, Sand, Aggregate, Silica Fume, Fly Ash, Slag, Water, Polypropylene (P-P) and Basalt (B) fiber.	1: 2.27: 2.91: 0: 0: 0 & w/c ratio 0.36. P-P-F length =50 mm. B-F length =19 mm. Hybrid Fiber (H-F) = (P-P+B) content = (0.63+0, 0+0.22, 0.51+0.04, 0.42+0.07, 0.32+0.11, 0.21+0.15, 0.13+0.17 %). By volume of PC.	C-S = Increased with H-F. C-S = Increased 14% with 0.63+0 % H-F content as per PC. T-S = Increased 24% with 0.63+0 % H-F content as per PC.
Note: Compressive-strength (C-S); Flexural-strength (F-S); Split-tensile-strength (S-T-S).			

V. SUSTAINABILITY WITH HFRC

The construction sector uses a lot of natural resources and has a lot of negative environmental consequences. Building block production accounts for about 40% of total energy consumption, greenhouse gas emissions for 30%, freshwater consumption for 17%, harvested wood for 25%, and 45% to 65% disposal in landfills, as reported by the world business council for sustainable development [48-51]. Consequently, controlling environmental problems in industry of construction has become a significant concern. Green construction, which aims to decrease the harmful effects of buildings construction on humans and the environment, has lately gained a lot of attention [52]. Therefore, the production of the fibers as reported in current research requires a large quantity of energy and raw materials, i.e., fossil fuel [53, 54]. The cost of the composite material rises as the sustainability is reduced, i.e., unavoidable greenhouse gas emissions while manufacturing of steel. [55]. To minimize the environmental effects and warning of deficiency by using the natural resource, an advanced number of researches have been conducted to utilizing the recycled materials as the fiber reinforcing in cement based composites. Similarly, the reproduction of the materials from the real life of tires; one of the most recent endeavors, for example, is to replace steel and polymeric fibers with new manufacturing fibers. Around 500 million discarded tires are reported to be improperly disposed-off, with few landfill disposal locations being one of the most significant dangers to human civilization [56, 57]. The massive volume of solid tire wastes might offer many environmental impacts, such as igniting fire and viruses etc. [58]. Furthermore, steel, polymer fibers, and rubber particles could be recoverable through particular processing phases. As a result, there may be a method to efficiently recycle a large amount of discarded tires for utilization in cementitious composites worldwide [59].

VI. CONCLUSIONS

In this paper, a review has been done. The purpose of this research is to explore the use of natural fibers hybridization with artificial fibers in cementitious composites for sustainable construction. This paper will provide a brief summary about the benefits of using natural hybrid fibers for sustainable construction. Also, it will promote the potential use of hybrid fibers in cementitious composites. One of the most important research fields in engineering is the production of environmentally sustainable materials. Concrete is a high-demand material for the building and construction sector in civil engineering and related disciplines. By minimizing the environmental toxicity effect and natural resource scarcity caused by landfilled solid waste, the appropriate use of hybrid fibers in concrete obtained from natural resources may enhance the building industry's sustainability. The goal of the current review is to discuss the hybridization effect of synthetic fiber (polypropylene) with natural fibers for the flexure, compressive, and splitting tensile strengths of hybrid fiber reinforced cementitious composites. After a detailed literature review, it was found that the use of hybrid fibers in cementitious composites can improve the mechanical properties. Further, hybrid fiber reinforced cement based composites provide strong resistance to the formation and generation of cracks at different level as per their scale size. Hence, the addition of hybrid polypropylene fibers with natural fibers could be an alternate solution for minimizing dangerous environmental effects with cost effectiveness in construction industry. Further study should be carried out on the utilization of artificial fibers with natural fibers hybridization in cement based composites for improved mechanical behavior as well as reduction in environmental pollution and global warming by utilizing natural resources. It is suggested to investigate the durability of hybrid fibers as a concrete fiber reinforcement. Furthermore, the study on the overall pore shape and pore continuity of the hybrid fibers material for the concrete application need to be explored in future.

VII. ACKNOWLEDGMENTS

The author would like to thank Engr. Prof. Dr. Majid Ali for his kind support and guidance.

VIII. REFERENCES

[1] M. K. Yew, I. Othman, M. C. Yew, S. Yeo, and H. Mahmud, "Strength properties of hybrid nylon-steel and polypropylene-steel fibre-reinforced high strength concrete at low volume fraction," *International Journal of Physical Sciences*, vol. 6, pp. 7584-7588, 2011.

[2] E. Awwad, M. Mabsout, B. Hamad, M. T. Farran, and H. Khatib, "Studies on fiber-reinforced concrete using industrial hemp fibers," *Construction and Building Materials*, vol. 35, pp. 710-717, 2012.

[3] T. Lecompte, A. Perrot, A. Subrianto, A. Le Duigou, and G. Ausias, "A novel pull-out device used to study the influence of pressure during processing of cement-based material reinforced with coir," *Construction and Building Materials*, vol. 78, pp. 224-233, 2015.

[4] L. Yan, "Plain concrete cylinders and beams externally strengthened with natural flax fabric reinforced epoxy composites," *Materials and Structures*, vol. 49, pp. 2083-2095, 2016.

[5] P. Bordes, E. Pollet, and L. Avérous, "Nano-biocomposites: biodegradable polyester/nanoclay systems," *Progress in Polymer Science*, vol. 34, pp. 125-155, 2009.

[6] L. Yan, N. Chouw, and K. Jayaraman, "On energy absorption capacity, flexural and dynamic properties of flax/epoxy composite tubes," *Fibers and Polymers*, vol. 15, pp. 1270-1277, 2014.

[7] A. A. Azeez, K. Y. Rhee, S. J. Park, and D. Hui, "Epoxy clay nanocomposites–processing, properties and applications: A review," *Composites Part B: Engineering*, vol. 45, pp. 308-320, 2013.

[8] S. Yin, R. Tuladhar, F. Shi, M. Combe, T. Collister, and N. Sivakugan, "Use of macro plastic fibres in concrete: A review," *Construction and Building Materials*, vol. 93, pp. 180-188, 2015.

[9] A. Sadrmomtazi, B. Tahmouresi, and A. Saradar, "Effects of silica fume on mechanical strength and microstructure of basalt fiber reinforced cementitious composites (BFRCC)," *Construction and Building Materials*, vol. 162, pp. 321-333, 2018.

[10] A. Enfedaque, D. Cendón, F. Gálvez, and V. Sánchez-Gálvez, "Analysis of glass fiber reinforced cement (GRC) fracture surfaces," *Construction and Building Materials*, vol. 24, pp. 1302-1308, 2010.

[11] S. Fallah and M. Nematzadeh, "Mechanical properties and durability of high-strength concrete containing macro-polymeric and polypropylene fibers with nano-silica and silica fume," *Construction and building materials*, vol. 132, pp. 170-187, 2017.

[12] R. Abaeian, H. P. Behbahani, and S. J. Moslem, "Effects of high temperatures on mechanical behavior of high strength concrete reinforced with high performance synthetic macro polypropylene (HPP) fibres," *Construction and Building Materials*, vol. 165, pp. 631-638, 2018.

[13] H. A. Toutanji, "Properties of polypropylene fiber reinforced silica fume expansive-cement concrete," *Construction and Building Materials*, vol. 13, pp. 171-177, 1999.

[14] J. Wei and C. Meyer, "Degradation mechanisms of natural fiber in the matrix of cement composites," *Cement and Concrete Research*, vol. 73, pp. 1-16, 2015.

[15] N. Saba, M. Paridah, and M. Jawaid, "Mechanical properties of kenaf fibre reinforced polymer composite: A review," *Construction and Building materials*, vol. 76, pp. 87-96, 2015.

[16] L. Yan, N. Chouw, and K. Jayaraman, "Flax fibre and its composites–A review," *Composites Part B: Engineering*, vol. 56, pp. 296-317, 2014.

[17] D. Hannant, "Durability of polypropylene fibers in Portland cement-based composites: eighteen years of data," *Cement and Concrete Research*, vol. 28, pp. 1809-1817, 1998.

[18] A. Richardson, "Electrical properties of Portland cement, with the addition of polypropylene fibres–regarding durability," *Structural Survey*, 2004.

[19] D. Wang, Y. Ju, H. Shen, and L. Xu, "Mechanical properties of high performance concrete reinforced with basalt fiber and polypropylene fiber," *Construction and Building Materials*, vol. 197, pp. 464-473, 2019.

[20] S. Jalasutram, D. R. Sahoo, and V. Matsagar, "Experimental investigation of the mechanical properties of basalt fiber ‐ reinforced concrete," *Structural Concrete*, vol. 18, pp. 292-302, 2017.

[21] W. He, X. Kong, Y. Fu, C. Zhou, and Z. Zheng, "Experimental investigation on the mechanical properties and microstructure of hybrid fiber reinforced recycled aggregate concrete," *Construction and Building Materials*, vol. 261, p. 120488, 2020.

[22] E. A. Alwesabi, B. A. Bakar, I. M. Alshaikh, and H. M. Akil, "Experimental investigation on mechanical properties of plain and rubberised concretes with steel–polypropylene hybrid fibre," *Construction and Building Materials*, vol. 233, p. 117194, 2020.

[23] M. Ali and N. Chouw, "Coir fibre and rope reinforced concrete beams under dynamic loading," in *Annual Australian Earthquake Engineering Society Conference, "Newcastle Earthquake–20 years on*, 2009.

[24] M. Ali, "Use of coconut fibre reinforced concrete and coconut-fibre ropes for seismic-resistant construction," *Materiales de Construcción*, vol. 66, p. 073, 2016.

[25] M. Ali, "Seismic performance of coconut-fibre-reinforced-concrete columns with different reinforcement configurations of coconut-fibre ropes," *Construction and Building Materials*, vol. 70, pp. 226-230, 2014.

[26] M. Ali, "Role of post-tensioned coconut-fibre ropes in mortar-free interlocking concrete construction during seismic loadings," *KSCE Journal of Civil Engineering*, vol. 22, pp. 1336-1343, 2018.

[27] V. Afroughsabet and T. Ozbakkaloglu, "Mechanical and durability properties of high-strength concrete containing steel and polypropylene fibers," *Construction and building materials*, vol. 94, pp. 73-82, 2015.

[28] L. Betterman, C. Ouyang, and S. P. Shah, "Fiber-matrix interaction in microfiber-reinforced mortar," *Advanced Cement Based Materials*, vol. 2, pp. 53-61, 1995.

[29] N. Banthia, F. Majdzadeh, J. Wu, and V. Bindiganavile, "Fiber synergy in Hybrid Fiber Reinforced Concrete (HyFRC) in flexure and direct shear," *Cement and Concrete Composites*, vol. 48, pp. 91-97, 2014.

[30] P. Song, J. Wu, S. Hwang, and B. Sheu, "Statistical analysis of impact strength and strength reliability of steel–polypropylene hybrid fiber-reinforced concrete," *Construction and building materials*, vol. 19, pp. 1-9, 2005.

[31] A. A. Nia, M. Hedayatian, M. Nili, and V. A. Sabet, "An experimental and numerical study on how steel and polypropylene fibers affect the impact resistance in fiber-reinforced concrete," *International Journal of Impact Engineering*, vol. 46, pp. 62-73, 2012.

[32] M. Khan and M. Cao, "Effect of hybrid basalt fibre length and content on properties of cementitious composites," *Magazine of Concrete Research*, pp. 1-12, 2020.

[33] R. Ralegaonkar, H. Gavali, P. Aswath, and S. Abolmaali, "Application of chopped basalt fibers in reinforced mortar: A review," *Construction and building materials*, vol. 164, pp. 589-602, 2018.

[34] S. Spadea, I. Farina, A. Carrafiello, and F. Fraternali, "Recycled nylon fibers as cement mortar reinforcement," *Construction and Building Materials*, vol. 80, pp. 200-209, 2015.

[35] A. Izaguirre, J. Lanas, and J. I. Alvarez, "Effect of a polypropylene fibre on the behaviour of aerial lime-based mortars," *Construction and Building Materials*, vol. 25, pp. 992-1000, 2011.

[36] H. Zhong and M. Zhang, "Experimental study on engineering properties of concrete reinforced with hybrid recycled tyre steel and polypropylene fibres," *Journal of Cleaner Production*, p. 120914, 2020.

[37] F. Qamar, T. Thomas, and M. Ali, "Use of natural fibrous plaster for improving the out of plane lateral resistance of mortarless interlocked masonry walling," *Construction and Building Materials*, vol. 174, pp. 320-329, 2018.

[38] Z. Tang, M. Ali, and N. Chouw, "Residual compressive and shear strengths of novel coconut-fibre-reinforced-concrete interlocking blocks," *Construction and Building Materials*, vol. 66, pp. 533-540, 2014.

[39] M. U. Farooqi and M. Ali, "Contribution of plant fibers in improving the behavior and capacity of reinforced concrete for structural applications," *Construction and Building Materials*, vol. 182, pp. 94-107, 2018.

[40] T. Hussain and M. Ali, "Improving the impact resistance and dynamic properties of jute fiber reinforced concrete for rebars design by considering tension zone of FRC," *Construction and Building Materials*, vol. 213, pp. 592-607, 2019.

[41] M. Khan, M. Cao, and M. Ali, "Cracking behaviour and constitutive modelling of hybrid fibre reinforced concrete," *Journal of Building Engineering*, vol. 30, p. 101272, 2020.

[42] Z. Deng, X. Liu, X. Yang, N. Liang, R. Yan, P. Chen, *et al.*, "A study of tensile and compressive properties of hybrid basalt ‐ polypropylene fiber ‐ reinforced concrete under uniaxial loads," *Structural Concrete*, vol. 22, pp. 396-409, 2021.

[43] E. Palanisamy and M. Ramasamy, "Dependency of Sisal and Banana Fiber on Mechanical and Durability Properties of Polypropylene Hybrid Fiber Reinforced Concrete," *Journal of Natural Fibers*, pp. 1-11, 2020.

[44] H. Huang, Y. Yuan, W. Zhang, and L. Zhu, "Experimental study on the mechanical properties and the microstructure of hybrid ‐ fiber ‐ reinforced concrete under an early stage," *Structural Concrete*, vol. 21, pp. 1106-1122, 2020.

[45] N. K. Singh and B. Rai, "Assessment of synergetic effect on microscopic and mechanical properties of steel ‐ polypropylene hybrid fiber reinforced concrete," *Structural Concrete*, vol. 22, pp. 516-534, 2021.

[46] F. Shi, T. M. Pham, H. Hao, and Y. Hao, "Post-cracking behaviour of basalt and macro polypropylene hybrid fibre reinforced concrete with different compressive strengths," *Construction and Building Materials*, vol. 262, p. 120108, 2020.

[47] Z. Deng, X. Liu, X. Yang, N. Liang, R. Yan, P. Chen, *et al.*, "A study of tensile and compressive properties of hybrid basalt ‐ polypropylene fiber ‐ reinforced concrete under uniaxial loads," *Structural Concrete*, 2020.

[48] B. Sisson and C. Van Aerschot, "Energy Efficiency Buildings: Business realities and opportunities," *World Business Council for Sustainable Development (WBCSD)*, 2008.

[49] U. Sbci, "Buildings and climate change: Summary for decision-makers," *United Nations Environmental Programme, Sustainable Buildings and Climate Initiative, Paris*, pp. 1-62, 2009.

[50] C. Say and A. Wood, "Sustainable rating systems around the world," *Council on Tall Buildings and Urban Habitat Journal (CTBUH Review)*, vol. 2, pp. 18-29, 2008.

[51] F. Smith Peter, "Architecture in a Climate of Change, A guide to sustainable design. ed," ed: ArchitectUral Press, Oxford, 2005.

[52] A. Sev, "A comparative analysis of building environmental assessment tools and suggestions for regional adaptations," *Civil Engineering and Environmental Systems*, vol. 28, pp. 231-245, 2011.

[53] M. Mastali, A. Dalvand, A. Sattarifard, Z. Abdollahnejad, and M. Illikainen, "Characterization and optimization of hardened properties of self-consolidating concrete incorporating recycled steel, industrial steel, polypropylene and hybrid fibers," *Composites Part B: Engineering*, vol. 151, pp. 186-200, 2018.

[54] O. Onuaguluchi and N. Banthia, "Scrap tire steel fiber as a substitute for commercial steel fiber in cement mortar: engineering properties and cost-benefit analyses," *Resources, Conservation and Recycling*, vol. 134, pp. 248-256, 2018.

[55] K. Liew and A. Akbar, "The recent progress of recycled steel fiber reinforced concrete," *Construction and Building Materials*, vol. 232, p. 117232, 2020.

[56] B. S. Thomas and R. C. Gupta, "A comprehensive review on the applications of waste tire rubber in cement concrete," *Renewable and Sustainable Energy Reviews*, vol. 54, pp. 1323-1333, 2016.

[57] J. Wang, Q. Dai, R. Si, and S. Guo, "Mechanical, durability, and microstructural properties of macro synthetic polypropylene (PP) fiber-reinforced rubber concrete," *Journal of Cleaner Production*, vol. 234, pp. 1351-1364, 2019.

[58] H. Zhong, E. W. Poon, K. Chen, and M. Zhang, "Engineering properties of crumb rubber alkali-activated mortar reinforced with recycled steel fibres," *Journal of Cleaner Production*, vol. 238, p. 117950, 2019.

[59] S. Gigli, D. Landi, and M. Germani, "Cost-benefit analysis of a circular economy project: a study on a recycling system for end-of-life tyres," *Journal of Cleaner Production*, vol. 229, pp. 680-694, 2019.

Treatment of Natural Fibers for Improving Cement Composites Behavior-An Overview

Sami Ullah
MS Student at Department of Civil Engineering
Capital University of Science and Technology
Islamabad, Pakistan
samiullahktk426@gmail.com

Majid Ali
Professor at Department of Civil Engineering
Capital University of Science and Technology
Islamabad, Pakistan
professor.drmajid@gmail.com

Abstract

Fiber-reinforced concrete (FRC) provides a convenient, practical and economical solution for reducing the microcracks and other similar types of deficiencies to enhance the properties of concrete. Natural fibers have a rough surface and absorb water, which decreases the strength of concrete with the passage of time. The improving of the natural fiber properties is necessary to enhance the surface of the fibers, reduce water absorption of the fibers and enhance the strengthening properties like flexural strength and ductility, etc. which intern enhance the properties of composites. For this purpose, different types of treatment techniques are used on natural fibers for improving their surface and enhance the properties of fiber-reinforced composites. In this paper different papers studies about the properties of natural fibers, the use of natural fibers in composites, treatment techniques used for enhancing the properties of the natural fibers, and effects of the treatment techniques on natural fiber for improving the composite behavior. To achieve these goals, the treatment techniques used on natural fibers to smooth the surface of the natural fibers and make fiber resist the absorption of water. The treatment techniques used for this purpose are chemical, physical, and surface treatment to improve the properties of the natural fiber and make the fiber more durable and sustainable than the non-treated natural fibers. The different treatment techniques of fibers used not only improve the contact between fiber and concrete but also increase the natural fiber's strength as well as reduce the water-absorbing capacity of concrete and mechanical properties of natural fibers increased which clearly show the enhancement of the behavior of the composite using treated natural fibers in the composites.

Keywords: *Natural fibers reinforced concrete, treatment techniques of natural fiber, enhance properties, reduce water absorption.*

I. INTRODUCTION

Pakistan is one of the amongst developing countries where natural fibers are abundantly available. The utilization of natural fibers for use in concrete has great interest nowadays, which making economical materials for infrastructure. The natural fibers like wheat straw etc. before used in clay works as well for reducing the number of cracks and cracks width in clay for use in houses and increase the contact on the wall as well as the ground. Nowadays the natural fibers used in concrete increase the properties of concrete as they are abundantly available at a very low cost [1]. The replacement of man-made fibers in concrete by natural fibers reduces the environmental problem as well as reduces the cost of concrete and improves the properties of concrete as like man-made fibers [2].

Fiber-reinforced composites play important role in Civil Engineering applications because of their efficient strength, high modulus, and reduced carbon content in the environment. Natural fiber from coir, oil palm, sisal, banana, jute, bamboo, rice husk, and kenaf, etc. are environmentally friendly materials that proved to be good reinforcement reducing the density and cost of the composites [3]. Natural fiber-reinforced composites have high corrosion and impact resistance, low maintenance requirements, and non-conductive. Different types of Fibers used as reinforcement material in concrete were glass, carbon, aluminum oxide, and Natural fibers, especially flax, hemp, jute, henequen, and many others were applied by researchers as fiber reinforcement in concrete.

Natural fibers used in concrete have low density, low cost, recyclable and biodegradable [4]. The mechanical properties of natural fibers are good and can compete with other types of fibers in strength and modulus. Natural fiber can be used in concrete for improving the properties of concrete and reduced the cost as well as reduce environmental problems [5]. The natural fiber also reduces microcrack, shrinkage cracks, and also increases the strength of the composites-like synthetic, artificial, and other man-made fibers. However, replacing other kinds of fibers with natural fibers, which take time, using cost for producing give economical solution to prepare fiber reinforced concrete. The main advantages of using natural fibers in composites are the environmental aspect as natural fibers absorb carbon content from the air especially plant fibers. The pineapple leaf (PALF) which has good flexural and tensile properties can be useful for construction and automotive industries [6].

This paper gives information about the different types of natural fibers using in composites for enhancing the composite behavior, using the treatments techniques for natural fibers for improving composite behaviors. For this purpose, different papers studied natural fiber using in composites, treatment techniques used for natural fibers, and their effects on natural fibers. The different techniques used for natural fiber commonly are physical, chemical, and physiochemical treatment techniques which depend on the fiber types, required properties of the fibers to be achieved. This paper

IEECP'21, July 29-30, 2021, Silicon Valley, San Francisco, CA – USA

DAI : *https://sci-index.com/DAI/2021.99101/IEECP/14811840*

basically about the need for treatment of fibers, types of treatment using and their effects on the behavior of composites.

II. USE OF NATURAL FIBERS IN CEMENT COMPOSITES

Natural fiber using in concrete and plaster, which improve the sustainability of the composite at low cost and abundantly available in many countries especially plant-based fibers [7]. The researchers utilizing natural fibers in construction to reduce waste, improve the construction material properties, and get low-cost construction materials. For improving the dynamic properties and impact resistance of concrete panels jute fiber is used as a reinforcing material, which improves properties and reduces the steel reinforcement up to 30% [8]. Some natural fibers like wheat straw were also used in concrete which shows enhance flexural strength up to 7.5%, toughness indices 11.1%, and energy absorption up to 30.4% [9]. The natural fibers were used in concrete for the road with a content of silica fume which enhances the mechanical properties and results in the reduction of road thickness up to 8% [10]. Types of fibers show in figure 01 below.

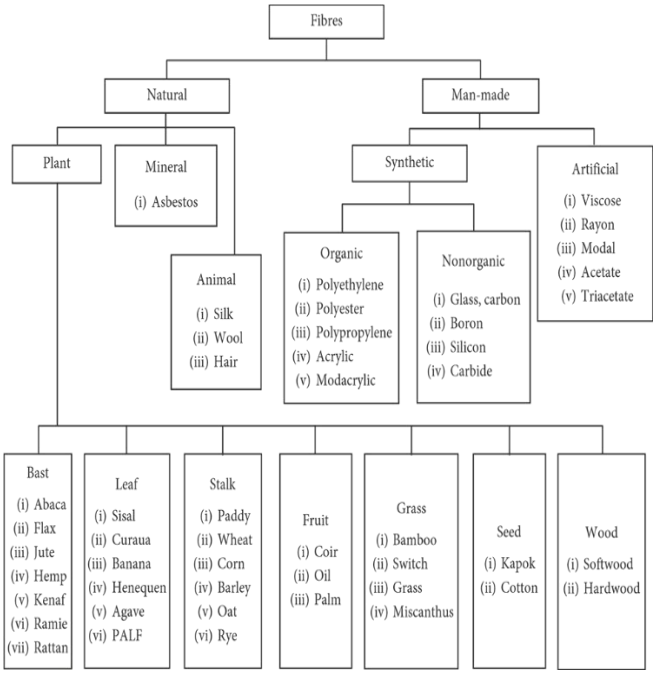

Figure 01: Fiber Classifications [11]

Natural fibers are used in plaster as well which effectively show lateral resistance of the mortarless interlocking masonry structures like sisal fiber and rice straw fibers [12]. A lot of work done on coconut fibers for use in concrete to enhance the properties of concrete and uses the ropes of coconut fiber as well in structural members which show improve in the lateral resistance of the structural members and improve dynamic properties of the structural members effectively [13]–[17]. Nowadays research work in progress on hybrid fibers which show better performance than the single fiber used in concrete to improve the fiber reinforced concrete properties and reduce cracks propagations [18]. The fibers using concrete enhance the properties like toughness indices, flexural strength, tensile strength and reduces wasting of materials as well as reduces cracks and cracks propagation of the fiber-reinforced concrete.

III. CHARACTERISTICS OF NATURAL FIBERS

The natural fibers are obtained from the product that is used, it is a waste material obtained from the waste of the product, and their use in concrete as fiber-reinforced concrete gives an economic solution for improving the concrete properties [19]. The natural fibers have low durability as they deteriorate in the alkaline cement matrix due to erosive behavior [20]. Table number 01 shows the chemical composition of the natural fibers as shown below.

Table 1. Chemical composition of Common Natural Fibers [21]

Fiber	Cellulose (%)	Lignin (%)	Hemicellulose (%)	Pectin (%)	Ash (%)
Fiber Flax	71	2.2	18.6 - 20.6	2.3	-
Seed Flax	43-47	21-23	24 - 26	-	5
Kenaf	31-57	15-19	21.5 - 23	-	2-5
Jute	45-71.5	12-26	13.6 - 21	0.2	0.5-2
Hemp	57-77	3.7-13	14 – 22.4	0.9	0.8
Ramie	68.6-91	0.6-0.7	5 - 16.7	1.9	-
Abaca	56-63	7-9	15 - 17	-	3
Sisal	47-78	7-11	10 - 24	10	0.6-1
Henequen	77.6	13.1	4 - 8	-	-

The chemical composition of common natural fibers shown in table number 01 which contain different content on different proportions. The treatment techniques improve not only the surface of the fiber but also enhances the chemical composition of the natural fibers. The treatment technique type using for natural fiber treatment depends on the type of fibers or chemical composition of the fiber as well to enhance the properties of the fiber to required or up to some level.

IV. TREATMENT TECHNIQUES USED

As natural fibers used in concrete have a rough surface, which causes a weakness in the bond between fiber and matrix. The natural fiber has water absorption capacity which tends to deteriorate the composite with the passage of time. The untreated natural fiber has low durability, sustainability, weak bond, and corrosive nature. To enhance the properties of fiber-reinforced concrete different treatment techniques of surface improving are used, which include physical treatments, chemical treatments, and physicochemical treatment techniques to modify the natural fiber surface and improve the desired properties of fibers. These treatment techniques are used mostly for the plant fibers to enhance their properties and to increase the life of the composite. These fiber treatment techniques are necessary to enhance the strength properties of the fibers and improve the durability of the fiber which in result will enhance the properties of the fiber-reinforced concrete. The different treatment techniques used for modification of natural fibers are followings. As can see different treatment techniques are using for fiber to improve the properties of the fibers. The technique selected for fiber treatment depends on the fiber properties improving and types of fiber. The most common techniques using are Physical treatment,

Chemical treatment, and Physiochemical treatment which are selected on the basis of fiber type and required properties to achieve.

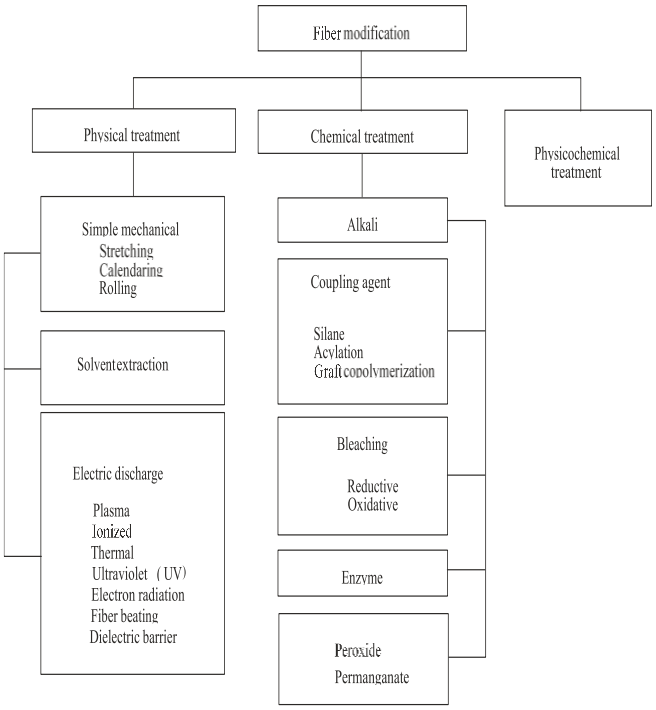

Figure 02: Fiber Modifications [11]

A. *Physical Treatment*

The physical treatment technique used for natural fibers can change the surface and structural characteristics of natural fibers, improve thermal properties as well as the mechanical bonding of the concrete without affecting the chemical characteristics of natural fibers. These treatment techniques are implemented on natural fibers only to separate the bundle of fiber into a single filament to improve their surface and other properties for composite applications. Physical treatment includes solvent extraction, simple mechanical and electric discharge techniques.

B. *Chemical Treatment*

The chemical treatment technique is used for the purpose of changing and activate the natural fiber structure by using a hydroxyl group, which modifies the composition of the fiber with a new element to connect with the matrix. By using chemical treatment techniques for the fiber modification increase the mechanical properties of the fiber and adhesion of the fiber for increasing the bonding of the fiber in composites and reducing the water absorption capacity of concrete. Chemical treatment includes Alkali, coupling agent, enzymes, and peroxide techniques.

C. *Physiochemical Treatment*

The physicochemical treatment technique is a combination of both physical and chemical treatment techniques. This technique has an advantage on physical and chemical techniques using separately because it is the combination of both techniques to support the chemical reaction as well as separate the bundle into filaments. This type of treatment provides high quality of fibers and these fibers have good mechanical properties and show significant improvement in mechanical properties of fibers.

V. EFFECTS OF TREATMENT OF NATURAL FIBERS ON COMPOSITE BEHAVIOR

The method used on natural fibers of surface treatment shows improvement in mechanical properties of concrete such as tensile, compressive, and flexural strength of the natural fibers as well as enhance the durability and sustainability of natural fibers as compared to untreated natural fibers. The bamboo fiber was treated with Ca $(OH)_2$ for the reinforced cement composite which enhances the properties of fiber and increases the flexural strength of the composite up to 40% after 90 days of curing period the untreated fibers [22]. The Kenaf fiber used in cement treated sandy soil was efficiently shown in enhancing the properties like unconfined compressive strength, splitting tensile strength, and decrease the brittle indices, modulus of elasticity, and ultrasonic wave velocity [23]. The treated coir fiber of 1% and pond ash 10% used with 4% of cement content in the cement-stabilized clay which enhances the unconfined compressive strength 3.72 times and split tensile strength 3.83 times while reducing the stiffness and brittle behavior of the composite change to ductile behavior [24]. Treated Hemp Fiber Reinforced Composite (THFRC) and untreated Hemp Fiber Reinforced Composite (UHFRC) properties are shown in table number 02.

Table 2. Effects of treatment on properties of Hemp Fiber [25]

Type of Fiber	Age (days)	Flexural Load (N) p_{max}	Modulus of Elasticity E(MPa)
UHFRC	14	1,907	17,584
	28	2,325	20,481
THFRC	14	2,158	17,015
	28	2,488	18,279

From table 02 it can be seen that the load sustained by THFRC is 7-13% more than the UHFRC while the modulus of elasticity of THFRC is 3-11% less than the UHFRC. This means that the flexural strength ductility of the composite increased by treating the hemp fibers. The flexural strength and ductility of the coconut fiber-reinforced composites also increased by treating the coconut fibers [26].

VI. CLEANER PRODUCTION

Cleaner production is basically the process of product and production process which focuses on utilizing the natural resources to minimize the waste generated. The utilization of natural resources like natural fibers in composites gives a better solution for reducing waste. As waste pollution is a major issue in many developing especially in Asia's countries. This waste of the natural fibers can be reduced by using the natural fibers in composite like in concrete, plaster. As natural fibers improving the properties of the composite like flexural strength, durability, ductility, and reducing the number of cracks as well as the propagation of the cracks of the composites. So, utilizing the natural fibers in composite gives a better solution for reducing waste pollution.

VII. CONCLUSION

The treated natural fibers used in composites show improvement in the behavior of the composites as compared to using untreated natural fibers. It has been observed from the review of the papers that treatment techniques used for natural fibers improve the

strength of the fibers, improve water absorption resistance of the fibers, and improve durability as well as the ductility of the composites. The selected treatment techniques depend upon the natural fiber type and the required properties of the fibers to be improved. The utilization of natural fibers reducing waste pollution as well which a major issue in many developing countries.

The following conclusion is made from the treatment of fibers

1. Treatment techniques used on natural fiber increase the quality of NF for use in concrete.
2. Treatment techniques of natural fiber increase the bonding strength of fiber and matrix.
3. Treatment techniques of natural fiber increase the durability as well as the sustainability of fibers.
4. Treatment techniques of natural fiber reduce water absorption of the fiber.

The replacement of man-made fibers in concrete with natural fibers has great potential nowadays. The natural fibers using in concrete reduce environmental problems and well as it has very low cost and economical which abundantly available. As the treatment techniques using on natural fibers improve the quality of fibers and enhance their mechanical properties of natural fibers. The bonding strength of fiber and matrix is also enhanced by treatment of NF as well as improving the durability and sustainability of NF. As the natural fiber has the capacity of absorbing water which can be reduced by the treatment of fibers. The physicochemical treatment is getting intention then using separately physical or chemical because it shows that it improves both physical as well as chemical properties of natural fibers. Natural Fiber as fiber-reinforced concrete will be very useful for utilizing to avoid waste pollution caused by natural fibers and enhance the concrete properties.

VIII. ACKNOWLEDGMENTS

The authors would like to acknowledge all organizations/persons who have helped in this literature research.

IX. REFERENCES

[1] Azam Ali, Khubab Shaker, Yasir Nawab, Madeha Jabbar, Tanveer Hussain, Jiri Milky, Vijay Baheti, “Hydrophobic treatment of natural fibers and their composites—A review”, Journal of industrial textiles, Sage, 2016.

[2] Mohit Sood, Gaurav Dwivedi, “Effect of fiber treatment on flexural properties of natural fiber-reinforced composites, A Review”, Egyptian Journal of petroleum, Elsevier, 2017.

[3] Adewale George Adeniyi, Damilola Victoria Onifade, Joshua O. Ighalo, Akorede Samson Adeoye, “A review of coir fiber reinforced polymer composites”, Composites part-B: Engineering, Elsevier, 2019.

[4] Libo Yan, Shen Su, Nawawi Chouw, “Microstructure, flexural properties and durability of coir fiber reinforced concrete beams externally strengthened with flax FRP composites”, Composites part-B: Engineering, Germany, Elsevier, 2015.

[5] M.A. Aziz, P. Paramasivam, and S. L. Lee, “Prospects for natural fiber reinforced concrete in construction”, The international journal of cement composites and lightweight concrete, Singapore, 1981.

[6] S.Sathees Kumar, R.Muthalagu, CH. Nithin Chakravarthy, “Effects of fiber loading on mechanical characterization of pineapple leaf and sisal fibers reinforced polyester composites for various applications”, Materials Today: Proceedings, Elsevier, 2020.

[7] Obinna Onuaguluchi, Nemkumar Banthia, “Plant-based natural fiber reinforced cement composites: A review”, Cement and Concrete Composites, Canada, Elsevier, 2016.

[8] Tasaddaq Hussain, Majid Ali, “Improving the impact resistance and dynamic properties of jute fiber reinforced concrete for rebars design by considering tension zone of FRC”, Construction and Building Materials, Elsevier, 2019.

[9] Muhammad Usman Farooqi, Majid Ali, “Contribution of plant fibers in improving the behavior and capacity of reinforced concrete for structural applications”, Construction and Building Materials, Elsevier, 2018.

[10] Mehran Khan, Abdul Rehman, Majid Ali, “Efficiency of silica-fume content in plain and natural fiber reinforced concrete for the concrete road”, Construction and Building Materials, Elsevier, 2020.

[11] R. Ahmad, R. Hamid, S. A. Osman, “Physical and Chemical modification of plant fibers for reinforcement in cementitious composites”, Advances in Civil Engineering, Hindawi, 2019.

[12] Furqan Qamar, Terence Thomas, Majid Ali, “Use of natural fibrous plaster for improving the out-of-plane lateral resistance of mortarless interlocked masonry walling”, Construction and Building Materials, Elsevier, 2018.

[13] Majid Ali, “Seismic performance of coconut-fiber-reinforced-concrete columns with different reinforcement configurations of coconut-fiber ropes”, Construction and Building Materials, Elsevier, 2014.

[14] Majid Ali, “Use of coconut fiber reinforced concrete and coconut-fiber ropes for seismic-resistant construction”, Materiales De Construccion, 2016.

[15] Majid Ali, “Role of Post-tensioned Coconut-fibre Ropes in Mortar-free Interlocking Concrete Construction During Seismic Loadings”, KSCE Journal of Civil Engineering, 2017.

[16] Majid Ali, and Nawawi Chouw, “Coir Fibre and Rope Reinforced Concrete Beam Under Dynamic Loading”, Department of Civil and Environmental Engineering, the University of Auckland, New Zealand.

[17] Zhenghao Tang, Majid Ali, Nawawi Chouw, “Residual compressive and shear strengths of novel coconut-fiber-reinforced-concrete interlocking blocks”, Construction and Building Materials, Elsevier, 2014.

[18] Luca Sorelli, Nemkumar Banthia, Giovanni Plizzari, “Constitutive Modeling of Hybrid Fiber Reinforced Concrete”.

[19] J.M.L Reis, Fracture and flexural characterization of natural fiber-reinforced polymer concrete, Construction and Building Materials, Elsevier, 2006.

[20] Jianqiang Wei, Christian Meyer, “Improving degradation resistance of sisal fiber in concrete through fiber surface treatment”, Applied surface science, New York: Elsevier, 2013.

[21] Xue Li, Lope G. Tabil, Satyanarayan Panigrahi, “Chemical treatment of natural fiber for use in natural fiber-reinforced composites: A review”, Journal of polymers and the Environment, Springer, 2007.

[22] Luz Adriana Sanchez-Echeverri, Jorge Alberto Medina-Perilla, and Eshmaiel Ganjian, “Nonconventional Ca(OH)2 treatment of bamboo for the reinforcement of cement composites”, Materials, Colombia, MDPI, 2020.

[23] Moein Ghadakpour, Asskar Janalizadeh Choobbasti, and Saman Soleimani Kutanaei, “Investigation of the kenaf fiber hybrid length on the properties of the cement-treated sandy soil”, Transportation Geotechnics, Iran, Elsevier, 2019.

[24] Jitendra Singh Yadav, Suresh Kumar Tiwari, “Behavior of cement stabilized treated coir fiber-reinforced clay-pond ash mixtures”, Journal of Building Engineering, Elsevier, 2016.

[25] Xianming zhou, Harmeet Saini, Gediminas Kastiukas, “Engineering properties of treated natural hemp fiber-reinforced concrete”, Frontier Built Environment, 2017.

[26] Vivi anggraini, Afshin Asadi, Agusril Syamsir, Bujang B.K. Huat “Three-point bending flexural strength of cement-treated tropical marine soil reinforced by lime treated natural fiber”, Measurement, Malaysia, Elsevier, 2017.

Numerical Modeling of Heat Flow of Kangding Area with New Borehole Data for Purpose of Geothermal Resources Development Evaluation

Chao Zhang
Key Laboratory of Ministry of Education on Safe Mining of Deep Metal Mines
Northeastern University
ShenYang, China
chaozhan2017@foxmail.com

Ming Wu
Key Laboratory of Ministry of Education on Safe Mining of Deep Metal Mines
Northeastern University
ShenYang, China
754359418@qq.com

ZaoBao Liu*
Key Laboratory of Ministry of Education on Safe Mining of Deep Metal Mines
Northeastern University
ShenYang, China
liuzaobao@mail.neu.edu.cn

Abstract

Terrestrial heat flow is a surface indicator of potential geothermal resources in depth, and its measurement and compilation are important for evaluating the merits of geothermal resources. The Kangding area locates in the western Sichuan Province of China where regional thermal fractures develops showing good potential for geothermal energy development but with barely precise heat flow data. We collect the borehole temperature data from the geological survey report of the Sichuan-Tibet Railway that passes through the Kangding area where geothermal survey data are in lack. In total, 50 sets of high-quality data are compiled. The average heat flow in the study area is calculated as $86.96 \pm 39.73\ mW/m^2$, which fills the gap of heat flow data in Western Sichuan. With the obtained heat flow data incorporating into the heat flow database, the regional heat flow is numerically studied by the Kriging interpolation method to obtain the map of the geothermal flow in Sichuan Province. A preliminary assessment of the exploitation of geothermal energy resources is finally made in the Kangding area of western Sichuan. The results indicates that Kangding area has the good potential for geothermal exploitation.

Keywords: Terrestrial Heat Flow; Kriging interpolation; geothermal energy in Kangding area; Sichuan-Tibet railway;

I. INTRODUCTION

As a new type of clean energy, geothermal energy resources have environmental and economic advantages over conventional energy sources[1]. China has abundant reserves of geothermal energy resources, of which hydrothermal geothermal resources are equivalent to 1,250 billion tons of standard coal, and the reserves of dry hot rock resources are equivalent to 856 trillion tons of standard coal [2]. According to the evaluation results of geothermal energy resources in mainland China by Guocheng Ren et al. [3], hot dry rock resources at a depth of 3~10km in mainland China total 21×106EJ. If calculated by 2% of the exploitable resources, it is traditional Hydrothermal geothermal energy resources are 16.8 times, approximately equivalent to 4,400 times the total energy consumption of mainland China in 2010.

As an important transportation and tourist route for Sichuan-Tibet Highway and Sichuan-Tibet Railway, Ganzi Prefecture of Sichuan Province has abundant geothermal energy reserves. According to the summary of previous work, there are 264 hot spring spots and 17 geothermal wells in the prefecture [4]. Geothermal energy resources in the form of high-temperature steam and underground hot water can provide a wide range of uses for local tourism, heating, power generation, agricultural planting, etc.

However, the current assessment of the distribution of geothermal energy reserves in Western Sichuan mainly relies on existing hot spring spots and geothermal wells. Spatial distribution characteristics, the resulting evaluation results only have a certain reference value for the surrounding areas of the existing data points, and no research has been conducted to evaluate the regional distribution characteristics of geothermal energy resources in western Sichuan. The main reasons are: sparsely populated areas in western Sichuan, inconvenient transportation, and low local utilization of geothermal energy resources, resulting in a lack of data related to geothermal energy.

This paper supplements the existing heat flow database based on the 50 sets of borehole temperature measurement data screened and calculated based on the borehole temperature measurement data of the Kangding Formation of the Linzhi to Ya'an section of the newly built Sichuan-Tibet Railway, and combined the existing data to draw the Terrestrial Heat Flow map of the Kangding area. An assessment of the regional distribution of geothermal energy and heat storage in Kangding County and surrounding areas in Ganzi Prefecture will lay the foundation for the future development of the geothermal energy industry in this region.

II. OVERVIEW

The Ganzi Prefecture is located in the eastern part of the Qinghai-Tibet Plateau and belongs to the Tethys tectonic domain. Due to the convergence-collision-orogeny of the Indian and Eurasian plates, many lithospheric-scale strike-slip, thrust fault zones and volcanic island arcs have been formed. The average altitude is above 4000m in the plateau area [4]. Frequent geological tectonic movements have made the Ganzi area rich in geothermal resources [5].

There are 264 hot spring spots and 17 geothermal wells in Ganzi Prefecture, including 35 hot springs and 13 geothermal wells in Kangding County (the highest water vapor temperature at the well head reaches 198°C), which has high utilization potential.

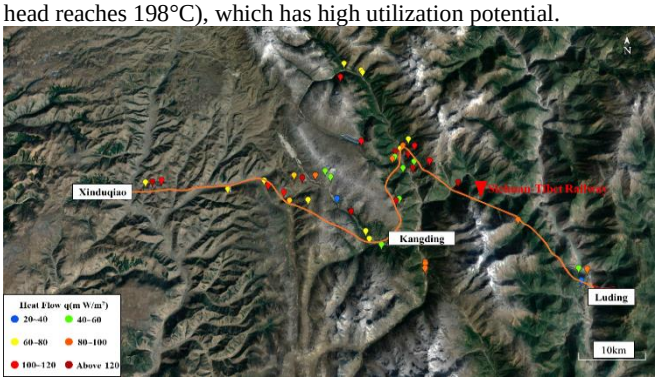

Figure 1 Geographical distribution map of newly increased Terrestrial Heat Flow measurement point

IEECP'21, July 29-30, 2021, Silicon Valley, San Francisco, CA – USA

DAI : *https://sci-index.com/DAI/2021.99101/IEECP/14899509*

The new Kangding area of the Nyingchi-Ya'an section of the Sichuan-Tibet Railway is a key control project of the Sichuan-Tibet Railway. During the survey and design stage, a lot of survey work has been done along the line. Therefore, multiple sets of borehole temperature measurement data have been obtained, which is not only for the safety construction of the Sichuan-Tibet Railway, but also provides a data source for understanding the distribution of geothermal energy resources along the line. Figure 1 shows the geographical distribution of new boreholes with temperature measurement.

III. BOREHOLE TEMPERATURE MEASUREMENT AND HEAT FLOW DATA IN KANGDING AREA

The ground heat flow value is defined as the heat flow value through a unit area of the earth's surface per unit time, which is a necessary parameter for evaluating the potential of geothermal energy resources [6]. The study of China's Terrestrial Heat Flow began in the 1960s when Shanfeng Yi reported three heat flow data in the Northeast Mesozoic basin. In 1979, the Geothermal Group of the Institute of Geology of the Chinese Academy of Sciences officially announced the first batch of 25 Terrestrial Heat Flow data [7]. Wang Jiyang et al. [7-10] successively summarized and updated heat flow data in mainland China, and up to now a total of 1230 sets of heat flow data have been collected.

The China Terrestrial Heat Flow Database ((http://chfdb.xyz/) produced by the Geothermal Resources Research Center of the Institute of Geology and Geophysics, Chinese Academy of Sciences (http://chfdb.xyz/) compiles all currently publicly published data of China's Terrestrial Heat Flow, and the distribution of existing heat flow data in Sichuan Province (see Figure 2) are mainly distributed in the eastern and southern regions of Sichuan. There are very few data in the northern part and no data in the western part.

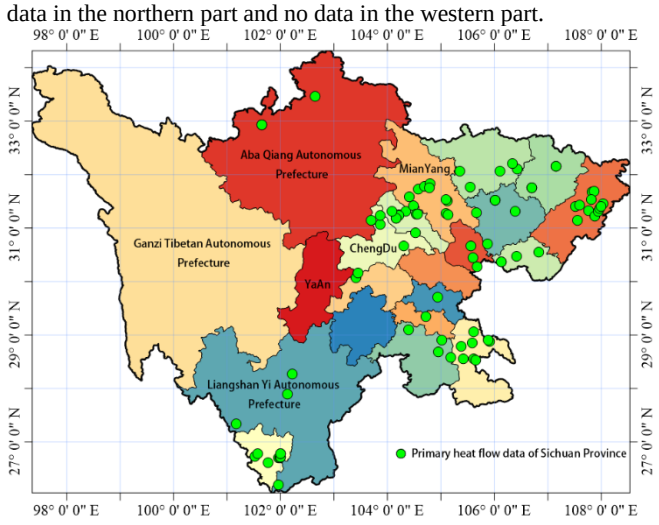

Figure 2. Distribution of existing heat flow data in Sichuan Province

The existing 89 sets of heat flow data in Sichuan Province (see Figure 3) meet the characteristics of normal distribution. The minimum, the maximum, and the average heat heat flow values are respectively 27.4 mW / m^2 , 94.7 mW / m^2 , and 53.75 ± 12.24 mW / m^2 . Compared with the 4th edition of the statistical results of heat flow in mainland China [7] with average of 61.5 ± 13.9 mW / m^2 , the average of this area is smaller, indicating that the existing heat flow data belong to the middle and low heat flow areas. The high-temperature hot water activity in western Sichuan is rich in geothermal resources, but the utilization rate is less than 8% [11].

On one hand, it is because of inconvenient transportation and sparsely populated people. On the other hand, it is mainly due to the lack of geothermal drilling information. The present research data is mainly derived from the central, eastern, and southern regions of Sichuan province. As consequence, it is impossible to accurately quantify the Terrestrial Heat Flow in the western Sichuan region so as to evaluate the geothermal energy storage.

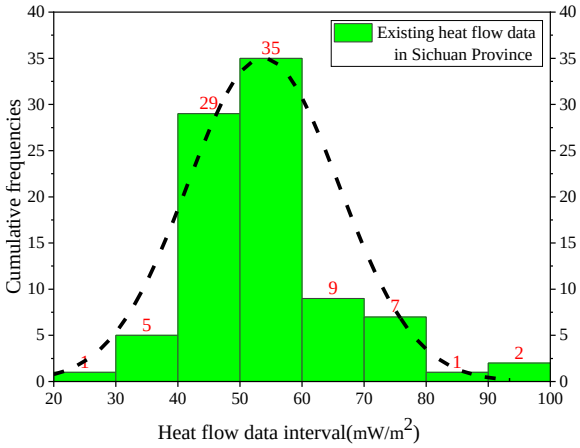

Figure 3. Bar statistics of existing heat flow data in Sichuan Province

The values of the borehole geothermal gradient and rock thermal conductivity are based on the field test results. For a single formation, the relationship between the Terrestrial Heat Flow value and the geothermal gradient and rock thermal conductivity is:

$$q = k\frac{dT}{dx} \tag{0.1}$$

where q is the earth heat flow value, k is the thermal conductivity of the rock, and dT/dx is the geothermal gradient;

Considering the complexity and diversity of actual engineering geology, the stratum in the borehole cannot be single. The rock thermal conductivity can be calculated according to the weighted average of the thickness of different rock layers in the borehole.

$$k = \sum_i k_i \frac{H_i}{H} \tag{0.2}$$

For a set of borehole temperature measurement data, k_i is the thermal conductivity of the rock, H_i is the stratum thickness, and H is the borehole depth.

The value of rock thermal conductivity refers to the empirical values provided in the "Code for Geological Survey of Geothermal Resources" (GB/T 11615-2010) [12], as shown in Table 1.

Table 1 Rock thermal conductivity

Rock name	Thermal conductivity(W/m℃)
granite	2.721
Limestone	2.010
sandstone	2.596
Sandy clay	0.921

Using the above formula, filtering and calculating on-site data can get 50 sets of heat flow data as shown in Table 2.

Table 2 Newly added Sichuan heat flow data in this article

Numbering	longitude	latitude	Heat flow value（mW/m^2）
1	102°12'25.20"	29°55'50.88"	37.80
2	101°56'02.40"	30°05'59.28"	40.50
3	101°55'31.44"	29°59'22.92"	72.90
4	101°38'39.84"	30°03'49.32"	62.10
5	101°55'15.24"	30°07'03.72"	48.60
6	101°51'52.92"	30°08'28.68"	62.10
7	101°48'13.32"	30°05'25.08"	43.20
8	101°47'15.72"	30°05'03.48"	81.00
9	101°45'57.96"	30°04'50.16"	162.00
10	101°45'09.36"	30°05'04.56"	81.00
11	101°42'36.72"	30°04'12.00"	110.00
12	101°49'22.80"	30°02'52.44"	34.56
13	102°13'18.48"	29°56'44.16"	86.50
14	102°12'26.64"	29°56'48.48"	42.39
15	102°06'56.88"	30°00'59.76"	86.40
16	102°01'30.00"	30°04'39.36"	180.90
17	101°58'40.44"	30°06'32.04"	116.30
18	101°56'38.76"	30°07'21.36"	133.00
19	101°57'16.92"	30°08'04.56"	115.00
20	101°56'43.44"	30°08'49.20"	64.80
21	101°56'08.88"	30°08'13.56"	83.70
22	101°57'12.24"	30°06'39.24"	32.40
23	101°57'03.24"	30°06'02.88"	170.10
24	101°55'53.40"	30°08'00.60"	67.50
25	101°55'21.72"	30°07'50.88"	197.10
26	101°54'59.40"	30°06'49.32"	97.20
27	101°55'09.12"	30°02'42.00"	175.50
28	101°55'27.48"	30°02'53.88"	51.30
29	101°46'34.32"	30°02'40.92"	62.10
30	101°44'09.60"	30°03'32.40"	110.70
31	101°52'06.96"	29°59'58.92"	74.25
32	101°52'26.76"	29°59'18.24"	67.50
33	101°44'44.88"	30°02'42.72"	91.80

34	101°42'10.44''	30°04'40.08''	74.25
35	101°48'45.00''	30°04'51.96''	45.90
36	101°50'43.80''	30°01'44.04''	145.00
37	101°33'05.76''	30°04'44.76''	54.00
38	101°32'00.60''	30°04'43.68''	108.75
39	101°31'04.80''	30°04'37.92''	132.30
40	101°30'25.20''	30°04'32.52''	75.60
41	101°53'33.72''	29°58'44.40''	56.70
42	101°57' 50.04''	29°57' 14.76''	79.89
43	101°57' 50.04''	29°57' 14.76''	82.12
44	101°57' 37.80''	29°56' 43.08''	73.85
45	101°57' 50.04''	29°57' 06.84''	82.22
46	101°52' 04.80''	30°16' 13.80''	77.36
47	101°50' 15.36''	30°16' 56.64''	78.50
48	101°50' 15.36''	30°16' 58.08''	77.56
49	101°52' 13.80''	30°15' 58.32''	74.94
50	101°13' 15.24''	30°51' 10.44''	87.16

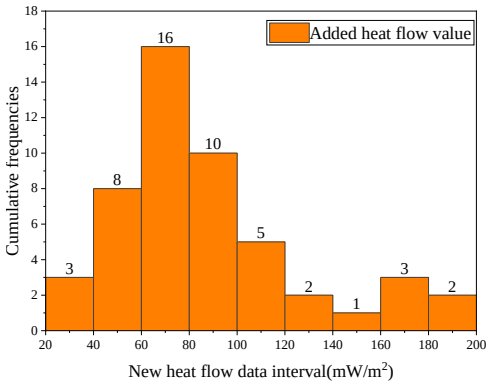

Figure 4 Newly added bar graph of heat flow data

IV. HEAT FLOW MODELING

In recent years, with the rapid development of Geographic Information System (GIS), spatial interpolation methods have been widely used. Among them, Kriging Interpolation is the most widely used.

Kriging interpolation (Kriging), also known as spatial local interpolation [15], is a method of unbiased optimal estimation of regionalized variables in a limited area based on the theory of variogram and structural analysis. One of the main contents of statistics, which is widely used in rainfall distribution, petroleum engineering, hydrology, meteorology, geology and other fields.

Based on the newly added 50 sets of heat flow data in this paper and the existing heat flow data in Sichuan Province and surrounding areas, Surfer commercial software is used to complete the drawing of heat flow maps in this paper.

A. Heat flow data collection

In order to avoid the influence of the interpolation boundary error on the heat flow inversion, we collected 400 sets of heat flow data in Sichuan and surrounding areas(see Figure 5). In Sichuan Province, there are 89 sets of existing heat flow data and 50 sets of new data, for a total of 139 sets of data.

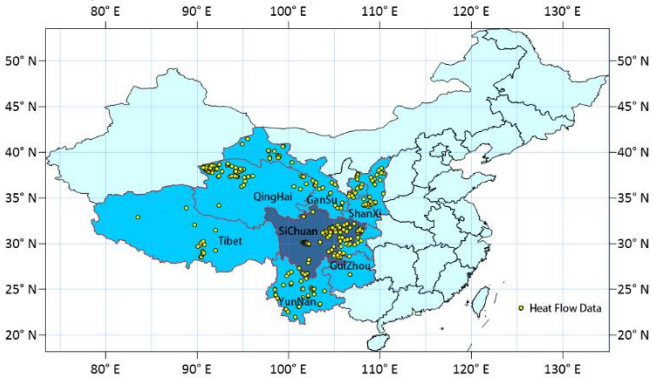

Figure 5 Heat flow data distribution map

B. Verification of the correctness of the interpolation method

In order to verify the accuracy of the Kriging interpolation method, we firstly draw the heat flow map of the China area and compare it with previous work.

The data for drawing China's Terrestrial Heat Flow map comes from the official website of the International Heat Flow Commission (IHFC). The latest database shows that China has 1621 sets of heat flow data. Figure 6 shows the use of Surfer to map the terrestrial heat flow in China and the Terrestrial Heat Flow map drawn by surfer can be seen in Figure 6.

By comparing with the heat flow map drawn by Jiang et al. [16, 17], the overall distribution characteristics and the heat flow distribution characteristics in the structural geological zone in this paper are basically the same as the previous work. Such as Qinghai The Republic Basin, the Guangdong-Hong Kong-Macao Greater Bay Area, the Asia-Europe plate-Pacific plate, and the Asia-Europe plate-Indian Ocean plate junctions have obvious high heat flow area characteristics, which also verifies the accuracy of the heat flow mapping method in this paper.

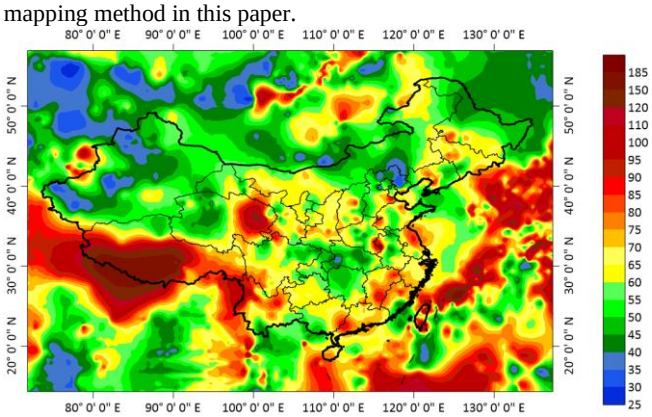

Figure 6 Terrestrial Heat Flow map in China mainland

C. Heat flow data plotting

The land-continent collision of the India-Eurasian plate is the main cause of the intense crustal activity and abnormal regional heat flow on the Qinghai-Tibet Plateau. The Western Sichuan Plateau is affected by the global geological structure and the accompanying regional fault structures, giving the Western Sichuan Plateau a tectonic background and geothermal conditions that give birth to intense hydrothermal activity. Figure 7 shows the distribution of hot springs along the fault zone in the Western Sichuan region.

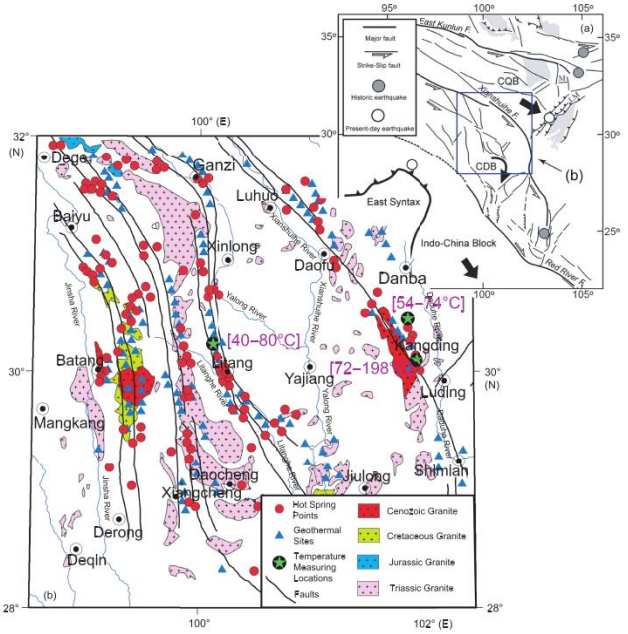

Figure 7 Geothermal geological map of western Sichuan [11]

Using the Kriging interpolation method, in order to improve the accuracy of the interpolation results, the raster data spacing is set to $0.1^{\circ} \times 0.1^{\circ}$, and the Terrestrial Heat Flow map of Sichuan Province and Kangding area is drawn as shown in Figure 8 and Figure 9.

From the inversion results of the Terrestrial Heat Flow in Sichuan Province, Fig. 8 shows that the Terrestrial Heat Flow in Sichuan Province is decreasingly distributed from west to east, and is obviously higher in the west and lower in the east. The areas of high heat flow are mainly distributed in Derong, Xiangcheng, Daocheng in the southwest and along the northwest. It is spread near the deep fault zone area.

Due to the land-continent collision of the Cenozoic India-Eurasian plate along the Yarlung Zangbo suture zone and the magmatism of the Mediterranean-Himalayan geothermal activity zone, resulting in a high heat flow distribution in the southwest of Sichuan Province. And there is a long-range diminishing effect of heat transfer from the east structural junction along the north-east direction. But it does not continue to decrease, because the Xianshuihe, Ganzi-Litang, Dege-Xiangcheng, Jinshajiang, and Batang fault zones are still affected in western Sichuan. It shows that the deep fault zone is the main controlling factor of the geothermal anomaly area in western Sichuan [11].

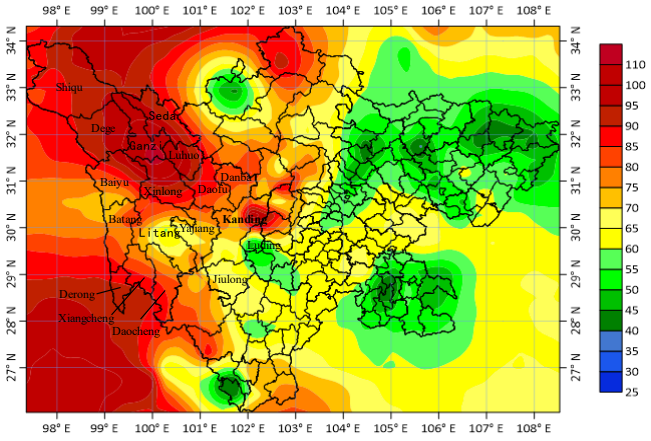

Figure 8 Terrestrial Heat Flow map of Sichuan Province

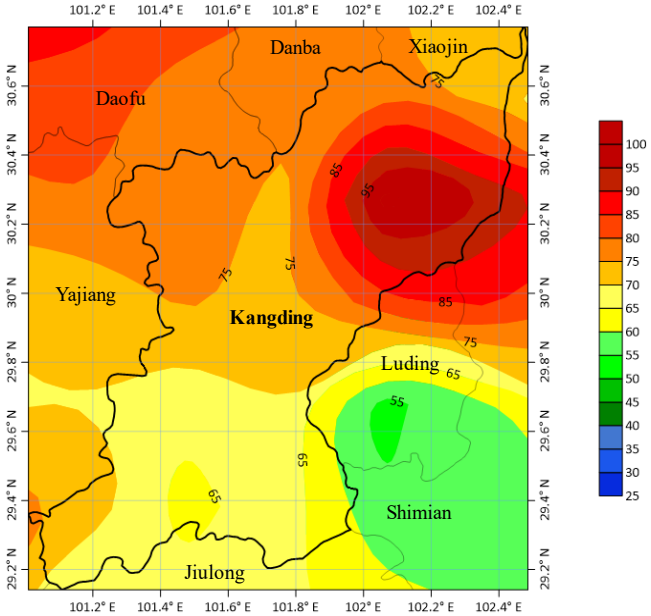

Figure 9 Terrestrial Heat Flow map in Kangding area

V. EVALUATION OF GEOTHERMAL POTENTIAL IN KANGDING AREAS

Analyzing the heat flow map of Kangding County, we can find that the Terrestrial Heat Flow values of Kangding County vary from 64 to 101, which are higher than the original average heat flow data of Sichuan Province ($53.75 \pm 12.24\ mW/m^2$), the average heat flow value of mainland China ($61 \pm 15.5\ mW/m^2$) and the global average heat flow value. ($65 \pm 1.6\ mW/m^2$) [13]. The overall heat flow value is high, and it has the potential for geothermal exploitation. The heat flow value in the north is higher than that in the south, and reaches the highest value of $101\ mW/m^2$ in the

northeast of Kangding. The Kangding County is affected by the Xianshuihe fault zone, which is a deep and large high-temperature shear zone and characterized by intense hydrothermal activity, high geothermal gradient and high heat flow, inducing high heat flow value of this area.

Daofu County, Danba County and the northeastern part of Kangding County are all located nearby the Xianshuihe fault zone. The heat flow value is high and distributed along the northwest. The heat flow value ranges from 75~101 mW/m^2, and the heat flow value reaches the highest value of 101 in the northeast of Kangding County. The heat flow value of Xiaojin County, which borders the northern part of Kangding County, ranges from 72~ 77 mW/m^2. The heat flow value of Yajiang County, which borders the eastern part of Kangding County, ranges from 70~80 mW/m^2. The Jiulong County, which borders the southern region of Kangding County, the Luding County, which borders the central region, and the Shimian County presents the phenomenon of long-distance decline in heat transfer from east to east, with heat flow values ranging from 54~64 mW/m^2. In the southern part of Luding, the lowest heat flow is 54 mW/m^2. The result shows that the heat flow distribution in Kangding area is significantly affected by regional tectonic effects and high heat flow areas. The formation of the zone is the result of the combined effect of the East structure and the Xianshuihe fault zone.

The heat flow in the Xianshuihe fault zone is significantly higher, indicating that the Xianshuihe fault zone is the main reason for the formation of the high heat flow zone according to the above earth heat flow values. The distribution characteristics provide the evidence that it has good potential to exploit and utilize the geothermal resources in Kangding area.

VI. CONCLUSION

In this paper, by processing the borehole data in the geological survey report of the Kangding area of the Sichuan-Tibet Railway, 50 sets of high-quality data are initially obtained. Based on the newly added heat flow data, a heat flow map of Sichuan Province and Kangding area was drawn. The following conclusions can be drawn from the work done:

1) The average heat flow value in the Kangding area is 86.96 ± 39.73 mW/m^2 obtained from the borehole temperature data of Sichuan-Tibet Raiway geological survey.

2) The high heat flux zone is distributed along the northwest of Kangding area. The terrestrial heat flow value of Kangding County ranges from 64~101 mW/m^2 with the highest value of 101 mW/m^2 in the northeast Kangding County.

3) The formation of the high heat flux zone in Kangding area is the result of the joint action of the Xianshuihe fault zone and the eastern structure junction. Due to the diminishing effect of the heat transfer of the east structure junction, the high heat flow zones are mainly distributed along the northwest, and the active Xianshuihe fault zone is the main reason for the formation of the high heat flow zones in Kangding County and its surrounding areas.

The above opinions on the exploitation and utilization of geothermal energy resources in different areas of Sichuan Province need to be specifically investigated in conjunction with the specific local engineering geological conditions, which is also the work to be done in future.

VII. ACKNOWLEDGEMENTS

The authors appreciate the support received from China Railway Engineering Equipment Group Co., Ltd. The granted supports from the Fundamental Research Funds for Central Universities of China (N180105031), the Young Talent Program of Liaoning Province (XLYC1807094), and the Research Project of China Railway Eryuan (no.KYY2019004(19-22)) are also acknowledged. The work is partially supported by the 111 Project (B17009) and under the framework of Sino-Franco Joint Research Laboratory on Multiphysics and Multiscale Rock Mechanics.

VIII. REFERENCES

[1] Ze-wei Q U, Heng Z, Ya-zhao H U, et al. "General situation and development regional division of geothermal resources in western sichuan region "[J]. Mineral Exploration, 2019, 10(5): 1233-42.

[2] Gui-ling W, Wei Z, Ji-yun L, et al. "Evaluation of Geothermal Resources Potential in China "[J]. Acta Geoscientica Sinica, 2017, 38(4): 448-59.

[3] Guocheng R. "Talking about the calculation method of geothermal resources and reserves "[J]. Western Prospecting Project, 2015, (11): 108-10.

[4] Dong S U N, Nan C A O, Xin-ze L I U, et al. "Geothermal Resources and Development in Garzê Prefecture, Sichuan "[J]. Journal of Sichuan Geology, 2019, 39(1): 133-8.

[5] bin W. Geophysical Exploration of Geothermal Rresources in the Songpam-Ganzi Area [D]; Chengdu University of Technology, 2013.

[6] Majorowicz J, Grasby S E. "Heat flow, depth-temperature variations and stored thermal energy for enhanced geothermal systems in Canada "[J]. Journal of geophysics and engineering, 2010, 7(3): 232-41.

[7] Jiyang W, Shaopeng H. "Compilation of Heat Flow data for continental area of China "[J]. Scientia Geologica Sinica, 1988, (02): 196-204.

[8] Jiyang W. "Compilation of heat flow data in the continental area of China (2th edition) "[J]. Seismic geology, 1990: 351-63,66.

[9] Hu S, Lijuan H, Jiyang W. "Compilation of heat flow data in the continental area of China (3th edition) "[J]. 2001, 44(5): 611-26.

[10] Guangzheng J, Takashi, Song R, et al. "Compilation of heat flow data in the continental area of China (4th edition) "[J]. Chinese Journal of Geophysics, 2016, 59(8): 2892-910.

[11] Jian Zhang, WY Li, XC Tang, et al. "Geothermal data analysis at the high-temperature hydrothermal area in Western Sichuan "[J]. Scientia Sinica（Terrae）, 2017, 47(8): 899-915.

[12] ""Regulations for Geothermal Resources Geological Prospecting" for public comments "[J]. Geothermal Energy, 2008: 29.

[13] Xujuan L, Feng L, Zhiming L, et al. "Terrestrial Heat Flow in Guide Basin,Qinghai "[J]. Bulletin of Geological Science and Technology, 2016, 35(03): 227-32.

[14] Zhijie L, Ping Z. Yunnan-Tibet tropical zone: geothermal resources and typical geothermal system [M]. China Science and Technology Press, 1999.

[15] Junxiao L, Chaokui L. "ArcGIS Based Kriging Interpolation Method and Its Application "[J]. Bulletin of Surveying and Mapping, 2013, (9): 87-90,7.

[16] Jiang G, Hu S, Shi Y, et al. "Terrestrial Heat Flow of continental China: Updated dataset and tectonic implications "[J]. International Journal of Geotectonics and the Geology and Physics of the Interior of the Earth, 2019, 753: 36-48.

[17] Jiyang W, Shengbiao H U, Zhonghe P, et al. "Estimate of Geothermal Resources Potential for Hot Dry Rock in the Continental Area of China "[J]. Science and Technology Review, 2012, 30(32): 25-31.

Intensified extractive distillation process for the separation of n-heptane-toluene mixture using the ionic liquid 1-Ethyl-4-methylpyridinium Bis(trifluoromethanesulfonyl)imide

Fadia Guella
dept. of Chemical Engineering
University of Sciences and Technology of Oran Mohamed Boudiaf
Oran, Algeria
guella.fadia11@gmail.com

Hassiba Benyounes
dept. of Chemical Engineering
University of Sciences and Technology of Oran Mohamed Boudiaf
Oran, Algeria
benyounes.hassiba@gmail.com

Abstract

Ionic liquids (ILs) have emerged in recent years as promising green solvents to replace conventional solvents. This work aims to the separation of n-heptane-toluene mixture by extractive distillation using ionic liquid (IL) to enhance the performance of the process. The ionic liquid [4EMPy] [NTF_2], "1-ethyl-4-methylpyridiniumBis(trifluoromethane-sulfonyl)imide", was proposed due to its high selectivity compared to the conventional solvent "Sulfolane".

The calculation of the VLE of n-heptane-toluene mixture in the presence of the solvent was performed using the NRTL activity coefficient model. The effect of the concentration of the IL showed that the relative volatility of n-heptane (1) to toluene (2) in the presence of [4EMPy] [NTF_2] increases at a smaller solvent concentration compared to Sulfolane. The best operating conditions for the extractive distillation process were determined to recover n-heptane with a high purity of 99.9 mol. %. It was found that the ionic liquid [4EMPy] [NTF_2] is more efficient than sulfolane for separating n-heptane/toluene close boiling point mixture even it is used in small amounts and it is less energy consuming.

Keywords: n-heptane/toluene, close boiling point, NRTL, [4EMPy] [NTF_2], extractive distillation, energy consumption.

1 INTRODUCTION

The separation of aromatic-aliphatic hydrocarbon mixtures is one of the most difficult separations in the chemical and petrochemical industries due to their close boiling points and the formation of azeotropes. These types of separations were first studied 42 years ago in a European project [32].

The separation of toluene from n-heptane mixture is an aromatic-aliphatic separation. This separation is useful for the production of low aromatic fuels which are widely recommended nowadays [3]. Research has shown that this mixture can be separated by extractive distillation or by azeotropic distillation [7, 8, 14, 26, 28].

The currently used organic solvents for n-heptane/toluene separation such as sulfolane [5, 4, 6, 16, 39], N-methyl pyrrolidone (NMP) [16], N-formyl morpholine (NFM), and ethylene glycol [1, 34, 39] show some disadvantages. Although, their boiling point is high, they still have some volatility that eventually pollutes the top product and large amounts of solvent or high reflux ratios are needed to obtain the desired product purity. Recently, ionic liquids as a new kind of "green" solvents have been proposed for being a potential solvent for separation process [9, 10, 12, 20, 22-24, 38, 40] and as a substituent of the organic solvents due to their high separation ability, negligible vapor pressure, relative low melting point and recyclability [31, 36, 37]. Many studies have demonstrated the great ability of these new class of solvents to separate complex mixtures by extractive distillation [7, 8, 14, 17-19, 26, 28].

In this work, to evaluate the thermodynamic and the energy efficiency of the extractive distillation process of the close-boiling point mixture n-heptane/toluene using IL"1-ethyl-4-methylpyridinium Bis (trifluoromethanesulfonyl) imide [4EMPy] [NTF_2], the sensitivity analysis of the key operating parameters of the process was performed using Aspen Plus software V.10.

2 METHODS

Physical and thermodynamic properties of the ionic liquid [4EMPy][NTF_2] were estimated, such as critical properties using an extended group contribution method, which is based on the well-known concepts of Lydersen and Joback and Reid [2], and vapor pressure using the Antoine equation [29]. The standard enthalpy of vaporization was predicted with Verevkin's method [33] and the

IEECP'21, July 29-30, 2021, Silicon Valley, San Francisco, CA – USA

DAI : *https://sci-index.com/DAI/2021.99101/IEECP/14811834*

heat capacity was correlated with a group contribution method developped by Sattari and al. [30].

The ionic liquid molecule [4EMPy][NTF_2] was introduced into Aspen Plus with the properties listed in Tab. 1.

The thermodynamic behavior of the n-heptane/toluene mixture in the presence of sulfolane and [4EMPy] [NTF_2] ionic liquid was studied. The Non-Random two liquids NRTL model was used to calculate the vapor-liquid equilibrium based on the experimental data of the n-heptane (1) - toluene (2) system in the presence of the organic solvent sulfolane and the ionic liquid [4EMPy] [NTF_2] [15, 21, 25, 35] using Aspen plus software v10.

Table 1. Physical properties of the ionic liquid [4EMPy] [NTF2]

Properties	Mw (g/mol)	T_b (K)	T_c (K)	P_c (bar)
[4EMPy][NTF_2]	402.3	806.12	1465.08	25.88

In distillation, the separation efficiency of two constituents is often denoted by a quantity called the relative volatility α_{ij} which define the ease of separation of a given mixture

$$\alpha_{ij} = \frac{y_i/x_i}{y_j/x_j} = \frac{\gamma_i P_i^0}{\gamma_j P_j^0} \qquad (1)$$

Where x is the mole fraction in the liquid phase, y is the mole fraction in the vapor phase, γ is the activity coefficient, and P_i^0 is the vapor pressure of the pure component.

The solvent is introduced to increase the relative volatility as far from unity as possible. Since the ratio of P_i^0 / P_j^0 is constant at small temperature changes, the added solvent enhances the relative volatility as the ratio γ_i / γ_j changes in the presence of the solvent, this ratio is called selectivity S_{ij} [19]:

$$S_{ij} = \left(\frac{\gamma_i}{\gamma_j}\right)_S \qquad (2)$$

3 RESULTS AND DISCUSSION

3.1 Calculation of vapor - liquid equilibrium for n-heptane-toluene-solvent system

The regression of the NRTL binary interaction parameters was done without considering the temperature dependence. The regressed parameters are grouped in Tab. 2.

Table 2. Regressed binary interaction parameters of NRTL model

Component i	Component j	A_{ij}	A_{ji}	α
n-heptane	Toluene	-33.2	153.8	0.3
n-heptane	Sulfolane	1329.7	934.6	0.3
Toluene	Sulfolane	889.0	17.7	0.3
n-heptane	[4EMPy][NTF_2]	944.1	741.9	0.4
Toluene	[4EMPy][NTF_2]	363.0	-399.2	0.4

3.1.1 Effect of the solvent concentration on the selectivity of sulfolane and [4EMPy] [NTF_2]

Figure 1 (a) and (b) respectively show the variation of the selectivity of sulfolane and the ionic liquid [4EMPy] [NTF_2] as a function of the mole fraction of n-heptane in the pseudo-binary mixture.

It can be seen from Fig. 1 that the selectivity reaches its maximum value at infinite dilution of n-heptane in toluene, which confirms that sulfolane and [4EMPy] [NTF_2] are selective solvents with respect to toluene.

From Fig.1 we notice that, the selectivity is proportional to the solvent mole fraction (x_3) in the mixture. The ionic liquid [4EMPy] [NTF_2] have a high selectivity toward toluene (Fig. 1 (b)) compared to sulfolane (Fig. 1 (a)), thus, for a solvent fraction of 0.5, the selectivity of sulfolane and [4EMPy] [NTF_2] are respectively equals to 3.2 and 5.2.

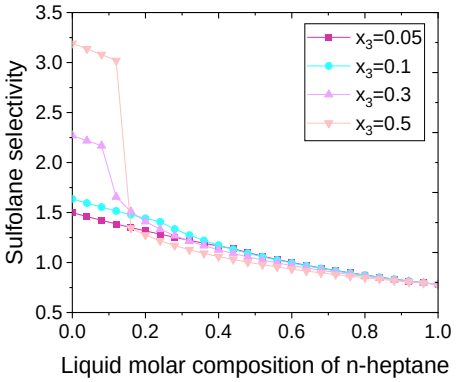

(a)

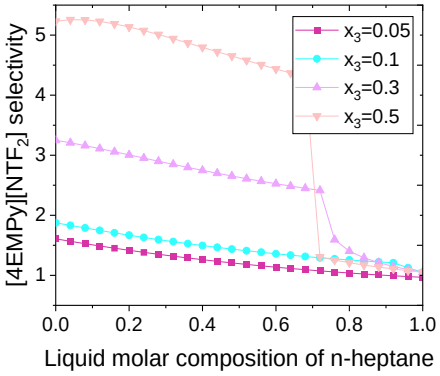

(b)

Figure 1. Variation of selectivity as a function of the n-heptane mole fraction in the pseudo binary mixture, (a): sulfolane, (b): [4EMPy][NTF_2]

3.1.2 Effect of the solvent concentration on the relative volatility of n-heptane to toluene in the presence of sulfolane and [4EMPy] [NTF2]

A relative volatility close to unity means that separation of the two component is likely to be difficult, whereas a relative volatility greater than unity means that few equilibrium stages are required for separation. For a binary system, equation (1) can be rearranged to give:

$$y_i = \frac{\alpha_{ij} x_i}{1+(\alpha_{ij}-1)x_i} \qquad (3)$$

The vapor-liquid equilibrium curves are plotted in Fig. 2 at different solvent concentrations, from which it can be seen that in the absence of the solvent, the relative volatility of n-heptane is very close to unity over the composition range from 0.8 to 1. The vapor-liquid equilibrium curve moves away from the diagonal as the mole fraction of the solvent (x_3) increases.

The relative volatility of n-heptane to toluene increases notably in the presence of [4EMPy] [NTF_2] (Fig. 2 (b)) compared to sulfolane (Fig. 2 (a)) for the same solvent concentrations. As a result, the ionic liquid [4EMPy] [NTF_2] is more efficient for n-heptane/toluene separation in comparison with the organic solvent sulfolane.

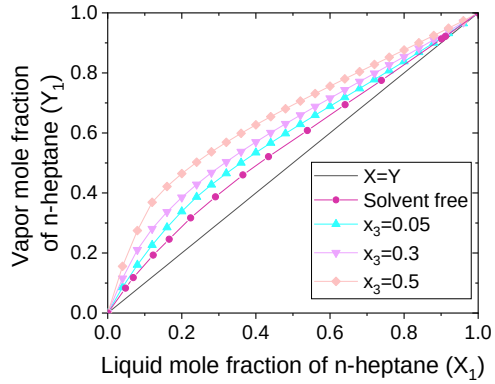

(a)

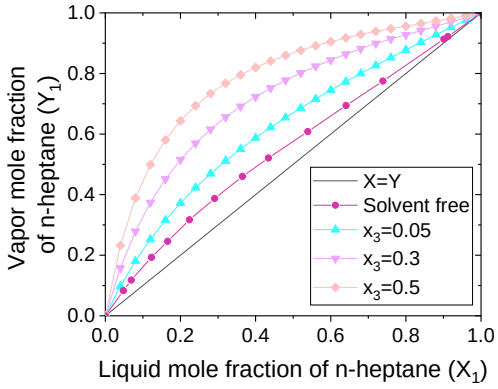

(b)

Figure 2. Effect of the solvent molar fraction of sulfolane (a) and [4EMPy][NTF_2] (b) on the relative volatility of n-heptane

3.2 Simulation of the extractive distillation process for the sepration of n-heptane-toluene mixture

The simulated process flowsheet, as presented in Fig. 3, consists of two columns, an extractive distillation column for the separation of the n-heptane/toluene mixture using a heavy entrainer and a recovery column for the solvent regeneration. In extractive distillation column, the entrainer is fed continuously above the main feed mixture, bringing an additional extractive section in the column, between the stripping and the rectifying sections [11]. N-heptane is recovered at the top of the extractive distillation column, and the mixture toluene + entrainer removed at the bottom is sent to the regeneration column. At the bottom of the regeneration column, the solvent is recovered with a high purity, and then recycled back to the extractive distillation column.

The rigorous simulation of the extractive distillation process was carried out using Aspen plus V.10. The operating pressure of the extractive distillation process was set to 1 atm, the feed is assumed to be in the boiling liquid state and the solvent feed temperature was fixed to 25°C. The molar feed flow rate (F) was set to 100 kmoles/hr and the mixture was chosen for an equimolar composition. The n-heptane purity in the distillate of the extractive distillation column and the solvent purity at the bottom of the regeneration column must be higher than 99.9 mol%.

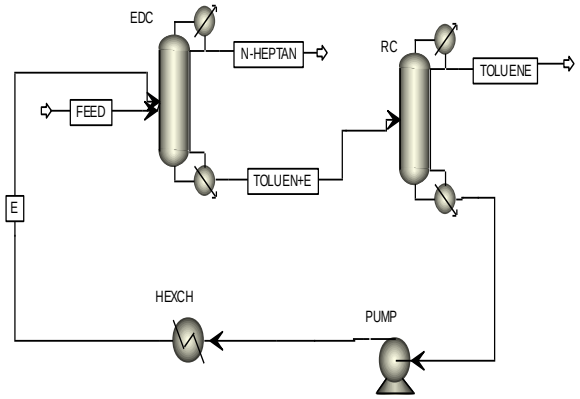

Figure 3. Extractive distillation process flowsheet for separating n-heptane from toluene using either sulfolane or [4EMPy] [NTF_2] as an entrainer

3.2.1 Sensitivity analysis of extractive distillation column using sulfolane and [4EMPy] [NTF_2]as solvents

3.2.1.1 Effect of solvent-to-feed molar ratio and reflux ratio on the n-heptane purity

The effect of the solvent-to-feed ratio and the reflux ratio on the purity of n-heptane in the distillate shows that the purity is proportional to the solvent rate and to the reflux ratio in the presence of both sulfolane (Fig. 4 (a)) and [4EMPy] [NTF_2] (Fig. 4 (b)). It can be seen from Fig. 4 (a) that the optimal values of the reflux and the solvent ratio to get a purity greater than 99.9 mol. % are respectively 0.5 and 0.8 using sulfolane, while using [4EMPy] [NTF_2] (Fig. 4 (b)) the values of these parameters can be reduced to 0.1 for the reflux ratio and 0.4 for the solvent ratio.

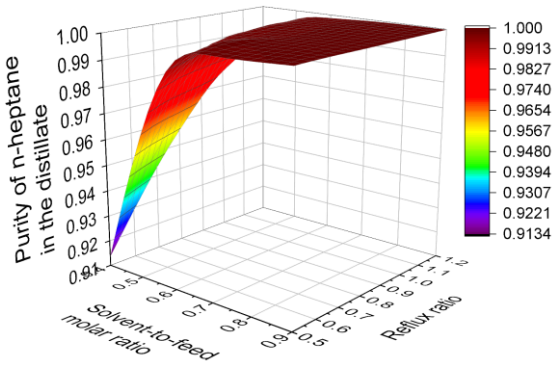

(a)

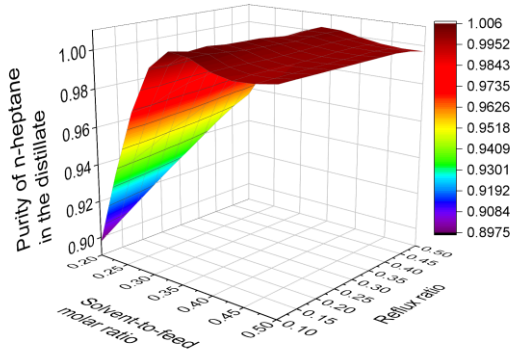

(b)

Figure 4. Effect of solvent-to-feed molar ratio and reflux ratio on the n-heptane purity in the distillate using Sulfolane (a) and [4EMPy] [NTF$_2$] (b)

3.2.1.2 *Effect of the solvent feed stage and the main feed stage on the n-heptane purity*

The effects of solvent feed stage and feed stage of initial mixture on the purity of n-heptane in the distillate using sulfolane and [4EMPy] [NTF$_2$] are represented in Fig. 5 (a) and (b). We notice from Fig. 5 (a) that the high purity of n-heptane can be reached in column with extractive sections of 17, 16, 15 and 14 stages. It can be noted from this analysis that the minimum and the maximum number of stage in the extractive section allowing to obtain a purity higher than 99.9 mol. % using sulfolane are 14 and 17 stages respectively, the best feed stage is N_F=20 and the entrainer stage can be chosen from 3 to 6 stages from the top of the column.

When using the ionic liquid [4EMPy] [NTF$_2$] (Fig. 5 (a)), the purity of n-heptane reaches its maximum for the entrainer feed stage from 2 to 6, and mixture feed stage from 20 to 22. This means that the minimum and the maximum number of stage in the extractive section to achieve purity greater than 99.9 mol. % are 14 and 19 stages respectively.

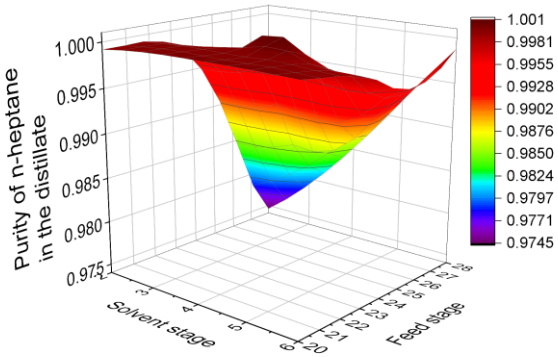

(a)

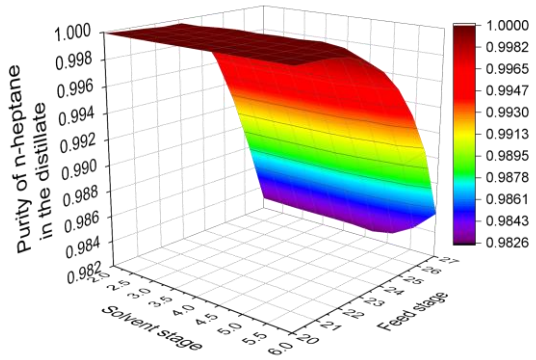

(b)

Figure 5. Effect of solvent stage and feed stage on the n-heptane purity in the distillate using Sulfolane (a) and [4EMPy] [NTF$_2$] (b)

3.2.1.3 *Effect solvent-to-feed molar ratio and reflux ratio on the reboiler duty*

The reboiler heat duty as a function of the solvent-to-feed molar ratio and reflux ratio at fixed purity of n-heptane is represented in Fig. 6 (a) and (b). It was shown that the reboiler duty is proportional to both solvent rate and reflux ratio. The best operating parameters of F_E/F and R are determined by minimizing the energy consumed in the reboiler (Q_R) of the extractive distillation column.

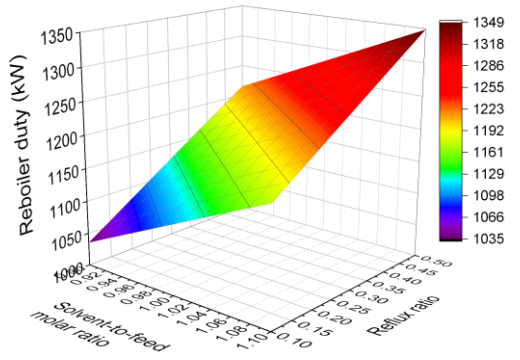

(a)

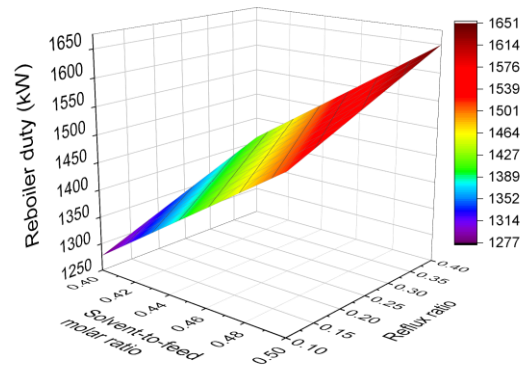

(b)

Figure 6. Effect of the solvent-to-feed molar ratio and the reflux ratio on the reboiler duty using sulfolane (a) and [4EMPy] [NTF$_2$] (b)

3.2.2 *Design parameters for the extractive distillation column using sulfolane and [4EMPy] [NTF$_2$]*

The best operating parameters for the extractive distillation column were determined by the sensitivity analysis for a feed containing 50 mol. % of n-heptane to recover n-heptane in the distillate with a high purity of 99.97 mol. %. The total number of stages was fixed to 30 stages. The operating parameters of the extractive distillation column using sulfolane and [4EMPy] [NTF$_2$] are displayed in Tab. 3.

Table 3. Design parameters of the extractive distillation column using Sulfolane and [4EMPy] [NTF$_2$]

Parameters	Solvent	
	Sulfolane	[4EMPy][NTF$_2$]
Number of stages	30	30
N_E	5	3
N_F	22	20
F_E/F	1	0.33
R	0.2	0.06
n-heptane purity in mol.%	99.97	99.97
Q_R (kW)	1149.53	1078.55
Bottom temperature (°C)	123.38	133.13

For the both solvents sulfolane and [4EMPy] [NTF$_2$], the separation requires 17 stages in the extractive section to get a purity of n-heptane of 99.97% in the distillate for the same total number of stages of the extractive distillation column. In addition, [4EMPy] [NTF$_2$] needs less stages in the rectifying section compared to sulfolane and more stages for the stripping section, this means that the separation of n-heptane from toluene is easy when using the ionic liquid and that the affinity of [4EMPy] [NTF$_2$] for toluene is higher than that of sulfolane. It is also noted that the extractive distillation column using [4EMPy] [NTF$_2$] consumed less solvent flow rate for low reflux ratio and is less energy consuming.

3.2.3 *Design parameters for the regeneration column using sulfolane and [4EMPy] [NTF2]*

The separation of toluene from the solvent was achieved in a distillation column. The pressure of the regeneration column of sulfolane was set to 1 atm, however, the [4EMPy] [NTF$_2$] ionic liquid is regenerated at a vacuum pressure to avoid decomposition of the ionic liquid [9]. The thermal decomposition temperature for the pyridinium ionic liquids is between 510-720 K, according to Jacob and al. The decomposition temperature of the used IL is not mentioned, nevertheless, it may be equal to or slightly less than the [BMPy] [NTF$_2$] which is 670 K [13], for this purpose, the bottom temperature of the regeneration column using [4EMPy] [NTF$_2$] should not exceed 396.85 °C. The operating parameters of the regeneration column using sulfolane and [4EMPy] [NTF$_2$] are represented in Tab. 4.

Table 4. Design parameters of the solvent regeneration column using Sulfolane and [4EMPy] [NTF$_2$]

Parameters	Solvent	
	Sulfolane	[4EMPy][NTF$_2$]
Pressure (bar)	1.013	0.1
Number of stages	6	4
Feed stage	3	3
R	0.4	0.12
Solvent purity in mol.%	99.97	99.97
Q_R (kW)	1650.41	1597.07
Bottom temperature (°C)	286.26	323.48

It can be seen from Tab. 4, that the separation of toluene from the ionic liquid [4EMPy] [NTF2] to be regenerated required less number of stages, reflux ratio and less energy consumption compared to sulfolane to get the same solvent purity.

CONCLUSION

In this work, the extractive distillation process for the separation of n-heptane-toluene mixture using [4EMPy] [NTF$_2$] ionic liquid and sulfolane was investigated. The vapor-liquid equilibrium of the n-heptane-toluene close boiling point mixture in the presence of different concentrations of solvent was calculated by the NRTL model using Aspen plus software. The binary interaction parameters of the model were regressed from the VLE experimental data.

The thermodynamic study show that the ionic liquid [4EMPy] [NTF$_2$] have a high selectivity for toluene compared to sulfolane. Furthermore, this ionic liquid is more efficient for n-heptane-toluene separation comparing to sulfolane because it increases the relative volatility of n-heptane even at low amounts

The rigorous simulation of the extractive distillation process shows that the extractive distillation column using [4EMPy] [NTF$_2$] requires lower values of solvent-to-feed molar ratio and reflux molar ratio compared to sulfolane to get a high purity of 99.97 mol.% of n-heptane.

Finally, we conclude that extractive distillation using the ionic liquid [4EMPy] [NTF$_2$] is feasible and even very advantageous compared to the conventional process using sulfolane, as well as, the solvent flow rate and the overall energy consumption using the ionic liquid [4EMPy] [NTF$_2$] can be reduced up to 67% and 4.44% respectively. Thereby, extractive distillation using ionic liquids can be considered as a potential energy saving technology for separating a close-boiling point mixtures if a suitable ILs with a high selectivity are chosen to replace the organic solvents which are in most cases toxic, more volatile and not easily recyclable.

4 REFERENCES

[1] Al-Sahhaf, T.A. and Kapetanovic, E. 1996. Measurement and prediction of phase equilibria in the extraction of aromatics from naphtha reformate by tetraethylene glycol. Fluid Phase Equilib. 118 (2), 271– 285.

[2] Alvarez, V.H. and Valderrama, J.O. 2004. A modified Lydersen-Joback-Reid method to estimate the critical properties of biomolecules. Alimentaria, 254, 55-66.

[3] Billard, P., Nguyen, Q.T., Leger, C. and Clement, R. 1998. Diffusion of organic compounds through chemically asymmetric membranes made of semi-interpenetrating polymer networks. Sep. Purif. Technol. 14, 221–232.

[4] Chen, J., Li, Z. and Duan, L. 2000. Liquid– liquid equilibria of ternary and quaternary systems including cyclohexane, 1-

heptane, benzene, toluene, and sulfolane at 298.15 K, J. Chem. Eng. Data 45, 689–692.

[5] Chen, J.,. Duan, L.P.,. Mi, J.G, Feio, W.Y. and Li, Z.C. 2000. Liquid– liquid equilibria of multi-component systems including n-hexane, n-octane, benzene, toluene, xylene and sulfolane at 298.15 K and atmospheric pressure. Fluid Phase Equilib. 173, 109– 119.

[6] Choi, Y.J., Cho, K.W., Cho, B.W. and Yeo, Y.K. 2002. Optimization of the sulfolane extraction plant based on modeling and simulation. Ind. Eng. Chem. Res. 41, 5504–5509.

[7] Díaz, I., Palomar, J., Rodríguez, M., de Riva, J., Ferro, V. and Gonzalez, E.J. 2016. Ionic liquids as entrainers for the separation of aromatic−aliphatic hydrocarbon mixtures by extractive distillation. Chem. Eng. Res. Des., 115, 382−393.

[8] Dong Y., Dai, C. and Lei, Z. 2018. Extractive distillation of methylal/ methanol mixture using the mixture of dimethylformamide (DMF) and ionic liquid as entrainers. Fuel, 216, 503−512.

[9] Dong, Y. C., Dai, C. N. and Lei, Z. G. 2018. Separation of the methanol-ethanol-water mixture using ionic liquid. Ind. Eng. Chem. Res, 57, 11167-11177.

[10] Ferro, V. R., de Riva, J., Sanchez, D., Ruiz, E., Palomar, J. 2015. Conceptual design of unit operations to separate aromatic hydrocarbons from naphtha using ionic liquids. COSMO-based process simulations with multicomponent 'real' mixture feed. Chem. Eng. Res. Des, 94, 632-647.

[11] Gerbaud, V. and Rodriguez-Donis, I. 2010. Distillation of non-ideal mixtures. Azeotropic distillation and extractive distillation. Choice of the entrainer, J 2612 V1, Paris.

[12] Gonzalez, E. J., Navarro, P., Larriba, M., Garcia, J., Rodriguez, F. 2015. Use of selective ionic liquids and ionic liquid/salt mixtures as entrainer in a vapor + liquid system to separate n-heptane from toluene. J. Chem. Thermodyn., 91, 156-164.

[13] Jacob Crosthwaite, M., Mark Muldoon, J., JaNeille Dixon, K., Jessica Anderson, L. and Joan Brennecke F. 2005. Phase transition and decomposition temperatures, heat capacities and viscosities of pyridinium ionic liquids. J. Chem. Thermodynamics 37, 559–568.

[14] Jongmans, M. T. G., Schuur, B. and de Haan, A. B. 2011. Ionic Liquid Screening for Ethylbenzene/Styrene Separation by Extractive Distillation. Ind. Eng. Chem. Res., 50, 10800−10810.

[15] Ko, M., Im, J., Sung, J. Y., Yong Sung, J. and Kim, H. J. 2007. Liquid - Liquid Equilibria for the Binary Systems of Sulfolane with Alkanes. Chem. Eng. Data, 52, 1464-1467.

[16] Krishna, R., Goswami, A.N., Nanoti, S.M., Rawat, B.S., Khana, M.K. and Dobhal, J. 1987. Extraction of aromatics from 63–69-C naphtha fraction for food grade hexane production using sulpholane and NMP as solvents. Ind. J. Technol. 25, 602–606.

[17] Kulajanpeng, K., Suriyapraphadilok, U. and Goni, R. 2016. Systematic screening methodology and energy efficient design of ionic liquid-based separation processes. J. Cleaner Prod., 111, 93−107.

[18] Lei, Z., Dai, C., Zhu, J. and Chen, B. 2014. Extractive Distillation with Ionic Liquids: A Review. AIChE J., 60, 3312−3329. 26

[19] Lei, Z., Li, C. and Chen, B. 2003. Extractive Distillation: A Review. The Key Laboratory of Science and Technology of Controllable Chemical Reactions. Separation and purification reviews, Vol. 32, No. 2, 121–213. 27

[20] Li, Q. S., Zhang, J. G., Lei, Z. G., Zhu, J. Q., Zhu, J. J., Huang, X. Q. 2009. Selection of ionic liquids as entrainers for the separation of ethyl acetate and ethanol. Ind. Eng. Chem. Res., 48, 9006-9012.

[21] Michishita, T., Arai, Y., Saito, S. and Kogaku, K. 1971. Vapor-liquid equilibria of hydrocarbons at atmospheric pressure, 35(1), 111-116. 19

[22] Mokhtarani, B., Gmehling, J. Vapour-liquid equilibria of ternary systems with ionic liquids using headspace gas chromatography. 2010. J. Chem. Thermodyn., 42, 1036-1038.

[23] Navarro, P., Ayuso, M.; Palma, A. M.; Larriba, M., Delgado-Mellado, N., Garcia, J.; Rodriguez, F., Coutinho, J. A. P. and Carvalho, P. J. 2018. Toluene/n-heptane separation by extractive distillation with tricyanomethanide-based ionic liquids: Experimental and CPA EoS modeling. Ind. Eng. Chem. Res., 57, 14242-14253.

[24] Navarro, P., Larriba, M., Garcia, J.; Radriguez, F. 2017. Design of the recovery section of the extracted aromatics in the sparation of BTEX from naphtha feed to ethylene crackers using [4empy][Tf2N] and [emim][DCA] mixed ionic liquids as solvent. Sep. Purif. Technol., 180, 149-156.

[25] Navarro, P.,. Larriba, M, García, J., Gonzalez, E. J. and Rodríguez, F. 2016. Vapor−Liquid Equilibria of n‑Heptane + Toluene+1-Ethyl-4-methylpyridinium Bis(trifluoromethylsulfonyl)imide Ionic Liquid. J. Chem. Eng. Data, 61, 458−465.

[26] Paduszynski, K., Krolikowski, M., Zawadzki, M. and Orzet, P. 2017. Computer-Aided Molecular Design of New Task-Specific Ionic Liquids for Extractive Desulfurization of Gasoline. ACS Sustainable Chem. Eng., 5, 9032−9042.

[27] Rebelo, L. P., Canongia, J. N., Esperanca, J. M. and Filipe, E. 2005. On the Critical Temperature, Normal Boiling Point, and Vapor Pressure of Ionic Liquids. J. Phys. Chem. B. vol 109, No 13, pp. 6040–6043.

[28] Rodríguez-Cabo, B., Rodríguez, H., Rodil, E., Arce, A. and Soto, A. 2014. Extractive and oxidative-extractive desulfuration of fuels with ionic liquids. Fuel, 117, 882−889.

[29] Rudkin, J. 1961. Equation predicts vapor pressures. Chem. Eng., april 17, 202-203.

[30] Sattari, M., Gharagheizi, F., Ilani-Kashkouli, P., Mohammadi, A.H., Ramjugernathand, D. 2013. Development of a group contribution method for the estimation of heat capacities of ionic liquids. J Therm Anal Calorim, Akademiai Kiado, Budapest, Hungary.

[31] Sheldon, R. 2001. Catalytic reactions in ionic liquids. J. Chem. Soc., Chem. Commun. , 2399-2407.

[32] Smitha, B., Suhanya, D., Sridhar, S. and Ramakrishna, M. 2004. Separation of organic–organic mixtures by pervaporation – a review. J. Membr. Sci. 241, 1–21. 2

[33] Verevkin, S. P. 2008. Predicting enthalpy of vaporization of ionic liquids: A simple rule for a complex property. Angewandte Chemie - International Edition, 47, 5071-5074.

[34] Wang, W., Gou, Z.M. and Zhu, S.L. 1998. Liquid– liquid equilibria for aromatics extraction systems with tetraethylene glycol. J. Chem. Eng. Data 43 (1), 81– 83.

[35] Wang, Z., Huang, L., Xia, S. and Ma, P. J. 2011. Isobaric (vapour + liquid) equilibria for sulfolane with toluene, ethylbenzene, and isopropylbenzene at 101.33 kPa. Chem. Thermodyn., 43(12), 1865-1869.

[36] Wasserscheid, P.; Keim, W. 2000. Ionic Liquids-New "Solutions" for Transition Metal Catalysis. Angew. Chem., Int. Ed., 39, 3772-3789.

[37] Welton, T. 1999. Room-Temperature Ionic Liquids. Solvents for Synthesis and Catalysis. Chem. Rev., 99, 2071-208.

[38] Wishart, J. F. and Castner, J. E. W. 2007. The physical chemistry of ionic liquids. J. Phys. Chem. B, 111, 201-208.

[39] Yorulmaz, Y. and Karpuzcu, F. 1985. Sulpholane versus diethylene glycol in recovery of aromatics. Chem. Eng. Res. Des. 63, 184– 190.

[40] Zhang, S. J., Liu, X. M., Yao, X. Q., Dong, H. F., Zhang, X. P. 2009. Forefront, development and application of ionic liquid. Sci. China Ser. B: Chem., 39, 1134-1144.

Recycling of waste plastic with least effect to environment: A review

Aaroon Joshua Das
Department of Civil Engineering
Capital University of Science and Technology
Islamabad. Pakistan
email: ajodas@yahoo.com

Majid Ali
Department of Civil Engineering
Capital University of Science and Technology
Islamabad. Pakistan
mali078@aucklanduni.ac.nz

Abstract

There is a rising problem of plastic waste which is effecting the environment. The main reason is that plastic is present in most of the daily use things. This enormous use increases the waste production and unfortunately it does not have a proper complete life cycle. The quantum of waste recycling in marginal and studies are required to put this plastic to reuse. The overall aim of the research program is to reutilize plastic in construction industry. The present study compiles the review of the techniques available for recycling plastic and the environmental concerns of recycling plastic. Recycling primarily depend upon the type of plastic. The techniques have already been bifurcated into primary, secondary, tertiary and quaternary. The energy recovery techniques are incineration and pyrolysis which effect the environment at large. The plausible reuse of waste plastic which least effect on environment is the use in construction industry. The construction industry has the capacity to use the waste plastic in bulk quantum to reduce landfill and other waste plastic problems. The research shall provide a novel material to be used in different structural members for low paid housing in construction industry.

Keywords: Recycling, Waste Plastic, Sustainability

I. INTRODUCTION

The man made inventions have polluted the natural environment in its true form. The spread of unnecessary pollution has evolved manifold and is presently out of control. It has been the essence of all sustainability researches to retrieve the natural environment. The contamination and pollution is hard to eradicate. Reutilization and recycling of wastes are being explored to cap up the issue. Among such menace plastic pollution is a much evaluated area for recycling. The large level pollution is not only the problem it has been studied that the effects are also severe at micro level. Plastic as a material is strong, lightweight, synthetic natural polymers practically non-breakable under repetitive loads and durable. The plastic recycling is uncontrollable and 79% is being accumulate as piles on the pounds and filling land. Statistically only 9% of plastic produced globally has been recycled, the second disposal option is incineration from which 12% plastic gets a life cycle [1]. A rough idea was developed for Asian countries from available sources by Liang, et al., 2021, wherein, it was recorded that MSW municipal solid waste contains 79 Mt plastic waste 42 Mt of plastic waste is available from industrial waste [2]. The policy makers of the Asian countries are seriously putting an effort to control the plastic import and the details of 2021 have shown that the use is also being limited by the countries because of the problems of plastic waste[2].

In literature the formulation of plastic goes back to 1869 when John Wesley Hyatt developed the first known artificial plastic. The word plastic comes from “plastiko" which is Greek meaning a strand of repeating molecule. At some places it has been termed as moldable and having inherent property. The plastic product formation started from a unique plastic called Bakelite. Then further development added the use of coloring agents and other additives [3]. Due to the diverse nature of the material the industrial development grew large. In 2014 it has been reported that the industrial production goes beyond 300 Mt [4]. This uncontrollable production led to develop ideas that the material needs to be reused and recycled. This notion is still not being followed with commitment. In 2017, it was assessed that whether the people have awareness to recycle the plastic or not and it was found that a substantial quantum of people have an inclination towards recycling based on their individual set knowledge. People are also being benefitted with plastic products in different spheres of life. [5]. People are outwardly willing to to participate in plastic recycling but the problem of structured process is lagging. The system understands the stakes and linkages need to be drawn with a set of finance allocation to manage this problem efficiently [6].

This idea of recycling has put together the motivation for this study and a life cycle chain is required to make use of plastic and reduce waste. The data found in literature also reveals that plastic recycling are being considered as main stream activities and over the past few decades a substantial increase is also found in this area. The structured disposal and recycling in all modes starts from sorting either from disposal points or any other sorting done at individual use source. Some countries are pressing on banning of the plastic bags This study enacts to provide that this problem of plastic waste is increasing and becoming a bloating problem. The plastic although comes from different sector of use such as automotive, household, packing, electrical sports etc. This is not being recycled at large and producing heaps of waste. The present research program is directed to use waste plastic for construction industry for an efficient reuse for plastic.

IEECP 21, July 29-30, 2021, Silicon Valley, San Francisco, CA – USA

DAI : *https://sci-index.com/DAI/2021.99101/IEECP/14811831*

II. CONVENTIONAL RECYCLING OF WASTE PLASTIC

The recycling process is not just a figurative word it encompasses of different conversion methods. These conversion methods start from primary methods and ends to incineration or energy recovery. In such bifurcation the mechanical recycling is the most difficult and final product is often questioned in terms of contents. The properties are also deviated and a set of rules apply to control the system [7]. Gu, et al. 2017, studied extrusion process and presented that mechanical recycling is the most efficient and has least environmental impact [8]. The recycling methods segregated in research steps up from land fill or disposal at marine, then to reuse, then secondary recycling involving additive additions and mechanical recycling, then comes energy recovery and then monomerization [9]. In studies carried out at Qatar by Al-Maadeed et al., 2012, the mechanical recycling was appreciated and found most appropriate when other products are being drawn [10]. The first step for all methods are sorting, back in 1984, Lohani stated that the scavenging is the best method for sorting and collection. The solid waste management still have issues at collection point even after almost 40 years. The reason is presumably the lack of coordinated scale wise structure for plastic recycling. This has a societal impact as it can draw cleanliness and incentives for plastic recollection [11].

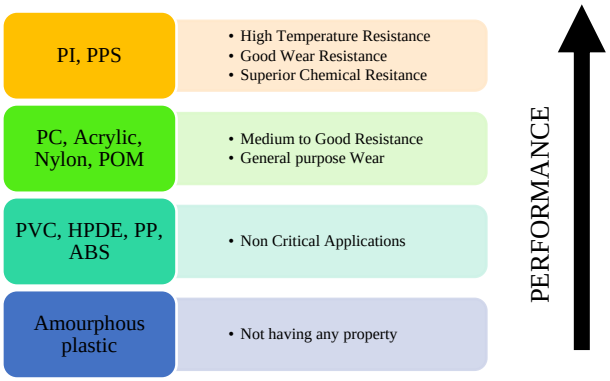

Figure 1: Performance of different Thermoplastic [12]

The recycling of the different type of thermoplastic gives a different performance level. Figure 1 shows the hierarchal depiction of some high performance plastics and also the low amorphous plastic. The second aspect which has remained under discussion is the cost adhered to recycle. Drain, et al., 1981, in their research highlighted that the cost is an important part of the recycling process. This process should be centralized to form a part of the circular economy and not only individual gains should play lead role. The study is equally applicable for all waste management system [13].

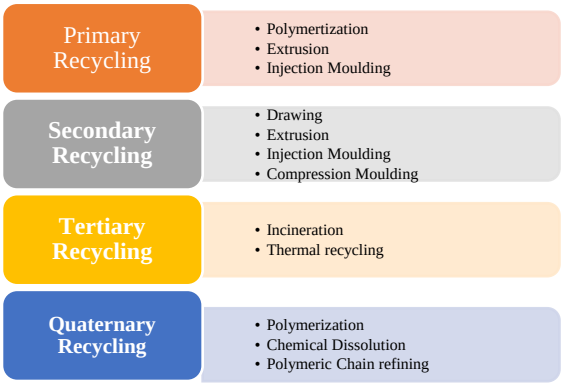

Figure 2: Thermoplastic Recycling Methods [17]

Kiran et al., 2000, studied degradation which is a sort of low temperature pyrolysis. This employs thermos gravimetric analysis [14]. The frequent set of plastic that comes to mind is the PET bottles. These bottles can be used twice and multiple reuse makes the bottles worth far more reliable than any other material. The economy of reuse definitely vary from person to person and involves hygiene issues [15]. The secondary methods are more stringent. This after collection synthesizes the waste for recycling [16]. The synthesis method effects the cost of the recycling.

The resin size after the first sort also require determination from the treatment after collection. These methods are the inert steps available to recycle the plastic. The sort is washed sometime was water and sometimes with chemical treatment. The pellets further require removal of contaminants and degraded material [18]. The stream branches off to other variants of recycling and recycling method for energy recovery are tertiary. The recycled products in all such methods are fuels [19]. Other methods include depolymerization, solvolysis, thermolysis each involving braking the molecular chain of the plastic polymer [7]. Figure 2 shows the available thermoplastic plastic recycling methods.

III. RECYCLING IMPACT ON ENVIRONMENT

The climate change, global warming and odor in the environment are prime drivers which shows the impact of plastic on the environment. The virgin plastic developed from polymerization has a different set of formulation. The plastic recycling has a different environmental impact than the virgin plastic. The comparison of two may result that recycling plastic pellets reuse are less harmful than virgin plastic. The process of recycling also signifies the environmental hazard for marine, land and air. [20][21]. Presently the pharma industries are also considering upon the demand of the plastic and due to the pandemic situation may questions are being asked to control the outburst of medical and municipal waste [22]. Plastics are widely used as essentials in health care. Blood bags, waste syringes and other items are also formed from plastic. Due to prevalent situation masks gloves, sanitizer bottles, face shields are required which are made up of plastic. This is a growing concern that plastic consumption has increased manifold it requires media publicity and social awareness [23]. The footprint should be reduced to achieve sustainability. The viable option is construction industry that might have the solution for its circular reuse by producing blocks, rebars, sheets etc.

Table 1: Waste Plastic Generation in Asian Countries[2]

Sr. No.	Country	Total Plastic Waste (2018)
1	China	49.71
2	Pakistan	5.51
3	Koera,Rep.	4.38
4	Vietnam	3.3
5	Israel	1.03
6	Yemen Rep	0.93
7	Srilanka	0.56
8	Mongolia	0.46
9	Tajikistan	0.36
10	Watar	0.25
11	Turkmenistan	0.16
12	Brunei Darussalum	0.05
13	India	17.66
14	Japan	11.19
15	Turkey	6.28
16	Thailand	5.96
17	Iran, Islamic rep	3.24
18	Saudi Arabia	3.11
19	Indonesia	3.101
20	Philipine	2.61
21	Malaysia	2.65
22	Singapore	1.24

In the literature a compilation for the year 2018 was found and has been redrawn at Table 1 which shows the plastic which goes to landfill in Asian countries [2]. Since the research Lohani, 1984 who provided a review which was cursory that Asian countries are opting for Solid Waste Management [11]. These when compared with the statistics of Liang et al., 2021, shows that 40 years are not even sufficient to cater the issue of plastic waste [2]. The reason is probable population growth, increase in demand, easy availability of the material and so forth. Plastic produced from fishing gears and other also in parallel describes that marine areas are also being polluted at large. Deshpande, et al., have also depicted the increase of the adverse effect of social, economic, and environmental in Norway due to this plastic waste [24]. The people of China have also brought their thoughts for quantification of the waste produced from PET materials. This quantification shall enable proper recycling and waste management control to this menace. This idea has also been implemented in different areas of the world. As quantification reduces uncertainty and provides a relationship of demand and supple. In a small island of Grenada this idea was implemented by Elgie, et al., 2021, an economic model was devised and the advantage of the area was that everything is imported [25]. About 7421 tons of plastic was imported. The control highlighted that it is feasible to control the plastic once the original figures are in place.

The polyethylene amongst the other plastic is becoming an issue and in very near future it will become a problem [26]. Some uses derived for plastic also covers soil improvement. The properties of soil improve by optimizing Plastic-Eucalyptus wood char in soil [27]. This was recorded to increase the soil fertility making a sustainable use of the plastic. Environmental, social and economic aspect of this present day plastic problem requires a solid waste network discussed by Mamashli & Javadian, 2021, [28]. This study states that in order to manage the solid waste facilities which includes vehicles, equipment etc. are required to setup the system for recycling. The well-established factors determine the planning and implementation of recycling techniques The underutilization of the potential of waste is also waste [29]. The trend of construction waste and other waste are catered during execution of each project. However, the life cycle of plastic is still under debate and entails the attitude and assessment of the life cycle to be developed for plastic [30][31].

IV. MINIMIZING ENVIRONMENT CONCERNS DURING RECYCLING

The main source of waste comes from the Municipal Plastic Waste (MPW). A depiction of different portions of plastic in MSW is shown in Figure 3. In order to target the plastic waste and reduce environmental concerns the detail bifurcation analysis is required from source MSW. This identification helps reduce the effort of recycling and provides a target plastic for recycling. The bifurcation shows that MSW contains 8% of (PET) polyethylene terephthalate, about 10% (PVC) Polyvinyl Chloride and (uPVC) un-plasticized, about 30% of (HDPE) High Density Polyethylene & (LDPE) low density polyethylene, about 19% proportion of (PP) Polypropylene, (PS) Polystyrene in proportion of about 6% and other plastic of about 19% [32][33][34]. These plastics have a recyclable value. Polyethylene group is the largest to be available in the MSW and becomes an important nominee for use in recycling. The recycling of PE would reduce by 35-30% of the plastic waste. All plastics are not recyclable and many become amorphous prior to any treatment. In fact, due to presence of impurities the plastics after repetitive recycling degrade and are not stable. This is added with a touch of additive to improve the process. The additives not only give the required property but also provides a solution to reduce environmental concerns.

The plastic recycling is not easy and a proper set of skill development is required. The plastic recycling provides a large scale of employment and money minting solutions. The use of plastic extends to making toys and stationary items which also has a societal impact [20]. The leading sector for plastic reuse is undoubtedly packaging. [35]. Other than industry household also bears a quantum for recycling. Jiang, et al., 2021, have also highlighted that in present era social media can play a vital role to enlighten the societal drive for waste plastic management [36].

Recently in Bangladesh plastic PET bottles have been suggested as eco-friendly solution to replace bricks [37]. Plastic recycling advocacy is making its place in the construction industry in building, roads and other uses. Sharma and Bansal, 2016, used different type of waste plastic and used it in the concrete being used as additive usually provide crack arrest and decrease the strength component in concrete. This method utilizes the waste in the concrete such variants are not preferred for significant structural work. Sharma & Bansal, 2016, reviewed the compilations of different studies where plastic was used in concrete[38]. Plastic waste reutilization in construction industry is being studied for roads, soil improvement concrete filler and production of other building products. This industry shall provide a platform for a huge quantum of waste recycling.

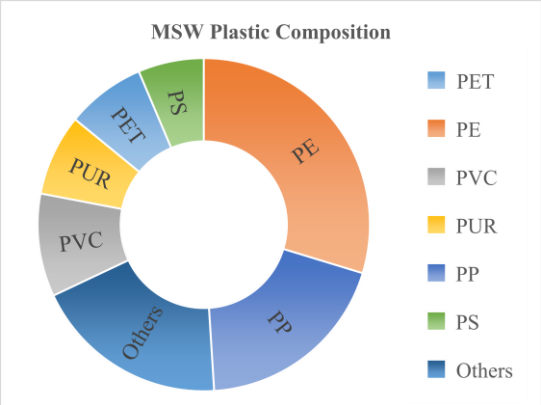

Figure 3: General Composition of plastic in MSW[32][33][34]

V. CONCLUSION

The plastic waste disposed produces landfill and pollutes the Environment. The Asian countries are generating waste plastic at large and if the issue is not addressed to complete the life cycle of plastic then this menace shall further create problems. The literature is evident that recycling methods does not completely eliminate all type of plastic waste. The present recycling methods also employ incineration which produces environmental hazards. The construction industry however can provide a sustainable solution for waste plastic reutilization. The societal aspect considering the present pandemic situation has gained much attention in providing awareness for plastic reuse. The involvement at individual level is required for plastic disposal. The present study shall form a basis to explore plastic reuse in construction industry to develop rebars, sheets, blocks and other construction variant.

VI. ACKNOWLEDGMENTS

Our thanks to thank CE department, Capital University of Science and Technology and members of SMaRG for providing assistance in the research.

VII. REFERENCES

[1] R. Geyer, J. R. Jambeck, and K. L. Law, “Production, use, and fate of all plastics ever made,” *Sci. Adv.*, vol. 3, no. 7, pp. 25–29, 2017, doi: 10.1126/sciadv.1700782.

[2] Y. Liang, Q. Tan, Q. Song, and J. Li, “An analysis of the plastic

waste trade and management in Asia," *Waste Manag.*, vol. 119, pp. 242–253, 2021, doi: 10.1016/j.wasman.2020.09.049.

[3] M. Kutz, *Applied plastics engineering handbook: processing and materials*. William Andrew, 2011.

[4] I. Muise, M. Adams, R. Côté, and G. W. Price, "Attitudes to the recovery and recycling of agricultural plastics waste: A case study of Nova Scotia, Canada," *Resour. Conserv. Recycl.*, vol. 109, pp. 137–145, 2016, doi: 10.1016/j.resconrec.2016.02.011.

[5] R. Afroz, A. Rahman, M. M. Masud, and R. Akhtar, "The knowledge, awareness, attitude and motivational analysis of plastic waste and household perspective in Malaysia," *Environ. Sci. Pollut. Res.*, vol. 24, no. 3, pp. 2304–2315, 2017, doi: 10.1007/s11356-016-7942-0.

[6] J. Van Engeland, J. Beliën, L. De Boeck, and S. De Jaeger, "Literature review: Strategic network optimization models in waste reverse supply chains," *Omega (United Kingdom)*, vol. 91, 2020, doi: 10.1016/j.omega.2018.12.001.

[7] S. M. Al-Salem, P. Lettieri, and J. Baeyens, "The valorization of plastic solid waste (PSW) by primary to quaternary routes: From re-use to energy and chemicals," *Prog. Energy Combust. Sci.*, vol. 36, no. 1, pp. 103–129, 2010, doi: 10.1016/j.pecs.2009.09.001.

[8] F. Gu, J. Guo, W. Zhang, P. A. Summers, and P. Hall, "From waste plastics to industrial raw materials: A life cycle assessment of mechanical plastic recycling practice based on a real-world case study," *Sci. Total Environ.*, vol. 601–602, pp. 1192–1207, 2017, doi: 10.1016/j.scitotenv.2017.05.278.

[9] D. Lazarevic, E. Aoustin, N. Buclet, and N. Brandt, "Plastic waste management in the context of a European recycling society: Comparing results and uncertainties in a life cycle perspective," *Resour. Conserv. Recycl.*, vol. 55, no. 2, pp. 246–259, 2010, doi: 10.1016/j.resconrec.2010.09.014.

[10] M. Al-Maaded, N. K. Madi, R. Kahraman, A. Hodzic, and N. G. Ozerkan, "An Overview of Solid Waste Management and Plastic Recycling in Qatar," *J. Polym. Environ.*, vol. 20, no. 1, pp. 186–194, 2012, doi: 10.1007/s10924-011-0332-2.

[11] B. N. Lohani, "Recycling potentials of solid waste in Asia through organised scavenging," *Conserv. Recycl.*, no. 2, pp. 181–190, 1984.

[12] A. Das *et al.*, "Current understanding and challenges in high temperature additive manufacturing of engineering thermoplastic polymers," *Addit. Manuf.*, vol. 34, no. April, p. 101218, 2020, doi: 10.1016/j.addma.2020.101218.

[13] K. F. Drain, W. R. Murphy, and M. S. Otterburn, "Polymer waste - resource recovery," *Conserv. Recycl.*, vol. 4, no. 4, pp. 201–218, 1981, doi: 10.1016/0361-3658(81)90025-4.

[14] N. Kiran, E. Ekinci, and C. E. Snape, "00/03732 Recycling of plastic wastes via pyrolysis," *Fuel Energy Abstr.*, vol. 41, no. 6, pp. 417–418, 2000, doi: 10.1016/s0140-6701(00)94792-1.

[15] K. Hamad, M. Kaseem, and F. Deri, "Recycling of waste from polymer materials: An overview of the recent works," *Polym. Degrad. Stab.*, vol. 98, no. 12, pp. 2801–2812, 2013, doi: 10.1016/j.polymdegradstab.2013.09.025.

[16] D. J. da Silva and H. Wiebeck, "Current options for characterizing, sorting, and recycling polymeric waste," *Prog. Rubber, Plast. Recycl. Technol.*, vol. 36, no. 4, pp. 284–303, 2020, doi: 10.1177/1477760620918603.

[17] R. Kumar, "Tertiary and quaternary recycling of thermoplastics by additive manufacturing approach for thermal sustainability," *Mater. Today Proc.*, vol. 37, no. Part 2, pp. 2382–2386, 2020, doi: 10.1016/j.matpr.2020.08.183.

[18] J. Li *et al.*, "Rapid biodegradation of polyphenylene sulfide plastic beads by Pseudomonas sp.," *Sci. Total Environ.*, vol. 720, p. 137616, 2020, doi: 10.1016/j.scitotenv.2020.137616.

[19] I. A. Ignatyev, W. Thielemans, and B. Vander Beke, "Recycling of polymers: A review," *ChemSusChem*, vol. 7, no. 6, pp. 1579–1593, 2014, doi: 10.1002/cssc.201300898.

[20] K. P. Gopinath, V. M. Nagarajan, A. Krishnan, and R. Malolan, "A critical review on the influence of energy, environmental and economic factors on various processes used to handle and recycle plastic wastes: Development of a comprehensive index," *J. Clean. Prod.*, vol. 274, p. 123031, 2020, doi: 10.1016/j.jclepro.2020.123031.

[21] L. Shen, E. Worrell, and M. K. Patel, "Open-loop recycling: A LCA case study of PET bottle-to-fibre recycling," *Resour. Conserv. Recycl.*, vol. 55, no. 1, pp. 34–52, 2010, doi: 10.1016/j.resconrec.2010.06.014.

[22] C. S. G. Penteado and M. A. S. de Castro, "Covid-19 effects on municipal solid waste management: What can effectively be done in the Brazilian scenario?," *Resour. Conserv. Recycl.*, vol. 164, no. June 2020, p. 105152, 2021, doi: 10.1016/j.resconrec.2020.105152.

[23] V. Thakur, "Framework for PESTEL dimensions of sustainable healthcare waste management: Learnings from COVID-19 outbreak," *J. Clean. Prod.*, vol. 287, p. 125562, 2021, doi: 10.1016/j.jclepro.2020.125562.

[24] P. C. Deshpande, C. Skaar, H. Brattebø, and A. M. Fet, "Multi-criteria decision analysis (MCDA) method for assessing the sustainability of end-of-life alternatives for waste plastics: A case study of Norway," *Sci. Total Environ.*, vol. 719, p. 137353, 2020, doi: 10.1016/j.scitotenv.2020.137353.

[25] A. R. Elgie, S. J. Singh, and J. N. Telesford, "You can't manage what you can't measure: The potential for circularity in Grenada's waste management system," *Resour. Conserv. Recycl.*, vol. 164, no. May 2020, p. 105170, 2021, doi: 10.1016/j.resconrec.2020.105170.

[26] J. Chu, Y. Cai, C. Li, X. Wang, Q. Liu, and M. He, "Dynamic flows of polyethylene terephthalate (PET) plastic in China," *Waste Manag.*, no. 124, pp. 273–282, 2021.

[27] K. R. Vanapalli, J. Bhattacharya, B. Samal, S. Chandra, I. Medha, and B. K. Dubey, "Optimized production of single-use plastic-Eucalyptus wood char composite for application in soil," *J. Clean. Prod.*, vol. 278, p. 123968, 2021, doi: 10.1016/j.jclepro.2020.123968.

[28] Z. Mamashli and N. Javadian, "Sustainable design modifications municipal solid waste management network and better optimization for risk reduction analyses," *J. Clean. Prod.*, vol. 279, p. 123824, 2021, doi: 10.1016/j.jclepro.2020.123824.

[29] L. A. Guerrero, G. Maas, and W. Hogland, "Solid waste management challenges for cities in developing countries," *Waste Manag.*, vol. 33, no. 1, pp. 220–232, 2013, doi: 10.1016/j.wasman.2012.09.008.

[30] K. Kabirifar, M. Mojtahedi, C. Wang, and V. W. Y. Tam, "Construction and demolition waste management contributing factors coupled with reduce, reuse, and recycle strategies for effective waste management: A review," *J. Clean. Prod.*, vol. 263, p. 121265, 2020, doi: 10.1016/j.jclepro.2020.121265.

[31] J. Hopewell, R. Dvorak, and E. Kosior, "Plastics recycling: Challenges and opportunities," *Philos. Trans. R. Soc. B Biol. Sci.*, vol. 364, no. 1526, pp. 2115–2126, 2009, doi: 10.1098/rstb.2008.0311.

[32] P. E. Alejandro Villanueva, *End-of-waste criteria for waste plastic for conversion*. 2014.

[33] C. Areeprasert *et al.*, "Municipal Plastic Waste Composition Study at Transfer Station of Bangkok and Possibility of its Energy Recovery by Pyrolysis," *Energy Procedia*, vol. 107, no. September 2016, pp. 222–226, 2017, doi: 10.1016/j.egypro.2016.12.132.

[34] H. Zhang, S. Pap, M. A. Taggart, K. G. Boyd, N. A. James, and S. W. Gibb, "A review of the potential utilisation of plastic waste as adsorbent for removal of hazardous priority contaminants from aqueous environments," *Environ. Pollut.*, vol. 258, no. xxxx, p. 113698, 2020, doi: 10.1016/j.envpol.2019.113698.

[35] S. Serranti and G. Bonifazi, *Techniques for separation of plastic wastes*, no. January 2018. Elsevier Ltd, 2019.

[36] P. Jiang, Y. Van Fan, and J. J. Klemeš, "Data analytics of social media publicity to enhance household waste management," *Resour. Conserv. Recycl.*, vol. 164, no. June 2020, p. 105146, 2021, doi: 10.1016/j.resconrec.2020.105146.

[37] M. Oyinlola and T. Whitehead, "Recycling of Plastics for Low Cost Construction," *Encycl. Renew. Sustain. Mater.*, pp. 555–560, 2020, doi: 10.1016/b978-0-12-803581-8.11523-1.

[38] R. Sharma and P. P. Bansal, "Use of different forms of waste plastic in concrete - A review," *J. Clean. Prod.*, vol. 112, pp. 473–482, 2016, doi: 10.1016/j.jclepro.2015.08.042.

A Review on Durability Methods for Natural Fibers in Polymer Matrices from Sustainability Aspects

1st Blawal Hasan
Department of Civil Engineering
Capital University of Science and Technology
Islamabad, Pakistan
blawalhasan@gmail.com

2nd Majid Ali
Department of Civil Engineering
Capital University of Science and Technology
Islamabad, Pakistan
professor.drmajid@gmail.com

Abstract

The researchers around the globe are working hard to develop new material which would improve the quality of product environmentally, as this world needs eco-friendly materials. This article gives a critical review of the treatment methods/techniques that can improve durability for natural fibers in polymers. The natural fibers are very low cost as compared to other fibers and having specific high properties. These natural fibers are not abrasive and can biodegradable. The natural fiber polymer proffers certain properties which are similar to traditional fiber polymers. However, while preparation of these polymers, the critical issue is frequently the reduction of the strength of natural fibers in polymer matrices which is caused by unsuited fibers and less resistive against. The durability can be achieved by increasing strength, better workability, good mixing and by enhancing the bond strength of fibers with the surrounding. These require very low energy which is consumed during the production and hold mechanical properties of superior quality. By using such materials with properly treated natural fibers in construction works, it is quite possible to produce more sustainable material by minimum construction waste.

Keywords: *Durability Methods, fiber reinforced composites, natural fiber reinforced polymers.*

I. INTRODUCTION

The use of fibrous material in the construction industry is growing day by day. In the construction industry, fiber reinforced concrete and fiber reinforced polymers are the most common composites composed of fibers. Many researchers investigated the effect of fibers on the properties of the composite [1-3]. The dynamic and mechanical properties of the composite improved by the addition of the fiber [4, 5]. The addition of fibers has enhanced the resistance against the cracking of the composite [6, 7]. In comparison with construction materials like concrete and steel, fiber reinforced polymers (FRP) have several benefits. In the construction industry, the use of FRP is limited in building and construction [8–10]. Natural fiber reinforced polymer (NFRP) is a composite of natural fiber reinforcement and with a polymer matrix [11]. In general, FRP is used in the automotive, aerospace and marine industry. FRP materials are lightweight high strength materials compared to other composites. The FRP composites with reinforcement of fibers have comprehensive use in the civil engineering construction industry in complementary applications, such as bathrooms and vanities, kitchen, ornamentation and finishing, for many years. The ballistic performance of bulletproof vests and helmets was enhanced by the distribution of natural fibers in the composites [12]. In the last year of the 20th century, the second-largest consumer of FRP materials industry in this world was the construction industry by consuming 35% of the around the globe [13]. From the beginning of the 21st century until now, there have been a lot of efforts and research work done to shift fiber reinforced polymers (FRPs) into the construction sector to be used as basic material for load-bearing members of civil structures and condemnatory applications. The use of FRP composites is being increased in the construction works as time passes and has significant importance for larger use in civil works and buildings, as well as it also includes large primary structures [14]. Now construction industry is the most consuming industry of polymers and their composites. These days, the increment has been seen in the preparation of load-bearing structural implementations in construction works. As a substitution of steel in concrete, FRP has been initiated as a feasible, aggressive choice for retrofit and convalescence of medieval civil structures [15]. In a research study, it was observed that jute fiber reinforced polymer composite is better than the polypropylene fiber reinforced polymer composite for external strengthening of concrete [16]. Nowadays, the use of NFRP is going to be traditional material like concrete and masonry due to the incremental use of these composites in civil and structural engineering sectors [17].

FRP composites are composed of fibers and a polymer matrix in which fiber act as reinforcement. There are two types of fibers either artificial fibers, such as aramid, glass and carbon fibers, or natural fibers, such as plant and animal fibers. Artificial FRP composites are more likely used in the aerospace and automobile industry in high-performance applications because of the fact of their better mechanical qualities and lightweight. Anyhow, these fibers are expensive, then the natural fibers, need large energy in production. Synthetic or artificial fibers are not eco-friendly. If not recycled properly, hence, their immense usage can lead to environmental pollution [18]. Due to ensure competitive cost, energy consumption while production, reduce dependency on nonrenewable resources

IEECP'21, July 29-30, 2021, Silicon Valley, San Francisco, CA – USA

DAI : *https://sci-index.com/DAI/2021.99101/IEECP/14811837*

and non-eco-friendly, hence, have changed the focus to use natural fibers as reinforcement instead of synthetic fibers [19–21]. In both the academic and construction industry, NFRPs are gaining increased attention. Due to their preferable properties and ease of availability, natural fibers like jute, sisal, flax and hemp are commonly used as reinforcement in FRPs [22]. A FRP composite part made of natural fibers will be light in weight than others produced with synthetic fibers such as glass fibers. This is because of the variance between the densities. The density of natural fibers is lies between 1.2 to 1.6 g/cm3 and synthetic such as glass fibers lie between 2.16 to 2.68 g/cm3 [23, 24]. On the other way around, NFRP composites have a lot of disadvantages, such as high moisture content, poor fire aversion, poor linking adhesion, low aversion to microbiological attack and a need to use at low refining temperatures [22]. The flexural strength, as well as thermal and physical properties of the composite, are highly dependent upon the interfacial adhesion conditions [25]. The use of different lengths of natural fibers has shown different effects on flexural strength physical properties of NFRP [26]. However, many of these issues can be tackled with suitable surface treatment methods. The use of NFRP composites can be different according to interest from section to section, for example, the NFRP is used for structural applications like railing, decking and fencing in the United States region, while in the Europe region NFRPs are primarily used in the automotive industry [27].

In this study, different methods were elaborated for the durability of natural fiber in polymers. The use of NFRP in the construction sector has been scrutinized by many researchers, who have investigated the properties and characteristics of different types of NFRPs, for example, modification of fiber, fiber biodegradability, crystallinity and thermal stability. However, the majority of work has based on plastic materials reinforced with natural fibers. And few studies have been conducted considering polymers reinforced by natural fibers and their functionality in the building and construction industry. Furthermore, the main focus of the review has been on moisture content, fiber matrix and adhesion property to the surrounding of fiber with polymers. The purpose and focus of this article are to examine the durability for the engineering purposes of polymers reinforced with natural fiber as filler material and their functionality in the construction industry. It has been claimed that even after some treatment of durability for natural fiber, NFRPs properties are superior to those without some treatment of fibers for durability, and thus, more sustainable material can be obtained with the help one these durability methods. In this study, different methods were elaborated for the durability of natural fiber in polymers. The use of NFRP in the construction sector has been scrutinized by many researchers, who have investigated the properties and characteristics of different types of NFRPs, for example, modification of fiber, fiber biodegradability, crystallinity and thermal stability. However, the majority of work has based on plastic materials reinforced with natural fibers. And few studies have been conducted considering polymers reinforced by natural fibers and their functionality in the building and construction industry. Furthermore, the main focus of the review has been on moisture content, fiber matrix and adhesion property to the surrounding of fiber with polymers. The purpose and focus of this article are to examine the durability for the engineering purposes of polymers reinforced with natural fiber as filler material and their functionality in the construction industry. It has been claimed that even after some treatment of durability for natural fiber, NFRPs properties are superior to those of without some treatment of fibers for durability, and thus, more sustainable material can be obtained with the help one these durability methods.

II. FACTS ABOUT REDUCED DURABILITY OF FIBERS IN FRP

During the serviceable life, FRP materials aspect a diversity of climate circumstances developing from artificial or/and natural factors. These factors consist of fluctuating temperature and humidity, vital ultraviolet rays caused by the sun or any other human activities, and chemical reactions such as chemical liquids in storing tanks and pipes connected with it, and atmospheric ozone and oxygen. The durability reduction factors like the fiber's degradation, cracking of matrix, and de-bonding were presented from applicable records to control for the climate effects on behavior on composites of FRP [28]. FRP materials react to environmental factors which cause a reduction in durability. These factors cause the change in the structure of material chemical and physical and its formation. Effects of these kinds of changes are permanent decay of the mechanical properties and characteristics of a commodity. Aesthetic looks/conditions, like color and shine, go through permanent change. The material may also develop into brittle and cracks can occur. In practice, degradation is defined as any change that affects the material properties related to advisable properties. As shown in Figure 1, this can also be caused by the FRP helix rupture at failure [29].

Mostly, the degradation caused by the environment is a slow process

Figure 1. FRP spiral broke at failure.

that can last up to many years before effects are probable [30]. Degradation caused by environmental can result from environmental effects like temperature, humidity, climate type, overburden resulting in debonding, impacts and rusting of the actual reinforced steel [31]. The alkaline polymer's environment can also result in the degradation of fiber. The most of study work has been done on the fiber, nonetheless, the resin has turn into the study focus. This is the major review in FRP composite is the durability in the field and service life. The concrete structures are which are exposed to the environment, there still need to understand the long-term durability of FRP [32]. In research work, it was concluded that meaningful reflection has been managed to the durability of fiber reinforced polymers commodity in infrastructure functions [33]. The researchers spotted a long-term data deficiency related to the service life of more than 75 years of civil structures [34]. A study conducted by the Civil Engineering Research Fund to bridge cracks in long-term durability data associated with construction industry functionalities spotted the points that are needed like effects of moisture, alkaline solution, creep, fatigue and deterioration [35]. Degradation of natural fibers, i.e., bamboo fibers, accelerates in an alkaline environment than the glass fibers [36]. The effect of

ultraviolet rays (UV) also affects the durability of fibers in FRP. Table 1 shows the comparison between the strengths of unseasoned and seasoned fibers and FRPs affected by the UV rays.

Table 1. UV's effects on natural fibers and FRP [37]**.**

Composite	Unseasoned		Seasoned	
	Tensile Strength (MPa)	Young's Modulus (GPa)	Tensile Strength (MPa)	Young's Modulus (GPa)
Jute	45.55	3.89	25.45	2.77
Epoxy	20.62	1.98	19.18	1.02
EFB	22.61	2.23	21.20	2.17

III. DURABILITY METHODS IN FRP

A. Proper Good Mixing of Fibers in Polymers

1. Specifications

Arbitrarily blended palmyra reinforced composites were set up with various fiber lengths and distinctive fiber content (49%–54%). At 30 mm and 40 mm fiber length, the impact, flexural and tensile properties were achieved with 54% fiber content. At 50 mm fiber length, every one of the static mechanical properties was higher with 55% fiber content. Further expanding the fiber substance will diminish the mechanical properties [38]. After the manufacturing, the FRP was placed in resin for 24 hours. A research study was performed on test beams of size 152 mm 254 mm 2743 mm reinforced by NFRP fabrics and plates to assess durability exposing 10,000 h in severe environmental conditions [20]. Glass transformation temperatures were the same for the two resins. Across the whole 152 mm width of beam NFRP plate and two fabrics were applied to meet the strength of 1.2 mm thick NFRP plate. No information regarding epoxy thickness was provided.

2. Technology involved and method implementation

The exposures to the environment considered were fully humidity, salty water, alkaline solution, frost and thaw, expansion due to thermal energy and dry due to heat at 60 °C. ASTM testing standards were adopted for the salty water, alkaline solution and frost and defrost vulnerability. For thermal expansion and frost and defrost testing, two specimens were tested after 1000 h, 3000 h, 10,000 h excepting. To determine fatigue the effect caused by imitated loads, reinforced beams were applied constant magnitude but imitated load repetitions at 3.25 Hz with the load limiting from 15, 25 and 40 percent of ultimate load of reinforced beams.

B. Increase of Bond Strength

1. Specifications

The mechanical properties of hybrid fiber reinforced polymer's properties were investigated with various fiber treatment, ratio and loading. The FRPs were also manufactured with different chemically treated fibers. The bond strength of fibers dispersed longitudinally was higher than transversely dispersed fibers [39]. Bond strength also depends upon the chemical used for the treatment of fibers and the surface texture of the fibers. It was observed that the tensile strength and hardness properties were improved when the chemically treated fibers were used for the manufacturing of the hybrid reinforced composite [40].

2. Technology involved and method implementation

The FRP can be prepared by using different types of methodologies with different weights and directions of dispersion of the fibers. Different researchers used different types of methodologies to improve the bond strength. In a research study, for the manufacturing of the FRP composite, hydraulic press technology was used to improve the bond strength [41]. The hand layup and cold press technique was adopted for the manufacturing of the hybrid fiber reinforced composite [42]. Another research used hot press technology along with the epoxy resin for FRP's manufacturing [43].

IV. LESSONS LEARNT FOR ENHANCING DURABILITY TO ENSURE SUSTAINABILITY

The use of FRP is being increasing day by day in the construction industry. As the 35% total manufactured FRP material is being used in the construction industry only. The construction sector is the second largest industry that uses FRP as a building material. The FRP is a more sustainable and lightweight material than concrete. The bond of fibers with the surrounding matrix of polymer composite directly affects the sustainability of the material. The sustainability of FRP also depends upon the methodology adopted for the mixing and resins type. There is no standardized design code available for FRP. Different researchers used different types of methodology for the manufacturing of the FRP. The different technology of pressing and different types of resins were used. Mechanical properties, brittleness of fiber, characteristics of fiber can be damaged by the execution of loading, variation of temperature and exposure to climate situations. The durability of FRPs is considerable interest durability of FRPs for its extensive functionality, if any, soon exceed the rule of conventional building materials. The durability depends upon the matrix and the fibers used for making them more durable than the fibers themselves. However, the strength is more influenced by making the fiber strong in tension. Collective effect causing by joined action of humidity and temperature is known to be harmful and damaging.

V. CONCLUSIONS

In civil engineering, the use of FRPs allows engineers to gain outstanding achievements in the applicability, economy and safety of construction. The strength to density ratio of FRP is high ratio as these are lightweight and high performance, may be altered to possess specific mechanical properties, have better corrosion resistance behavior, convenient magnetic, electrical and thermal characteristics to be considered as a blessing to the construction industry and its applications. The pursuing conclusions were realized/noticed from recent and past studies on durability of fiber reinforced polymer composites:

- Natural fibers degradation accelerates in an alkaline environment like seawater structures, so the fiber should properly be treated using resins to enhance the durability of natural fibers in the polymers.
- By improving the bond strength between the fiber and polymer, the durability for fibers in polymers enhances. Hence, a more sustainable composite material can be produced.
- To improve the durability of natural fibers in polymers, it is concluded that durability can be improved by increasing the strength of the composite.
- The change in external appearance and look polymer composite material occurred by UV radiation effects.
- While aging of moisture absorption, swelling of the fiber, rusting of fiber, water flow between matrix and fiber surfaces and babble are created in composites.
- Due to ultraviolet radiations, the moisture-absorbing capacity is more of natural fiber as compared to synthetic fibers, FRP material's durability and mechanical characteristics may be lightly enhanced by providing an outside boundary layer as synthetic fibers on exposure of the NFRP composite materials.

- Capillary action of the flow of water is low on synthetic fiber made FRP, hence, provision of the layer of synthetic fiber enhances NFRP materials.
- Proper good mixing of the composite can enhance the durability of the FRP.

It can be observed that FRP is a blessing/gift to the civil and construction works, finding some very alluring functions along with the issues of involvement for their broad acceptance and functionality. These issues, somehow, can be overcome and control by enhancing the durability of natural fibers in the polymer.

ACKNOWLEDGMENTS

The authors would like to thank all the persons who have helped in this research work.

VI. REFERENCES

[1] M. Ali, A. Liu, H. Sou, and N. Chouw, "Mechanical and dynamic properties of coconut fibre reinforced concrete," Construction and Building Materials, vol. 30, pp. 814–825, 2012.

[2] M. Khan, M. Cao, and M. Ali, "Effect of basalt fibers on mechanical properties of calcium carbonate whisker-steel fiber reinforced concrete," Construction and Building Materials, vol. 192, pp. 742–753, 2018.

[3] M. Khan and M. Ali, "Effect of super plasticizer on the properties of medium strength concrete prepared with coconut fiber," Construction and Building Materials, vol. 182, pp. 703–715, 2018.

[4] M. Ali and N. Chouw, "Experimental investigations on coconut-fibre rope tensile strength and pullout from coconut fibre reinforced concrete," Construction and Building Materials, vol. 41, pp. 681–690, 2013.

[5] M. Ali, "Seismic performance of coconut-fibre-reinforced-concrete columns with different reinforcement configurations of coconut-fibre ropes," Construction and Building Materials, vol. 70, pp. 226–230, 2014, doi: https://doi.org/10.1016/j.conbuildmat.2014.07.086.

[6] A. Zia and M. Ali, "Behavior of fiber reinforced concrete for controlling the rate of cracking in canal-lining," Construction and Building Materials, vol. 155, pp. 726–739, 2017.

[7] M. Khan and M. Ali, "Use of glass and nylon fibers in concrete for controlling early age micro cracking in bridge decks," Construction and Building Materials, vol. 125, pp. 800–808, 2016.

[8] R. E. Chambers, "Structural fiber glass-reinforced plastics for building applications," Plastics in Buildings. Reinhold Publishing Co., New York, pp. 72–118, 1965.

[9] L. Hollaway, Glass reinforced plastics in construction: engineering aspects. John Wiley & Sons Incorporated, 1978.

[10] Z. S. Makowski, "SYMBIOSIS OF ARCHITECTURE AND ENGINEERING IN THE DEVELOPMENT OF STRUCTURAL USES OF PLASTICS," 1981.

[11] O. Hag-Elsafi, S. Alampalli, and J. Kunin, "Application of FRP laminates for strengthening of a reinforced-concrete T-beam bridge structure," Composite structures, vol. 52, no. 3–4, pp. 453–466, 2001.

[12] N. M. Nurazzi et al., "A review on natural fiber reinforced polymer composite for bullet proof and ballistic applications," Polymers, vol. 13, no. 4, p. 646, 2021.

[13] A. Weaver, "Composites: world markets and opportunities," Materials Today, vol. 2, no. 1, pp. 3–6, 1999, doi: 10.1016/s1369-7021(99)80012-1.

[14] D. Kendall, "Building the future with FRP composites," Reinforced plastics, vol. 51, no. 5, pp. 26–33, 2007.

[15] A. Seco, A. M. Echeverria, S. Marcelino, B. Garcia, and S. Espuelas, "Durability of polyester polymer concretes based on metallurgical wastes for the manufacture of construction and building products," Construction and Building Materials, vol. 240, p. 117907, 2020.

[16] K. Madhavi, V. V Harshith, M. Gangadhar, V. C. Kumar, and T. Raghavendra, "External strengthening of concrete with natural and synthetic fiber composites," Materials Today: Proceedings, vol. 38, pp. 2803–2809, 2021.

[17] T. Nicolae, O. Gabriel, I. Dorina, E. Ioana, M. Vlad, and B. Catalin, "Fibre reinforced polymer composites as internal and external reinforcements for building elements," Buletinul Institutului Politehnic din lasi. Sectia Constructii, Arhitectura, vol. 54, no. 1, p. 7, 2008.

[18] S. K. Ramamoorthy, M. Skrifvars, and A. Persson, "A review of natural fibers used in biocomposites: plant, animal and regenerated cellulose fibers," Polymer Reviews, vol. 55, no. 1, pp. 107–162, 2015.

[19] M. R. Sanjay, G. R. Arpitha, and B. Yogesha, "Study on mechanical properties of natural-glass fibre reinforced polymer hybrid composites: A review," Materials today: proceedings, vol. 2, no. 4–5, pp. 2959–2967, 2015.

[20] J. L. Thomason and J. L. Rudeiros-Fernández, "A review of the impact performance of natural fiber thermoplastic composites," Frontiers in Materials, vol. 5, p. 60, 2018.

[21] C. Grazide, E. Ferrier, and L. Michel, "Rehabilitation of reinforced concrete structures using FRP and wood," Construction and Building Materials, vol. 234, p. 117716, 2020.

[22] K. Rohit and S. Dixit, "A review-future aspect of natural fiber reinforced composite," Polymers from Renewable Resources, vol. 7, no. 2, pp. 43–59, 2016.

[23] G. Navaneethakrishnan et al., "Structural analysis of natural fiber reinforced polymer matrix composite," Materials today: proceedings, vol. 21, pp. 7–9, 2020.

[24] Hm. Akil, M. F. Omar, A. A. M. Mazuki, S. Safiee, Z. A. M. Ishak, and A. A. Bakar, "Kenaf fiber reinforced composites: A review," Materials & Design, vol. 32, no. 8–9, pp. 4107–4121, 2011.

[25] C. H. Lee, A. Khalina, and S. H. Lee, "Importance of Interfacial Adhesion Condition on Characterization of Plant-Fiber-Reinforced Polymer Composites: A Review," Polymers, vol. 13, no. 3, p. 438, 2021.

[26] J. B. Sajin, P. B. Aurtherson, J. S. Binoj, N. Manikandan, M. S. S. Saravanan, and T. M. Haarison, "Influence of fiber length on mechanical properties and microstructural analysis of jute fiber reinforced polymer composites," Materials Today: Proceedings, vol. 39, pp. 398–402, 2021.

[27] Y. Gao, H. Zhang, M. Huang, and F. Lai, "Unsaturated polyester resin concrete: A review," Construction and Building Materials, vol. 228, p. 116709, 2019.

[28] K. Mayandi, N. Rajini, M. Manojprabhakar, S. Siengchin, and N. Ayrilmis, "Recent studies on durability of natural/synthetic fiber reinforced hybrid polymer composites," in Durability and Life

Prediction in Biocomposites, Fibre-Reinforced Composites and Hybrid Composites, Elsevier, 2019, pp. 1–13.

[29] T. Ibell, A. Darby, and S. Denton, "Research issues related to the appropriate use of FRP in concrete structures," Construction and building materials, vol. 23, no. 4, pp. 1521–1528, 2009.

[30] E. K. Ngoy, "Modelling and prediction of the environmental degradation of fibre reinforced plastics." University of the Witwatersrand, 2010.

[31] J. R. Brown, "Infrared Thermography Inspection of Fiber-reinforced Polymer Composites Bonded to Concrete," p. 291, 2005.

[32] S. M. Homam, S. A. Sheikh, P. Collins, G. Pernica, and J. Daoud, "Durability of fiber reinforced polymers used in concrete structures," in Proc. 3rd International Conference on Advanced Materials in Bridges and Structures, Ottawa, Canada, August, 2000, pp. 751–758.

[33] K. Liao, C. R. Schultesiz, D. L. Hunston, and L. C. Brinson, "Long-term durability of fiber-reinforced polymer-matrix composite materials for infrastructure applications: a review," 1998.

[34] V. M. Karbhari and S. Zhang, "Durability of fibre reinforced composites in civil infrastructure–issues, results and implications," Developments in Design Standards for Advanced Composites in Infrastructure Applications, CRC-ACS, Australia, 1999.

[35] V. Karbhari, J. W. Chin, and R. Reynaud, "Gap analysis for durability of fiber reinforced polymer composites in civil infrastructure," CERF, ASCE, 2001.

[36] F. Guo, S. Al-Saadi, R. K. S. Raman, and X. L. Zhao, "Durability of fiber reinforced polymer (FRP) in simulated seawater sea sand concrete (SWSSC) environment," Corrosion Science, vol. 141, pp. 1–13, 2018.

[37] A. M. Hameed and M. T. Hamza, "Characteristics of polymer concrete produced from wasted construction materials," Energy Procedia, vol. 157, pp. 43–50, 2019.

[38] S. Mishra et al., "Studies on mechanical performance of biofibre/glass reinforced polyester hybrid composites," Composites science and technology, vol. 63, no. 10, pp. 1377–1385, 2003.

[39] M. A. A. Ghani, Z. Salleh, K. M. Hyie, M. N. Berhan, Y. M. D. Taib, and M. A. I. Bakri, "Mechanical properties of kenaf/fiberglass polyester hybrid composite," Procedia Engineering, vol. 41, pp. 1654–1659, 2012.

[40] M. Zhan, R. P. Wool, and J. Q. Xiao, "Electrical properties of chicken feather fiber reinforced epoxy composites," Composites Part A: Applied Science and Manufacturing, vol. 42, no. 3, pp. 229–233, 2011.

[41] M. J. John, B. Francis, K. T. Varughese, and S. Thomas, "Effect of chemical modification on properties of hybrid fiber biocomposites," Composites Part A: Applied Science and Manufacturing, vol. 39, no. 2, pp. 352–363, 2008.

[42] M. Jacob, S. Thomas, and K. T. Varughese, "Mechanical properties of sisal/oil palm hybrid fiber reinforced natural rubber composites," Composites science and Technology, vol. 64, no. 7–8, pp. 955–965, 2004.

[43] P. Noorunnisa Khanam, G. Ramachandra Reddy, K. Raghu, and S. Venkata Naidu, "Tensile, flexural, and compressive properties of coir/silk fiber-reinforced hybrid composites," Journal of Reinforced Plastics and Composites, vol. 29, no. 14, pp. 2124–2127, 2010.

Aspergillus Niger A Local Isolate From Rice Husk as Potential Source of Single Cell Protein Production

R. Monisha
Department of Applied Microbiology
Sri Padmavati Mahila Visvavidyalayam,
Tirupati-517502
monishamoni3063@gmail.com
70931486943
Corresponding Author
R. Jaya Madhuri
Department of Applied Microbiology
Sri Padmavati Mahila Visvavidyalayam,
Tirupati-517502
drjayaravuri@gmail.com
8639278826

Abstract:

Aim: In protein supplementation *Aspergillus niger* was used to produce single cell protein from rice husk through fermentative production.

Methodology: Under optimal conditions using different parameters like carbon sources, nitrogen sources, concentration of solid substrate, level of inoculum, temperatures, pH and incubation period have been optimized for obtaining more yield of single cell protein under submerged fermentation. In the current research various substrates such as brans of wheat,rice,rice husk ,whey, molasses, orangepeel,soyameal.

Result: The maximum yield of *Aspergillus niger* 5.428% or 13.57gms was analyzed with following optimized parameters substrate(rice husk) 0.75gms , carbon source(glucose) 1.45gms, nitrogen source(ammonium sulphate) 1.16gms, pH(5.5) 0.35gms, temperature(20°) 1.1gms, incubation period 5days , inoculum concentration 1ml/100ml for 5days fungal culture. These analysis indicate that Rice husk was used for the maximum yield of *Aspergillus niger*. By using Lowry protein assay the amount of protein concentration in solution is 1.021mgl/ml.

Key words: *Aspergillus niger* rice husk, C/N ratio, submerged fermentation

IEECP'21, July 29-30, 2021, Silicon Valley, San Francisco, CA – USA

DAI : ***https://sci-index.com/DAI/2021.99101/IEECP/14999190***

Submerged Fermentative production of L-Asparaginase Enzyme by *Asparagillus niger*

K.Sowbhagya Lakshmi
Dept.of Applied Microbiology
Sri Padmavati Mahila Visvavidyalayam
Tirupati, Andhra Pradesh, India.
Sowbhagya.ms98@gmail.com

Dr. M.Bhargavi
Dept. of Applied Microbiology
Sri Padmavati Mahila Visvavidyalayam
Tirupati, Andhra Pradesh, India.
vkrbhargavi@gmail.com

Dr.R.Jaya Madhuri
Dept. of Applied Microbiology
Sri Padmavati Mahila Visvavidyalayam
Tirupati, Andhra Pradesh, India.
drjayaravuri@gmail.com

Abstract:

Microbial L-asparaginase (ASNase) is an important anticancer agent that is used extensively worldwide. L-Asparaginase catalyzes the degradation of Asparagine, an essential amino acid for leukemic cells into ammonia and aspartic acid. In this study we are focused on Collection, isolation, screening, microbial identification, enzyme assay, Submerged fermentative production, partial purification and molecular weight determination of partially purified extracellular L-Asparaginase enzyme producing *Asparagillus niger* collected from onion peel. The fungal culture was isolated by standard tissue isolation technique. The screening process done by using potato dextrose broth supplemented with 0.3ml of 2.5% phenol red indicator at p^H 6.5 and L-asparagine as sole nitrogen source for microbial growth. Microbial identification by Lacto phenol cotton blue staining technique. Optimize the media with different nitrogen sources like Sodium nitrate, urea and yeast extract. Urea showing highest enzyme activity, used for Submerged fermentative production. Partial purification carried out in two steps Ammonium sulphate precipitation and dialysis. The dialyzed compound used for molecular weight determination by SDS PAGE technique and found to be 79 KDA.

Key Words:

L-asparaginase, *Asparagillus niger*, onion peel, potato dextrose broth, Partial purification and urea.

D!f : *https://sci-index.com/DAI/2021.99101/IEECP/14904888*

Gradient algorithms for artificial neuron network teaching

1st Erkin Uljaev
faculty of Electronics and Automation
Tashkent State Technical University
named after Islam Karimov
Tashkent, Uzbekistan
e.uljaev@mail.ru

2nd Shohrukh Narzullayev
faculty of Electronics and Automation
Tashkent State Technical University
named after Islam Karimov
Tashkent, Uzbekistan
narzullayevsh@tdtu.uz

3rd Utkirjon Ubaydullaev
faculty of Electronics and Automation
Tashkent State Technical University
named after Islam Karimov
Tashkent, Uzbekistan
utkir2005@mail.ru

4th Elyor Khudoyberdiyev
faculty of Electronics and Automation
Tashkent State Technical University
named after Islam Karimov
Tashkent, Uzbekistan
elyor125rqt11@gmail.com

Abstract

This article is devoted to the study and application of the basic features of algorithms for "teaching" multilayer artificial neural networks, in particular, gradient algorithms. The article states that scientific research is being carried out on the development of intelligent measuring devices for controlling the moisture content of scattering materials based on functions such as automatic adjustment of measuring range, self-calibration, linear static characteristics, high measurement accuracy and reliability, data processing, decision making. As a result of the research, it was considered that the requirements for measuring the moisture content of scattering materials by control and management systems can be met by high-precision moisture meters developed using intelligent technologies. Today, a wide range of new opportunities for the construction of intelligent systems for the control of technological processes are developing through the use of artificial neural networks. Symbols are widely used in issues such as recognition, prediction and diagnostics, optimization, signal processing under the influence of noise. The authors have built an artificial neural network for an intelligent device that measures the moisture content of scattering materials. The main parameters of the artificial neural network were determined and "training" was carried out on the basis of gradient algorithms. In an intelligent device that measures the moisture content of scattering materials, the factors that affect the measurement accuracy are minimized as a result of gaining knowledge base through experiments. Based on the above results, it is stated that an artificial neural network has been used in an intelligent device.

Keywords: Artificial neural network, gradient algorithm, humidity, weight coefficients, constant shift (bias).

1. INTRODUCTION

In the era of globalization, where science and information and communication technologies are rapidly developing and leading to the fourth industrial revolution, public and social governance, economics, industry, social protection, education, science, medical diagnostics, agriculture, defense and security, tourism in developed countries and the widespread use of modern information technology and artificial intelligence in many areas.

The solution of technical problems such as management, control and measurement of technological processes in all sectors of industrial production in the world is being intelligent. The intellectualization of such technological processes requires the expansion of the functional capabilities of technical means of management, control, and measurement, the improvement of technical characteristics, the solution of new scientific and technical problems of efficient use of energy resources. Therefore, a class of intelligent devices and sensors is emerging. They have the ability to self-adapt to the operating principle, images of input signals, technical condition and external factors affecting the measuring system due to changes in control and measurement conditions [1].

Intelligent devices and sensors differ from other analogues of this type in that they have functions such as automatic adjustment of the measuring range, self-calibration, data processing, decision making [2,3].

Nowadays, measuring instruments that measure temperature, humidity, pressure and other quantities are rapidly being developed by specialists in various fields. However, the accuracy of measuring instruments used in many industries is insufficient, and the measurement error differs from the specified "range". By optimizing the controlled and controlled parameters, it is possible to improve the quality of manufactured products and reduce defects. This makes it necessary to create new measuring instruments.

2. PURPOSE OF THE WORK

Construction of an artificial neural network based on gradient algorithms for an intelligent device that measures the moisture content of scattering materials.

3. PROBLEM STATEMENT

It is known that moisture is one of the most important technological parameters, which directly affects the cost, technological structure, and other properties of substances and materials [4-8]. High-precision moisture meters, which are involved in moving technological processes, are used directly to organize the quality control of moisture in the process of spraying materials (wheat, barley, rice, millet, etc.). Therefore, the selection of measuring instruments for each control system, the study of their principles of operation, design, and other parameters is of great importance [9-12].

IEECP '21, July 29-30, 2021, Silicon Valley, San Francisco, CA – USA

DAI : *https://sci-index.com/DAI/2021.99101/IEECP/14904897*

The following requirements can be set for devices used to measure the moisture content of spray materials:

• measuring device - measures moisture in the technological process and does not damage the measured substance;

• the absence of elements in the design of the measuring device that affect the accuracy of the measurement of scattering materials;

• measuring device - low sensitivity to the external environment and a stable measuring system;

• Measuring device - should be an intelligent device with a microprocessor that measures with high accuracy on the basis of modern technologies.

An analysis of the available moisture metering devices shows that the above requirements for measuring the moisture content of spray materials by control and management systems can be met by moisture metering devices developed using intelligent technology.

Today, scientific research is being carried out on the development of intelligent measuring devices for automatic control of the measuring range, calibration, linear static characteristics, high measurement accuracy and reliability, data processing, decision-making to control the moisture content of dispersed materials [11,13- 15].

Factors that directly affect the measuring accuracy of the device for measuring the moisture content of scattering materials can include changes in the density of the material under study, dielectric constant, temperature, the chemical composition of the substance, and other parameters. These factors cause errors in the measurement process. Therefore, these errors should be minimized as much as possible.

Extensive new possibilities for building intelligent process control systems are being developed through the use of artificial neural networks, and they are widely used in issues such as image recognition, prediction, and diagnostics, optimization, signal processing under the influence of noise [16]. In an intelligent device based on artificial neural networks that measure the moisture content of scattering materials, the factors that affect measurement accuracy are brought closer to the minimum value as a result of gaining a knowledge base through experiments.

3.1. SOLUTION METHOD OF THE PROBLEM

Properly distributed artificial neural networks are now widely used to solve problems in intelligent systems. Therefore, we use properly distributed cross-linked neural networks in an intelligent device that measures the moisture content of scattering materials. Because the system is static, all neurons in the given vectors of the signals of the neurons in the input layer form a single value of the signal vector in the output layer. A neural network consists of a number of inputs and outputs, consisting of a set of interconnected neurons, and performs a nonlinear change. A model of an artificial neural network performing the given problem is shown in Figure 1 [17-20].

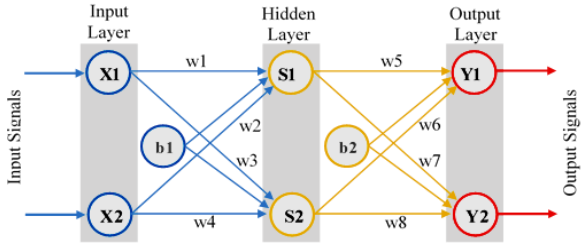

Figure 1. The structure of an artificial neural network

Several algorithms for teaching multilayer artificial neural networks have been developed. We can divide these algorithms into two groups [16-18, 21-22]:

- gradient algorithms;

- stochastic algorithms.

The algorithms of the first group include the calculation of the product of the error function and the neural networks that correct the weights according to the found product. Each subsequent step is directed towards the antigradient of the error function. The basis of these algorithms is the algorithm of inverse distribution of errors. This algorithm serves to minimize the deviation of the actual values of the neurons in the neural network output layer from the required value. Errors are found using the quadratic error function for each output neuron, and they give the total error of the output neuron. Examples of this algorithm are moment study, autonomous gradient algorithm, and second-order methods.

In stochastic algorithms, however, random changes in weight and shear (bias) coefficients are made while maintaining the previous changes. This leads to an improvement in neural network parameters. Stochastic algorithms include random directional search algorithms, Cauchy learning algorithms, Boltsman learning algorithms, evolutionary algorithms. The main disadvantages of this algorithm include the high demand for technical means, the long duration of learning time, and so on. Nevertheless, these algorithms are used because they provide global optimization. In gradient algorithms, however, local minimums of the error function can be found. Currently, hybrid algorithms based on the combined use of the above two algorithms are also used.

3.2. RESEARCH METHODS AND THE RECEIVED RESULTS

Frequency input signals describing changes in temperature and capacitance (dielectric constant) of the scattering materials under study (e.g., wheat) were taken. The actual values of the quantities received as the input signal vary in frequency and temperature of range through the corresponding functions. To perform artificial neural network training, we interact with input layer neurons through and input signals equal to and.

Each of the neurons in the hidden layer is associated with neurons in the input layer that have a certain weight. It describes the interdependence of the elements of the layers and determines the magnitude of the communication efficiency of the elements. We know that each element of the neural network operates in a discrete-time and forms the resulting signal based on the received signal. Table 1 shows the random weight coefficients of the input and hidden layer neurons and the values of the constant shifts (bias).

According to Figure 1, the input signals coming to the hidden layer neurons are the cumulative signal by their respective weights [17, 23-26].

$$S = w \times X + b \qquad (1)$$

Where - weight coefficients of neurons; - signal given by neurons of the input layer; - constant displacement (bias); - the sum of input signals.

We calculate the sum of the input signals using the random weight coefficients given in Table 1.

$$S_1 = w_1 \cdot X_1 + w_2 \cdot X_2 + b_1,$$
$$S_1 = 0{,}20 \cdot 0{,}10 + 0{,}25 \cdot 0{,}70 + 0{,}60 = 0{,}795,$$
$$S_2 = w_3 \cdot X_1 + w_4 \cdot X_2 + b_1,$$
$$S_2 = 0{,}30 \cdot 0{,}10 + 0{,}35 \cdot 0{,}70 + 0{,}60 = 0{,}875$$

Table 1.

Weight coefficients of layers of the artificial neural network, constant shifts (bias), and values of required output signals

X_1	X_2	w_1	w_2	w_3	w_4	w_5	w_6	w_7	w_8	b_1	b_2	Y_1^*	Y_2^*
0,10	0,70	0,20	0,25	0,30	0,35	0,40	0,45	0,50	0,55	0,60	0,65	0,35	0,65

Using activation functions, we convert the results in hidden layer neurons into output signals. Several types of activation functions are currently used in practice [27,28]. We use the activation function in the sigmoid view. The activation function in the sigmoid view is nonlinear and the given multidimensional function can be polished with arbitrary precision per unit cross-section [27,29,30]. As a result, the output layer also has a nonlinear characteristic. It has the following appearance:

$$f(S)=\frac{1}{1+e^{-S}}$$

From the above expression, we calculate the output value of each neuron in the hidden layer.

$$f(S_1)=\frac{1}{1+e^{-S_1}}=\frac{1}{1+e^{-0,795}}=0,6889039179\ \ 7695\ ,$$

$$f(S_2)=\frac{1}{1+e^{-S_2}}=\frac{1}{1+e^{-0,875}}=0,7057850278\ \ 3701$$

The resulting values are the output value for the hidden layer neurons and the input signals for the output neurons in the second layer.

We also determine the values of the neurons in the next layer using the random weight coefficients in Table 1 using expression (1).

$$S_3=w_5\cdot f(S_1)+w_6\cdot f(S_2)+b_2,$$

$$S_3=0,40\cdot 0,6889039179\ \ 7695+0,45\cdot 0,7057850278\ \ 3701+$$
$$+0,65=1,2431648297\ \ 1744$$

$$S_4=w_7\cdot f(S_1)+w_8\cdot f(S_2)+b_2,$$

$$S_4=0,50\cdot 0,6889039179\ \ 7695+0,55\cdot 0,7057850278\ \ 3701+$$
$$+0,65=1,3826337242\ \ 9883$$

Equation (2) calculates the values of the output signals from the expression. We find the true values of the output signals using the activation function in the sigmoid view. We know that the activation function in the sigmoid view is both a negative and a monotonous growth function. Therefore, the values of the output signals also consist of positive results.

$$Y_1=f(S_3)=\frac{1}{1+e^{-S_3}}=\frac{1}{1+e^{-1,24316482971744}}=0,7761144182\ \ 1532$$

,

$$Y_2=f(S_4)=\frac{1}{1+e^{-S_4}}=\frac{1}{1+e^{-1,38263372429883}}=0,7994136548\ \ 4440$$

These values are the output signals of the artificial neural network we are looking for.

The most complex process in building multilayer artificial neural networks is “training” (Figure 2). The unknown parameters of "training" neurons are the identification of weight and bias coefficients. In the teaching of multilayer neural networks, gradient search methods are used to minimize the criterion functions that depend on the parameters of the neurons.

This process is iterative, and in each iteration, all the coefficients of the network are found first for the output layer, then for the hidden layer, and for the input layer (the method of inverse distribution of errors) [16-17, 31-33]. Other forms of minimum search, such as genetic algorithms and the least-squares method, are also used.

We calculate the errors for each output neuron using the error inverse distribution method.

$$E_\Sigma=\sum\frac{1}{2}(Y*-Y)^2 \qquad (3)$$

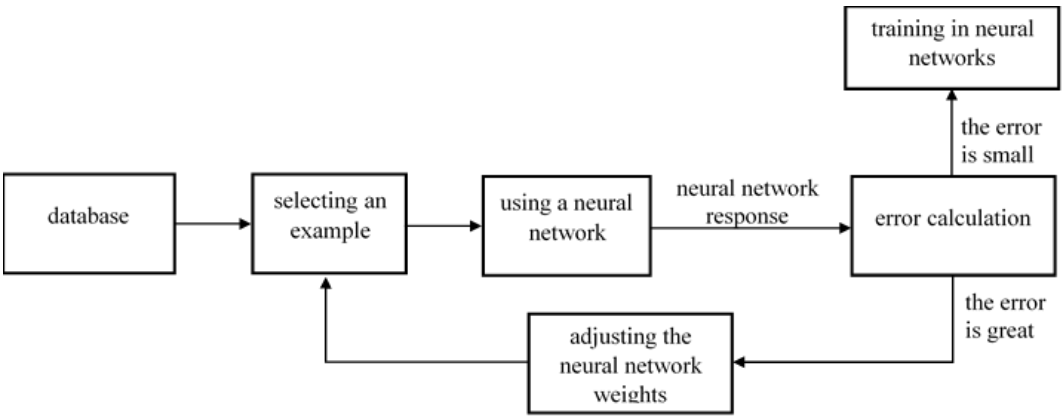

Figure 2. The process of "training" the neural network

Where, and are the required and actual output values of the neural network accordingly. The sum of the errors is performed on the output layer and the whole set of neurons in the neural network training.

We calculate the errors of the neurons at the output of the neural network through the expression (3).

$$E_1=\frac{1}{2}(Y_1^*-Y_1)^2=\frac{1}{2}(0,35-0,77611441821532)^2=0,09078674870549$$

,

$$E_2=\frac{1}{2}(Y_2^*-Y_2)^2=\frac{1}{2}(0,65-0,79941365484440)^2=0,01116222012698$$

The sum of these errors gives a total error.

$$E_\Sigma=E_1+E_2=0,09078674870549+0,01116222012698=0,10194896883247$$

The purpose of using the inverse error distribution method is to update each weighting coefficient and bias in the neural network. This is because we can minimize the total error in each output neuron and by bringing the actual values of the

neurons in the output layer of the neural network closer to the required values.

Now we determine that each weighting coefficient in the output layer of the artificial neural network affects the total error (Fig. 3.).

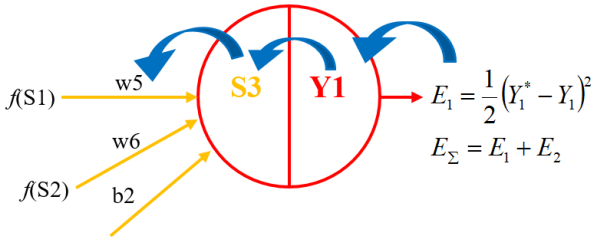

Figure 3. Structural view of the effect of weighting coefficients on the output of the total error

consider the effect of the weight coefficient w_5 on the overall error.

$$\frac{\partial E_\Sigma}{\partial w_5} = \frac{\partial E_\Sigma}{\partial Y_1} \cdot \frac{\partial Y_1}{\partial S_3} \cdot \frac{\partial S_3}{\partial w_5} \quad (4)$$

We can calculate this expression by dividing it into parts, such as the complex rule product (chain rule). First, we determine the effect of the output signal on the overall error.

$$E_\Sigma = E_1 + E_2 = \frac{1}{2}(Y_1^* - Y_1)^2 + \frac{1}{2}(Y_2^* - Y_2)^2,$$

$$\frac{\partial E_\Sigma}{\partial Y_1} = -2 \cdot \frac{1}{2}(Y_1^* - Y_1)^{2-1} + 0 = -(Y_1^* - Y_1) = -(0{,}35 - 0{,}77611441821532) =$$

$$= 0{,}42611441821532$$

We express the effect of the input signal S_3 on the output signal Y_1 using the following product

$$Y_1 = f(S_3) = \frac{1}{1 + e^{-S_3}},$$

$$\frac{\partial Y_1}{\partial S_3} = Y_1(1 - Y_1) = 0{,}7761144182\ 1532 \cdot (1 - 0{,}7761144182\ 1532) = 0{,}1737608280\ 5362$$

Finally, we consider the effect of the weight coefficient on the overall expression.

$$S_3 = w_5 \cdot f(S_1) + w_6 \cdot f(S_2) + b_2,$$

$$\frac{\partial S_3}{\partial w_5} = f(S1) + 0 + 0 = 0{,}6889039179\ 7695$$

Based on expression (4), we combine the results found above.

$$\frac{\partial E_\Sigma}{\partial w_5} = 0{,}42611441821532 \cdot 0{,}17376082805362 \cdot$$

$$\cdot 0{,}68890391797695 = 0{,}05100781986798$$

We use the following expression to find the new weight coefficient.

$$w_5^* = w_5 - \eta \cdot \frac{\partial E_\Sigma}{\partial w_5}$$

where, η is the training coefficient. η is a gradient that allows you to control the amount of weight coefficient in each iteration, which is one of the parameters of the neural network training algorithm [16-17, 34-37]. Its value $(0 \le \eta \le 1)$ varies in the range. Selecting a zero value is useless because in this case, the value of the weight coefficients does not change. Learning algorithm runs faster (less time is required to minimize error function) in the interval of $0{,}7 \le \eta \le 1$, but the accuracy of neural network error function minimization can be reduced, which exacerbates the training error.

At small values of the training coefficient, the $0{,}1 \le \eta \le 0{,}3$ number of cycles of finding the extremum increases, but the accuracy of minimizing the error function is higher. This in turn can lead to a reduction in teaching error. In practice, the value of the training coefficient is usually chosen experimentally or arbitrarily. Assume that the training coefficient is equal to $\eta = 0{,}5$.

$$w_5^* = w_5 - \eta \cdot \frac{\partial E_\Sigma}{\partial w_5} = 0{,}40 - 0{,}5 \cdot 0{,}05100781986798 =$$

$$= 0{,}37449609006601$$

We also perform the above sequence of actions for the remaining neurons w_6, w_7, w_8 in the output layer.

The effect of the weight coefficient w_6 on the total error is as follows.

$$\frac{\partial E_\Sigma}{\partial w_6} = \frac{\partial E_\Sigma}{\partial Y_1} \cdot \frac{\partial Y_1}{\partial S_3} \cdot \frac{\partial S_3}{\partial w_6},$$

$$\frac{\partial E_\Sigma}{\partial w_6} = 0{,}05225773090557$$

From this, we calculate a new weight coefficient w_6^*.

$$w_6^* = w_6 - \eta \cdot \frac{\partial E_\Sigma}{\partial w_6} = 0{,}42387113454722$$

For the weight coefficient w_7, we also perform the above sequence of actions.

$$\frac{\partial E_\Sigma}{\partial w_7} = \frac{\partial E_\Sigma}{\partial Y_2} \cdot \frac{\partial Y_2}{\partial S_4} \cdot \frac{\partial S_4}{\partial w_7},$$

$$\frac{\partial E_\Sigma}{\partial w_7} = 0{,}01650524105286$$

The new value of the weight coefficient w_7^* is as follows:

$$w_7^* = w_7 - \eta \cdot \frac{\partial E_\Sigma}{\partial w_7} = 0{,}49174737947357$$

Determine the final weight coefficient w_8 in the output layer:

$$\frac{\partial E_\Sigma}{\partial w_8} = \frac{\partial E_\Sigma}{\partial Y_2} \cdot \frac{\partial Y_2}{\partial S_4} \cdot \frac{\partial S_4}{\partial w_8},$$

$$\frac{\partial E_\Sigma}{\partial w_8} = 0{,}01690969046912$$

Based on the results found, we calculate the new weight coefficient .

$$w_8^* = w_8 - \eta \cdot \frac{\partial E_\Sigma}{\partial w_8} = 0{,}54154515476544$$

We perform network updates after we have calculated for neurons in the hidden layer as well. When finding new values of the weight coefficients in the hidden layer, we use the values of the initial weight coefficients and shifts (bias), rather than the values found above. Figure 4 shows the effect of each weighting coefficient and bias on the total error in the hidden layer of the artificial neural network.

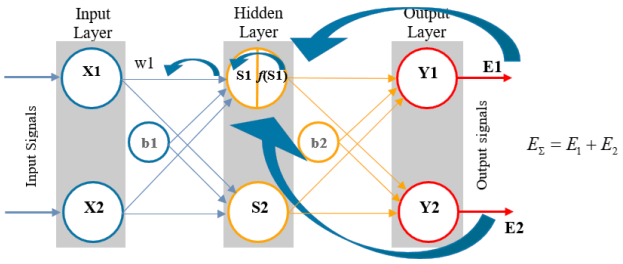

Figure 4. Structural view of the effect of hidden layer weight coefficients on the total error

Through the calculations, we found new values of weight coefficients representing the connections of neurons in the hidden and output layers. Now we also need to calculate the new values of the weight coefficients that represent the connections between the input and hidden layer neurons.

The hidden layer weight coefficients affect all output signals. Therefore, their effect on all neurons in the output layer should be taken into account [17-18,23].

$$\frac{\partial E_\Sigma}{\partial w_1} = \frac{\partial E_\Sigma}{\partial f(S_1)} \cdot \frac{\partial f(S_1)}{\partial S_1} \cdot \frac{\partial S_1}{\partial w_1} \quad (5)$$

We know that $f(S_1)$ affects both errors in the output signals. Therefore, the effect of the expression $\frac{\partial E_\Sigma}{\partial f(S_1)}$ on the error in both output signals must be taken into account.

$$\frac{\partial E_\Sigma}{\partial f(S_1)} = \frac{\partial E_1}{\partial f(S_1)} + \frac{\partial E_2}{\partial f(S_1)} \quad (6)$$

We calculate the product of E_1 to.

$$\frac{\partial E_1}{\partial f(S_1)} = \frac{\partial E_1}{\partial S_3} \cdot \frac{\partial S_3}{\partial f(S_1)} \quad (7)$$

we find the value of $\frac{\partial E_1}{\partial S_3}$ by the results calculated above

$$\frac{\partial E_1}{\partial S_3} = \frac{\partial E_1}{\partial Y_1} \cdot \frac{\partial Y_1}{\partial S_3} = 0{,}4261144182\ \ 1532 \cdot 0{,}1737608280\ \ 5362 = 0{,}0740419941\ \ 5468$$

The value of $\frac{\partial S_3}{\partial f(S_1)}$ the expression is calculated as follows.

$$S_3 = w_5 \cdot f(S_1) + w_6 \cdot f(S_2) + b_2,$$
$$\frac{\partial S_3}{\partial f(S_1)} = w_5 = 0{,}40\ .$$

We combine the results found in expression (7).

$$\frac{\partial E_1}{\partial f(S_1)} = 0{,}0740419941\ \ 5468 \cdot 0{,}40 = 0{,}0296167976\ \ 6187$$

Now we calculate the second component of expression (6).

$$\frac{\partial E_2}{\partial f(S_1)} = \frac{\partial E_2}{\partial S_4} \cdot \frac{\partial S_4}{\partial f(S_1)} \quad (8)$$

For this expression, too, we perform the sequence of actions in expression (7).

$$\frac{\partial E_2}{\partial S_4} = \frac{\partial E_2}{\partial Y_2} \cdot \frac{\partial Y_2}{\partial S_4} = 0{,}1494136548\ \ 4440 \cdot 0{,}1603514632\ \ 9272 = 0{,}0239586981\ \ 9021$$

$$S_4 = w_7 \cdot f(S_1) + w_8 \cdot f(S_2) + b_2,$$
$$\frac{\partial S_4}{\partial f(S_1)} = w_7 = 0{,}50\ .$$

Determine the value of the expression (8).

$$\frac{\partial E_2}{\partial f(S_1)} = 0{,}0239586981\ \ 9021 \cdot 0{,}50 = 0{,}0119793490\ \ 9511$$

We put these results in expression (6) and calculate the value of $\frac{\partial E_\Sigma}{\partial f(S_1)}$.

$$\frac{\partial E_\Sigma}{\partial f(S_1)} = 0{,}02961679766187 + 0{,}01197934909511 = 0{,}04159614675698\ .$$

From the activation function in the form of sigmoid in expression (5) we find the product of the sum of the input signals S_1.

$$f(S_1) = \frac{1}{1+e^{-S_1}},$$
$$\frac{\partial f(S_1)}{\partial S_1} = f(S_1) \cdot (1 - f(S_1)) = 0{,}68890391797695 \cdot$$
$$\cdot (1 - 0{,}68890391797695) = 0{,}21431530977296$$

Here, we calculate the effect w_1 on the total error using the sum of the input signals.

$$S_1 = w_1 \cdot X_1 + w_2 \cdot X_2 + b_1,$$
$$\frac{\partial S_1}{\partial w_1} = X_1 = 0{,}10\ .$$

In that case, the value $\frac{\partial E_\Sigma}{\partial w_1}$ is equal to the following.

$$\frac{\partial E_\Sigma}{\partial w_1} = 0{,}04159614675698 \cdot 0{,}21431530977296 \cdot 0{,}10 = 0{,}00089146910775\ .$$

From the results obtained we find the new weight coefficient of w_1.

$$w_1^* = w_1 - \eta \cdot \frac{\partial E_\Sigma}{\partial w_1} = 0{,}20 - 0{,}5 \cdot 0{,}00089146910775 = 0{,}19955426544612$$

.

We also perform the above steps for the weight coefficients w_2, w_3 and w_4.

$$\frac{\partial E_\Sigma}{\partial w_2} = \frac{\partial E_\Sigma}{\partial f(S_1)} \cdot \frac{\partial f(S_1)}{\partial S_1} \cdot \frac{\partial S_1}{\partial w_2} = 0{,}0062402837\ \ 5431$$

$$w_2^* = w_2 - \eta \cdot \frac{\partial E_\Sigma}{\partial w_2} = 0{,}25 - 0{,}5 \cdot 0{,}00624028375431 = 0{,}24687985812285$$

$$\frac{\partial E_\Sigma}{\partial w_3} = \frac{\partial E_\Sigma}{\partial f(S_2)} \cdot \frac{\partial f(S_2)}{\partial S_2} \cdot \frac{\partial S_2}{\partial w_3} = 0{,}00086375447928,$$

$$w_3^* = w_3 - \eta \cdot \frac{\partial E_\Sigma}{\partial w_3} = 0{,}30 - 0{,}5 \cdot 0{,}00086375447928 = 0{,}29956812276036\ .$$

$$\frac{\partial E_\Sigma}{\partial w_4} = \frac{\partial E_\Sigma}{\partial f(S_2)} \cdot \frac{\partial f(S_2)}{\partial S_2} \cdot \frac{\partial S_2}{\partial w_4} = 0{,}00604628135496,$$

$$w_4^* = w_4 - \eta \cdot \frac{\partial E_\Sigma}{\partial w_4} = 0{,}35 - 0{,}5 \cdot = 0{,}00604628135496 = 0{,}34697685932252$$

We found new values of all weight coefficients. Now we can make updates. Initially as input signals $X_1 = 0{,}10$ and $X_2 = 0{,}70$ when we gave the values, the error in the neural network was 0.1019489683247. After we updated the weight coefficients, the error was 0.1019458256412. We continue the process to the allowable value of the error.

4. Conclusions

Studies have shown that the use of artificial neural networks in an intelligent device that measures the moisture content of scattering materials can significantly increase the accuracy and timing of measurements. The layers of the artificial neural network and the basic parameters of the neurons were found separately for each period, and an activation function in the form of a sigmoid was used. In the creation of multilayer artificial neural networks, training based on gradient algorithms with a "teacher" was used. As a result, neuro model data generalization and training time was reduced.

REFERENCES

[1] Michael T., McGrath, Cliodhna Ni Scanaill. Sensor Technologies. *Apress Media*. LCC, New York (NY). USA, 2014. – 321 p.

[2] Gaskarov D.V. Intellektualnыe informatsionnыe sistemы[Intellectual information system].- M.: Izd-vo: Vыssh. shk., 2003 g. - 432 s.

[3] Randy Frank. Understanding Smart Sensors. *Artech House*, Boston London, MA, USA, 2000. – 389 p.

[4] M.A.Berliner, Izmereniya vlazhnosti [Moisture measurements]. Izd. 2-e, pererab. Moskva: Energiya, 1973. 400 p. (in Russian).

[5] Theory and practice of rapid control of humidity of solid and liquid materials. Ed. E.S. Krichevsky. - M.: Energy, 1980.

[6] M.V. Kulakov, Tekhnologicheskie izmereniya i pribory dlya khimicheskikh proizvodstv [Technological measurements and devices for chemical production]. Izd. 3-e, pererab. i dop. Moskva: Mashinostroenie, 1983. 424 p. (in Russian).

[7] E.Uljaev, U.M.Ubaydullaev, Sh.N.Narzullaev, E.F.Xudoyberdiev, F.G.Haydarov, "Classification of Detectors of Capacitive Humidity Transducers of Bulk Materials", *International Journal of Advanced Science and Technology*, vol. 29(11s), pp.1949 – 1953, 2020. Retrieved from http://sersc.org/journals/index.php/IJAST/article/view/21858.

[8] E.Uljaev, Sh.N.Narzullaev, F.G.Xaydarov, "K voprosu razrabotki intellektualnogo kombinirovannogo ustroystva kontrolya vlajnosti sipuchix materialov"[On the issue of developing an intelligent combined device for controlling the moisture content of bulk materials], *Materiali mejdunarodnoy nauchnoy konferensii «Innovatsionnie resheniya injenerno-texnologicheskix problem sovremennogo proizvodstva»*, vol. 2, 14-16 noyabrya 2019 g, Buxara-2019, pp.204-206. (in Russian).

[9] Arbuzov V.P., Mishina M.A., Belыnseva P.N. Sistematizatsiya sposobov fazovogo razdeleniya kanala izmeritelnыx sepey yemkostnыx datchikov // Izvestiya vыsshix uchebnыx zavedeniy. Povoljskiy region. Texnicheskie nauki, 2017. № 1(41). S. 85-95.

[10] Frayden Dj. Sovremennыe datchiki: spravochnik. –M.: Texnosfera, 2005 g. -592 s.

[11] E. Uljaev, U.M. Ubaydullaev, and Sh.N. Narzullaev, "Capacity transformer of coaxial and cylindrical form of humidity meter", *Chemical Technology, Control and Management*. 4(4):23-30, 2020. DOI: https://doi.org/10.34920/2020.4.23-30.

[12] Umarov E.O., Mardonov U.T., Shoazimova U.Kh. Influence of the Magnetic Field on the Viscosity Coefficient of Lubricoolant that is used in the Cutting Process. *International Journal of Mechatronics and Applied Mechanics*,8(2):144-149 . https://www.doi.org/10.17683/ijomam/issue8.50.

[13] Ernest O.D. Measurement Systems: Application and design. McGraw - Hill. Higher Education. - New York, 2004 – 1078 p.

[14] E.Uljayev, U.M.Ubaydullayev, Sh.N.Narzullayev, and L.N.Nasimxonov, "Optimization of the sizes of the cylindrical measuring transducer", *Chemical Technology, Control and Management*: Vol. 2020: Iss. 5, Article 5, 2020. DOI: https://doi.org/10.34920/2020.5-6.29-32.

[15] E.Ulzhaev, Sh.N.Narzullaev, & O.N.Norboev, "Substantiation of application of artificial neural networks for creation of humidity measuring devices". *International Virtual Conference On Innovative Thoughts, Research Ideas and Inventions in Sciences*, no.1(1), New York, USA, January, 2021, pp.86-91.

[16] N.R.Yusupbekov, R.A.Aliev, R.R.Aliev, A.N.Yusupbekov, *Intellektual'ny'e sistemy' upravleniya i prinyatiya resheniy [Intelligent management and decision-making systems]*. Tashkent: Uzbek-skaya nacional'naya e`nciklopediya, 2014, 490 p. (in Russian).

[17] M. A. Nielsen, Neural networks and deep learning. Determination Press, 2015.

[18] V.G. Spitsyn, Yu.R. Tsoj, *Predstavlenie znanij v informatsionnykh sistemakh [Knowledge representation in information systems]*. Uchebnoe posobie, Tomsk: Izd-vo TPU, 2006, 146 p. (in Russian).

[19] P.P.Mal'tsev, K.M.Ponomarev, Yu.I.Stepanov, "«Umnaya pyl'» na osnove mikrosistemnoj tekhniki" ["Smart dust" based on microsystem technology], *«Intellektual'nye robototekhnicheskie sistemy – 2021»: materialy molodezh. nauch. shkoly*, Taranrog.: Izd-vo TRTU, 2001, pp. 220-232. (in Russian).

[20] A.V.Gavrilov, *Gibridnye intellektual'nye sistemy [Hybrid intelligent systems]*. Novosibirsk: Izd-vo NGTU, 2003, 164 p. (in Russian).

[21] Dias M.B., Stentz A. A Free Market Architecture for Distributed Control of a Multirobot System. Proceedings of the 6th International Conference on Intelligent Autonomous Systems (IAS), Venice, Italy, July, 2000, pp. 115 - 122.

[22] Stentz A., Dias M.B. A Free Market Architecture for Coordinating Multiple Robots tech. report CMU-RI-TR-99-42, Robitics Institute, Carnegie Mellon University, December, 1999.

[23] Aliyev R.A., Vahidov R.M., Aliyev R.R. Artificial Neural Networks: Theory and Practice. –Tabriz: Tabriz University Press, 1993, 193 p.

[24] Uljayev E., Ubaydullayev U.M., Tadjitdinov G.T., Narzullayev S. (2021) Development of Criteria for Synthesis of the Optimal Structure of Monitoring and Control Systems. In: Aliev R.A., Yusupbekov N.R., Kacprzyk J., Pedrycz W., Sadikoglu F.M. (eds) 11th World Conference "Intelligent System for Industrial Automation" (WCIS-2020). WCIS 2020. Advances in Intelligent Systems and Computing, vol 1323. Springer, Cham. https://doi.org/10.1007/978-3-030-68004-6_73E.

[25] A.R.Marakhimov, Kh.Z.Igamberdiev, A.N.Yusupbekov, I.Kh.Siddikov, *Nechetko-mnozhestvennye modeli i intellektual'noe upravlenie tekhnologicheskimi protsessami [Fuzzy-set models and intelligent process control]*. Tashkent: TashGTU, 2014, 240 p. (in Russian).

[26] Yu. A.Kravchenko, "Postroenie prognoznykh modelej dinamicheskikh sistem na osnove integratsii nejronnykh setej

i geneticheskikh algoritmov" [Building predictive models of dynamic systems based on the integration of neural networks and genetic algorithms], *Izvestiya Taganrog. gos. radiotekh. un-ta*, vol. 64, no. 9, pp. 103–104, 2006. (in Russian).

[27] Szandała T. (2021) Review and Comparison of Commonly Used Activation Functions for Deep Neural Networks. In: Bhoi A., Mallick P., Liu CM., Balas V. (eds) Bio-inspired Neurocomputing. Studies in Computational Intelligence, vol 903. Springer, Singapore. https://doi.org/10.1007/978-981-15-5495-7_11

[28] Chigozie Nwankpa, Winifred Ijomah, Anthony Gachagan, Stephen Marshall, Activation functions: Comparison of trends in practice and research for deep learning. Machine Learning (cs.LG); Computer Vision and Pattern Recognition (cs.CV), arXiv preprint arXiv:1811.03378, 2018.

[29] A. Hertz, Introduction to the theory of neural computation. CRC Press, 2018.

[30] Y. LeCun, L. Bottou, G.B. Orr, and K.R. Müller, "Efficient backprop," in Neural networks: Tricks of the trade, Berlin, Heidelberg: Springer Berlin Heidelberg, 1998, pp. 9–50.

[31] T.A.Gavrilova, V.F. Khoroshevskij, *Bazy znanij intellektual'nykh sistem [Knowledge bases of intelligent systems]*. Sankt-Peterburg: Piter, 2000, 382 p. (in Russian).

[32] E. Ulzhaev, Sh.N. Narzullaev, E.F. Khudoyberdiev, Sh.A. Sulaimonova, Algorithm of the process of creation of neural networks for measuring qualitative parameters of bulk materials. Proceeding of International Conference on Scientific Endeavors and opportunities, Telavi, Georgia, March, 2021, pp. 78-81.

[33] Robbins, H., Monro, S.: A stochastic approximation method. Ann. Math. Statist.22, pp. 400–407.

[34] Bengio, Y. Practical recommendations for gradient-based training of deep architectures. arXiv 2012, arXiv:1206.5533.

[35] Rumelhart, D.E.; Hinton, G.E.; Williams, R.J. Learning representations by back-propagating errors. Nature 1986, 323, 533–536.

[36] Kelley, C.T. Iterative methods for linear and nonlinear equations. In Frontiers in Applied Mathematics; SIAM: Philadelphia, PA, USA, 1995.

[37] Kelley, C.T. Iterative Methods for Optimization. In Frontiers in Applied Mathematics; SIAM: Philadelphia, PA, USA, 1999.

Modeling and Finite Element Validation of a Wind Turbine with a Direct Drive Permanent Magnet Synchronous Generator.

Henda Zorgani Agrebi
Department of Electrical Engineering
National School of Engineering of Gabes
Tunisia
henda.zorganiagrebi@enis.tn

Naourez Benhadj
Department of Electrical Engineering
National School of Engineering of Sfax
Tunisia
naourez.benhadj@enis.tn

Mohamed Chaieb
Departement of Electrical Engineering
National School of Engineering of Chartage
Tunisia
Mohamed.Chaieb@enichartage.tn

Rafik Neji
Departement of Electrical Engineering
National School of Engineering of Sfax
Tunisia
rafik.neji@enis.tn

Abstract

In this paper, the analytical modeling of a wind turbine conversion chain is carried out according to multi-physical disciplines of the system. The chain represents a 3 bladed horizontal axis wind turbine coupled directly to a permanent magnet synchronous generator PMSG delivering power in a battery through a diode rectifier. For the considered chain, four models are developed. Mechanical model describes the power generation from kinetic movement of the wind to its transmission to the generator. Geometric Model clarify the design method of the turbine components. Magnetic Model summarizes the phenomena arising from the influence of the permanent magnets within the generator. Electrical Model determine the parameters and the electrical performance of the machine. Developed models are tested with the Finite Element Analysis FEA to evaluate their reliability. The FEA, by MATLAB-FEMM software, describes the electromagnetic behavior of the PMSG, the main component of the considered simplified chain.

Keywords: Horizontal-Axis Wind Turbine, Analytical Modeling, Direct Drive Permanent Magnet Synchronous Generator, Finite Element Validation.

I. INTRODUCTION

In recent decades, the development of the wind power sector is being a challenge in modern times to supply the global energy needs and to face the ecosystem barriers [1]. By the way, the investment in developing effective models to the wind turbine chain is of vital importance. Analytical modelling intervenes in the elaboration of system optimization models thus they ensure optimal design [2]. It participates in the reliable formulation of dynamic models to describe the system behavior according to wind fluctuations and operating conditions [3]. They allow the analysis of the system from a magnetic and thermal point of view basing on the finite element method [4]. In this way, the development of effective models for a simple wind turbine conversion chain is elaborated. The chain is composed from 3 bladed horizontal axis turbine connected to a gearless synchronous generator with surface permanent magnets having a radial flux and glued to an inner rotor. The choice of such structure is based on several advantages. The absence of the gearbox is considered as an achievement in the wind power generation system offering a higher efficiency with lower vibration and noise and a reduction of the maintenance of the turbine [5-6]. For the PMSGs, they are the most popular electrical machines for the direct drive wind turbines .they benefit with an excellent efficiency and energy yield [7]. In addition, the permanent magnets PM replace the excitation circuits in the rotor so it assures a permanent magnetic field. Therefore, the maintenance in the rotor are removed and the efficiency is improved.

In this paper, four models are treated. Several disciplines existing within the turbine are taken into account. Mechanical model processes the parameters of the dynamic behavior of the wind turbine to predict the torque generated at the turbine shaft from the kinetic torque of the wind. Geometric Model Allows to have a feasible structure for the design and analysis of the system. Magnetic model illustrates the influence of the permanent magnets by producing a permanent magnet flux within the machine. Electrical model determine the characteristics and the parameters of the generator. The relevance of the elaborated models is tested by the design in 2D of the PMSG with the MATLAB-FEMM software and the study of the system electromagnetic behavior by the finite element method FEM.

II. CURRENT STATUS OF WIND ENERGY IN THE WORLD ENERGY PLAN

In recent years the exploitation of wind energy power is increasing. It is exploited since antiquity and has underwent a boom in the latest thirteen years since the oil shocks. In fact, according to the statistics of the International Energy Agency IEA, the global energy consumption from wind power has increased from 3.4 TWh in 1990 to 790 TWh in 2016 [8]. In an other hand, the statistics given by the World Wind Energy Association WWEA, mentioned in "Figure 1", show that the global capacity of wind farms is changing annually from 435.284 GW in 2015 to reach 744 GW in 2020 [9]. This capacity has provided 7% of global demand for electricity in 2020 [9]. In fact, the wind Turbine Installations in 2020 have an energy capacity of 93 GW equivalent to 50% more than in 2019 and more than ever installed in one year [9].

IEECP'21, July 29-30, 2021, Silicon Valley, San Francisco, CA – USA

DII: https://sci-index.com/DAI/2021.99101/IEECP/16366077

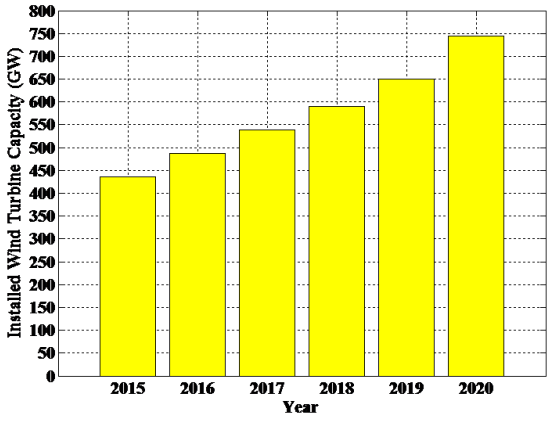

Figure 1. The Evolution of Installed Wind Turbines Capacity between years 2015 and 2020

Many regions from the advanced nations had the courage to invest in the installation of wind Turbines. The WWEA followed up the evolution of installed wind turbines in different zone between 2018 and 2020 as clarified "Figure 2" [9]. By the way, China and United-States have achieved new records in wind turbines installation. For European countries, they show slight growth due to the coronavirus crisis which has caused supply chain disruptions and luck of manpower.

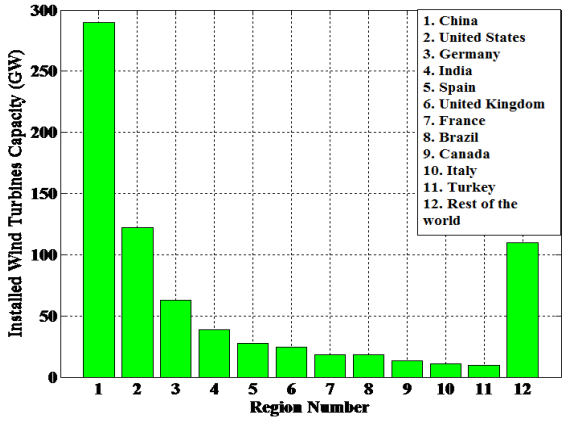

Figure 2. The Evolution of Installed Wind Turbines Capacity in different regions in 2020

A report of Global Wind Energy Council GWEC affirms that experts consider the year 2021 to be decisive year in confronting the barriers imposed by global climate change caused by the carbon emission and the harmful waste for the ecosystem [10]. They claim that wind power is the most favorable source that offers the greatest amount of de-carbonization per MW. They encourage the global wind industry to be united to highlight the major role that can play this energy in overcoming the barriers that threaten the world evolution in the future.

III. WIND TURBINE MODELLING

The modelling of a wind turbine is an important issue especially in the elaboration of optimal design [11]. Therefore, the structure of the wind conversion chain to be modeled in the study is a simplified chain dedicated to small scale wind production as clarified "Figure 3". It is a horizontal-axis turbine with three blades coupled directly to a permanent magnet synchronous generator. This generator presents surface permanent magnets with radial flux glued to an inner rotor. The electrical energy produced is stored to a battery through a diode bridge rectifier. The direct transmission of the turbine torque to the generator rotor encounters 2 types of losses which are friction torque and inertia torque.

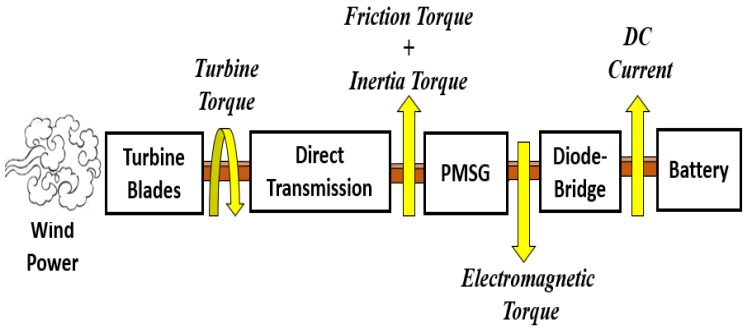

Figure 3. Simplified Wind Power Conversion Chain

A. Mechanical Model

Wind is the only variable that stimulate the mechanical movement of the turbine. It represents the only input variable of the turbine model. Its speed V_v in terms of time is described by a mathematical model. Referring to [12], an analytical wind model related to an urban site is given in "Equation 1" and represented in "Figure 4".

$$V\_v\,(t) = 10 + 0.2\sin(0.1047t) + 2\sin(0.2665t) + \sin(1.2930t) + 0.2\sin(3.6645t) \quad (1)$$

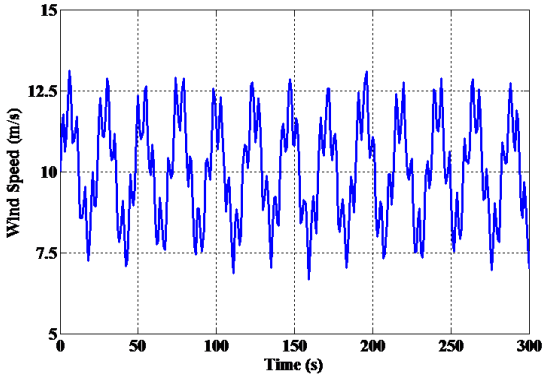

Figure 4. The Wind Profile as function of Time

The performance of the turbine in generating power is evaluated by the power coefficient C_p which represents the ratio of the power captured by the wind turbine and the kinetic power of the wind. For a setting fixed angle, the C_p analytical model of the commercialized BERGEY brand turbine is function of the reduced speed λ as expressed in "Equation 2".

$$C_p = -3{,}89.10^{-8}\lambda^7 - 4{,}21.10^{-6}\lambda^6 + 2{,}1.10^{-4}\lambda^5 - 3{,}1.10^{-3}\lambda^4 + 1{,}64.10^{-2}\lambda^3 - 1{,}76.10^{-2}\lambda^2 + 1{,}74.10^{-2}\lambda - 1{,}93.10^{-3} \quad (2)$$

The tip speed ratio λ, as defines "Equation 3", is the ratio of the tangential speed at the end of the blade $R_T\Omega$ to the instantaneous wind speed V_v. The blade radius of the chosen turbine R_T is equal to 1.25m [12-13].

$$\lambda = \frac{R_T \Omega}{V_v} \quad (3)$$

According to C_p curve mentioned in "Figure 5", the power Turbine reaches its maximum for the optimal values of $C_{p.opt}$ equal to 0.442 and $\lambda_{p.opt}$ equal to 6.9.

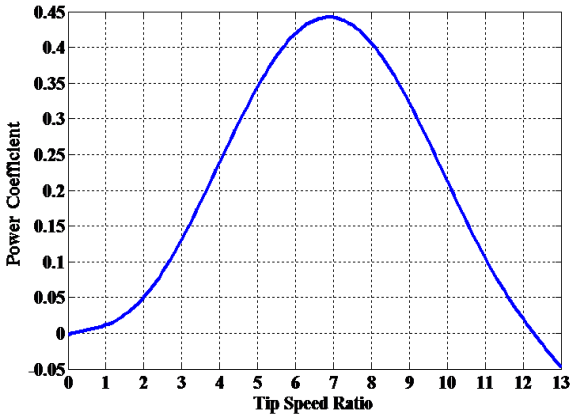

Figure 5. Aerodynamic Power Coefficient with respect to the Tip Speed Ratio

The associated wind turbine power P_T is defined as [14-15]:

$$P_T = \frac{1}{2}\rho S_T C_p(\lambda) V_v^{\,3} \quad (4)$$

With ρ the air density (Kg.m-3) and S_T represents the surface swept by the turbine blades (m^2).

The surface of the turbine S_T differs depending on its type. For horizontal axis wind turbines, the area swept by the blades is given as follows.

$$S_T = \pi R_T^{\,2} \quad (5)$$

The intervention of the angular rotation speed Ω of the rotor shaft product a turbine torque T_T illustrated in "Equation 6" [14-15].

$$T_T = \frac{P_T}{\Omega} = \frac{\frac{1}{2}\rho R S_T C_p(\lambda) V_v^{\,2}}{\lambda} \quad (6)$$

The characteristics of the turbine through the power extraction curves are shown in "Figure 6" as a function of the rotation speed Ω for different wind values included in the wind interval admissible for the turbine blades drive.

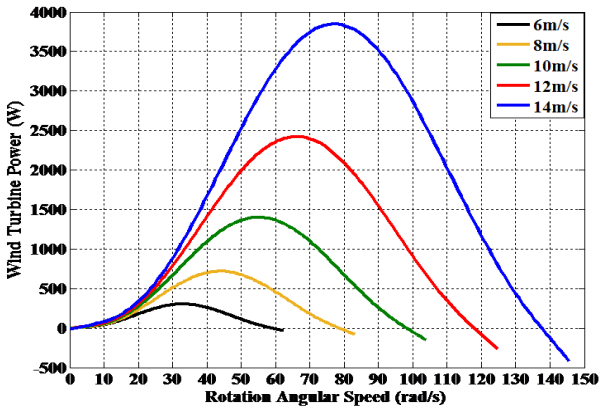

Figure 6. Wind Turbine Power vs. Rotation Angular Speed

The dynamic coupling characterizing the turbine-Generator mechanical behavior is given by the empirical "Equation 7" relating the turbine torque T_T and the electromagnetic torque T_{em} with the rotation angular speed Ω, the turbine inertia J_T and the generator friction coefficient f_m.

$$T_T - T_{em} = J_T \frac{d\Omega}{dt} + f_m \Omega \quad (7)$$

B. Geometric Model

The geometric part of the turbine is summed up in the design of the blades and the generator.

1)Blades Geometric Model

The studied turbine consists of 3 blades located on a horizontal axis sweeping a circular surface shown in "Figure 7" and equal to:

$$S_T = \pi R_T^{\,2} \quad (8)$$

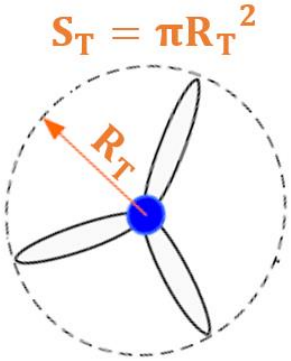

Figure 7. Geometric Model of the turbine Blades

2)PMSG Geometric Model

The principle of this methodology is based on fixing the electromagnetic torque of the generator imposed by the rotor turbine on the nominal value. According to the relation given in "Equation 9", the bore radius r_s will be calculated and geometric parameters are deduced [12]. This equation connect the fixed electromagnetic torque T_{em} of the generator with its bore radius r_s, its active length l_r, the magnet fundamental induction peak value B_{1a} and the linear current effective value K_{1s} [12-14]

$$T_{em} = 2\pi r_s l_r B_{1a} K_{1s} \quad (9)$$

The machine length l_r is given as follow [12-15]

$$l_r = \frac{r_s}{R_{rl}} \quad (10)$$

With R_{rl} is a virtual parameter chosen according to the designer expertise.

The generator air gap g is deduced from the empirical relation under below [12-15].

$$g = 0.001 + 0.003\sqrt{r_s l_r} \quad (11)$$

The angular width of the magnet per pole w_m is calculated as mentioned in "Equation 12". For the magnet thickness l_m, it is deduced as shown in "Equation 13" [12-15].

$$w_m = \frac{2\ \alpha_{magnet}}{p}\ r_s \quad (12)$$

With p is the number of the generator pole pairs and α_{magnet} is the magnet angle.

$$l_m = K_c g\ \frac{\mu_r}{B_r/B_a - 1} \quad (13)$$

With K_c is the crankcase coefficient, μ_r is the magnet's relative permeability, B_a is the induction magnet peak value in the air-gap and B_r is the magnet's remanent induction.

To simplify the design process, the stator and rotor depth, d_y and d_r, have equal values which is the same case for the slot and tooth width, w_s and w_T. [12-15]. The expressions of these graders are given in "Equation 14" to "Equation 15".

$$d_y = d_r = \frac{r_s\ B_a}{p\ B_y}\ \alpha_{magnet} \quad (14)$$

Where B_y represents the induction in the stator yoke.

$$w_s = w_T = \frac{4\pi r_s}{3N_{slots}} \quad (15)$$

With N_{slots} is the slots number.

The slot trapezoidal shape is presented in "Figure 8" having a depth d_s given in "Equation 16" [15]

$$d_s = R_{dr} r_s \quad (16)$$

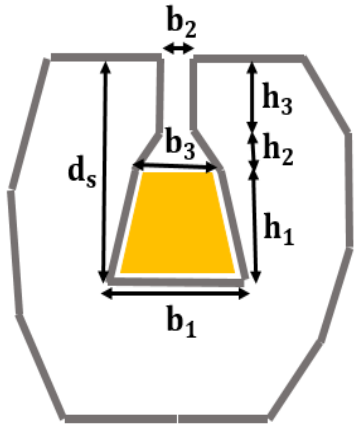

Figure 8. Characteristics of the trapezoidal slot

With:

$$\begin{cases} h_3 = 0.02 r_s & b_1 = w_s \\ h_2 = \frac{w_s}{8} & b_2 = \frac{w_s}{2} \\ h_1 = d_s - h_2 - h_3 & b_3 = \frac{3w_s}{4} \end{cases}$$

C. Magnetic Model

Permanent magnets cause the presence of a permanent magnet field in the air gap of the PMSG. In fact, the magnet fundamental induction peak value B_{1a} is expressed in "Equation 17" as function of the magnet angle α_{magnet} and the induction magnet peak value in the air gap B_a [12].

$$B_{1a} = \frac{4}{\pi} B_a \sin(\alpha_{magnet}) \quad (17)$$

The magnet angle α_{magnet} is a function of the filling factor of the pole K_p as mentioned bellow [12].

$$\alpha_{magnet} = \frac{4}{\pi} K_p \quad (18)$$

The induction magnet peak value in the air gap B_a is given as follows [12].

$$B_a = B_r \frac{l_{m/\mu r}}{K_c\, g + l_{m/\mu r}} \quad (19)$$

The vacuum magnetic flux received by a stator phase for a single conductor per slot Φ_{s1} is expressed as mentioned in "Equation 20" [12-14].

$$\Phi_{s1} = 2K_b N_{spp} B_{1a} r_s l_r \quad (20)$$

The total vacuum magnetic flux generated in a stator phase, expressed in "Equation 21", is function of the conductor number per slot N_{cs} [12-14].

$$\Phi_s = N_{cs} \Phi_{s1} \quad (21)$$

D. Electrical Model

The electrical part of the wind turbine lies in the electromagnetic behavior of the generator. The calculation of the electrical graders is based on the geometric model of the considered machine.

The linear current effective value K_{1s} characterizes the current distributed along the air gap per unit of length. It depends, as cited in "Equation 22" on the surface density of the current J_s, the tooth width w_T, the slot width w_s, the slot depth d_s, the winding factor K_{B1} and the slot filling coefficient K_r [12].

$$K_{1s} = \frac{J_s w_s d_s}{w_s + w_T} K_{B1} K_r \quad (22)$$

The winding factor K_{B1} is limited to the fundamental term of the distribution factor K_{z1}. It is deduced from the number of slots per pole and per phase N_{spp} as clarified in "Equation 23" [12].

$$K_{z1} = K_{B1} = \left| \frac{\sin\left(\frac{\pi}{6}\right)}{N_{spp} \sin\left(\frac{\pi}{6N_{spp}}\right)} \right| \quad (23)$$

The slot filling factor K_r is characterized by the ratio between the slot surface actually filled with copper S_{copper} and the total slot surface S_{slot} as given in "Equation 24" [12].

$$K_r = \frac{S_{copper}}{S_{slot}} \quad (24)$$

Therefore, the magnetizing inductance L_{m1} , the leakage inductance L_{f1}, the mutual inductance between stator phases M_{s1}, the generator phase inductance L_{s1}, and the electrical resistance for a phase R_{s1} are explained for a single conductor per slot as follow in equations below [12-14].

$$L_{m1} = \frac{4\mu_0 l_r r_s}{\pi(K_c g + l_m)} {N_{spp}}^2 {K_{B1}}^2 \quad (25)$$

$$L_{f1} = 2\mu_0 l_r p N_{spp} \lambda_{slot} \quad (26)$$

$$M_{s1} = \frac{-L_{m1}}{2} \quad (27)$$

$$L_{s1} = L_{m1} - M_{s1} + L_{f1} \quad (28)$$

$$R_{s1} = 2\rho_{copper}\left[l_r + \frac{\pi^2(r_s + 0.5d_s)}{2p}\right]\frac{pN_{slots}}{\pi r_s d_s K_r} \quad (29)$$

The current in stator windings for a single conductor per slot I_{s1} is function of the current density J_s as shows "Equation 30" [15].

$$I_{s1} = \frac{J_s d_s K_r \pi r_s}{6pN_{spp}} \quad (30)$$

The vacuum electromotive force E generated in the stator windings is given by "Equation 31" [12].

$$E = p\Omega\Phi_s \quad (31)$$

With Ω is the rotational angular speed of the generator rotor.

The study is devoted to three-phase generator delivering on an alternating voltage source of maximum amplitude V_{dim}. For the case referred to in this paper, the voltage source delivers to a battery of accumulators with voltages V_{bat} through a diode bridge. Consequently, V_{dim} is related with V_{bat} as expressed in "Equation 32" [12].

$$V_{dim} = \frac{2}{\pi} V_{bat} \quad (32)$$

The generative operation of the machine is described by the fundamental "Equation 33". Therefore, the Fresnel Diagram is obtained at the base dimensioning point as illustrated in "Figure 9". In fact, the base dimensioning point is characterized by the sizing voltage V_{dim}, electrical angular speed ω_{dim}, and electromagnetic design torque T_{em_dim} [12-14].

$$\underline{E} = \underline{V_{dim}} + R_s\underline{I_s} + j\,L_s\omega_{dim}\underline{I_s} \quad (33)$$

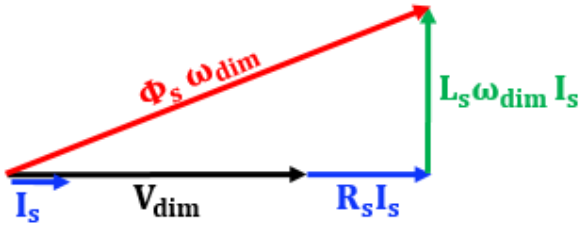

Figure 9. Generator Fresnel Diagram at Base Point

The purpose of this diagram is to calculate the number of conductors per slot N_{cs}. Indeed, the generator electrical parameters are a function of the number of conductors per slot and the calculated graders for a single conductor per slot as mentioned in equations bellow [12-14].

$$L_f = {N_{cs}}^2 L_{f1} \quad (34)$$

$$L_m = {N_{cs}}^2 L_{m1} \quad (35)$$

$$L_s = {N_{cs}}^2 L_{s1} \quad (36)$$

$$R_s = {N_{cs}}^2 \quad (37)$$

$$I_s = \frac{I_{s1}}{N_{cs}} \quad (38)$$

As a conclusion, the number of conductors in a single slot is obtained by solving the quadratic "Equation 39" obtained by replacing the electrical quantities expressions developed above in the formula spelled out from generator electrical diagram of "Figure 8".

$$ {N_{cs}}^2 - \frac{2V_{dim}R_{s1}I_{s1}}{(\Phi_{s1}\omega_{dim})^2 - [{R_{s1}}^2 + (L_{s1}\omega_{dim})^2]{I_{s1}}^2} N_{cs} - \frac{{V_{dim}}^2}{(\Phi_{s1}\omega_{dim})^2 - [{R_{s1}}^2 + (L_{s1}\omega_{dim})^2]{I_{s1}}^2} = 0 \quad (39)$$

IV. FINITE ELEMENT ANALYSIS OF THE PMSG

In order to design the generator in 2D, a MATLAB-FEMM code is elaborated. This code has as input parameters geometric graders resulting from structural model of the machine. The main target of this part is to evaluate the performance of the interconnected models. For a reference machine with electromagnetic torque of 27.5 N.m, the bore radius is equal to 83.2 mm. The obtaining of the bore radius value is due to expertise of the designer in design of electrical machines and basing on several hypothesis. In fact, simplifying hypotheses are cited. At first, the filling factor K_p is chosen equal to 0.833. Thus, the angular width of the magnet α_{magnet} is equal to 75°. Such a value minimize the harmonics of the electromotive force EMF and ensure a good ratio between the volume of the magnet and the effective value of the induction in the air gap [12, 15]. The slot fill factor K_r is fixed to 0.35. The permanent magnets used are Neodymium Iron Boron Magnets NdFe30 having residual magnetization B_r equal to 1.1 T and relative permeability μ_r equal to 1.05. Subsequently, generator characteristics coming from analytical models are calculated.

As a result, the 2D geometric model of the reference machine is obtained by finite element software FEMM. It is represented in "Figure 10" having 36 trapezoidal slots with 47 conductors per slot and 12 magnets. All parameters of the reference machine are given in the table in the appendix.

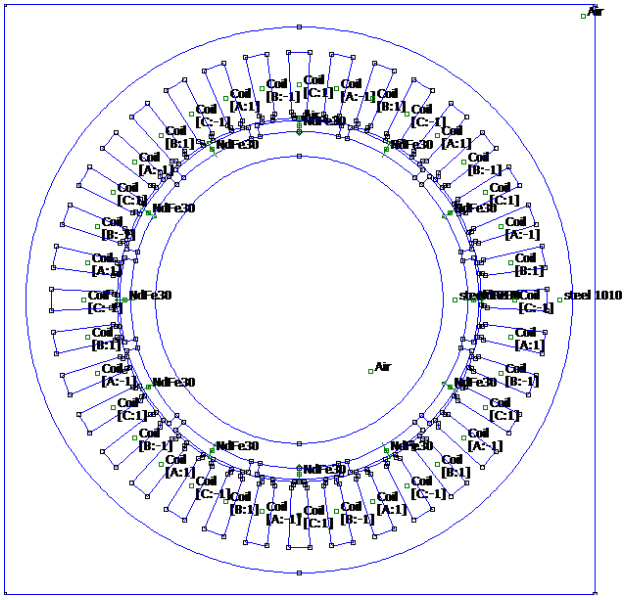

Figure 10. 2D Geometric Model of the PMSG with FEMM.

The induction variation B_a in the air-gap is shown in "Figure 11". Its peak value is 0.9 T. It is close to the analytical value 0.846 T.

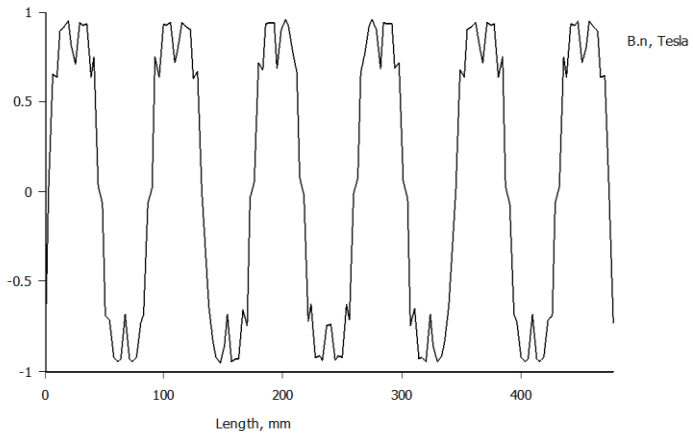

Figure 11. Induction as function of the air-gap perimeter length.

The magnetic field lines generated by the rotation of the permanent magnets glued to the rotor are represented in the stator and rotor yoke as mentioned in "Figure 12".

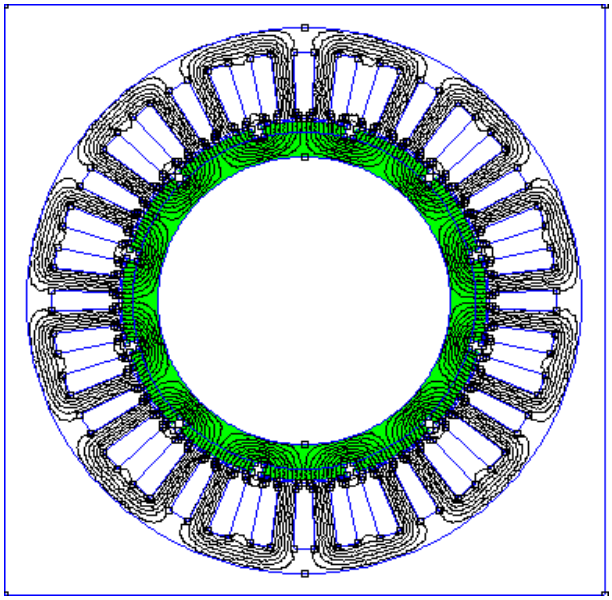

Figure 12. Field Lines Distribution in the PMSG.

The rotational movement of the magnets-rotor assembly highlighted in green in "Figure 12" is generated by the rotational movement of the turbine. According to the induction phenomena, an induced electromotive force EMF and an induced current in the three phase's stator windings. There will be a generation of an electromagnetic torque. For the studied case, the electromagnetic torque curve obtained by the finite element method with MATLAB-FEMM software is represented in "Figure13". Its average value is equal to 23.5 N.m. Comparing to 27.5 N.m, a tolerable error of 17% is introduced between analytical and numerical results given the smoothness of the finite element analysis approach and considering the effect of the winding type.

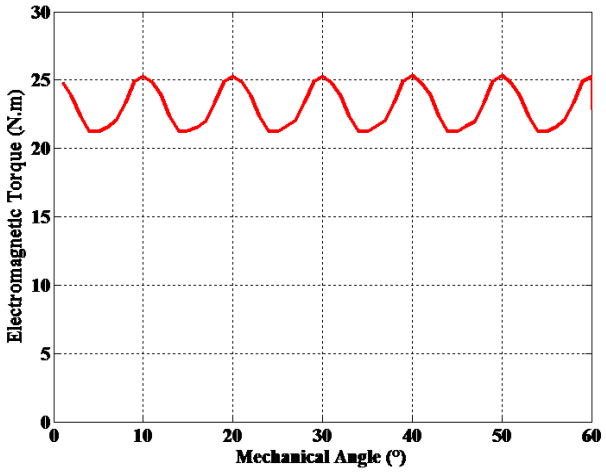

Figure 13. Electromagnetic Torque Curve Obtained by the Finite Element Method

The simulation results curves allow the validation of the PMSG analytical models. The feasible structure of the machine proved the reliability of the geometric model. The induction curve and the safe distribution of the field lines in the machine confirmed the magnetic model. Indeed, the average value of the electromagnetic torque is at the base of the determination of the parametric modelling of the whole chain. Such curve look and value support the analytical approach for the modeling of the wind turbine chain. Therefore, the analytical models are validated.

V. CONCLUSION

In this paper, a modelling method of a wind chain is described. The analytical resolution of the mechanical-geometric parameters of the airfoils, the geometric sizes of the PMSG and the calculation of the electrical and magnetic graders allows the parameterized evaluation of the wind power conversion chain. The performance of the generator are tested with the finite element analysis using MATLAB-FEMM software. A 17% error between analytical and numerical value of the electromagnetic torque of the PMSG is tolerable given the reliability of the considered method. As a perspective, models are suitable for the elaboration of an optimization model of the wind turbine to product optimal design to the wind market.

VI. Appendix

The attached table summarizes the Characteristics of the reference machine used in the case studied.

Machine Parameter	Unit	Value
r_{dr}	--	0.366
r_{rl}	--	2.025
J_s	A/mm^2	2.7
p	--	6
B_y	T	1.4
N_{spp}	--	1
Ω_{dim}	rad/s	40
r_s	mm	83.16
l_r	mm	41.06
w_m	mm	36.28
g	mm	1.17
l_m	mm	4.94
w_s	mm	9.68
d_y	mm	11.3
d_s	mm	30.44

VII. REFERENCES

[1] M. Santosh, C. Venkaiah and D. M. V. Kumar, "*Current Advances and Aproaches in Wind Speed and Wind Power Forecasting for Improved Renewable Energy Integration: A Review",* Engineering Reports, 2(6), April 2020.

[2] A F Reines and B Svingen, *"Analysis and Improvement of a Mathematical Turbine Model",* Journal of Physics: Conference Series, Vol. 1608, March 2020.

[3] C H Chong, A R Rigit and I Ali, *"Wind Turbine Modelling and Simulation Using MATLAB-SIMULINK",* IOP Conference Series: Materials Science and Engineering, October 2020.

[4] L Golebiowski, M Golebiowski, D Mazur and A Smolen, *"Analysis of Axial Flux Permanent Magnet Generator"*, The International Journal for Computaion and Mathematics in Electrical and Electronic Engineering, January 2020.

[5] A. Hemeida, P. Sergeant, A. Rasekh and J. Vierendeels, *"An Optimal Design of a 5MW AFPMSM for Wind Turbine Applications Using Analytical Model",* 2016 XXII International Conference on Electrical Machines, DOI: 10.1109/ICELMACH.20167732691.

[6] K. Latoufis, A. Rontogiannis, V. Karatasos, P. Markopoulos and N. Hatziargyriou, *"Thermal and Structural Design of Axial Flux Permanent Magnet Generators for Locally Manufactured Small Wind Turbines",* 2018XIII International Conference on Electrical Machines, pp. 2381-4802, September 2018.

[7] K.Sindhya, A. Mannien, K. Miettinen and J. Pippuri, *"Design of permanent magnet synchronous generator using interactive Mulitiobjective optimization"*, IEEE Transactions on Industrial Electronics, vol. 64, pp. 9776-9783, December 2017.

[8] World Energy Outlook, iea.org.

[9] World Wind Energy Asociation, wwindea.org.

[10] Global Wind Energy Council, gwec.net.

[11] L. Gang, Z. Hanguo, G. Youguang, L. Chengcheng and M. Bo, *"A Review of Design Optimization Methods for Electrical Machines"* , Energies, November 2017.

[12] D. Tran, "*Conception Optimale Intégrée d'une chaine éolienne « passive » : Analyse de robustesse et validation expérimentale", National Institute o Polytechnic of Toulouse*, 2010.

[13] N. Ben Halima, S. Ammous and A. Walha, *" Constant-Power Management algorithms of a hybrid wind energy system"*, Journal of Renewable and Sustainable Energy, October 2018.

[14] A. Abdelli, *"Optimisation Multicritère d'une chaine éolienne passive"*, National Institute o Polytechnic of Toulouse, 2007.

[15] B. Sareni, A. Abdelli, X. Roboam and D.H. Tran, *"Model simplification and optimization of a passive wind turbine generator",* Renewable Energy, vol. 34, p. 2640-2650, April 2009.

A Linguistic MCDM Framework for Sustainable Agriculture Design

Gülçin Büyüközkan *
Department of Industrial Engineering
Galatasaray University
Istanbul, Turkey
gbuyukozkan@gsu.edu.tr

Deniz Uztürk
Department of Business Administration
Galatasaray Univeristy
Istanbul, Turkey
duzturk@gsu.edu.tr

Abstract

In the direction of being sustainable, agriculture must satisfy the necessities of present and future generations while guaranteeing expediency, ecological health, and social and economic equity. Therefore, concerning only the environmental or the economic aspect of the agricultural development is not enough to satisfy the issues stated above. The social, economic, and environmental aspects of the agricultural transition are crucial. One cannot be separated from others. So, planning and evaluating the current situation in agriculture is essential for reaching a well-designed strategy for sustainable agriculture (SA). The inclusion of stakeholders, collaborative working of governments, municipalities, and practitioners are complete resolutions to create shared knowledge and awareness. Starting from this point of view, this paper suggests group decision-making (GDM) based design framework SA. For this purpose, the Axiomatic Design (AD) technique is provided. To create a flexible environment for decision-makers (DMs) and simplify the computations, the AD technique is integrated with a 2-tuple linguistic model. The 2-tuple model facilitates the interpretation of the assessments by providing linguistic outputs. A case study is presented to test the applicability of the suggested methodology, and the results and analysis are provided followingly.

Keywords: Sustainable agriculture, sustainable design, MCDM, Axiomatic Design, 2-Tuple linguistic model

I. INTRODUCTION

In 2015, United Nations generated an agenda covering seventeen different goals as the 2030 Sustainable Development Goals (SDGs). Zero hunger (goal 1), clean water (goal 6), sustainable cities and communities (goal 11), responsible consumption and production (goal 12), and climate action (goal 13) are the crucial ones that are highly related to the agriculture industry [16]. Consequently, the revision of existing agricultural systems is one of the essential targets to reach sustainable development. Agriculture stands at an important place for humanity by providing food for a living. Nevertheless, to be able to meet the increasing demand with accelerated population growth, to overcome the loss of biodiversity and food loss and waste, a novel agricultural approach is needed [40].

The sustainable Agriculture (SA) notion is on the agenda since the 1970s [4]. In these years, still the importance of recycling, having less waste, and improving productivity were assigned as the significant issues about SA. Today the expectations from SA remain the same as before. Currently, novel digital technologies started to involve in the traditional agricultural systems. We are facing a new era with more automized, controllable, and transparent food production. However, the rising hunger and malnutrition, and overexploitation of natural resources continue. Accordingly, to achieve a durable and robust plan for SA, a design methodology in which all the stakeholders can be integrated may be a quality solution [5, 32, 36]. Considering the stakeholder's expectations, an action/solution prioritization may be handy for practitioners, governments, or municipalities. From this point of view, this paper suggests a linguistic design framework for SA. The SA design procedure is approached as multi-criteria decision-making (MCDM) process, and the design parameters are based on the stakeholders' expectations from SA.

As an MCDM technique, the Axiomatic Design (AD) approach is suggested regarding its benefits, such as reducing design iterations and random searches for solutions [20]. In favor of fortifying the AD technique's use of linguistic variables, the AD is extended with the 2-tuple linguistic model [24]. The 2-tuple linguistic model enables the creation of computations with linguistic variables, and it provides interpretability of the results via linguistic variables closer to human thinking. A group decision-making (GDM) approach is also followed in this recommended framework to mimic the stakeholder integration. Aggregation of multiple evaluations is handled with the 2-tuple model's operators [22]. To the best of our knowledge, the main contributions of this work can be summarized as follows:

- Integrating AD technique to SA design subject for the first time,
- Integrating the 2-tuple linguistic model and AD model for the first time in the SA design problem.

The remaining parts of the paper are as follows: Section II presents the theoretical background of the methodology by explaining the SA notion and its expectations. Section III provides the methodological background by giving the preliminaries about suggested techniques.

IEECP'21, July 29-30, 2021, Silicon Valley, San Francisco, CA – USA

D!t: *https://sci-index.com/DAI/2021.99101/IEECP/15056949*

* Corresponding author / *Galatasaray University, Ortakoy, Cıragan Cd. No:36, 34349 Besiktas/Istanbul*

Section IV provides the case study to test the applicability of the suggested framework. The following section gives the results and analysis of the case study. Finally, Section VI gives the concluding remarques.

II. THEORETICAL BACKGROUND

A. Sustainable Agriculture

In the direction of being sustainable, agriculture must satisfy the necessities of present and future generations while guaranteeing profitability, environmental health, and social and economic equity [17]. Therefore, concerning only the environmental or the economic aspect of the agricultural development is not enough to satisfy the issues stated above. The social, economic, and environmental aspects of the agricultural transition are crucial. One cannot be separated from others. In the literature, the transition/transformation to the SA is commonly associated with the social movements created by the stakeholders [3, 32, 36].

The need for a practice change and redesigning the farming systems are the critical enablers for SA. Recently, the integration of innovative technologies into the traditional farming environment speeded up this transition for farmers [10, 12, 29]. However, technological availability is not the same for every region in the world. So, planning and evaluating the current situation in agriculture is essential for reaching a well-designed strategy for SA.

The inclusion of stakeholders, collaborative working of governments, municipalities, and practitioners are the key enablers for social transition. Food and Agriculture Organization of the United Nations (FAO) emphasizes five main principles for food and agriculture sustainability [40]:

- Adding value to food systems by augmenting production and employment,
- Conserve and intensify natural resources,
- Support inclusive economic growth,
- Reinforce resistance of communities and ecosystems,
- Governance adaptation.

Concerning these main principles, this paper generates the main expectations of stakeholders from academic and industrial literature.

Furthermore, the powerful solutions/actions based on the five main principles of FAO are generated from the literature as well. The details of the expectations and the actions will be given in Section II.C. The following section will present the background of the SA and the MCDM applications in the literature.

B. Sustainable Agriculture and MCDM

As aforementioned, the primary success factor for SA is the evaluation of economic, social, and environmental components together. MCDM approach is a possible way to investigate the interactions and system components behaviors [26]. From groundwater zone determination to the land suitability assessment MCDM approaches proposed various techniques to analyze and investigate complex models with multiple criteria and alternatives. The design tools such as AD and the Quality Function Deployment are also common techniques used in alternative selection problems. However, in this paper, the AD technique is utilized thanks to its design nature. It aims to prioritize the most suitable actions/solutions that can cover all the expectations.

When the "sustainable agriculture" and "multi-criteria decision-making" words are search on the Scopus database together, eleven different works were obtained. Their focused area and applied techniques are listed in Table 1.

Table 1. MCDM based SA studies

Year and Reference	The objective of the study	Technique	Linguistic Technique	Case Study
2020 [28]	Land suitability analysis	AHP and WCL	No	Yes
2020 [2]	Land suitability assessment	AHP	No	Yes
2019 [41]	Suitability mapping for rice cultivation	AHP	No	Yes
2019 [13]	Assessment of sustainable sugarcane farms	VIKOR, TOPSIS, VTOPES	No	Yes
2019 [42]	Agricultural supply chain risk management	SWARA and FMEA	No	Yes
2019 [15]	Agriculture supply chains	TOPSIS	Yes	Illustrative Example
2018 [30]	Crop selection pattern	TOPSIS	Yes	Yes
2017 [11]	Land suitability evaluation for wheat cultivation	AHP	No	Yes
2016 [23]	Representation of groundwater potential	AHP	No	Yes
2014[25]	Selecting peach ideotypes	ELECTRE-Tri and DRSA	No	Yes
2005 [26]	Economic and environmental analysis of farming practices	MODAM	No	Yes

As Table 1 states, the most common technique for SA studies is the AHP approach suggested by Saaty [31]. When the "sustainable agriculture design" is searched on the Scopus database, two different works are obtained, one is focused on the design and analysis of the hydraulic structures for SA [34], and the other is concentrated on risk analysis and design of activities concerning the risk factor [37].

When the whole related literature is analyzed, we can deduct that the MCDM tools are potent solutions to handle complex decision problems in the SA area. Moreover, we found that there is a lack of a roadmap for policymakers and stakeholders. Consequently, this paper aims to fulfill this gap and propose a design methodology for policymakers and farmers. The model is based on linguistic variables and the AD technique. The following section will give the details of obtained expectations, solutions/actions, and the decision-making model.

C. Sustainable Agriculture Expectations

The expectations of all stakeholders for SA activities are derived from the academic and industrial literature. Moreover, the industrial experts who also helped assess the case study validated the listed expectations and the potential solutions.

Figure 1 here presents the suggested decision model with the expectations [1, 10, 17, 26, 29, 36], and followingly Table 2 gives the identified actions/solutions [6, 17, 26, 39] for the SA approach.

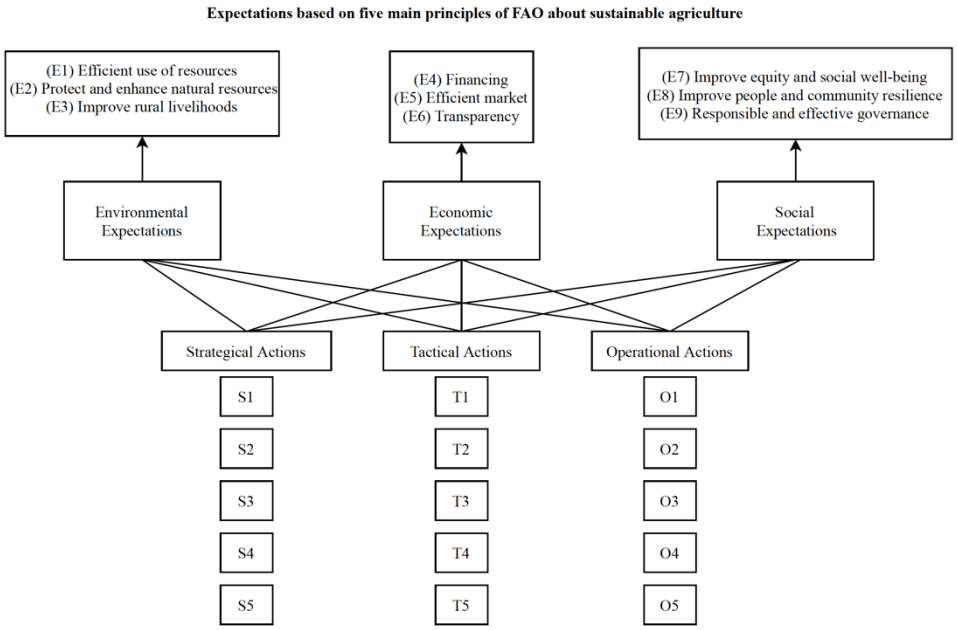

Figure 1. Suggested decision-making model for action prioritization

Table 2. Actions to prioritize for SA

Stakeholder dialogue	Strategical	**S1**
Co-constructed knowledge with awareness rising	Strategical	**S2**
Creating inclusive platforms	Strategical	**S3**
Regulations and standards based on climate-change mitigation and adaptation	Strategical	**S4**
Enhance gender equity	Strategical	**S5**
Developing decentralized capacity	Tactical	**T1**
Develop financial incentive packages to support private investment and enable equitable distribution of benefits	Tactical	**T2**
Decentralize decision-making	Tactical	**T3**
Apply mediation and other conflict resolution mechanisms in resource governance	Tactical	**T4**
Generalize risk assessment/management and communication	Tactical	**T5**
Encouraging flexibility in production systems	Operational	**O1**
Promote small/medium enterprises	Operational	**O2**
Improve rural nutrition: production of more and affordable nutritious and diverse foods, including fruits & vegetables	Operational	**O3**
Increase/protect farmers' access to resources, such as pasture, water, credit	Operational	**O4**
Increase rural job opportunities e.g., in small and medium enterprises sustainability and related activities	Operational	**O5**

The listed actions in Table 2 are divided into three leading groups as strategical, tactical, and operational. In favor of designing strategies for SA, knowing the possible effects of the actions at the managerial level also may guide the practitioners to create a better transition plan.

III. METHODOLOGICAL BACKGROUND

This section will provide the methodological background with preliminary information about the 2-Tuple linguistic model and the AD technique. First, the main benefits and properties of the 2-Tuple model and AD are given, and later the principal methodology for GDM aggregation is presented.

A. 2-Tuple Linguistic Model

Herrera and Martinez first represent this model in 2000 [24]. The 2-tuple linguistic model and its extensions have been applied to various topics, mainly decision-making and decision analysis problems [24, 27, 35]. Basic definitions are as follows [24]:

The 2-Tuple fuzzy linguistic representation model represents the linguistic information using a 2-Tuple (S, α) here; S is a linguistic label, and α is a numerical value representing the value of the symbolic translation. The function is defined as:

$$\Delta_s : [0, g] \rightarrow \bar{S}$$
$$\Delta_s(b) = (S_i, a), with \begin{cases} i = round(b) \\ a = b - i \end{cases} \quad (1)$$

The linguistic term set S could be converted into 2-Tuple form by adding zero value as in the following relation:

$$S_i \in S \Rightarrow (S_i, 0) \quad (2)$$

For further details, the readers can refer to [24]. The main benefits of a 2-tuple linguistic model have augmented the accuracy and interpretability of the results, the possibility of dealing with variables closer to human beings' cognitive processes, and increased accuracy of computations. Regarding these benefits to create a flexible environment for the decision-makers (DMs) and better analysis and knowledge about the SA area, the suggested 2-Tuple methodology is integrated with the AD technique.

B. Axiomatic Design

AD is a technique first introduced by Suh [38]. For the selection problem, a linguistic-based AD is proposed; it is used with 2-Tuple linguistic information to overcome the multi-granularity arising from multiple experts. The AD technique uses two axioms: the first one is the independence axiom, which sets out that function requirements (FRs) must be independent, and the second one is the information axiom, which sets out that the design with the minimum information content is better than all the other designs that satisfy the FRs [38].

AD is based on the information content (I), which is represented by the probability function for fulfilling an FR. In 2-tuple AD, fuzzy membership functions for linguistic variables are used instead of probability functions. Figure 1 represents the System Range (SR) and Design Range (DR) for fuzzy membership functions.

I_i is calculated as the following relation for Fuzzy AD [7]:

$$I_i \begin{cases} \infty & ,no\ intersection \\ log_2\left(\frac{area\ of\ SR}{common\ ares}\right) & ,otherwise \end{cases} \quad (3)$$

Then the weighted total information content (I) is calculated with:

$$I = \sum_{i=1}^{n} w_i \times I_i \quad (4)$$

where n is the number of criteria, w_i is the weight of criteria and I_i is the non-weighted information content calculated with Eq. (3).

Finally, the prioritization of alternatives is obtained by ranking the options with increasing order. The alternative with the minimum information content is the most appropriate one for the solution.

C. Aggregation Technique for GDM

This paper proposed a linguistic SA design framework with a GDM approach. The main benefit of the GDM approach is to create an unbiased, objective decision-making environment where the final solution is beneficial to each DM. The GDM approach is based on the aggregation of different opinions from multiple DMs [9]. GDM is a commonly adopted method preferred over a single DM due to its superiority in avoiding partiality and bias [8, 21].

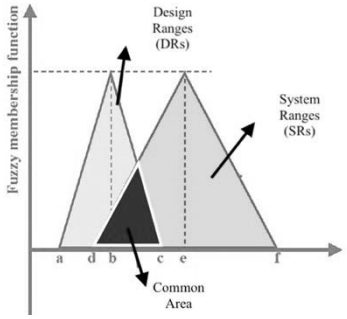

Figure 1. System ranges, design ranges, and common area in fuzzy membership functions [7]

Regarding all the benefits mentioned above, the 2-tuple linguistic model's *Linguistic Hierarchies (LH)* approach is selected as an aggregation technique for this GDM methodology. The methodology is based on the experts' knowledge; however, the experience level and knowledge may differ concerning the interest of DMs. So, providing different granulated linguistic evaluations set to each DM may be a powerful solution to balance the knowledge difference rising from different backgrounds.

LH [24] approach unifies the multigranular linguistic input under the one unified linguistic set. A transformation equation exists to normalize label sets with different granularity. The following equation gives the relations:

$$TF_{t'}^{t}(S_i^{n(t)}, a^{n(t)}) = \Delta\left(\frac{\Delta^{-1}(S_i^{n(t)}, a^{n(t)}) \cdot (n(t') - 1)}{n(t) - 1}\right) \quad (5)$$

where *TF* is the transformation function for *LH*, and the transformation is from t^{th} level to t'^{th} level.

Furthermore, for aggregating normalized linguistic variables *Weighted Aggregation Operator (WAO)* of 2-Tuple model is recommended as well. The following equation gives the formulation:

$$\vec{x} = \left(\frac{\sum_{i=1}^{n} \Delta^{-1}(e_i, \alpha_i) \times \Delta^{-1}(w_i, \alpha_i)}{\sum_{i=1}^{n} \Delta^{-1}(w_i, \alpha_i)}\right) = \Delta\left(\frac{\sum_{i=1}^{n} \beta_i \times w_i}{\sum_{i=0}^{n} w_i}\right) \quad (6)$$

where, (e_i, α_i) is the assessments provided by each expert; (w_i, α_i) stands for the weights of experts and n represents the number of experts and β_i is the β values for ith criterion's importance.

The detailed steps of the suggested methodology will be given in the next section.

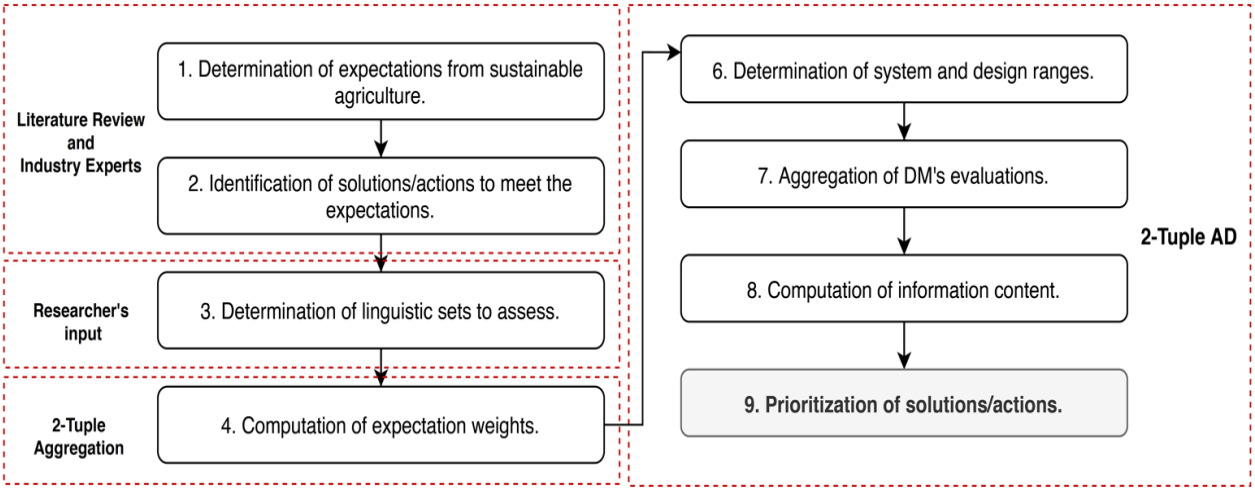

Figure 2. Detailed steps of the suggested framework.

D. Suggested Framework

The preliminaries provided in the previous section forms the methodological basis of the SA design framework. Here Figure 2 presents the flow of the recommended framework. Followingly, in the case study, the indicated steps will be followed in order to test the applicability of the design model.

IV. CASE STUDY

The case study is designed to test the applicability of the suggested framework. When the framework is formed, the first step was creating a decision-making group and validating the framework to them.

The decision-making group comprises three competent experts in sustainable agriculture, sustainable design and agriculture, and sustainable supply chain and its design. The DMs working on sustainable agriculture and design are assessed by using nine scaled linguistic sets. Due to the volatile background of DMs, two different linguistic sets are provided. The third DM works on sustainable supply chains, and their design used five scaled linguistic sets. The details of linguistic sets are as follows:

The second level five scaled (Very Low(VL)- Low (L)- Medium (M)- High(H)-Perfect (P)) and the third level nine scaled (Very low (VL)- Low(L)-Medium Low (ML)- Almost Medium (AM)- Medium (M)- Medium High (MH)- High (H)- Very High (VH)- Perfect (P)) hierarchy of letters [18].

The Delphi [23] method is followed for the separate meetings with each DM. Their judgments are collected separately and aggregated by using the 2-tuple model's LH approach.

As stated in Figure 2, the first three steps of the framework are completed as explained above. Then for the following steps, the weights of the expectations are obtained first by normalizing assessment under nine scaled sets then unifying them using Eq. (6). Table 3 gives the individual assessments of DMs and the aggregated importance of expectations.

The exact process is conducted for the assessment of relations between expectations and actions. Due to the page restriction, only the aggregated decision matrix for AD is given in Table 4.

Table 3. Expectation weights

	Five scaled set	Nine scaled set		Unified under nine scaled
	DM1	DM2	DM3	Aggregated
E1	P	VH	P	(P,-0.39)
E2	P	P	P	(P,0)
E3	H	H	VH	(H,0.39)
E4	M	AH	H	(AH,0.17)
E5	M	H	VH	(VH,-0.04)
E6	H	VH	VH	(VH,-0.22)
E7	H	VH	H	(H,0.39)
E8	M	AH	AH	(AH,-0.22)
E9	P	P	P	(P,0)

Table 4. The aggregated assessment matrix for 2-tuple AD.

	DRs	S1	S2	S3	S4	S5	T1	T2	T3	T4	T5	O1	O2	O3	O4	O5
E1	LAM	(L,0)	(H,0)	(P,0)	(VH,0.22)	(VL,0)	(M,0)	(VL,0)	(L,0)	(H,0)	(H,0)	(H,0)	(M,-0.39)	(M,0)	(P,0)	(L,0)
E2	LAM	(AM,0.22)	(AM,0.22)	(AH,0.22)	(P,0)	(L,-0.43)	(H,-0.43)	(VL,0)	(L,0)	(L,0)	(H,0)	(H,0)	(M,-0.39)	(H,0)	(P,0)	(M,-0.43)
E3	LMH	(AH,0.22)	(H,0)	(L,0.43)	(P,0)	(AM,-0.22)	(M,0)	(AM,-0.22)	(M,-0.39)	(H,0)	(M,-0.39)	(L,0)	(AH,0.22)	(H,-0.43)	(VH,-0.22)	(H,0)
E4	LAM	(AH,-0.22)	(M,0)	(VH,-0.22)	(H,0)	(L,0)	(AH,-0.22)	(P,0)	(M,0)	(M,0)	(H,0)	(M,0)	(P,0)	(AM,-0.22)	(AM,0.22)	(H,0)
E5	LAM	(M,-0.43)	(AM,0.22)	(H,0)	(H,0)	(M,0)	(M,0)	(VH,-0.17)	(M,0)	(L,0)	(L,0)	(M,0)	(H,0)	(L,0)	(AM,0.22)	(M,0)
E6	LAM	(VH,-0.22)	(AM,0.22)	(VH,-0.22)	(P,0)	(AM,-0.22)	(AH,-0.22)	(H,0)	(VH,-0.22)	(AH,-0.22)	(H,0)	(L,0)	(AM,0.22)	(AM,0.22)	(M,0)	(M,0)
E7	LMH	(H,0)	(H,0.39)	(H,0)	(M,0)	(P,0)	(VH,-0.22)	(L,0)	(M,-0.39)	(M,0)	(M,0)	(L,0)	(AH,0.22)	(M,0)	(H,0)	(P,-0.39)
E8	LAM	(P,0)	(P,-0.39)	(VH,-0.22)	(AH,-0.22)	(P,0)	(H,0)	(AM,-0.22)	(M,0)	(M,0)	(L,0)	(L,0)	(H,0)	(H,0.39)	(P,0)	(P,-0.39)
E9	LMH	(AH,-0.22)	(P,-0.39)	(VH,-0.22)	(L,0)	(AM,-0.22)	(M,0)	(H,-0.43)	(H,0)	(P,0)	(H,0)	(M,0)	(M,0)	(H,-0.43)	(H,-0.43)	(H,0.39)

For the design ranges (DRs) in the AD technique, a nine-scaled assessment set is suggested to DMs, and their compromise assessment is obtained as a consensus. The suggested assessment set is as follows: *At least very low (LVL)- at least low (LL) - at least medium low (LML) - at least almost medium (LAM) - at least medium (LM) - at least medium high (LMH) - at least high (LH) - at least very high (LVH) at least perfect (LP).*

According to the design ranges and the aggregated DMs assessment, as in Figure 1, the intersection area of both assessments is calculated to obtain each action's information content. The information content is obtained with Eq.(3). Then, the expectation importance will be multiplied to obtain the final ranking as in Eq (4).

The results and their analysis will be given in the next section.

V. RESULTS AND ANALYSIS

After applying the steps stated in Figure 2, the final relation matrix where the weighted information values are stated is given in Table 5.

The ∞ refers to no intersection between the system and design ranges. That means the solutions do not meet the expectations. Therefore, the AD provided a pre-elimination to reach the most efficient solutions for SA. The elimination of less effective actions narrows down the design process, and it only suggests and ranks the most efficient actions. The information content is calculated by taking the intersection of each system range with the assigned design ranges. The design ranges and the intersection of a system range are presented as an example in Figure 3.

Moreover, all the operational solutions are eliminated. The operational solutions contain the solutions for operational, short-term

actions. We can assume that the short-term actions are not as powerful as tactical and strategical solutions for SA.

As the existing literature confirms that the tactical and strategical transition is the critical enabler for SA [17, 18], our suggested methodology validated the same result by eliminating short-term actions as a solution.

Table 5. Ultimate relation matrix with information contents

	S1	S2	S3	S4	S5	T1	T2	T3	T4	T5	O1	O2	O3	O4	O5
E1	∞	0.03	0.00	0.00	∞	0.18	∞	∞	0.03	0.03	0.03	∞	0.18	0.00	∞
E2	0.08	0.08	0.01	0.00	∞	0.61	∞	∞	∞	0.04	0.04	∞	0.04	0.00	∞
E3	0.03	0.09	0.47	0.00	∞	1.00	∞	∞	0.09	∞	∞	0.03	∞	0.23	0.09
E4	0.29	0.15	0.05	0.03	∞	0.29	0.00	0.15	0.15	0.03	0.15	0.00	∞	0.07	0.03
E5	∞	0.05	0.02	0.02	0.11	0.11	0.02	0.11	∞	∞	0.11	0.02	∞	0.05	0.11
E6	0.06	0.08	0.06	0.00	∞	0.36	0.04	0.06	0.36	0.04	∞	0.08	0.08	0.19	0.19
E7	0.08	0.00	0.08	0.81	0.00	0.19	∞	∞	0.81	0.81	∞	0.02	0.81	0.08	0.99
E8	0.00	0.08	0.04	0.27	0.00	0.03	∞	0.14	0.14	∞	∞	0.03	0.00	0.00	0.08
E9	∞	1.30	0.24	∞	∞	1.07	∞	0.10	0.00	0.10	1.07	1.07	∞	∞	0.00
Sum:		**1.88**	**0.97**	**1.13**		**3.84**									

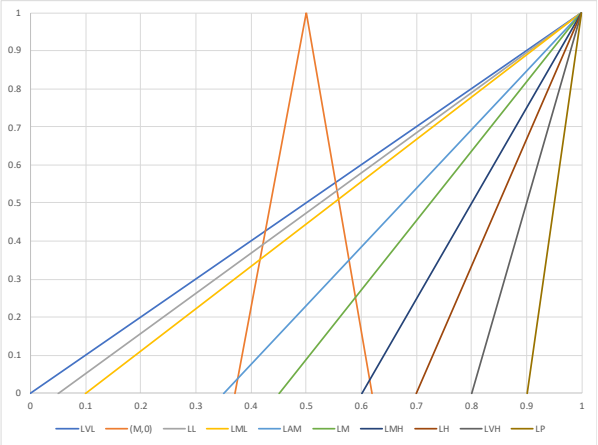

Figure 3. The intersection of design ranges and system range

Table 6. Ranking of the feasible solutions

S#	Solution	Rank
S2	Co-constructed knowledge with awareness rising	3
S3	Creating inclusive platforms	1
S4	Regulations and standards based on climate-change mitigation and adaptation	2
T1	Developing decentralized capacity	4

Furthermore, among appropriate solutions, the majority are the strategical solutions that can transform the mentality of the conventional agricultural systems. The ranking of the feasible solutions concerning their weighted information values is given in Table 6.

Creating inclusive platforms is selected as the most potent solution for SA design. As stated in the literature, inclusive platforms are significant enablers for long-term capacity building, knowledge sharing, and consensus-based decision making [14, 17, 19, 33]. Therefore, for building shared knowledge and joint actions for SA design, these platforms are the primary facilitator for technological innovations as well.

VI. CONCLUSIONS

The accelerated population growth and the consumption of natural resources to feed the increasing population are two significant challenges that agriculture faces today. Plus, the severe effects of climate change related to the extending natural sources cause vulnerabilities at various stages of the agricultural value chain.

As a result, SA is recommended by various policymakers and nongovernmental organizations. The SA approach suggested, yet the need for an appropriate roadmap or a “to do” list for practitioners was a gap in the literature. Therefore, this paper suggested a linguistic design framework for SA design.

The framework is built with the integration of the 2-tuple linguistic model with the AD technique. The 2-tuple linguistic model provided interpretability of the assessments closer to human thinking, and also it enables to make computations with multi-granular data. The multi-granular data eliminated the knowledge and background differences of DMs. They felt comfortable while evaluating the relations between the expectations and the solutions. As a result, a ranking of four solutions is obtained. The majority of the results were strategic solutions. The methodology also validated the existing literature by emphasizing the importance of strategic approaches for a successful SA design.

The SA expectations were generated from the academic and the industrial literature as a significant input to the framework. Also, they are validated by the experts. However, future studies can improve the number of expectations, and real field research can be applied to reach real stakeholders.

As a limitation, the number of DMs can be stated. In this paper, the recommended methodology is tested with three DMs; however, the framework can work with DMs up to more high numbers. Also, a sensitivity analysis can be performed to investigate the solution rankings by changing the design ranges.

Furthermore, for future studies, the same methodology can be followed for other industries as well. The same methodology can serve as valuable guidance for strategy and solution detection for various sectors by improving the expectations according to the industries.

VII. ACKNOWLEDGMENTS

Our thanks to experts for their valuable assessments and guidance for the design model. This work has been supported by the Scientific Research Projects Commission of Galatasaray University (Project Number: 19.102.002).

VIII. REFERENCES

[1] Agarwal, P. et al. 2019. Sustainable Smart-Farming Framework: Smart Farming. *Smart Farming Technologies for Sustainable Agricultural Development*. Igi Global. 147–173.

[2] Ali, S. et al. 2020. Assessment of land use suitability for natural rubber using GIS in the U-tapao River Basin, Thailand. *Kasetsart Journal of Social Sciences*. 41, 1 (2020), 110–117.

[3] Anderson, C.R. et al. 2019. Transformative agroecology learning in Europe: building consciousness, skills and collective capacity for food sovereignty. *Agriculture and Human Values*. 36, 3 (Sep. 2019), 531–547.

[4] Balfour, L.E. Towards a Sustainable Agriculture--The Living Soil. 7.

[5] Borsellino, V. et al. 2020. Agri-food markets towards sustainable patterns. *Sustainability (Switzerland)*. 12, 6 (2020).

[6] Building partnerships for sustainable agriculture and food security: *https://www2.deloitte.com/jp/en/pages/about-deloitte/articles/nva-country-partnership-guide.html*. Accessed: 2021-06-03.

[7] Buyukozkan, G. et al. 2017. RFID service provider selection: An integrated fuzzy MCDM approach. *Measurement*. 112, (Dec. 2017), 88–98.

[8] Büyüközkan, G. and Feyzioğlu, O. 2005. Group decision making to better respond customer needs in software development. *Computers & Industrial Engineering*. 48, 2 (2005), 427–441.

[9] Buyukozkan, G. and Guleryuz, S. 2015. Extending Fuzzy QFD Methodology with GDM Approaches: An Application for. *International Journal of Fuzzy Systems*. 17, 4 (Dec. 2015), 544–558.

[10] Collado, E. et al. 2019. Smart farming: A potential solution towards a modern and sustainable agriculture in Panama. *Aims Agriculture and Food*. 4, 2 (2019), 266–284.

[11] Dadhich, G. et al. 2017. Agriculture land suitability evaluation for wheat cultivation using geomatics for Patan District, India. *International Journal of Agricultural Resources, Governance and Ecology*. 13, 1 (2017), 91–108.

[12] De Clercq, M. et al. 2018. Agriculture 4.0: The future of farming technology. *Proceedings of the World Government Summit, Dubai, UAE*. (2018), 11–13.

[13] Deepa, N. et al. 2019. An efficient ensemble VTOPES multi-criteria decision-making model for sustainable sugarcane farms. *Sustainability (Switzerland)*. 11, 16 (2019).

[14] Ebitu, L. et al. 2021. Citizen science for sustainable agriculture – A systematic literature review. *Land Use Policy*. 103, (2021).

[15] El Alaoui, M. et al. 2019. Type 2 fuzzy TOPSIS for agriculture MCDM problems. *International Journal of Sustainable Agricultural Management and Informatics*. 5, 2–3 (2019), 112–130.

[16] #Envision2030: 17 goals to transform the world for persons with disabilities | United Nations Enable: 2016. *https://www.un.org/development/desa/disabilities/envision2030.html*. Accessed: 2021-06-02.

[17] FAO ed. 2014. *Building a common vision for sustainable food and agriculture: principles and approaches*. Food and Agriculture Organization of the United Nations.

[18] FAO et al. 2001. *The state of food insecurity in the world 2001*. FAO.

[19] Golicz, K. et al. 2021. Old problem, the Millennial solution: using mobile technology to inform decision making for sustainable fertilizer management. *Current Opinion in Environmental Sustainability*. 49, (2021), 26–32.

[20] Harutunian, V. et al. 1996. Decision Making and Software Tools for Product Development Based on Axiomatic Design Theory. *CIRP Annals*. 45, 1 (Jan. 1996), 135–139.

[21] Herrera, F. et al. 2001. Multiperson decision-making based on multiplicative preference relations. *European Journal of Operational Research*. 129, 2 (Mar. 2001), 372–385.

[22] Herrera, F. and Martínez, L. 2001. A model based on linguistic 2-tuples for dealing with multigranular hierarchical linguistic contexts in multi-expert decision-making. *IEEE Transactions on Systems, Man, and Cybernetics, Part B (Cybernetics)*. 31, 2 (2001), 227–234.

[23] Mandal, U. et al. 2016. Delineation of Groundwater Potential Zones of Coastal Groundwater Basin Using Multi-Criteria Decision-Making Technique. *Water Resources Management*. 30, 12 (2016), 4293–4310.

[24] Martínez, L. et al. 2015. *The 2-tuple Linguistic Model*. Springer International Publishing.

[25] Memmah, M.-M. et al. 2014. Multi-criteria sorting methods to select virtual peach ideotypes. *International Journal of Multicriteria Decision Making*. 4, 4 (2014), 348–366.

[26] Meyer-Aurich, A. 2005. Economic and environmental analysis of sustainable farming practices - A Bavarian case study. *Agricultural Systems*. 86, 2 (2005), 190–206.

[27] Mi, C. et al. 2018. Product redesign evaluation: An improved quality function deployment model based on failure modes and effects analysis and 2-tuple linguistic. *Advances in Mechanical Engineering*. 10, 11 (Nov. 2018), 1687814018811227.

[28] Mufungizi, A.A. et al. 2020. A land suitability analysis of the Vhembe District, South Africa, the case of maize and sorghum. (2020), 1023–1030.

[29] Oswald Spring, U. 2019. Climate-Smart Agriculture and a Sustainable Food System for a Sustainable-Engendered Peace. *Climate Change, Disasters, Sustainability Transition and Peace in the Anthropocene*. H.G. Brauch et al., eds. Springer International Publishing Ag. 95–123.

[30] Qureshi, M.R.N. et al. 2018. Decision support model to select crop pattern for sustainable agricultural practices using fuzzy MCDM. *Environment, Development and Sustainability*. 20, 2 (2018), 641–659.

[31] Saaty, T.L. 1982. The Analytic Hierarchy Process: A New Approach to Deal with Fuzziness in Architecture. *Architectural Science Review*. 25, 3 (Sep. 1982), 64–69.

[32] Sadovska, V. et al. 2020. Reviewing value creation in agriculture - A conceptual analysis and a new framework. *Sustainability (Switzerland)*. 12, 12 (2020).

[33] Sanner, T.A. and Nielsen, P. 2019. Software Platforms for Inclusive Innovation. *Information and Communication Technologies for Development. Strengthening Southern-Driven Cooperation as a Catalyst for ICT4D* (Cham, 2019), 218–230.

[34] Santiago-Collazo, F.L. and Silva-Araya, W.F. 2019. Computational Model for Gradually Varied Flow in Channel Networks with Hydraulic Structures. *Journal of Irrigation and Drainage Engineering*. 145, 6 (2019).

[35] Singh, A. and Gupta, A. 2020. Best criteria selection based PROMETHEE II to aid decision-making under 2-tuple linguistic framework: Case-study of the most energy efficient region worldwide. *International Journal of Management and Decision Making*. 19, 1 (2020), 44–65.

[36] Slimi, C. et al. 2021. Exchanges among farmers' collectives in support of sustainable agriculture: From review to reconceptualization. *Journal of Rural Studies*. 83, (2021), 268–278.

[37] Stigter, K. 2010. Improving coping strategies with weather and climate risks in agricultural production, including the improved use of insurance approaches: Multiple cropping. *Applied Agrometeorology*. 531–534.

[38] Suh, N.P. 1998. Axiomatic Design Theory for Systems. *Research in Engineering Design*. 10, 4 (Dec. 1998), 189–209.

[39] Sustainable food & agriculture | Sustainability | McKinsey & Company: *https://www.mckinsey.com/business-functions/sustainability/how-we-help-clients/sustainable-food-and-agriculture*. Accessed: 2021-06-03.

[40] Sustainable Food and Agriculture: *http://www.fao.org/sustainability/en/*. Accessed: 2021-06-02.

[41] Ujoh, F. et al. 2019. Suitability mapping for rice cultivation in Benue State, Nigeria using satellite data. *Geo-Spatial Information Science*. 22, 4 (2019), 332–344.

[42] Yazdani, M. et al. 2019. A multi-criteria decision-making framework for agriculture supply chain risk management under a circular economy context. *Management Decision*. (2019).

Sustainable Farm Building Design with 2-Tuple House of Quality

Gülçin Büyüközkan [1]
Department of Industrial Engineering
Galatasaray University
Istanbul, Turkey
gbuyukozkan@gsu.edu.tr

Deniz Uztürk
Department of Business Administration
Galatasaray Univeristy
Istanbul, Turkey
duzturk@gsu.edu.tr

Abstract

Sustainability could be a good strategy or a path to follow for any industry to achieve a durable and adaptable system. In the construction sector, where a non-stop activity to build a new environment exists, sustainability is a massive necessity for continuity. Sustainable construction and design facilitate adaptable solutions with nature rather than producing solutions against it. Hence, this paper aims to propose a methodology for designing farm buildings for sustainable agriculture. The need for structures in the rural lands is a necessity for farming activities and stocking. Creating a sustainable building for farming practices is also an essential step to transition to sustainable agriculture. For this purpose, the House of Quality (HoQ) of the Quality Function Deployment (QFD) is suggested with the 2-tuple linguistic model integration. The group decision-making (GDM) approach is applied to simulate stakeholder inclusion for the design phase. The 2-tuple model helps to compute with multi-granular linguistic information. The use of multi-granular information augments the accuracy of computations and transforms the design phase closer to human thinking. To test the plausibility of the recommended methodology, a case study from Turkey is presented with the results and the analysis. Finally, the concluding remarques are provided at the end.

Keywords: Building design, sustainable farm building, HoQ, QFD, 2-tuple linguistic model, GDM

I. INTRODUCTION

Sustainability becomes one of the critical trending notions in our century with the rising awareness about the human effects on our earth. When it comes to sustainability, the idea is addressed in three dimensions: environmental, economic, and social. These three notions are the three main components of sustainability. The primary purpose of these components is to be stable or sustained in any situation. For this purpose, efficient usage of economic, environmental, and social sources is significant.

Sustainability could be a good strategy or a path to follow for any industry to achieve a durable and adaptable system. In the construction sector, where there is non-stop activity to build a new environment, sustainability is necessary to have continuity. In the building sector, the realization of sustainable building remains at a low rate, despite the increased need for it [13]. This low rate is a consequence of challenges of environmental and economic issues. To achieve an appropriate level of sustainability in a building, some principles must be applied, such as [1]:

- Lowering the energy demand and the consumption of operating materials,
- Utilization of reusable or recyclable building products and materials,
- Extension of the lifetime of products and buildings,
- Risk-free return of materials to the natural cycle,
- Comprehensive protection of natural areas and use of all possibilities for space-saving construction.

For some, these principles could be challenging and hard to apply. However, a prioritization of these principles could be done to achieve a sustainable building step by step. Different multi-criteria decision-making (MCDM) approaches could be used to handle the complications of this application. In this paper, the House of Quality (HoQ) of the Quality Function Deployment Method (QFD) is recommended to translate customer requests into building design requirements. The customer requests are treated as the sustainability requirements for operating a methodology that serves for sustainable design.

As an application area, the agricultural buildings are selected. The agricultural systems have immense impacts on their environments [30]. And the need for structures in the rural lands is a necessity for farming activities and stocking. Therefore, designing a sustainable building for farming practices is also an important step to transition to sustainable agriculture.

Consequently, this paper suggests an HoQ based framework for a sustainable farm building design. The HoQ technique is extended with the 2-tuple linguistic model to fortify its ability to deal with linguistic variables. Plus, the 2-tuple model facilitates the interpretation of outputs with linguistic variables, creating an assessment model closer to human thinking. A group decision-making (GDM) approach is followed to mimic the stakeholder or end-user inclusion in the designing phase. By integrating the end-user and the sustainability issues into the building design, this

IEECP'21, July 29-30, 2021, Silicon Valley, San Francisco, CA – USA

D!f: *https://sci-index.com/DAI/2021.99101/IEECP/15057072*

[1] Corresponding author - *Galatasaray University, Ortakoy, Cıragan Cd. No:36, 34349 Besiktas/Istanbul*

methodology aims to propose valuable guidance for farmers for their buildings.

The main contribution of this paper can be summarized as a first-time proposition of a linguistic model for a sustainable farm building design. The suggested linguistic-based design framework may guide farmers and policymakers to reach a sustainable agriculture environment. Plus, policymakers can use this methodology to create regulations for their rural areas.

The remaining parts are organized as follows: The following section gives the existing literature about HoQ and the building design area. Moreover, the same section provides a detected customer needs (CNs) and design requirements (DRs) for sustainable farm building design. Section III presents the preliminaries about the recommended methodology. Section IV gives the case study, and the results and analysis are presented followingly. Finally, in Section VI, the concluding remarques are provided.

II. LITERATURE REVIEW

This section gives the theoretical background about building design and QFD and the suggested 2-tuple HoQ framework components.

A. Building Design and QFD

Shigeru Mizuno and Yoji Akao first introduced QFD at the end of the ’60s. Concerning transferring customer expectations, QFD is a robust approach with suitable applications[2]. Various studies discussed QFD and its applications in different areas. The main idea of the QFD approach is how to balance CNs. Prearranging CN is the leading and first step for QFD. In this paper, it is recommended to use for the design of a sustainable farm building. For this purpose, detailed research about sustainable building requirements and their design requirements is done.

In the literature, Uztürk et al. suggested a fuzzy linguistic-based approach for a hospital building design [24]. The healthcare sector is the one sector that a QFD model is suggested for the building design [8, 25]. Other studies commonly focus on building envelop design [21–23] or building design management [19, 26, 27] with QFD methodology.

As seen from the existing literature, the QFD and its HoQ are potent tools to handle building design decisions. Moreover, its extension with the fuzzy linguistic creates more accurate and unbiased findings for the designers and construction teams. So, by generating robust CNs and DRs, the recommended model may be convenient for the building designers and construction firms. The detected customer expectations and the technical requirements for a sustainable farm building will be given in the next section.

B. Sustainable Farm Building Design

Sustainable construction and design facilitate adaptable solutions with nature rather than producing solutions against it. In the long term, it also helps for energy-saving and cost-saving for farming activities [14]. The construction phase and the design phase are both proposing solutions for sustainable building. Among them, the design phase has a more critical role in the life cycle of the building [3, 21]. The initial decisions in the designing phase have an immense effect on the long-term of the construction site and the building’s land use.

Consequently, a better analysis of the desired sustainability issues should be addressed in the design phase. Considering the value of the design components, in this paper, two groups of requirements are generated from a comprehensive academic literature review.

The first group covers the CNs in the HoQ, and the second one contains the DRs to reach the CNs. The CNs are assigned as the sustainability requirements that a farm building has for its future life. Table 1 and Table 2 present the detected CNs and the DRs for a sustainable farm building design.

Table 1. CNs for the farm building design [3–5, 10, 11].

CN#	CNs
CN1	Flexible interiors
CN2	Quick construction
CN3	Low cost
CN4	Less site preparation
CN5	Durability
CN6	Natural Ventilation
CN7	Natural Lighting
CN8	Less resource usage
CN9	Accessibility
CN10	Adaptability to the field

These ten requirements form the basis of sustainable design. According to these dimensions, technical requirements for a building will be evaluated. Their relations will be studied thanks to the HoQ technique, and the 2-Tuple linguistic model will help to better analyze the relations with linguistic variables.

As aforementioned, the GDM approach will be used to obtain an objective weighting of dimensions and relations. Forming a group will help to simulate a project group for the construction projects.

Table 2. DRs for sustainable farm building [5, 10, 14, 18, 29].

DR#	DRs
DR1	Sensor utilization
DR2	Types, sizes, and shapes of openings
DR3	Fixed light windows for skylights
DR4	Flexible building envelop design
DR5	Non-toxic, low VOC glues and paints
DR6	Rainwater storage
DR7	Local material use for construction
DR8	Recycled material use
DR9	Life-cycle cost analysis before the construction
DR10	Innovative architecture
DR11	Heat emitting windows
DR12	Proper building operations and maintenance

As Table 2 states, twelve technical attributes are derived from the literature. The main aim is to prioritize them according to the CNs. As a result, their prioritization will be obtained, and the results will serve the practitioners as a roadmap for their construction projects.

The following section will present the preliminaries for the suggested methodology and the detailed steps of the framework.

III. METHODOLOGY

As aforementioned, the selected primary tool for a farm building design is HoQ. This section will give the details of the HoQ technique and the 2-tuple linguistic model.

A. 2-Tuple Linguistic Model

Herrera and Martinez first represent this model in 2000 [15]. The 2-tuple linguistic model and its extensions have been applied to various

topics, mainly decision-making and decision analysis problems [15, 17, 20]. Basic definitions are as follows [15]:

The 2-Tuple fuzzy linguistic representation model represents the linguistic information using a 2-Tuple (*S, α)* here; *S* is a linguistic label, and α is a numerical value representing the value of the symbolic translation. The function is defined as:

$$\Delta_s : [0, g] \to \bar{S}$$
$$\Delta_s(b) = (S_i, a), with \begin{cases} i = round(b) \\ a = b - i \end{cases} \quad (1)$$

The linguistic term set *S* could be converted into 2-Tuple form by adding zero value as in the following relation:

$$S_i \in S \Rightarrow (S_i, 0) \quad (2)$$

For further details, the readers can refer to [15]. The main benefits of the 2-tuple linguistic model are the augmented accuracy and interpretability of the results and the possibility to deal with variables closer to the human beings' cognitive processes. Regarding these benefits, to create a flexible environment for the DMs and better analysis and knowledge about the sustainable building design area, the suggested 2-Tuple methodology is integrated with the HoQ technique.

B. Aggregation Technique for GDM

The main benefit of the GDM approach is to create an unbiased, objective decision-making environment where the final solution is beneficial to each DM. The GDM approach is based on the aggregation of different opinions from multiple DMs [7]. GDM is a commonly adopted method preferred over a single DM due to its superiority in avoiding partiality and bias [6, 12].

Regarding all the benefits mentioned above, the 2-tuple linguistic model's *Linguistic Hierarchies (LH)* approach is selected as an aggregation technique for this GDM methodology. The methodology is based on the experts' knowledge; however, the level of experience and expertise may differ concerning the interest of DMs. So, providing different granulated linguistic evaluation sets to each DM may be a powerful solution to balance the knowledge difference rising from diverse backgrounds.

LH [15] approach is used to unify the multigranular linguistic input under the one unified linguistic set. A transformation equation exists to normalize label sets with different granularity. The following equation gives the relations:

$$TF_{t'}^{t}(S_i^{n(t)}, a^{n(t)}) = \Delta\left(\frac{\Delta^{-1}(S_i^{n(t)}, a^{n(t)}) \cdot (n(t') - 1)}{n(t) - 1}\right) \quad (5)$$

where *TF* is the transformation function for *LH*, and the transformation is from t^{th} level to t'^{th} level.

Furthermore, for aggregating normalized linguistic variables *Weighted Aggregation Operator (WAO)* of 2-Tuple model is recommended as well. The following equation gives the formulation:

$$\vec{x} = \left(\frac{\sum_{i=1}^{n} \Delta^{-1}(e_i, \alpha_i) \times \Delta^{-1}(w_i, \alpha_i)}{\sum_{i=1}^{n} \Delta^{-1}(w_i, \alpha_i)}\right) = \Delta\left(\frac{\sum_{i=1}^{n} \beta_i \times w_i}{\sum_{i=0}^{n} w_i}\right) \quad (6)$$

where, (e_i, α_i) is the assessments provided by each expert; (w_i, α_i) stands for the weights of experts and n represents the number of experts and β_i is the β values for ith criterion's importance.

C. 2-Tuple HoQ Framework for Sustainable Farm Building Design

The computational steps of 2-Tuple QFD are as follows [9, 16, 28]:

1. Assigning an objective of the study. Then defining a problem related to it. Afterward, detect requirements for this objective and form a decision-making group to solve the problem.
2. Selecting a linguistic comparison scale for each DM to represent their own opinion about the problem assigned. Different scales could be chosen according to the experience of experts in the case study. Tables 3 and 4 show the different scales for experts.

Table 3. Label Set for DMs [15]

Label Set for five scale	Abbreviation	S_i^5
VL	VL	S_0^5
Low	L	S_1^5
Medium	M	S_2^5
High	H	S_3^5
Perfect	P	S_4^5

Table 4. Label set for DMs

Label Set for nine scale	Abbreviation	S_i^9
Very Low	VL	S_0^9
Almost Low	AL	S_1^9
Low	L	S_2^9
Almost Medium	AM	S_3^9
Medium	M	S_4^9
Almost High	AH	S_5^9
High	H	S_6^9
Very High	VH	S_7^9
Perfect	P	S_8^9

3. Detecting the CNs about the problem and taking their related importance from the DM group. The importance taken from the DM group is in a Label Set form.
   - 3.1. Normalizing the multi-granulated assessments under the highest granularity (S_i^9) by Eq. (5).
   - 3.2. Aggregating DMs normalized assessments with Eq. (6).
4. Detecting DRs for QFD according to the CNs.
   At this step, DRs need to be well evaluated according to CNs to get logical relations between them during the relation matrix construction.
5. Constructing the relation matrix for HoQ to determine pairwise relations between CNs and DRs.
   This step is to determine the level of relations between CNs and DRs. The DMs can perform their evaluations again in the label set form, and the same steps as 3.1 and 3.2 are to follow to aggregate the DMs assessments.
6. Calculating the importance of DRs and ranking them in decreasing order.

Figure 1 represents the HoQ components and structure, and followingly, Figure 2 summarizes the suggested framework's steps.

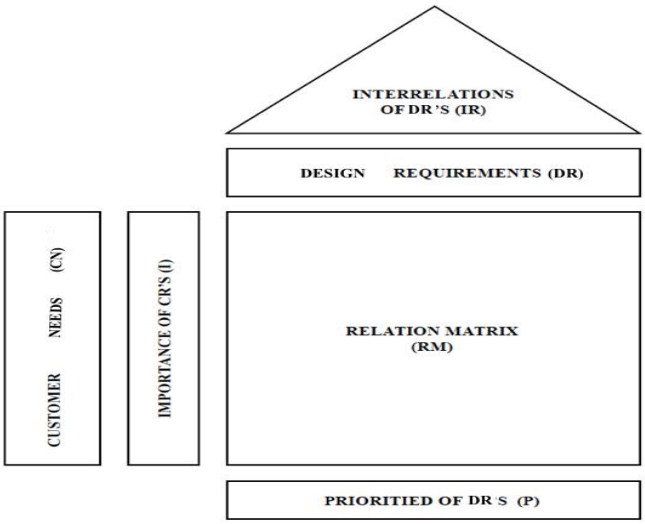

Figure 1. The HoQ structures[2].

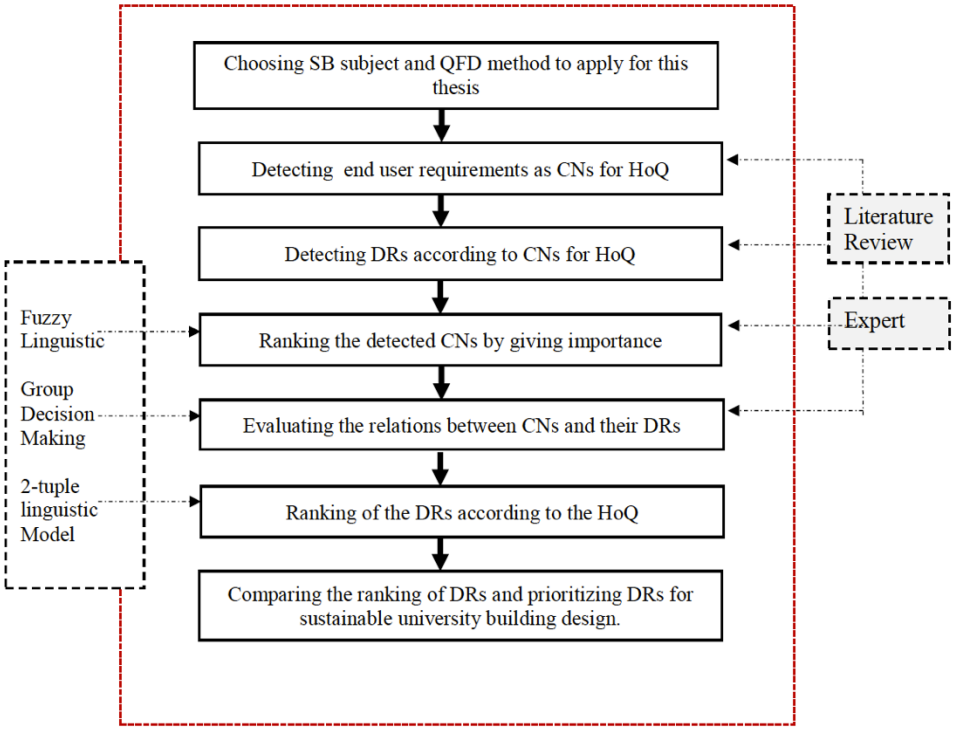

Figure 2. Summary of the suggested methodology

IV. CASE STUDY

In this section, a case study from Turkey is presented to test the plausibility of the recommended methodology.

An organic farm closer to Istanbul city is chosen as a case study. The selected farm also provides accommodation to its visitors in sustainable buildings. So, the farm's strategy is familiar with sustainability and sustainable design. Besides its accommodation areas, the farm also continues to produce organic food in the rural regions of Kandıra. They plan to design a farming building closer to their greenhouses and the production field. Therefore, we have proposed our methodology as guidance for their farm building project.

Consequently, a decision-making group is formed from two owners/managers of the farm and one academician. Two DMs from the farm had different experiences about the sustainable building and design area so that S_i^5 and S_i^9 are provided to them. The academician also made her assessments with S_i^9 label set.

As stated in Section III, Step 4, the DMs are asked to evaluate CNs (Table 1) separately. Here Table 5 gives the individual assessments of each DM and their aggregated importance.

Table 5. DMs assessments and the aggregated importance of CNs

DM1	DM2	DM3	Aggregated	Beta values
M	AH	P	(H,-0.04)	5.96
H	AM	M	(M,0.04)	4.04
M	H	P	(H,0.35)	6.35
P	VH	AH	(H,-0.43)	6.43
P	P	P	(P,0)	8.00
P	P	P	(P,0)	8.00
P	VH	P	(P,-0.39)	7.61
H	H	H	(H,0)	6.00
M	AM	AM	(M,-0.39)	3.61
H	AH	P	(H,0.39)	6.39

As stated in Section III.C, Step 5, the relation matrix is constructed to investigate the relations between the CNs and DRs. The following Table 6 gives the aggregated ultimate relation matrix for the case study.

During the formation of aggregated relation matrix, each DMs' assessments were collected separately. The normalization and the aggregation steps in Section III are followed, and finally, the relation matrix is obtained. Afterward, using the CNs importance, prioritization for the DRs is obtained.

The details of the obtained results and the sensitivity analysis will be given in the next section.

V. RESULTS AND ANALYSIS

The obtained beta values for each DR are given in Figure 3. By using Eq. (1), the beta values can be presented in linguistic label set form.

When the DRs are ranked according to their final beta values, the most critical five technical requirements are detected as:

1. Innovative architecture
2. Local material use for construction
3. Flexible building envelop design

Table 6. Final aggregated relation matrix.

			DR1	DR2	DR3	DR4	DR5	DR6	DR7	DR8	DR9	DR10	DR11	DR12
	DRs / CNs	CNs Importan	Sensor utilization	Types, sizes and shapes of openings	Fixed high windows for skylights	Flexible building envelop design	Non-toxic low VOC glues and paints	Rainwater storage	Local material use for construction	Recyled material use	Life-cycle cost analysis before the construction	Innovative architecture	Heat emitting windows	Proper building operations and maintenance
CN1	Flexible interiors	(H,-0.04)		(AM,0.22)		(P,0)		(M,-0.43)	2.78		(AM,-0.22)	(AH,-0.22)		(AH,-0.22)
CN2	Quick construction	(M,0.04)		(H,0)		(M,0)			(P,0)		(L,0)	(M,0)		(AH,-0.22)
CN3	Low cost	(H,0.35)	(L,0)		(AL,0.22)	(AL,0.22)		(AH,-0.22)	(H,0)	(P,0)	(VH,0.22)		(H,0)	(L,0.29)
CN4	Less site preperation	(H,-0.43)							(H,0.39)			(P,0)		(L,0.29)
CN5	Durability	(P,0)		(L,0)		(AH,0.22)	(AH,0.22)		(H,0.39)		(P,0)	(L,0)		(VH,-0.22)
CN6	Natural Ventilation	(P,0)	(M,0)	(VH,0.17)		(M,0)						(VH,-0.22)	(AH,-0.22)	
CN7	Natural Lighting	(P,-0.39)	(H,0)	(VH,0.17)	(P,0)	(AH,-0.22)						(VH,-0.22)		
CN8	Less resourse usage	(H,0)	(M,0)					(P,0)	(VH,0.17)	(VH,0.22)				(AH,-0.22)
CN9	Accessibility	(M,-0.39)									(L,0)	(M,0)		
CN10	Adaptability to the field	(H,0.39)				(AH,-0.22)	(AH,-0.22)					(M,0.39)		(L,-0.39)

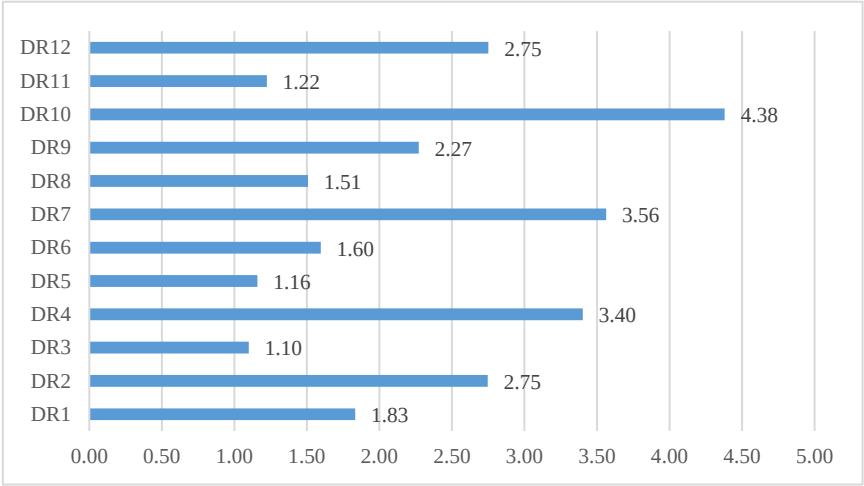

Figure 3. Obtained beta values for the final ranking of DRs.

4. Types, sizes, and shapes of openings
4. Proper building operations and maintenance
5. Fixed light windows for skylights

The ranking of DRs proposes a roadmap to follow to reach a sustainable farm building. By changing the CNs importance, each project can have its road for designing with their preferences. Accordingly, testing the robustness and the replicability of the model is essential. For that purpose, a sensitivity analysis is conducted. Figure 4 gives the results of the sensitivity analysis.

Ten different scenarios are created; each scenario emphasizes one CN. Ten different rankings are obtained, and the values show that the suggested model ranks the DRs according to CN weights.

The same sensitivity analysis also enables us to investigate DR-CN relations more carefully. The changing ranking of DR shows us which CN has a significant impact on which technical attributes. Accordingly, by analyzing these differences more comprehensive understanding of the sustainable farm building design can be obtained.

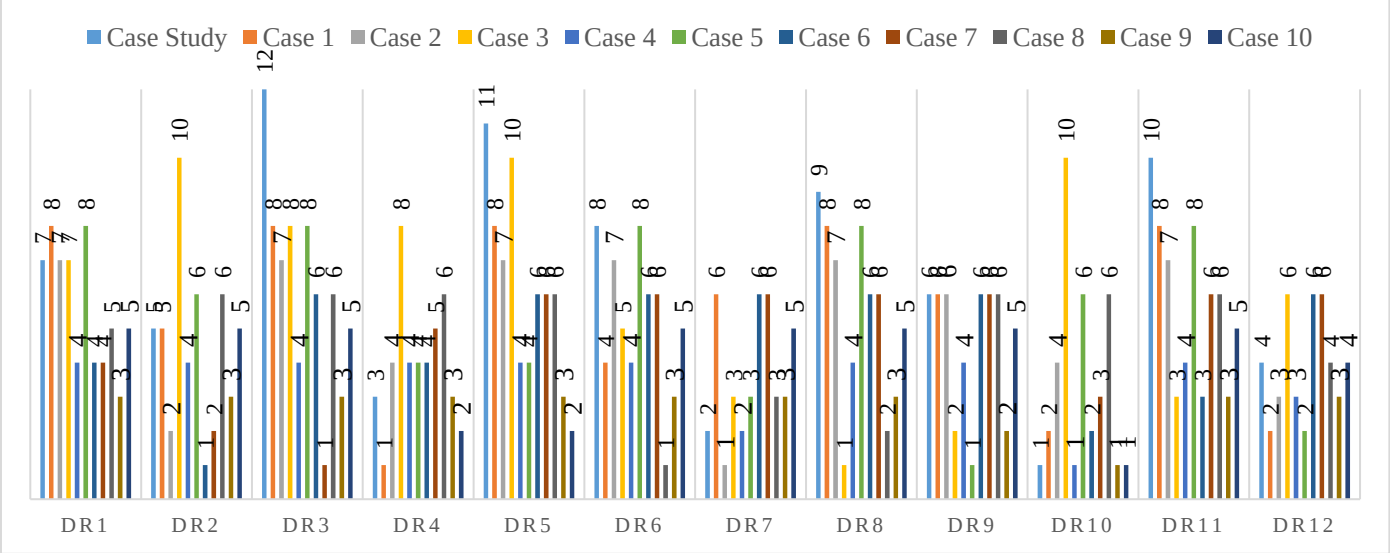

Figure 4. Sensitivity analysis

VI. CONCLUSIONS

Nowadays, where sustainability is a critical issue for creating more durable and flexible systems, this paper proposes a valuable framework for sustainable agriculture. Transition to sustainable agriculture is a process which is needed to be designed carefully. One of the agricultural system components is the farm buildings that are located in the farming fields. So, to reach a sustainable agricultural system, whole system components should design concerning the sustainability issues. Consequently, a comprehensive design approach is needed for environmentally friendly agriculture fields.

The well-known design tool, HoQ, is suggested for designing sustainable farm buildings. Moreover, the HoQ technique is extended with the 2-tuple linguistic model to create a model that can operate with the linguistic information. To test the applicability of the recommended framework, a real case study from Turkey is presented. The results from the case study showed that the innovative architecture, local material usage, and the envelop design are the primary first three steps to follow for a sustainable farm building.

This paper aims to present guidance for practitioners and construction companies to follow during their projects. The methodology is adaptable for different cases; by changing the CNs' weights, each project can obtain its roadmap for its projects.

As a limitation, the number of DMs can be stated. In this paper, the recommended methodology is tested with three DMs; however, the framework can work with DMs up to higher numbers.

Furthermore, for future studies, the same methodology can be followed for other industries as well. The same methodology can serve as valuable guidance for strategy and solution detection for various sectors by improving the CNs according to the sectors.

VII. ACKNOWLEDGMENTS

Our thanks to experts for their valuable assessments and guidance for the design model. This work has been supported by the Scientific Research Projects Commission of Galatasaray University (Project Number: 19.102.002).

VIII. REFERENCES

[1] Abdellatif, M. and Al-Shamma'a, A. 2015. Review of sustainability in buildings. *Sustainable Cities and Society*. 14, 1 (2015), 171–177.
[2] Akao, Y. 2004. *Quality Function Deployment*. Productivity Press.
[3] Alibrandi, U. et al. 2015. *The Method of the Independent Components for Sustainable Building Design*. Ieee.
[4] Arroyo, P. et al. 2016. Collaborating in decision making of sustainable building design: An experimental study comparing CBA and WRC methods. *Energy and Buildings*. 128, (Sep. 2016), 132–142.
[5] Awadh, O. 2017. Sustainability and green building rating systems: LEED, BREEAM, GSAS, and Estidama critical analysis. *Journal of Building Engineering*. 11, (May 2017), 25–29.
[6] Büyüközkan, G. and Feyzioğlu, O. 2005. Group decision making to better respond customer needs in software development. *Computers & Industrial Engineering*. 48, 2 (2005), 427–441.

[7] Buyukozkan, G. and Guleryuz, S. 2015. Extending Fuzzy QFD Methodology with GDM Approaches: An Application for. *International Journal of Fuzzy Systems*. 17, 4 (Dec. 2015), 544–558.
[8] Dehe, B. and Bamford, D. 2017. Quality Function Deployment and operational design decisions - a healthcare infrastructure development case study. *Production Planning & Control*. 28, 14 (2017), 1177–1192.
[9] Dursun, M. and Karsak, E.E. 2012. Supplier Selection Using an Integrated Decision Making Approach Based on QFD and 2-Tuple Fuzzy Representation. *World Congress on Engineering and Computer Science, Wcecs 2012, Vol Ii*. Int Assoc Engineers-Iaeng. 1309–1315.
[10] Gillis, W. 2013. Understanding the Design Impacts Among LEED Certification - Technische Informationsbibliothek (TIB). (2013).
[11] Gillis, W.L. and Cudney, E.A. 2014. A New Methodology for Eco-friendly Construction: Utilizing Quality Function Deployment to Meet LEED Requirements. *Eco-Innovation and the Development of Business Models: Lessons from Experience and New Frontiers in Theory and Practice*. S.G. Azevedo et al., eds. Springer International Publishing. 245–273.
[12] Herrera, F. et al. 2001. Multiperson decision-making based on multiplicative preference relations. *European Journal of Operational Research*. 129, 2 (Mar. 2001), 372–385.
[13] Kang, H.J. 2015. Development of a systematic model for an assessment tool for sustainable buildings based on a structural framework. *Energy and Buildings*. 104, (Oct. 2015), 287–301. DOI
[14] Kim, J. 2020. Green building strategies for LEED-certified laboratory buildings: Comparison between gold and platinum levels. *International Journal of Sustainable Building Technology and Urban Development*. 11, 3 (2020), 153–173.
[15] Martínez, L. et al. 2015. *The 2-tuple Linguistic Model*. Springer International Publishing.
[16] Mei, Y. et al. 2018. A Multi-Granularity 2-Tuple QFD Method and Application to Emergency Routes Evaluation. *Symmetry-Basel*. 10, 10 (Oct. 2018), 484.
[17] Mi, C. et al. 2018. Product redesign evaluation: An improved quality function deployment model based on failure modes and effects analysis and 2-tuple linguistic. *Advances in Mechanical Engineering*. 10, 11 (Nov. 2018), 1687814018811227.
[18] Obata, S.H. et al. 2019. LEED certification as booster for sustainable buildings: Insights for a Brazilian context. *Resources, Conservation and Recycling*. 145, (2019), 170–178.
[19] She, Y. 2009. The Application of Fuzzy Comprehensive Evaluation to Quantify Design Space. *2009 WRI World Congress on Software Engineering* (May 2009), 499–503.
[20] Singh, A. and Gupta, A. 2020. Best criteria selection based PROMETHEE II to aid decision-making under 2-tuple linguistic framework: Case-study of the most energy efficient region worldwide. *International Journal of Management and Decision Making*. 19, 1 (2020), 44–65.
[21] Singhaputtangkul, N. 2017. A decision support tool to mitigate decision-making problems faced by a building design team. *Smart and Sustainable Built Environment*. 6, 1 (2017), 2–18.
[22] Singhaputtangkul, N. et al. 2013. Knowledge-based Decision Support System Quality Function Deployment (KBDSS-QFD) tool for assessment of building envelopes. *Automation in Construction*. 35, (Nov. 2013), 314–328.
[23] Singhaputtangkul, N. and Low, S.P. 2015. Modeling a Decision Support Tool for Buildable and Sustainable Building Envelope Designs. *Buildings*. 5, 2 (Jun. 2015), 521–535.
[24] Uztürk, D. et al. 2020. Fuzzy linguistic integrated methodology for sustainable hospital building design. *Advances in Intelligent Systems and Computing*. 1029, (2020), 1180–1188.
[25] Uztürk, D. and Büyüközkan, G. 2018. Stakeholder Preference Based 2-Tuple Integrated Method for Sustainable Hospital Design. (2018), 6.
[26] Van Luu, T. et al. 2009. Quality improvement of apartment projects using fuzzy-QFD approach: A case study in Vietnam. *KSCE Journal of Civil Engineering*. 13, 5 (Sep. 2009), 305–315.
[27] Yang, Y.Q. et al. 2003. A fuzzy quality function deployment system for buildable design decision-makings. *Automation in Construction*. 12, 4 (Jul. 2003), 381–393.
[28] Zhang, X. and Su, J. 2018. An integrated QFD and 2-tuple linguistic method for solution selection in crowdsourcing contests for innovative tasks. *Journal of Intelligent & Fuzzy Systems*. 35, 6 (2018), 6329–6342.
[29] 2018. BREEAM UK New Construction 2018. 3 (2018), 403.
[30] Building Sustainable Farms, Ranches and Communities. *SARE*.

'Impact of window wall ratio in office building envelopes on operational energy consumption in the temperate climatic zone of India'

Deepali Sahu
Centre of Sustainable Built Environment
Manipal School of Architecture and Planning,MAHE
Manipal,Karnataka,India
deepali.sahu732@gmail.com

Pradeep Kini*
Centre of Sustainable Built Environment
Manipal School of Architecture and Planning,MAHE
Manipal,Karnataka,India
Pradeep.kini@manipal.edu

Pranav Kishore
Centre of Sustainable Built Environment
Manipal School of Architecture and Planning,MAHE
Manipal,Karnataka,India
pranav.kishore@manipal.edu

Anir Upadhyay
School of Built Environment
UNSW
Australia
anir. upadhyay@unsw.edu.au

Kiran Kamath
Dept of Civil Engineering
Manipal Institute of Technology,MAHE
Manipal,Karnataka,India
Kiran.kamath@manipal.edu

Abstract

The construction of predominantly glazed facades in commercial buildings has become a standard practice in India irrespective of the climate and in particularly in cities such as Bangalore, an Indian IT hub with temperate climate. In recent decades, urbanisation has been rapid and fully glazed buildings have increased, resulting in high energy consumption and demand. The development and implementation of energy efficiency codes and initiatives can help ensure a sustainable future. Window wall ratio is one of the key parameters and if designed properly, could have a substantial impact on the overall energy consumption of a building. In order to understand the impact of solar radiation and daylight entering through the building envelope, a reference high rise office building with an operation period of 24 hours was simulated and after optimization of WWR with daylight utilization, the average EPI of 350 kWh/m2/yr. (BEEP India 2013) improved to 306 kWh/m2/yr. The building envelope is evaluated with reference to different WWR and orientation (North, South, East and West). The optimum WWR was selected on the basis of the lowest energy consumption while at the same time achieving the lighting threshold as specified in the ECBC. The building has been modelled and analysed using Energy Plus and COMFEN.

Keywords*: *Optimum WWR, orientation, EPI, daylight utilization, Annual energy consumption, office building

I. INTRODUCTION

The Fast-increasing world energy consumption levels have already raised concerns over the excessive usage of resources and subsequent environmental impacts. According to WEO (2009), energy is accounting for 65% of the World's Greenhouse gas (GHG) emissions. Being a developing country, power consumption has been increasing at greater pace in India. (Nagaraju Kaja,2015). Unfortunately, the current building stock is oriented towards high energy consumption (Hirst, 2013) and the commercial sector has become the fastest growing energy demand sector globally (EIA, 2016). The commercial sector accounts for 8.6% of total electricity consumption of India and increasing with 5% rate annually due to rapid urbanization. The building's major energy consuming end-uses are air-conditioning including heating, cooling, lighting, and equipment during the operational phase (Bhatnagar et al, 2019). The average annual electricity consumption for space conditioning and lighting in India is around 160 KWh/m2 for commercial (Nagaraju Kaja,2015). In a typical commercial office building, the major share of energy is from Cooling-25%, Equipment 28%, Lighting 30%.(Central Electric Authority). Energy savings in the building sector are critical for the achievement of sustainable development. Current trends of energy use indicate that buildings' energy demands and related emissions will continue to increase.

However, buildings offer great opportunities to reduce growth in energy demand in terms of design and architects have a great role to play in it. The energy conscious design approach helps designers and building owners to economically reduce building operating costs, while improving comfort for the building's occupants. The energy consumed by a building depends on its use (whether residential, commercial or industrial), the type of building (air-conditioned or naturally ventilated and the climate classification. Architects have to ensure that the design of the built form suits the intended use of the building and the specific needs of the user within the framework of the prevailing climatic conditions.

The construction of predominantly glazed facades in commercial building has become a standard practice in India irrespective of the climate which has led to high energy consumption in such buildings. The glazed components of the building allow heat and solar gain which primarily determines the operational energy requirement of buildings.

Especially in cities like Bangalore, an IT hub of India which has a temperate climate. It has seen rapid urbanization in the past few decades and rise in fully glazed buildings without any consideration for energy efficiency which has resulted in high energy demand and consumption. Heat loss or gain through the

IEECP'21, July 29-30, 2021, Silicon Valley, San Francisco, CA – USA

DAI : ***https://sci-index.com/DAI/2021.99101/IEECP/14899533***

building envelope and solar gain should be considered together with internal energy demands in assessing the energy performance of glazed building components (Grynning, 2013).

Optimizing the glazing system considering area, thermal performance, and localization of glazed building components in a building envelope are ways to reduce energy consumption in buildings (Grynning, 2013). Window wall ratio restricted up to 40% in Energy Conservation Building Code (ECBC) is one of the key parameters, if designed properly, could have a substantial impact on the overall energy consumption of a building. Hence, the analysis and optimization of WWR is an important way to achieve efficiency in the energy performance of a building. But there is an apparent lack of understanding amongst practitioners of what might be considered appropriate in the temperate climatic context of Bangalore.

II. BACKGROUND STUDY

A. WWR- Window to Wall ratio

The window-to-wall ratio is the measure of the percentage area determined by dividing the building's total glazed area by its exterior envelope area. Window-to-wall ratio (WWR) is an important variable affecting energy performance in a building and determining thermal and visual comfort indoors. Window area will have impacts on the building's heating, cooling, and lighting, as well as the indoor environment in terms of access to daylight, ventilation, comfort and views. The Window Wall Ratio is restricted up to 40% in ECBC.

B. Daylighting

Daylight has qualities that cannot be replicated by artificial lighting. The design of a window and choice of glazing can dramatically affect the quantity and quality of daylight in a space and how it is experienced. Daylight design is far more sophisticated than simply providing a window with a high enough visible transmittance. More daylight does not necessarily equate to better lighting conditions. It is a matter of balancing daylight admission with glare control, as well as providing uniform light distribution.

The usability of daylight is dependent on the task. For some tasks, bright illumination improves visual acuity and glare is of little concern. For computer tasks, glare may be problematic and it is better to control illuminance levels. The average annual daylight illuminance is linearly related to the product of the window-to-wall ratio and visible transmittance (VT*WWR).

The Useful Daylight Illuminance (UDI) is a holistic analysis method measuring the useful daylight as well as glare on the work plane.

The ECBC defines UDI between 300 to 500 Lux as useful daylight. We are considering 500 lux as the threshold daylight level on the work plane in an office space for this study.

C. EPI-Energy Performance Index

Energy performance index (EPI) is total energy consumed in a building over a year divided by total built up area in kWh/sq.m./year or MJ/sq.m./year **(where 1kWh= 3.6MJ)** and is considered as the simplest and most relevant indicator for qualifying a building as energy efficient or not. Most commercial buildings in India have EPI between 200-400kWh/m2/year. Energy conscious buildings in India have achieved EPIs of 100-150kWh/m2/year. The national benchmark is 180kWh/ m2/year. Buildings with EPI of 180kWh/m2/year are ECBC compliant.

In order to understand the impact of solar heat and daylight entering through the façade of a reference high rise office building with an operation period of 24 hours and an average EPI index of 350 kWh/m2/yr (approx.) as mentioned in Table 1.

Table 1. Averages Annual Energy Consumption for different office building typologies (Source: Building Energy Benchmarking study undertaken by the USAID ECO-II Project)

No. of Buildings	Building Type	Floor Area (sq.m.)	Annual Energy Consumption (kWh)	Benchmarking Indices	
				kWh/sq.m./year	kWh/sq,m,/hour
145	One shift Building	16,716	20,92,364	149	0.068
55	**Three shifts Building**	**31,226**	**88,82,824**	**349**	**0.042**
88	Public Sector Buildings	15,799	18,38,331	115	0.045
224	Private Sector Buildings	28,335	44,98,942	258	0.064
10	Green Buildings	8,382	15,89,508	141	-

D. Research gap

Previous research has clearly established the role and benefits of building envelope optimization on the overall energy performance of the building. But there is lack of understanding of daylight integration to reduce artificial lighting energy consumption in an office building. This research paper fills that gap as it aims to determine an optimum WWR for different orientation of a building whilst achieving a threshold lighting level and studying the impact on the building's energy performance.

III. AIM

The main aim of the paper is to determine an optimum WWR for each orientation of a building situated in Bangalore, which lies in temperate climatic zone to reduce the overall energy consumption whilst achieving a threshold lighting level as mentioned in ECBC.

IV. OBJECTIVE

In order to meet the aim, the study focuses on the following objectives:

1. To understand the importance of energy efficiency in the current commercial building sector in India.
2. Optimization of WWR of the glazing systems taking daylight utilization into consideration in different orientation using simulation tools- Modelling, input data, shoebox analysis
3. To study and analyze the results of the simulation and formulate solutions for future reference.

V. SCOPE & LIMITATION

The study of daylight use was one of the main objectives of this work and shading devices were not considered. Additional optimization of features for each orientation will require more study, with shading included. This methodology could be

followed during the initial stages of designing to determine fenestration levels which would lead to a building with better energy performance.

VI. METHODOLOGY & RESEARCH DESIGN

In order to understand the impact of solar heat and daylight entering through the façade of a reference high rise office building with an operation period of 24 hours and an average EPI of 350 kWh/m2/yr. (acc. to BEEP India 2013), the building fenestration is assessed with reference to different WWR and orientation. The optimum WWR was selected on the basis of least energy consumption whilst achieving a threshold lighting level as mentioned in ECBC. The building has been modelled and analysed using Design Builder, Energy Plus and COMFEN.

A. To understand the importance of energy efficiency in the current commercial building sector.

A detailed literature study of the current trends in commercial building design and its impact on the energy performance of the building was conducted. A major issue identified was increased levels of energy consumption due to lack of attention paid to climatic responsive design instead following international trends of extensively glazed facades. Through the literature study, the relation between specific components of building envelope and their impact on the overall energy consumption.

Optimization of WWR of the glazing systems in different orientation using simulation tools- Modelling, input data, shoebox analysis.

A baseline building as mentioned above was modelled using Design Builder. COMFEN (COMmercial FENestration), an energy modeling tool developed by LBNL (Lawrence Barkley National Laboratory), for comprehensive analysis of building glazing systems with respect to energy efficiency and comfort was used to achieve the objectives of this study. COMFEN also uses the powerful calculation engine of Energy Plus. A reference building envelope was referred for the baseline building specifications and inputs.

The impact of altering WWR on the energy consumption of a building with daylight utilization was studied for each orientation (north, south, east, west). The energy use intensity (EUI), in MJ/m2-yr for each variant was determined to find the optimum WWR.

Investigation of the optimum WWR with daylight utilization required the use of a dynamic daylight performance metric. For this, DA (Daylight Autonomy) was used to implement daylighting in a building. DA is regarded as a comprehensive parameter since it considers the effects of orientation, climate and fenestration optical properties to describe the daylighting performance of the space. With daylight utilization, identification of optimum WWR for each orientation was based on the lowest energy consumption for the parameters at which the work plane illuminance threshold criteria of 500 lux were met by daylight alone for 50% of the occupancy time during the year. Annual energy consumption and daylight availability at the work plane were calculated.

COMFEN -Input data

The input data was derived from the reference building modelled in previous research where they studied around 200 office buildings. According to ASHRAE 2010 the perimeter and interior zones need to be separated for energy modelling. So, a reference room which is 4m wide, 3.05m high (floor to ceiling height) with a perimeter zonal depth of 4.57m (thermal and daylight lighting zone depth as per ASHRAE standard 90.1 and International Energy Conservation Code (IECC).It was assumed that the reference office room forms part of a perimeter zone of an office building (as per the reference building zoning). The base case glazing was double glazed, clear glass (DGI). It was assumed that there was no shading from additional shading devices or any surrounding buildings.

Input data required in this study for an office building/reference room including thermostat set points, schedules (occupancy, lighting, equipment), and outdoor air flow rate were set according to the default values of COMFEN. The loads for each schedule were set according to reference building specifications. Work place density, miscellaneous equipment power and artificial Lighting Power Density (LPD) for an office building were specified as 14 m2 / person, 16.14 W/m2 and 8.32 W/m2 respectively. The illumination level of 500 lux was specified at the work plane height during office hours as recommended by ASHRAE standards and IESNA (Illuminating Engineering Society of North America). Daylight control logic is embedded in the software COMFEN. Continuous lighting controls were modeled in this study as providing continuous dimming control based on daylight levels to maintain constant, undisturbed, fluorescent light levels during office hours.

Since a building can have maximum glazing of about 40%, the WWRs considered for simulation are 10%, 15%, 20%, 25%, 30%, 35%, 40% (Fig.1) respectively for each orientation (North, South, East, West) considering the building is perfectly aligned in the N-S direction. Window position has significant effect on lighting energy demand when there is a daylight control system. Windows positioned in the center of the façade were considered in this study as being most advantageous when daylight controls are to be used (Bokel, 2007). The outdoor climatic data used in this study included monthly average temperatures, horizontal solar radiations, horizontal illuminance were set according to an in-built file in COMFEN with climatic details of the city.

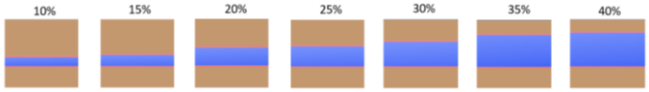

Figure 1. Different WWRs considered for simulation

B. To study and analyze the results of the simulation and formulate solutions for future reference.

Shoebox modelling is a good practice in the energy modelling process, as it helps the architects/engineers to take informed decision on what passive measures to integrate in the building design. In shoebox modelling we plot a graph between the annual energy consumption derived from the simulation and the different WWRs selected for the study and a linear relation between the two variables is established which is then compared and analyzed further to draw conclusions and derive an optimum WWR which is case specific.

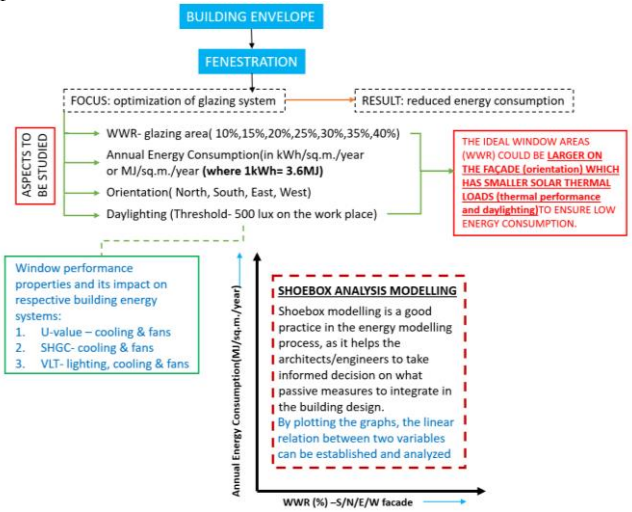

Figure 2. Methodology- Research Design Outline

VII. RESULT & DISCUSSION

It was found from the simulation results that daylight utilization reduced building energy demand significantly by reducing the artificial lighting requirement and also the cooling load associated with artificial lighting. Optimum WWR selection with daylight utilization was based on the lowest energy consumption for the parameters which satisfied the preset threshold criteria of 500 lux provided at the work plane by daylight alone. For this purpose, intermediate WWRs between the two with lowest energy consumption were simulated to investigate the optimum condition for energy demand reduction and find the minimum WWR that provided the required daylighting.

A. North Orientation

It was derived from Figure 3 for North orientation, WWRs between 20% and 25% have to be simulated to find the optimum condition for energy demand reduction in order to find the minimum WWR that provided the required daylighting.

Table 2. Total energy consumption and heat gain for North orientation with daylight utilization

Scenario /Sr. No.	WWR	Average Daylight Illuminance lux	Cooling MJ/m2-yr	Fans MJ/m2-yr	Lighting MJ/m2-yr	Total energy consumption MJ/m2-yr	Window total heat gain MJ/m2-yr
1.	10 %	79.49	347.32	96.45	150.69	594.47	55.43
2.	15 %	131.13	349.89	97.55	132.30	579.75	89.81
3.	**20 %**	**205.15**	**354.44**	**98.70**	**115.02**	**568.17**	**129.12**
4.	**25 %**	**264.98**	**361.84**	**100.56**	**108.67**	**571.07**	**164.45**
5.	30 %	338.36	377.83	110.01	105.33	593.18	201.62
6.	35 %	425.72	388.49	113.21	103.32	605.01	238.96
7.	40 %	492.89	399.13	116.45	102.39	617.97	275.51

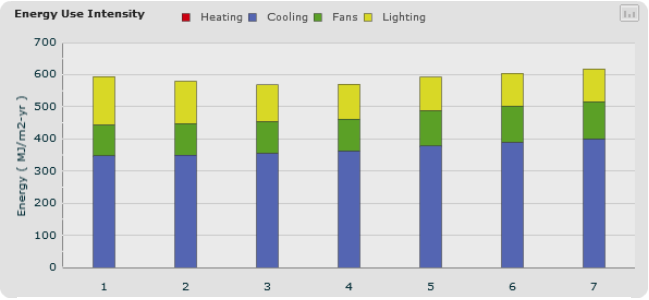

Figure 3. Comparison of energy consumption of different WWRs for North orientation with daylight utilization.

After comparing all the WWRs for daylight availability for north orientation, a WWR of 20% (Table 3) was identified as optimum for north orientation, providing the required threshold daylight illumination levels of 500 lux throughout the working time. As direct sunlight does not strike the north façade at this latitude in the northern hemisphere, higher WWRs on the north orientation were found to provide sufficient daylight levels throughout the occupancy hours with reasonable energy demand. If required, a higher WWR up to 25% could most readily be planned on the north façade due to low solar gains from this direction.

Table 3. Annual average hourly daylight (lux) at different (intermediate) WWRs for North orientation

WWR	Annual average hourly daylight (lux) for five counted hours				
	10:00 am	11.00 am	12:00 pm	1:00 pm	2:00 pm
20%	**469.43**	**542.87**	**562.96**	**591.83**	**537.268**
23%	537.03	593.86	620.71	643.53	676.32
25%	605.51	668.25	697.52	732.51	763.38

B. South Orientation

It was derived from Figure 4 for south orientation, WWRs between 15% and 20% have to be simulated to find the optimum condition for energy demand reduction in order to find the minimum WWR that provided the required daylighting.

Table 4. Total energy consumption and heat gain for South orientation with daylight utilization.

Scenario /Sr. No.	WWR	Average Daylight Illuminance lux	Cooling MJ/m2-yr	Fans MJ/m2-yr	Lighting MJ/m2-yr	Total energy consumption MJ/m2-yr	Window total heat gain MJ/m2-yr
1.	10 %	111.80	356.03	95.08	139.62	590.73	83.44
2.	**15 %**	**184.35**	**364.25**	**95.86**	**122.51**	**582.62**	**137.62**
3.	**20 %**	**288.14**	**376.51**	**96.65**	**109.76**	**582.92**	**201.96**
4.	25 %	372.48	389.92	97.99	106.46	594.37	258.21
5.	30 %	475.94	411.92	106.41	104.36	622.69	317.85
6.	35 %	599.91	427.93	109.02	102.81	639.77	377.68
7.	40 %	695.07	443.09	111.52	102.03	656.65	435.61

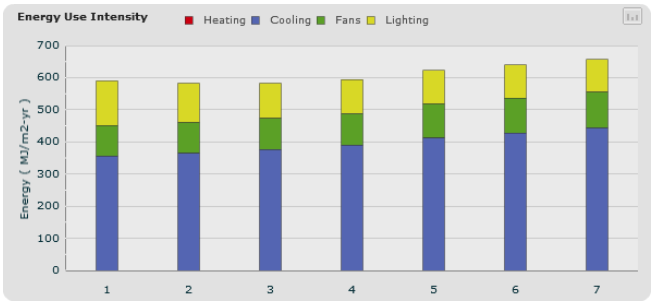

Figure 4. Comparison of energy consumption of different WWRs for South orientation with daylight utilization.

A WWR of 18% (Table 5) was identified as optimum glazing size for south orientation satisfying the pre-set criteria for the working duration with lowest energy consumption of 579.81 MJ/m-yr.

The south orientation was found to be better than north, east and west orientations for useful daylighting as it receives direct sunlight throughout the working time. However, minimum energy demand

was found with a WWR of 18%, allowing natural light to bathe the space for most of the working time without causing glare or overheating.

Table 5. Annual average hourly daylight (lux) at different (intermediate) WWRs for South orientation.

WWR	Annual average hourly daylight (lux) for five counted hours				
	10:00 am	11.00 am	12:00 pm	1:00 pm	2:00 pm
15%	440.16	524.95	568.94	586.09	575.45
18%	**611.15**	**728.13**	**791.20**	**820.33**	**815.48**
20%	678.72	808.01	877.23	909.03	903.64

C. East Orientation

It was derived from Figure 5 that for East orientation, WWRs between 10% and 15% have to be simulated to find the optimum condition for energy demand reduction in order to find the minimum WWR that provided the required daylighting.

Table 6. Total energy consumption and heat gain for East orientation with daylight utilization

Scenario /Sr. No.	WWR	Average Daylight Illuminance lux	Cooling MJ/m2-yr	Fans MJ/m2-yr	Lighting MJ/m2-yr	Total energy consumption MJ/m2-yr	Window total heat gain MJ/m2-yr
1.	**10 %**	**119.51**	**387.91**	**126.85**	**143.53**	**658.29**	**87.49**
2.	**15 %**	**203.90**	**413.80**	**146.68**	**127.67**	**688.15**	**144.45**
3.	20 %	338.57	446.60	171.01	114.52	732.13	212.85
4.	25 %	443.02	477.41	193.68	109.02	780.11	272.54
5.	30 %	561.40	511.20	218.72	105.55	835.47	336.18
6.	35 %	789.80	546.65	245.33	103.25	895.23	400.43
7.	40 %	928.25	580.16	269.95	102.21	952.33	462.42

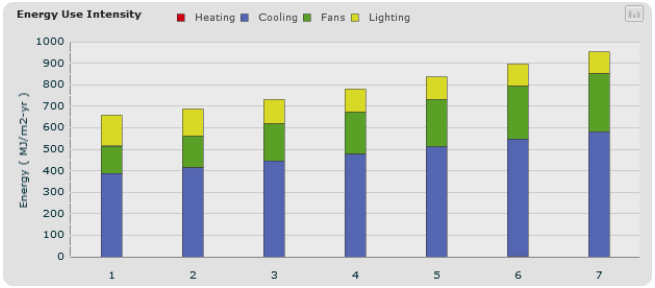

Figure 5. Comparison of energy consumption of different WWRs for East orientation with daylight utilization.

A WWR of 15% (Table 7) was found to be optimum for east orientation, providing the required illumination at the work plane with daylight alone for 55% of the working time. High illumination levels (causing glare or visual discomfort) were observed during morning hours for east orientation due to low solar altitudes.

Table 7. Annual average hourly daylight (lux) at different (intermediate) WWRs for East orientation.

WWR	Annual average hourly daylight (lux) for five counted hours				
	9:00 am	10:00 am	11.00 am	12:00 pm	1:00 pm
10%	469.62	512.33	415.17	288.72	226.36
12%	**568.63**	**622.79**	**505.58**	**351.43**	**275.39**
15%	773.73	842.58	681.93	474.19	371.69

D. West Orientation

It was derived from Figure 6 that for West orientation, WWRs between 10% and 15% have to be simulated to find the optimum condition for energy demand reduction in order to find the minimum WWR that provided the required daylighting.

Table 8. Total energy consumption and heat gain for West orientation with daylight utilization.

Scenario /Sr. No.	WWR	Average Daylight Illuminance lux	Cooling MJ/m2-yr	Fans MJ/m2-yr	Lighting MJ/m2-yr	Total energy consumption MJ/m2-yr	Window total heat gain MJ/m2-yr
1.	**10 %**	**132.26**	**365.72**	**105.40**	**133.82**	**604.93**	**91.59**
2.	**15 %**	**217.09**	**379.17**	**109.51**	**119.38**	**608.06**	**149.05**
3.	20 %	336.79	413.18	132.62	109.32	655.12	214.97
4.	25 %	440.11	442.97	151.93	105.57	700.48	273.95
5.	30 %	623.35	474.81	172.64	103.59	751.04	335.85
6.	35 %	801.90	506.25	193.02	102.37	801.64	397.89
7.	40 %	923.84	537.05	213.47	101.71	852.23	485.90

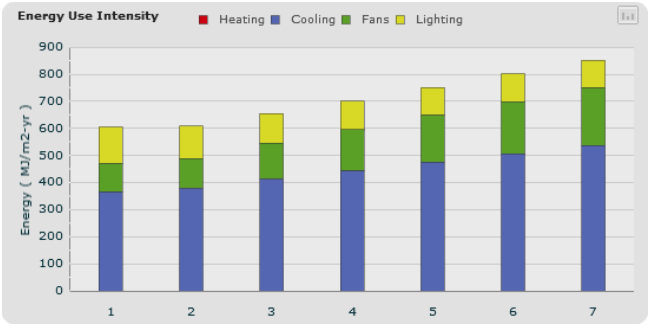

Figure 6. Comparison of energy consumption of different WWRs for West orientation with daylight utilization.

A WWR of 12% (Table 9) was found to be optimum for west orientation, providing the required illumination at the work plane with daylight alone for 55% of the working time. High illumination levels (causing glare or visual discomfort) were observed during evening hours for west orientation due to low solar altitudes.

Table 9. Annual average hourly daylight (lux) at different (intermediate) WWRs for West orientation.

WWR	Annual average hourly daylight (lux) for five counted hours				
	1:00 pm	2:00 pm	3:00 pm	4:00 pm	5:00 pm
10%	260.36	376.72	484.27	491.52	390.49
12%	**316.68**	**457.79**	**587.49**	**594.64**	**470.88**
15%	427.96	621.04	800.09	813.40	729.68

By optimizing WWR for all orientations from the presently traditional (reference building model) 30% WWR, a total of 4% to 19% of the energy could be saved as shown in Table 10. Owing to different solar conditions, the optimal glazing size varies for different orientations in daylight use. With daylight utilization, energy demand is reduced by 19% by use of optimum WWR for east and west, while 6.88% and 4.21% reductions are available from optimum WWRs for south and north orientations, respectively, compared to 30% WWR. For more than 50% of the working time, these optimum WWRs have daylighting levels above 500 lux at desk level.

Table 10: Total reduction in annual energy consumption optimum WWR for East, West, North and South orientation with daylight utilization.

Orientation	Baseline scenario		Optimized scenario		Reductions in overall energy requirement %
	WWR	Total energy consumption MJ/m2-yr	WWR	Total energy consumption MJ/m2-yr	
North	30%	593.18	20%	568.17	4.21%
South	30%	622.69	18%	579.81	6.88%
East	30%	835.47	12%	668.68	19.96%
West	30%	751.04	12%	604.95	19.45%

VIII. CONCLUSION

This study illustrated that by using optimized WWRs, substantial energy savings in glazed commercial buildings are possible in cooling dominant climates. By optimizing WWR for all orientations from the presently traditional (reference building model) 30% WWR, a total of 4% to 19% of the energy could be saved as shown in Table 10. Owing to different solar conditions, the optimal glazing size varies for different orientations in daylight use. With daylight utilization, energy demand is reduced by 19% by use of optimum WWR for east and west, while 6.88% and 4.21% reductions are available from optimum WWRs for south and north orientations, respectively, compared to 30% WWR. For more than 50% of the working time, these optimum WWRs have daylighting levels above 500 lux at desk level. The results showed that the heat gained through windows is responsible for the excessive energy demand in Bangalore (a cooling dominant region).

Therefore, the control of penetration of solar radiations through windows is essential for saving energy. Daylight use lowered the energy demand for buildings by reducing the energy requirements for artificial lighting and the cooling load associated with artificial lighting. Therefore, a choice needs to be made between taking advantage of natural daylighting by optimal WWR in order to minimize energy demands; hence, decreasing the use of artificial lighting and decreasing WWR to suitable sizes to minimize heat gains via windows.

Buildings with EPI of 180 kWh/m2/year or 648 MJ/sq.m./year are ECBC compliant. The average EPI index of a standard 24 hours operation high rise office building is 350 kWh/m2/yr. which reduced to 306 kWh/m2/yr. after optimization of WWR with daylight utilization..

IX. REFERENCES

[1] Hirst, N. (2013). Buildings and Climate Change. In: R. Yao, ed., *Design and Management of Sustainable Built Environments*, Springer London.

[2] Grynning, S. (2013). Windows and glazing material. In: *Windows in the buildings of tomorrow: energy losers or energy gainers?* Norway.

[3] Kaja, N. (2015). International Journal of Science and Research. In: A*n overview of energy sector in India.* School of Planning and Architecture, Vijayawada.

[4] Farheen Bano, Mohammad Arif Kamal (2016). *Examining the Role of Building Envelope for Energy Efficiency in Office Buildings in India.* Aligarh, India.

[5] Bureau of Energy Efficiency (2017), *Energy Conservation Building Code,* New Delhi, India

[6] ASHRAE (2010) *ASHRAE standard 90.1-2010. Energy Standard for Buildings except Low-Rise Residential Buildings*. American Society of Heating, Refrigerating and Air-Conditioning Engineers.

[7] Ghisi, E. and Tinker, J.A. (2005). An ideal window area concept for energy efficient integration of daylight and artificial light in buildings. *Building and Environment.*

[8] Mayank Bhatnagar, Jyotirmay Mathura, Vishal Garg (2019), Journal of Building Engineering. In: *Development of reference building models for India.* Hyderabad, India

[9] Lee, J., Jung, H., Park, J., Lee, J. and Yoon, Y. (2013). Optimization of building window system in Asian regions by analyzing solar heat gain and daylighting elements. *Renewable Energy.* Seoul, South Korea

Energy Conservation Building Code compliant material optimization of lightweight building envelope wall construction for different climate zones of India

Pranav Kishore
Centre of Sustainable Built Environment, MSAP
Manipal Academy of Higher Education
Manipal, India
pranav.kishore@manipal.edu

Vanshika Chanani
Manipal School of Architecture and Planning
Manipal Academy of Higher Education
Manipal, India
vanshika.chanani@learner.manipal.edu

Stuthi Shetty*
Centre of Sustainable Built Environment, MSAP
Manipal Academy of Higher Education
Manipal, India
stuthisshetty@gmail.com

Srijan Didwania
M.S. Addition & Associates
Phoenix, AZ, USA
srijandidwania@gmail.com

Vatsala Bajpai
Centre of Sustainable Built Environment, MSAP
Manipal Academy of Higher Education
Manipal, India
vatsala.bajpai09@gmail.com

Pradeep Kini
Centre of Sustainable Built Environment, MSAP
Manipal Academy of Higher Education
Manipal, India
pradeep.kini@manipal.edu

Abstract

India is key within the many global corporates around the world when it comes to development and revolution as one of the rapid economic growth is seen within India, which not only opens up a lot of opportunities in the building and construction field but also needs to set a balance for the mass construction. This paper suggests an integrated design solution involving the mass of construction materials to help reduce the dead loads on the structural frame of the building, releasing pressure off the beams, columns, and footing. This resolves into keeping a healthy balance of resource utilization and reducing any sort of material exploitation. This study incorporates the use of optimization techniques to obtain the best possible solution for various cases under consideration in five climate zones by minimizing the mass of the wall assembly while meeting the U-Value constraints specified by ECBC.

Keywords: dead weight, mass optimization, lightweight construction

I. INTRODUCTION

A. Urbanization

India is one of the fastest-growing economies in the world. Industrialization, commercialization, social benefits and services, employment opportunities, modernization and changes in the standard of living, rural-urban transformation, and spread of education are some of the reasons for massive urbanization across the country. With an increasing number of people, there is an evident increase in demand for employment around the country. Thus there is a dire need for infrastructure to support this growth. Increased population also increases demand in the residential sector. The construction industry contributes up to 8% of India's GDP. The commercial building stock is expected to increase five times in over ten years from now. There is a potential 70% of floor space that is yet to be constructed over a period until 2030 in India [1].

B. Resource Optimization

Throughout the life-cycle of a building, it can contribute significantly to emissions and waste generation as it consumes an enormous amount of material and energy resources to develop and sustain the built environment. This is why the construction industry is capable of making a noteworthy contribution to the objectives of sustainability. The current and anticipated pace of global urbanization makes it imperative for the process to be accountable in all three platforms of sustainability: environmental, social, and economic [10] .

Brundtland Commission's report of " Our Common Future" from 1987, outlines various sustainable development options including sustainable construction which underscores the idea of meeting the present-day needs of housing, infrastructure, etc., without having to compromise with the future requirements. The construction industry can walk the path of sustainable construction by reducing its ecological footprint and be more socially supporting, while also creatively responding to the high demand for built spaces.

Newer technology will inevitably replace the current trend of construction. But until then we must maximize the essence of the current building practices to make it more sustainable and approachable. The current resources are getting exhausted and therefore there is a need for resource optimization to support sustained infrastructural growth.

IEECP'21, July 29-30, 2021, Silicon Valley, San Francisco, CA – USA

D!f: https://sci-index.com/DAI/2021.99101/IEECP/14904861

II. LITERATURE REVIEW

It is impossible to stunt the growth of construction in India. The increasing population and the demand will continue to grow over the years increasing the landmass of construction. Old buildings get replaced with new ones. This will lead to construction waste across the country, defying the whole concept of sustainable construction or resource optimization. Yet we need to continue with the mass construction keeping in mind the impact and trying to reduce the construction wastage as much as possible. Using newer and better materials is one-way approach to the problem but better accessibility to such material probes an issue to many cities within the country. Hence a better use and balance of the currently available materials will be the most sound option in such scenarios. One such example for better material optimization and resource management is from a study by Kishore et al., in their paper, they have analyzed the current material library users across the country and have suggested the best possible mix of the wall composition that not only will be of constrained thickness but also confides within the u-value defined as per Energy Conservation Building Code (ECBC), India. This helps everyone to follow the basic norms of sustainability in terms of thermal heat barrier that should be maintained by the external wall without having to worry about using newer materials which demand a higher level of transportation, skilled professionals, or even increased costing [2].

Sustainable construction is defined as "the creation and responsible management of a healthy built environment based on resource efficiency and ecological principles".

The Organisation for Economic Co-operation and Development (OECD) is an international platform that works to "build better policies for better lives", a project that identifies majorly five objectives for sustainable buildings: Correlation with the environment including environmental assessment; resource efficiency; prevent pollution which includes indoor air quality and noise abatement; resource efficiency; energy efficiency which includes greenhouse gas emission control and finally integrated and systematic approaches including environmental management strategies [3].

A. Gap Identification:

The domain of the paper focuses on construction materials for non-load bearing structures. This paper takes references to code compliance for wall construction specific to India like the Energy Conservation Building Code, 2017 which applies to "buildings or building complexes that have a connected load of 100 kW or greater or a contract demand of 120 kVA or greater and are intended to be used for commercial purposes" [7]. A connected load of 100 kW indicates that the building in conversation is mostly a G+2 and G+3 or more commercial structure which is normally advised to be of load-bearing structural construction. To make full use of the FAR (Floor Area Ratio) it is inevitable to go higher, thus building up great structural pressure on the beams, columns, and footing. This paper aims to lessen the dead weight of the building structure through walls, a major part of the building is consumed by walls. Using a new technique or material to achieve this goal is one approach but it's not advisable to be used across the country without this being normalized, causing problems in costing, transportation, skilled labor requirement, etc. Hence this an attempt to optimize the currently available materials in the construction market to achieve the task without facing any above-mentioned problems and also creating alternative for easier acceptance in the construction and architectural field of today. Table 1 highlights the research findings of various lightweight construction-related topics that show the importance of lightweight construction and also the current status in the field.

III. METHODOLOGY

A. Code compliance-based wall construction in India

Thermal transmittance is one of the critical parameters for understanding heat loss or gain from the envelope of a building. Walls constitute a major part of the building envelope and receive maximum solar radiation along with exposure to extreme temperature and other weather conditions. To maintain steady indoor thermal comfort conditions, it is necessary to reduce heat transfer through exterior walls. It is very important to consider the heat storage capacity of the wall along with its thermal conduction properties. Energy Conservation Building Code (ECBC) for commercial buildings 2017 regulates the compliance conditions for the wall assemblies in terms of its U-factor(Thermal Transmittance). ECBC, ECBC +, and ECBC Super are the three categories for compliance specified in ECBC 2017 [7] for five climate zones in India as classified by the Indian Meteorological Department (IMD) which are "C1-Composite, C2-Hot and Dry, C3-Warm and humid, C4-Temperate and C5-Cold". Thermal transmittance in terms of the opaque wall construction assemblies (U- factor limitations), maximum U-factor (W/m^2.K) mentioned for E1-ECBC, E2-ECBC +, and E3-ECBC Super categories in different climate zones of India for different building typologies namely B1- All building types except the following, B2- No star hotel <10000 sq.m AGA, B3- Business <10000 sq.m AGA, B4- School <10000 sq.m AGA and B5- unconditioned building, are detailed in table 2, 3, and 4.

The Bureau of Indian Standards approved 'Handbook for the functional requirement of buildings other than industrial buildings', SP-41, divided into four sections which include climatology, heat insulation, ventilation, and lighting [8]. The calculation methodology for thermal heat transfer through the wall surface is acquired from this handbook as a reference. "Total Thermal Resistance (Rt) is the sum of the thermal resistance of each layer of the wall section."

"$R_t = R_1 + R_2 + \ldots + R_n = L_1/K_1 + L_2/K_2 + \ldots + L_n/K_n$

Where $L_{1\text{-}n}$ is the thickness and $K_{1\text{-}n}$ is the thermal conductivity for all the layers of the assembly."

U-factor is given by:

$U = 1/R_t$ where,

$R_t = 1/h_i + 1/h_o + L_1/K_1 + L_2/K_2 + \ldots + L_n/K_n$

Where, h_i and h_o represent the inside and outside air heat transfer coefficients. The heat transfer for the inside and outside film of air is stated in the Heat Insulation section of the SP-41 handbook. At an air velocity of 8km/h, the outside film coefficient (h_0) is 19.86W/m^2 K and for still air, the inside film coefficient (h_i) is 9.36W/m^2 K [8].

B. Mass calculation and considerations

Mass = Density * Volume

To compare results among the various combination of wall assemblies comprising of various inside finish material, outside finish material, and block material making up the assembly type, the cross-section of that wall is taken as per 1m^3 volume of the assembly, for the calculation of the mass of each assembly type.

C. Data collection

The materials selected for the wall assemblies in the study are code amenable with ECBC 2017 and verified and tested per the Indian standards[2]. The study pivots on the mass of these materials listed in the paper which are currently being used in India. Tables 5 and 6 list the materials classified as block opaque wall material, exterior finish material, and interior finish material respectively. Thickness (T) is shown in meters(m) and conductivity (k) is measured by the unit W/mK. Density is represented in kg/m^3 and the rate is identified as Indian Rupees per sqm (INR/m^2).

Table 1. Literature review and gap finding

Sl. No.	About	Title	citation	input variables	output variables	aim of the study	usefulness(to your research/ or to a particular topic)	GAP IDENTIFICATION
1	lightweight construction	Functional assessment of lightweight construction solutions in view of sustainability	Braganca, L., & Mendonca, P. (2005). Functional assessment of lightweight construction solutions in view of sustainability. ResearchGate, DOI: 10.1201/9780203970843.ch64.	construction materials	minimum transport cost, reduced raw material requirement	* The study highlights the relevance of use of lightweight construction materials in terms of thermal, acoustic and visual comfort. * Optimizing the total primary energy consumption (PEC) of construc-tion materials and their transport and reducing the energy operating consump-tions for maintaining thermal comfort, even using the maximum possible passive solar gains are two main focuses in this study. * The study makes use of mixed-weight housing principle, which uses thermal zoning concept and passive solar indirect gain to determine the weight reduction on construction without increase in the operating energy.	* Almost all the materials mentioned within this study is easy to dismantle and reusable/recyclable compared to steel reinforced concrete structure with clay hollow brick walls and pavements popularly used in Portugal. * Despite the recent popularity of lightweight maaterials and systems, durability and stability are considerations that are still in process. * The study concludes that solar passive optimized solution is more sustainable in a Sunspace configuration then in a Trombe wall configuration.	** the study highlights how environmentally acceptable the concept of lightweight materials and systems could be. ** Durability and stability are still two aspects of lightweight materials that still needs work on.
2	polystyrene waste- wall panels	Utilization of polystyrene waste for wall panel to produce green construction materials	Siswosukarto, S., Suputra, A., & Kafrain , I. Y. (2017). Utilization of polystyrene waste for wall panels to produce green construction materials. Elsevier, Procedia Manufacturing, Sustainable civil engineering structures and construction materials, 664 – 671.	polystyrene		* The study exhibits the importance of reusing the polystyrene waste as wall panel to create a lightweight wall panel construction. * The study asks for particular attention towards tensile characteristics of the concrete mix for better use of this technique.	*compressive strength, flexural strength, density and water absorption are certain parameters explain within the paper * Researches also simulated the action of forces on wall to study the behavior of the wall panel under repeated load.	** Polystyrene wall panel for lightweight construction indicates the various studies taking place across the world to promote and benefit from lightweight construction.
3	lightweight concrete vs reinforced concrete	A Review Paper on Comparative Study of Lightweight Concrete and Reinforced Concrete	Jagtap, P. J., Rathod, M. R., & Sheikh Murtuja, S. S. (2020). A Review Paper on Comparative Study of Lightweight Concrete and reinforced concrete. International research journal of engineering and technology, Volume: 07 Issue: 03.	lightweight concrete, reinforced concrete	compressive strength, flexural strength, density	*Based on properties, uses, ingredients, characteristics, the difference between lightweight concrete and reinforced concrete is analysed.	*reduction of dead load, faster building rates in construction and lower haulage and handling costs are some of the advantages of lightweight concrete over reinforced concrete specified in the study. * lightweight concrete has low density and thermal conductivity which proves to be effective characteristics for building construction, however, It is important that the cement to water ratio has to be sufficient for adequate cohesion between cement and water.	** reinforced concrete utilises more quantity of raw materials and increases the overall mass of the building whereas, lightweight concrete with low density and thermal conductivity proves a better and sustainable solution.
4	thermal mass	THERMAL MASS IMPACT ON ENERGY PERFORMANCE OF A LOW, MEDIUM, AND HEAVY MASS BUILDING IN BELGRADE	Andjelkovic, B. V., Stojanovic, B. V., Stojlkovic, M. M., Janevski, J. N., & Stojanovic, M. B. (2012). THERMAL MASS IMPACT ON ENERGY PERFORMANCE OF A LOW, MEDIUM, AND HEAVY MASS BUILDING IN BELGRADE. Thermal Science, 16, Suppl. 2, pp. S447-S459.	heavy mass materials	energy performance, thermal comfort	* the main agenda of this study was to bring out the effect of thermal mass has on internal environment of a building, resulting in lower energy requirements from the mechanical systems. *A three-dimensional building model was generated to represent a typical office building. Building shape, orientation, glazing to wall ratio, envelope insulation thickness, and indoor design conditions were held constant while location and thickness of building mass (concrete) was varied between cases in a series of energy simulations.	*The simulation results indicated that with addition of thermal mass to the building envelope and structure: 100% of all simulated cases experienced reduced annual space heating energy requirements, 67% of all simulated cases experienced reduced annual space cooling energy requirements, 83% of all simulated cases experienced reduced peak space heating demand and 50% of all simulated cases experienced reduced peak space cooling demand. * the space heating and cooling demand indicates that lightweight consumes 1.5kW and higher thermal mass consumes lesser i.e., 1.1 kW. In the case of peak cooling demand also the higher thermal mass consumes lesser than lightweight construction. * The simulations demonstrated that radiation had a positive impact on lowering the space heating and cooling requirement than convection, radiation being an important aspect of thermal mass. *The location of the thermal mass located at the inner side of the insulation also affected in bringing down the requirement of cooling and heating demands.	** lightweight construction reacts positively towards lesser raw material consumtion and reduced dead loads on the building, but this study helps rethink the solution for thermal mass can provide a better insulation of the envelope reducing the energy requirement of the entire building making it more efficient.
5	foam concrete	Foam Concrete: A State-of-the-Art and State-of-the-Practice Review	Fu, Y., Wang, X., Wang, L., & Li, Y. (2020). Foam Concrete: A State-of-the-Art and state of the practice review. Advance in materials science and engineering, Volume 2020, Article ID 6153602, 25 pages; https://doi.org/10.1155/2020/6153602.			*Foam concrete (FC) has the potential of being an alternative to ordinary concrete, as it reduces dead loads on the structure and foundation, contributes to energy conservation, and lowers the cost of production and labor cost during the construction and transportation.	*method of preparation of foam, type of foaming agent, the accuracy of the mixture, type of surfactants and additives used, usage of nano particles and mix design, etc are some of the factors to be considered for better efficiency of foam concrete. * Foam Concrete with uniformly distributed closed circular air pores exerts good thermal and mechanical properties.	** foam concrete is one such material that can be a lightweight material but with the efficiency of providing the qualities of a higher thermal mass material because air molecules embedded within the concrete act as a great thermal resistance.
6	seismic performance	Seismic Performance of Lightweight Concrete Structures	Vandanapu, S., & Krishnamurthy, M. (2018). Seismic Performance of Lightweight Concrete Structures. Advances in civil engineering, Hindawi, Volume 2018, Article ID 2105784, 6 pages; https://doi.org/10.1155/2018/2105784.			*Due to the mass of the concrete, the building is usually prone to earthquakes. *In order to reduce the impact of earthquake forces on buildings, use of lightweight building materials enables structural designers to cut loads off the structural members of the building. *This paper attempts to predict the seismic response of a six-storied reinforced concrete frame with the use of lightweight concrete.	*A comparison between normal weight concrete and lightweight concrete shows that the bending moment and shear forces are reduced to 15% and 20 %, respectively, in lightweight concrete. The density difference observed was 28% lower when compared normal weight concrete to lightweight concrete. *A building using lightweight concrete when subjected to seismic analysis resulted in reduction of cross section of members or to reduce the steel in moment and shear resisting sections.	** against a seismic situation a lightweight construction is preferred over conventianal methods to reduce overall dead load of the structure.

D. Mass and u value distribution

A Business as Usual wall in India consists of the wall assembly shown in Figure 1.

The objective of this paper is to focus on finding the optimized solution for the wall section that not only abide by the thermal transmittance constraint imposed by ECBC India but also with the least possible mass to reduce the overall dead load of the structure reducing the load on the structural components of the building like beams, columns, and footings.

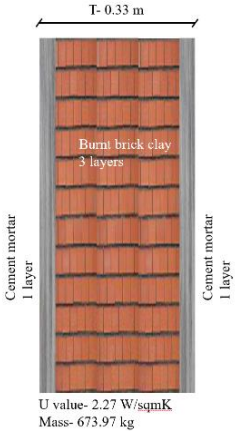

Figure 1. Wall assembly for a Business as Usual wall in India

Table 2 ECBC compliance category suggested maximum U-factor for various climate zones of India and different building categories [7]

Type of building	Composite	Hot & dry	Warm & humid	Temperate	Cold
1.All building types except below	0.4	0.4	0.4	0.55	0.34
2.No star hotel <10000 sqm aga	0.63	0.63	0.63	0.63	0.4
3.Business< 10000 sqm aga	0.63	0.63	0.63	0.64	0.4
4.School <10000sqm aga	0.85	0.85	0.85	1	0.4

Table 3 ECBC + compliance category suggested maximum U-factor for various climate zones of India and different building categories [7]

Building typology	Composite	Hot & dry	Warm & humid	Temperate	Cold
1.All building types except below	0.34	0.34	0.34	0.55	0.22
2.No star hotel <10000 sqm aga	0.44	0.44	0.44	0.44	0.34
3.Business< 10000 sqm aga	0.44	0.44	0.44	0.55	0.34
4.School <10000sqm aga	0.63	0.63	0.63	0.75	0.44

Table 4 ECBC Super compliance category suggested maximum U-factor for various climate zones of India and different building categories [7]

Building typology	Composite	Hot & dry	Warm & humid	Temperate	Cold
1.All building types	0.22	0.22	0.22	0.22	0.22

Table 5. Material dataset for block material and exterior wall finish materials [2]

S no.	Material- Block	Thickness (m)	K-value (W/m.K)	Density (kg/m^3)	Rate (INR/sqm)	S no.	Material-Exterior finish	Thickness (m)	K-value (w/m.K)	Density (kg/m^3)	Rate (INR/sq m)
1	Aerated autoclaved concrete block	0.2032	0.18	642	726.56	1	Ac sheet	0.006	0.25	1145	279.86
2	Aerated autoclaved concrete block	0.1016	0.18	642	363.28	2	Aluminium	0.004	212.2	2700	1399.31
3	Armor rock boulders	0.2032	0.07	270	1076.39	3	Armor rock boulders	0.025	0.07	270	645.83
4	Autoclaved aerated concrete block	0.1524	0.18	642	322.92	4	Asbestos sheet	0.008	0.51	1377	753.47
5	Autoclaved aerated concrete block	0.2032	0.18	642	430.56	5	Black coarse granite	0.025	2.54	3473	1184.03
6	Brick - burnt red clay	0.1016	1.27	2049	538.2	6	Black fine granite	0.019	2.44	3535	1506.95
7	Brick - burnt red clay	0.0762	1.27	2048	403.65	7	Brick cladding	0.02	1.27	1892	538.2
8	Cellular concrete	0.2032	0.19	704	645.83	8	Brick tile	0.015	0.8	1892	459.26
9	Cellular concrete	0.1016	0.19	704	322.92	9	Cement board	0.01	0.44	1340	215.28
10	Cement stabilized soil block	0.0762	1.3	1900	1216.32	10	Cement board	0.016	0.44	1340	322.92
11	Cement stabilized soil block	0.1016	1.3	1900	1621.76	11	Cement bonded particle board	0.016	0.33	1251	355.21
12	Cement stabilized soil block	0.1016	0.84	1700	807.29	12	Cement fibre board	0.016	0.39	1376	430.56
13	Compressed mud blocks	0.09	1.21	1840	555.18	13	Cement mortar	0.012	0.72	1648	161.46
14	Compressed mud blocks	0.15	1.21	1840	926.87	14	Cement mortar	0.015	0.72	1648	215.28
15	Fly ash brick	0.0762	0.64	1240	236.81	15	Cement plaster	0.015	1.21	1880	236.81
16	Fly ash brick size -9x4x3in density-40kg/m4 4 inch	0.1016	0.64	1240	315.74	16	Clay roof tile	0.012	0.63	2531	484.38
17	Foam cement block	0.0508	0.16	481	322.92	17	Clay ceiling tile	0.012	0.63	2531	322.92
18	Foam cement block	0.0762	0.16	481	484.38	18	Composite marble	0.02	2.44	3146	2960.07
19	Foam concrete	0.1016	0.07	320	322.92	19	Concrete paver tiles	0.06	1.72	2210	699.65
20	Foam concrete	0.2032	0.07	320	645.83	20	Dholpuri stone	0.02	3.08	2262	807.29
21	Perforated burnt clay brick	0.0762	0.63	1520	645.83	21	Floor board– Shera wood type – fibre cement	0.015	0.27	954	968.75
22	Perforated burnt clay brick	0.1016	0.63	1520	861.11	22	Granite - lakha red	0.018	3.57	2569	3229.17
23	Solid burnt clay brick	0.0762	0.62	1400	301.39	23	Jaisalmer yellow stone	0.02	2.74	3006	861.11
24	Solid burnt clay brick	0.1016	0.62	1400	401.85	24	Kota stone	0.02	3.02	3101	484.38
25	Solid concrete block	0.1016	1.4	2427	363.28	25	Kota stone	0.03	3.02	3010	592.01
26	Solid concrete block	0.2032	1.4	2427	726.56	26	Mangalore roof tile	0.02	0.61	2531	129.17
27	Solid concrete block	0.1524	1.4	2427	411.72	27	Mild steel	0.004	44.12	7823	1076.39
28	Solid concrete block	0.2032	1.4	2427	548.96						
29	Solid concrete block	0.2032	1.4	2427	484.38						

Table 6. Material dataset for interior wall finish materials [2]

S no.	Material- Interior finish	Thickness (m)	K value (W/m.K)	Density (kg/m^3)	Rate (INR/sq m)	S no.	Material- Interior finish	Thickness (m)	K value (W/m.K)	Density (kg/m^3)	Rate (INR/sq m)
1	Acrylic sheet	0.01	0.22	1145	699.65	28	Hard board	0.014	0.28	979	376.74
2	Ambaji marble	0.019	2.81	3128	775	29	Hard board	0.016	0.28	979	452.08
3	Asbestos cement board	0.015	0.47	1404	322.92	30	Italian black granite	0.019	2.36	2911	5920.15
4	Asbestos mill board	0.01	0.25	1397	376.74	31	Italian marble	0.019	2.78	2630	4843.76
5	Asbestos sheet	0.008	0.51	1377	753.47	32	Laminated particle board	0.019	0.18	656	484.38
6	Bamboo	0.015	0.2	913	3928.82	33	Medium density fibreboard	0.012	0.2	133	538.2
7	Black fine granite	0.019	2.44	3535	1506.95	34	Melamine fibreboard	0.012	0.25	807	269.1
8	Calcium silicate board	0.016	0.28	1016	322.92	35	Oak laminated floor tiles	0.012	0.27	949	807.29
9	Cement mortar	0.012	0.72	1648	161.46	36	Plain particle board	0.012	0.27	902	322.92
10	Cement mortar	0.015	0.72	1648	215.28	37	Pop board	0.01	0.5	1080	484.38
11	Ceramic frit glass	0.006	0.69	2520	861.11	38	Pumice square - bronze tile	0.01	0.99	2327	861.11
12	Ceramic tile	0.005	1.6	2700	538.2	39	Rajnagar marble	0.019	5.64	3332	699.65
13	Ceramic tile	0.005	0.8	2549	699.65	40	Rubber wood	0.008	0.17	472	1754.52
14	Chile wood 15 mm	0.015	0.14	362	1345.49	41	Saag wood	0.02	0.29	959	3229.17
15	Engineer wood floored tile	0.015	0.25	570	1883.68	42	Sandstone	0.019	3.01	2530	861.11
16	Ghana teak wood	0.02	0.21	529	2095.5	43	Soft board	0.012	0.09	249	1076.39
17	Granite - cat eye	0.019	3.44	2660	1237.85	44	Steam beech wood	0.012	0.23	241	1453.13
18	Granite - green galaxy	0.019	2.62	2690	968.75	45	Teak wood	0.075	0.24	665	15607.66
19	Granite - ivory fantasy	0.019	2.55	2540	1776.04	46	Udaipur brown marble	0.019	2.92	3197	1076.39
20	Granite - Kashmiri gold	0.019	2.47	2710	2690.98	47	V-board	0.018	0.3	1191	376.74
21	Granite - tan brown	0.019	2.95	2610	1399.31	48	Veneered particle board	0.012	0.24	788	322.92
22	Green marble	0.019	2.37	2650	807.29	49	Veneered particle board	0.016	0.24	788	484.38
23	Gypsum board	0.012	0.25	623	484.38	50	Vitrified tile	0.006	1.48	2719	376.74
24	Gypsum plaster	0.002	0.51	1120	258.33	51	Wall board	0.006	0.05	2622	269.1
25	Hard board	0.006	0.28	979	193.75	52	Wall board	0.008	0.05	2622	322.92
26	Hard board	0.01	0.28	979	258.33	53	Wall board	0.01	0.05	2622	376.74
27	Hard board	0.012	0.28	979	301.39	54	Wall board	0.012	0.05	2622	409.03

E. Optimization

Optimization is the technique of selecting the best and most effective resources while conforming to a set of rules and precisely achieving the solution for a given problem statement. The objective function is represented as f(x_1, x_2, … x_n). This function is inclusive of variables and their constraints. The function can achieve minima or maxima at some values of variables ranging from x_1 to x_n. A tangent is drawn just before the point 'x' to determine a point of minima or maxima.

Using an exhaustive search method of optimization, the best practicable wall assembly scenarios are attained with the minimum possible mass for each U-value constraint as provided by ECBC 2017 for five different climate zones with the wall thickness constraints of T1- 0.15m, T2- 0.2m, T3- 0.25m, T4-0.3m, T5-0.35m, T6-0.4m, and T7- 0.45m. The algorithm ceaselessly tries to obtain the results every time it runs for every probable case considered. The optimization algorithm does not make any supposition. Constraints are added to the optimizer to keep in check the inputs along with variables ensuring that the optimizer resolves every possible case and gives the best possible solution which will be practically possible to consider. If the constraints are not satisfied, the system re-runs.

Inside finish material, outside finish material, and opaque block material and their respective thicknesses are mentioned in the dataset considered for the study in the paper [2]. Constraints comprise U-values specified by ECBC 2017, the number of layers of finish materials and block materials that can be used to form a particular wall assembly, and various thicknesses of wall section practically possible are included within the study. Figure 2 gives an overall flow of the process that has been adopted in this study. Keeping in mind the practical possibility of the number of layers of materials that can be used to comprise a wall assembly, the minimum and maximum limit for the number of layers of each material is 0-3 i.e., it was decided not to exceed 3 layers of material for either of Inside finish material nor outside finish material. The lower and upper limit of layers for block material is considered from 1-3 layers. The four different combinations of finish material are represented as, F1- no interior wall finish, opaque, no exterior wall finish; F2- interior wall finish, opaque, exterior wall finish; F3- no interior wall finish, opaque, exterior wall finish; F4- interior wall finish, opaque, no exterior wall finish. The objective function of mass was minimized to understand the feasibility of lightweight wall construction with respect to the 'The Code 2017'.

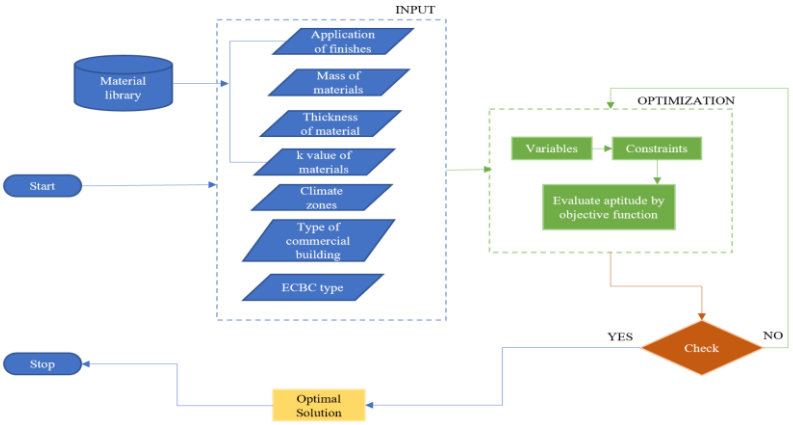

Figure 2. Process flow chart of evolutionary optimization

IV. RESULTS, DISCUSSION, AND ANALYSIS

Graphs 1 to 4 depict the scenarios as a result of minimizing the objective function i.e., mass construction for a wall section that conforms with the ECBC criteria of thermal transmittance for various building typologies, across five climate zones of India. The x-axis of the graph explains the hierarchy of the combination of constraints that are applied to the six variables considered in the study i.e., type of wall finish materials (interior and exterior), block material and their respective thicknesses. The primary y-axis of the graph shows the mass of the construction assembly in kg/sq.m while the secondary y-axis shows thermal transmittance in W/sq.m.K. The constraints include various u-values for different categories of compliance, namely ECBC, ECBC +, and ECBC Super, different for different category of building and five climate zones of India. Graph 1-4 shows ECBC and ECBC + results only. The cases included within the study are the different climate zones, overall thickness of the wall assembly from T1-T7 and the type of ECBC compliance category. There are scenarios shown in the graphs for which no practical solution exist, which indicates that there is no possible solution i.e., there is no combination of material from the dataset that abides by the given level of ECBC compliance category for that particular climate zone

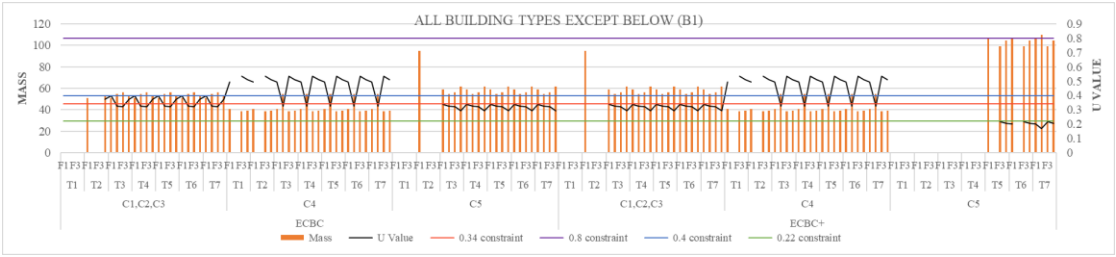

Graph 1 shows the least mass obtained for the case all building types (B1)

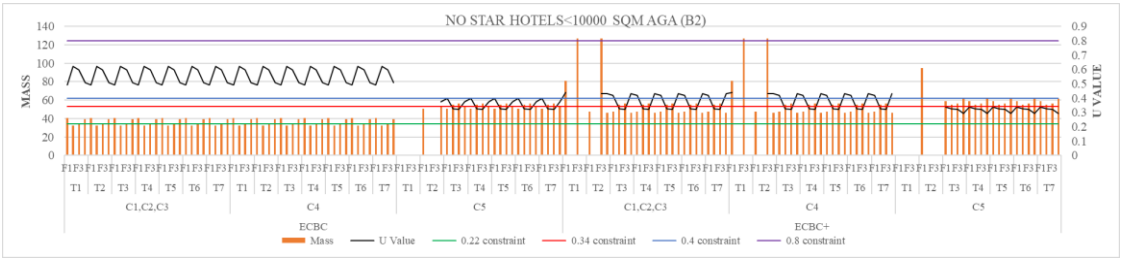

Graph 2 shows the least mass obtained for the cases of no star hotels<10000 sqm AGA (B2)

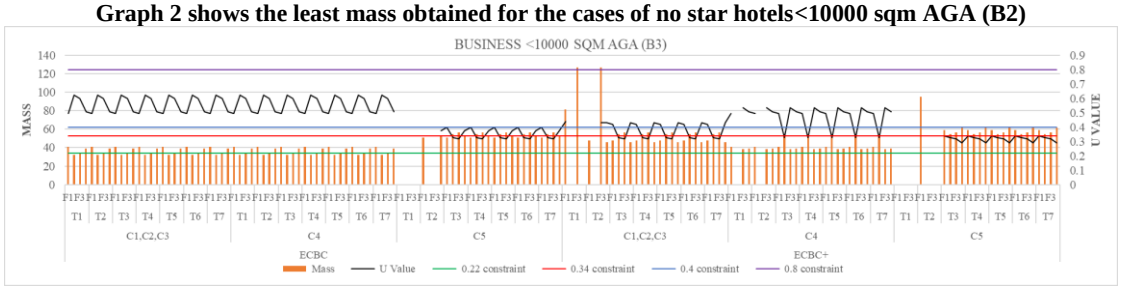

Graph 3 shows the least mass obtained for the cases business<10000 sqm AGA (B3)

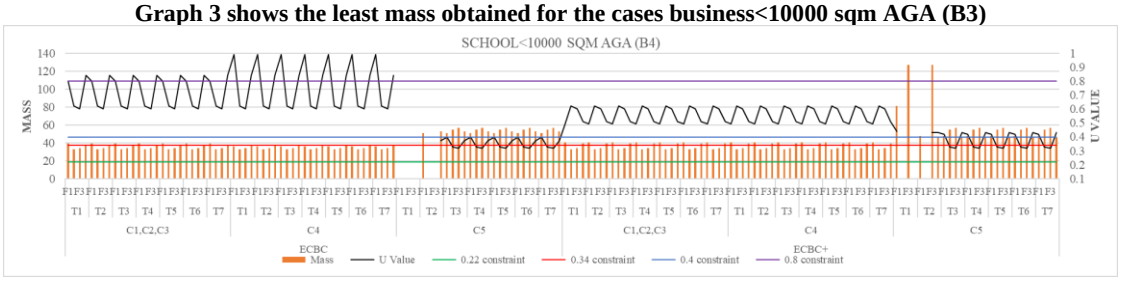

Graph 4 shows the least mass obtained for the cases of school<10000 sqm AGA (B4)

Graph 5 shows the results obtained for unconditioned building (naturally ventilated building) type mentioned in The Code 2017 manual. The hierarchy of the x-axis remains the same and also the graph shows the possible solutions for only two levels of the ECBC compliance category i.e., ECBC + and ECBC. The thickness, climate zones, and ECBC constraint are considered the same for all four wall finish types throughout this study.

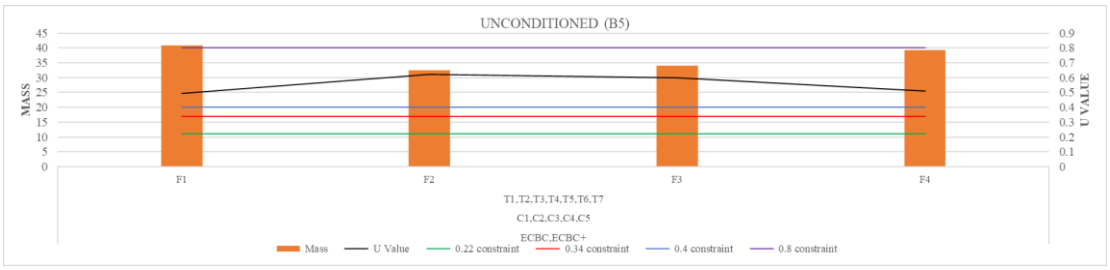

Graph 5 shows the least mass obtained for the cases of unconditioned buildings (B5)

Graph 6 is a compiled result of all building typologies from B1- All building types except the following, B2-no-star hotels<10000 sqm AGA, B3-School <10000 sqm AGA, B4-Business<10000 sqm AGA and B5-Unconditioned type. This is because the ECBC Super compliance category states the same value of thermal transmittance irrespective of different building typologies and different climate zones. The variations shown in the graph are for seven wall thicknesses and four combination of wall finish.

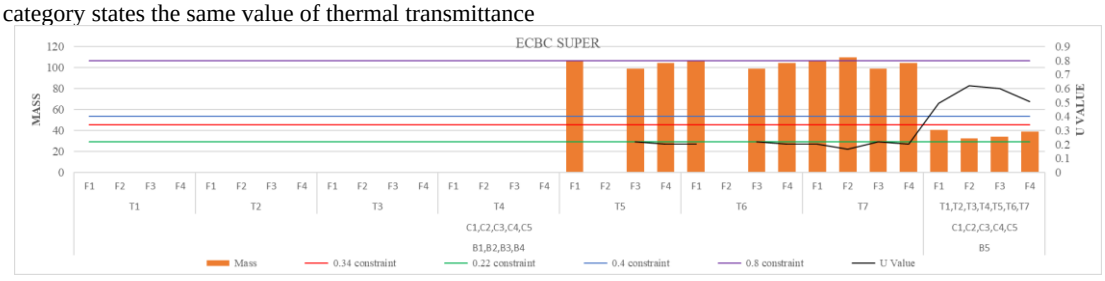

Graph 6 shows the least mass obtained in all five building categories for ECBC Super criteria

V. CONCLUSION

The results of the optimization show that foam concrete is the most recurring solution to the least mass construction material that can be used as a block material for minimum mass construction than the rest of twenty-eight block materials from the material library. Higher mass construction in buildings has a higher saving on building energy consumption because of the time lag provided by thermal mass but adversely impacts on the dead load of the structure and results in unbalanced material utilization. This paper suggests a lower mass solution for wall construction while conforming with the thermal transmittance requirements per ECBC, 2017. This makes it an efficient and practical solution that is more sustainable. Foam concrete has reduced mass due to air pockets embedded within the block. This in turn acts as an extra layer of insulation as air is the bad conductor of heat. Lesser mass also helps with lowering the dead load overall. In solid mechanics bending moment is a reaction that is seen in structural elements when an external force is applied which causes the element to 'bend'. The moment is given by force * distance; force is given by mass * acceleration. This relation shows the connectivity of how mass will affect the practicality of beams and columns in construction. Reduced dead loads through walls are indicative of reduced sizes of these structural elements which lower the cost of construction materials and helps with sustainability by reducing resource consumption. Lean structures help tackle lateral forces such as earthquakes and wind load better than the conventional heavier buildings. The conventional mode of construction does not allow mass as an element of consideration in construction or design. The best solution can come up from what is already available to us and our ability to integrate it into our design to result in a sustainable yet achievable solution. Considering mass along with thermal transmittance is an Integrated Design Approach (IDA) to reduce the dead weight of the non-structural and structural elements of the building without compromising the energy efficiency. This paper sets a foreground to further exploit the chance of increasing lightweight construction within the country which can be done by a trade-off between mass and u-value of the wall assembly with feasible cost. Hence this paper offers a solution that is efficient in a more justified way.

VI. REFERENCES

[1]TERI, t. e. (2015). *Green growth and sustainable development in India.* Seoul, South Korea: Global and green growth Institute

[2] Shetty, S., Kishore, P., Kini, P., Acharya, R. R., & Raj, A. (2019). Energy Conservation Building Code based optimum wall composition with respect to thermal transmittance and thickness for different commercial pockets of Tier-1 cities in the temperate climatic zone of India. *Procedia Manufacturing, Elsevier*, 229-236.

[3] OECD. (2021). *OECD secretary general's report to ministers.* Paris, https://doi.org/10.1787/8cd95b77-en: OECD Publishing.

[4] Braganca, L., & Mendonca, P. (2005). Functional Assessment of lightweight construction solutions in view of sustainability. *Improvement of Buildings' structural quality by new technologies, Taylor and Francis Group*.

[5] Jagtap, P. J., Rathod, M. R., & Sheik Murtuja, S. (2020). A review paper on comparative study of lightweight concrete and reinforced concrete. *International research journal of engineering and technology*.

[6] Vandanapu, S. N., & Krishnamurthy, M. (2018). Seismic performance of lightweight concrete structures. *Advances in civil engineering, Hindawi*, https://doi.org/10.1155/2018/2105784.

[7] ECBC. (2017). *Energy Conservation Building Code.* Bureau of Energy Efficiency, Ministry of Power, Government of India.

[8] SP-41. (1987). *Handbook on functional requirements of building (other than industrial building).* Bureau of Indian Standards.

[9] Mirsaeedie, L., Zabihi, H., & Habib, F. (2012 December). Sustainability in Building and construction: Revising definitions and concepts. *International Journal of Emerging science and engineering, ResearchGate*, 570-578.

[10] U. S., Bhuvandas, N., & Aggarwal, V. (2012). Impacts of urbanization on environment. *International Journal of Research in Engineering and Applied Sciences*, Volume 2, Issue 2 ; ISSN: 2249-3905.

Understanding the impact of Green Walls on the Indoor Environment of Buildings in different climatic zones of India.

Akash N Achar
Manipal School of Architecture and Planning,
Manipal Academy of Higher Education
Manipal, India
akashachar5@gmail.com

Pradeep Kini
Centre for Sustainable Built Enviroment
Manipal School of Architecture and Planning,
Manipal Academy of Higher Education
Manipal, India
pradeep.kini@manipal.edu

Pranav Kishore
Centre for Sustainable Built Enviroment
Manipal School of Architecture and Planning,
Manipal Academy of Higher Education
Manipal, India
pranav.kishore@manipal.edu

Kiran Kamath
Department of Civil Engineering
Manipal Institute of Technology
Manipal, India
kiran.kamath@manipal.edu

Abstract

The world's population is on a rise, and this has resulted in a huge loss of natural green spaces as the demand for housing increases. As the land is limited in an urban area, green spaces are being cleared out to set up high-rise buildings as they can accommodate more people. The absence of green spaces in an urban area has resulted in increased pollution levels, temperature etc. To cope up with these problems faced by the urban population, green facades are an excellent solution. These methods can be applied to high-rise or mid-rise buildings which contribute a lot towards the increase in temperature around an urban area. Green walls are also a great to reduce the internal temperatures within buildings. This paper aims to discuss and assess the benefits of inculcating green facades in high rise buildings in an Indian-Urban scenario.
Design builder is the simulation software used to simulate buildings in 5 urban locations in India, and the advantages and disadvantages of introducing green walls is assessed.

Keywords: Green walls, High-rise buildings, temperature, India

1.INTRODUCTION

With the ever-growing population of the planet, the demand for housing has rapidly increased, which has resulted in a large chunk of the population hunting for job opportunities and hence moving into cities and urban areas. As the demand for housing rises, much greenery eventually gets removed, and the cities tend to expand horizontally. As per the UN report, Today, 55% of the world's population lives in urban areas, which is foreseen to increase to 68% by 2050. Predictions show that urbanization, the progressive shift in the residence of the human population from rural to urban areas, coupled with the global growth of the world's population, might add another 2.5 billion people to urban areas by 2050, with near to 90% of this increment taking place in cities in Asia and Africa. To accommodate such a drastic change in the population with limited land availability, the most acceptable option is to go vertical in the form of Skyscrapers and Multifunctional High rises. While these buildings are being designed, the designers and construction companies need to keep sustainability in mind. Increasing temperatures in urban areas due to the Urban heat island effect is also a growing problem. Urban building elements are another reason that urban areas trap heat. Many modern building materials are impervious and rugged surfaces. This means that water cannot flow through surfaces like a brick or a patch of cement like it would through a plant. Without a cycle of running and evaporating water, these surfaces have nothing to cool them down. Planting gardens on urban roofs can also help to cool down the city too. A study conducted in California estimated that changes like these would be enough to avoid close to $100 million per year in energy costs. Green Walls were especially important in the Arts & Crafts and Modern style movements in Europe, which led to an increase in its significance as an aesthetic element and a sustainable one. At the beginning of the 20th century, some movements like the 'Jugendstil Movement' used various climbing plants on building façades to merge buildings with their gardens. In England, Garden Cities are exceptional examples of Green Walls. William Robinson and Gertrude Jekyll designed outdoor vegetated rock walls used for screens and boundaries in gardens. Green Walls and climbing

IEECP'21, July 29-30, 2021, Silicon Valley, San Francisco, CA – USA

DAI : *https://sci-index.com/DAI/2021.99101/IEECP/14899587*

plants' usage on the façade declined after the 1930′s due to development of new building techniques and people's fear about compromises of wall life and durability. Stanley Hart White (University of Illinois Urbana-Champaign) developed the modern Green Wall with integrated hydroponics in 1931-1938. White owns the first known patent for a green wall or vertical garden, conceptualizing this new type of garden to solve the problem of modern garden design. Studies done imply that vegetated facades can decrease the effect of urban heat island around 2 degrees Celsius, improving air quality, thermal comfort, and human health, with savings in electricity consumption of up to 5% to 10%.

1.1 Green walls

Green walls are vertical surfaces /structures that have different types of plants or other greenery growing on or attached to them. The greenery is planted in a growth medium such as soil, stone, or water. A green wall will also usually have a built-in water supply system so as to irrigate the plants. According to the CTBUH guide, the main elements of green walls are:

i) Plants
ii) Planting media
iii) Structures that support and attach plants to the façade
iv) The irrigation system

Green walls can be broadly divided in two categories:

i) Façade Supported Green Walls
ii) Façade Integrated Green Walls

Façade supported green walls include 2D and 3D systems in the form of vertical cables, rods, trellis, nets etc whereas the Façade integrated green walls include climbing plants and Living walls. These Living walls usually have the irrigation system integrated. within the green wall panels.

1.2 Background Study

In the Thermal Performance Simulation of Hydroponic Green Wall conducted in Shahrekord City, Iran which enjoys cold climate, where a green wall was modelled at a distance of 20cm from the exterior walls of a school building using Energy Plus Software. Results showed that during the warmer seasons, the indoor temperatures reduced by a maximum of 1.13°C and a minimum of 0.7°C. During the colder seasons, the temperatures increased by an average of 1.46°C. [1]

In the study mentioned in the book "Green Walls in High-Rise Buildings: An output of the CTBUH Sustainability Working Group" wherein several case studies of high rise buildings with green walls is included, Consorcia Santiago Building in Chile, with a Mediterranean climate, experienced a reduction in energy consumption in floors of the building having external green walls of up to 35% and operation costs of up to 25% as compared to the floors without the green walls. [2]

In Athens City, which falls under the Mediterranean climate zone, while testing the thermal performance of a green wall using the design builder software, it was observed that the application of a green wall on the East side brings a reduction of the building heating need to about 10%. Average decrease in the internal surface temperatures of the eastern walls of two rooms was 1.08 and 1.48 Celsius, respectively [3].

In Cairo, Egypt the simulation of a green wall was conducted using the Design Builder Software on three typical Residential buildings. It was observed that in Arid Climates such as the one Cairo Experiences, the results show that an extensive soil thickness of 15cm performs better in the arid climates. Annual electricity consumption reduced by 17% to 25% per annum when a vegetated layer was added, in addition to enhancing the indoor air temperature by 5°C [4].

In a simulation study conducted using the TRNSYS software in two cities La Rochelle with an oceanic climate and Athens with a Mediterranean climate it was found that the green walls decrease the surface heat transfer from indoor to outdoor and the façade surface temperature. As a result, the green walls will contribute, also, to the urban microclimate mitigation. The difference in the operative temperature was more prominent in Athens where average reduction of 1.5 °C between the reference building and the vegetated building [5].

In a field experiment conducted by the Department of Architecture, NUM, Malaysia in a tropical climate on two identical thermal labs, one with a green wall and one without, the results indicated that indoor air temperature of thermal lab with the green façade is always lower than indoor air temperature of reference thermal lab at all times. Maximum reduction of indoor air temperature is 1.7°C. Daily average of indoor air temperature with Green Facades is 1.0°C lower compared to indoor air temperature of reference thermal lab, with 29.8°C and 30.8°C, respectively [6]. In another live study and monitoring of summertime indoor temperatures of a 5 storeyed building in Shanghai, where green wall was integrated within a double skin glass façade, the results showed that the indoor thermal improvement by the Vertical Greening System, evaluated by operative temperature, is 1.1 °C averagely and 2.7 °C maximally on the South-facing office, and 0.6 °C averagely and 1.9 °C maximally on the North-facing office. [7]

To assess the benefits of a green wall in an urban microclimate, Envimet Software was used to model a locality in Hong-Kong. The urban temperature was recorded. It was found that when 30% of each building's façade was incorporated with greenery, the urban temperature dropped by 1°C. This proved that the green walls are not only beneficial for better indoor temperatures but also helps in reducing the temperatures in an urban level. [8]

2. METHODOLOGY

The research will be conducted with the help of DesignBuilder Software. Design Builder is an Energy Plus based software tool which is used for energy, carbon, lighting and comfort measurement and control. Design Builder is developed to help in easing up the building simulation process.

Step 1: Selection of Urban Areas

The first step involved the selection of 5 urban areas in India. Since India is a large country with varying climate zones throughout the region, ECBC has divided the country broadly into 5 climatic zones i.e., Hot & Humid, Hot & Dry, Moderate, Composite, and Cold. An urban area from each of these climatic zones has been selected to run the simulation.

Step 2: Modelling of Reference Building

A 9 storeyed building (g+8) was modelled on the Design Builder Software. The reference building has an exterior dimension of 90m x 39m (aspect ratio of 1:2.3 [9]) The reference building was divided into various zones with Core and Perimeter Zones. A Perimeter width of 4.5m was considered. The details of the building envelope have been shown in table 1.

Table 1. Reference Building Model Envelope Details

City	Wall U-value	Roof U-Value	Window U-Value
Mumbai	1.26 - Fly Ash Brick Wall (200 mm) with plaster	1.18	2.05
Ahmadabad	1.46 - Brick Wall (200 mm) with plaster	0.64	2.05
Delhi	1.46 - Brick Wall (200 mm) with plaster	0.64	2.05
Bangalore	1.46 - Brick Wall (200 mm) with plaster	0.64	2.05
Srinagar	2.15	1.65	1.1

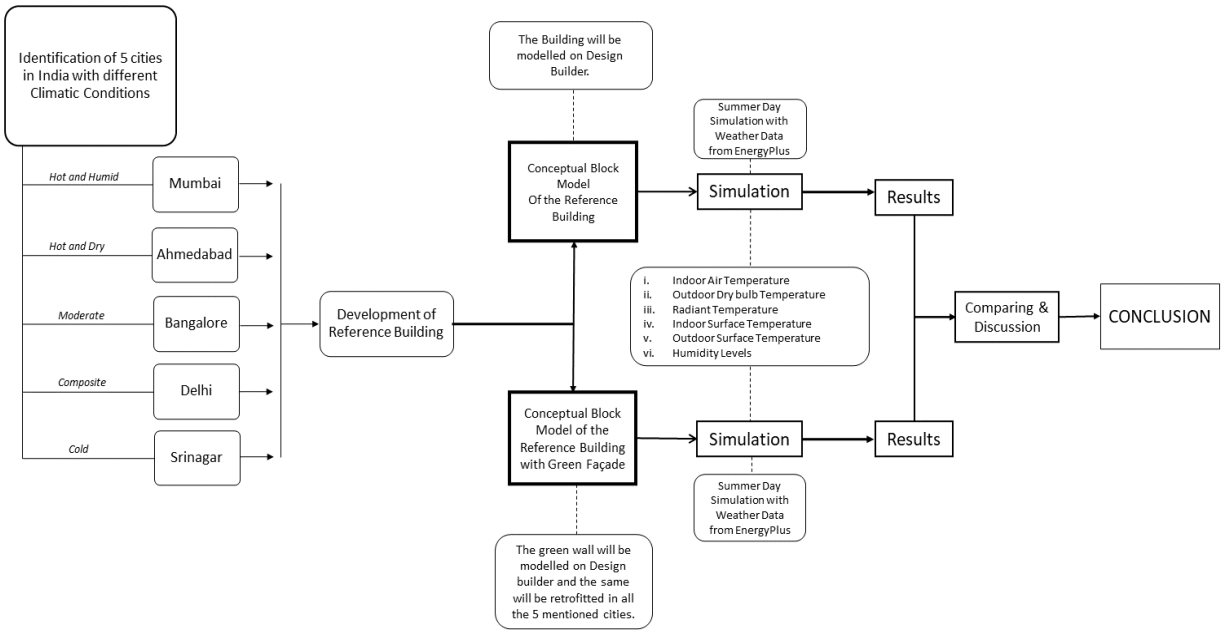

Figure 2: Methodology Flowchart

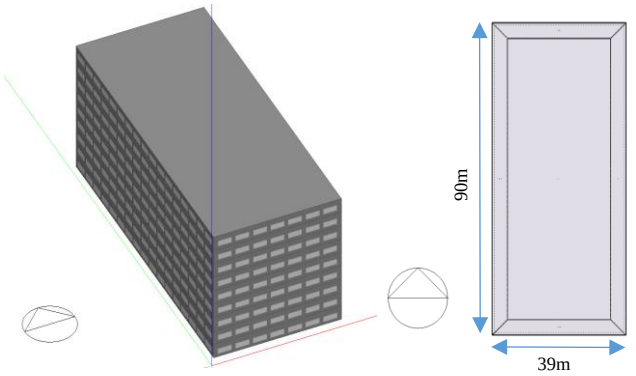

Figure 1: Reference Building Model Isometric View and thermal Zone Divisions on the floors.

Figure 3: Green Wall Cross Section

Step 3 : Retrofitting of Green wall

A façade integrated green wall was modelled on the Design Builder Software. This Green wall was then retrofitted into the existing walls of the Reference Building Model. An Air Gap of 8cm was considered between the existing wall and the green walls aluminum back panel for the provision of irrigation lines for the green wall. Peat soil has been chosen as the growing medium for the plants as peat soil is an organic matter that can be found throughout the country irrespective of the climatic region. The details of the Green Wall have been given in Table 2. A cross section of the green wall has been shown in figure 4.

Table 2: Details of Green Wall Given to Design Builder

Plant Height	0.2m
Leaf Area Index	3
Air Gap between Exterior wall and Green wall	0.08m thickness
Growing Medium: Peat soil with 133% Moisture	0.15m thickness
Vapour Permeable Felt	0.005m
Aluminium Backing	0.005

Step 4: Running of Simulation

The 8th Floor of the reference Building model was simulated for the summer day of May 19th to check the Indoor Air Temperatures, Radiant Temperatures, Inside Surface Temperature, Exterior Surface Temperature, Humidity Levels, and the Outside Dry Bulb Temperature in all the four perimeter zones of the floor. Once the Simulation was completed for the Reference building in a Climate Zone, the modelled green wall was retrofitted into the Exterior walls and the simulation was run again. The results where then Compared. The same Procedure was followed for all the 5 Cities.

3. RESULTS

Case 1: Hot and Humid

In Mumbai, the Outside Dry Bulb Temperature was 30.75°C. The average reduction in Air Temperature and the Radiant Temperature on the 8th floor was 1.13°C and 1.47°C, respectively.

The floors interior surface temperatures reduced by 1.65°C and the exterior surface temperatures reduced by 2.48°C. Figure 4 Graphically compares the temperature levels before and after retrofitting a green wall. It is observed that the highest temperature reduction is seen on the building's exterior Surface.

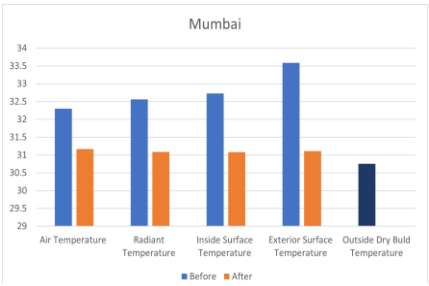

Figure 4: Graph of Average Temperature Levels before and After Retrofitting a green wall in Mumbai.

The maximum air and radiant temperature decrease is seen on the Northern perimeter zone, with a temperature dip of 1.1°C and 1.27°C respectively, and the least decrease in the air and radiant temperature is seen on the Western Perimeter with a dip of 0.76°C and 0.86°C, respectively. The inside surface temperatures experience a maximum dip of 1.33 on the northern zone and the least dip is observed on the Eastern Façade with a temperature decrease of 0.71°C. The exterior surface temperature reduction is the max on the southern wall with a decrease of 1.37°C and the least is observed on the Western side with a reduction of 0.31°C. The difference in the temperatures on the various perimeter zones before and after introducing a green wall is graphically represented in figure 5.

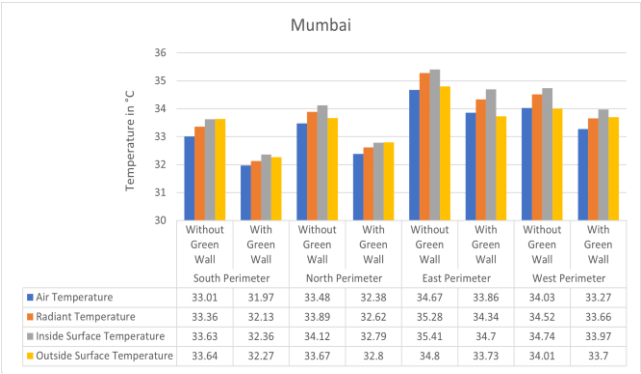

Figure 5: Perimeter Zone wise recorded temperatures before and after retrofitting a green wall in Mumbai.

Case 2: Temperate Climate

In Bangalore, the Outside Dry Bulb Temperature on the 19th of May was 27.74°C. The average reduction in Air Temperature and the Radiant Temperature on the 8th floor was 0.89°C and 1.09°C, respectively. The floors interior surface temperatures lowered by 1.25°C and the exterior surface temperatures decreased by 2.63°C. Figure 6, Graphically compares the temperature levels before and after retrofitting a green wall.

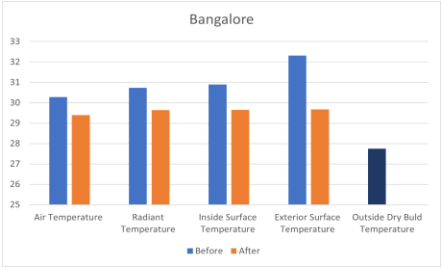

Figure 6: Graph of Average Temperature Levels before and After Retrofitting a green wall in Bangalore.

The maximum air temperature and radiant temperature decrease is seen on the Northern perimeter zone, with a temperature dip of 0.59°C and 0.72°C respectively, and the least decrease in the air and radiant temperature is seen on the Western Perimeter with a dip of 0.39°C and 0.49°C, respectively. The inside surface temperatures experience a maximum dip of 0.9°C on the Southern zone and the least reduction is observed on the Western Façade with a temperature decrease of 0.46°C. The exterior surface temperature reduction is the max on the southern wall with a decrease of 4.59°C and the least is observed on the Western side with a reduction of 0.47°C. The difference in the temperatures on the various perimeter zones with and without the green wall is graphically represented in figure 7.

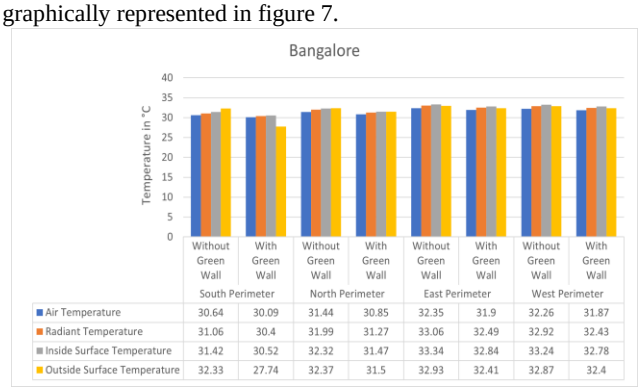

Figure 7: Perimeter Zone wise recorded temperatures before and after retrofitting a green wall in Bangalore.

Case 3:Hot and Dry

In Ahmadabad, the Outside Dry Bulb Temperature on the 19th of May was 34.27°C. The average reduction in Air Temperature and the Radiant Temperature on the 8th floor was 2.27°C and 2.77°C, respectively. The floors average interior surface temperatures lowered by 3.05°C and the exterior surface temperatures decreased by 5.32°C. Figure 8, Graphically compares the temperature levels before and after retrofitting a green wall.

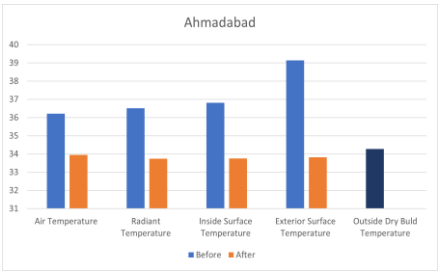

Figure 8: Graph of Average Temperature Levels before and After Retrofitting a green wall in Ahmadabad.

The maximum air temperature and radiant temperature decrease is seen on the Northern perimeter zone, with a temperature dip of 2.64°C and 3.19°C respectively, and the least decrease in the air and radiant temperature is seen on the Western Perimeter with a dip of 2.22°C and 2.61°C, respectively. The inside surface temperatures experience a maximum decline of 3.47°C on the Southern zone and the least reduction is observed on the Western

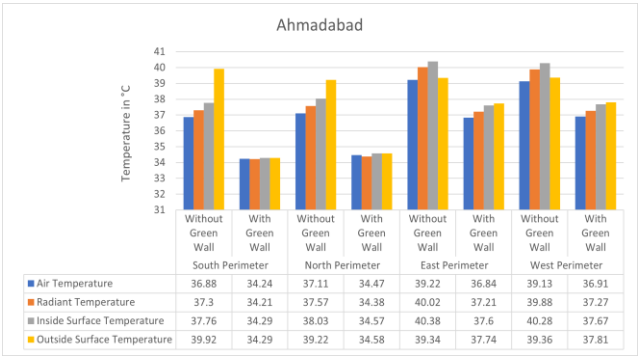

Figure 9: Perimeter Zone wise recorded temperatures before and after retrofitting a green wall in Ahmadabad.

Façade with a temperature decrease of 2.61°C. The exterior surface temperature reduction is the max on the southern wall with a decrease of 5.63°C and the least reduction is observed on the Western side with a reduction of 1.55°C. The difference in the temperatures on the various perimeter zones with and without the green wall is graphically represented in figure 9.

Case 4: Composite Climate

In Delhi, the Outside Dry Bulb Temperature on the 19th of May was 32.06°C. The average reduction in Air Temperature and the Radiant Temperature on the 8th floor was 1.9°C and 2.37°C, respectively. The floors average interior surface temperatures lowered by 2.7°C and the exterior surface temperatures decreased by 6.1°C. Figure 10, Graphically compares the temperature levels before and after retrofitting a green wall.

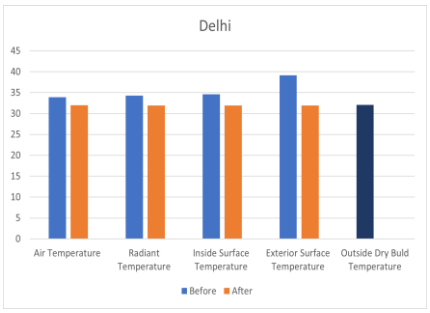

Figure 10: Graph of Average Temperature Levels before and After Retrofitting a green wall in Delhi.

The highest air temperature and radiant temperature decrease is seen on the Northern perimeter zone, with a temperature dip of 2.02°C and 2.22°C respectively, and the least decrease in the air and radiant temperature is seen on the Eastern Perimeter with a dip of 1.65°C and 1.95°C, respectively. The inside surface temperatures experience a maximum decline of 2.71°C on the Southern zone and the least reduction is observed on the Eastern Façade with a temperature decrease of 1.98°C. The exterior surface temperature reduction is the max on the southern wall with a decrease of 6.1°C and the least reduction is observed on the Eastern side with a reduction of 3.3°C. The difference in the temperatures on the various perimeter zones with and without the green wall is graphically represented in figure 11.

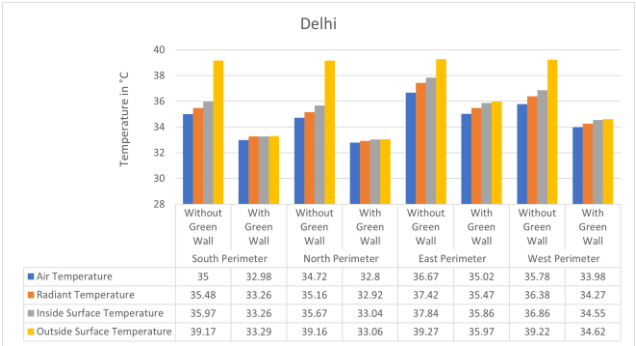

Figure 11: Perimeter Zone wise recorded temperatures before and after retrofitting a green wall in Delhi.

Case 5: Cold Climate

In Srinagar, the Outside Dry Bulb Temperature on the 19th of May was 14.24°C. The Air Temperature and the Radiant Temperature on the 8th floor increased by 1.46°C and 2.34°C, respectively. The floors average interior surface temperatures increased by 2.89°C and the exterior surface temperatures increased by 5.41°C. Figure 12, Graphically compares the temperature levels before and after retrofitting a green wall.

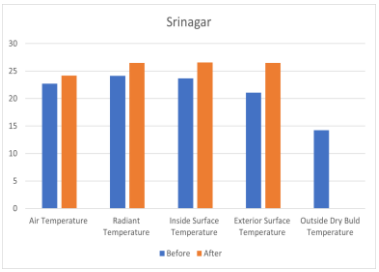

Figure 12: Graph of Average Temperature Levels before and After Retrofitting a green wall in Srinagar.

The maximum increase in air temperature and radiant temperature is seen on the Western perimeter zone, with a temperature rise of 1.77°C and 2.97°C respectively, the other perimeter zones experience a similar result with the least increase seen in the eastern perimeter zone with 1.63°C and 2.73°C.The inside surface temperatures experience a maximum increase of 3.46°C on the Eastern zone while the other perimeter zones also had a similar result. The maximum average exterior surface temperature increase is seen on the eastern façade with an increase of 6.41°C. The least increase is seen on the south perimeter with 5.27°C. The difference in the temperatures on the various perimeter zones with and without the green wall is graphically represented in figure 13.

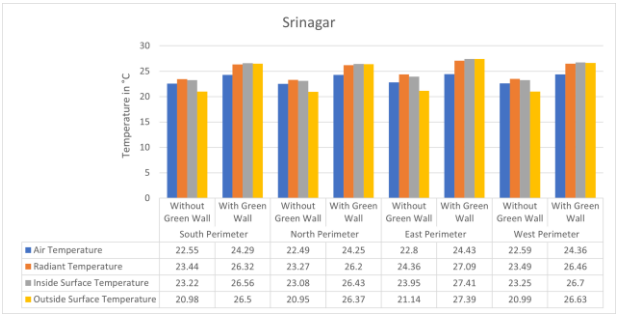

Figure 13: Perimeter Zone wise recorded temperatures before and after retrofitting a green wall in Srinagar.

Humidity

Although the green walls help in having a better ambient temperature within the building's environment and its surrounding, a major drawback of green walls are its potential to increase the humidity levels within the building and its surroundings. The Average increase in the humidity levels in the all the 5 cities is 5.26% with the maximum increase seen in Bangalore with a Temperate climate. The least increase is observed in Srinagar of cold climate with an increase of 3.27%. Figure 14 graphically represents the increase in humidity in the 5 mentioned cities.

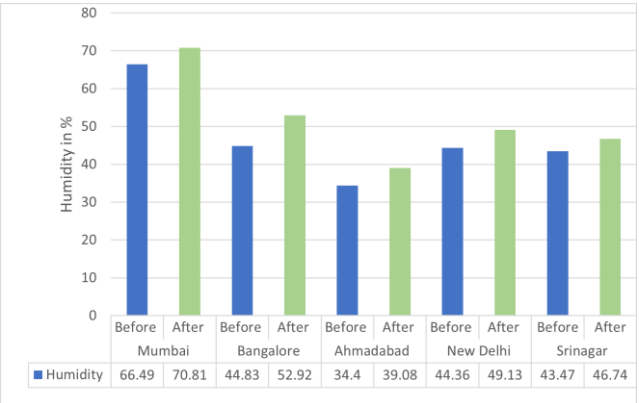

Figure 14: Graphically representation of change in the humidity levels in the 5 mentioned cities.

4. DISCUSSIONS

The simulation' results suggest that the green walls thermal impacts on the building and its surroundings are dependent on the climatic zone of the building site. In terms of temperature reduction pertaining to the interior of the building, the green wall seems to be the least effective in Bangalore with a temperate climate, where the Air temperature, Radiant Temperature and the interior surface temperature reduced by 0.89 °C, 1.09°C, 1.25°C, respectively. Whereas the results suggest that the green wall is most affective in Ahmadabad with Hot and Dry climate, where the Air temperature, Radiant Temperature, and the interior temperatures reduced by 2.27°C, 2.77°C and 3.05°C, respectively.

Though Ahmadabad and Delhi fall under two different climate zones, during the summer month of May, both the cities experience Excessive heat and very low air humidity which are the two most significant climatic indicators. The reduction in the temperatures in both of these two cities are the highest and similar.

Figure 15 shows the percentage wise change in the temperature levels in all the 5 climatic zones. It can be inferred that, a green wall is most effective in a hot and dry climate, where the average reduction in interior surface temperatures in Ahmadabad and Delhi is 3.05°C and 2.07°C. The effectiveness of green walls is reduced with the decrease in the outdoor dry bulb temperature and the increase in the humidity levels. This is evident in the case of Mumbai, when compared with the results of that of Ahmadabad and Delhi. In the case of Srinagar with a cold climate, it is observed that the results are different than the rest. Here the green wall is increasing the temperature levels within the building as well as the exterior wall temperature.

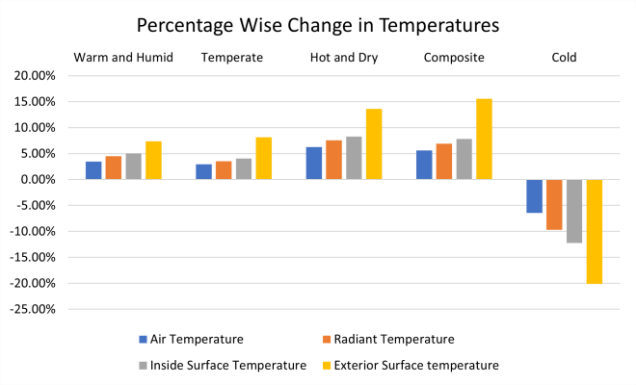

Figure 15: Changes in the temperature levels in the 5 climatic zones

The exterior walls of a high-rise building are one of the highest contributors of heat in an urban canyon. A bare plastered wall would re-radiate the suns heat into the surroundings which results in the central business districts of a city to have higher temperatures than the exterior of the city. Figure 15 suggests that the maximum change in the temperature levels is happening at the exterior surface, whereas in cities like Delhi, a reduction in the temperature by 15.58%. This would suggest that a green wall not only helps in having better interior ambient temperature levels but also contributes to having a better microclimate within a city.

The exteriors wall temperatures are reducing the most towards the southern façade. This is probably due to the direct solar heat gain on the south façade experienced by most of the buildings in the northern hemisphere. Because of the presence of a constant inbuilt irrigation system and the process of evapotranspiration undertaken by the plants, in all the climatic zones, it is observed that the humidity levels are increasing with the introduction of a green wall.

5. CONCLUSION

The results of the study have shown that the green walls help in reducing the internal temperatures in warmer regions and in a colder climate such as Srinagar a green wall helps in increasing the temperatures. This shows that they also act as insulation assisting to regulate a building's temperature, keeping it warmer in Winter and cooler in Summer. Results show that the green walls not only contribute to having better interior temperatures, but also contributes to regulating the temperatures on the building's exterior, which would lead to a better urban microclimate. Humidity is one of the key parameters in thermal comfort. When installing green walls to reduce temperature, attention must be given to ventilation and humidity control especially in cities such as Mumbai with an already prevailing humid climate.

The climate of the area is a crucial factor for the magnitude of the thermal effect of green walls in a building's microclimate. It is observed that areas with higher temperature and lower humidity (hot and dry regions), tend to benefit more from green walls.

REFERENCES

[1] S. R. A. G. Maryam Farhadian, "Thermal Performance Simulation of Hydroponic Green Wall in a Cold Climate," December 2019.

[2] Council on Tall Buildings and Urban Habitat, Council on Tall Buildings and Urban Habitat, 2014.

[3] R. F. D. M. F. d. R. Margarita-Niki Assimakopoulos, "GreenWall Design Approach Towards Energy Performance and Indoor Comfort Improvement: A Case Study in Athens," 2020.

[4] B. A. K. K. M. N. Sherine M. Wahba, "Effectiveness of Green Roofs and Green Walls on Energy Consumption and Indoor Comfort in Arid Climates," Civil Engineering Journal, October 2018.

[5] E. B. R. B. Rabah Djedjig, "INTEGRATION OF A GREEN ENVELOPE MODEL IN A TRANSIENT BUILDING SIMULATION PROGRAM AND EXPERIMENTAL COMPARISON".

[6] J. L. F. Gabriel Pérez, "Vertical Greenery Systems (VGS) for energy saving," *RenewableandSustainableEnergyReviews*, 2014.

[7] F. Y. F. Q. FengYang, "Summertime thermal and energy performance of a double-skin green facade: A case study in Shanghai," May 2018.

[8] A. L. K. K.-L. L. E. N. Tobi Eniolu Morakinyo, "Thermal benefits of vertical greening in a high-density city: Case study of," Hongkong, 2017.

[9] V. G. M. B. Jyotirmay Mathur, "Development of reference building models for India," *Journal of Building Engineering*, pp. 267-277, 2019.

Design Guidelines to achieve Optimum Shading Strategies for different window orientations across various geographical locations in India

Pranav Kishore
Center of Sustainable Built Environment, MSAP
Manipal Academy of Higher Education
Manipal, India
pranav.kishore@manipal.edu

Bysani Sathwik
Manipal School of Architecture and Planning
Manipal Academy of Higher Education
Manipal, India
bysanisatwik66@gmail.com

Vatsala Bajpai*
Center of Sustainable Built Environment, MSAP
Manipal Academy of Higher Education
Manipal, India
vatsala.bajpai09@gmail.com

Srijan Didwania
M .S. Addison & Associates
Phoenix, AZ, USA
srijandidwania@gmail.com

Stuthi Shetty
Center of Sustainable Built Environment, MSAP
Manipal Academy of Higher Education
Manipal, India
stuthisshetty@gmail.com

Pradeep Kini
Center of Sustainable Built Environment, MSAP
Manipal Academy of Higher Education
Manipal, India
pradeep.kini@manipal.edu

Abstract

Shading devices are used to maintain thermal and visual comfort in a space. They aid in reducing the cooling loads and visual glare by reducing the amount of direct solar radiation entering the space. However, it also leads to an increase in the heating load for a heating-dominated climate or winter season. Therefore, a universal solution or a one size fits all approach for the type and characteristics of shading devices cannot work for every space or building and will depend on the location and orientation. This study suggests optimum shading strategies like horizontal louvers, vertical louvers, inclined louvers and overhangs, their characteristics like the number of louvers and angle of inclination that are location and orientation specific for India. A shading device is an imperative design component for an architect and hence, the optimum solutions from this study can be used by an architect or designer for window design.

Keywords: shading device, angle of inclination, direct solar radiation, optimization

I. INTRODUCTION

A. UNSDGs and the built environment

The United Nations' 2030 agenda for Sustainable Development defined 17 sustainable development goals (UNSDGs) for a holistic approach towards sustainable development [1]. UNSDG 3: Good Health and Well Being, highlights the importance of healthy living and a healthy built environment. Indoor climates are of major importance because humans spend a majority of their time indoors, which in turn has major effects on health [2,3]. Goal 7: Affordable and Clean Energy and Goal 9: Industry, Innovation and Infrastructure, highlight how the built environment is a major contributor to energy consumption hence, energy efficiency is the need of the hour [4,5]. By the year 2022, it is expected that the Indian building and construction market will become the third-largest in the world [6].

B. Indian climate and shading devices

ECBC 2017 has classified the Indian climate into five climate zones [7]. Except for the regions classified under the cold climate typology, the other regions experience harsh summer. Hence, India can be characterized as a country that prominently has a warm climate [8]. The impact of heat from solar radiation that enters the buildings are mitigated using external shading devices. External shading devices also help control the amount of daylight and glare entering the building thereby aiding in maintaining visual comfort which in turn affects the productivity of the users [9, 10]. The use of daylight has been associated with a large set of benefits for architectural spaces, energy-saving and the occupants' visual comfort [11]. But in the field of view, certain limits have been defined for Luminance ratios. If the value is too high, the eyes would have difficulty adapting. Glare from daylight can cause visual discomfort and hamper the execution of a task (disability glare) or decreases the performance of the viewer (discomfort glare). Disability glare is caused due to bright light while discomfort glare is caused due to visual contrast [12]. Hence, it is imperative to control the glare and design an appropriate external shading device that can be a viable solution.

C. Indian building codes- shading device design

The National Building Code (NBC-2016) suggest ways to design shading device after fixing one parameter like the overhang depth and then the calculation of spacing and louvers [13]. BIS SP-41 has divided India into geographical zones and has given recommendations for the type of overhang [8]. However, location specific overhang design has not been specified.

II. LITERATURE STUDY

Daylight availability and daylight glare index has been used to calculate the type of fixed shading device required for a space [14]. Genetic optimization for an office building space with a south-facing window has been studied for the design of an optimal fixed shading device to minimize the overall energy consumption. Genetic optimization proved to be a viable tool for the designer to get the solutions [15]. UDI (useful daylight index) and DA (daylight autonomy) have been used as parameters to decide the effectiveness

IEECP'21, July 29-30, 2021, Silicon Valley, San Francisco, CA – USA

***DAI* : https://sci-index.com/DAI/2021.99101/IEECP/14904867**

of a shading device. Results obtained showed that the use of a shading device decreased the DA but increased the UDI for an indoor space [16]. For composite, hot and humid and hot and dry climatic zones appropriate shading devices can decrease the cooling loads and the polluting effects of the building [17].

III. GAP FINDING

Studies providing the type of shading device and its characteristics like, the number of louvers and angle of inclination according to the architect's need for various locations and orientations have not been conducted in the Indian context. Overhang design that can abide by the overhang depth requirements while optimizing the construction cost for a specific location and orientation has not been explicitly defined for India. The proposed study covers the above-mentioned aspects of shading device design.

IV. METHODOLOGY

A. Location and orientation selection

Twenty-nine states and six union territories (UTs) have been considered with five cities taken up from each state according to the demarcation as Central, North, East, West and South zones (C-N-E-W-S) [18]. Eight cardinal and sub cardinal directions have been considered for the orientation of the window for which the shading design needs to be provided. North (N) is taken as 0 degrees similarly, in clockwise direction North-East (NE) is 45˚, East (E) is 90˚, South-East (SE) is 135˚, South (S) is 180˚, South-West (SW) is 225˚, West (W) is 270˚ and North-West (NW) is 315˚ [19]. A window of 1200mm height (according to the standard window sizes in India) [13,20] and 900mm width (according to Indian ergonomics) [21] has been considered for shading device calculations in the algorithm but they can be changed according to the architect's need and specifications.

B. Solar position angles and shadow angles

Azimuth and altitude angles are the solar position angles that define the sun's position in the sky. They depend on the declination, latitude and hour angle [19]. The equations are mentioned below:

$$\text{Alititude} = \sin^{-1}(\sin Declination \times \sin Latitude + \cos Declination \times \cos Latitude \times \cos Hour\ angle) \dots\dots\dots\dots\dots (1)$$

$$\text{Azimuth} = \cos^{-1}[(\cos Latitude \times \sin Declination - \cos Declination \times \sin Latitude \times \cos Hour\ angle)/\cos Altitude] \dots\dots\dots\dots\dots\dots\dots\dots\dots\dots\dots\dots (2)$$

Horizontal shadow angle (HSA) equation (3) and Vertical shadow angle (VSA) equation (4) express the sun's position for a building façade in a specific orientation [8,19]. They are used for shading device calculation. Equations are as follows:

$$HSA = Azimuth - Orientation \quad \dots\dots\dots (3)$$

$$VSA = \tan^{-1}\frac{\tan Altitude}{\cos HSA} \quad \dots\dots\dots\dots (4)$$

The shadow angles have been used to calculate the required overhang depth to prevent the direct radiation component of the sun to enter through the window [9].

$$Horizontal\ overhang\ depth = \frac{Window\ height}{\tan VSA} \dots (5)$$

$$Vertical\ fin\ depth = \frac{Window\ width}{\tan HSA} \dots\dots\dots\dots (6)$$

The maximum depth of the required horizontal or vertical shading device has been calculated from 365 or 366 days of the year between the timings of 9 a.m. and 4 p.m. The depth of the required shading device has a constraint of 1200mm beyond which the algorithm does not give a solution. To obtain the maximum number of louvers possible, for horizontal louvers the height of the window is divided by a value taken as the minimum spacing between the louvers i.e., 250mm; and the window width is divided by 250mm to get the number of vertical louvers. For the angle of inclination calculations in the case of inclined louvers the maximum angle of inclination possible is calculated using the equation below:

$$Max.\ angle\ of\ inclination = \tan^{-1}\frac{Depth\ of\ louver}{Spacing\ between\ the\ louvers} \dots\dots\dots (7)$$

C. Shading device types and cost optimization

Eight overhang typologies have been considered in the study that is explained in the following table:

Table 1. Shading devices

S. No.	Overhang type
1	Horizontal shading device – one overhang
2	Vertical shading device – one fin
3	Horizontal inclined shading device – one overhang
4	Vertical inclined shading device – one fin
5	Horizontal louvers
6	Vertical louvers
7	Horizontal inclined louvers
8	Vertical inclined louvers

The type of shading device, the angle of inclination and the number of louvers has been taken as variables in the algorithm to get the optimum solution. The type of shading device varies from 1 to 8. The angle of inclination varies from 0 (which means normal to the wall) to the maximum value calculated from the above-mentioned formula in equation (7). To calculate the volume of the shading device, Reinforced Cement Concrete (RCC) has been considered as the building material with overhang/louver thickness of 50mm. A market study has been conducted and the cost of RCC per cubic meter is derived as 6000 INR. Excel solver has been used for optimization, keeping cost minimization as the objective function. Therefore, the results generated are first and second-best strategies for a certain location and orientation with their specifications i.e., angle of inclination and number of louvers that are feasible with minimal cost. Shading device depths have been rounded up to the nearest hundred millimeters (mm). The angle of inclination has been rounded into an integer and number louvers have been rounded up to the nearest whole number.

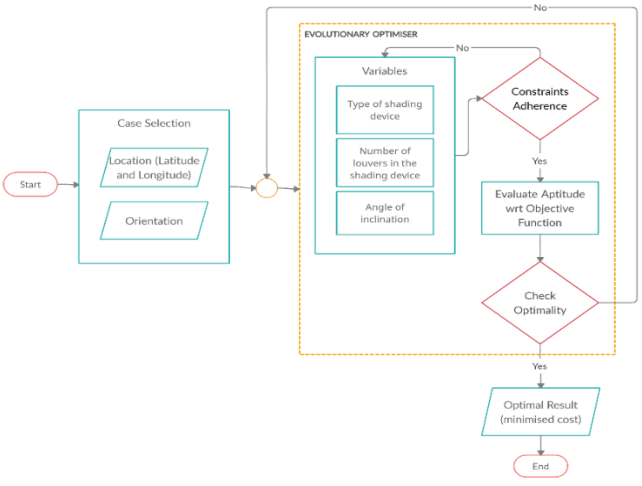

Figure 1. Process flowchart for the algorithm

V. RESULTS AND DISCUSSION

Table 2 and figures (graphs) 2,3,4 and 5 have been used for denoting the results. Graphs have been presented for 6 states and 6 UTs. The selection criteria of states for which graphs have been presented is based on a logic to cover all five climate zones defined by ECBC, where mostly one state belongs to a specific climate zone.

The graphs denote the type of overhang/louver (ref. Table 1) and the number of louvers on the primary y-axis. The secondary y-axis shows the overhang depth (in cm) and angle of inclination. The x-axis denotes the state, city and orientations in alphabetical order.

Figure 2. Graph showing best and next best shading device strategies for the states Karnataka and Kerala

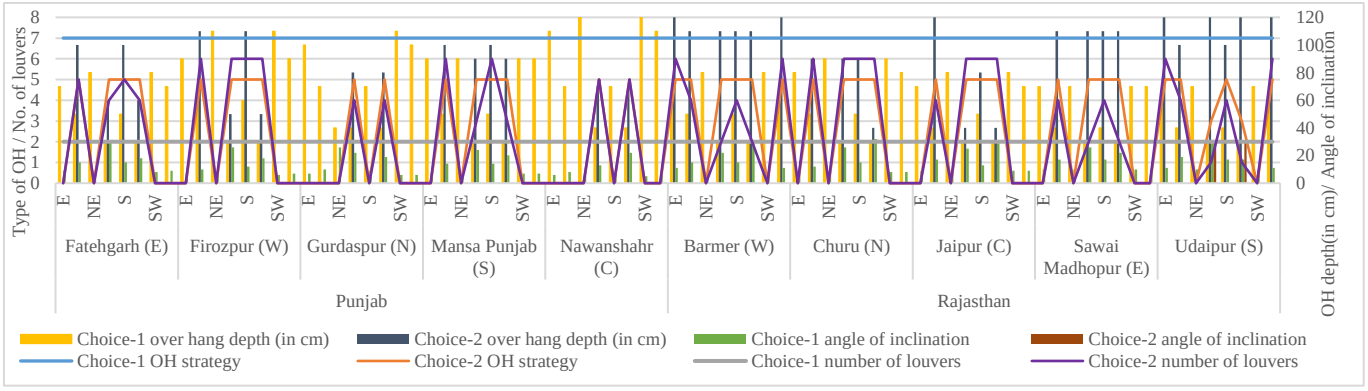

Figure 3. Graph showing best and next best shading device strategies for the states Punjab and Rajasthan

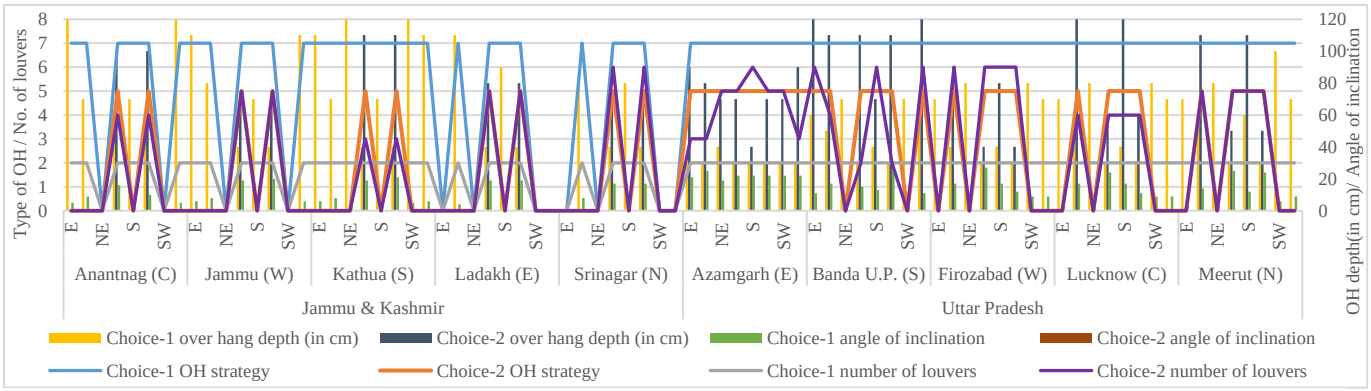

Figure 4. Graph showing best and next best shading device strategies for the states Jammu & Kashmir and Uttar Pradesh

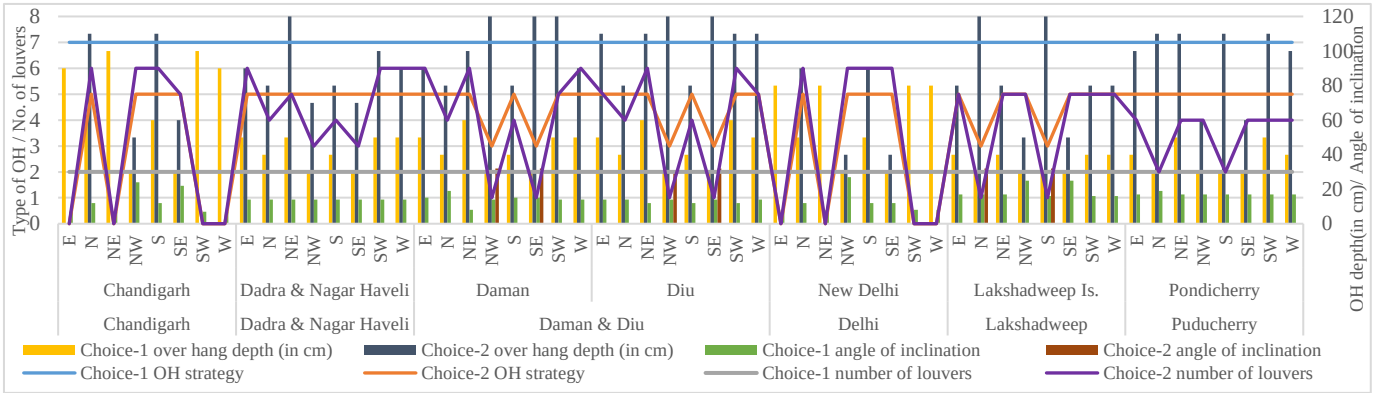

Figure 5. Graph showing best and next best shading device strategies for the six Union Territories

In Figure 2, the orientations at which the windows have been considered are arranged as E, N, NE, NW, S, SE, SW and W in the graphs. For the states of Karnataka (which has Bangalore which falls under the Temperate climate zone) and Kerala (Warm and Humid Climate zone), the best shading device strategy is 7 i.e., Horizontal inclined louvers and the number of louvers that would serve the purpose at minimal cost is 2. For Karnataka, the depth of horizontal inclined louvers varies from 300mm to 500mm and for Kerala it varies from 300mm to 400mm. The angle of inclination varies from 11 degrees to 26 degrees for Karnataka, while for Kerala it varies from 17 to 26 degrees as per the orientation. The next-best strategy for Karnataka is 5 i.e., horizontal louvers without any inclination for all five cities and eight orientations under consideration except for Gulbarga in the NW and SE orientations where the suitable strategy suggested is 3 i.e., one inclined horizontal overhang with a depth of 1200mm and angle inclination as 31 and 32 degrees respectively. For all the cases where horizontal louvers without any inclination (strategy 5) is the solution, the number of louvers varies from 2 to 6 and the louver depth varies from 400mm to 1200mm. The next-best strategy for Kerala is also 5 except for the N and S orientations in Calicut, Cochin and Quilon where one inclined horizontal overhang (strategy 3) is the most feasible solution with overhang depth as 1200mm and angle of inclination is 32 degrees. For the other cases where strategy 5 is the solution, the number of louvers vary from 3 to 6 and louver depths varies from 400mm to 1200mm.

In Figure 3, for the states of Punjab (Composite climatic zone) and Rajasthan (mostly Hot and Dry climatic zone), the best shading device strategy is 7 i.e., Horizontal inclined louvers and the number of louvers which would serve the purpose at minimal cost is 2. For Punjab, the depth of horizontal inclined louvers varies from 300mm to 1200mm while for Rajasthan it varies from 300mm to 900mm. The angle of inclination varies from 5 to 31 degrees for Punjab and 7 to 32 degrees for Rajasthan. The next-best strategy for Punjab is 5 i.e., horizontal louvers without any inclination for all cities of Punjab for the NW and SE window orientations with the louver depth varying from 500mm to 1200mm and the number of louvers varying from 4 to 6. For Rajasthan also the next best strategy 5 i.e., horizontal louvers without any inclination for all cities with window orientations as N, NW, S and SE. The louver depth varies from 400mm to 1200mm and the number of louvers varies from 2 to 6.

In Figure 4, for the cities of Jammu and Kashmir (Cold climatic zone) there is no shading strategy following the defined constraints of the algorithm that can completely shade the windows in all orientations except for the city of Kathua where shading strategy 7 i.e., Horizontal inclined louvers (having 2 louvers) is the optimum solution for all 8 orientations with the angle of inclination varying from 5 to 21 degrees and louver depth ranging from 700mm to 1200mm. The next-best strategy for all cities of Jammu and Kashmir under consideration is horizontal louvers without any inclination (strategy 5) for NW and SE window orientations. For Uttar Pradesh (Composite climatic zone) Horizontal inclined louvers (strategy 7) is the optimum solution for all cities and orientations with the number of louvers required being 2. The louver depths vary from 300mm to 1000mm and the angle of inclination varies from 6 to 31 degrees. The next-best shading strategy for both the states for orientations where solutions are possible is strategy 5 i.e., horizontal louvers without any inclination. For Jammu and Kashmir horizontal louvers without any inclination (strategy 5) gives the second-best solution for all 5 cities with window orientations as NW and SE with louver depths varying from 700mm to 1100mm. In Uttar Pradesh, the city of Azamgarh shows horizontal louvers without any inclination (strategy 5) as the second-best solution for all 8 orientations where the louver depth varies from 400mm to 900mm.

In figure 5, which represents the details of the optimum and next-best shading device strategies for 6 union territories (UTs). For all UTs the optimum shading strategy is 7 i.e., Horizontal inclined louvers (having 2 louvers) for all 8 orientations. For Chandigarh, the louver depths vary from 300mm to 1000mm and angle of inclination ranges from 7 to 24 degrees. For Dadra & Nagar Haveli, the louver depth varies from 300mm to 500mm and the angle of inclination of the louver is 14 degrees for windows in all orientations. For Daman and Diu, the louver depth varies from 400 mm to 600 mm and the angle of inclination ranges between 8 to 19 degrees. For New Delhi, the louver depth varies from 300 mm to 800 mm and the angle of inclination ranges from 8 to 27 degrees. For Lakshadweep Islands, the louver depth varies from 300 mm to 400 mm and the angle of inclination ranges from 16 to 25 degrees. For Puducherry, the louver depth varies from 300 mm to 500 mm and the angle of inclination ranges from 17 to 19 degrees. For Chandigarh, the next best shading strategy is 5 i.e., horizontal louvers without any inclination for N, NW, S and SE window orientations where the louver depth varies from 500 mm to 1100 mm and the number of louvers to used are 5 or 6. For Dadra & Nagar Haveli, horizontal louvers without any inclination (strategy 5) is the next-best shading strategy for all 8 orientations where the number of louvers varies between 3 to 6, the louver depth varies from 700 mm to 1200 mm. At Daman and Diu, for NW and SE window orientations the next-best strategy is 3 i.e., one inclined horizontal overhang with a depth of 1200mm and angle inclination as 32 degrees. For all other orientations in Daman and Diu horizontal louvers without any inclination (strategy 5) is the next-best shading strategy where the number of louvers ranges from 4 to 6 and the louver depth varies from 800 mm to 1200 mm. For New Delhi, the next best strategy for N, NW, S and SE window orientations is horizontal louvers without any inclination (strategy 5) where the number of louvers is 6 and the louver depth varies from 400 mm to 900 mm. At Lakshadweep Islands, for N and S window orientations the next-best shading strategy is 3 i.e., one inclined horizontal overhang with a depth of 1200mm and angle of inclination as 32 degrees; for all other window orientations the next-best shading strategy is horizontal louvers without any inclination (strategy 5) where the number of louvers is 5 and the louver depth varies from 500 mm to 800 mm. For Puducherry, the next-best shading strategy for all 8 window orientations is horizontal louvers without any inclination (strategy 5) where the number of louvers ranges from 2 to 4 and the louver depth is either 1000 mm or 1100 mm.

The following table (Table 2) shows results for optimum and next-best shading strategy for 8 different orientations and cities of the remaining 23 states. The results also provide information about the depth of the shading device, the angle of inclination and the number of louvers. Results for different states and cities (according to zones C-N-E-W-S) are represented in the order: **Shading device strategy number (refer Table 1) / shading device depth / number of louvers / angle of inclination of the shading device.**

The results mentioned in the table are the optimum solution for a window of height 1200 mm and width 900 mm which is a standard dimension of a window in the Indian scenario [13,20]. However, these results can be used to extract data for windows of different dimensions. For e.g.: - the first city for which the results have been presented in the table is Guntur, Andhra Pradesh. According to the results, the optimum shading strategy for a window (1200mm*900mm) is 7 i.e., horizontal inclined louvers where the number of louvers required is 2. For a North oriented window, the depth of the required louvers is 300 mm at an angle of inclination as 24 degrees. From the tabular data, it can be inferred that the 2 horizontal inclined louvers would be installed at a gap of 600 mm for a window height of 1200 mm. Hence, for a window height of 1800 mm the number of louvers required would be 3 placed at 600 mm distance from each other. In the case of a window height of 1500 mm, 2 louvers of 300 mm depth would not serve the purpose but 3 louvers placed at a 500 mm distance from each other would be a functional solution. A similar method can be followed for vertical shading devices. Hence, a functional overhang design can be derived from the results for any given window size.

Table 2. Results of 23 states and their respective cities for the 8 cardinal and sub cardinal orientations

State	City	Results	N	NE	E	SE	S	SW	W	NW
Andhra Pradesh	Guntur (C)	Choice 1 OH	7/300/2/24	7/500/2/15	7/400/2/16	7/300/2/16	7/300/2/20	7/500/2/15	7/400/2/16	7/300/2/24
		Choice 2 OH	5/900/3/0	5/900/6/0	5/800/6/0	5/1100/2/0	5/900/3/0	5/900/6/0	5/800/6/0	5/1100/2/0
	Vishakhapatnam (N)	Choice 1 OH	7/200/2/30	7/300/2/26	7/300/2/26	7/300/2/26	7/200/2/28	7/300/2/26	7/300/2/26	7/300/2/26
		Choice 2 OH	3/1100/1/31	5/900/3/0	5/1100/2/0	5/900/3/0	3/1100/1/32	5/900/3/0	5/1100/2/0	5/900/3/0
	Nellore (E)	Choice 1 OH	7/300/2/26	7/400/2/17	7/500/2/17	7/300/2/17	7/300/2/17	7/400/2/17	7/500/2/17	7/300/2/17
		Choice 2 OH	5/800/3/0	5/1200/4/0	5/1100/4/0	5/600/4/0	5/600/4/0	5/1200/4/0	5/1100/4/0	5/600/4/0
	Kurnool (W)	Choice 1 OH	7/300/2/23	7/500/2/14	7/400/2/17	7/300/2/17	7/300/2/21	7/500/2/12	7/400/2/17	7/300/2/17
		Choice 2 OH	5/500/5/0	5/1000/5/0	5/900/5/0	5/1100/2/0	5/500/5/0	5/1000/5/0	5/900/5/0	5/1100/2/0
	Chittoor (S)	Choice 1 OH	7/300/2/17	7/400/2/17	7/400/2/17	7/300/2/17	7/300/2/17	7/400/2/17	7/400/2/17	7/300/2/17
		Choice 2 OH	5/1200/2/0	5/900/5/0	5/700/6/0	5/400/6/0	5/400/6/0	5/900/5/0	5/700/6/0	5/400/6/0
Arunachal Pradesh	Doporijo (C)	Choice 1 OH	7/300/2/23	7/400/2/15	7/300/2/19	7/400/2/19	7/300/2/26	7/400/2/19	7/300/2/19	7/400/2/19
		Choice 2 OH	5/500/5/0	5/800/5/0	5/600/5/0	5/800/5/0	5/500/5/0	5/800/5/0	5/600/5/0	5/800/5/0
	Yingkiong (N)	Choice 1 OH	7/300/2/21	7/400/2/19	7/300/2/19	7/400/2/19	7/300/2/25	7/400/2/19	7/300/2/19	7/400/2/19
		Choice 2 OH	5/500/5/0	5/800/5/0	5/600/5/0	5/800/5/0	5/500/5/0	5/800/5/0	5/600/5/0	5/800/5/0
	Chonglong (E)	Choice 1 OH	7/500/2/14	7/300/2/22	7/800/2/8	7/1000/2/7	7/500/2/14	7/300/2/22	7/800/2/8	7/1000/2/7
		Choice 2 OH	5/1200/5/0	5/900/3/0	0/0/0/0	0/0/0/0	5/1000/6/0	5/900/3/0	0/0/0/0	0/0/0/0
	Upper Subansi (W)	Choice 1 OH	7/300/2/19	7/400/2/19	7/300/2/19	7/400/2/19	7/300/2/19	7/400/2/19	7/300/2/19	7/400/2/19
		Choice 2 OH	5/800/3/0	5/800/5/0	5/600/5/0	5/800/5/0	5/800/3/0	5/800/5/0	5/600/5/0	5/800/5/0
	Itanagar (S)	Choice 1 OH	7/300/2/32	7/300/2/22	7/300/2/22	7/300/2/22	7/300/2/22	7/300/2/22	7/300/2/22	7/300/2/22
		Choice 2 OH	5/800/3/0	5/1200/3/0	5/700/4/0	5/900/4/0	5/600/4/0	5/900/4/0	5/700/4/0	5/900/4/0
Assam	Tezpur (C)	Choice 1 OH	7/300/2/17	7/300/2/26	7/200/2/28	7/300/2/26	7/300/2/26	7/300/2/26	7/300/2/26	7/400/2/17
		Choice 2 OH	5/400/6/0	5/600/6/0	5/700/4/0	5/900/4/0	5/600/4/0	5/900/4/0	5/700/4/0	5/900/4/0
	Dibrugarh (N)	Choice 1 OH	7/300/2/22	7/400/2/19	7/300/2/19	7/400/2/19	7/300/2/19	7/400/2/19	7/300/2/19	7/400/2/19
		Choice 2 OH	5/600/4/0	5/1000/4/0	5/600/5/0	5/800/5/0	5/600/4/0	5/1000/4/0	5/600/5/0	5/800/5/0
	Jorhat (E)	Choice 1 OH	7/300/2/19	7/300/2/22	7/300/2/22	7/300/2/22	7/300/2/22	7/300/2/22	7/300/2/22	7/300/2/22
		Choice 2 OH	5/800/3/0	5/1200/3/0	5/700/4/0	5/900/4/0	5/600/4/0	5/900/4/0	5/700/4/0	5/900/4/0
	Barpeta (W)	Choice 1 OH	7/300/2/22	7/300/2/22	7/300/2/22	7/300/2/22	7/300/2/22	7/300/2/22	7/300/2/22	7/300/2/22
		Choice 2 OH	5/600/4/0	5/700/5/0	5/900/3/0	5/700/5/0	5/800/3/0	5/700/5/0	5/900/3/0	5/700/5/0
	Silchar (S)	Choice 1 OH	7/300/2/22	7/400/2/22	7/300/2/22	7/400/2/22	7/300/2/22	7/400/2/22	7/300/2/22	7/400/2/22
		Choice 2 OH	5/1100/2/0	5/700/5/0	5/900/3/0	5/700/5/0	5/1100/2/0	5/700/5/0	5/900/3/0	5/700/5/0
Bihar	Patna (C)	Choice 1 OH	7/300/2/15	7/300/2/24	7/600/2/12	7/1000/2/6	7/700/2/9	7/300/2/25	7/300/2/25	7/400/2/19
		Choice 2 OH	5/1100/2/0	5/700/5/0	5/900/3/0	5/700/5/0	5/1100/2/0	5/700/5/0	5/900/3/0	5/700/5/0
	Darbhanga (N)	Choice 1 OH	7/300/2/22	7/300/2/22	7/300/2/22	7/300/2/22	7/300/2/22	7/300/2/22	7/300/2/22	7/300/2/22
		Choice 2 OH	5/600/4/0	5/700/5/0	5/900/3/0	5/700/5/0	5/600/4/0	5/700/5/0	5/900/3/0	5/1200/3/0
	Siwan (E)	Choice 1 OH	7/300/2/22	7/300/2/22	7/300/2/22	7/400/2/17	7/300/2/29	7/400/2/19	7/300/2/22	7/300/2/22
		Choice 2 OH	5/800/3/0	5/700/5/0	5/900/3/0	5/700/5/0	5/600/4/0	5/700/5/0	5/900/3/0	5/700/5/0
	Katihar (W)	Choice 1 OH	7/300/2/22	7/400/2/14	7/300/2/24	7/400/2/22	7/300/2/22	7/400/2/22	7/300/2/22	7/400/2/22
		Choice 2 OH	5/1100/2/0	5/700/5/0	5/900/3/0	5/700/5/0	5/1100/2/0	5/700/5/0	5/900/3/0	5/1200/3/0
	Nawada (S)	Choice 1 OH	7/300/2/15	7/400/2/12	7/300/2/23	7/400/2/21	7/300/2/17	7/400/2/17	7/300/2/25	7/400/2/22
		Choice 2 OH	5/1100/2/0	5/700/5/0	5/900/3/0	5/700/5/0	5/1100/2/0	5/700/5/0	5/900/3/0	5/700/5/0
Chhattisgarh	Raipur (C)	Choice 1 OH	7/400/2/20	7/600/2/12	7/500/2/13	7/300/2/13	7/400/2/13	7/600/2/12	7/500/2/14	7/300/2/20
		Choice 2 OH	5/1100/3/0	5/1100/6/0	5/1000/6/0	3/1200/1/29	5/1100/3/0	5/1100/6/0	5/1000/6/0	3/1200/1/32
	Baikunthpur (N)	Choice 1 OH	7/300/2/14	7/400/2/14	7/300/2/23	7/400/2/19	7/300/2/19	7/400/2/19	7/300/2/23	7/400/2/19
		Choice 2 OH	3/1200/1/32	5/800/4/0	5/500/5/0	5/800/4/0	3/1200/1/29	5/800/4/0	5/500/5/0	5/800/4/0
	Raigarh (E)	Choice 1 OH	7/300/2/17	7/300/2/20	7/300/2/20	7/300/2/20	7/300/2/17	7/300/2/17	7/300/2/17	7/300/2/17
		Choice 2 OH	3/1200/1/29	5/600/5/0	5/800/3/0	5/1000/3/0	3/1200/1/29	5/600/5/0	5/800/3/0	5/1000/3/0
	Kawardha (W)	Choice 1 OH	7/400/2/18	7/600/2/10	7/500/2/14	7/300/2/14	7/400/2/14	7/600/2/12	7/500/2/14	7/300/2/14
		Choice 2 OH	5/700/5/0	5/1100/6/0	5/1000/6/0	3/1200/1/31	5/700/5/0	5/1100/6/0	5/1000/6/0	3/1200/1/30
	Bijapur (S)	Choice 1 OH	7/300/2/18	7/500/2/14	7/500/2/14	7/300/2/14	7/300/2/20	7/500/2/14	7/500/2/14	7/300/2/14
		Choice 2 OH	5/1000/3/0	5/1200/5/0	5/1000/5/0	3/1200/1/32	5/600/5/0	5/1200/5/0	5/1000/5/0	3/1200/1/32
Goa	Panjim (C)	Choice 1 OH	7/300/2/22	7/500/2/15	7/400/2/17	7/300/2/17	7/300/2/23	7/500/2/13	7/400/2/17	7/300/2/17
		Choice 2 OH	5/500/5/0	5/1000/5/0	5/1100/4/0	5/1100/2/0	5/500/5/0	5/1000/5/0	5/1100/4/0	5/1100/2/0
	Marmagao (S)	Choice 1 OH	7/300/2/22	7/500/2/15	7/400/2/17	7/300/2/17	7/300/2/23	7/500/2/13	7/400/2/17	7/300/2/17
		Choice 2 OH	5/500/5/0	5/1000/5/0	5/1100/4/0	5/1100/2/0	5/500/5/0	5/1000/5/0	5/1100/4/0	5/1100/2/0
Gujarat	Ahemadabad (C)	Choice 1 OH	7/400/2/19	7/600/2/11	7/600/2/11	7/300/2/16	7/400/2/14	7/600/2/11	7/600/2/11	7/400/2/11
		Choice 2 OH	5/1000/4/0	5/1200/6/0	5/1100/6/0	3/1200/1/30	5/1200/3/0	5/1200/6/0	5/1100/6/0	3/1200/1/32
	Palanpur (N)	Choice 1 OH	7/400/2/16	7/700/2/10	7/600/2/10	7/300/2/28	7/400/2/16	7/700/2/10	7/600/2/10	7/300/2/21
		Choice 2 OH	5/1000/4/0	5/1200/6/0	5/1100/6/0	3/1200/1/31	5/600/6/0	5/1200/6/0	5/1100/6/0	3/1200/1/31
	Vadodara (E)	Choice 1 OH	7/300/2/22	7/600/2/11	7/500/2/14	7/300/2/14	7/300/2/22	7/600/2/11	7/500/2/14	7/300/2/14
		Choice 2 OH	5/700/5/0	5/1200/6/0	5/1000/6/0	3/1200/1/32	5/700/5/0	5/1200/6/0	5/1000/6/0	3/1200/1/32
	Jamnagar (W)	Choice 1 OH	7/300/2/22	7/600/2/11	7/500/2/14	7/300/2/14	7/300/2/22	7/600/2/11	7/500/2/14	7/300/2/14
		Choice 2 OH	5/1200/3/0	5/1200/6/0	5/1000/6/0	3/1200/1/32	5/700/5/0	5/1200/6/0	5/1000/6/0	3/1200/1/30
	Bhavnagar (S)	Choice 1 OH	7/400/2/14	7/600/2/12	7/500/2/13	7/300/2/13	7/400/2/13	7/600/2/12	7/500/2/13	7/300/2/13
		Choice 2 OH	5/700/5/0	5/1100/6/0	5/1000/6/0	3/1200/1/30	5/700/5/0	5/1100/6/0	5/1000/6/0	3/1200/1/31
Haryana	Rohtak (C)	Choice 1 OH	7/500/2/14	7/300/2/28	7/400/2/16	7/700/2/10	7/600/2/10	7/300/2/21	7/300/2/22	7/600/2/11
		Choice 2 OH	5/1100/5/0	0/0/0/0	0/0/0/0	5/500/5/0	5/1100/5/0	0/0/0/0	0/0/0/0	5/500/5/0
	Kaithal (N)	Choice 1 OH	7/600/2/10	7/1000/2/7	7/800/2/8	7/300/2/20	7/500/2/14	7/1000/2/7	7/800/2/8	7/300/2/22
		Choice 2 OH	5/1200/5/0	0/0/0/0	0/0/0/0	5/900/3/0	5/1200/5/0	0/0/0/0	0/0/0/0	5/900/3/0
	Panipat (E)	Choice 1 OH	7/500/2/14	7/900/2/7	7/800/2/8	7/300/2/21	7/500/2/14	7/900/2/7	7/800/2/8	7/300/2/23
		Choice 2 OH	5/1200/5/0	0/0/0/0	0/0/0/0	5/900/3/0	5/1200/5/0	0/0/0/0	0/0/0/0	5/900/3/0
	Sirsa (W)	Choice 1 OH	7/400/2/17	7/800/2/9	7/700/2/9	7/300/2/20	7/400/2/17	7/800/2/9	7/700/2/9	7/300/2/31
		Choice 2 OH	5/1200/4/0	0/0/0/0	0/0/0/0	5/600/4/0	5/1200/4/0	0/0/0/0	0/0/0/0	5/600/4/0
	Rewari (S)	Choice 1 OH	7/500/2/15	7/800/2/8	7/800/2/8	7/300/2/25	7/500/2/12	7/800/2/8	7/800/2/8	7/300/2/23
		Choice 2 OH	5/900/6/0	0/0/0/0	0/0/0/0	5/400/6/0	5/900/6/0	0/0/0/0	0/0/0/0	5/400/6/0

State	City	Results	N	NE	E	SE	S	SW	W	NW
Himachal Pradesh	Mandi (C)	Choice 1 OH	7/700/2/8	7/1100/2/6	7/900/2/7	7/400/2/20	7/700/2/9	7/1100/2/6	7/900/2/7	7/400/2/15
		Choice 2 OH	5/1200/6/0	0/0/0/0	0/0/0/0	5/800/4/0	5/1200/6/0	0/0/0/0	0/0/0/0	5/800/4/0
	Chamba (N)	Choice 1 OH	7/700/2/10	7/1200/2/5	7/1200/2/5	7/400/2/22	7/700/2/8	7/1200/2/5	7/1100/2/6	7/400/2/16
		Choice 2 OH	0/0/0/0	0/0/0/0	0/0/0/0	5/700/5/0	0/0/0/0	0/0/0/0	0/0/0/0	5/700/5/0
	Kullu (E)	Choice 1 OH	7/700/2/10	7/1100/2/6	7/1000/2/6	7/400/2/12	7/600/2/11	7/1100/2/6	7/1000/2/6	7/400/2/22
		Choice 2 OH	0/0/0/0	0/0/0/0	0/0/0/0	5/800/4/0	5/1200/6/0	0/0/0/0	0/0/0/0	5/800/4/0
	Dharamsala (W)	Choice 1 OH	7/700/2/9	7/500/2/25	7/1100/2/6	7/400/2/15	7/700/2/10	7/500/2/25	7/1100/2/6	7/400/2/22
		Choice 2 OH	0/0/0/0	0/0/0/0	0/0/0/0	5/1100/3/0	0/0/0/0	0/0/0/0	0/0/0/0	5/1100/3/0
	Shimla (S)	Choice 1 OH	7/600/2/9	7/1100/2/6	7/900/2/7	7/300/2/21	7/600/2/12	7/1100/2/6	7/900/2/7	7/300/2/19
		Choice 2 OH	5/1100/6/0	0/0/0/0	0/0/0/0	5/500/6/0	5/1100/6/0	0/0/0/0	0/0/0/0	5/500/6/0
Jharkhand	Ranchi (C)	Choice 1 OH	7/300/2/19	7/400/2/22	7/700/2/8	7/1200/2/5	7/1100/2/6	7/400/2/16	7/700/2/10	7/1100/2/6
		Choice 2 OH	3/1200/1/29	5/800/4/0	5/500/5/0	5/800/4/0	3/1200/1/30	5/800/4/0	5/500/5/0	5/800/4/0
	Hazaribag (N)	Choice 1 OH	7/300/2/16	7/400/2/16	7/300/2/21	7/400/2/21	7/300/2/21	7/400/2/21	7/300/2/21	7/400/2/21
		Choice 2 OH	5/700/3/0	5/1100/3/0	5/900/3/0	5/1100/3/0	5/700/3/0	5/1100/3/0	5/900/3/0	5/1100/3/0
	Dumka (E)	Choice 1 OH	7/300/2/21	7/400/2/21	7/300/2/21	7/400/2/21	7/300/2/21	7/400/2/21	7/300/2/21	7/400/2/21
		Choice 2 OH	3/1200/1/32	5/1100/3/0	5/900/3/0	5/1100/3/0	3/1200/1/32	5/1100/3/0	5/900/3/0	5/1100/3/0
	Latehar (W)	Choice 1 OH	7/300/2/21	7/400/2/21	7/300/2/21	7/400/2/21	7/300/2/21	7/400/2/21	7/300/2/21	7/400/2/21
		Choice 2 OH	5/700/3/0	5/800/4/0	5/500/5/0	5/800/4/0	5/700/3/0	5/800/4/0	5/500/5/0	5/800/4/0
	Chaibasa (S)	Choice 1 OH	7/300/2/21	7/400/2/21	7/300/2/26	7/400/2/19	7/300/2/19	7/400/2/19	7/300/2/22	7/400/2/19
		Choice 2 OH	3/1200/1/30	5/800/4/0	5/500/5/0	5/800/4/0	3/1200/1/31	5/800/4/0	5/500/5/0	5/800/4/0
Madhya Pradesh	Sagar (C)	Choice 1 OH	7/300/2/24	7/500/2/12	7/400/2/14	7/300/2/14	7/300/2/14	7/400/2/16	7/400/2/16	7/300/2/16
		Choice 2 OH	5/1000/4/0	5/1200/6/0	5/1100/6/0	5/700/3/0	5/1000/4/0	5/1200/6/0	5/1100/6/0	5/700/3/0
	Gwalior (N)	Choice 1 OH	7/400/2/17	7/700/2/10	7/700/2/10	7/300/2/25	7/500/2/15	7/800/2/8	7/700/2/9	7/300/2/26
		Choice 2 OH	5/900/5/0	0/0/0/0	0/0/0/0	5/1100/2/0	5/900/5/0	0/0/0/0	0/0/0/0	5/1100/2/0
	Umaria (E)	Choice 1 OH	7/400/2/19	7/600/2/11	7/600/2/11	7/300/2/18	7/400/2/18	7/600/2/11	7/600/2/11	7/300/2/29
		Choice 2 OH	5/800/5/0	5/1200/6/0	5/1100/6/0	5/700/3/0	5/1000/4/0	5/1200/6/0	5/1100/6/0	5/700/3/0
	Indore (W)	Choice 1 OH	7/300/2/22	7/600/2/11	7/500/2/14	7/300/2/14	7/300/2/22	7/600/2/11	7/500/2/12	7/300/2/27
		Choice 2 OH	5/600/6/0	5/1200/6/0	5/1000/6/0	3/1200/1/29	5/900/4/0	5/1200/6/0	5/1000/6/0	3/1200/1/29
	Betul (S)	Choice 1 OH	7/400/2/19	7/600/2/10	7/500/2/14	7/300/2/14	7/400/2/14	7/600/2/12	7/500/2/13	7/300/2/13
		Choice 2 OH	5/700/5/0	5/1100/6/0	5/1000/6/0	3/1200/1/32	5/700/5/0	5/1100/6/0	5/1000/6/0	3/1200/1/32
Maharashtra	Parbhani (C)	Choice 1 OH	7/300/2/24	7/300/2/25	7/500/2/15	7/800/2/8	7/700/2/9	7/300/2/26	7/400/2/19	7/600/2/11
		Choice 2 OH	5/500/6/0	5/1000/6/0	5/900/6/0	5/700/3/0	5/1000/3/0	5/1200/5/0	5/900/6/0	5/700/3/0
	Jalgaon (N)	Choice 1 OH	7/400/2/14	7/600/2/12	7/500/2/13	7/300/2/13	7/400/2/13	7/600/2/12	7/500/2/13	7/300/2/13
		Choice 2 OH	5/1100/3/0	5/1100/6/0	5/1100/5/0	3/1200/1/29	5/1100/3/0	5/1100/6/0	5/1100/5/0	3/1200/1/31
	Chandrapur (E)	Choice 1 OH	7/400/2/13	7/500/2/13	7/500/2/13	7/300/2/13	7/400/2/13	7/500/2/13	7/500/2/13	7/300/2/13
		Choice 2 OH	5/800/4/0	5/1000/6/0	5/900/6/0	5/700/3/0	5/800/4/0	5/1200/5/0	5/900/6/0	5/700/3/0
	Mumbai (W)	Choice 1 OH	7/300/2/22	7/500/2/14	7/500/2/14	7/300/2/14	7/300/2/18	7/500/2/14	7/500/2/14	7/300/2/14
		Choice 2 OH	5/600/5/0	5/1200/5/0	5/900/6/0	5/700/3/0	5/1000/3/0	5/1200/5/0	5/900/6/0	5/700/3/0
	Satara (S)	Choice 1 OH	7/300/2/25	7/500/2/15	7/400/2/16	7/300/2/16	7/300/2/25	7/500/2/15	7/400/2/17	7/300/2/17
		Choice 2 OH	5/700/4/0	5/900/6/0	5/800/6/0	3/1200/1/31	5/700/4/0	5/900/6/0	5/800/6/0	3/1200/1/32
Manipur	Imphal (C)	Choice 1 OH	7/300/2/17	7/400/2/17	7/300/2/20	7/400/2/20	7/300/2/20	7/400/2/20	7/300/2/20	7/400/2/20
		Choice 2 OH	5/1100/2/0	5/700/5/0	5/900/3/0	5/700/5/0	5/1100/2/0	5/700/5/0	5/900/3/0	5/700/5/0
	Senapati (N)	Choice 1 OH	7/300/2/22	7/400/2/22	7/300/2/22	7/400/2/22	7/300/2/22	7/400/2/22	7/300/2/22	7/400/2/22
		Choice 2 OH	5/1100/2/0	5/700/5/0	5/900/3/0	5/700/5/0	5/1100/2/0	5/700/5/0	5/900/3/0	5/700/5/0
	Kamjong (E)	Choice 1 OH	7/300/2/22	7/400/2/22	7/300/2/22	7/400/2/22	7/300/2/22	7/400/2/22	7/300/2/22	7/400/2/22
		Choice 2 OH	5/1100/2/0	5/700/5/0	5/900/3/0	5/700/5/0	5/1100/2/0	5/700/5/0	5/900/3/0	5/700/5/0
	Tamenglong (W)	Choice 1 OH	7/300/2/20	7/400/2/20	7/300/2/20	7/400/2/20	7/300/2/20	7/400/2/20	7/300/2/20	7/400/2/20
		Choice 2 OH	5/1100/2/0	5/700/5/0	5/900/3/0	5/700/5/0	5/1100/2/0	5/700/5/0	5/900/3/0	5/700/5/0
	Churachandpur (S)	Choice 1 OH	7/200/2/37	7/300/2/26	7/300/2/26	7/300/2/26	7/200/2/26	7/300/2/26	7/300/2/26	7/300/2/26
		Choice 2 OH	3/1200/1/32	5/1100/3/0	5/900/3/0	5/1100/3/0	3/1200/1/32	5/1100/3/0	5/900/3/0	5/1100/3/0
Meghalaya	West-khasi-hills(C)	Choice 1 OH	7/300/2/22	7/400/2/22	7/300/2/22	7/400/2/22	7/300/2/22	7/400/2/22	7/300/2/22	7/400/2/22
		Choice 2 OH	5/1100/2/0	5/700/5/0	5/900/3/0	5/700/5/0	5/1100/2/0	5/700/5/0	5/900/3/0	5/700/5/0
	Ribhoi (N)	Choice 1 OH	7/300/2/22	7/400/2/22	7/300/2/22	7/400/2/22	7/300/2/22	7/400/2/22	7/300/2/22	7/400/2/22
		Choice 2 OH	5/1100/2/0	5/700/5/0	5/900/3/0	5/700/5/0	5/1100/2/0	5/700/5/0	5/900/3/0	5/700/5/0
	Jaintia Hills (E)	Choice 1 OH	7/300/2/22	7/400/2/22	7/300/2/22	7/400/2/22	7/300/2/22	7/400/2/22	7/300/2/22	7/400/2/22
		Choice 2 OH	5/1100/2/0	5/700/5/0	5/900/3/0	5/700/5/0	5/1100/2/0	5/700/5/0	5/900/3/0	5/700/5/0
	Garo Hills (W)	Choice 1 OH	7/300/2/26	7/400/2/22	7/300/2/22	7/400/2/22	7/300/2/22	7/400/2/22	7/300/2/22	7/400/2/22
		Choice 2 OH	5/1100/2/0	5/700/5/0	5/900/3/0	5/700/5/0	5/1100/2/0	5/700/5/0	5/900/3/0	5/700/5/0
	East-khasi-hills (S)	Choice 1 OH	7/300/2/22	7/400/2/22	7/300/2/22	7/400/2/22	7/300/2/22	7/400/2/22	7/300/2/22	7/400/2/22
		Choice 2 OH	5/1100/2/0	5/700/5/0	5/900/3/0	5/700/5/0	5/1100/2/0	5/700/5/0	5/900/3/0	5/700/5/0
Mizoram	Lunglei (C)	Choice 1 OH	7/300/2/26	7/400/2/22	7/300/2/22	7/400/2/22	7/300/2/22	7/400/2/22	7/300/2/22	7/400/2/22
		Choice 2 OH	3/1200/1/32	5/800/4/0	5/500/5/0	5/800/4/0	3/1200/1/30	5/800/4/0	5/500/5/0	5/800/4/0
	Aizawl (N)	Choice 1 OH	7/300/2/22	7/400/2/22	7/300/2/22	7/400/2/22	7/300/2/22	7/400/2/22	7/300/2/22	7/400/2/22
		Choice 2 OH	5/700/3/0	5/800/4/0	5/500/5/0	5/800/4/0	5/700/3/0	5/800/4/0	5/500/5/0	5/800/4/0
	Champhoi (E)	Choice 1 OH	7/300/2/21	7/400/2/21	7/300/2/21	7/400/2/21	7/300/2/21	7/400/2/21	7/300/2/21	7/400/2/21
		Choice 2 OH	3/1200/1/30	5/800/4/0	5/500/5/0	5/800/4/0	3/1200/1/30	5/800/4/0	5/500/5/0	5/800/4/0
	Mamit (W)	Choice 1 OH	7/300/2/15	7/400/2/15	7/300/2/21	7/400/2/21	7/300/2/21	7/400/2/21	7/300/2/21	7/400/2/21
		Choice 2 OH	5/700/3/0	5/1100/3/0	5/900/3/0	5/1100/3/0	5/700/3/0	5/1100/3/0	5/900/3/0	5/1100/3/0
	Saiha (S)	Choice 1 OH	7/300/2/17	7/400/2/17	7/300/2/26	7/400/2/19	7/300/2/19	7/400/2/19	7/300/2/24	7/400/2/19
		Choice 2 OH	3/1200/1/32	5/800/4/0	5/500/5/0	5/800/4/0	3/1200/1/32	5/800/4/0	5/500/5/0	5/800/4/0

State	City	Results	N	NE	E	SE	S	SW	W	NW
Nagaland	Zunheboto (C)	Choice 1 OH	7/300/2/22	7/400/2/22	7/300/2/22	7/400/2/22	7/300/2/22	7/400/2/22	7/300/2/21	7/400/2/21
		Choice 2 OH	5/600/4/0	5/700/5/0	5/900/3/0	5/700/5/0	5/600/4/0	5/700/5/0	5/900/3/0	5/700/5/0
	Mon (N)	Choice 1 OH	7/300/2/22	7/300/2/22	7/300/2/22	7/300/2/22	7/300/2/22	7/300/2/22	7/300/2/22	7/300/2/22
		Choice 2 OH	5/600/4/0	5/700/5/0	5/900/3/0	5/700/5/0	5/600/4/0	5/700/5/0	5/900/3/0	5/700/5/0
	Kiphire (E)	Choice 1 OH	7/300/2/22	7/400/2/22	7/300/2/22	7/400/2/22	7/300/2/22	7/400/2/22	7/300/2/22	7/400/2/22
		Choice 2 OH	5/600/4/0	5/700/5/0	5/900/3/0	5/700/5/0	5/600/4/0	5/700/5/0	5/900/3/0	5/700/5/0
	Mokokchung (W)	Choice 1 OH	7/300/2/20	7/300/2/22	7/300/2/22	7/300/2/22	7/300/2/22	7/300/2/22	7/300/2/22	7/300/2/22
		Choice 2 OH	5/1200/2/0	5/700/5/0	5/900/3/0	5/700/5/0	5/1200/2/0	5/700/5/0	5/900/3/0	5/700/5/0
	Kohima (S)	Choice 1 OH	7/300/2/22	7/400/2/22	7/300/2/22	7/400/2/22	7/300/2/22	7/400/2/22	7/300/2/22	7/400/2/22
		Choice 2 OH	5/1100/2/0	5/700/5/0	5/900/3/0	5/700/5/0	5/1100/2/0	5/700/5/0	5/900/3/0	5/700/5/0
Odisha	Deogarh (C)	Choice 1 OH	7/500/2/17	7/700/2/10	7/600/2/11	7/300/2/31	7/500/2/15	7/800/2/8	7/600/2/11	7/300/2/28
		Choice 2 OH	3/1200/1/31	5/500/6/0	5/400/6/0	5/500/6/0	3/1200/1/31	5/500/6/0	5/400/6/0	5/500/6/0
	Baleshwar (N)	Choice 1 OH	7/300/2/28	7/300/2/19	7/300/2/19	7/300/2/19	7/300/2/19	7/300/2/19	7/300/2/19	7/300/2/19
		Choice 2 OH	3/1200/1/31	5/500/6/0	5/400/6/0	3/1200/1/31	3/1200/1/31	5/500/6/0	5/400/6/0	3/1200/1/31
	Cuttack (E)	Choice 1 OH	7/200/2/26	7/300/2/26	7/300/2/26	7/300/2/26	7/200/2/26	7/300/2/26	7/300/2/26	7/300/2/26
		Choice 2 OH	3/1200/1/29	5/500/6/0	5/400/6/0	5/500/6/0	3/1200/1/29	5/500/6/0	5/400/6/0	5/500/6/0
	Sonepur (W)	Choice 1 OH	7/300/2/26	7/300/2/26	7/300/2/26	7/300/2/26	7/300/2/26	7/300/2/26	7/300/2/26	7/300/2/26
		Choice 2 OH	3/1200/1/29	5/500/6/0	5/400/6/0	5/500/6/0	3/1200/1/29	5/500/6/0	5/400/6/0	5/500/6/0
	Rayagada (S)	Choice 1 OH	7/200/2/26	7/300/2/26	7/300/2/26	7/300/2/26	7/200/2/26	7/300/2/26	7/300/2/26	7/300/2/26
		Choice 2 OH	3/1100/1/28	5/700/4/0	5/600/4/0	5/700/4/0	3/1200/1/25	5/700/4/0	5/600/4/0	5/700/4/0
Sikkim	Mangan (N)	Choice 1 OH	7/300/2/17	7/400/2/17	7/300/2/19	7/400/2/19	7/300/2/19	7/400/2/19	7/300/2/19	7/400/2/19
		Choice 2 OH	5/800/3/0	5/1000/4/0	5/1000/3/0	5/1000/4/0	5/600/4/0	5/1000/4/0	5/500/6/0	5/800/5/0
	Gangtok (E)	Choice 1 OH	7/300/2/19	7/400/2/19	7/300/2/19	7/400/2/19	7/300/2/19	7/400/2/19	7/300/2/19	7/400/2/19
		Choice 2 OH	5/600/4/0	5/1000/4/0	5/700/4/0	5/1000/4/0	5/600/4/0	5/1000/4/0	5/700/4/0	5/1000/4/0
	Gezingo (W)	Choice 1 OH	7/300/2/22	7/400/2/19	7/300/2/19	7/400/2/19	7/300/2/19	7/400/2/19	7/300/2/19	7/400/2/19
		Choice 2 OH	5/600/4/0	5/1000/4/0	5/700/4/0	5/1000/4/0	5/600/4/0	5/1000/4/0	5/700/4/0	5/1000/4/0
	Namchi (S)	Choice 1 OH	7/300/2/22	7/400/2/19	7/300/2/19	7/400/2/19	7/300/2/19	7/400/2/19	7/300/2/19	7/400/2/19
		Choice 2 OH	5/800/3/0	5/1000/4/0	5/700/4/0	5/1000/4/0	5/800/3/0	5/1000/4/0	5/700/4/0	5/1000/4/0
Tamil Nadu	Tiruchirappalli (C)	Choice 1 OH	7/300/2/26	7/300/2/19	7/300/2/19	7/300/2/19	7/300/2/19	7/300/2/19	7/200/2/26	7/300/2/26
		Choice 2 OH	5/700/3/0	5/700/6/0	5/800/5/0	5/600/4/0	5/700/3/0	5/700/6/0	5/800/5/0	5/600/4/0
	Tiruvannamalai (N)	Choice 1 OH	7/300/2/19	7/400/2/17	7/400/2/17	7/300/2/17	7/300/2/17	7/400/2/17	7/400/2/17	7/300/2/17
		Choice 2 OH	5/1100/2/0	5/1100/4/0	5/1000/4/0	5/600/4/0	5/1100/2/0	5/1100/4/0	5/1000/4/0	5/600/4/0
	Thanjavur (E)	Choice 1 OH	7/300/2/17	7/400/2/17	7/400/2/17	7/300/2/17	7/300/2/17	7/400/2/17	7/400/2/17	7/300/2/17
		Choice 2 OH	5/700/3/0	5/700/6/0	5/1000/4/0	5/600/4/0	5/700/3/0	5/700/6/0	5/1000/4/0	5/600/4/0
	Erode (W)	Choice 1 OH	7/300/2/17	7/400/2/17	7/400/2/17	7/300/2/17	7/300/2/17	7/400/2/17	7/400/2/17	7/300/2/17
		Choice 2 OH	3/1200/1/32	5/700/6/0	5/1000/4/0	5/600/4/0	3/1200/1/32	5/700/6/0	5/1000/4/0	5/600/4/0
	Virudunagar (S)	Choice 1 OH	7/300/2/17	7/400/2/17	7/400/2/17	7/300/2/22	7/300/2/22	7/400/2/19	7/400/2/19	7/300/2/22
		Choice 2 OH	3/1200/1/30	5/1000/4/0	5/1000/4/0	5/500/5/0	3/1200/1/30	5/800/5/0	5/800/5/0	5/500/5/0
Telangana	Hyderabad (C)	Choice 1 OH	7/300/2/22	7/500/2/15	7/400/2/16	7/300/2/16	7/300/2/20	7/500/2/15	7/400/2/17	7/300/2/17
		Choice 2 OH	5/900/3/0	5/900/6/0	5/800/6/0	3/1200/1/31	5/900/3/0	5/900/6/0	5/800/6/0	3/1200/1/31
	Jagtial (N)	Choice 1 OH	7/300/2/18	7/500/2/14	7/500/2/14	7/300/2/14	7/300/2/23	7/500/2/14	7/500/2/14	7/300/2/14
		Choice 2 OH	5/600/5/0	5/1200/5/0	5/1000/5/0	3/1200/1/32	5/500/6/0	5/1000/6/0	5/1000/5/0	3/1200/1/32
	Warangal (E)	Choice 1 OH	7/300/2/24	7/500/2/15	7/500/2/15	7/300/2/15	7/300/2/20	7/500/2/15	7/500/2/15	7/300/2/15
		Choice 2 OH	5/700/4/0	5/900/6/0	5/1000/5/0	3/1200/1/32	5/700/4/0	5/900/6/0	5/1000/5/0	3/1200/1/32
	Medak (W)	Choice 1 OH	7/300/2/22	7/500/2/15	7/400/2/15	7/300/2/15	7/300/2/25	7/500/2/15	7/400/2/15	7/300/2/15
		Choice 2 OH	5/700/4/0	5/900/6/0	5/800/6/0	3/1200/1/32	5/700/4/0	5/900/6/0	5/800/6/0	3/1200/1/32
	Nalgonda (S)	Choice 1 OH	7/300/2/26	7/500/2/15	7/400/2/17	7/300/2/17	7/300/2/20	7/500/2/15	7/400/2/17	7/300/2/17
		Choice 2 OH	5/900/3/0	5/900/6/0	5/800/6/0	5/1100/2/0	5/900/3/0	5/900/6/0	5/800/6/0	5/1100/2/0
Tripura	Gomati (C)	Choice 1 OH	7/300/2/19	7/300/2/14	7/300/2/23	7/500/2/14	7/500/2/14	7/300/2/14	7/300/2/24	7/500/2/15
		Choice 2 OH	3/1200/1/30	5/800/4/0	5/500/5/0	5/800/4/0	5/700/3/0	5/800/4/0	5/500/5/0	5/800/4/0
	Dharmanagar (N)	Choice 1 OH	7/300/2/22	7/400/2/22	7/300/2/22	7/400/2/22	7/300/2/22	7/400/2/22	7/300/2/22	7/400/2/22
		Choice 2 OH	3/1200/1/30	5/1100/3/0	5/900/3/0	5/1100/3/0	3/1200/1/32	5/1100/3/0	5/900/3/0	5/1100/3/0
	Ambassa (E)	Choice 1 OH	7/300/2/22	7/400/2/22	7/300/2/22	7/400/2/22	7/300/2/22	7/400/2/22	7/300/2/22	7/400/2/22
		Choice 2 OH	5/700/3/0	5/1100/3/0	5/900/3/0	5/1100/3/0	5/700/3/0	5/1100/3/0	5/900/3/0	5/1100/3/0
	Agartala (W)	Choice 1 OH	7/300/2/17	7/400/2/17	7/300/2/24	7/400/2/22	7/300/2/22	7/400/2/22	7/300/2/22	7/400/2/22
		Choice 2 OH	5/700/3/0	5/800/4/0	5/500/5/0	5/800/4/0	5/700/3/0	5/800/4/0	5/500/5/0	5/800/4/0
	Belonia (S)	Choice 1 OH	7/300/2/22	7/400/2/22	7/300/2/22	7/400/2/22	7/300/2/22	7/400/2/22	7/300/2/22	7/400/2/22
		Choice 2 OH	3/1200/1/32	5/800/4/0	5/500/5/0	5/800/4/0	3/1200/1/29	5/800/4/0	5/500/5/0	5/800/4/0
Uttarakhand	Almora (C)	Choice 1 OH	7/500/2/14	7/900/2/7	7/800/2/8	7/300/2/25	7/500/2/14	7/900/2/7	7/800/2/8	7/300/2/26
		Choice 2 OH	5/1200/5/0	0/0/0/0	0/0/0/0	5/900/3/0	5/1000/6/0	0/0/0/0	0/0/0/0	5/900/3/0
	Chamoli (N)	Choice 1 OH	7/600/2/12	7/1000/2/7	7/800/2/8	7/300/2/22	7/600/2/12	7/1000/2/7	7/800/2/8	7/300/2/25
		Choice 2 OH	5/1100/6/0	0/0/0/0	0/0/0/0	5/700/4/0	5/1100/6/0	0/0/0/0	0/0/0/0	5/700/4/0
	Pithoragarh (E)	Choice 1 OH	7/500/2/14	7/900/2/7	7/800/2/8	7/300/2/21	7/500/2/14	7/900/2/7	7/800/2/8	7/300/2/24
		Choice 2 OH	5/1000/6/0	0/0/0/0	0/0/0/0	5/900/3/0	5/1000/6/0	0/0/0/0	0/0/0/0	5/900/3/0
	Dehra Dun (W)	Choice 1 OH	7/600/2/12	7/900/2/7	7/800/2/8	7/300/2/26	7/600/2/12	7/900/2/7	7/800/2/8	7/300/2/20
		Choice 2 OH	5/1100/6/0	0/0/0/0	0/0/0/0	5/700/4/0	5/1100/6/0	0/0/0/0	0/0/0/0	5/700/4/0
	Nainital (S)	Choice 1 OH	7/500/2/14	7/900/2/7	7/800/2/8	7/300/2/26	7/500/2/14	7/900/2/7	7/800/2/8	7/300/2/26
		Choice 2 OH	5/1200/5/0	0/0/0/0	0/0/0/0	5/900/3/0	5/1200/5/0	0/0/0/0	0/0/0/0	5/900/3/0
West Bengal	Berhampur (C)	Choice 1 OH	7/200/2/39	7/300/2/22	7/600/2/12	7/1000/2/7	7/800/2/8	7/300/2/25	7/500/2/14	7/900/2/7
		Choice 2 OH	3/1100/1/29	5/700/4/0	5/600/4/0	5/700/4/0	3/1200/1/29	5/700/4/0	5/600/4/0	5/700/4/0
	Jalpaiguri (N)	Choice 1 OH	7/300/2/26	7/300/2/22	7/300/2/22	7/300/2/22	7/300/2/22	7/300/2/22	7/300/2/22	7/300/2/22
		Choice 2 OH	5/600/4/0	5/900/4/0	5/700/4/0	5/900/4/0	5/600/4/0	5/900/4/0	5/700/4/0	5/900/4/0
	Kolkata (E)	Choice 1 OH	7/300/2/22	7/400/2/22	7/300/2/22	7/400/2/22	7/300/2/22	7/400/2/22	7/300/2/22	7/400/2/22
		Choice 2 OH	3/1200/1/32	5/800/4/0	5/500/5/0	5/800/4/0	3/1200/1/30	5/800/4/0	5/500/5/0	5/800/4/0
	Puruliya (W)	Choice 1 OH	7/300/2/22	7/400/2/22	7/300/2/22	7/400/2/22	7/300/2/22	7/400/2/22	7/300/2/22	7/400/2/22
		Choice 2 OH	3/1200/1/30	5/800/4/0	5/500/5/0	5/800/4/0	3/1200/1/30	5/800/4/0	5/500/5/0	5/800/4/0
	Tamluk (S)	Choice 1 OH	7/300/2/22	7/400/2/22	7/300/2/22	7/300/2/22	7/300/2/22	7/400/2/22	7/300/2/22	7/400/2/22
		Choice 2 OH	3/1200/1/32	5/800/4/0	5/600/4/0	5/800/4/0	3/1200/1/31	5/800/4/0	5/600/4/0	5/800/4/0

In Table 2 for certain cities and orientations, the result shown is '0/0/0/0', which means that no results are possible for that specific orientation for the selected location, which adhere to the shading device depth constraints specified in the algorithm. For the window orientations where the results are '0/0/0/0', has a design implication that for that space inside a building windows should not be provided for those wall orientations during the specified hours and if necessary then there should be a provision of a buffer space or a portico which can shade the window. Hence, an optimum shading strategy for a window of standard dimensions (1200mm*900mm) has been suggested for the selected locations in all cardinal and sub cardinal directions for most of the cases.

Limitations of the study are that an optimum and the next-best solution have been provided only for a window of standard dimensions (1200mm*900mm). For other window dimensions, sub-optimal solutions that provide functional shading device design can be derived from the results.

VI. CONCLUSION

The design of shading devices should be location and orientation specific to get the optimum benefit and tradeoff between first cost and operational energy cost. Use of horizontal inclined louvers (with two louvers) is the best strategy for all locations because it prevents direct radiation to enter a space or building while keeping the cost minimum. Horizontal louvers without any inclination and one inclined horizontal overhang are the next-best suggested shading device strategies. The Architects and designers can incorporate the results presented in the study to provide shading device strategies for windows in building design. A universal solution or a one size fits all approach for the type and characteristics of shading device that is used in standard practice cannot work for every space or building and will depend on the location and orientation. This gap has been covered by making the results location and orientation specific with shading device characteristics like the angle of inclination of the overhang/louvers, the number of louvers and the overhang/louver depth being defined explicitly for all cases. The results from this paper can also be incorporated into the Indian building codes to provide the architects and designers with a much more precise and location specific shading strategy. Further studies can explore how the different shading strategies affect the natural lighting inside spaces in a building. The shading strategies will also affect the overall carbon emission of a building by changing the heating and cooling loads.

VII. REFERENCES

[1] United Nations, The 17 Goals - Sustainable Development, Retrieved from https://sdgs.un.org/goals.

[2] K. Iwamura, Summary Of Architecture Guide to the UN 17 Sustainable Development Goals, UIA Commission on SDGs & JIA Editing Committee of SDGs, 2019, p. 7.

[3] Sustainable Development Goals, Goal 3:Ensure healthy lives and promote well-being for all at all ages, Retrieved from https://www.un.org/sustainabledevelopment/health/.

[4] Sustainable Development Goals, Goal 7: Ensure access to affordable, reliable, sustainable and modern energy, Retrieved from https://www.un.org/sustainabledevelopment/energy/.

[5] Sustainable Development Goals, Goal 9: Build resilient infrastructure, promote sustainable industrialization and foster innovation, Retrieved from https://www.un.org/sustainabledevelopment/infrastructure-industrialization/.

[6] IBEF: Growth of Construction Equipment Industry in India – Infographic, June 1 2021, Retrieved from https://www.ibef.org/industry/infrastructure-sector-india/infographic.

[7] BEE- Energy Conservation Building Code (ECBC) 2017, Bureau of Energy Efficiency, Ministry of Power, Govt. of India.

[8] SP 41 (1987): Handbook on Functional Requirements of Buildings (Other than Industrial Buildings), Bureau of Indian Standards, New Delhi.

[9] G. Evola, F. Gullo and L. Marletta, "The role of shading devices to improve thermal and visual comfort in existing glazed buildings", Energy Procedia, vol. 134, October 2017, pp. 346-355.

[10] Don Prowler, WBDG: Sun Control And Shading Devices, 2016, Retrieved from https://www.wbdg.org/resources/sun-control-and-shading-devices.

[11] S. Altomonte, "Daylight and the Occupant: Visual and physio-psychological well-being in built environments", PLEA2009 - 26th Conference on Passive and Low Energy Architecture, Quebec City, Canada, June 2009, pp. 22-24.

[12] W. Osterhaus, "Discomfort glare assessment and prevention for daylight applications in office environments", Solar Energy, August 2005, vol. 79, pp. 140-158.

[13] National Building Code of India 2016 volume 2 (NBC -2016), Bureau of Indian Standards, New Delhi.

[14] A. K. Yener, "A method of obtaining visual comfort using _xed shading devices in rooms", Building and Environment, 1999, vol. 23, pp. 285-291.

[15] M. Manzen, "Genetic optimization of external fixed shading devices", Energy and Buildings, 2014, vol. 72, pp. 431–440.

[16] K. S. Lee, K. Han and J. Lee, "The Impact of Shading Type and Azimuth Orientation on the Daylighting in a Classroom – Focusing on Effectiveness of Façade Shading, Comparing the Results of DA and UDI", Energies, 2017, vol. 10, pp. 1-20.

[17] A. Kirimtat, B. Koyunbaba, I. Chatzikonstantinou and S. Sariyildiz, "Review of simulation modeling for shading devices in buildings", Renewable and Sustainable Energy Reviews, 2016, vol. 53, pp. 23–49.

[18] Maps of India: Indian States and Union Territories, Retrieved from https://www.mapsofindia.com/states/

[19] S. V. Szokolay, "Solar Geometry", PLEA International, Department of Architecture, The University of Queensland, Brisbane, 2007, pp.22-23

[20] M. Bhatnagar, J. Mathur and V. Garg, "Development of reference building models for India", Journal of Building Engineering, vol. 21, 2019, pp. 267–270.

[21] D. Chakrabarti, "Indian Anthropometric Dimensions For Ergonomic Design Practice", National Institude of Design, 1997, pp. 35-38.

Cryptocurrency Mining: As a Green Energy Drive

Nazenin Gure
Department of Mechanical Engineering
Faculty of Engineering and Architecture
Beykent University)
Istanbul, Turkey
nazeningure@beykent.edu.tr
https://orcid.org/0000-0001-7903-7655

Abstract

In this paper, a new insight of cryptocurrency mining usage related to renewables, reuse of excess heat from mining rigs into heating, drying, energy generation and growing crops in greenhouses as well as defining green-coins are presented. Finally, possible energy harvesting case for boosting mining energy economy and efficiency is suggested for the first time in literature and open web.

As the effects of climate change are increasing, environmental awareness, actions towards energy economy and emission reduction are increasing. Meanwhile, unless renewables are subsidized by government, collaborative projects and feed-in-tariff, implementation of renewable power plants is facing difficulties due to long period of redemption. Cryptocurrency mining is commonly indicated as giant source of energy consumption and one of the greatest sources of resulted greenhouse-gas emissions due to traceable structure based on transparency of blockchain. However, cheap energy is the fundamental step for mining to cover mining costs and generate profit. The chronological shift to receive cheap energy started from: (i) Locating in cold regions to both cool mining hardware and receive cheaper electricity; (ii) to locating in hot regions with solar power plants to achieve self-sustaining energy generating mining farms where the cooling energy is also covered and profit upon mining. Meanwhile, another trend is that (iii) localization of mining farms near renewable power plants. The latter two (ii and iii) opened a new financially sustainable model for renewable energy. Cryptocurrency mining reduced the period of redemption of renewables from 5 years to a year as well as tripling the profit. Additionally, the option (i) is also evolved into: (1) mining rig heaters for households (brands such as Hotmine and Qarnot), (2) novel bio-generation plant, (3) heating greenhouse crops like strawberries and tomatoes ("cryptomatoes") and (4) Canadian well ventilation together with heating greenhouses. Novel bio-generator (2) consumes biofuel, has trigeneration that feeds mining, adsorption unit upon waste-heat and heat pump. Eventually, energy distribution is looped to feed mining, heat the building, cool mining rigs; and mining results in financial profit stem from mining reward, transaction fees and minimized maintenance cost due to efficient cooling. UnitedCorp's BlockchainDome (4) collect rising waste-heat and feed greenhouses via well ventilation. Rejected heat is then exchanged to subsoil which is chilled underground and pumped to cool the mining rigs without the need of fan or air conditioning.

While the green-coin definition started as a metaphor due to cryptocurrency mining empowered by renewable energy sources, green-crop producing sustainable mining models are introducing additional layer for the real meaning of green.

Pioneer application suggestions of this study are: (A) Thermo-electric generator (TEG) implementation on mining hardware (application-specific integrated circuit chips, ASICs) as energy harvesting from cryptocurrency mining; and finally, (B) Desalination of salt water from the waste-heat of mining. Reuse of waste-heat from cryptocurrency mining for desalination and greenhouse heating together would also provide irrigation of the crops in greenhouse. Therefore, fully sustainable profit-making green mining model is projected.

Keywords: *Blockchain, Cryptocurrency Mining, Mining Rigs, ASICs, Renewable Cryptocurrency Mining, Green-Coins, Climate Change, Green Mining, Energy Harvesting, Energy Harvesting from Mining*

IEECP'21, July 29-30, 2021, Silicon Valley, San Francisco, CA – USA

DAI : *https://sci-index.com/DAI/2021.99101/IEECP/15031614*